AFWAL-TR-80-4131
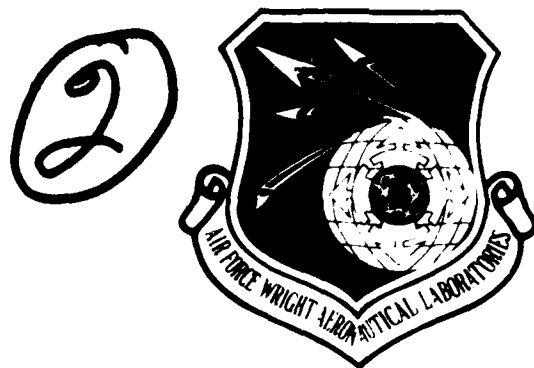
AD A100642

CRACK GROWTH BEHAVIOR OF ALLOY IN 100 UNDER SUSTAINED LOAD AT 732°C (1350°F)

Robert C. Donath

Metals Behavior Branch
Metals and Ceramics Division

April 1981

TECHNICAL REPORT AFWAL-TR-80-4131

Final Report for Period July 1977 - June 1980

DTC FILE COPY

MATERIALS LABORATORY
AIR FORCE WRIGHT AERONAUTICAL LABORATORIES
AIR FORCE SYSTEMS COMMAND
WRIGHT-PATTERSON AIR FORCE BASE, OHIO 45433

NOTICE

When Government drawings, specifications, or other data are used for any purpose other than in connection with a definitely related Government procurement operation, the United States Government thereby incurs no responsibility nor any obligation whatsoever; and the fact that the government may have formulated, furnished, or in any way supplied the said drawings, specifications, or other data, is not to be regarded by implication or otherwise as in any manner licensing the holder or any other person or corporation, or conveying any rights or permission to manufacture use, or sell any patented invention that may in any way be related thereto.

This report has been reviewed by the Office of Public Affairs (ASD/PA) and is releasable to the National Technical Information Service (NTIS). At NTIS, it will be available to the general public, including foreign nations.

This technical report has been reviewed and is approved for publication.

R. C. DONATH, Project Engineer
Metals Behavior Branch
Metals and Ceramics Division

WALTER H. REIMANN, Acting Chief
Metals Behavior Branch
Metals and Ceramics Division

REPORT DOCUMENTATION PAGE		READ INSTRUCTIONS BEFORE COMPLETING FORM
1. REPORT NUMBER AFWAL-TR-80-4131	2. GOVT ACCESSION NO. AD-A100642	3. RECIPIENT'S CATALOG NUMBER
4. TITLE (and Subtitle) CRACK GROWTH BEHAVIOR OF ALLOY IN-100 UNDER SUSTAINED LOAD AT 732°C (1350°F)		5. TYPE OF REPORT & PERIOD COVERED July 1977-June 1980
		6. PERFORMING ORG. REPORT NUMBER
7. AUTHOR(s) Robert C. Donath		8. CONTRACT OR GRANT NUMBER(s)
9. PERFORMING ORGANIZATION NAME AND ADDRESS Air Force Wright Aeronautical Laboratories MLLN Wright-Patterson AFB, OH 45433		10. PROGRAM ELEMENT, PROJECT, TASK AREA & WORK UNIT NUMBERS 2307P102
11. CONTROLLING OFFICE NAME AND ADDRESS Materials Laboratory Air Force Wright Aeronautical Laboratories Wright-Patterson Air Force Base, Ohio 45433		12. REPORT DATE April 1981
		13. NUMBER OF PAGES 343
14. MONITORING AGENCY NAME & ADDRESS(if different from Controlling Office)		15. SECURITY CLASS. (of this report) UNCLASSIFIED
		15a. DECLASSIFICATION DOWNGRADING SCHEDULE

16. DISTRIBUTION STATEMENT (of this Report)

Approved for public release, distribution unlimited.

17. DISTRIBUTION STATEMENT (of the abstract entered in Block 20, if different from Report)

18. SUPPLEMENTARY NOTES

19. KEY WORDS (Continue on reverse side if necessary and identify by block number)

Creep
Crack growth
Elevated temperature
Fracture mechanics

20. ABSTRACT (Continue on reverse side if necessary and identify by block number)

Sustained load crack growth in IN-100 at 1350°F (732°C) is studied using two specimen geometries, a standard compact tension specimen and a radially cracked ring loaded in tension. The effects of specimen thickness on the growth rate are investigated covering a range from 0.22 inch (5.6mm) to 0.72 inch (18.3mm) in thickness. Only the thinnest specimens show a crack growth rate which is lower than that obtained from all of the other thickness specimens. Stress intensity factor, net section stress, load line displacement rate, and the C*-integral are investigated as possible crack growth rate correlating parameters. In addition,

DD FORM 1473 EDITION OF 1 NOV 65 IS OBSOLETE
1 JAN 73

a crack driving force function, $\mathcal{G}$, is developed for a linear elastic creeping solid which represents the excess of energy available for creating new crack surfaces. In particular, the crack growth rate is observed to decrease from an initially higher value to a "steady state" rate which depends on the stress intensity factor, net section stress or load line displacement rate. In the correlation of the stress intensity factor, the magnitude of this initial growth rate is about double the "steady state: creep crack growth rate.

The concept of an "effective" crack length determined from specimen compliance measurements is introduced as a measure of crack length for severely tunneled crack front geometries. Neither net section stress, load line displacement rate nor C* are found to be acceptable as crack growth parameters based on data from both test geometries. Although the stress intensity factor, K, provides fair correlation, the phenomenology of creep crack growth prevents its description adequately with only a single parameter. The crack driving force appears to correlate creep crack growth for the two geometries based on a limited number of tests. Results show that the inelastic energy which goes into the deforming material all goes into driving the crack.

FOREWORD

iii

TABLE OF CONTENTS

TABLE OF CONTENTS (Concluded)

LIST OF TABLES

LIST OF ILLUSTRATIONS

LIST OF ILLUSTRATIONS (Continued)

LIST OF ILLUSTRATIONS (Continued)

LIST OF ILLUSTRATIONS (Continued)

LIST OF ILLUSTRATIONS (Continued)

LIST OF ILLUSTRATIONS (Continued)

LIST OF ILLUSTRATIONS (Continued)

LIST OF ILLUSTRATIONS (Continued)

LIST OF ILLUSTRATIONS (Continued)

LIST OF ILLUSTRATIONS (Concluded)

NOMENCLATURE

a, a_i, a_j, a_0	=	crack length, ith, jth and initial value, respectively
$\bar{a}$	=	effective crack length
ASTM	=	American Society for Testing Materials
B	=	specimen thickness
C, C_i, C_j, C_0	=	compliance, ith, jth and initial value, respectively
C^*	=	C*-integral
COD	=	crack opening displacement
CT	=	compact tension
e_{ij}	=	strain components
E	=	Young's modulus of elasticity
E'	=	elastic part of strain energy of deformation
E''	=	plastic part of strain energy of deformation
G	=	shear modulus
$\mathscr{G}$	=	strain energy release rate
$\overline{\mathscr{G}}$	=	crack driving force
$\widetilde{\mathscr{G}}$	=	strain energy release rate for fracture toughness
$\widetilde{\mathscr{G}}_c$	=	critical value of $\widetilde{\mathscr{G}}$ for fracture toughness
$\mathscr{G}_I$	=	strain energy release rate for Mode I crack extension
J	=	J-integral
K	=	stress intensity factor
K_I	=	stress intensity factor for Mode I cracking
K_{Ic}	=	plane strain fracture toughness
LEFM	=	linear elastic fracture mechanics
P	=	load
R_i, R_0	=	inner, outer ring specimen radii

NOMENCLATURE (Concluded)

t	=	time
T_i	=	components of the traction vector
T'	=	work of the external forces on a body
u_i	=	components of the displacement vector
U	=	potential energy
W	=	specimen width
$W(e_{mn})$	=	strain energy density
$W*(e_{mn})$	=	strain energy density rate
$\bar{W}$	=	stored nonlinear elastic strain energy
α	=	crack length per unit width, a/W, for the compact tension specimen and $a/(R_o-R_i)$ for the ring specimen
$\hat{\alpha}$	=	specimen geometry-dependent coefficient
γ	=	unit crack surface energy
Γ	=	path around a crack tip in the counterclockwise sense
$\bar{\Gamma}$	=	total crack surface energy
$\delta, \delta_i, \delta_j, \delta_o$	=	displacement, ith, jth and initial value, respectively
δ_{el}, δ_{in}	=	elastic and inelastic deformation, respectively
$\varepsilon, \varepsilon_c, \varepsilon_e, \varepsilon_o$	=	strain, creep, elastic and reference, respectively
$\sigma, \sigma_c, \sigma_e, \sigma_o$	=	stress, creep, elastic and reference, respectively
σ_{ij}	=	stress components
σ_K	=	rupture stress
σ_{net}	=	net section stress
σ_y	=	yield stress in tension
ν	=	Poisson's ratio

SECTION I

INTRODUCTION

In recent years, requirements in the use of high-strength nickel-based superalloys in turbojet engine applications has created the need for a clearer understanding of fracture behavior in these materials. Operating environments at higher and higher temperatures have become increasingly hostile in the turbine end of aircraft engines. This places in question the direct applicability of linear elastic fracture mechanics as a methodology for predicting life performance in aircraft engines. Complexities arise in the determination of the material fracture toughness as well as in the characterization of crack growth at these temperatures.

Recent advances in understanding the crack growth behavior of turbine disc alloys have emphasized cyclic crack growth (Reference 1), cycle-dependent growth with hold times at constant load (Reference 2) or with peak overloads (Reference 3). The applicability of linear elastic fracture mechanics to high temperature crack growth has been investigated (References 3, 4, 5) within the limitations on time-dependent behavior imposed by specimen geometry and loading conditions. One of the features of the load spectrum which is seen by turbine disc materials is the existence of sustained load for various periods of time. Therefore, it is important to have an understanding of the growth of cracks under a sustained load in order to be able to accurately predict the crack growth behavior in these materials.

In a survey of quasi-static crack growth in metals at elevated temperatures, Fu showed (Reference 6) that slow stable crack growth is observed at stress intensities well below a material's fracture toughness, K_{1c}. Cracks in the stable growth region may grow not only for conditions of load reversal, but also as a result of sustained load combined with exposure to high temperatures and corrosive environments. The interaction between fatigue and creep crack growth is found to be highly complex and is frequency-dependent. A detailed account of the empirical results of creep crack growth and it's microscopic and macroscopic descriptions are given in (Reference 6).

The present study was undertaken in an attempt to correlate sustained load crack growth behavior with one or more fracture mechanics parameters using a typical aircraft engine material at a temperature considered to be the maximum design value. The material chosen was IN-100, a nickel-based superalloy used as a turbine disc material in the F-100 engine. Toward this end, two specific aspects play an important rôle. One is the effect of creep strain on crack growth behavior under sustained load; the second is the possible effect of specimen thickness and the subsequent triaxial stress field on the growth of cracks under sustained load conditions. The effect of temperature on creep crack growth behavior in Inconel 718 was studied by Floreen (Reference 7). Mills (Reference 8) characterized the decrease of fracture toughness with increasing temperature in alloy A-286, an iron-based superalloy using compact tension specimens. Thickness is also a consideration in the phenomenon of crack growth in the stable region defined by plane strain fracture toughness. Green and Knott (Reference 9) examined the effect of a range of specimen thicknesses on the critical value of crack opening displacement in a mild steel. They found that for a given constant applied load, the crack opening displacement below which failure will not occur is inversely proportional to the thickness for specimen width greater than 10 mm, and that crack growth can occur above the crack opening displacement (COD) limiting values.

In this study, the characterization of crack growth rate is based on the method of compliance. In this approach, the Hookian response of the test specimen to incremental load measured with respect to displacement in the line of load application forms the basis for establishing an "effective" crack length as a function of test time. The use of this technique coupled with the procedure of heat tinting fracture surfaces of tests with interruptions in the region of stable crack growth allows a means whereby a more rational description of the extent of crack tunneling may be achieved under conditions of sustained load. The procedure is readily applicable to related studies of crack growth involving cyclic loading interspersed with peak or hold-time loads.

The results show that any fracture mechanics parameter that is related to crack growth as a monotonically increasing function can be shown to correlate with crack growth rate. However, the "goodness" of suitability and it's application to life prediction is relatively dependent on the limitations of the testing procedure and on inherent scatter which the test results invariably demonstrate. It is felt that these restrictions inherent in the feasibility of making accurate experimental measurements, particularly of compliance for those materials which are of the family of high strength nickel-based alloys, is too severely limiting to adequately demonstrate the superiority of any one of the fracture mechanics parameters selected for study in this research. Within the range of thicknesses tested, it is shown that only the thinnest specimens consistently demonstrate plane stress thickness effects within the range of experimental scatter.

SECTION II

THEORETICAL CONSIDERATIONS

1. INTRODUCTION

The demand of a more fundamental and quantitative design procedure for advanced structures, such as modern gas turbine engines, in the presence of crack-like defects at elevated temperature has led to recent thrusts in applying fracture mechanics concepts and techniques to characterize crack growth at extreme temperature and loading conditions. McEvily and Wells (Reference 10) first reviewed the application of these concepts to safe design in the creep regime. Much experimental work and some theoretical analysis followed in studying the three important basic aspects of fracture at elevated temperature: (1) the definition and the determination of fracture toughness at high temperatures, (2) the characterization of crack growth by any particular fracture parameter, and (3) the roles of creep and environment, such as oxidation, in the determination of fatigue crack propagation. A review of the literature on the latter two aspects can be found in a recent article by Fu (Reference 6).

In what follows, basic concepts in linear elastic fracture mechanics and their limitations in application are first discussed and then the extension and application of these concepts to elevated temperature conditions are described.

2. LINEAR ELASTIC FRACTURE MECHANICS

Fracture mechanics provides the basis for a rational design in terms of a single parameter that characterizes the highly stressed and complexly deformed crack tip region. There are four major variants of this parameter: the strain energy release rate, $\mathscr{G}$, the stress intensity factor, K, the crack tip opening displacement, COD, and the path independent integral, J. Each of these parameters is related to another in a definitive manner within the context of linear elasticity:

$$\mathscr{G} = J = \frac{(1-\nu^2)K^2}{E} = \frac{(1-\nu^2)\sigma_y(COD)}{2} \tag{1}$$

where E, ν, and σ_y are Young's modulus, Poisson's ratio and yield stress in tension, respectively. For the plane stress case, the quantity $(1-\nu^2)$ must be replaced by unity.

a. Strain Energy Release Rate, $\mathscr{G}$

Employing the principle of conservation of energy, and the solution for an elliptical crack in an infinite plate, Griffith (Reference 11) found the energy required for creating new surfaces during crack extension as

$$\mathscr{G} = \frac{(1-\nu^2)\pi\sigma^2 a}{E} \tag{2}$$

where σ is applied stress and 2a is the length of the crack. Irwin (Reference 12) and Orowan (Reference 13) later extended this concept to non-brittle materials.

b. The Stress Intensity Factor, K

Irwin (Reference 14) computed the stresses in a center cracked infinite plate by employing the Westergaard stress functions and showed the dominant term that describes the "near-tip" field is characterized by a coefficient that depends only upon loading and crack length. This coefficient is called the stress intensity factor. Irwin's initial derivation was confined to crack openings in the direction perpendicular to the crack faces (Mode I). He later extended the idea to crack openings in the directions parallel to the crack surfaces (Modes II and III).

Stress intensity factors can be computed by first finding the elasticity solution of cracked structural members. For members of finite size, approximate numerical methods have been employed such as by a boundary collocation method (Reference 15), a boundary integral equation method (Reference 16), a finite element method (References 17, 18), and by the method of lines (References 19, 20). The stress intensity factor usually takes the form

$$K = \hat{\alpha}\sigma\sqrt{\pi a} \tag{3}$$

where σ and a are applied stress and crack length respectively, and $\hat{\alpha}$ is a function of the specimen geometry.

5

Although K was initially developed and used as a parameter which controls the onset of unstable crack growth, it was subsequently extended by Paris (Reference 21) and others (References 22, 23) to characterize the growth rate of cracks under cyclic loading, even though the mechanisms of unstable crack growth and fatigue crack propagation are different, and considering that there is no fundamental reason why K should be able to predict fatigue crack growth rate (Reference 24). Thus, it is not surprising that K can also be considered as a possible governing parameter for slow stable creep crack growth, even though the mechanisms here are different from either the case of unstable crack growth or fatigue crack growth.

Reidel (Reference 25) established that for a correlation to uniquely exist between the stress intensity factor and creep crack growth rates, conditions of small scale yielding are required as well as crack growth rates which are steady state. However, as Fu demonstrated (Reference 6), for conditions such as those mentioned above, where slow stable crack growth is occurring, $(K < K_{Ic})$, K may not be the appropriate parameter to include in a linear elastic fracture mechanics correlation with experimental data. Failure of K to correlate creep crack growth rate in certain circumstances (References 7, 26, 27) has led to the investigation of other parameters (References 26, 27, 28) which may better correlate the steady state crack growth rate. In addition to K, parameters which have been used include crack opening displacement (Reference 27), net section stress (Reference 29), the J-integral (References 4, 25), and the C*-integral (References 26, 28).

c. The Crack Opening Displacement, COD

Wells (Reference 30) first proposed the use of the crack face displacement at or near the crack tip as the measure of fracture potential. Irwin (Reference 14) and McClintock (Reference 31) pointed out that this is equivalent to an opening displacement and an average strain criterion in the case of small scale plasticity.

A vigorous analysis was performed by Burdekin and Stone (Reference 32), employing the Dugdale plastic strip yield model (Reference 33). They showed, for a crack of length 2a in an infinite plate under uniform biaxial stress, that the crack opening displacement is

$$COD = \frac{\pi \sigma^2 a}{E \sigma_y} \tag{4}$$

For the plane strain case, a triaxiality factor anywhere between 2 and 2.2 must be used to augment the value of σ_y.

d. The Path Independent Integral, J

The J-integral is defined (Reference 22) as a line integral around a path surrounding the crack tip for the two-dimensional case as

$$J = \int_\Gamma \left[W dx_2 - T_i \frac{\partial u_i}{\partial x_1} ds \right] \tag{5}$$

where x_1 and x_2 are Cartesian coordinates, W is the strain energy density, T_i are the components of the traction vector, u_i are the components of the displacement vector and Γ is any path around the crack tip in a counterclockwise sense. The strain energy density is given by

$$W = \int_0^{e_{mn}} \sigma_{ij} de_{ij} \tag{6}$$

If, and only if, the strain energy density can be expressed as a function of the strains, e, only, i.e.,

$$W(e_{mn}) = \int_0^{e_{mn}} \sigma_{ij} de_{ij} \tag{7}$$

then the integral is path independent. Thus, the J-integral as a path independent integral is applicable only for materials where the stresses are derivable from a strain energy density function as

$$\sigma_{ij} = \frac{\partial W}{\partial e_{ij}} \tag{8}$$

The J-integral is thus limited to nonlinear elastic materials, although the usage is commonly associated with elastic-plastic materials which obey the deformation theory of plasticity (Reference 34). The integral has no useful interpretation for actual materials. However, in Eshelby's (Reference 35) phraseology, "if we do not call the material's bluff by unloading", the integral can be used for these materials. If the assumptions of the J-integral are satisfied, then the integral can be interpreted as the energy release rate due to crack extension as

$$J = -\frac{dU}{da} \tag{9}$$

where U, the potential energy, is the total absorbed energy (the area under the load/load point displacement curve), and the calculation is made under the condition of constant load point displacement, δ.

3. MACROSCOPIC MODELING OF CREEP CRACK GROWTH

At elevated temperatures, metals commonly exhibit nonlinear time-dependent deformation. Under sustained uniaxial tensile loading, the strain in a smooth bar increases until rupture occurs. The time-dependent regime of crack growth propagation can be generalized by three distinct states. These are categorized as the primary, secondary, and tertiary stages of crack propagation in the creeping solid. After an initial instantaneous strain resulting from the initial application of a load, a material under constant load at elevated temperature often undergoes a period of transient response where the strain rate, $d\epsilon/dt$, decreases with time to a minimum steady state value that persists for a substantial portion of the total life. These two strain-time regimes are referred to as the transient (primary) and steady state (secondary) stages, respectively, of creep. Final failure occurs relatively soon after the initiation of tertiary creep, during which the creep rate increases. Although it has been commonly observed that creep crack propagation possesses these three distinct states, there has been no general agreement, with sometimes seemingly contradictory results, on the

characterization of the creep crack growth rate. There are available
empirical data supporting any one of the following predictions of the
creep crack growth rate:

$$\frac{da}{dt} = AK^{\alpha} \tag{10}$$

$$\frac{da}{dt} = B\sigma_n^{\beta} \tag{11}$$

$$\frac{da}{dt} = c(dy/dt)^{\gamma} \tag{12}$$

$$\frac{da}{dt} = D(C^{\star})^{\tau} \tag{13}$$

where K is the stress intensity factor, σ_n is either net section stress,
reference stress or skeletal stress, dy/dt is the load line crack opening
displacement rate, and C* is a line integral related to the rate of change
of potential energy release per unit crack advancement. Haigh (Reference 27)
reviewed previous work on the microscopic and macroscopic mechanisms of
creep crack growth and gave a table summarizing test results. Van Leeuwen
(Reference 36) presented a summary including some references to research
employing net section stress and the C*-integral as possible correlating
parameters for creep crack growth.

According to Nicholson (Reference 37) the exponent β in Equation 11
and n in the creep strain rate/stress relation

$$\dot{\epsilon} = \Gamma \sigma^n \tag{14}$$

should be equal for the same material at the same temperature while Taira
and Ohtani (Reference 38) disagreed. Based upon Townsend's work
(Reference 39), Williams and Price (Reference 40) indicated that metals
at elevated temperature can be classified as creep brittle (intergranular)
if p (or n) is less than 5, and creep ductile (transgranular) if p (or n)
is greater than 5.

9

Any macroscopic description of creep crack growth must identify a criterion for the initiation of crack growth and a mechanism of crack propagation after initiation, i.e., whether the crack propagates continuously or discontinuously and how the near-tip characterization changes as the crack advances. The validity of the result hinges largely on the modeling.

a. Barnby's Critical Strain Model

Assuming that the elastic strains are small compared to creep strains during steady state creep, Hoff's (Reference 41) mathematical analogy showed that creep rates are numerically equal to the elastic strains calculated for the purely elastic case, i.e.,

$$\frac{\dot{\epsilon}_c}{\dot{\epsilon}_o} = \frac{\dot{\epsilon}_e}{\dot{\epsilon}_o} = \frac{\dot{\epsilon}_e}{\dot{\epsilon}_o} = \frac{K}{\sigma_o (2\pi x)^{1/2}} \tag{15}$$

where the subscripts c, e and o refer to "creep", "elastic" and "reference" states, respectively. Barnby (References 42, 43) used the above relation and computed the creep stress near the crack tip as

$$\frac{\sigma_c}{\sigma_o} = \left(\frac{\dot{\epsilon}_c}{\dot{\epsilon}_o} \right)^{1/m} = \left(\frac{K'}{\sigma_o (2\pi x)^{1/2}} \right)^{1/m} \tag{16}$$

where Norton's creep law is used and K' is determined by satisfying the equilibrium conditions across the plane y = 0, the crack plane. For a center cracked plate of width 2W, crack length 2a and thickness B, the equilibrium condition requires that

$$P = B \int_0^{W-a} \sigma_c dx = B\sigma_o \int_0^{W-a} \left(\frac{K'}{\sigma_o (2\pi x)^{1/2}} \right)^{1/m} dx \tag{17}$$

and a simple manipulation gives

$$K' = \sigma_o (2\pi)^{1/2} \left(\frac{P}{B\sigma_o} \cdot \frac{2m-1}{2m} (W-a)^{-(2m-1)/m} \right)^m \tag{18}$$

It is of interest to note that for large m, say $m \geq 5$, $(2m-1)/2m \to 1$ and K' is related to the net section stress as

$$K' = \sigma_0 (2\pi)^{1/2} \left(\frac{\sigma_{net}}{\sigma_0} \right)^m \tag{19}$$

Due to the approximation used, Equation 19 becomes incorrect in units.

Barnby used a critical strain condition at a distance d_c, say the distance of closest creep void or grain boundary fissure, ahead of the main crack as the condition for crack advancement. Since

$$\frac{\dot{\varepsilon}_c}{\dot{\varepsilon}_0} = \frac{K'}{\sigma_0 (2\pi x)^{1/2}} \tag{20}$$

by his assumption, he scaled his crack growth rate to creep rate as

$$\frac{da}{dt} = \dot{\varepsilon}_c \left(\frac{x}{d_c} \right)^{1/2} \tag{21}$$

which is again incorrect in units. Inserting the value of K' he obtained

$$\frac{da}{dt} = \frac{\dot{\varepsilon}_0}{d_c^{1/2}} \left(\frac{\{P/B\sigma_0\}\{(2m-2)/2m\}}{(W-a)^{(2m-1)/2m}} \right)^m \tag{22}$$

In an attempt to relate his results to the crack growth rate in a linear elastic material, he defined a new parameter K" for which

$$P = \sigma_0 B \int_0^{W-a} \frac{K'' \, dx}{\sigma_0 (2\pi x)^{1/2}} \tag{23}$$

and forced K" = K' at m = 1. Thus he obtained

$$K/Y(a,W) = K''/N(a,W) \tag{24}$$

11

where $N(a,W)$ is obtained from $K'' = K'$ at $m = 1$. Finally, the crack growth rate was obtained as

$$\frac{da}{dt} = \{\varepsilon_0/\sigma_0 (2\pi d_c)^{1/2}\} K \frac{N(a,W)}{Y(a,W)} \quad , \quad m = 1 \tag{25}$$

His model predicts a faster crack growth in a material which creeps than a linear elastic model.

The approximate analysis used here applies only to the stress component directly ahead of the crack and normal to the crack plane. If damage is not localized, then the approximation is no good.

b. Critical Plastic Zone Size Model

Assuming that the damage zone ahead of the crack tip is a thin strip, To (Reference 44) used the plane stress analysis by Dugdale (Reference 33) where the size of the yield zone is

$$R = c_0 \{Sec[1/2\pi(\sigma/\sigma_y)]-1\} \tag{26}$$

and the yield zone is under uniform biaxial stress of magnitude σ_y, the uniaxial yield stress. The crack tip stresses are characterized by a time-independent analysis for the sake of simplicity.

He then introduced a time-dependent process through the use of Kachanov's (Reference 45) theory of creep rupture, i.e., through the use of the continuity equation

$$d\phi/dt = - c'(\sigma/\phi)^n \tag{27}$$

where c', n are material constants related to a uniaxial creep test and ϕ is the continuity parameter. For a perfect material $\phi = 1$ while for a ruptured material $\phi = 0$. The parameter n is in general less than the creep exponent and is equal to the inverse slope of a conventional log-log curve of stress against rupture life.

Integrating Equation 27 for constant stress, the rupture time is obtained as

$$t_R = T_K(\sigma_K/\sigma_y)^n \phi_0^{n+1} \tag{28}$$

where

σ_K = material rupture stress in the absence of a crack

T_K = rupture time corresponding to σ_K

ϕ_0 = regional continuity before the arrival of a crack with its associated plastic zone.

To then used a cumulative damage procedure to determine the initial continuity ϕ_0 before the arrival of the crack tip plastic zone. Let the half crack length at time t_n be c_n. At each time interval t_R the crack travels a distance equal to its plastic zone size. Note that the plastic zone size is a function of the current crack length and therefore it tends to become larger as the crack advances. Using this procedure, a first approximation to the crack growth rate was found to be

$$\frac{dc_n}{dt} = \frac{\ln \sec \frac{\pi}{2} \frac{\sigma}{\sigma_y} c_0}{q_0} \left(\frac{K}{K_0}\right)^2 \cdot \left[1 + \frac{2q_1 q_0}{\ln \sec \frac{\pi}{2} \frac{\sigma}{\sigma_0}} \ln \frac{K}{K_0} \right] \qquad (29)$$

where K and K_0 are the current and initial stress intensity factors and

$$q_0 = \sum_m (-1)^m \left[\frac{2(\sec \frac{\pi}{2} \frac{\sigma}{\sigma_y} + 1)}{\pi^2 (0.5) + \sum_{2 \le m' \le m} \left(\sec \frac{\pi}{2} \frac{\sigma}{\sigma_y}\right)^{m'-1}} \right]^{\eta m/2} \qquad (30)$$

$$q_1 = 0.5(\sigma/\sigma_y)^\eta \qquad (31)$$

$$t_i = T_K (\sigma_K/\sigma_y)^\eta \qquad (32)$$

To noted that his derived crack growth rate is of the power law form

$$\frac{dc_n}{dt} = A(K/K_0)^\eta \qquad (33)$$

13

AFWAL-TR-80-4131

and made a comparison with data obtained by Siverns and Price (Reference 46).
He showed a straight line on a log-log plot of dc/dt versus K/K_0.

If the second term in Equation 29 is taken into consideration,
a decrease in slope results as K increases or the crack extends. The
model does not include work hardening and hence does not admit a
singularity at the crack tip. Since both A and n in Equation 33 are
stress dependent, the implication here is that either the stress intensity
factor K is not a convenient parameter to use in crack growth rate
prediction or that the power law is not the proper function relation for
creep crack growth.

c. A Continuous Rupture Model

In this simplified model, the crack tip stress configuration is
characterized by a linear elastic solution (Reference 47). The crack tip
region is assumed to be in a uniaxial loading situation which is not
realistic. Purushothaman and Tien (Reference 47) estimated the crack
tip normal stress to be the same as given by Orowan and Irwin:

$$\sigma_y(x) = \sigma_t(a/\rho+x)^{1/2} \tag{34}$$

Taking a uniaxial stretching situation, the creep rate is calculated as

$$\dot{\epsilon}(x) = A\{\sigma_y(x)/E(T)\}^m \exp(-q_c/RT) \tag{35}$$

Using Equations 34 and 35 and an assumed empirical relation of creep rate
and rupture time as,

$$t_R = B\dot{\epsilon}^{-x} \tag{36}$$

The crack growth rate is derived as

$$\frac{da}{dt}\bigg|_{x=0} = \frac{2A\alpha}{\alpha m B} \cdot \rho^{1-\alpha m/2} (K/YE)^{\alpha m} \cdot \exp(-\alpha Q_c/RT) \tag{37}$$

14

where y is a geometrical factor and $K = Y\sigma_t(\pi a)^{1/2}$ and ρ is the crack tip radius. The derivation is straightforward. The functional relation between creep rate and temperature (Equation 35) is assumed to correlate with experimental observation. The model predicts continuous crack growth and does not account for any contribution to the rupture time that a point experiences before the arrival of the crack tip. The theory is therefore not complete. Furthermore, Van Leeuwen (Reference 48) found that the relation expressed in Equation 37 was unreliable for materials other than purely annealed metals.

d. A Critical C*-Integral Model

For a material that follows a creep law of the form

$$\dot{\varepsilon}/\varepsilon_0 = A(\sigma/\sigma_0)^n \tag{38}$$

in uniaxial tension, Goldman and Hutchinson (Reference 49) showed that there exists a singularity in strain rate at the crack tip whose amplitude is

$$\dot{K}_\varepsilon = (C^*/A\ \sigma_0 \varepsilon_0 \cdot I_n)^{n/n+1} \tag{39}$$

where I_n is a constant which is tabulated for a given range of n by Hutchinson (Reference 50) and C* is a line integral which was later used by Landes and Begley (Reference 28) to describe creep crack growth and is defined in Section II.3.f.

$$C^* = -\frac{d\dot{U}}{da} = \int_\Gamma \{W^*(\dot{\varepsilon}_{mn})dy - T_i \cdot \frac{\partial \dot{u}_i}{\partial x}ds\} \tag{40}$$

It can easily be shown that the C*-integral is equivalent to

$$C^* = A\ \sigma_0\ \varepsilon_0\ (\dot{K}_\varepsilon)^{(n+1)/n}\ I_n \tag{41}$$

$$= A\ \sigma_0\ \varepsilon_0\ \dot{K}_\sigma \dot{K}_\varepsilon\ I_n \tag{42}$$

15

It should be noted that Equations 39 and 40 apply only to steady state creep and are approximate solutions since the elastic strains are ignored (Reference 41). Nikbin, Webster and Turner (Reference 5) used the same definition but termed it J̇.

An experimental determination of C* can be obtained by controlling the displacement rate. By monitoring load and crack length at constant displacement rate, a crack growth rate (ȧ) versus C* plot can be obtained. A data reduction scheme is given in Reference 28. This experimental procedure requires data from several specimens, say, six to ten.

Webster (Reference 51) and Nikbin et al (Reference 5) employed nonlinear beam theory and derived the following approximate relation for C*:

$$C^* = \frac{P}{B} \cdot \frac{1}{n+1} \cdot \frac{d\Lambda}{d\dot{a}} \tag{43}$$

in a double cantilever beam specimen for conditions of constant loading. The load point displacement is denoted by Δ. Since beam theory was used and no account is taken of the deformation ahead of the crack, behind the beam arms, the method can only apply to cases where this deformation is small in relation to the overall deformation seen at the loading points.

In analogy to the theoretical estimation of the J-integral, Harper and Ellison (Reference 52) suggested a method for determining C* through a limit analysis.

Assuming that the multiaxial creep behavior of the material is given by

$$\dot{\varepsilon}_{ij} = B_n \phi^n \partial\phi/\partial\sigma_{ij} \tag{44}$$

where $\partial\phi/\partial(\sigma_{ij})$ is an effective stress associated with a flow rule (e.g. Von Mises, Tresca) and is a homogeneous first power function of stress σ_{ij}, and ignoring the singular behavior at the crack tip, they showed that

$$\dot{U}^* = -\frac{P}{n+1} B_n \cdot 1 (P/mBW)^n \qquad \text{(constant load)} \tag{45}$$

$$\dot{U}^* = \frac{P}{n+1} B_n \cdot 1 \cdot (P/mBW)^n \qquad \text{(constant displacement rate)} \tag{46}$$

16

where m is the yield load ratio defined as the tensile limit load of a cracked specimen to the limit load of an uncracked specimen and l is a characteristic length term, for example, the gauge length of a uniaxial specimen which when subjected to a reference stress of (P/mBW) will give a creep dissipation rate identical to that of a cracked specimen.

Differentiating U* with respect to a and dividing by B, they arrived at

$$C^* = - \frac{1}{n+1} \frac{P\Delta}{BW} \left(\frac{1}{m} \cdot \frac{dm}{d(a/W)} \right) \tag{47}$$

Relations of m in terms of (a/W) have been derived and given by Ewing and Richards (Reference 53) and by Haigh and Richards (Reference 54). The analysis is approximate in nature. In general, it applied to deep notched specimens where fully plastic conditions are achieved. Therefore, it is not an efficient method to use in studying creep crack growth. For creep crack growth studies, a determination of C* for limited plasticity is needed.

e. The C*-Integral

From the brief review sketched in the previous sections, it may be stated that the use of fracture mechanics on structural materials is fairly well established and practiced both for linear and nonlinear behavior regimes. It's use is generally restricted to conditions where materials do not exhibit plasticity or time dependent inelastic deformation. Thus, applications of fracture mechanics are usually confined to lower temperatures below which extensive ductility does not occur.

It was postulated by Landes and Begley (Reference 28) that the nonlinear fracture mechanics parameter C* may be a better descriptor of the behavior of the crack tip under elevated temperature and creep loading conditions than the linear stress intensity factor K. They showed that crack growth rates on discaloy center-cracked panels and on compact tension specimens tested in the creep range at 1200°F (649°C) related with the C*-integral through a power law relation. Sadananda and Shahinian (Reference 26) studied the relationship of C* to creep crack growth rate on compact tension specimens of Alloy 718 at 1000°F (538°C)

and 1200°F (649°C). Landes and Begley's data were obtained as a result of testing at a constant displacement rate whereas the results of the latter were obtained under constant load.

The C*-integral or $\dot{J}$-integral as it is also referred to, is obtained directly from the J-integral by replacing the strain terms by strain rate terms, i.e.,

$$C^* = \int_\Gamma \left(W^* \, dx_2 - T_i \, \frac{d\dot{U}_i}{dx_1} \, ds \right) \tag{48}$$

where

$$W^* = \int_0^{\dot{e}_{mn}} \sigma_{ij} \, d\dot{e}_{ij} \tag{49}$$

is the strain energy density rate. Dots denote differentiation with respect to time. As in the case of the J-integral, the C*-integral is path independent, and thus single-valued, if, and only if

$$W^* = W^*(\dot{e}_{mn}) = \int_0^{\dot{e}_{mn}} \sigma_{ij} \, d\dot{e}_{ij} \tag{50}$$

The existence of a strain energy density rate requires a material constitutive law such that

$$\sigma_{ij} = \frac{\partial W^*(\dot{e}_{ij})}{\partial \dot{e}_{ij}} \tag{51}$$

where $\dot{U}$ is the potential energy rate. For computational purposes, $\dot{U}$ is interpreted as the absorbed energy rate which is the area under the load/load point displacement rate curve, evaluated at constant $\dot{\delta}$. Comparison of the operational definitions of J and C* above shows the reason why C* is considered analogous to $\dot{J}$.

The path-independent C*-integral is meaningful only for materials which are creeping solids, that is, only those that can be characterized through the use of a strain energy rate function $W^*(\dot{e}_{ij})$. This restricts its use to materials where stress is a single-valued function of strain rate, or vice versa, for materials which have only creep type or time dependent strains associated with them. It thus cannot accommodate material behavior involving elastic strains.

f. A Critical Crack Opening Displacement Model

A phenomenological theory of creep crack growth has been developed by Vitek (Reference 55) using the results of a calculation of the time dependent development of the damage zone, which Vitek called the plastic zone, ahead of a crack tip. The whole matrix is assumed to be undergoing creep deformation. The plastic zone is represented by an array of dislocations coplanar with the crack as in the model of Bilby, Cottrell and Swinden (Reference 56).

Vitek showed that at any given point in the plastic zone, the dislocation density rate, $\partial B/\partial t$, is proportional to the negative of $\partial\dot{\epsilon}(x,t)/\partial x$,

$$\frac{\partial B(x,t)}{\partial t} = -h \frac{\partial\dot{\epsilon}(x,t)}{\partial x} \tag{52}$$

where h is the plastic zone width. The plastic zone is confined to a region of length, S, given by

$$S = a \left[\sec\left(\frac{\pi\sigma}{2\sigma_1^F} - 1\right)\right] \tag{53}$$

where σ_1^F is the apparent functional stress. He used an approximate expression for COD as

$$\phi = \frac{4(1-\nu)}{\pi} a \left(\frac{\sigma_1^F}{G}\right) \ln \sec \frac{\pi}{2} \frac{\sigma}{\sigma_1^F} \tag{54}$$

19

Using a critical crack opening displacement criterion and
assuming the crack advances through a fixed distance, be it any distance
d, the plastic zone size, or a critical length, Vitek derived the equation
of the creep crack growth rate as

$$\frac{V}{V_0} = A \cdot K^\alpha \tag{55}$$

where V_0 is a constant and A and α depend on σ/G, and regions of the
stress relaxation σ_1^F/σ. Equation 55 may be used for either one of the
three modes of loading. A singular integral equation for B is obtained
by satisfying the equilibrium conditions. The stress at a point x is

$$\tau(x,t) = \tau^{C+appl.}(x) + \int_a^\infty \alpha(x',t) \left[\frac{G}{2\pi(1-\nu)} \left\{ \frac{1}{x-x'} - \frac{1}{x+x'} \right\} \right.$$
$$\left. + \tau^{dim.}(x,x') - \tau^{dim.}(x,-x') \right] dx' \tag{56}$$

where $\tau^{C+appl.}$ is the stress due to the crack and the applied stress and
$\tau^{dim.}$ is the stress due to the image stress field of a unit dislocation
which results from zero traction on the crack surface. Vitek (Reference
57) found $\tau^{C+appl.}$ and $\tau^{dim.}$ by conveniently using a conformal mapping
function

$$z = \frac{1}{2} a (\zeta + 1/\zeta) \tag{57}$$

and known results for an elliptically shaped crack.

It was found that at any time that 95 percent of the dislocations
modeling α_i depend upon σ/G. This equation can be applied to different
modes of cracking and different degrees of stress and relaxation.

The theory applies when creep is localized at the crack tip.
It does not apply when the stress exponent is greater than, say 5. In
general, different exponents α have to be used for three different ranges
of K depending upon the degree of stress relaxation.

Since the model is basically an uniaxial model, it cannot be readily extended to a comparison of experimental data generated using typical two-dimensional specimens such as the compact tension specimen. This is the only theoretical development that attempts to describe all three stages of creep crack growth.

4.   THE ROLE OF COMPLIANCE

Experimental observations of the crack front features under sustained load or creep crack growth in IN-100 at 1350°F (732°C), and in other materials show a characteristic thumbnail shape. Thus, surface crack lengths are unreliable as a measure of the effective damage, or crack length, for calculations of any parameter which may govern crack growth behavior on the interior of the specimen where the actual crack length is greater than on the surface. Conversely, if the crack growth behavior of the entire specimen is dominated by the surface behavior, or if there is no thumbnail effect, then the surface crack length measurements are reliable parameters for characterization of the growth rate. However, observations of typical creep crack growth behavior have demonstrated two common features: an apparent incubation period where no growth occurs, and a tunneling effect where the crack growth initiates at the interior of the specimen. Thus the parameters which are proposed to govern creep crack growth behavior cannot be evaluated or calculated because the internal crack length cannot be measured directly during an experiment.

In linear elastic fracture mechanics, the stress intensity factor can be obtained from measurements or calculations of the strain energy release rate (Reference 58). From a global viewpoint this depends on determining the load line displacements and applied load for different crack lengths. The difference in stored elastic energy is a measure of crack extension or difference in crack length. If the behavior is nonlinear, the slope of the load vs. load line displacement curve in the vicinity of the origin where nonlinear effects are nonexistent can be used as an alternate measure of crack length. This slope is a measure of the stiffness of the specimen; its reciprocal the specimen compliance. Using linear elastic fracture mechanics concepts, crack length can be

related to compliance. For a crack that is not straight, as in the case
of tunneling, the compliance of the specimen can be used as a measure of
"effective" crack length. For the case of creep crack growth, this crack
length will be larger than the measured length at the surface of the
specimen because of the tunneling of the crack front as the deformation
proceeds. According to Bubsey et al (Reference 58), useful applications
of the compliance method is restricted to cracks of simple shape, in this
case, to plane cracks extending under Mode I relative displacements
(normal to the crack plane).

Compliance assumes linear elastic material behavior throughout the
entire body in order to have any physical meaning; thus it has the same
restrictions as LEFM. For a body containing a crack, the compliance can
be related to the stress intensity factor, K associated with the geometry
of the crack under certain conditions depending upon the dimensions of
the crack, and the position and direction of the load (Reference 58).
Therefore, compliance changes with crack length as the specimen becomes
less stiff as the crack grows. The rate of strain energy release, $\mathscr{G}_I$,
with crack extension associated with Mode I displacement is related to K_I
by

$$\mathscr{G}_I = \frac{K_I^2}{E} \qquad \text{for plane stress} \tag{58}$$

and

$$\mathscr{G}_I = \frac{K_I^2(1-\nu^2)}{E} \qquad \text{for plane strain} \tag{59}$$

in the region comprising the immediate vicinity in front of the crack.
For the case of a two-dimensional plane crack, and linear behavior,
strain energy release rate and compliance, C, are related through
(Reference 59)

$$\mathscr{G}_I = \frac{P^2}{2B} \frac{dC}{da} \tag{60}$$

22

where P is the load and B the specimen thickness. Compliance can be expressed in dimensionless form EBC, where E is the "effective" modulus of elasticity, and letting W be specimen width,

$$\frac{d(EBC)}{d(a/W)} = \frac{2B^2WK^2}{P^2} = f\left(\frac{a}{W}\right)$$
(61)

then

$$EBC = \frac{2B^2W}{P^2} \int_0^{a/W} K^2 d\left(\frac{a}{W}\right) = F\left(\frac{a}{W}\right) - F_0\left(\frac{a}{W}\right)$$
(62)

a. The Compact Tension Specimen

Theoretical solutions for the compact tension specimen exist for K as a function of a/W for a range of relative crack length $0.45 < a/W < 0.55$ (Reference 60). Srawley (Reference 61) presented an alternative expression valid over a wider range of a/W $(0.2 \leq a/W \leq 1.0)$,

$$f(\alpha) = \frac{2+\alpha}{(1-\alpha)^{3/2}} \cdot (.866 + 4.64\alpha - 13.32\alpha^2 + 14.72\alpha^3 - 5.6\alpha^4)$$
(63)

where $\alpha = a/w$, and

$$K = \frac{P}{B\sqrt{W}} f(\alpha)$$
(64)

where P is the load, B is the thickness, and W is the width as shown in Figure 1.

However, knowing stress intensity at a presumed crack length does not give compliance, but only its variation with crack length. It has already been established that compliance is a measure of crack length assuming no inelastic or creep deformation during rapid loading and unloading of the specimen. That is, the material is assumed to be linear and elastic. An initial value for compliance is required at a known crack length in order to use the relation between compliance and K in Equation 62. Once the value of some initial compliance, which is equated to a constant of integration in Equation 62, $F_0(a/W)$, is

established by finite element analysis or some other means, all other values of compliance related to crack extension can be derived.

The K analysis, being based on point load application at the pins for a compact tension specimen, determines the stress field at the crack tip. If St. Venant's principle is invoked, it should make no difference where the load is actually applied on the specimen along the load line provided it is far enough away from the vicinity of the crack tip. The stress field at the tip of the crack should be the same. Therefore, the point of load application does not effect stress intensity.

However, if an energy principle and compliance measurement is utilized, the actual manner of load application will effect the details of the specimen deformation. The method and actual point of application of loading is paramount, i.e., whether the load is distributed or concentrated, whether there is deformation around the pin holes, etc. The theoretical value of compliance, C, used in Equation 62 applies to idealized loading conditions and does not conform to a real loading situation. Therefore, in actual analysis, it is important to have theoretical values of displacements of the actual points where experimental measurements are being made based on realistic mathematical models of load application.

Rudolphi presented a method (Reference 62) for the integral equation solution for a bounded two-dimensional elastic medium with an edge crack, applicable to Mode I deformation. The procedure specifies the tractions and displacements on the boundary of a region and a numerical solution is obtained for the displacements within the body. The formulation allows for the direct evaluation of displacements on a compact tension specimen as a function of crack length. A solution by Rudolphi (Reference 63) over the crack growth range $0.3 \leq a \leq 0.7$ is reproduced in Figure 1 and compares mouth opening, crack opening load line, point load, and total height displacements per unit load as a function of crack extension. The load line displacements used in this research program correspond to δ_4 in Figure 1. The choice of measuring displacements off of the specimen directly is considered superior to measuring off the pins

because of the experimental problems associated with pin bending and rotation. The required relationship between displacement and crack length being provided (Figure 1) dimensionless compliance (EBC) was fitted to the polynomial

$$EBC = \ell + m\alpha^n \tag{65}$$

where $\alpha = a/W$. A best fit to the Rudolphi solution gives the coefficients over two segments

$$\left.\begin{array}{l} \ell = 11.51 \\ m = 248.8 \\ n = 3.167 \end{array}\right\} \qquad 0.25 \leq \alpha \leq 0.50 \tag{66}$$

$$\left.\begin{array}{l} \ell = 22.468 \\ m = 632.7 \\ n = 5.240 \end{array}\right\} \qquad \alpha > 0.50 \tag{67}$$

where continuity up to the first derivative has been assured at $\alpha = 0.50$ for the two segments.

From Equation 65, an "effective" crack length can be readily computed from experimental compliance based on an exact solution for displacements measured between the top and bottom of the specimen on the load line. Stress intensity for any given crack length is then readily calculated from the Srawley equation (Equation 63) or from Equation 69, and these are also exact solutions. Compliance measured experimentally at the start of the test provided an "effective" modulus of elasticity at 1350°F (732°.2C) for the CT specimen based on three-point averaged initial crack length (ASTM Standard E-399) measured directly on the fracture surface after test completion. Thus, neither plane stress modulus, E, nor plane strain modulus, $E/(1-\nu^2)$, had to be

assumed, but rather an "effective" modulus was obtained for each test specimen experimentally.

However, in the calculation of C* (Equation 57), where

$$C^* = -\left(\frac{d\dot{U}}{da}\right)_{\delta const.} \qquad (68)$$

$\dot{U}$ is based on actual load point displacements. Relative top to bottom load line displacements, δ_4, are used to calculate C* rather than load point displacements. Whereas displacements are measured off of plates rigidly affixed to the test specimens, changes due to additional bending of the pins or to local inelastic behavior between pins and specimen do not enter into the calculations.

b. The Ring Specimen

Grandt (Reference 64) demonstrated the feasibility of using a ring geometry for the study of crack growth at constant stress intensity. He reported the relative insensitivity of the stress intensity factor for the ring geometry loaded in remote compression over the midrange of crack lengths for specimens having an inner to outer radius ratio $R_i/R_o = 0.5$. A solution for remote tensile loading, which is the mode of loading in this investigation, was provided by Ahmad (Reference 65) using a finite element solution which best fits stress intensity to a polynomial in dimensionless crack length, α, where α is the crack length divided by by $(R_o - R_i)$, and

$$K = \frac{P}{2B\sqrt{R_o-R_i}} \cdot \sqrt{\pi\alpha} \; (6.5481-14.428\alpha+31.873\alpha^2-38.655\alpha^3+17.684\alpha^4) \quad (69)$$

K is constant within ± 2.5 percent for $0.4 \le \alpha \le 0.8$ where B, thickness, is 0.5 inch and load P is one pound (Figure 2).

The use of compliance as a means to study creep crack growth in the ring specimen is seriously limited by the inherent stiffness of the material as the crack grows. Because load line displacement rates decrease

26

in time during which the crack grows, it is not possible to calculate C*. The C* calculation for constant load depends on an increasing rate of displacement per increment of crack growth and the opposite is what occurs in the ring measurements. Therefore, the concept of C* as a meaningful fracture mechanics parameter is geometry limited and the C* results calculated for the compact tension specimens cannot be compared with the rings.

Since it is possible to use the compliance method to establish at least the boundary conditions on the compliance versus time relationship for the rings at the beginning and the end of the test (interrupted so as to tint the fracture surface as described elsewhere herein), it is not obvious how compliance is related to load line displacement during the time that the crack is growing. However, it is characteristic of the ring test that the compliance does not change significantly enough with respect to experimental scatter during the growth of the crack through the region of constant stress intensity. It was found that crack growth rates could best be related to the strain energy release rate and a corresponding energy rate function, $\overline{\mathcal{G}}$, discussed below, by assuming a simple linear relation for compliance with respect to load line displacement

$$C = z_1 + z_2 \delta \tag{70}$$

Using finite elements, Ahmad (Reference 66) solved the problem of a circular ring cracked radially from an inner diameter and tensile loaded on the inner diameter where the load line is perpendicular to the crack extension direction. From this analysis the relationship between displacement and crack length was given over a region where stress intensity is essentially constant. Based on this analysis, dimensionless compliance was fitted to the polynomial

$$EBC = p + q\alpha + r\, e^{-S\alpha} \tag{71}$$

where

$$\alpha = \frac{a}{R_o - R_i} \tag{72}$$

and a is crack length and R_o and R_i are outer and inner ring radii. A best fit to the Ahmad solution gives the coefficients

$$p = 11.3069$$

$$q = 0.311 \tag{73}$$

$$r = 1.56712$$

$$s = 7.80267$$

over the range $0.4 \leq \alpha \leq 0.8$.

An "effective" crack length can be computed for each value of load line displacement by substitution of the point value of compliance from Equation 70 into Equation 71 and solving for α by Newton-Raphson iteration. Crack growth rates are obtained from differentiation of compliance with respect to time

$$\frac{\partial C}{\partial t} = \frac{\partial C}{\partial \alpha} \cdot \frac{\partial \alpha}{\partial t} \tag{74}$$

Substitution of

$$\frac{\partial C}{\partial t} = z_2 \dot{\delta} \tag{75}$$

into Equation 74 and using Equation 71 differentiated with respect to time, gives for a particular set of (α_j, δ_j) a corresponding $\dot{\alpha}_j$,

$$\dot{\alpha}_j = \frac{EBz_2\dot{\delta}_j}{q - rse^{-s\alpha_j}} \tag{76}$$

5. ENERGY APPROACHES TO CRACK GROWTH

a. Linear Elastic Material

Griffith (Reference 11) assumed an energy balance for fracture in a linear elastic material. He postulated that the potential energy released by a crack extension from some length, a, to a length a + Δa in the time independent material is equivalent to the energy of the newly created surface plus the energy dissipated by inelastic deformation at the fracture load. Rice (Reference 67) showed that under this assumption, irrespective of the particular constitutive relation required, that the failure criterion is determined solely by local stresses and deformations near the crack tip. Therefore, the energy balance as originally postulated by Griffith is equivalent to equating the work done in stress removal from the newly formed crack surface to the work estimated for breaking of bonds at the growing crack surface, in the form of surface energy.

If T' represents the work of the external forces on the body, and W is the stored elastic strain energy, the potential energy of the system, U, is defined as

$$U = W - T' \tag{77}$$

The strain energy release rate, $\mathcal{G}$, is defined as

$$\mathcal{G} = -\frac{\partial U}{\partial a} = \frac{d}{da}(T' - W) \tag{78}$$

where a is the crack length and changes in T' or W occur due solely to crack extension. Thermal effects and kinetic energy due to inertia are neglected. $\mathcal{G}$ can be interpreted as a crack driving force which appears as the excess of work of the applied forces over the energy consumed in elastic deformation of the body. For the case of fixed grips, T'=0, since displacements are specified on the boundary and

$$\mathcal{G} = -\frac{dW}{da} \tag{79}$$

For dead weight loading, it can be shown that

$$\frac{dT'}{da} = 2 \frac{dW}{da} \tag{80}$$

also giving Equation 79. The elastic strain energy for any given crack length is the area under the (linear) load-displacement curve, thus

$$W = \frac{P\delta}{2} \tag{81}$$

where P is the applied load and δ the corresponding displacement. The compliance, C, of the system, for a given crack length, is

$$C = \frac{\delta}{P} \quad \cdot \tag{82}$$

and

$$W = \frac{P^2 C}{2} \tag{83}$$

The above formulation is obtained for a two-dimensional body of unit thickness. For a specimen of finite thickness, B, we obtain from the above,

$$\mathcal{G} = \frac{P^2}{2B} \frac{dC}{da} \quad \cdot \tag{84}$$

b. Nonlinear Elastic Material

In a non-brittle material, fracture is usually characterized by irreversible plastic and viscous deformation near the crack tip. Irwin (Reference 68) and Orowan (Reference 11) modified Griffith's approach to account for this phenomenon. They equated the decrease in elastic potential energy due to crack extension to the sum of the energy of the new surface and the work associated with inelastic dissipation. In this theory, the original Griffith surface energy is represented by a sum of the energy required to grow a new surface and the inelastic energy going into the body. The global elastic potential energy of a nonlinear elastic material is defined as

$$U = \overline{W} - T' \tag{85}$$

where $\overline{W}$ is the elastic strain energy which is, in general, nonlinear and can be broken down into a linear elastic and nonlinear part. The path independent J-integral can be expressed as

$$J = -\frac{\partial U}{\partial a} \tag{86}$$

It is noted that this formulation applies strictly to the class of materials which are nonlinear elastic or which satisfy the deformation theory of plasticity. This formulation is not valid for elastic plastic materials where elastic unloading occurs in the plastic region as might occur behind the tip of a growing crack as stresses are relaxed. For a linear elastic material, it is easy to see that $\mathcal{G} = J$.

c. Nonlinear Material

Eftis, Jones and Liebowitz (Reference 69) have introduced a non-linear energy function, $\widetilde{\mathcal{G}}$, which is used for defining fracture toughness or as a parameter applicable to sub-critical crack growth. Although they deal with the critical value of the parameter, $\widetilde{\mathcal{G}}_c$, for fracture toughness, a more general definition for any crack extension including fatigue could be written as

$$\widetilde{\mathcal{G}} = -\frac{\partial}{\partial a}(\overline{W} - T') \tag{87}$$

where $\overline{W}$ is the strain energy of deformation which can be considered to be composed of an elastic part E' and a plastic part E". The formulation is purely global and says nothing about localized plastic zones near the crack tip or small deformation limitations. For a linear elastic material, $\widetilde{\mathcal{G}} = \mathcal{G}$.

d. Linear Elastic Creeping Solid

For a body that exhibits linear elastic behavior over short time periods but creeps over an extended time regime, the nonlinear energy approach of Eftis, Jones and Liebowitz (Reference 69) can be followed to develop an energy function which will be called $\overline{\mathcal{G}}$. In this study, experimental observations showed essentially linear load displacement relations upon loading or unloading for any crack length from the initial fatigue crack to the highly extended and tunnelled creep crack, provided the loading or unloading was carried out in a short period of time, nominally

31

less than 100 seconds. The material can then be treated, from a global viewpoint, as one which sustains a combination of linear elastic and creep strains deformation.

The energy function $\overline{\mathcal{G}}$ can be derived in a manner similar to the derivation of $\mathcal{G}$ or $\tilde{\mathcal{G}}$. Let E' represent the stored (linear) elastic energy, E" the dissipated or stored inelastic energy, and $\overline{\Gamma}$ the total energy required to create new crack surfaces. Assuming negligible kinetic energy and heat flow out of the body, a global balance of energy requires that

$$\frac{\partial}{\partial t}(T' - E' - E") = \frac{\partial \overline{\Gamma}}{\partial t} \tag{88}$$

If it is assumed that all changes with time are related to changes in crack length, a, then

$$\frac{\partial}{\partial t} = \frac{\partial}{\partial a}\dot{a} \tag{89}$$

If the energy to create new crack surfaces $\overline{\Gamma}$ is linearly proportional to crack length, i.e., $\overline{\Gamma}=a\gamma$, or γ represents the energy to create a new unit crack surface, then

$$\frac{\partial}{\partial a}(T' - E' - E") = \gamma \tag{90}$$

The left side of this equation can be viewed as the crack driving force, $\overline{\mathcal{G}}$, or the excess of energy available for creating new crack surfaces.

Consider a load displacement diagram (Figure 3) which represents the condition for two times, one at A for some arbitrary crack length a_0 and one at C at some time later during which the crack extended under constant load to $a_0 + \Delta a = a_1$. For the initial crack, the load deflection curve, OA, is linear. Under sustained load, the load line deflection increases from point A to point C while the crack extends from a_0 to a_1. The compliance due to crack length a_1 is represented by the reciprocal of the slope of the line DC or OB. Point B represents the deflection due to purely elastic behavior which is denoted by δ_{el}. The remaining inelastic

deflection is denoted by δ_{in}. The work of the external forces is $P(\delta_{el}+\delta_{in})$. The change in stored elastic energy of the body in growing a crack from a_o to a_1 is $P\delta_{el}/2$. The remaining energy, represented by OACD, is available for either growing the crack, i.e., creating new surfaces, or permanently deforming the structure around and away from the crack. Thus, the amount of energy available for driving the crack can range from OAB to OACD. The inelastic energy OBCD goes either into creating new surfaces and driving the crack, or is dissipated as energy of inelastic deformation of the remaining structure.

The function $\mathcal{G}$ can be calculated from the work of the external forces and the stored and dissipated energies. The quantity which cannot be determined directly is the dissipated energy. This energy can go into the body as creep strains away from the crack tip or can all go into driving the crack or creating new surfaces. For finite increments of growth Δa, we can write

$$\Delta T' - \Delta E' = \Delta\overline{\Gamma} + \Delta E'' \tag{91}$$

The left-hand side represents all excess energy available for both creating new crack surfaces or inelastically deforming the body. Calculation of the left-hand side is easily done whereas

$$\Delta T' = P\delta_{el} + P\delta_{in} \tag{92}$$

$$\Delta E' = \frac{P\delta_{el}}{2} \tag{93}$$

and

$$\Delta T' - \Delta E' = \frac{P\delta_{el}}{2} + P\delta_{in} \tag{94}$$

Using Equation 89, the crack driving force is then defined by

$$\frac{d}{da}\{\Delta T' - \Delta E'\} = \frac{P}{2aB}\{\dot{\delta}_{el} + 2\dot{\delta}_{in}\} \tag{95}$$

If all of the inelastic energy goes into deforming the body and not directly into growing the crack, then the energy left to grow the crack is $P\delta_{el}/2$ which is equivalent to $\mathcal{G}$, i.e., the linear elastic fracture mechanics parameter. In this case, δ_{in} goes into deforming the body and hence from

$$\dot{\delta}_{el} = P\dot{C} \tag{96}$$

$$\text{and} \quad \dot{\delta}_{el} + 2\dot{\delta}_{in} = 2\dot{\delta}_{in} - P\dot{C} \tag{97}$$

where C is compliance,

$$\frac{P\dot{\delta}_{el}}{2\dot{a}B} = \frac{P^2\dot{C}}{2\dot{a}B} = \frac{P^2}{2B}\frac{dC}{da} \tag{98}$$

which is $\mathcal{G}$. At the other extreme, if all of the inelastic energy goes into driving the crack, then E' is zero and δ_{in} goes into growing the crack.

$$\overline{\mathcal{G}} = \frac{P\delta_{el}}{2} + P\delta_{in} \tag{99}$$

For unit thickness,

$$\overline{\mathcal{G}} = \frac{P\dot{\delta}}{2\dot{a}B} - \frac{P^2}{2B}\frac{dC}{da} \tag{100}$$

The quantity $\overline{\mathcal{G}}$ above can be calculated from the experimental displacement and compliance data and investigated as a possible crack growth criterion.

SECTION III

EXPERIMENTAL PROCEDURE

1. MATERIAL

IN-100 is an advanced turbine disc alloy used in the U.S. Air Force's F-100 turbofan engine. It is a nickel-based powder metallurgy material supplied in the form of a pancake by its manufacturer.* When super-plastically forged with a proprietary forging process known as "gatorizing", IN-100 becomes a fine-grained (as per ASTM 12-14) isotropic material. Typical chemical composition is 18.50Co-12.4Cr-4.98Al-4.32Ti-3.2Mo-0.78V-0.07C-0.06Zr-0.02B-balance nickel (Reference 3).

The pancake, identified as H59BIG, from which compact tension specimens and tensile/creep-rupture specimens were cut, was 1.5 inches (38 mm) thick and 16 inches (405 mm) in diameter. Compact tension specimen crack surfaces were in transverse planes, i.e., in planes perpendicular to the flat faces of the pancake. Specimen crack planes in the pancake were selected so that some were in the circumferential direction and some in the radial. From a feasibility study in the early stages of this program, it was determined that there was no observable effect on crack growth at 1350°F (732°.2C) within the limits of statistical variability due to selection of crack plane orientation with respect to the pancake. Therefore the claim of material isotropy as related to crack growth receives experimental support at least in planes orthogonal to the flat planes of the pancake. The effect of the transverse plane on crack growth was not investigated.

A second piece of IN-100, a portion of an undesignated turbine disc forging, supplied the material for the ring specimens. The chemical composition is 18.6co-11.8Cr-5.01Al-4.24Ti-3.38Mo-0.66V-0.07Zr-0.064C-.0.42Si-0.02B-balance nickel.

---

*Pratt and Whitney Aircraft Group, United Technologies Corporation.

2. MECHANICAL AND CREEP-RUPTURE PROPERTIES

Table 1 summarizes mechanical properties of IN-100. The modulus of elasticity at 71°F (21°.7C) was calculated from a single tensile specimen having 1.125 inch (29 mm) straight central length with a central section diameter of 0.25 inch (6 mm). Four electrical resistivity strain gages were equally spaced about the central diameter which eliminated specimen bending and temperature imbalance effects in the modulus determination. The modulus was calculated for each rotation of the test specimen in the testing machine grips at 45-degree intervals. The value in Table 1 is an average of those computations, and is used throughout this study.

Table 2 tabulates the results of stress-rupture tests on the same specimen geometry. On specimen C1, an extensometer was attached over a one-inch gage length. On specimen C2, the extensometer was attached to the shoulders and according to ASTM E-139, this corresponded to an effective gage length of 1.26 inches (32 mm). An applied load of 173 pounds (769.5 N) corresponding to a tensile stress of 72,000 psi (496.4 MPa) at 1350°F (732.2°C) resulted in a creep-rupture life of 92.5 hours on specimen C1 and 109 hours on specimen C2. The extensometer attached to the one-inch (25 mm) section of specimen C1 slipped at 71 hours. Due to variability in stress-rupture life in the two tests, it was not possible to equate the results of C2 to the strain history past 71 hours for C1. Failure location on C1 occurred at the extensometer knife edge which may account in part for the low elongation as compared to that listed in Table 1. Strain-time histories are shown in Figures 4 and 5.

3. COMPACT TENSION AND RING SPECIMENS

Five thicknesses were chosen for the CT specimens: 7/32", 11/32", 15/32", 19/32", and 23/32" (6 mm, 9 mm, 12 mm, 15 mm, and 18 mm) to be tested at initial nominal stress intensities of 30, 35, 40, and 45 ksi-inch$^{1/2}$, (33.0, 38.5, 44.0 and 49.5 MPa-m$^{1/2}$). A standard compact tension specimen geometry is used, its dimensions in accordance with ASTM E399-74 (Figure 6). Twenty-two CT specimens were fabricated to five

thicknesses and tested according to the schedule in Table 3. Seven ring specimens (Figure 7), 0.75 and 0.125 inch (6 and 3 mm) thickness were tested at the same temperature for nominal K values of 23, 30, 40, and 45 ksi-inch$^{1/2}$ (25.3, 33.0, 44.0 and 49.5 MPa-m$^{1/2}$). Prior to testing, all specimen flat surfaces were polished to machinist's standard PMS-2 to facilitate visual observation of the crack.

Specimens were cyclically loaded at room temperature in an MTS hydraulic servo-controlled testing machine for pre-cracking to a target total crack length of 0.65 inches (16.51 mm). Loads were adjusted to produce crack growth at stress intensity values of not more than 15,000 psi-inch$^{1/2}$) at a loading rate of 20 Hertz and stress ratio R=0.1. The actual fatigue-induced starter crack surface was measured after each test and the specimen pulled apart. The ASTM method (E-399) of averaging quarter point lengths on the crack surface showed that differences between these crack lengths and initial surface-measured crack lengths varied by 2 to 8 percent. Nominal stress intensity target values used to determine test loads were based on initial surface crack lengths. After the tests were completed, the adjusted and more accurate K-values were calculated from the post-test measured 3-point averaged initial crack lengths. These data are tabulated in Tables 4 and 5.

Punch marks placed on each CT specimen face 0.25 inches (6 mm) above and along the crack path at 0.25 inches (6 mm) intervals allowed monitoring crack growth by traveling microscope and 35 mm camera.

4. APPARATUS AND INSTRUMENTATION

Constant load was applied in a Swedish-manufactured 10,000 pound (44.48 kN) capacity creep test frame having a 20 to 1 loading ratio. The oven was resistance wire wound, inside dimensions 7" x 7" x 4" (178 x 178 x 102 mm), with viewing ports on either side. Specimens were mounted in Inconel clevises with IN-713 pin holding devices. Crack lengths during the test were measured to the nearest 0.0001 inch (0.03 mm) at five minute intervals through a traveling microscope on each side

of the specimen. Later, in the CT phase of the testing program, a 35 mm
camera was substituted for one of the microscopes. Photographs of the
advancing crack were taken every five minutes using Kodak high speed
Ektochrome film. By optimizing light conditions, the color of the speci-
men facilitated crack root identification and crack extension based on
fiducial markings on the specimen.

The displacement of the specimen due to crack opening in the plane
of load application (perpendicular to the crack plane) was measured using
a pair of linear variable differential transducers (LVDT) mounted below
the oven and attached to the specimen in the following manner. Two E-
shaped plates made of IN-718 were rigidly attached to the top and bottom
of the specimen. The use of a rigid fixture attached directly to the
specimen was demonstrated by Mills, et al (Reference 70). The E-plates
translate the load line displacement outside and around the loading
clevises on either side of the specimen far enough to intersect the
vertical load line plane containing the center line of the clevis pins.
These E-plates each contained two small pins which supported two stain-
less steel rod-in-sleeve (concentric tubing) extension arms, one on
either side of the specimen, which protrude down through the oven wall
and on which were attached the LVDTs. The LVDTs were bench calibrated
and linear over a midrange of 0.150 inches (4 mm).

A Daytronics LVDT Conditioner model 9010 provided AC signal for
the LVDTs and processed the change in the signals, converting it to
DC output in millivolts calibrated at a sensitivity of 10 MV per mil
of load line deflection. This output independently activated a Digitec
tape puncher at five minute intervals throughout the test. In parallel,
a Heath Dual Pen Recorder Model SR-206 plotted LVDT voltage sums.

5. CALIBRATION

Temperature variation from the test mean temperature of 1350°F
(732°.2C) on a CT specimen using thermocouples welded directly to the
specimen was not more than ± 8 degrees at the top and bottom and no more

than ± 4 degrees in the vicinity of the crack tip. These results were considered within reasonable limits of temperature variability.

The suitability of the LVDT/E-plate arrangement was demonstrated at room temperature using a 1/2-inch (13 mm) thick 304 stainless steel CT specimen mounted in the creep frame so that in addition to the E-plate attachments, a clip gauge was attached across the crack mouth opening in the load line, as recommended in ASTM Standard E-399. Response of both measuring devices showed linearity and equal slope of load-displacement over a 6 mil (.2 mm) range. Hence, there was no requirement to correct for load line displacement deviations such as arise from measurements made off the loading pins or from measuring load cross head movements.

6. EXPERIMENTALLY-DETERMINED COMPLIANCE

Pre-test compliance at room temperature was recorded on all specimens and the results used with Equations 65 and 71 to allow calculation of initial crack length for comparison with optically-measured surface crack lengths. Specimens were then soaked for one hour at test temperature and compliance again measured for one to two load-unload cycles and for the initial test loading. These values, averaged, provided the data for calculating an "effective" modulus of elasticity for each specimen. During the tests, compliance was taken at 30-minute intervals shedding 100 to 200 pounds (445 to 890 N) of load at a time up to 15 to 25 percent of total load. Loading and unloading curves were normally parallel lines and their average value was used to plot compliance as a function of load line displacement for each specimen test as shown in Figure 8 which combines data from all the tests on CT specimens, normalized for a unit thickness.

Those specimens in Tables 4 and 5 for which final surface crack measurements are recorded were not allowed to fail catastrophically. By stopping these tests before the cracks grew to a length at which

unstable crack growth occurred, fracture surfaces were heat-tinted.
Photographs of the fracture surfaces (Figures 229 through 250) show the
dramatic effect of crack front tunneling and demonstrate clearly how
misleading the use of surface crack measurement in fracture mechanics
applications really are.

SECTION IV

EXPERIMENTAL RESULTS AND DISCUSSION

1. DATA REDUCTION AND PRELIMINARY ANALYSIS

For each of 22 compact tension specimens of five different thicknesses and seven cracked ring specimens represented by two thicknesses, data were recorded for surface crack length and load line displacement as a continuous function of time. In addition, periodic measurements of specimen compliance were recorded. A data reduction scheme for the calculation of stress intensity versus crack growth rates, which forms the basis for an analysis of the C*-integral, is given in Figure 9. Step 1 of Figure 9 shows a typical load and load line displacement-time record. Load line displacement raw data in the form of two channels of LVDT output was averaged for each test and data were smoothed against time along with its first derivative using a seven-point averaging method making use of a least squares fit to a second degree polynomial. Smoothed displacement-time curves for each of the compact tension tests are given in Figures 10 through 30, and Figures 31 through 37 for the ring specimens. Load line displacement rates for the compact tension specimen tests were constant on the average of the first 40 percent of test life for initial nominal stress intensity of 45,000 psi-inch$^{1/2}$ (49.5 MPa·m$^{1/2}$) and first 62 percent for initial K of 30,000 psi-inch$^{1/2}$ (33.0 MPa·m$^{1/2}$). These rates increased rapidly as the crack grew toward the end of the stable growth region of the specimen. These rates are shown schematically in Step 2 of Figure 9.

In the case of the ring specimens, load line displacement rates were high at the beginning of each test and rapidly decayed exponentially with time. The difference in this behavior from the CT results is explained by the statics of load transference in the specimen whereby at complete failure along one half of a ring diameter, a limiting compliance is achieved. As the crack grows beyond the region where K is constant, the uncracked half of the ring carries more and more of the load. Hence, the crack growth rate actually decreases throughout the test.

2. EFFECTIVE CRACK LENGTH

From the outset of the experimental investigation, it was obvious that crack growth initiated in the center of the specimen and that tunneling occurred. This was based on observations of initial non-zero displacement rates coupled with apparent delay or an incubation period based on surface crack length measurements. This effect was more noticeable for the thicker specimens as was expected. The tunneling was further confirmed by observation of the fracture surfaces. In all cases, final crack lengths when the test was terminated before catastrophic failure, were considerably less then the internal dimension. The use of an "effective" crack length was therefore undertaken for all the experimental data. Crack growth-time data indicated that surface measurements began to lag behind effective lengths from the very beginning of the tests with the amount of lag becoming approximately constant after some small amount of growth. This would indicate that tunneling occurred from the beginning and appeared to reach a nearly steady state value of crack front advance. The limited number of actual crack profiles made it difficult to conclude as to the exact manner in which cracks grew internally.

A remarkable feature of the fracture surface was the presence of "fingers" extending into the uncracked region of the specimen. These fingers were more dramatically apparent on the thicker specimens (Figures 229 through 250). Mills (Reference 8) found "protrusions" ahead of the thumbnail zone in CT specimens of alloy A-286, an iron-based superalloy, which were loaded to various displacements at 800°F (427°C) and 1000°F (528°C) producing different amounts of crack extension. Boyd (Reference 7) reported a similar feature on the fracture surfaces of Ti-8Al-1Mo-IV, describing the almost vertical faces as cleavage facets. The extension of these fingers into uncracked material suggests that cracking is discontinuous, where the fingers form as a separate, rapid cleavage event leaving uncracked material between them, fcllowed by fracture of the intermediate material by creep/corrosion interaction.

Tunneling appeared to start immediately at the beginning of the tests and proceeded until making contact with the edges of the specimens. Examination of the fracture surfaces also revealed a significant amount of shear lip behavior along the edges of the specimens. The thickness of this edge increased with crack length as the corresponding tunnel width decreased containing the "fingering" to a narrowing central bank of material. The shear lip can be seen in Figures 229 through 243 on the CT specimens, along with the position of the measured surface crack length at test termination. It is apparent that the surface measurement is extremely inaccurate and, furthermore, highly nonconservative. The large amount of shear deformation could be observed ahead of the crack tip, but the position of the cracked region on the surface appeared to lag far behind the internal cracked region. This difference is even more apparent in the fracture surface of the ring specimens (Figures 244 through 250). Shear lips on rings were restricted to a narrow band along the surface edges. Crack front profiles tended to extend across the width of fracture surface similar to a fatigue crack profile which is not normally blunted significantly.

In Figures 229 through 250, the positions of the "effective" crack lengths are shown as a line across the specimens. These lengths were obtained from compliance measurements at room temperature after the creep crack growth tests had been terminated and before specimens were torn apart to reveal the heat-tinted zone which outlines the final creep crack profile. It is seen that in all of the specimens, the effective crack length was between the surface measurement and the maximum length on the centerline or in the interior region. Also, the effective crack length is still significantly shorter than the maximum crack length of the tunneled crack.

3. USE OF COMPLIANCE IN CRACK LENGTH DETERMINATION

    a. Compact Tension Specimen

        To obtain information of effective crack length against time, plots were made of load line displacement, δ, against compliance, C,

for each test. A straight line seemed to fit these data quite well, and an analytical expression for this line was obtained for each test. Figure 8 shows a plot of all these data for the CT specimens for all tests normalized for unit thickness. All the data fit into a band, the width of which is determined by experimental scatter. Thickness effects on the compliance-displacement relation are not evident within this scatter band.

The data of δ versus C (Figure 8), which were fit to a straight line for each test, indicate that there are two contributions to the increase in the load line displacement, δ, as the tests progressed. One contribution, which is the value to the straight line, whose slope is 1/P, is due solely to the growth of the crack for assumed linear elastic material behavior. For such a material, the experimental points would be expected to lie along the straight line, slope 1/P. This simply implies that for any given crack length, the compliance of the specimen changes according to the formula for compliance, C, versus crack length, a, from LEFM, and that if unloaded, δ would return to its initial value. The second portion of δ, from the straight line 1/P to the actual experimental curve, is an inelastic, nonrecoverable contribution. This contribution increases with δ, time and crack length. The significance of the linearity of the plot with δ or C is not apparent and does not appear to have any physical basis. Nonetheless, this inelastic portion of δ does increase during each test. It is quite likely that this is due, at least, in part, to creep behavior at and ahead of the crack tip.

In plotting the compliance-displacement results for each CT specimen, it was noted that in the majority of the tests, the second and third compliance on each specimen taken during the first 30 minutes of the test, were less than the initial compliance which invariably fell on the 1/P line. This anomaly, which appears to contradict physical law, has also been observed in the testing of CT specimens of aluminum alloy (Reference 72) and on polycarbonate three-point bend specimens

(Reference 73). If the observation then is real, it would imply an apparent shortening of the crack which is unrealistic. A possible explanation is that once load is applied to the front of the fatigue-induced crack, the crack is blunted. It is not obvious that the same value of compliance will result from two specimens having identical crack lengths and geometries, where one specimen has a sharp crack and the other blunt. Blunt notches have been utilized in specimens for experimental compliance measurements (Reference 58), but values of compliance identical to those from sharp cracks are not obtained. One possible explanation for the apparent drop in compliance is crack blunting combined with inelastic, time-dependent strains which occur ahead of the crack tip.

There was also a difference in the manner in which the initial loading compliance and subsequent compliance measurements were made. The initial compliance is based on a total load application whereas subsequent compliances were based on approximately 25 percent removal and replacement of total load. Hysteresis effects appeared not to be contributive to the observed lower values (second and third) since the incremental loading and unloading curves were invariably parallel.

In addition, an initial unloading and reloading was performed immediately after initial load-up in several tests. There was no apparent difference between the compliance measurements using both methods within experimental accuracy. No readily available explanation of this phenomenon has been found in the literature.

Step 4 of Figure 9 shows a typical plot of effective crack length against time for any fixed load. The effective crack length, $\bar{a}$, is calculated from a polynomial best fit of Rudolphi's displacement-crack length relation (Equation 65), for each CT test,

$$a_i = \left(\frac{EBC_i - \ell}{m} \right)^{1/n} \tag{101}$$

where the compliances, C_i, are calculated for selected values of δ_i using analytical expressions of the form

$$C_i = \bar{p}\ell_i + \bar{q} \tag{102}$$

Plots of $\bar{a}$ vs. time for all compact tension specimens are shown in Figures 38 through 58 and in Figures 59 through 65 for the rings. From δ, $\dot{\delta}$ and $\bar{a}$ information, stress intensities, K, and crack growth rates, $\dot{a}$, were calculated.

b. The Ring Specimen

Due to experimental complexities, it was difficult to use compliance as an effective means of describing the extent of the fracture surface in the rings. It was not possible to affix the E-plate directly to the specimen. Rather, load line displacement measurements were taken off the clevises using the rod-in-sleeve extensometers attached to either side of both upper and lower clevises. Although it was determined that the clevises did not contribute to total overall deformation there was measurable deformation introduced by bending and bearing stresses on the clevis (loading) pins as well as by inelastic indentation of the ring inner diameters at the pin load contact points. Initial compliance measurements at room and test temperature were experimentally determined as before but these values were twice as large as predicted by Ahmad's solution (Equations 71-73). Therefore, it was necessary to calibrate displacement-time measurements against a base displacement value which was forced to correspond to the compliance associated with quarter-point averaged initial crack length, using the relation (Equation 62)

$$EBC_0 = f(a_0) \tag{103}$$

The initial displacement, δ_0, corresponding to initial crack length, a_0, is defined by

$$\delta_0 = PC_0 \tag{104}$$

and is readily calculated from Equation 98. All experimental displace-
ments, δ_j, were adjusted by subtracting the difference between the total
experimental initial displacement due to loading the specimen, δ_ℓ, and
the theoretical initial displacement, δ_0,

$$\delta_i = \delta_j - (\delta_\ell - \delta_0) \tag{105}$$

The resulting calibrated displacements are the δ_i. Their
smoothed values are plotted against time in Figures 31 through 37.
It can be shown that the initial displacement lies on the 1/P line of
the corresponding compliance-displacement curve, regardless of the
shape of that curve.

Another difficulty in using the compliance method with ring
results was that a ring with a part-through crack is statically indeter-
minant and too stiff a geometry to allow compliance to change signifi-
cantly over the crack growth range. As the crack grows in the ring,
the load is transferred to the uncracked arm of the ring. The net
effect is a decreasing load line displacement rate and reduction of
energy available to progress the crack, which resulted in compliance
calculations which changed very little with crack length. To overcome
this difficulty, the experimental compliance data were plotted against
time for each ring test, and the resulting curves translated and rotated
to match the theoretical compliance associated with the experimentally
measured initial and final crack lengths. Due to the unreliability of
the compliance data between the initial and final points, a straight
line was fit to these two values as an approximation. Table 5 summar-
izes the data on the seven ring tests. Compliances shown therein are
calculated directly from Equations 71-73 from measured initial and
final crack lengths.

4. CORRELATION OF K WITH CRACK GROWTH RATE

Crack growth rate as a function of K for all tests of CT specimens
were plotted in Figures 66 through 87 and then re-plotted for groups of
specimens of the same thickness in Figures 88 through 92. A single

curve was drawn through each set of data for each thickness as shown
in Figure 93 as a representation of the data for each thickness. With
the exception of the 7/32 inch (6 mm) thickness, all of the data appear
to fit a single curve, that is, to fall within a scatter band repre-
senting thicknesses from 11/32 inch (9 mm) up to 23/32 inch (18 mm).
It appears that plane strain conditions for creep crack growth have been
achieved for thicknesses above approximately 0.3 inch (8 mm). These
are consistent with the observations of Wallace, Annis and Sims (Refer-
ence 3), for the same material at the same temperature for thicknesses
0.50 to 0.75 inch (13 to 19 mm) under sustained load.

One characteristic feature which was noted on nearly all of the
individual crack growth rate-K plots was an apparent high initial growth
rate which shows as a characteristic check mark on each of most of the
curves (Figures 66 through 87). Experimental findings of Hendricks
(Reference 74) using short hold time periods during cyclic loading on
the same material at 1350°F (732.2°C) have tended to verify this observa-
tion of an initial accelerated crack growth rate followed by a "steady
state" creep crack growth rate which depends on K or some other govern-
ing parameter. These initially high crack growth rates decreased to a
stable value after approximately the first 45 minutes of each test.
This time interval appeared to be independent of the total time in the
test as well as of specimen thickness. For example, the test results
for the 7/32" (6 mm) thick compact tension specimens show the same time
interval of approximately 45 minutes for the decreasing crack growth
rate as do the results for the 23/32" (18 mm) thick specimens. However,
in the matter of specimen thickness, it is also observed that the amount
of decrease is greater for the thinnest specimens than the thickest by
about 60 percent. Therefore, if gross plasticity governs in the initial
stage of crack initiation, then it could be postulated that crack growth
rates would decrease until a threshold value of stress intensity is
attained, after which linear fracture mechanics applies to describing
subsequent crack growth behavior. But under the load and temperature
conditions of the tests in question, such cannot be the case. It was

determined in an independent test during the course of this investigation on the same material at the same temperature that cracks could begin to grow at an initial nominal stress intensity of 10,000 psi-in$^{1/2}$ (4.4 MPa-m$^{1/2}$) which is a value of K well below the initial K levels used to determine test loads.

It is apparent that more than one mechanism is governing the initiation and early growth of the extending crack. Cracks were observed to begin to grow almost immediately, that is, there appeared in most tests to be little or no crack incubation time. Where observed, this incubation time was not seen to be more than eight minutes into any one test. It was also observed that for the thinner compact tension specimens, crack initiation and propagation was observed on the surfaces within two to three minutes after the test load was applied. However, changes in load line displacement for the thinner specimens tended to lag behind surface crack measurements. In the case of the thicker specimens, displacements were recorded from two to three minutes into the test with surface crack growth following by an amount of time up to eight minutes. It is logical to construct on physical grounds the manner in which the crack initiates and creates a plastic zone ahead of its frontal boundary which then extends into the plastically deformed region. In addition, the effect of oxidation can be expected to play a major role in the initiation of the crack front by the creeping mechanism. It is seen from very short time creep behavior that the crack begins by extending from the fatigue-induced pre-crack along the centerline of the fracture surface. Once initiated and growing on the fracture surface centerline and along the pre-crack front, the crack extends as a thumbnail shape into the material as the trailing edges of the crack on either side of the tunneling crack extended further and further along the front of the pre-crack. At some time within approximately two to eight minutes of the test, the tunneled crack front reaches a crack length long enough so that the trailing edges of the crack make contact with the surfaces of the specimen. From this time on, it is assumed that the thumbnail creep crack front

advances without any further change of shape in the region of stable
crack growth. Yet there are physical reasons for challenging this
assumption based on the tendency of the coursely textured and fingered
central region of the crack surface to funnel down in width as the crack
progresses.

In a manner of explanation, a model is formulated consisting of
two competing mechanisms of crack growth; one a creep mechanism which
governs over the stable crack growth region, and a second which in
addition to creep, is governed by chemical interaction with the triaxial
stress state which dominates the early portion of sustained load crack
initiation and propagation. In applying this conjecture to the experi-
mental observations, it is noticed that the fracture surface can be
divided into three zones (Figure 251); the central zone where the crack
front tunnels through the interior of the material (Zone I) and two
outer zones II and III which are enclosed between the centrally tunnel-
ed crack region and the outer edges of the specimen. The textured sur-
face of the interior region exhibits marked vertical ridges and troughs
running along the crack advance direction which culminates in fingers
which extend beyond the advancing curved crack front. As pointed out
previously, these fingers show cleavage type failure along one side
of it's ridge or trough. However, on the other side of the ridge,
in all cases, the sides facing the centerline of the specimen from
either side of the centerline do not show fracture and therefore did
not darken as a fracture surface due to heat tinting. The division
of the fracture surfaces into three characteristic zones can be readily
observed in the photographs of the compact tension specimens after
failure in Figures 229 through 243. The compact tension specimen whose
fracture surface has these three zones can be conceived as three
separate specimens, attached together in some manner where the conti-
nuity of displacements on joint surfaces is not violated. Hence, a
model whereby a constant load is applied to three specimens simultaneous-
ly in parallel is conceived where some time-dependent displacement field
is imposed between the flat specimen surfaces and displacements are con-
tinuous across these surfaces. In such a test, if it were possible to

design one, the unequal crack extension of the fracture surface due to tunneling in the creeping body is related to the stress states governing the three zones. The way in which the crack progresses over these three surfaces is modeled in the following way. Initially, the crack front grows from the fatigued pre-crack until the edges of the crack reach the side surfaces of the specimen. This, as noted, is seen to occur in the first eight minutes of the test. Then the crack begins to tunnel severely and the crack grows along the center zone (Zone I in Figure 251) at a faster rate than the cracks are growing in Zones II and III. The Zone I crack finally reaches a point where it is being retarded by the stress field of Zones II and III which is transmitted across the zone interfaces. In Zones II and III, the stresses are considerably lower than in Zone I and therefore cracks in the edge zones propagate more slowly then the advancing crack in Zone I.

Zone II fracture surfaces exhibit gross plasticity over the region which shows river lines typical of ductile fracture. The fracture surface in Zone I is characteristic of more brittle failure associated with a triaxial stress state at the crack tip. It can be argued that environmental effects due to chemical interaction with the stress field at the crack tip is more severe on the Zone II and III crack regions than on the material in the interior of the specimen because environment can influence the outer zone crack more effectively due to the greater access to the crack front material. But in these stress relieved zones, the stress field is of lower magnitude than in the interior. The overall effect is for the outer zone cracks to grow more slowly than Zone I cracks which are under higher stress. Hence, the outer zones act as a retardant on the centrally advancing thumbnail crack. In essence, due to this retarding effect, the stress intensity factor in the Zone I "specimen" is reduced and since K is a function of crack length, the crack length of the centrally failed region is slowed down until stable crack growth is achieved.

Under stable crack growth conditions, it is observed that Zone I thickness decreases as the crack length increases. Why not remove the

outer retarding material from the specimen by machining grooves along
each side? Such a test was performed by Ashbaugh (Reference 73) on a
19/32 inch thick specimen of IN-100 at 1350°F after machining a 1/16 inch
deep groove in both sides of the specimen. That test was interrupted
at one inch of crack length and the fracture surface heat tinted. It was
observed that the crack retarding effect was removed and that the crack
front did not tunnel. Deep fingers were characteristic of the mode of
failure as was observed on the tests discussed herein.

In the absence of a viable theory of creep flow and environmental
interaction with states of stress in nonlinear time-dependent materials,
even to the extent of being able to solve a simple three-dimensional
stress problem for a crack in a linear elastic material, it is argued
that explanations for the phenomena observed herein are not readily
available. It is noted that in the matter of coming into a better
understanding of the phenomenon of time-dependent deformation in cracked
metallic materials, it is not historically precedent that theories of the
creeping solid precede experimental observations of the material behavior
in the laboratory.

5. CORRELATION OF NET SECTION STRESS AND DISPLACEMENT RATE WITH
   CRACK GROWTH RATE

Net section stress was also examined as a possible correlating
parameter for crack growth rates. The data for all CT tests are pre-
sented in Figures 94 through 115 and re-plotted for groups of specimens
of the same thickness in Figures 116 through 120. A single curve was
drawn through each set of data for each thickness from Figures 116
through 120. These summarizing curves are shown in Figure 121 where
each curve is a best representation for each group of data by thickness.
The data of Figure 121 show no variation with specimen thickness except
for the thinnest, 7/32 inch (6 mm) specimens which show a lower crack
growth rate. To indicate the extent of possible overlapping of the
experimental scatter, the actual data for the 7/32 inch (6 mm) group are

shown with the single curve in the figure. The lower crack growth rate
for the 7/32 inch (6 mm) specimens is consistent with the results obtained
from the á-K plots, and in general, net section stress shows good corre-
lation with crack growth rate as a governing parameter for the compact
tension specimen data.

The data for load line displacement rates for all CT tests indicated
that during the early minutes of each test (up to the first 30 to 40
minutes), the load line displacement rate based on the smoothed displace-
ment-time data was decelerating. It was observed that displacement
increases were measurable on the specimens almost immediately after load
was applied or within the first 5 to 8 minutes. Total time in the test
appeared related in some manner to the way in which the crack was
influenced during the first few minutes into the test. An attempt to
describe this idea would be to state that it appeared that the material
ahead of the crack was able to sense what was going on at the crack
front, i.e., that material away from the crack was affected by crack
front tunneling, the three-dimensional stress state of the crack front as
influenced by oxidation, blunting of the crack tip, and specimen edge
effects. Perhaps the rate of displacement in the early portion of the
test was important in describing overall fracture behavior, hence it
was decided to examine load line displacement rates as a possible
governing parameter in creep crack growth. These data for all tests
are presented in Figures 122 through 143. As before, the data are
re-plotted for groups of each thickness in Figures 144 through 148. A
final plot showing a single curve for each thickness group is shown in
Figure 149. For comparison purposes, the actual data for the 7/32 inch
(6 mm) group are included along with its single curve in the figure.
It is seen that within a narrow range of crack growth rates, 7/32 inch
(6 mm) and 11/32 inch (9 mm) data show a lower and next to lower crack
growth rate.

6. A SCHEME FOR CALCULATING THE C*-INTEGRAL

From the definition of C*, it is obvious that C* cannot be calculated
from the results of a single test. Four tests at each thickness were

used to evaluate C*, each test corresponding to a different value of load and hence, different values of $\dot{\delta}$ for each crack length. A scheme was devised to obtain C* for constant load tests, similar to that of Landes and Begley for constant $\dot{\delta}$ tests. The data reduction scheme is outlined in Figure 150 where the various steps are shown schematically. In (a) (Figure 150), pairs of $(a_i, \dot{\delta}_i)$ at times, t_i, are plotted for each test to give curves of load vs. displacement rate. The areas under these curves give

$$\dot{U} = \int P d\dot{\delta} \qquad (106)$$

Therefore, it was necessary to determine a lower limit for the value of stress intensity at which cracks just start to grow. In order to ascertain what load governed this initial point for a given geometry, a 15/32 inch (12 mm) compact tension specimen was tested at 1350°F (732.2°C) at decreasing loads corresponding to initial stress intensities of 15,000, 10,000, and 8,000 psi-inch$^{1/2}$ (16.5, 11.0 and 8.8 MPa·m$^{1/2}$). At an initial K of 8,000 psi-inch $^{1/2}$ (8.8 MPa·m$^{1/2}$), no nonrecoverable crack growth nor load line displacement was observed over a five-day period. This value was used as a growth-limiting stress intensity for all thicknesses tested. An initial load, P_o, associated with each specimen's initial crack length at t = 0 was calculated as a lower bound of integration in the determination of $\dot{U}$. The area under each curve was integrated using a HP9820A table top calculator with plotter and digitizer. The form of the results for each test are shown in (b) (Figure 150), where $\dot{U}/B$ was plotted against $\dot{\delta}$ to give a family of curves at constant crack lengths.

For a set of selected $\dot{\delta}$, values of $\dot{U}/B$ for the curves in (b) are re-plotted for each crack length (c) (Figure 150). These curves are readily fitted to a straight line for the family of $\dot{\delta}$ curves. The negative of the slopes of the curves in (c) gives a set of C* values, over the range of $\dot{\delta}$. In (d) (Figure 150), the displacement rate data must be re-plotted against crack growth rate for each test. The $\dot{\delta}$ values were the same as used in (c). Crack growth rates were obtained through the intermediate plot, (e), using plots of crack length versus

crack length rate for each test where each crack length at a given time corresponded to the discrete value of $\dot{\delta}$. Using values of $\dot{\delta}$ associated with the C* determined in (c), a corresponding value of $\dot{a}$ was obtained for each load, P, giving pairs of values $(P,\dot{a})$ for each C*. The data assembled in a matrix takes the form:

$$
\begin{array}{c|cccc}
 & \dot{\delta}_1 & \dot{\delta}_2 & \dot{\delta}_3 & \dot{\delta}_4 \\
\hline
P_1 & a_{11} & a_{12} & a_{13} & a_{14} \\
P_2 & a_{21} & a_{22} & a_{23} & a_{24} \\
P_3 & a_{31} & a_{32} & a_{33} & a_{34} \\
P_4 & a_{41} & a_{42} & a_{43} & a_{44} \\
\hline
 & C^*_1 & C^*_2 & C^*_3 & C^*_4
\end{array}
$$

The last step (f) (Figure 150), plots crack growth rate versus C*. The actual results for C* versus $\dot{a}$ are presented in Figures 151 through 155 for the CT specimens for each thickness group. Finally, a straight line was drawn through each thickness group to represent that group by a single curve and these curves for the five thicknesses are shown in Figure 156. The actual data points calculated for the 7/32 inch (6 mm) group are plotted on the figure to provide guidance as to the effects of scatter. It is noted that the C* calculation required the use of data from several different tests and incorporated the statistical variation from test to test into the calculation. Thus, one single test may tend to bias the data even though many smoothing operations were performed in plotting, re-plotting, and cross-plotting the data to obtain C*. There appears to be no statistically significant deviation from crack growth rate with thickness in Figure 156.

The data from the ring tests were used to evaluate C*. It was noticed that by following the scheme for evaluating C* (Figure 150)

that values of C* would be negative. This was due to the load line
displacement rate which for the case of the ring results, was a decreas-
ing function in time and crack length. Therefore, C* does not provide
a means of correlating creep crack growth rate data as obtained from the
cracked ring geometry. Since the analytical derivation of C* is based
on a creeping solid and does not consider elastic strains or strain rates
in the body, a structure such as a cracked ring which is quite stiff is
poorly represented by such a model. Thus, the C* parameter cannot be
expected to provide a measure of creep crack growth rate when it is
obtained experimentally from load line displacements in a relatively
rigid and statically indeterminate structural configuration.

7. THE CRACK DRIVING FORCE, $\overline{\mathcal{G}}$, AS A CORRELATING PARAMETER

The use of a crack driving force, $\overline{\mathcal{G}}$, was investigated as a possible
parameter to characterize creep crack growth rates for both the compact
tension and the ring specimens. This energy dissipation function, $\overline{\mathcal{G}}$,
is related to complementary stored elastic energy and to the inelastic
energy available in creating new crack surfaces (Equation 99). The nature
of the parameter is such that two extremes of driving energy can be inves-
tigated experimentally to determine whether all of the inelastic energy
available in the test specimen goes into deforming the specimen and not
directly into growing the crack, in which case $\mathcal{G}$, which is equivalent to
K, governs, or whether all of the inelastic energy goes directly into
driving the crack in which case $\overline{\mathcal{G}}$, is the governing crack growth para-
meter.

Crack growth rates for each of the compact tension specimens
measured against the crack driving force, $\mathcal{G}$, is presented in Figures
157 through 178. It is seen that the shape of these curves for the CT
specimens are the same as those in the plots of da/dt versus K for the
same compact tension specimens (Figures 66 through 87) which demonstrates
the equivalency of $\mathcal{G}$ and K for a linear elastic material. These data
are re-plotted in Figures 179 through 183 for groups of specimens of the

same thickness. This allowed for a single curve to be drawn through each set of data for each thickness and the resulting plot of those curves, one for each thickness group, is presented in Figure 184. It is seen that the curve for the 7/32 inch (6 mm) thick group of compact tension specimens is apart from the others and as in the case of the da/dt versus K results (Figure 93), a thickness effect appears to be relevant for the thinnest group showing lower crack growth rates.

To investigate $\overline{\mathcal{G}}$ as a governing parameter, the same crack growth rate data were plotted against $\overline{\mathcal{G}}$ for the compact tension specimens in Figures 185 through 206. These curves are essentially the same as those for $\mathcal{G}$ in Figures 157 through 178 except that each curve is translated to the right on the abscissa in the direction of higher energy, for the same values of crack growth rate. These data are replotted in Figures 207 through 211 for groups of CT specimens of the same thickness and a single curve for each thickness group is presented in Figure 220.

The ring data for da/dt versus $\mathcal{G}$ are presented in Figures 213 through 219 and for $\overline{\mathcal{G}}$ in Figures 221 through 227. $\mathcal{G}$ and $\overline{\mathcal{G}}$ are constant for each ring specimen as seen in the figures. For the case of $\mathcal{G}$, this result is expected whereas $\mathcal{G}$ is equivalent to K and the ring solution is for constant stress intensity over the range of crack growth investigated. However, the shape of the $\overline{\mathcal{G}}$ curve depends on the assumed relationship between the compliance and the load line deflection. In this study, this relation was assumed to be linear (Equation 27). This means that for each incremental increase of crack growth from a crack of length a to length a+da, the relative increase of each incremental deflection due to elastic and inelastic deformation in the specimen is proportional in the same ratio.

The results for $\mathcal{G}$ for only the 8/32 inch (6 mm) thick ring tests are re-plotted in Figure 220 and re-plotted for $\overline{\mathcal{G}}$ in Figure 228. On each of these two figures for $\mathcal{G}$ and $\overline{\mathcal{G}}$, the curves for $\mathcal{G}$ and $\overline{\mathcal{G}}$ for the comparable thickness of compact tension specimen (7/32 inch) (6 mm)

are superimposed respectively. If one were to compare the results for $\mathcal{G}$ between the CT and ring specimen tests with those for $\overline{\mathcal{G}}$, it could be said that $\overline{\mathcal{G}}$ correlates better as a crack growth parameter than $\mathcal{G}$. Whereas $\mathcal{G}$ for the 7/32 inch (6 mm) CT tests correlates with the bottom parts of the 8/32 inch thick ring results as seen on Figure 228, it is suggested that $\overline{\mathcal{G}}$ is possibly a good correlating parameter for describing creep crack growth for more than just one geometry of material. It was already discussed that initial crack growth rates for the CT specimens were high and decreased until the steady state curve represented by $\mathcal{G}$ in Figures 220 and by $\overline{\mathcal{G}}$ in Figure 228 was reached. The vertical lines representing the results for the 8/32 inch rings in Figure 228 repeats the same phenomenon, that is, an initially high crack growth rate is shown which then decreases as the crack grows. This "check mark" effect on K curves for the CT specimen tests, indicates that for steady state conditions of crack growth, the $\overline{\mathcal{G}}$ curve for the 7/32 inch CT results and the lowest parts of the 8/32 ring curves show fairly good correlation. Therefore, it is apparent that the inelastic energy available for both crack extension and global deformation of the specimen is indeed all going into growing the crack. The results for $\mathcal{G}$ do not seem to correlate the two geometries in this fashion and hence $\mathcal{G}$ is not seen to be a good correlating parameter considering that a linear elastic material is assumed for the $\mathcal{G}$ calculations. The mechanisms of creep crack growth are extremely complex and apparently beyond the scope of applicability of K and $\mathcal{G}$ to adequately describe a crack growth law which does not take a three-dimensional stress field into consideration.

SECTION V

CONCLUSIONS

Sustained load crack growth in IN-100 is a highly complex phenomenon. The triaxiality of the crack tip stress and strain fields in creep crack growth is demonstrated by crack tunneling which is characteristic of fracture in this material under constant load at 1350°F. It was shown how cracks appear to grow first at the center of specimen fracture surfaces, tunnel into the material until the crack face intersects the edge surfaces, and then grow at a stable rate until a critical stress intensity value is reached and the growth becomes unstable. An approach was developed herein by which various fracture mechanics parameters could be studied as possible correlating parameters for creep crack growth. In addition to these correlative parametric investigations, the effect of thickness on the plane strain yielding of the crack tip and on stable creep crack growth was also researched using two geometries; the standard compact tension specimen and the cracked full ring in tensile loading. It is noted that although the phenomenon of creep crack growth has been observed in modern times for well over a century, there is yet no adequate mathematical model which admits for even a two-dimensional analysis of the creeping crack under the assumptions of linear elastic behavior. It is further noted that research in the area of understanding creep phenomena has been invariably empirical in the approach and that experimental observations have preceded analytical modeling and the creep laws upon which they were based.

The approach to a better understanding of the creep behavior in a structural alloy typically found in aircraft jet engines has resulted in three major contributions to further research in this area. Firstly, the development and analysis of an effective crack length is demonstrated. Surface crack measurements are misleading in materials where creep behavior is characterized by tunneling. But also, it is shown herein that in addition to crack tunneling, there is significant ductile edge zone cracking on both sides of the more brittle-behaving centerline tunneled crack. It is seen that an effective crack length can be a

better measure of a value of crack length that could hypothetically
characterize the stress field at the crack tip, even though it is still
not an adequate indicator in the absolute sense of the damage surface
location. Toward that end, the method of compliance is adopted herein
whereby an effective modulus of elasticity is calculated for all tests
based on the measured compliance asscciated with the essentially straight
fatigued pre-crack at 1350°F. The superiority of this approach negates
a reliance in analysis on assumptions of strictly plane stress or plane
strain fracture toughness. The effective modulus of elasticity was found
to lie between values of E for plane stress and $E/(1-\nu^2)$ for plane strain
for all tests. Table 4 lists these values for the compact tension speci-
mens.

It was found that the sustained load fracture surfaces exhibited
ductile fracture behavior in zones which lay between the centrally
tunneled fracture region and the edges of the fracture specimen. This
behavior is discussed in Section IV. It is seen that these side zones
increased in width for greater crack lengths. Creep crack growth is
also characterized in this material by "fingers" extending ahead of the
crack zone. Higher crack growth rates associated with more brittle
fracture behavior at the center of the specimen is characterized by
the phenomena of tunneling and vertical fracture planes along the "fin-
gers". Much work remains to be done to further characterize the damage
surface under this three-dimensional cracking process.

For all the compact tension tests, it is shown that a single
straight line can be reasonably fit to the data of compliance versus
load line displacement within experimental scatter (Figure 8). What
this implies is that for every increment of crack length, there is an
increase in load line displacement due to the growth of the crack from
the elastic deformations of the material and an additional inelastic
displacement due to nonlinear and time-dependent material behavior.
Each increment of inelastic displacement appears to be proportional to
the elastic component of the load line displacement for an increment
of crack growth.

It is shown that crack growth rates reasonably correlate with stress
intensity factors for stable creep crack growth. The initial growth
region is characterized by initially high crack growth rates which
decrease in time until stable creeping conditions are achieved. The
mechanisms attending to this phenomenon are discussed in Section IV.
Thickness effects were evident only for 7/32 inch thick compact tension
specimen results which exhibited lower crack growth rates than for
thicker specimens. Considerable scatter in test results attended all
test results.

A second significant contribution of this technical effort is the
scheme proposed and developed for the determination of the C*-integral
parameter using load line displacement data generated under constant
load. The rationale for the investigation of this parameter as a better
descriptor of the crack tip region is predicated upon the postulation
that high temperature creep behavior is not typically linearly elastic.
It is reasonable to assume that in applying C* to correlate creep crack
growth that the material is behaving according to a law which governs
steady state creep crack growth. It has been pointed out herein that
since the C*-integral is a path-independent energy rate line integral,
the assumption of it's suitability as a creep crack correlating para-
meter must apply not only to the crack tip area but to all points in the
specimen. The scheme used in this analysis was developed to uniquely
deal with the interpretation of the test data based on integration of
the load-displacement diagrams developed for each thickness group of
compact tension specimens. C* is directly based upon these results
and the scheme requires that the integration be performed at either
constant load line displacement rate or at constant load. In the
former case, the pseudo-potential energy is used and in the latter,
the complementary energy. For computational purposes, either approach
leads to the same result. The method employed herein was based on the
evaluation of C* for constant values of load line displacement rate.
The constant factor in these tests is the constant load used to gener-
ate the load line displacement data. Landes and Begley's (Reference 28)

tests were made by holding constant the displacement rate and their scheme
for C* is necessarily different than the one proposed herein in that re-
spect. Irrespective of the scheme used, there does not appear to be any
simple method for automating this procedure on a computer because of the
large amount of interpolation and human judgments necessary for selecting
appropriate values of parameters. Furthermore, a number of tests are
required covering a range of growth rates or displacement rates for each
specimen geometry for a given crack length range. The substantial amount
of experimental scatter from test to test, attributable primarily to
material property variability, makes the procedure for determining C*
very difficult because of the procedural complexities outlined previously.

Finally, the entire concept of an experimentally determined C* must
be questioned. The path independence and the operational definition of
C* is based upon the assumption that the material behavior is that of a
creeping solid throughout the entire specimen. The only strains allow-
able are those due to creep, i.e., from strain rates which depend on
stresses. There are no allowable elastic strains, even far away from
the crack tip. While the creeping solid assumption might be reasonable
in the vicinity of the crack tip, it appears to be unrealistic in the
far field. Thus, the C*-integral as a governing parameter for crack
growth would appear to be valid only if the integral were taken along
a path very close to the crack tip. This eliminates the possibility of
utilizing the operational definition of the C*-integral unless it can be
demonstrated that the far field load line displacements are due primarily
to the creep deformation in the vicinity of the crack tip. From a numeri-
cal computational point of view, this implies that the C*-integral has
to be taken around a path very close to the crack tip. To demonstrate
that the C*-integral is a successful correlating parameter, data should
be analyzed from more than one geometry, where it can be analyzed apart
from other stress field parameters. It is shown herein that for the
cracked fully circular ring geometry, that C* could not be calculated.
This was due to the manner in which energy going into the cracking ring
redistributed such that displacement decreased over time. Because of

the restrictive assumptions on the application of C* to creep crack
growth data, and because of the difficulties in obtaining C* as well
as its failure to categorize crack tip stress and strain fields in a
ring geometry, one has to seriously question the applicability of this
parameter for crack growth behavior predictions in real engineering
applications.

The third contribution of this research is the introduction of the
crack driving force, $\mathcal{G}$, which is defined for the linear elastic creeping
solid. $\mathcal{G}$ appears to correlate creep crack growth for the two geometries
studied. Results show that under the conditions of testing related herein,
the inelastic energy going into the deforming material all goes into driv-
ing the crack. Except for this conclusion which is based on a limited
number of test results, there appears to be no single function able to
correlate crack growth behavior for different geometries. Any function
which increases with crack length can be shown to correlate crack growth
for the compact tension specimen. Three-dimensional effects were not
taken into account in this investigation.

REFERENCES

1. D. E. Macha, "Fatigue Crack Growth Retardation Behavior of IN-100 at Elevated Temperature," Eng. Fract. Mech. Vol. 12, pp. 1-11, 1979.

2. D. E. Macha, A. F. Grandt, and B. J. Wicks, "Effects of Gas Turbine Engine Load Spectrum Variables on Crack Propagation." ASTM Symposium on Effect of Load Spectrum Variables on Fatigue Crack Initiation and Propagation, San Francisco, May 1979.

3. R. M. Wallace, C. G. Annis, Jr. and D. L. Sims, Application of Fracture Mechanics at Elevated Temperatures, AFML-TR-76-176 Part II, April 1977.

4. K. Sadananda and P. Shahinian, "Application of Fracture Mechanics Techniques to High-Temperature Crack Growth," Fracture Mechanics, ed. by Perrone, et al., U. Press of Virginia, 1978.

5. K. M. Nikbin, G. A. Webster, and C. E. Turner, "Relevance of Non-linear Fracture Mechanics to Creep Cracking," Cracks and Fracture, ASTM STP 601, 1976.

6. L. S. Fu, Quasi-Static Crack Growth in Metals at Elevated Temperatures - A Review, AFML-TR-78-136, March 1979.

7. S. Floreen, "The Creep Fracture of Wrought Nickel-Base Alloys by a Fracture Mechanics Approach," Metallurgical Transactions A, Vol. 6A, pp. 1741-1749, 1975.

8. W. J. Mills, "The Room Temperature and Elevated Temperature Fracture Toughness Response of Alloy A-286," J. of Eng. Mat. and Tech, Vol. 100, April 1978.

9. G. Green and J. F. Knott, "On Effects of Thickness on Ductile Crack Growth in Mild Steel," Jour. of Mech. and Phys. of Solids, Vol. 23, 1975.

10. A. J. McEvily and C. H. Wells, "On the Applicability of Fracture Mechanics to Elevated Temperature Design," International Conference on Creep and Fatigue in Elevated Temperature Applications. Philadelphia/Sheffield, Vol. 13, pp. 203.1-203.7, 1973.

11. A. A. Griffith, "The Phenomena of Rupture and Flow in Solids," Philosophical Transactions of the Royal Society, Series A., pp. 163-198, 1921.

12. G. R. Irwin, "Plastic Zone Near a Crack and Fracture Toughness," Proceedings Seventh Sagamore Ordnance Materials Research Conference, Syracuse University, 1960.

13. E. Orowan, "Energy Criteria of Fracture," Welding Research, Supplement, 1955.

REFERENCES (Continued)

14. G. R. Irwin, "Analysis of Stresses and Strains Near the End of a Crack Traversing a Plate," J. Applied Mech., Vol. 24, 1957.

15. B. Gross and J. E. Srawley, NASA Technical Notes; D-2603, January 1965; D-3092, December 1965; and D-3295, February 1966.

16. J. L. Swedlow and T. A. Cruse, "Formulation of Boundary Integral Equations to Elasto-Plastic Flow," International Journal Solids Structures, Vol. 7, pp. 1673-1683, 1971.

17. P. D. Hilton, "Elastic-Plastic Analysis for Cracked Members," Transactions, ASME, Journal Pressure Vessel Technology, Vol. 98, pp. 47-55, 1976.

18. J. L. Swedlow, "Elasto-Plastic Cracked Plates in Plane Strain," International Journal of Fracture Mechanics, Vol. 5, pp. 33-44, 1969.

19. L. S. Fu and S. N. Malik, "The Method of Lines Applied to Crack Problems Including Plasticity Effects," Proceedings, 4th International Conference on Structural Mechanics in Reactor Technology, Vol. G, 1977.

20. J. P. Ayekenyesi and A. Mendelson, "Stress Analysis and Stress Intensity Factors for Finite Geometry Solids Containing Rectangular Surface Cracks," Trans. ASME, J. Applied Mechanics, Vol. 45, 1978.

21. P. C. Paris, in Fatigue, An Interdisciplinary Approach, Syracuse Univ. Press, pp. 107-132, 1964.

22. J. R. Rice, Mathematical Analysis in the Mechanics of Fracture; Vol. II - Fracture, ed. H. Liebowitz, Academic Press, New York, 1968.

23. P. C. Paris and G. C. Sih, "Stress Analysis of Cracks," Fracture Toughness Testing and Its Applications, ASTM STP 381, 1965.

24. A. M. Freudenthal, "Fatigue and Fracture Mechanics," Inst. for the Study of Fatigue, Fracture and Structural Reliability Technical Rep. 11, Geo. Wash. Univ, May 1972 (also presented at Symp. on Fracture and Fatigue, GWU, May 3-5, 1972).

25. H. Reidel, "A Dugdale Model for Crack Opening and Crack Growth Under Creep Conditions; Mat. Sci. Eng., Vol. 30, 1977.

26. K. Sadananda and P. Shahinian, "Creep Crack Growth in Alloy 718, "Met. Trans. A., Vol. 8A, March 1977.

REFERENCES (Continued)

27. J.R. Haigh, "The Mechanisms of Macroscopic High Temperature Crack Growth, Parts I and II," Materials Science and Eng., Vol. 20, pp 213-235, 1975.

28. J.D. Landes and J.A. Begley, "A Fracture Mechanics Approach to Creep Crack Growth," Mechanics of Crack Growth, ASTM STP 590, pp. 128-148, 1975.

29. C.B. Harrison and G.N. Sandor, "High Temperature Crack Growth in Low Cycle Fatigue," Eng. Fract. Mech., Vol. 3, 1971.

30. A. A. Wells, "Proceedings of the Crack Propagation Symposium," (Cranfield, England), Vol. 1, p. 210. College of Aeronautics, Cranfield.

31. F.A. McClintock, "Local Criteria for Ductile Fracture," Int. J. Fracture Mech., Vol. 4, p. 101, 1968

32. F.M. Burdekin and D.E.W. Stone, "The Crack Opening Displacement Approach to Fracture Mechanics in Yielding Materials," J. of Strain Analysis, Vol. 1, pp. 145-153, January 1966.

33. D.S. Dugdale, "Yielding of Steel Sheets Containing Slits," Journal of Mechanics of Physics of Solids, Vol. 8, 1960.

34. J.R. Rice, "Elastic-Plastic Fracture Mechanics," The Mechanics of Fracture, ASME, AMD - Vol. 19, ed. F. Erdogen, pp. 23-53, 1976.

35. J.D. Eshelby, "Energy Relations and the Energy-Momentum Tensor in Continuum Mechanics," Inelastic Behavior of Solids, ed. M.F. Kanninen, et al, McGraw-Hill, pp. 77-115, 1970.

36. H.P. Van Leeuwen, "The Application of Fracture Mechanics to Creep Crack Growth," Engineering Fracture Mechanics, Vol. 9, pp. 951-974, 1977.

37. R.D. Nicholson, "The Effect of Temperature on Creep Crack Propagation in AISI 316 Stainless Steel," Materials Science Eng., Vol. 22, pp. 1-6, 1976.

38. S. Taira and R. Ohtani, "Creep Crack Propagation and Creep Rupture of Notched Specimens," Int. Conf. on Creep and Fatigue in Elevated Temperature Applications, Philadelphia, 1973 and Sheffield, 1974.

39. R.D. Townsend, "The Effect of Structure on the Creep Properties of Low Alloy, Ferritic Steels," CEGB Report RD/L/R, 1971, GEGB, U.K.

REFERENCES (Continued)

40. J.A. Williams and A.T. Price, "A Description of Crack Growth from Defects Under Creep Conditions," Trans. ASME, J. Eng. Materials and Tech., Vol. 97, pp. 214-222, July 1975.

41. J.T. Barnby, "Crack Tip Stresses Under Creep Conditions," Eng. Fracture Mechanics, Vol. 6, pp. 627-630, 1974.

42. J.T. Barnby, "Crack Propagation During Steady State Creep," Eng. Fracture Mechanics, Vol. 7, pp. 299-304, 1975.

43. N.J. Hoff, Q. Applications Math, Vol. 12, p. 49, 1954.

44. K.C. To, "Phenomenological Theory of Sub-Critical Creep Crack Growth Under Constant Loading in an Inert Environment," Int. J. Fracture, Vol. 11, pp. 641-648, 1975.

45. L.M. Kachanov, "On Rupture Time Under Conditions of Creep," Izv. Akad., USSR, Otd. Teckn. Nauk, No. 8, pp. 26-31, 1958.

46. M.J. Siverns and T.A. Price, "Crack Propagation Under Creep Conditions in a Quenched 2-1/4 Chromium 1 Molybdenum Steel," Int. J. Fracture, Vol. 9, pp. 199-207, 1973.

47. S. Purushothaman and J.K. Tien, "A Theory of Creep Crack Growth," Scripta Metall., Vol. 10, pp. 663-666, 1976.

48. H.P. Van Leeuwen, "Relating Rupture Time to Minimum Creep Rate and Ductility," NLR Report M, 2112, February 1966.

49. N.L. Goldman and J.W. Hutchinson, "Fully Plastic Crack Problems: The Center-Cracked Strip Under Plane Strain," Rep. DEAP A-7, Harvard Univ., 1974.

50. J.W. Hutchinson, "Singular Behavior at the End of a Tensile Crack in a Hardening Material," J. Mech. Phys. Solids, Vol. 16, pp. 13-31, 1968.

51. G.N. Webster, "The Application of Fracture Mechanics to Creep Cracking," Conf. on Mechanics and Physics of Fracture, Institute of Physics, England, 1975.

52. M.P. Harper and E.G. Ellison, "The Use of the C*-Parameter in Predicting Creep Crack Propagation Rates," J. Strain Analysis, Vol. 12, No. 3, pp. 167-179, 1977.

53. D.J.F. Ewing and C.E. Richards, "The Yield Point Loads of Singly-Notched Pin-Loaded Tensile Strips," J. Mech. Phys. Solids, Vol. 22, (1), pp. 27-36, 1974.

REFERENCES (Continued)

54. J.R. Haigh and C.E. Richards, "Yield Point Loads and Compliance Functions of Fracture Mechanics Specimens," C.E.G.B./C.E.R.L. Report RD/L/M461, 1974.

55. V. Vitek, "A Theory of the Initiation of Creep Crack Growth," Int. J. of Fracture, Vol. 13, pp. 39-50, 1977.

56. B.A. Bilby, A.H. Cotrell, and K.H. Swinden, Proc. Royal Society A272, p. 304, 1963.

57. V. Vitek, "Computer Simulation of the Development of Plastic Zone Ahead of a Crack Under Creep Conditions," Nucl. Metall, Vol.20, Pt. 1-2, 1976; Proc. Conf. on Computer Simulation for Materials Applications, Maryland, 1976, Part 2, pp. 909-916, 1976.

58. R.T. Bubsey, D.M. Fisher, M.H. Jones, and J.E. Srawley, "Compliance Measurements," Experimental Techniques in Fracture Mechanics, SESA Monograph No. 1, pp. 76-95, 1973.

59. G.R. Irwin and J.A. Kies, "Critical Energy Rate Analysis of Fracture Strength," Weld. Journal (Res. Supp.), Vol. 33, 1954.

60. "Standard Test Method for Plane-Strain Fracture Toughness of Metallic Materials," ASTM E399-78.

61. J.E. Srawley, "Wide Range Stress Intensity Factor Expressions for ASTM E399 Standard Fracture Toughness Specimens," Int. J. Fract., Vol. 12, 1976.

62. T.J. Rudolphi, An Integral-Equation Solution for a Bounded Elastic Body With an Edge Crack: Mode I Deformations, AFML-TR-78-113, July 1978.

63. T.J. Rudolphi, unpublished.

64. A.F. Grandt Jr., "Evaluation of a Cracked Ring Specimen for Fatigue Testing Under Constant Range in Stress Intensity Factor," Fract. Mech. and Tech: Vol. I, ed. G.C.Sih and C.L. Chow. Sijthoff and Noordhoff, 1977.

65. J. Ahmad, "Constant K_I Fracture Toughness Test Specimens," to be published.

66. J. Ahmad, private communication.

67. J.R. Rice, "An Examination of the Fracture Mechanics Energy Balance from the Point of View of Continuum Mechanics," Proc. First Int. Conf. on Fracture, Vol. 1, Sendai, Japan, 1965.

REFERENCES (Concluded)

68. G.R. Irwin, "Fracture", Handbuch der Physik, Springer, Berlin, Vol. 6, 1958.

69. J. Eftis, D.L. Jones and H. Liebowitz, "On Fracture Toughness in the Nonlinear Range," Eng. Fracture Mechanics, Vol. 7, pp. 491-503, 1975.

70. W.J. Mills, L.A. James, and J.A. Williams, "A Technique for Measuring Load-Line Displacements of Compact Ductile Fracture Toughness Specimens at Elevated Temperatures," J. of Testing and Evaluation, Vol. 5, No. 6, pp. 446-451, November 1977.

71. J.D. Boyd, "Stress-Corrosion Cracking of Ti-8Al-1Mo-1V in Aqueous Environments: 2. Plastic Zones, Crack Morphology and Fractography," Met. Trans., Vol. 4, pp. 1037-1045, April 1973.

72. A.F. Grandt Jr., private communication

73. N. Ashbaugh and R. Klinger, private communication.

74. T. Hendriks, to be published.

TABLE 1

SUMMARY OF MECHANICAL PROPERTIES OF IN-100
AT 71°F (22°C) AND AT 1350°F (732°.2C)

71°F	E = 31,000,000 psi
1350°F	E = 26,030,000 psi[a]
	σ_y = 152.000 psi
	σ_u = 164,400 psi
	23% elongation
	30% R.A.

a - average of three tests

TABLE 2

STRESS-RUPTURE PROPERTIES OF IN-100

SPEC. No.	Temp °F	Stress ksi	Life hr.	El. %	R.A. %
C_1	1350	72	92.5	6.6	12.8
C_2	1350	72	109.0	---	---

TABLE 3

IN-100 TEST SCHEDULE - NUMBER OF TESTS PER CONDITION
OF INITIAL NOMINAL STRESS INTENSITY

Thickness	Nominal Initial Stress Intensity, K $ksi - inch^{1/2}$				
CT	23	30	35	40	45
7/32"	--	1	1	1	1
11/32"	--	1	1	2	1
15/32"	--	1	1	1	1
19/32"	--	2	1	1	1
23/32"	--	1	1	--	2
RING					
1/8"	1	1	--	--	1
1/4"	1	1	--	1	1

TABLE 4

SUMMARY OF INITIAL AND FINAL TEST CONDITIONS
ON COMPACT TENSION SPECIMENS OF IN-100

Spec. No. (a)	Thick In.	Load Lbs.	Nominal Init K Ksi√IN	Eff. E x10⁻⁶ Psi (b)	Init a in. (c)	Final a Surface in. (d)	Final a "effect" in. (e)
7-1	.213	1762	35	27.62	.6617		(f)
7-2	.215	1524	30	29.50	.6642	1.234	1.281
7-3	.215	2034	40	26.88	.6637	1.104	1.218
7-4	.215	2280	45	27.42	.6634	0.920	1.075
11-2	.336	3168	40	29.41	.6717	0.988	1.197
11-3	.336	3170	40	26.36	.6702	0.713	0.904
11-4	.338	2788	35	25.00	.6729	1.336	(f)
11-5	.339	2406	30	24.95	.6719	1.104	(f)
11-6	.339	3608	45	31.00	.6709	1.039	1.278
15-2	.462	3784	35	26.68	.7060	1.269	(f)
15-6	.467	3304	30	24.62	.6860	1.261	1.469
15-7	.466	4394	40	26.12	.6810	1.026	1.102
15-8	.466	4942	45	24.55	.6800	0.996	1.101
19-1	.589	4080	35	25.82	.6903	1.266	(f)
19-2	.584	4138	30	28.68	.6866	1.224	(f)
19-3	.592	4220	30	25.39	.6884	1.242	1.375
19-4	.593	5328	40	26.39	.6770	1.032	1.197
19-6	.593	6336	45	24.20	.6833	1.090	1.142
23-1	.712	5886	35	29.54	.7037	1.214	(f)
23-2	.717	5067	30	25.20	.6943	1.270	1.525
23-3	.718	7450	45	25.89	.7217	1.121	1.213
23-4	.718	7760	45	23.76	.6830	0.973	1.091

Notes

(a) First number denotes nominal thickness in 32nds of an inch

(b) At 1350°F (732°.2C)

(c) ASTM 3-point average

(d) Average of both sides of specimen

(e) Based on post-test compliance at room temperature from $a=f-1$ (EBC) using measured compliance at 71°F (22°C)

(f) Fracture surface not tinted

TABLE 5

SUMMARY OF INITIAL AND FINAL TEST CONDITIONS ON RING SPECIMENS OF IN-100

Spec No	Thick In.	Load Lbs.	Nominal init K ksi$\sqrt{in}$	a_{init} in. (a)	δ_{init} mils (b)	$C_i \times 10^{-6}$ in/lb (c)	a_{final} in. (a)	δ_{final} mils (b)	$C_f \times 10^{-6}$ in/lb (c)	Test time min.(d)
8-1	.241	4354	45	.315	10.45	2.40	.674	16.75	3.09	61
8-A	.247	3960	40	.317	9.31	2.35	.695	21.60	3.06	360
8-3	.246	2970	30	.319	7.04	2.37	.612	10.60	2.92	220
8-4	.240	2226	23	.321	5.39	2.42	.619	8.49	3.00	270
4-1	.122	2194	45	.307	10.40	4.76	.603	15.80	5.89	63
4-2	.117	1084	23	.312	5.40	4.97	.571	10.20	6.00	792
4-3	.121	1454	30	.308	7.00	4.79	.583	11.25	5.86	420

(a) ASTM 3-point average

(b) Experimental $\delta_j - (\delta_\ell - \delta_o)$ (See Equation 57)

(c) EBC - $f(a)$

(d) Tests interrupted at these times

73
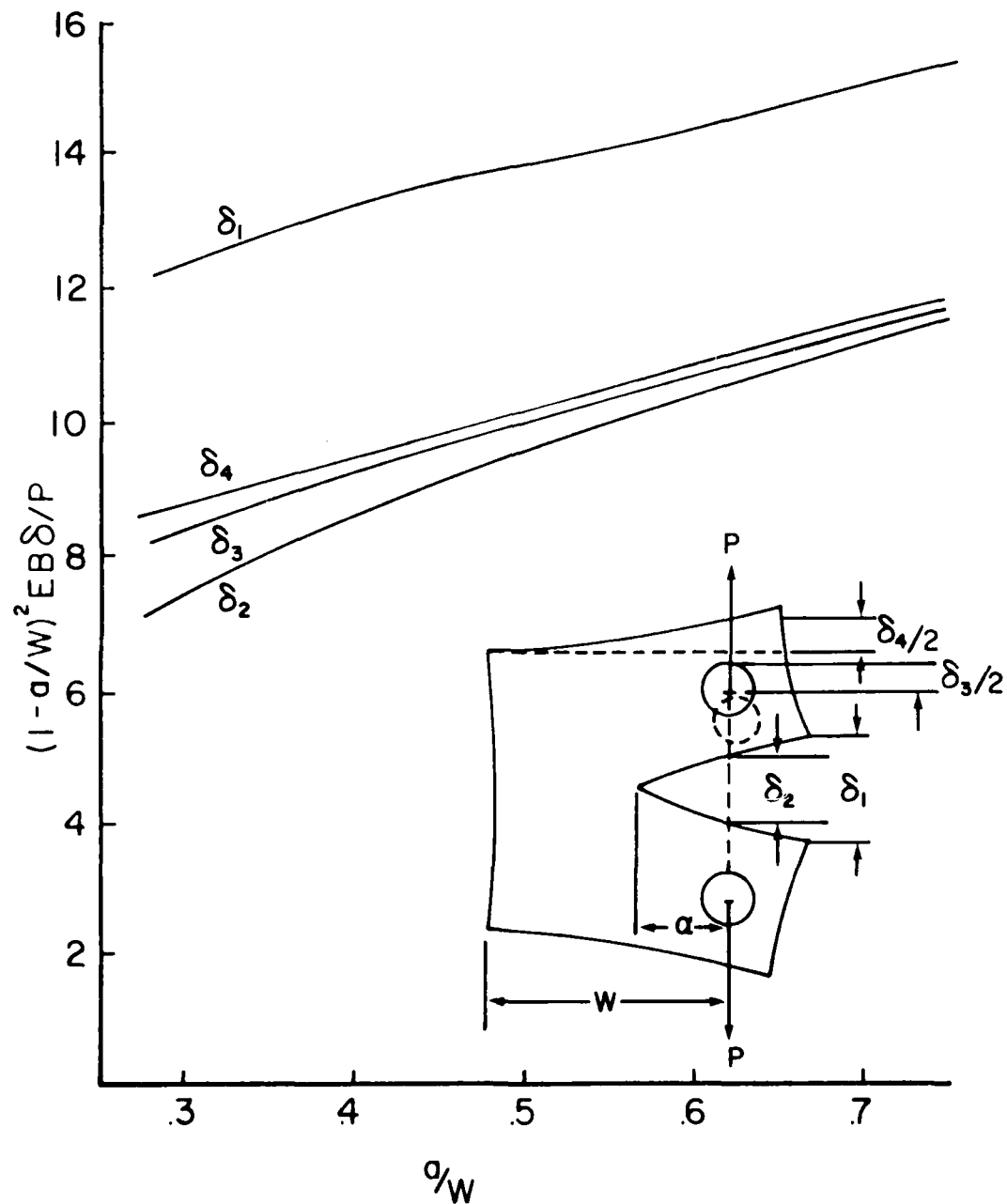
Figure 1. Compliance versus Crack Length Calibration Curve
for the CT Specimen for Four Different Displacement
Locations. (Rudolphi, Reference 41)
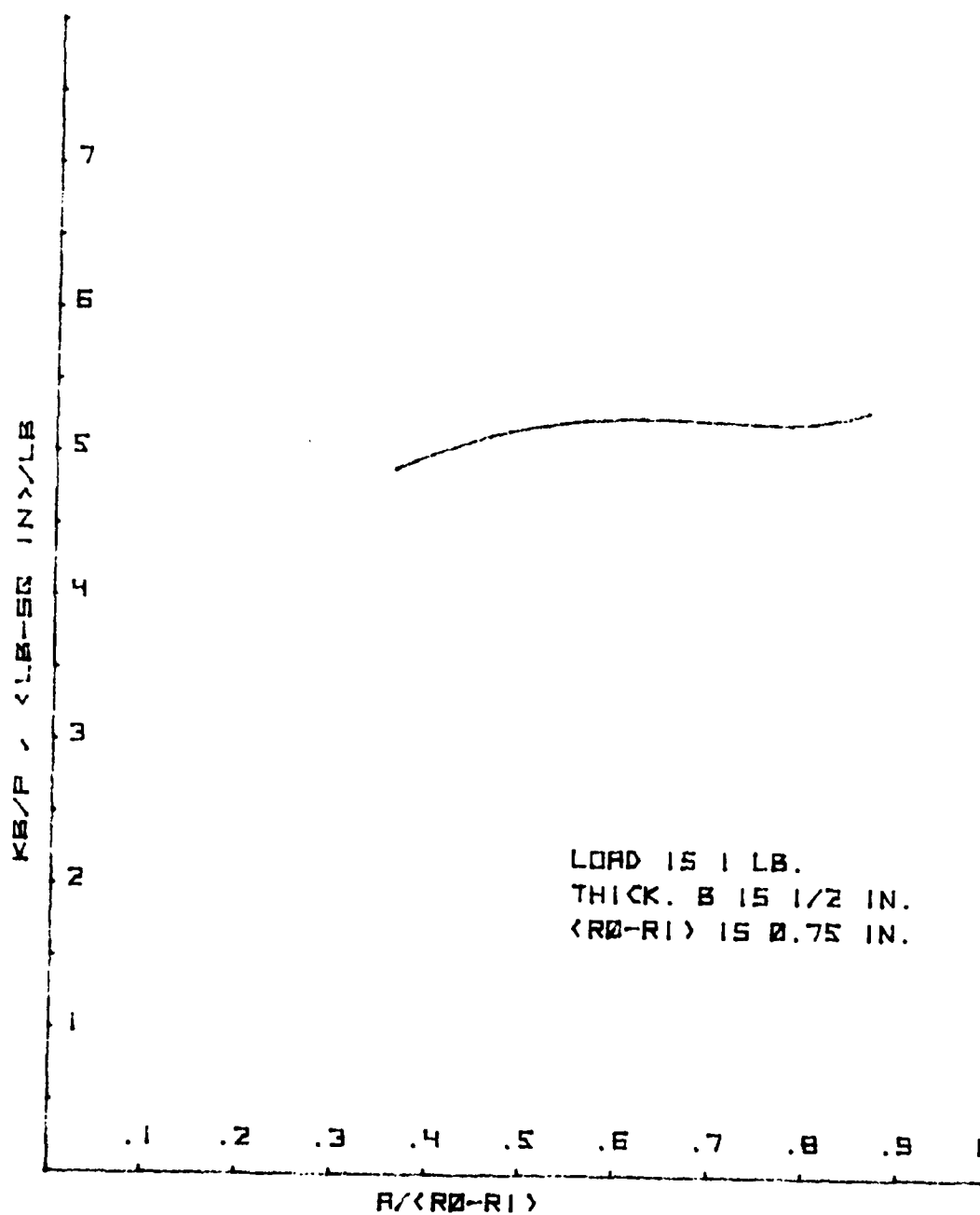
Figure 2. Stress Intensity for Remote Tensile Loading of a
Constant K 0.5 Inch (13 mm) Thick Ring Specimen
(Ahmad, Reference 43)
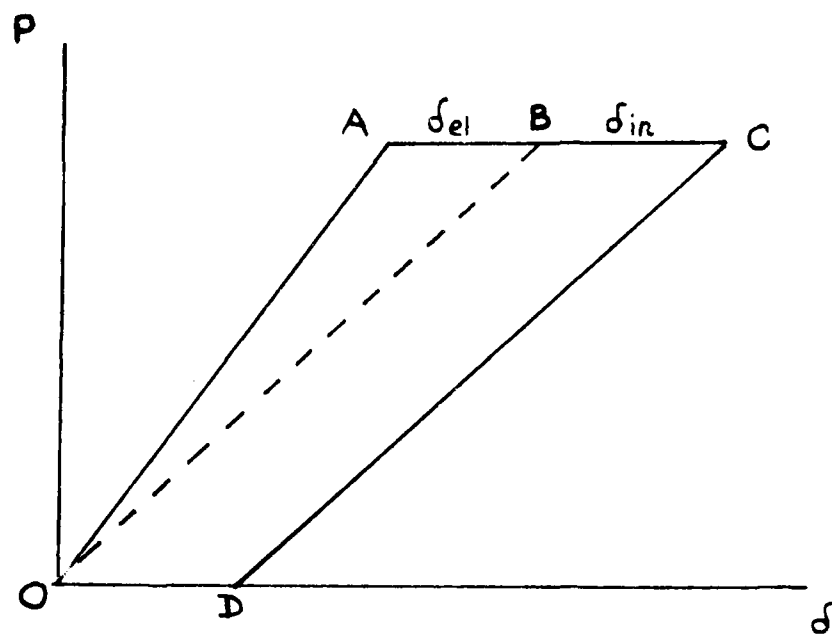
Figure 3.   Load-Displacement Diagram

2 of 4
AD
A100642
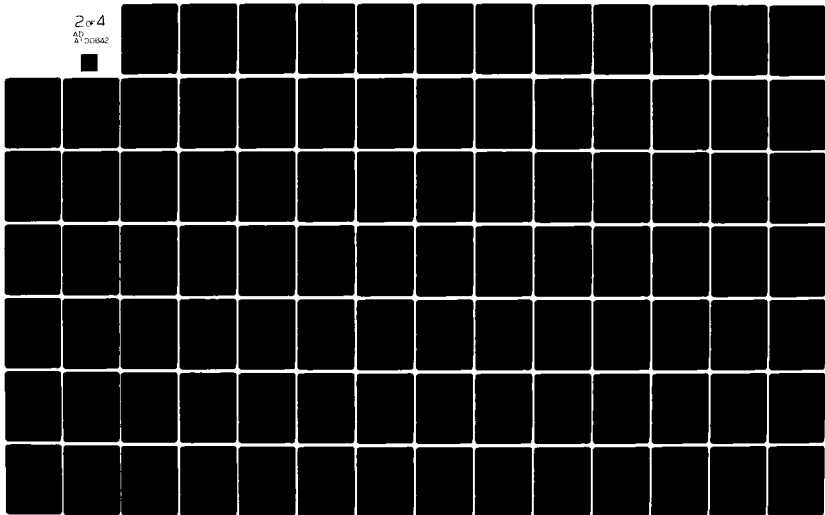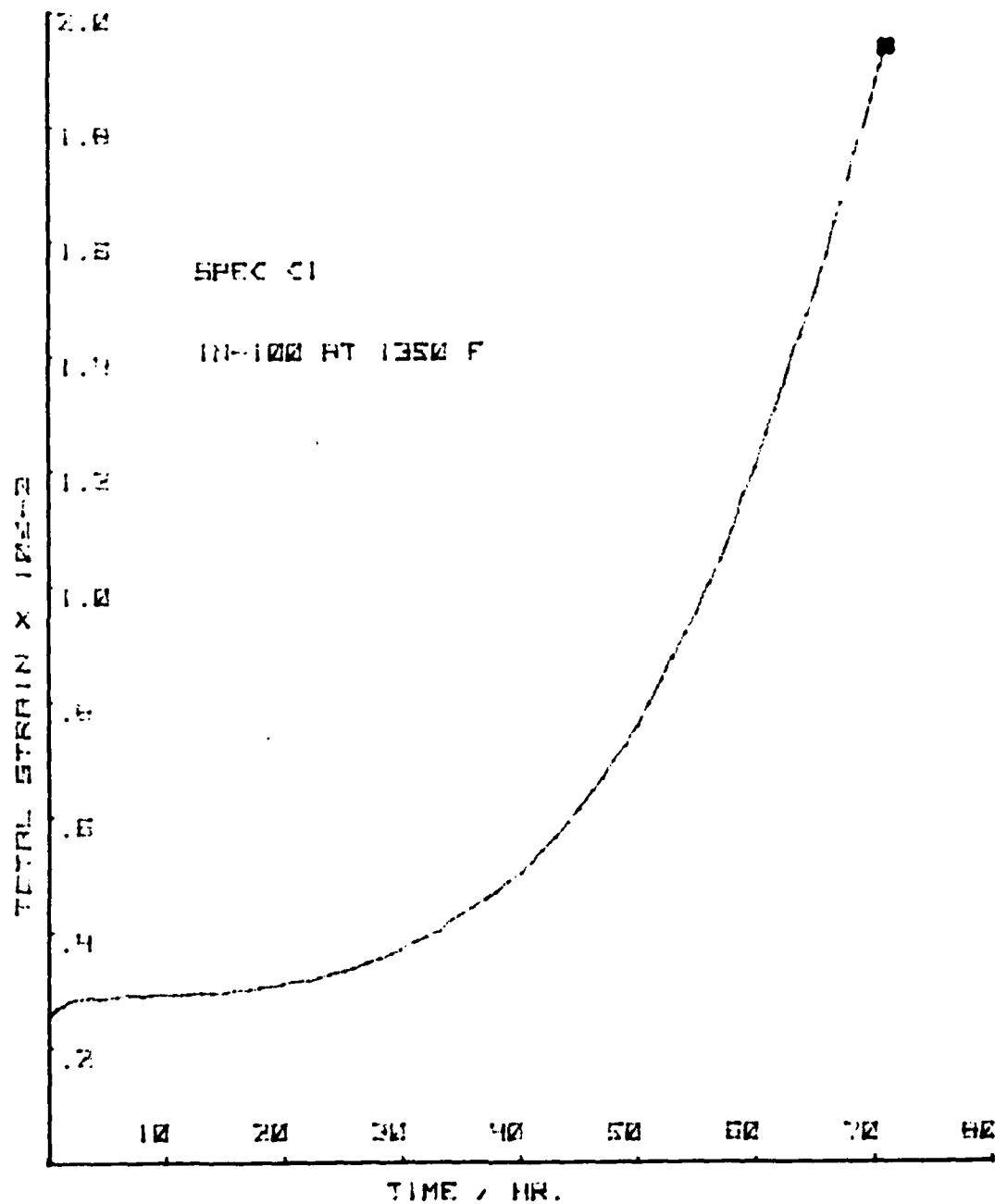
Figure 4.   Creep-Rupture Curve: IN-100 at 72,000 psi
(496.4 MPa) at 1350°F (732° .2C) Over a One Inch
(25 mm) Gage Length
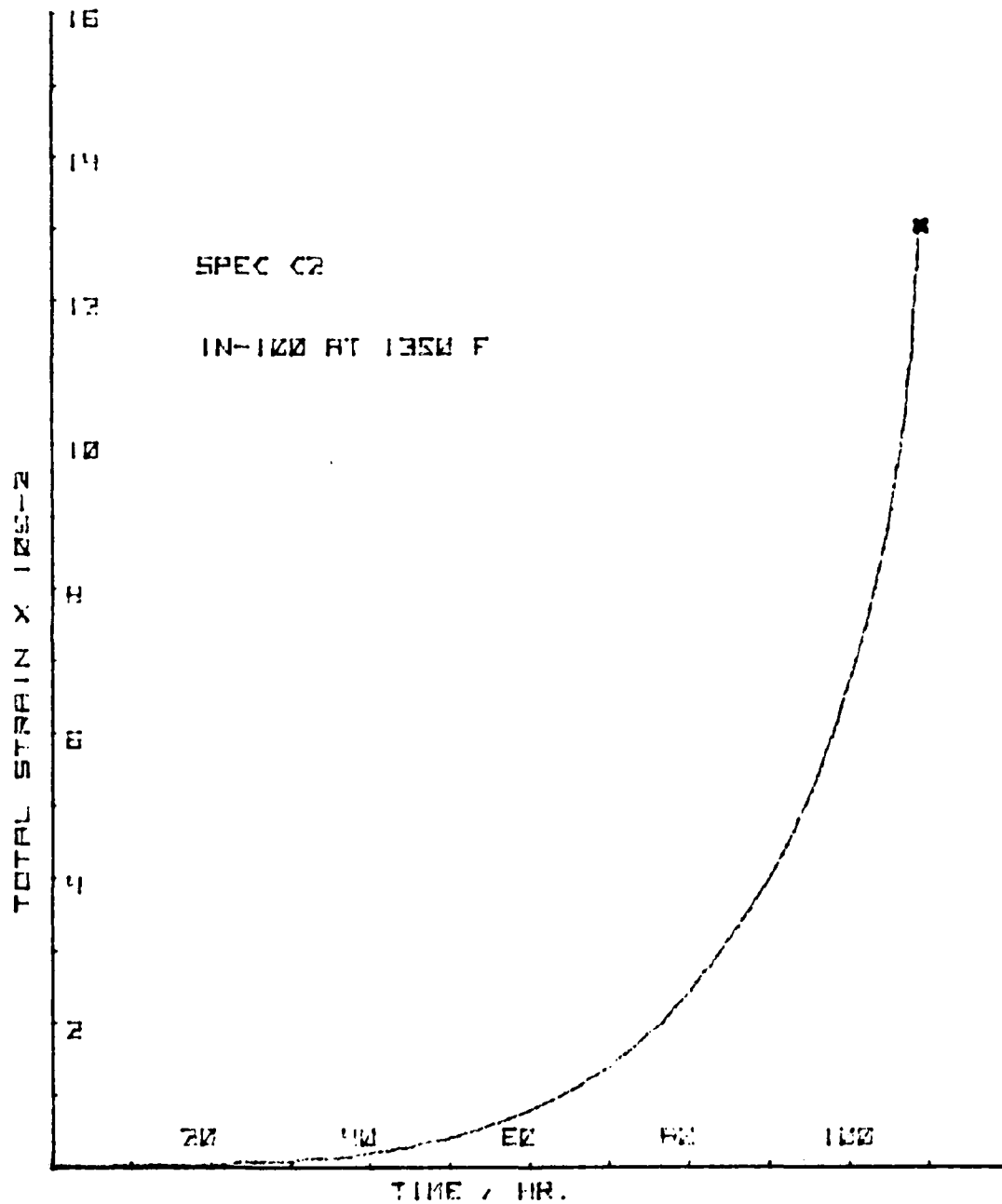
Figure 5.   Creep-Rupture Curve: IN-100 at 72,000 psi
(496.4 MPa) at 1350°F (732° .2C) - Shoulder-to-
Shoulder Gage Length
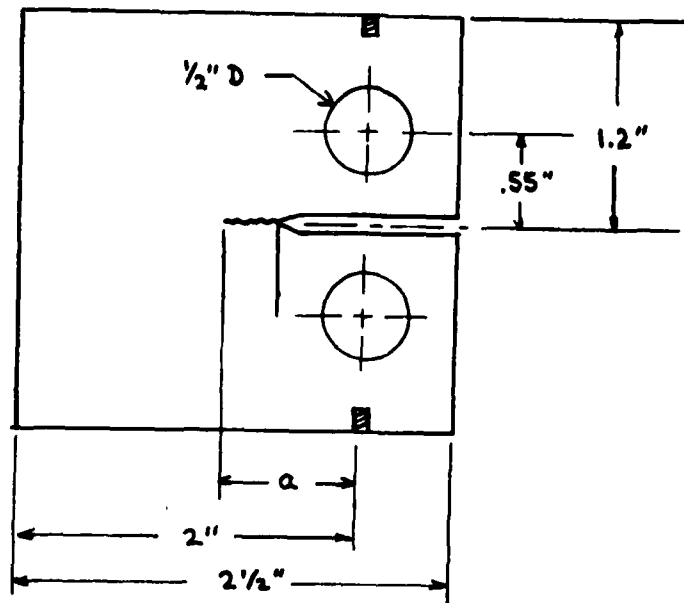
Figure 6.   Standard Compact Tension Specimen
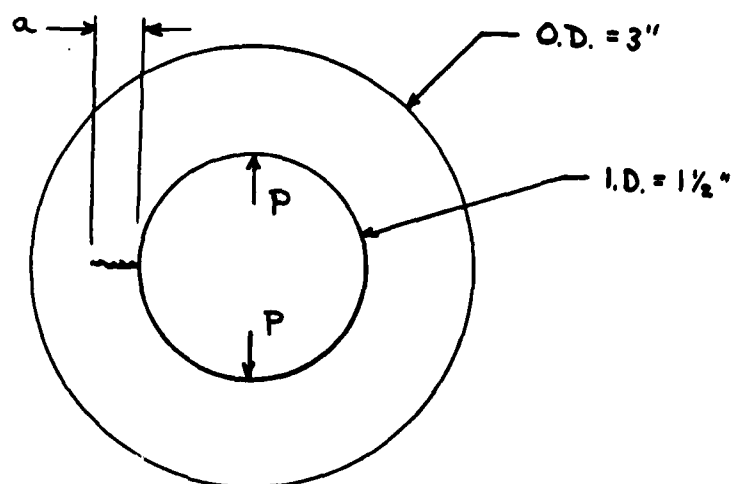
Figure 7.   Constant K Ring Specimen
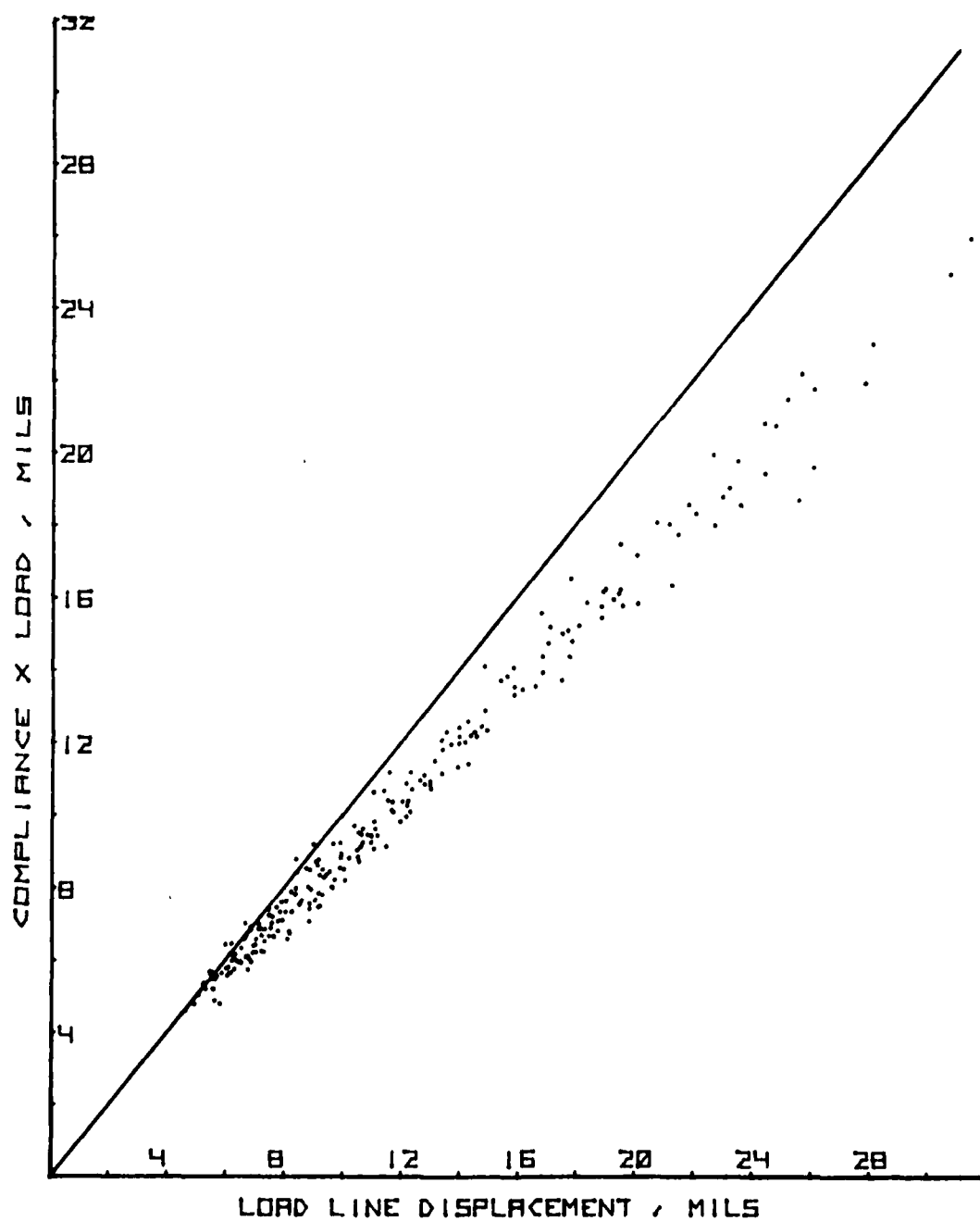
Figure 8.   Plot of Compliance-Load Line Displacement Data for
22 CT Specimens of IN-100
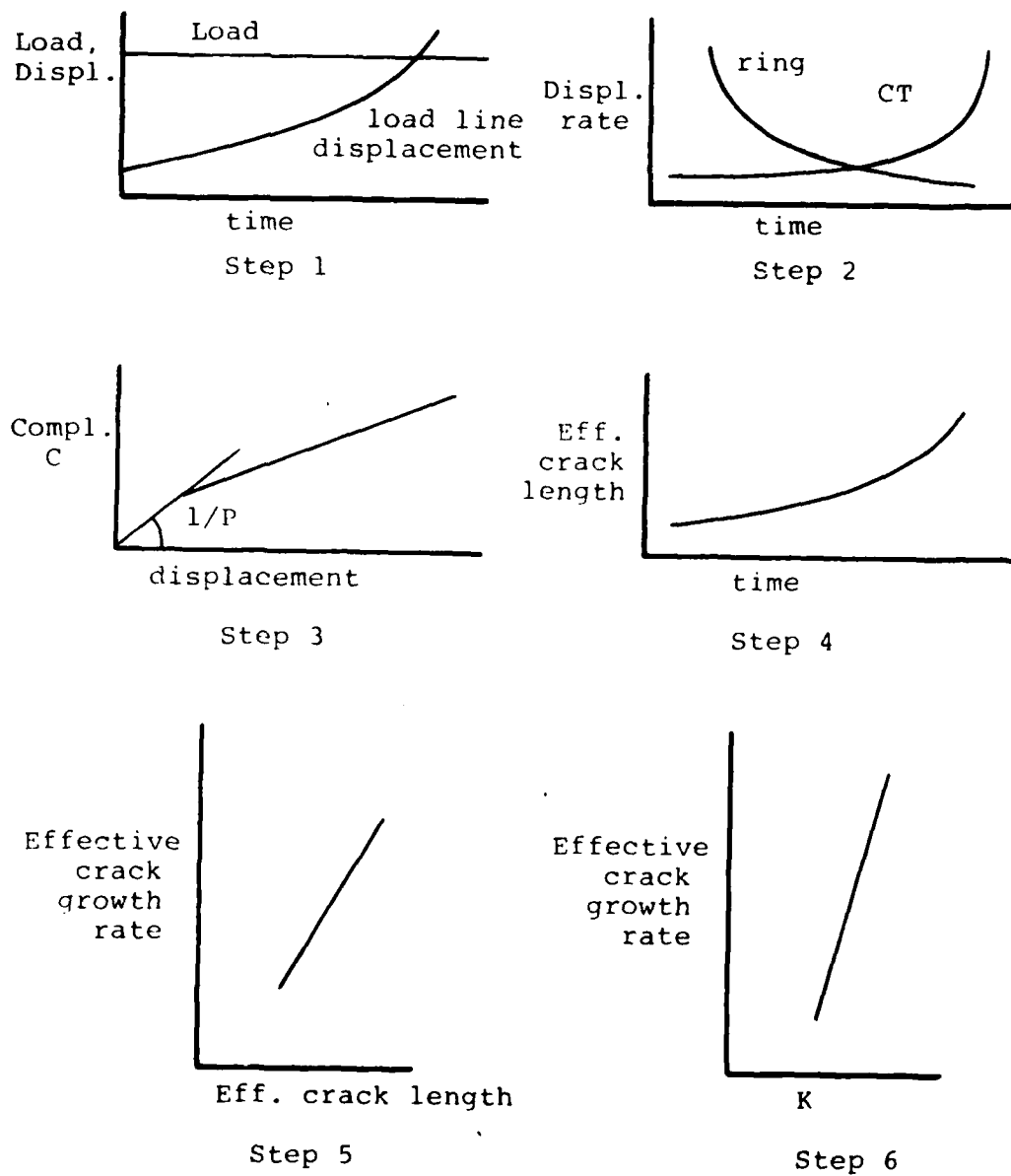
Figure 9.   A Data Reduction Scheme for the Calculation of
Effective Crack Length and Stress Intensity Factor
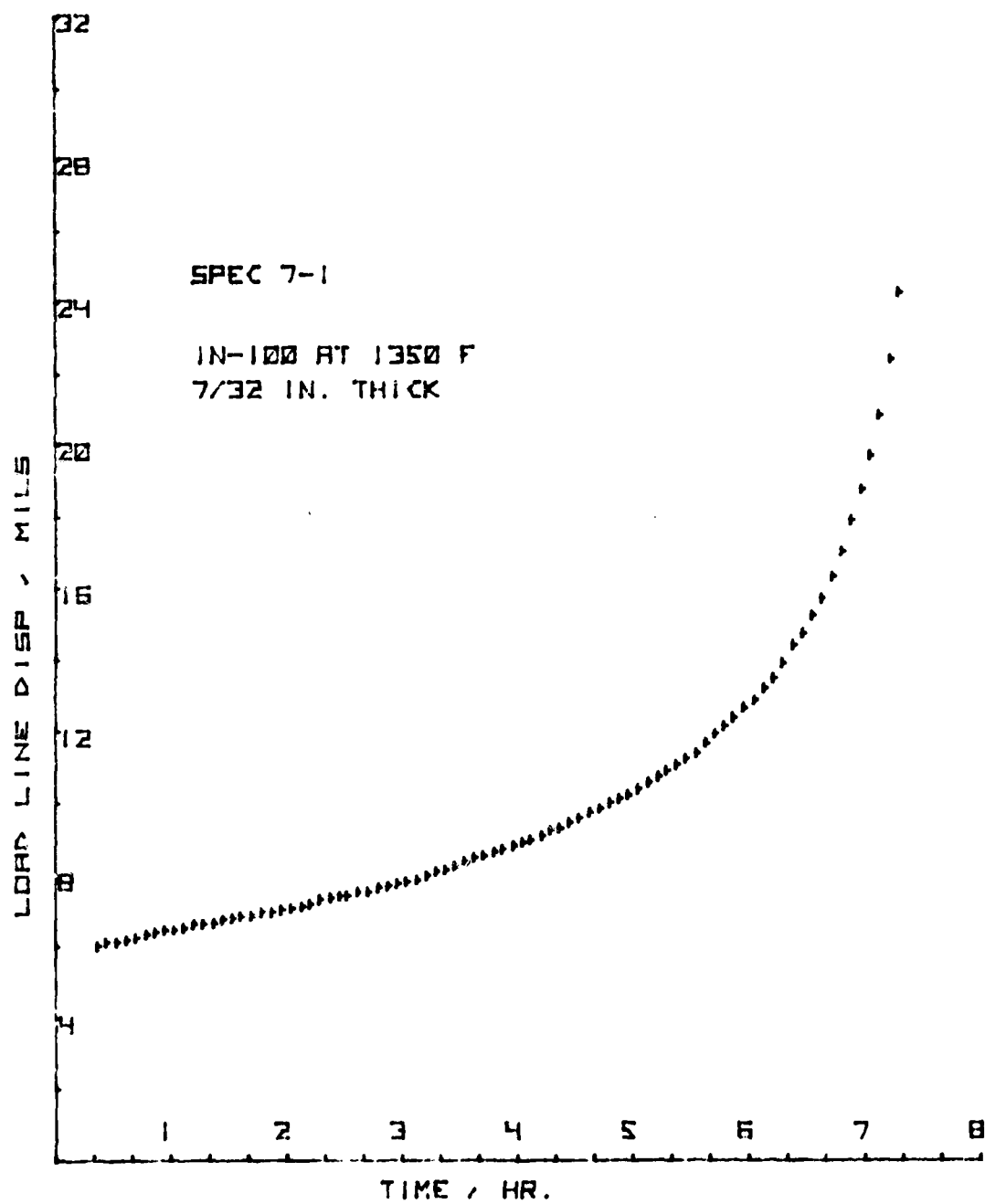
Figure 10.   LLD-Time Plot for CT Specimen 7-1
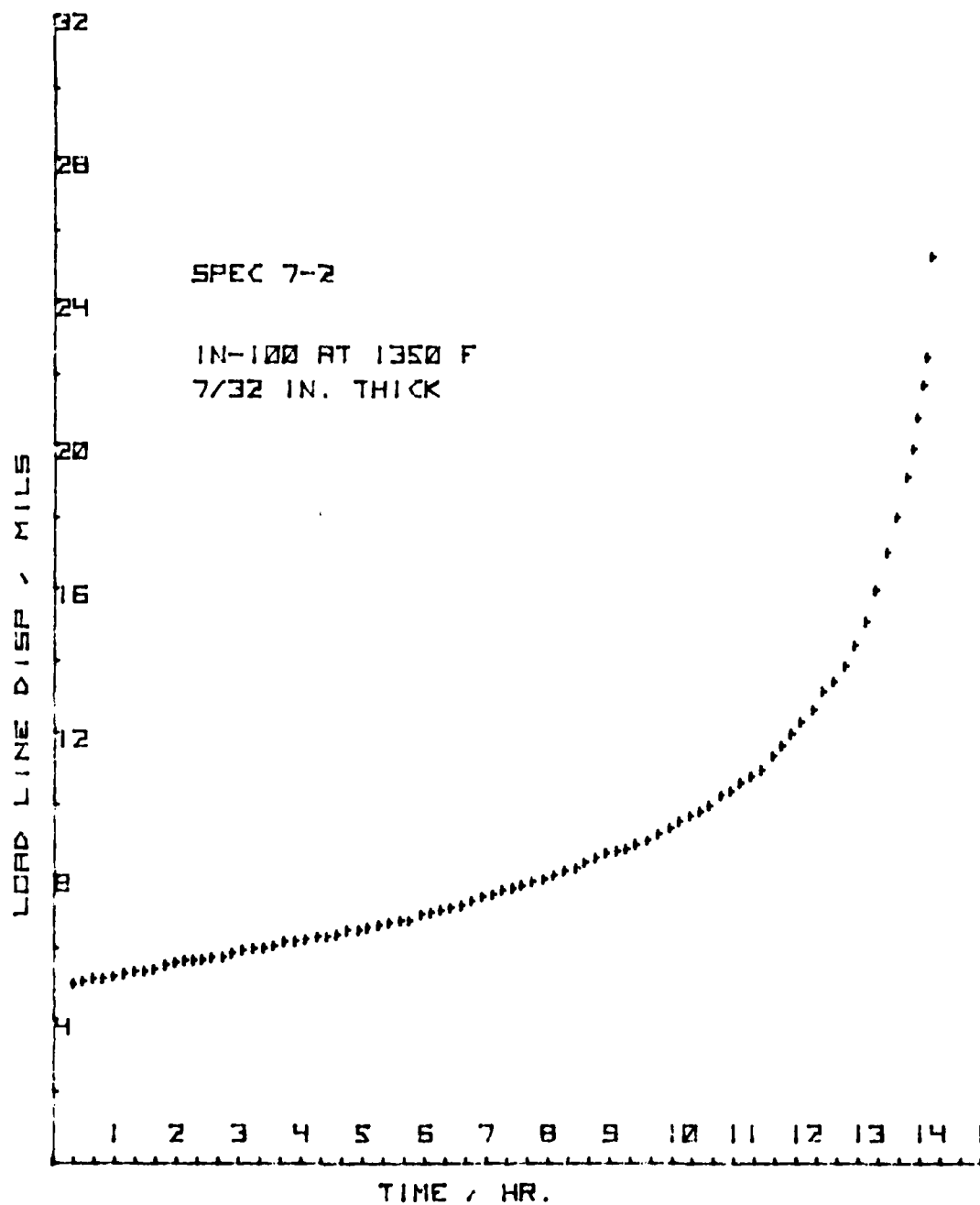
Figure 11. LLD-Time Plot for CT Specimen 7-2

83
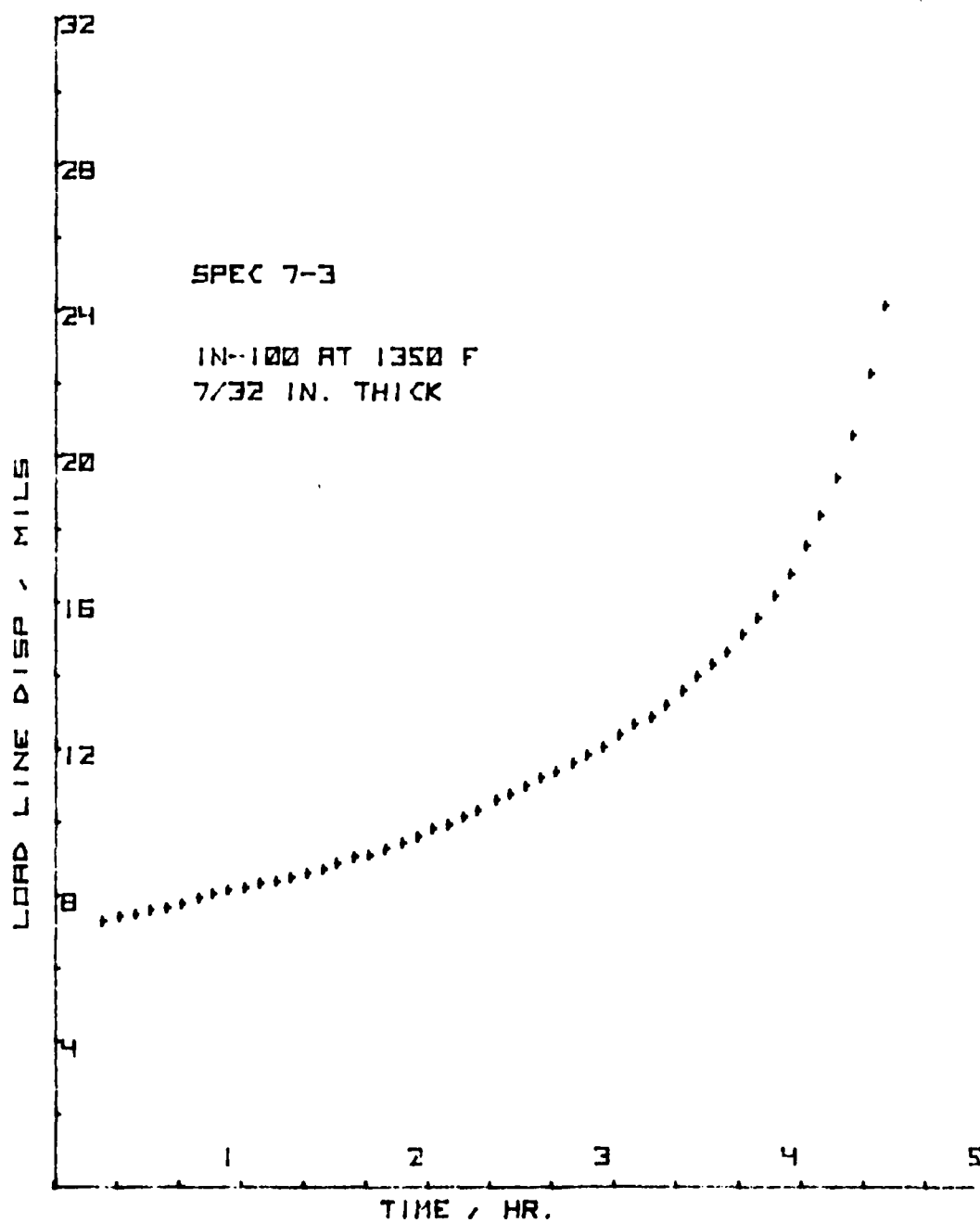
Figure 12. LLD-Time Plot for CT Specimen 7-3
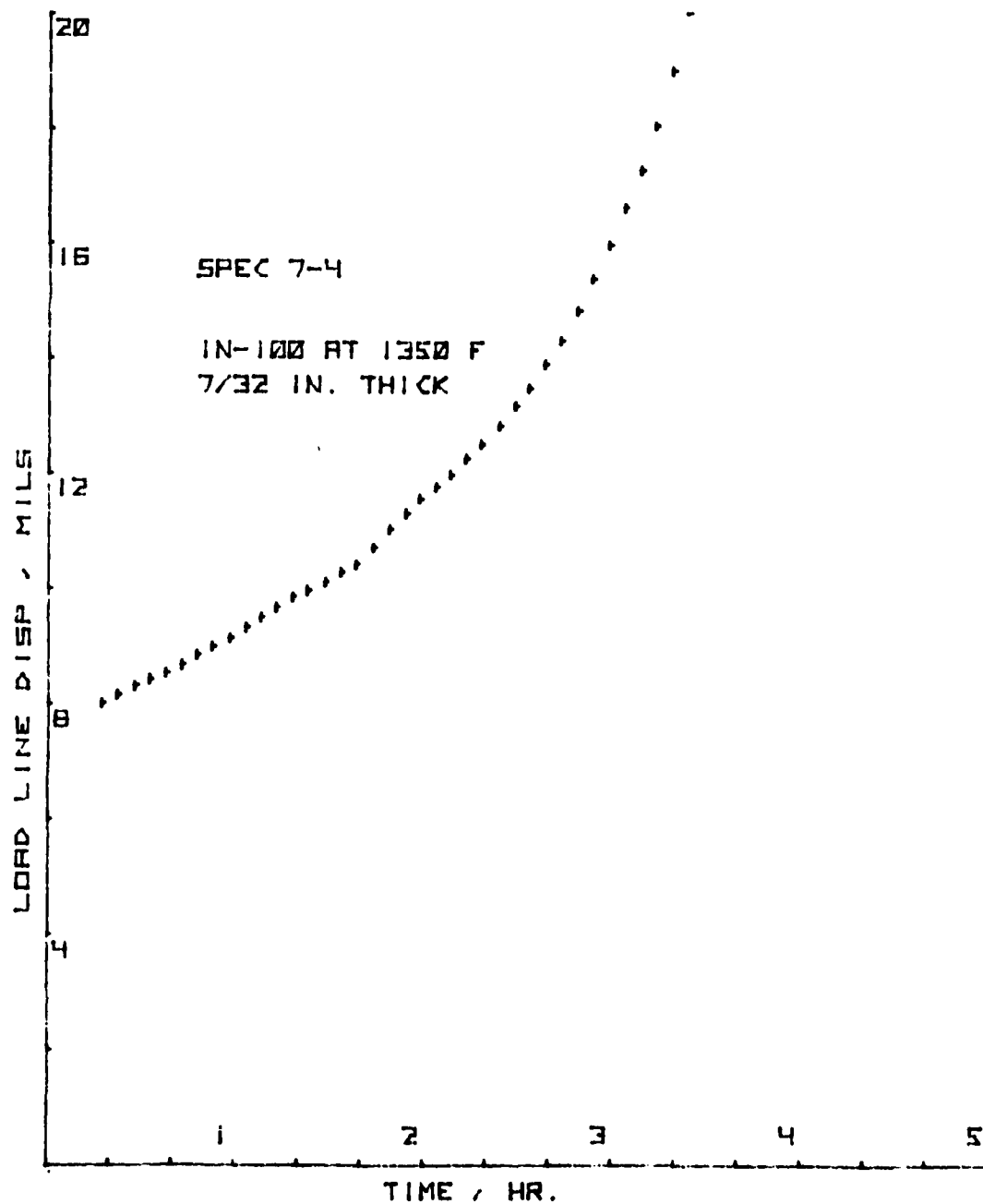
Figure 13.   LLD-Time Plot for CT Specimen 7-4
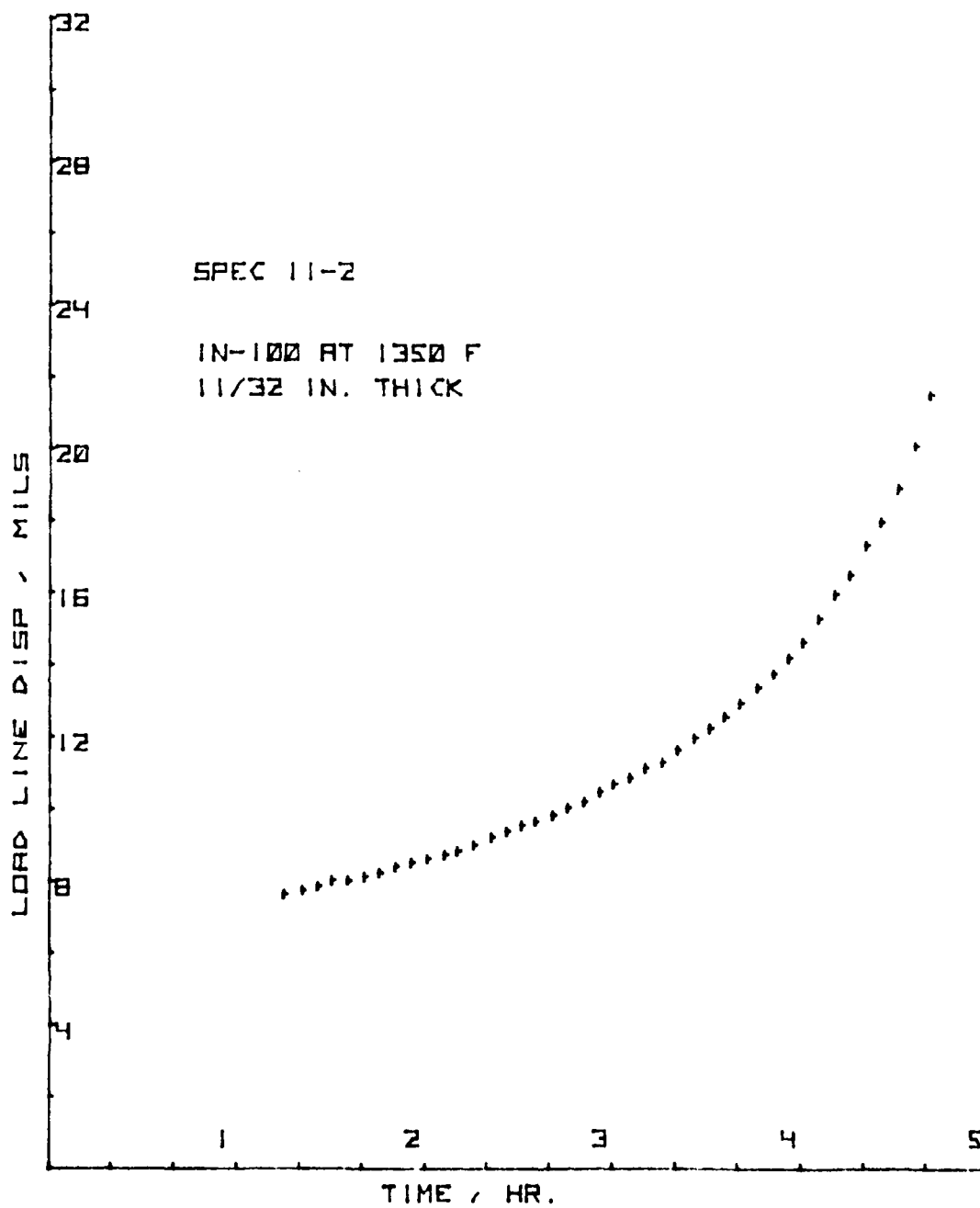
Figure 14. LLD-Time Plot for CT Specimen 11-2
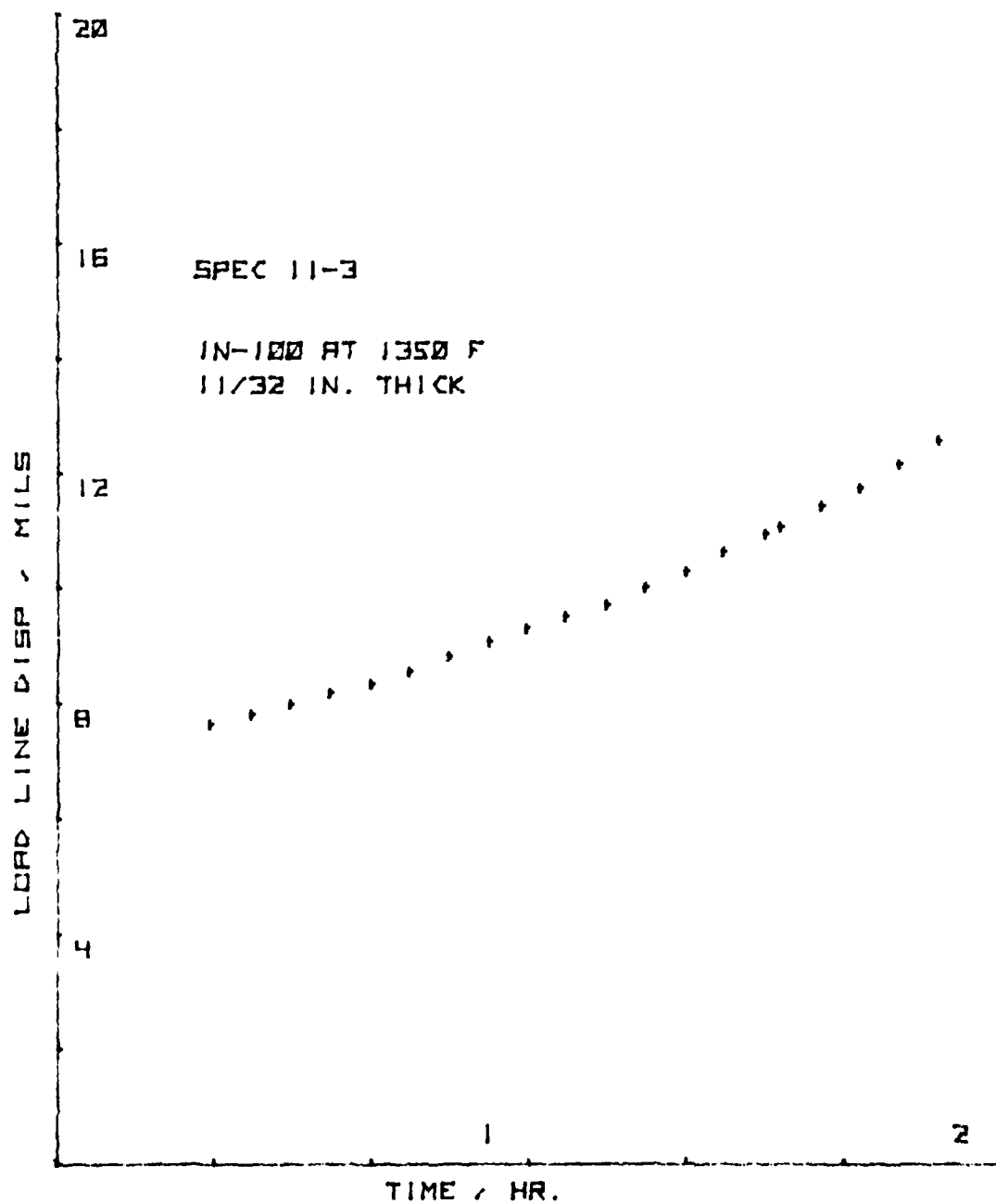
Figure 15. LLD-Time Plot for CT Specimen 11-3
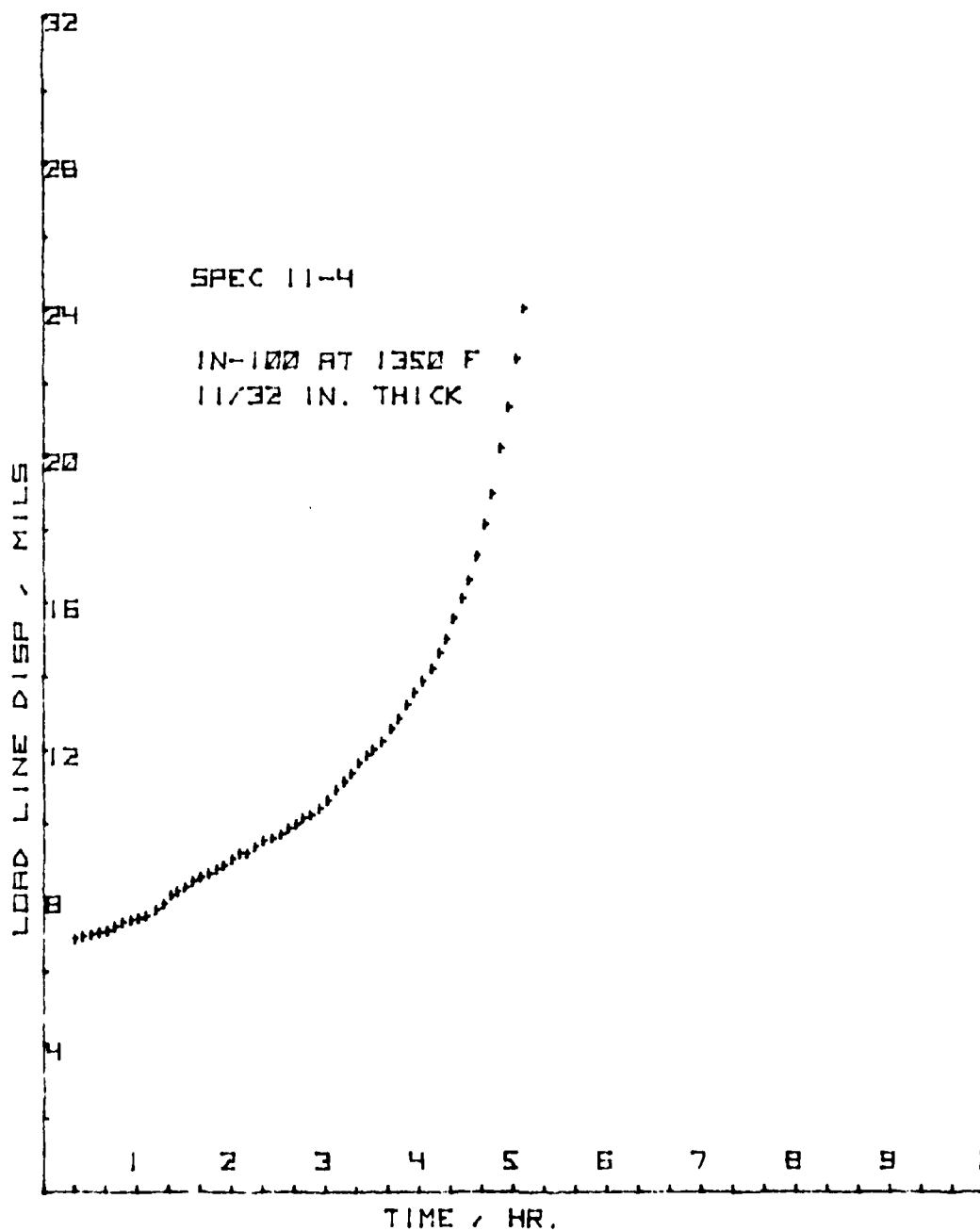
Figure 16. LLD-Time Plot for CT Specimen 11-4
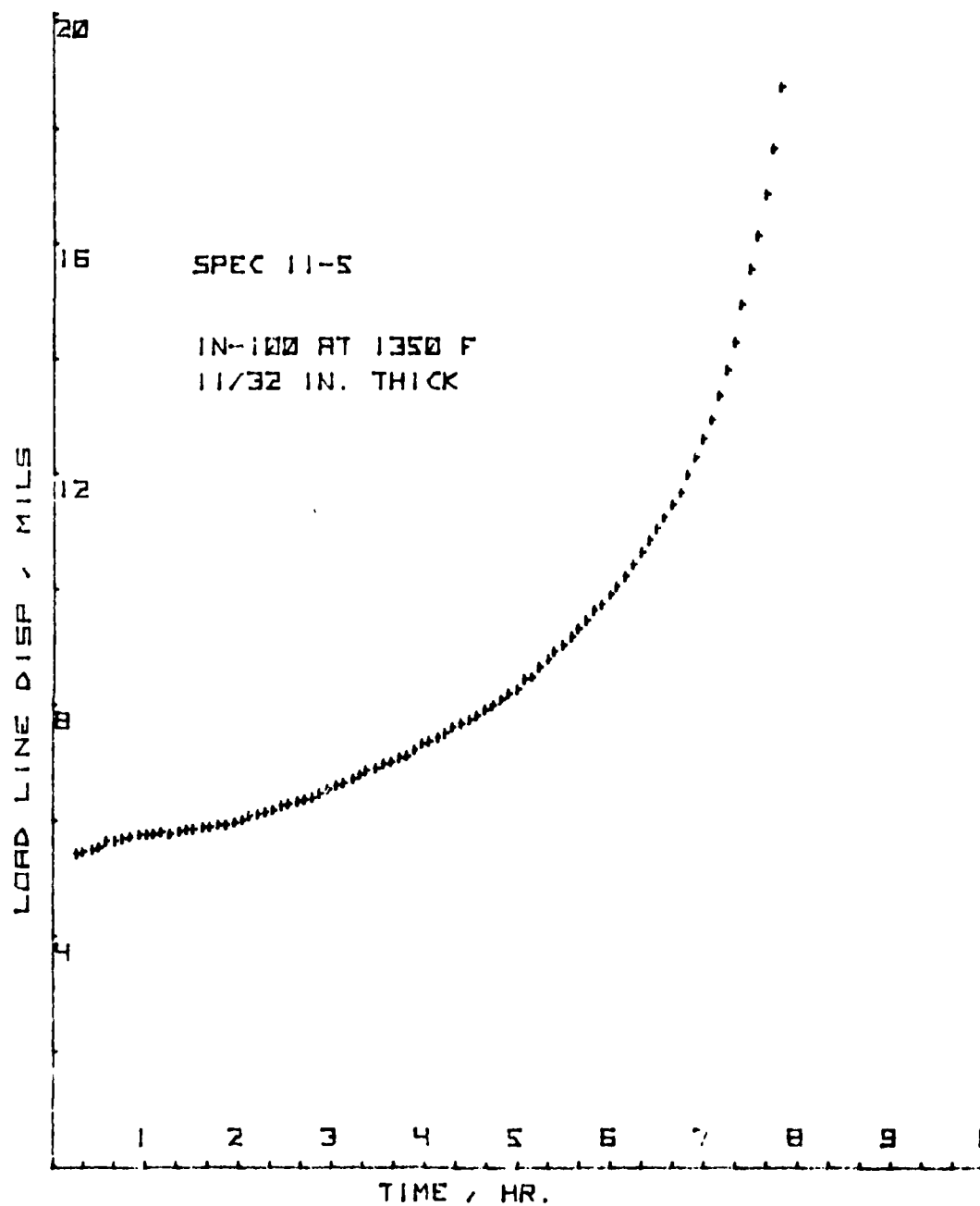
Figure 17. LLD-Time Plot for CT Specimen 11-5
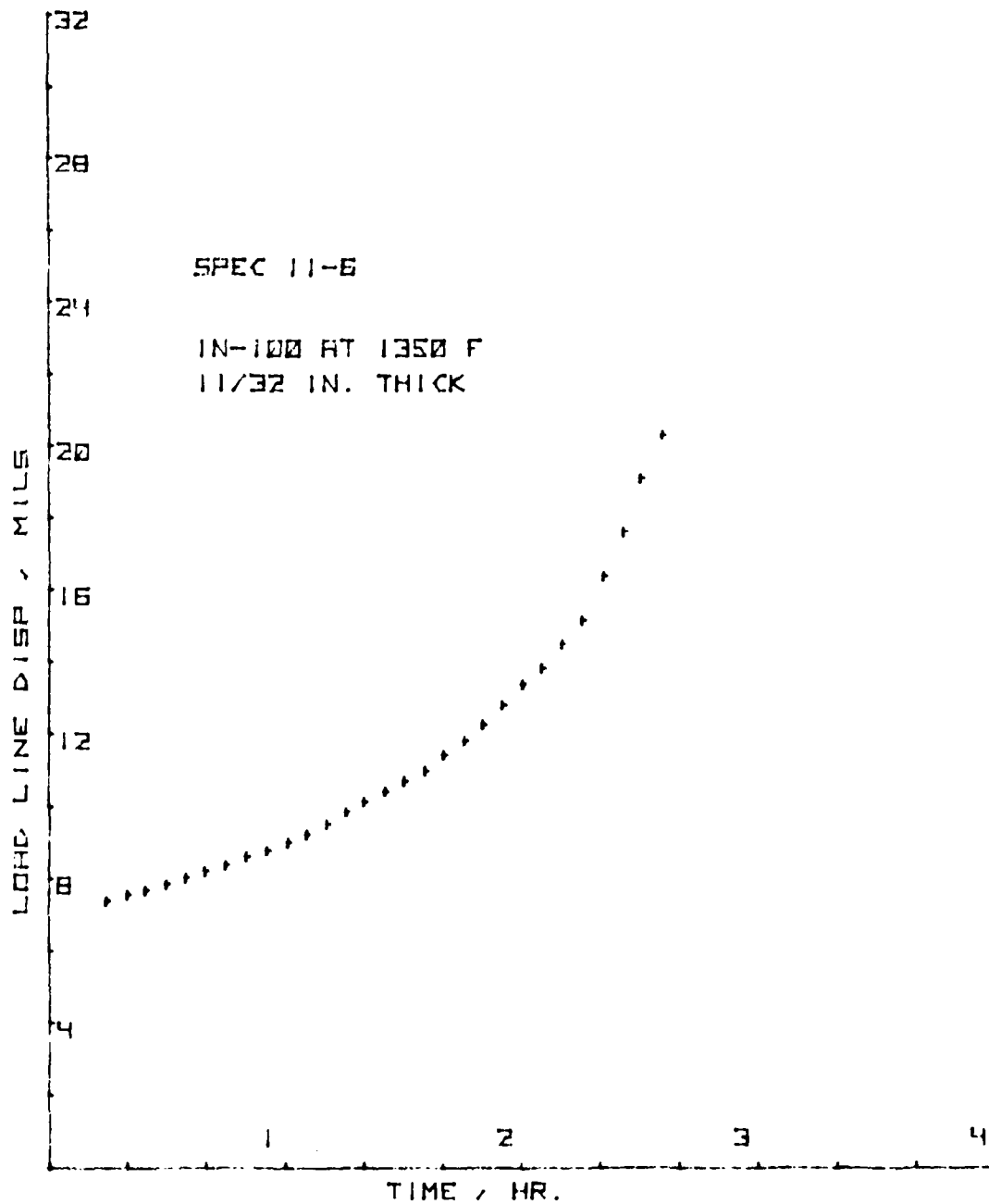
Figure 18. LLD-Time Plot for CT Specimen 11-6
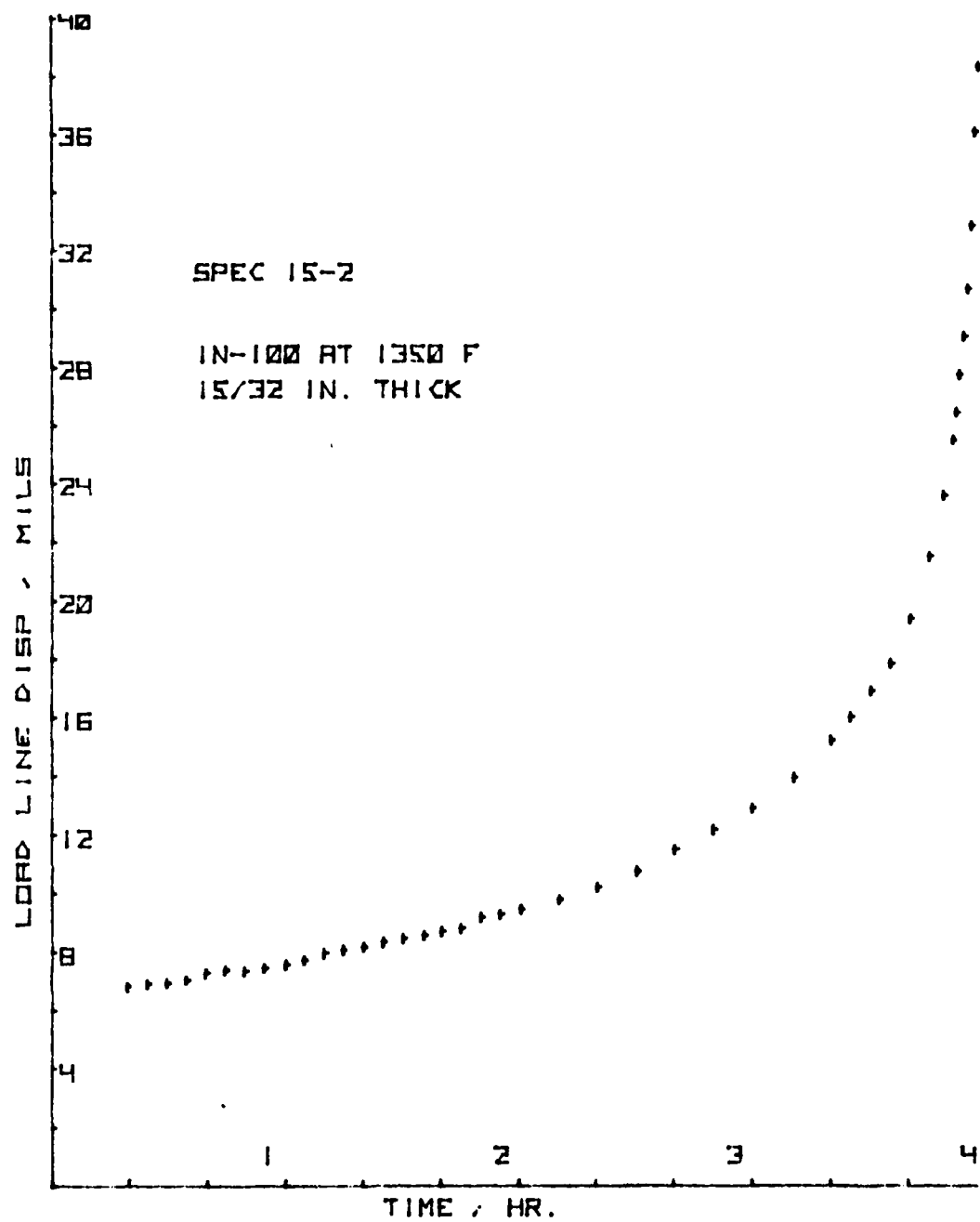
Figure 19.   LLD-Time Plot for CT Specimen 15-2
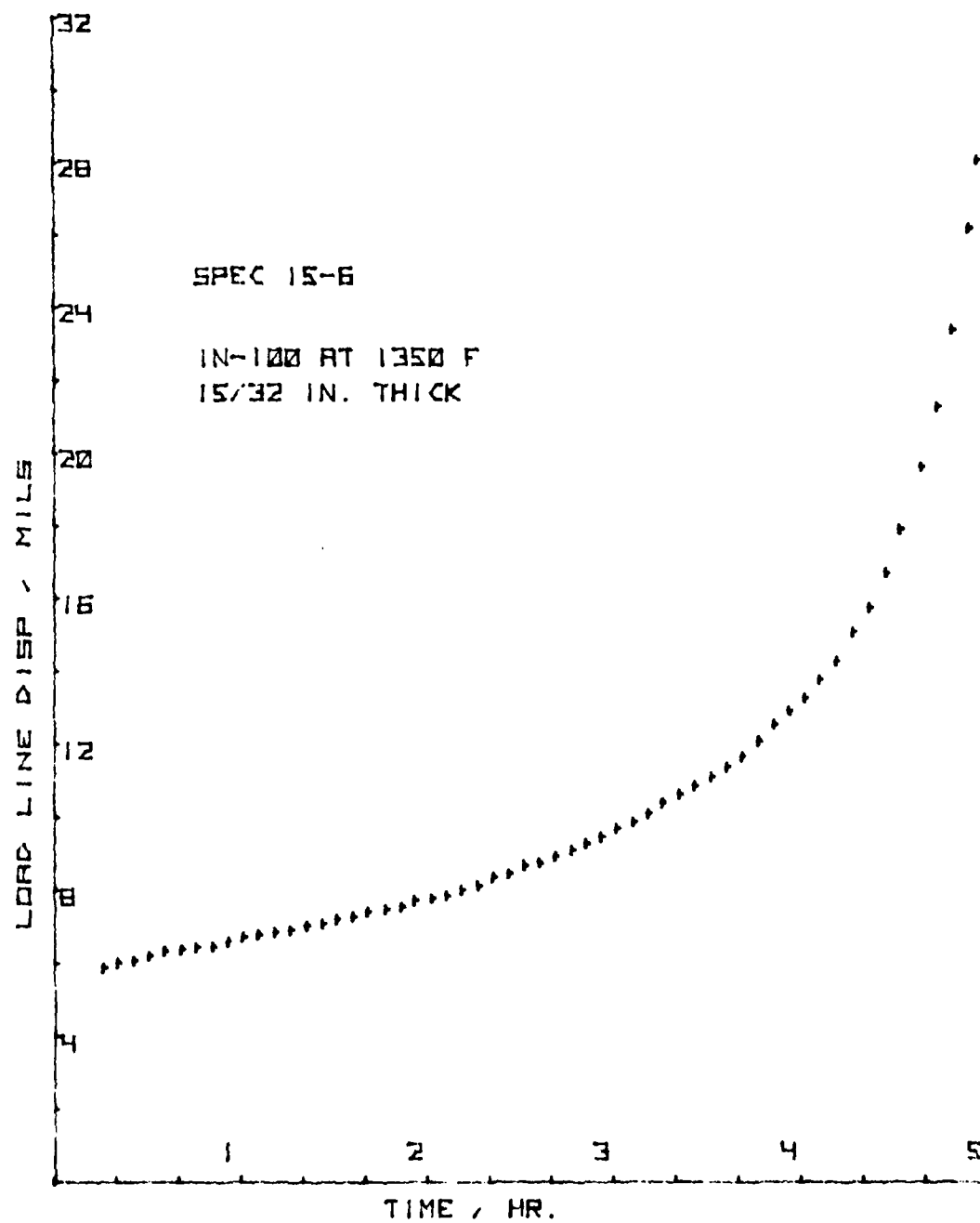
Figure 20. LLD-Time Plot for CT Specimen 15-6
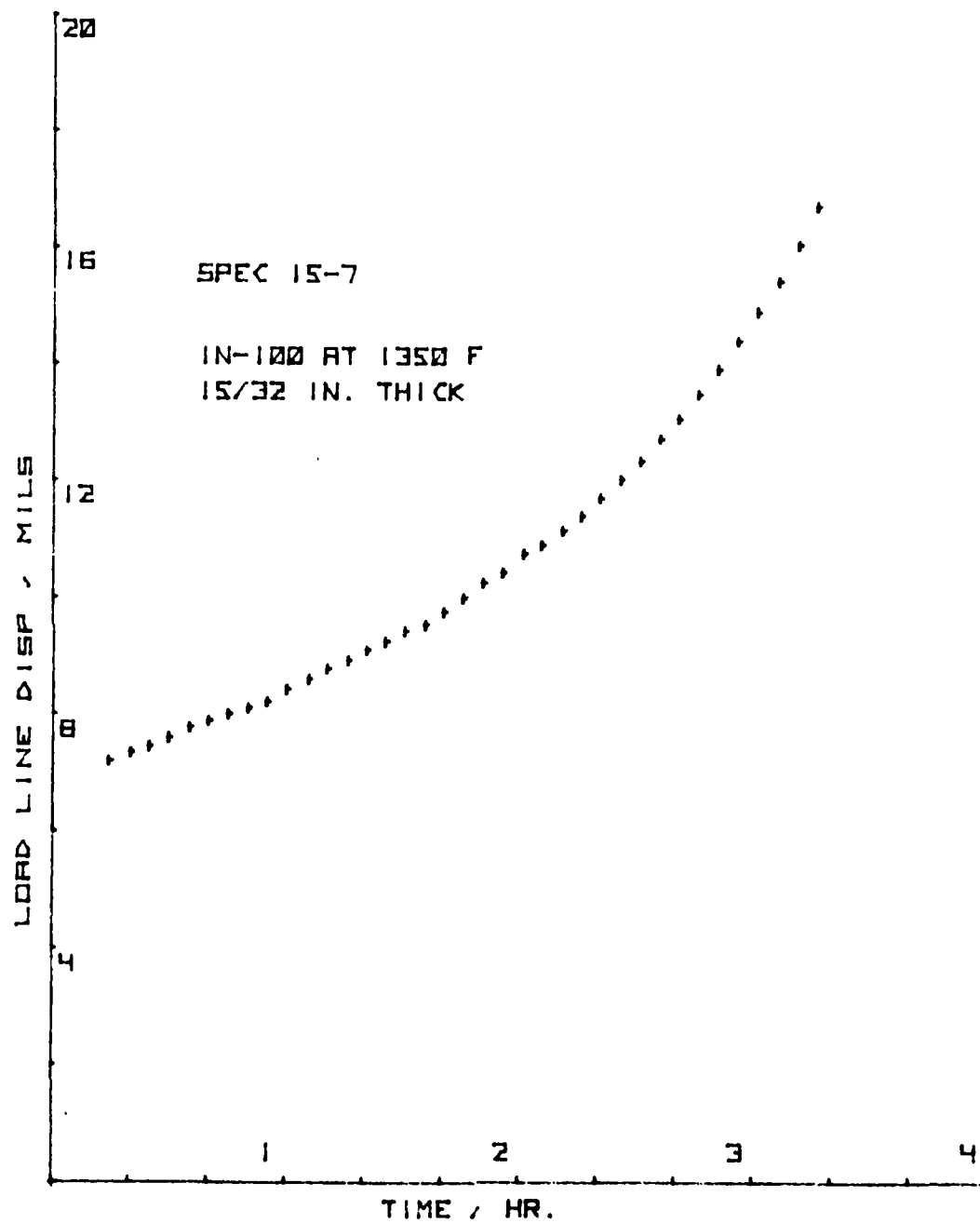
Figure 21. LLD-Time Plot for CT Specimen 15-7
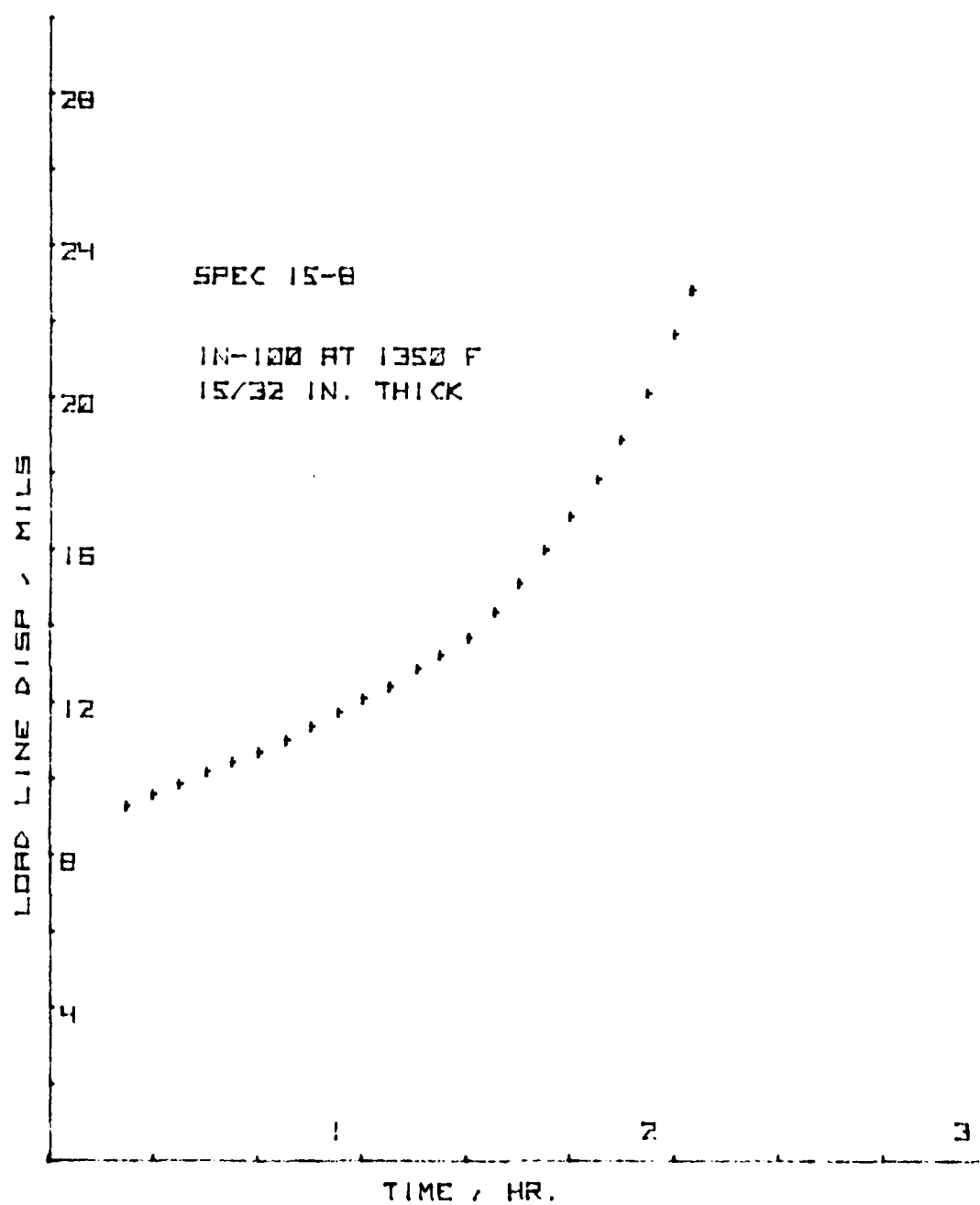
Figure 22. LLD-Time Plot for CT Specimen 15-8
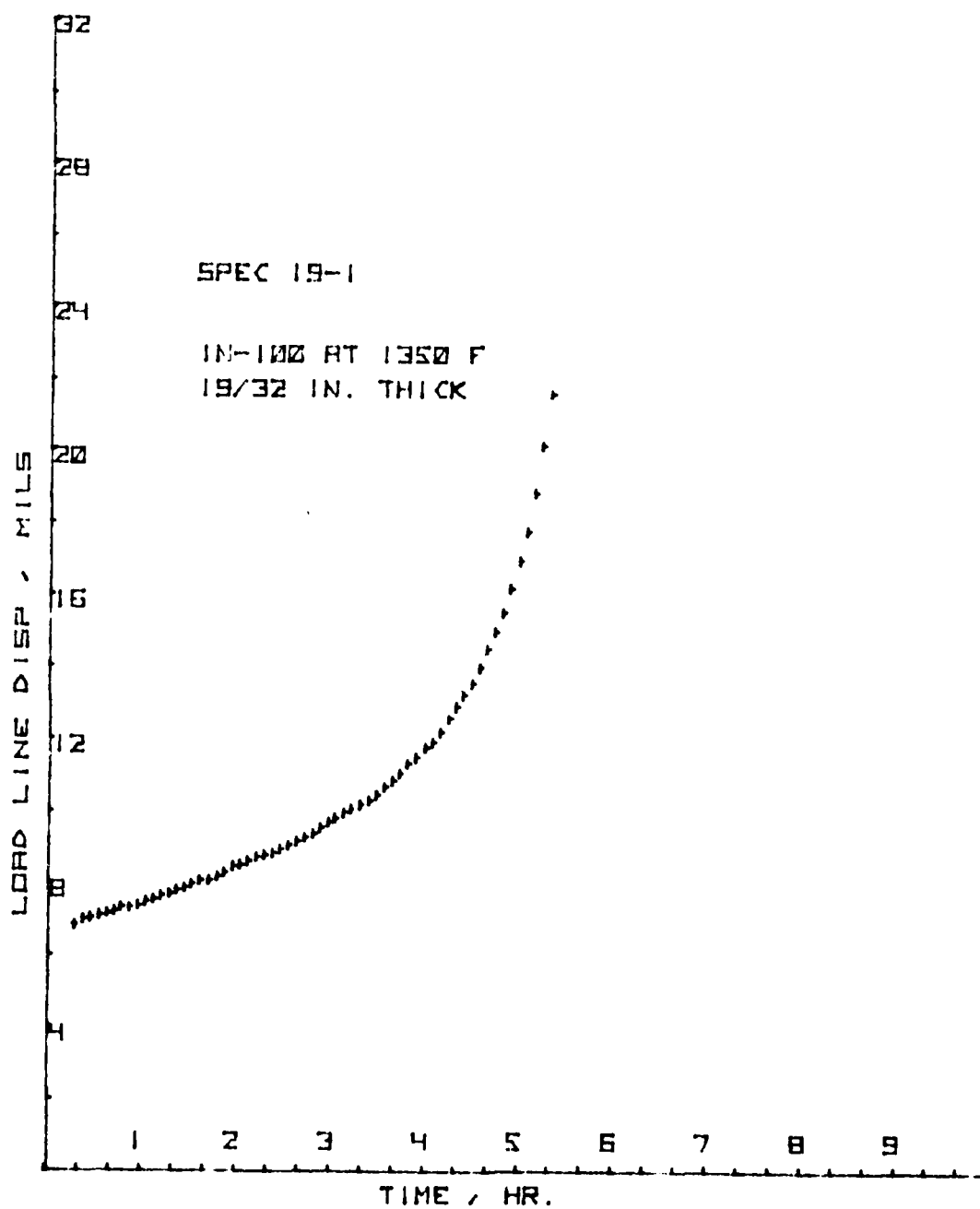
Figure 23.   LLD-Time Plot for CT Specimen 19-1
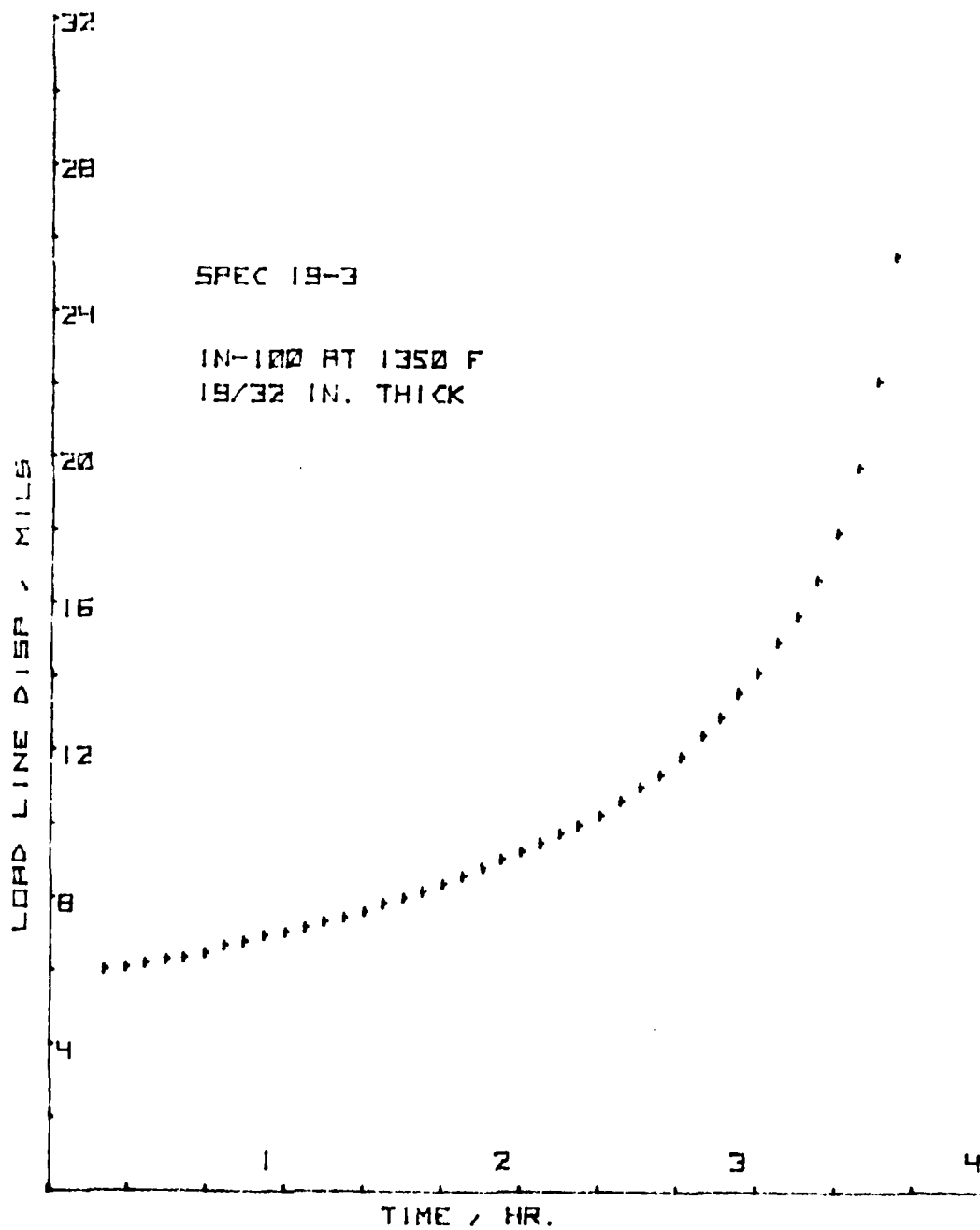
Figure 24.   LLD-Time Plot for CT Specimen 19-3
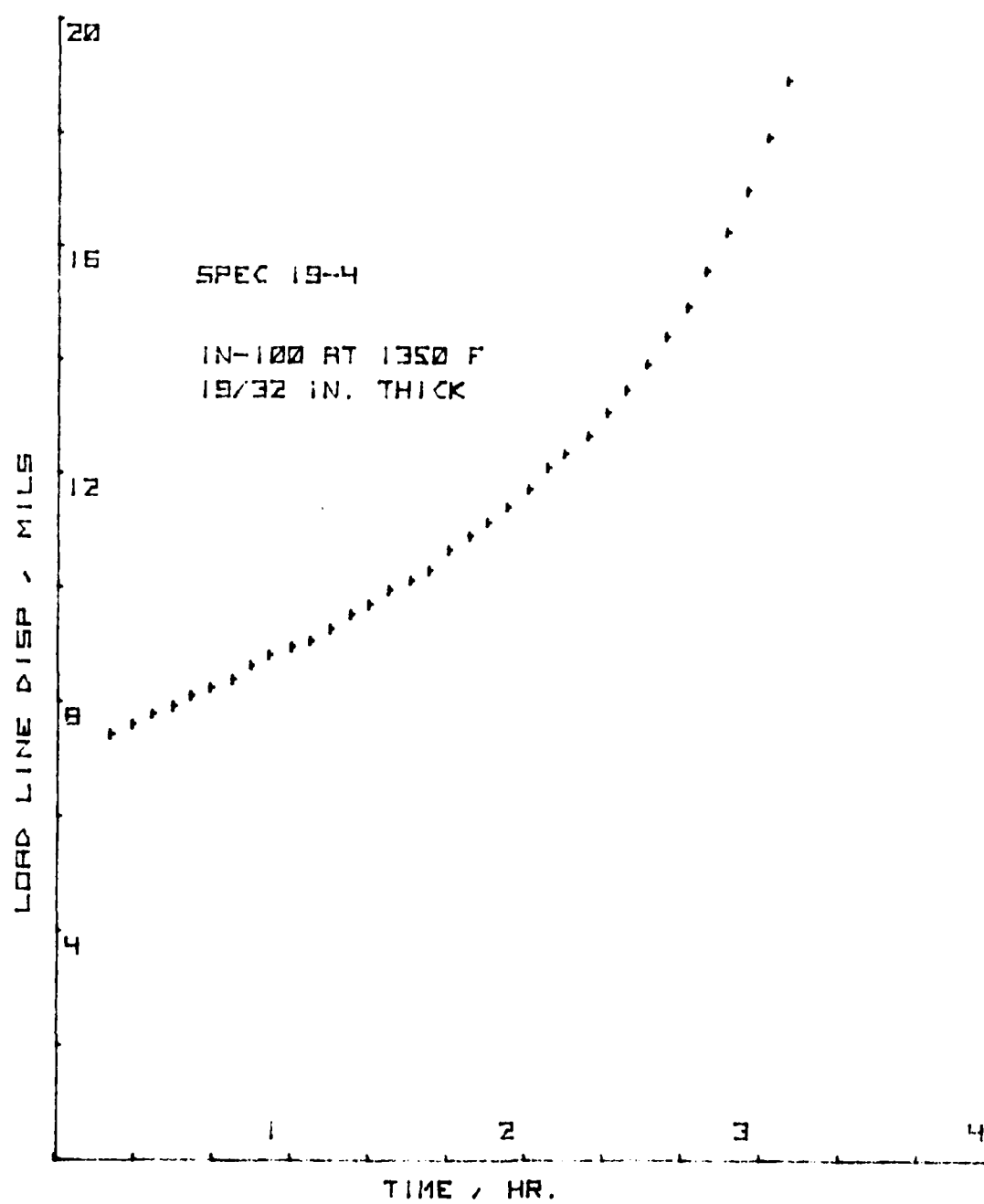
Figure 25. LLD-Time Plot for CT Specimen 19-4
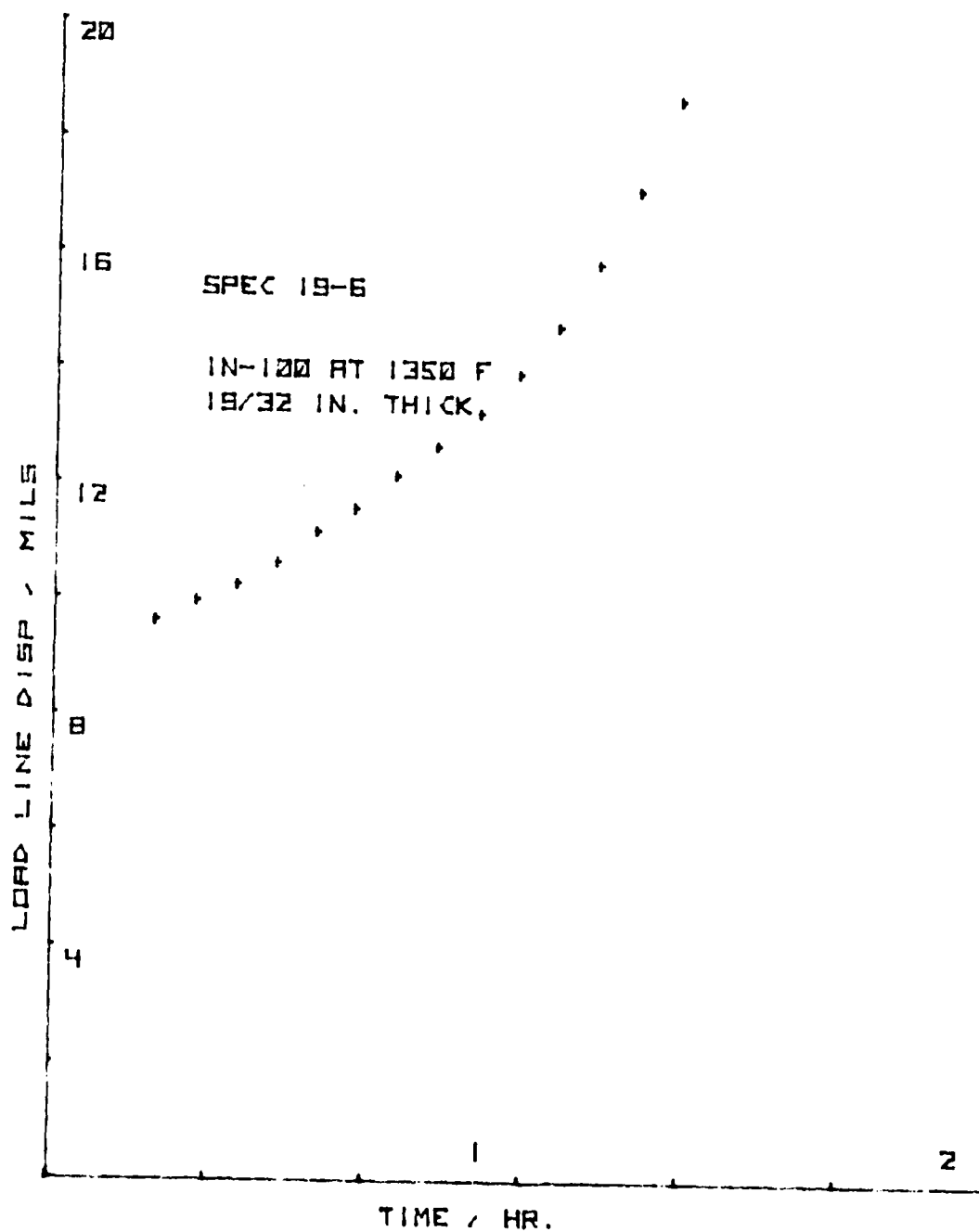
Figure 26.   LLD-Time Plot for CT Specimen 19-6
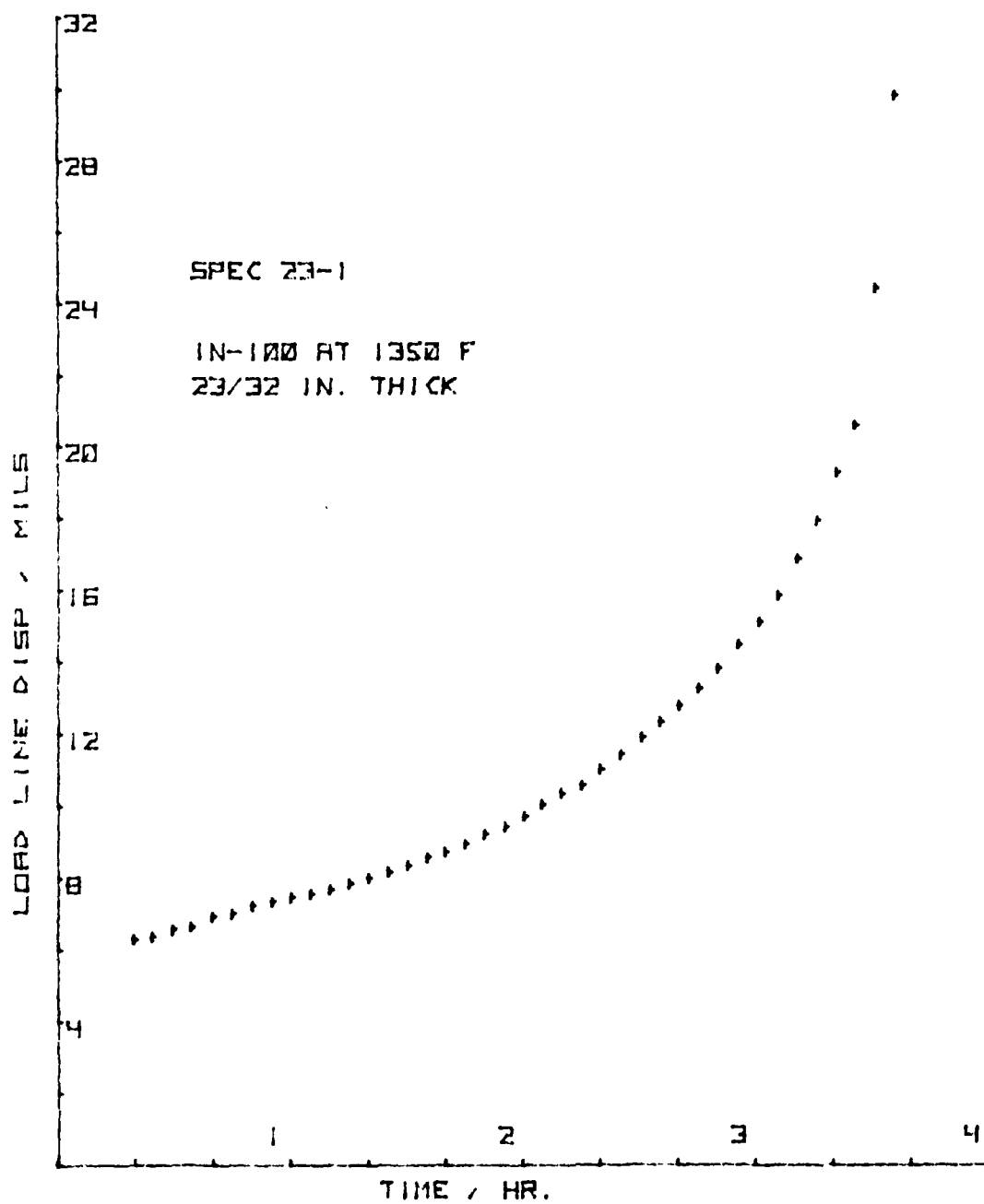
Figure 27. LLD-Time Plot for CT Specimen 23-1
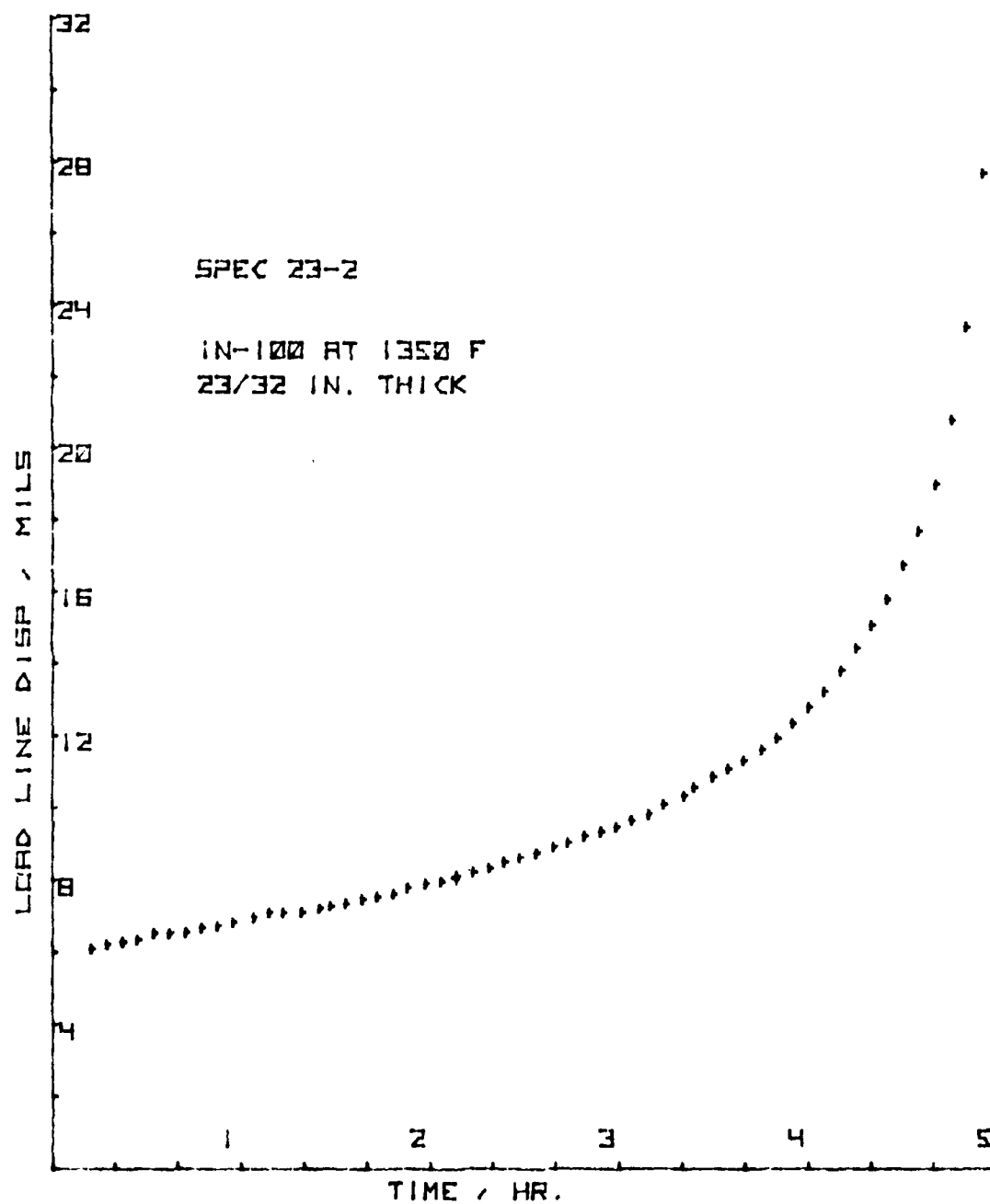
Figure 28. LLD-Time Plot for CT Specimen 23-2
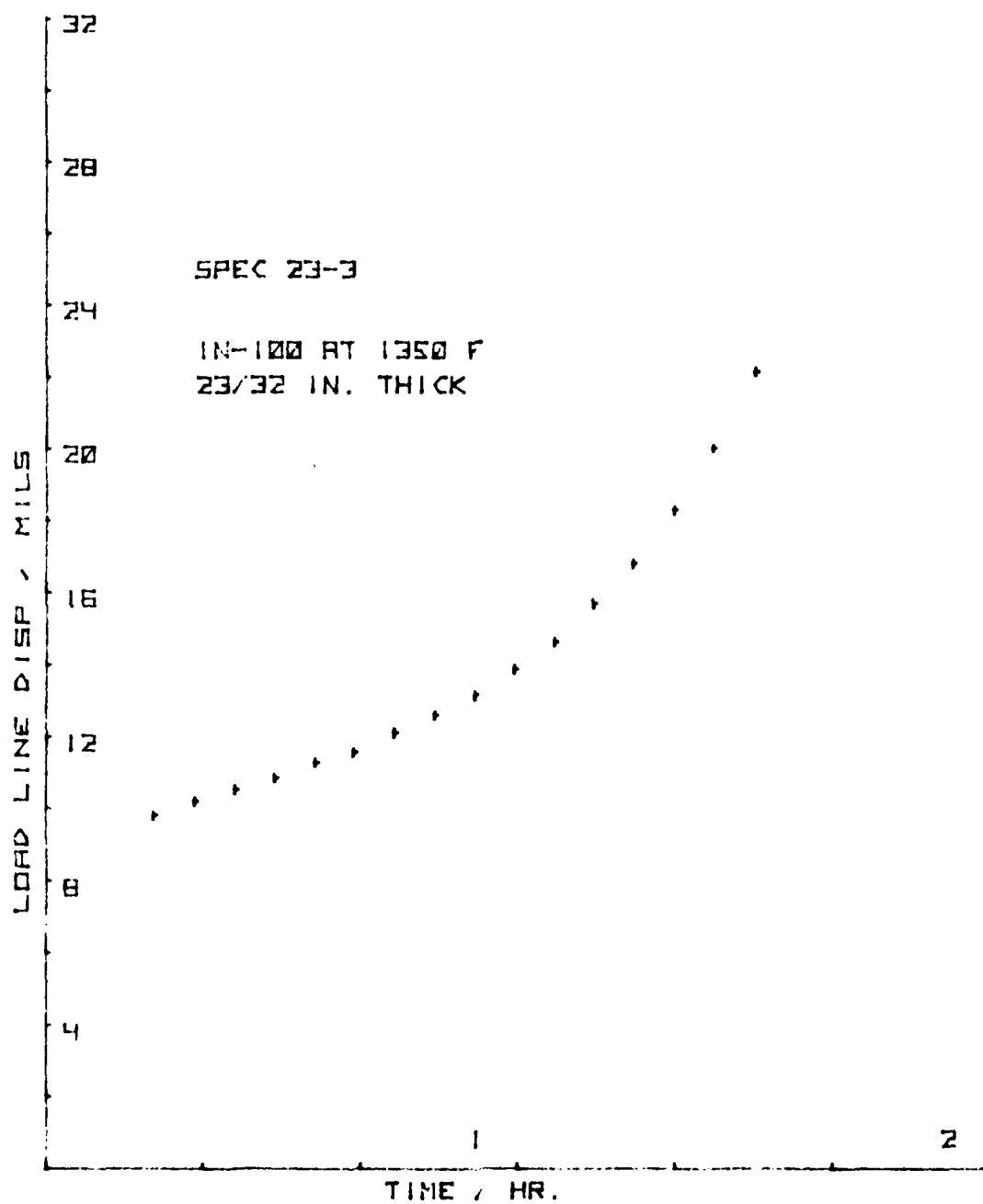
Figure 29. LLD-Time Plot for CT Specimen 23-3
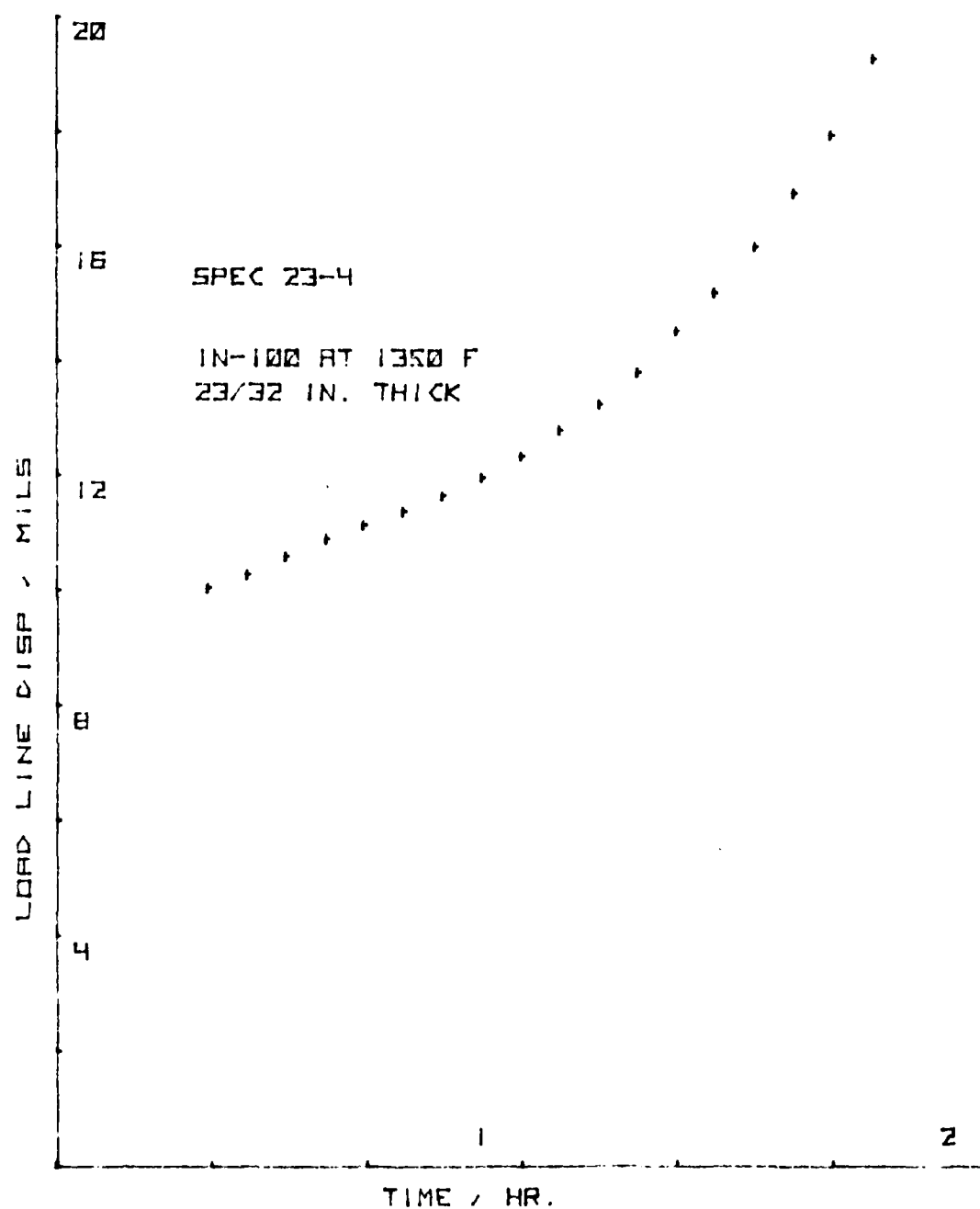
Figure 30. LLD-Time Plot for CT Specimen 23-4
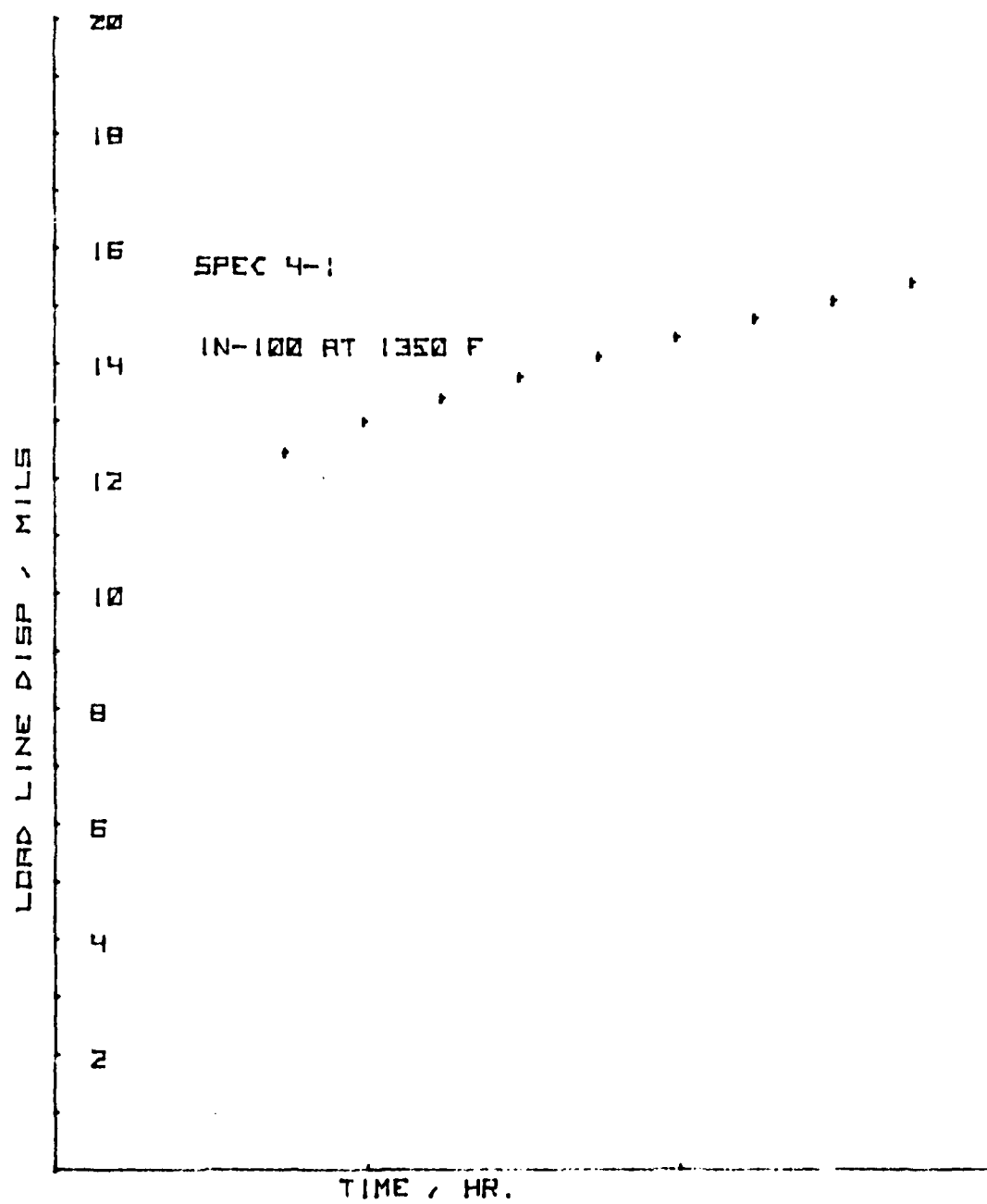
Figure 31. LLD-Time Plot for Ring Specimen 4-1
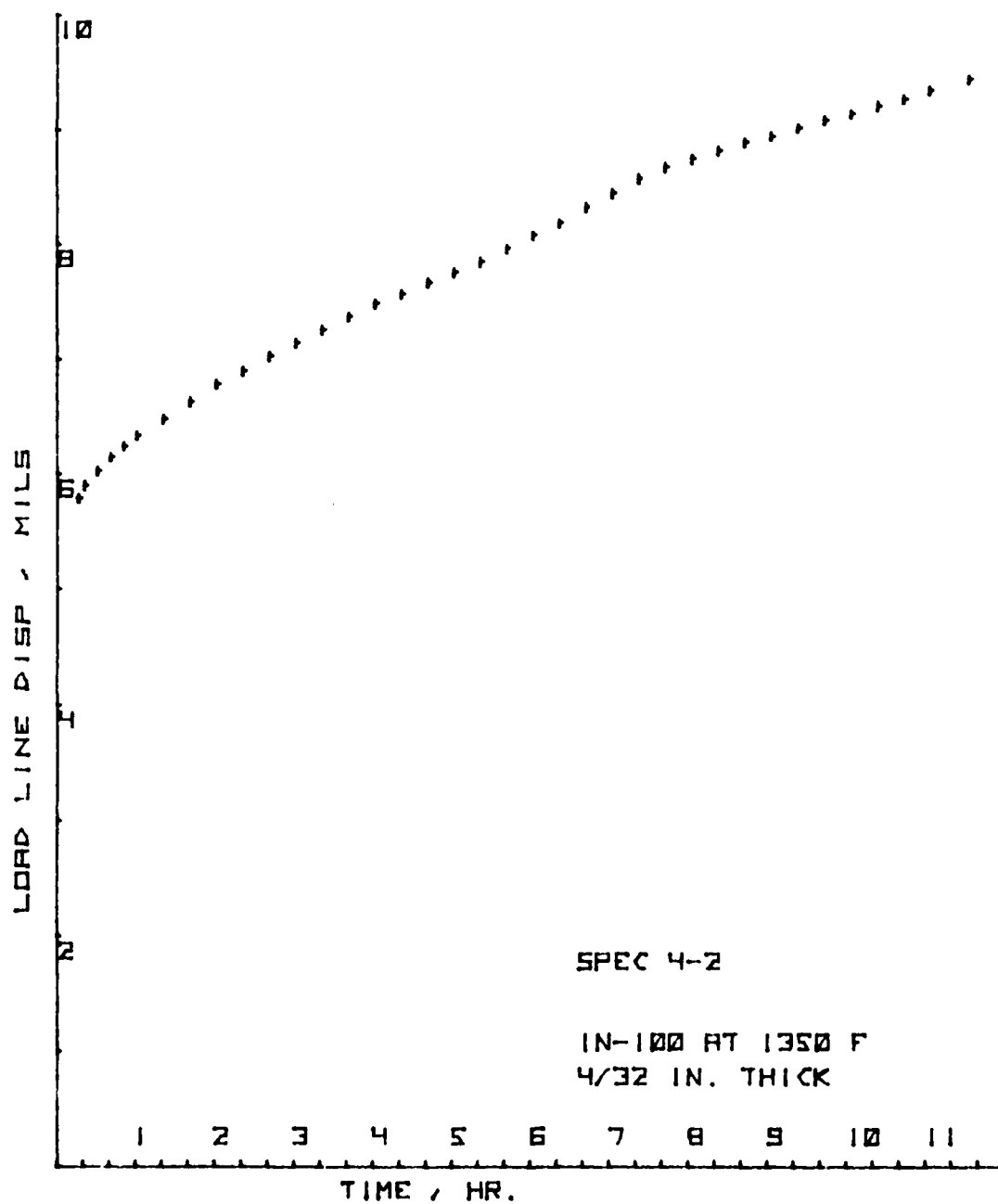
Figure 32. LLD-Time Plot for Ring Specimen 4-2
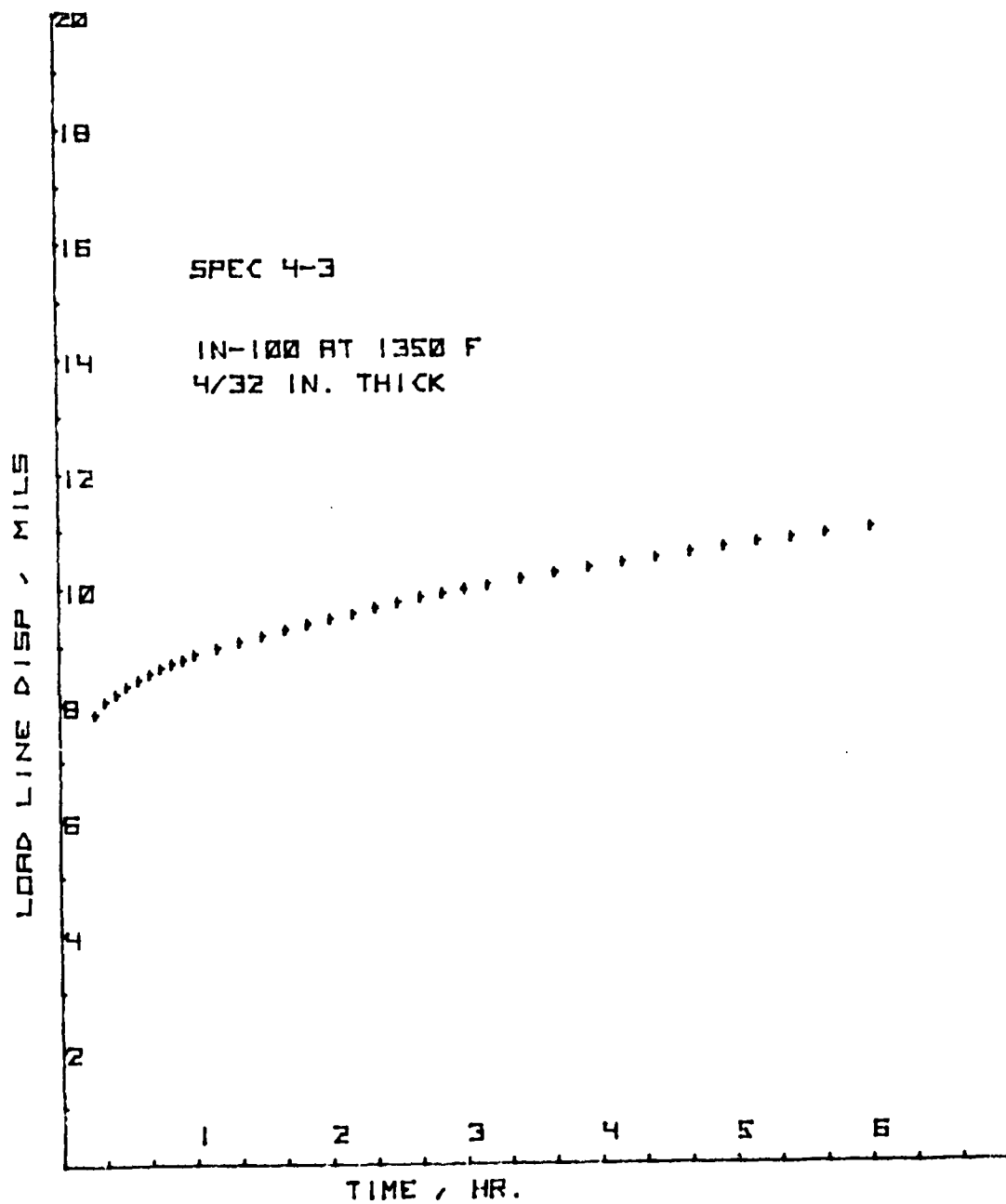
Figure 33. LLD-Time Plot for Ring Specimen 4-3
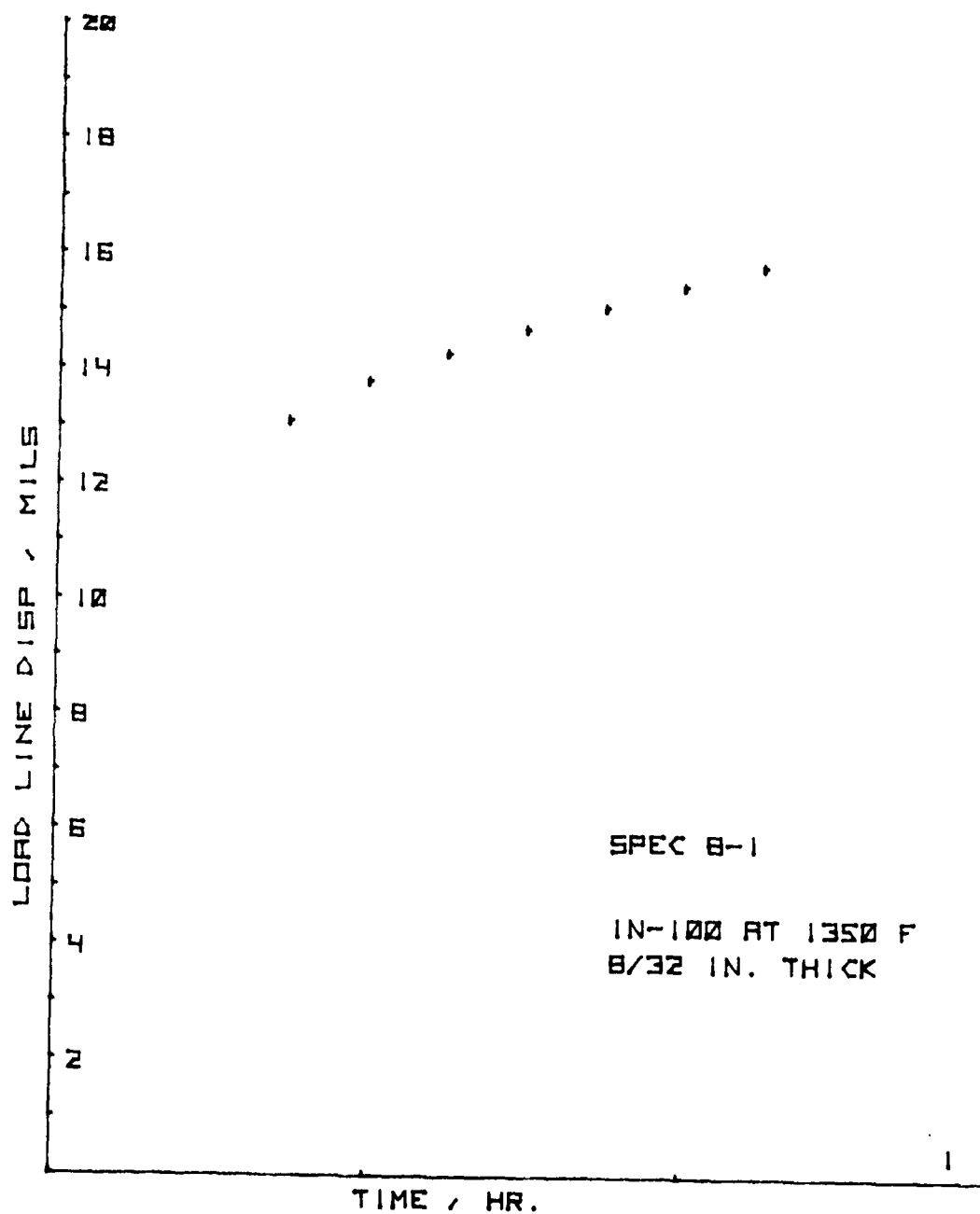
Figure 34. LLD-Time Plot for Ring Specimen 8-1
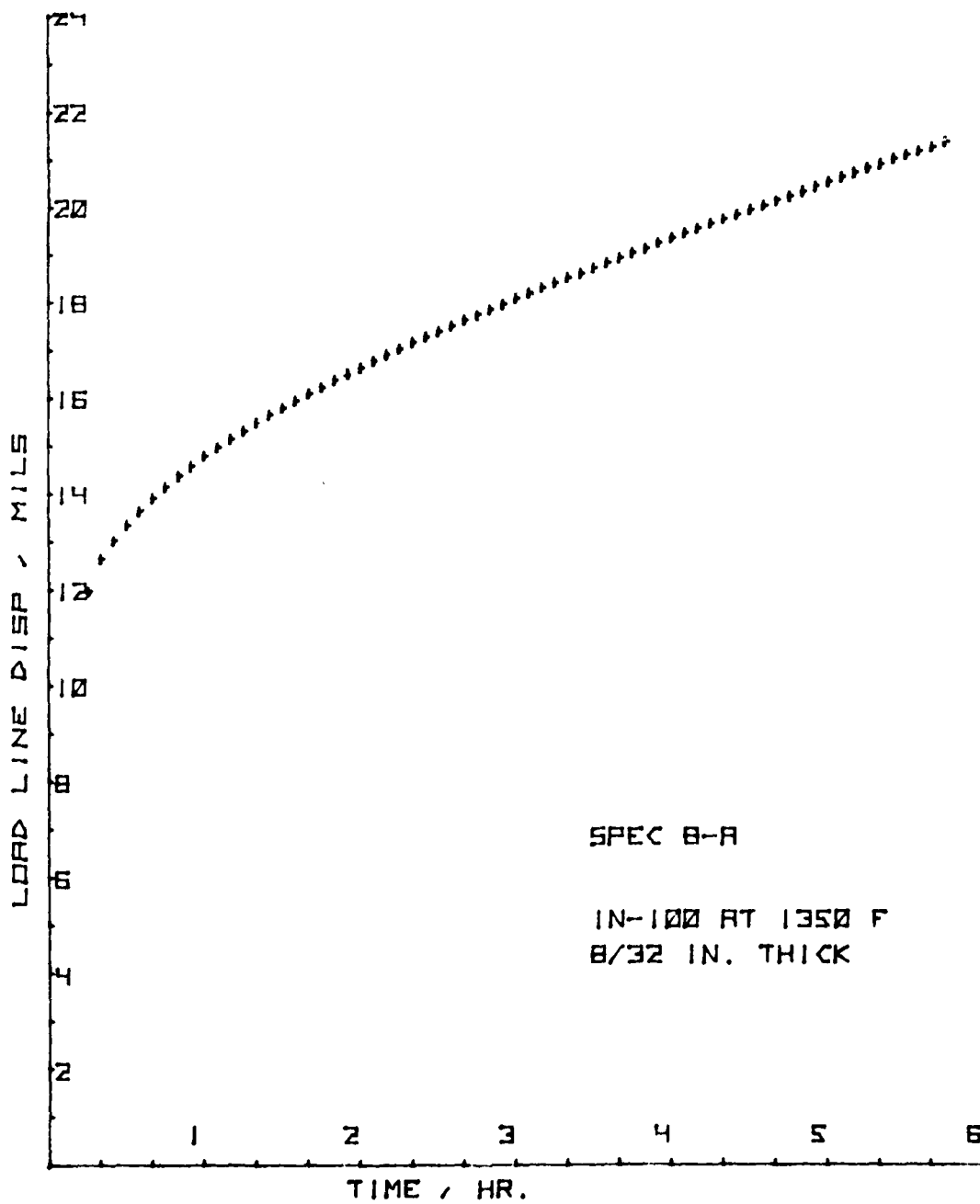
Figure 35. LLD-Time Plot for Ring Specimen 8-A
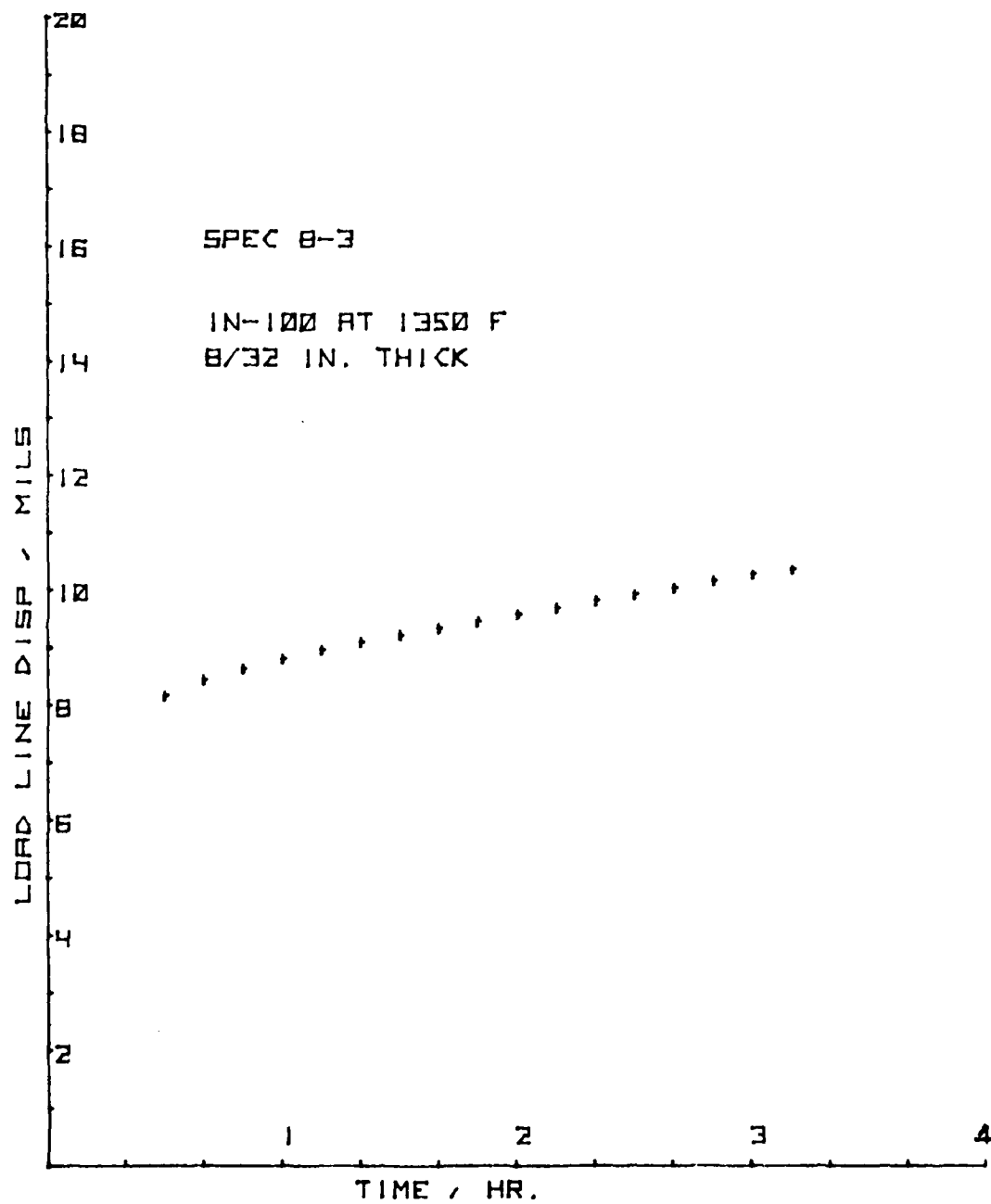
Figure 36. LLD-Time Plot for Ring Specimen 8-3
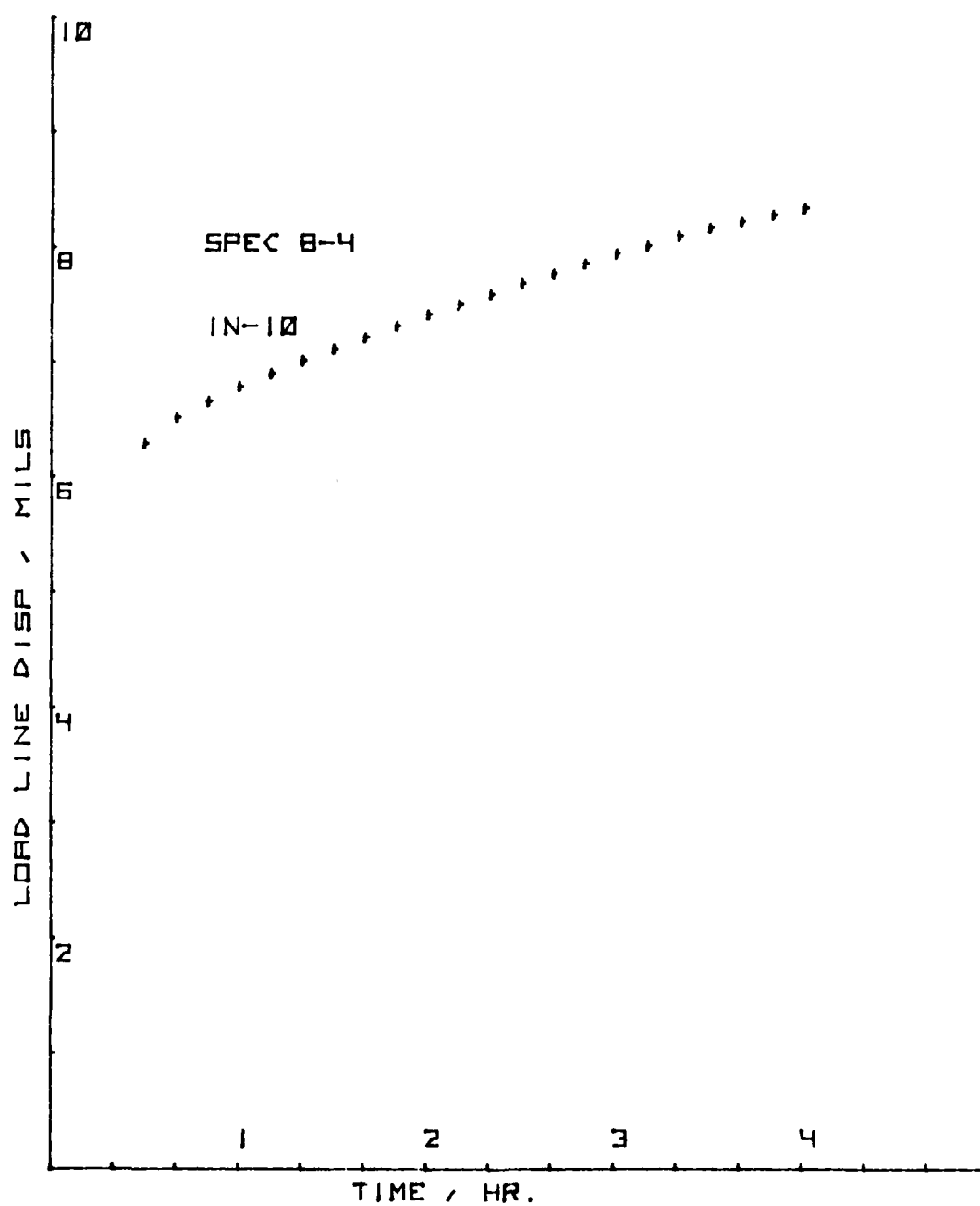
Figure 37.   LLD-Time Plot for Ring Specimen 8-4
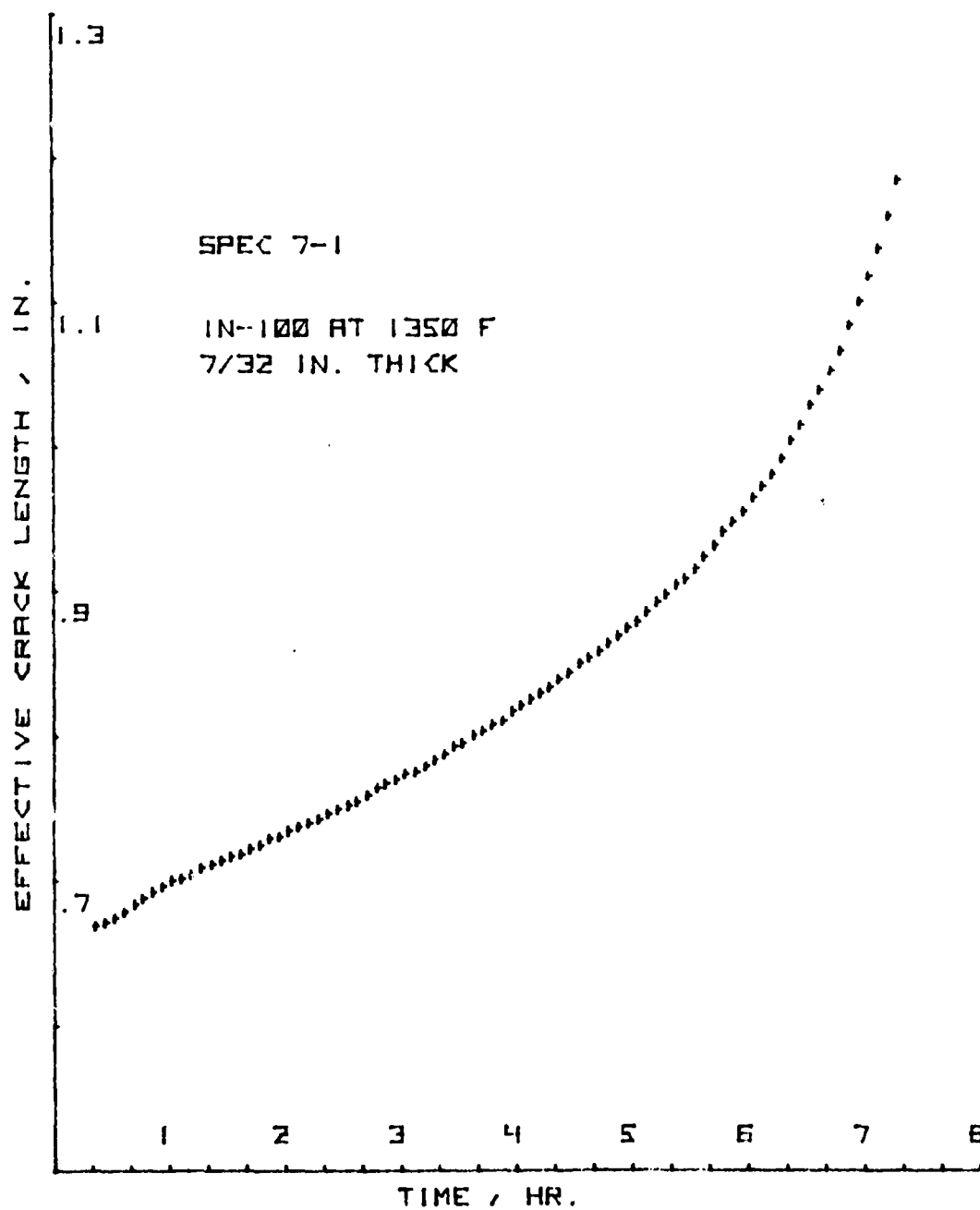
Figure 38. Effective Crack Length vs. Time Plot for CT
Specimen 7-1
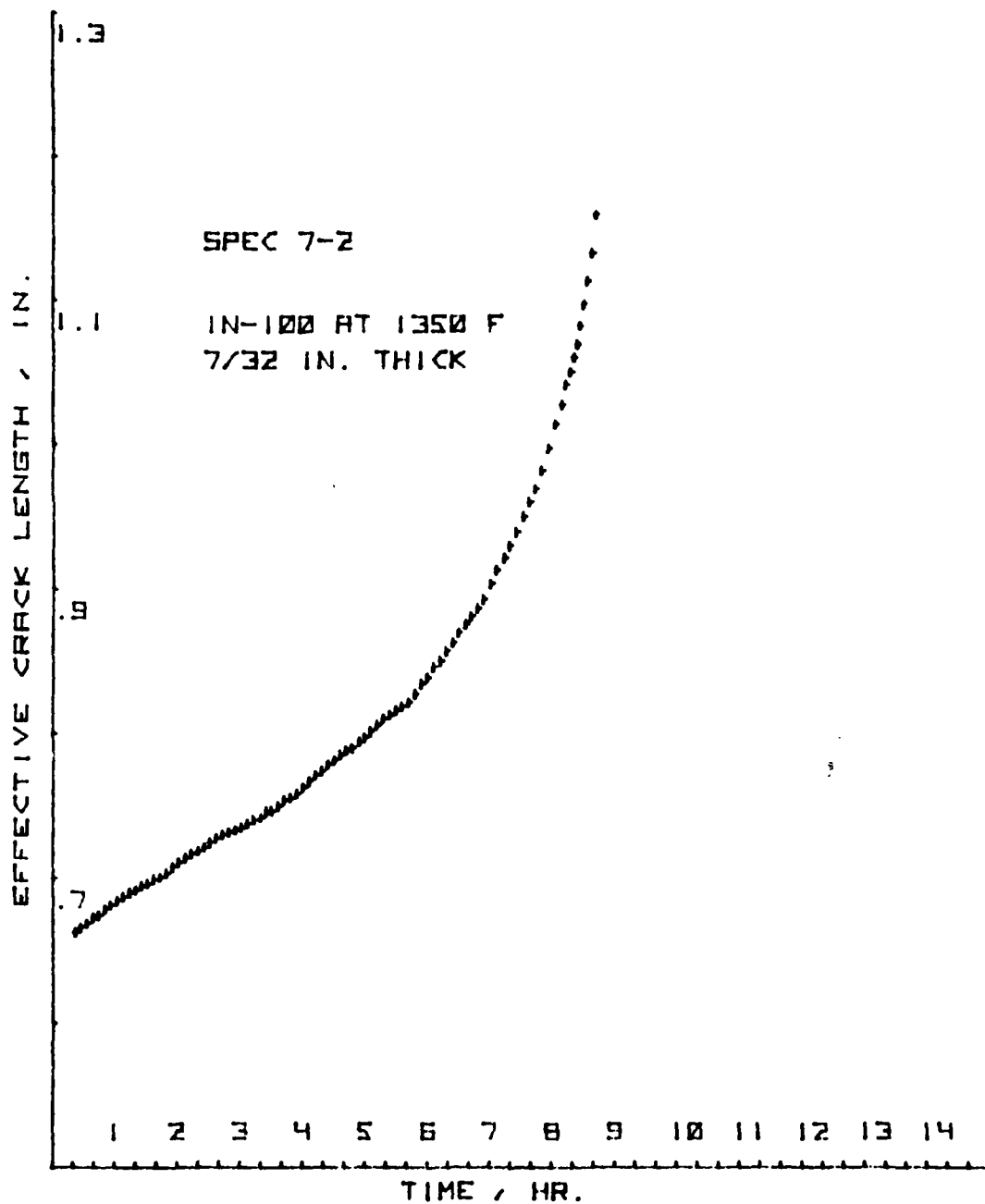
Figure 39. Effective Crack Length vs. Time Plot for CT
Specimen 7-2
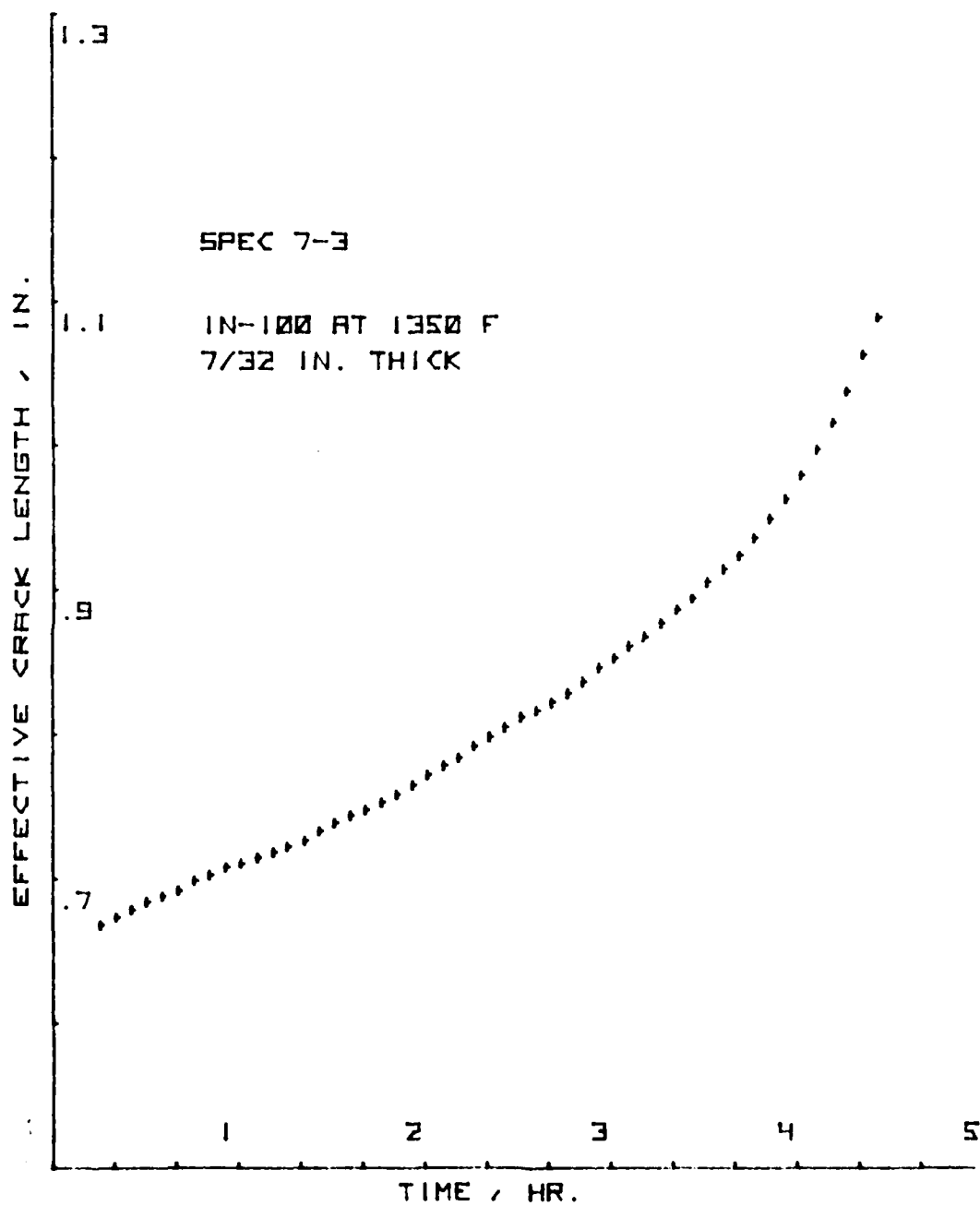
Figure 40. Effective Crack Length vs. Time Plot for CT
Specimen 7-3
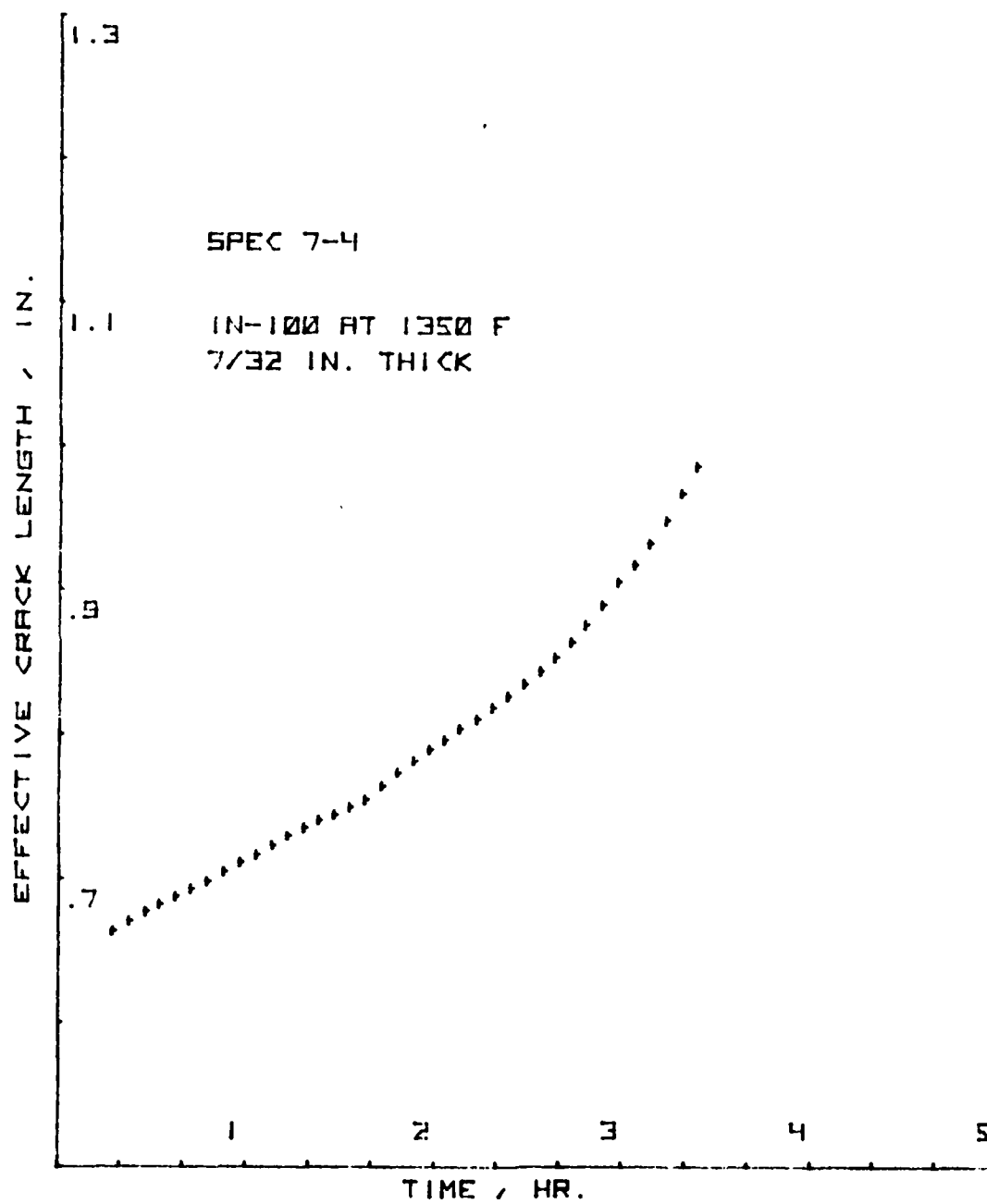
Figure 41. Effective Crack Length vs. Time Plot for CT
Specimen 7-4

Figure 42. Effective Crack Length vs. Time Plot for CT
Specimen 11-2
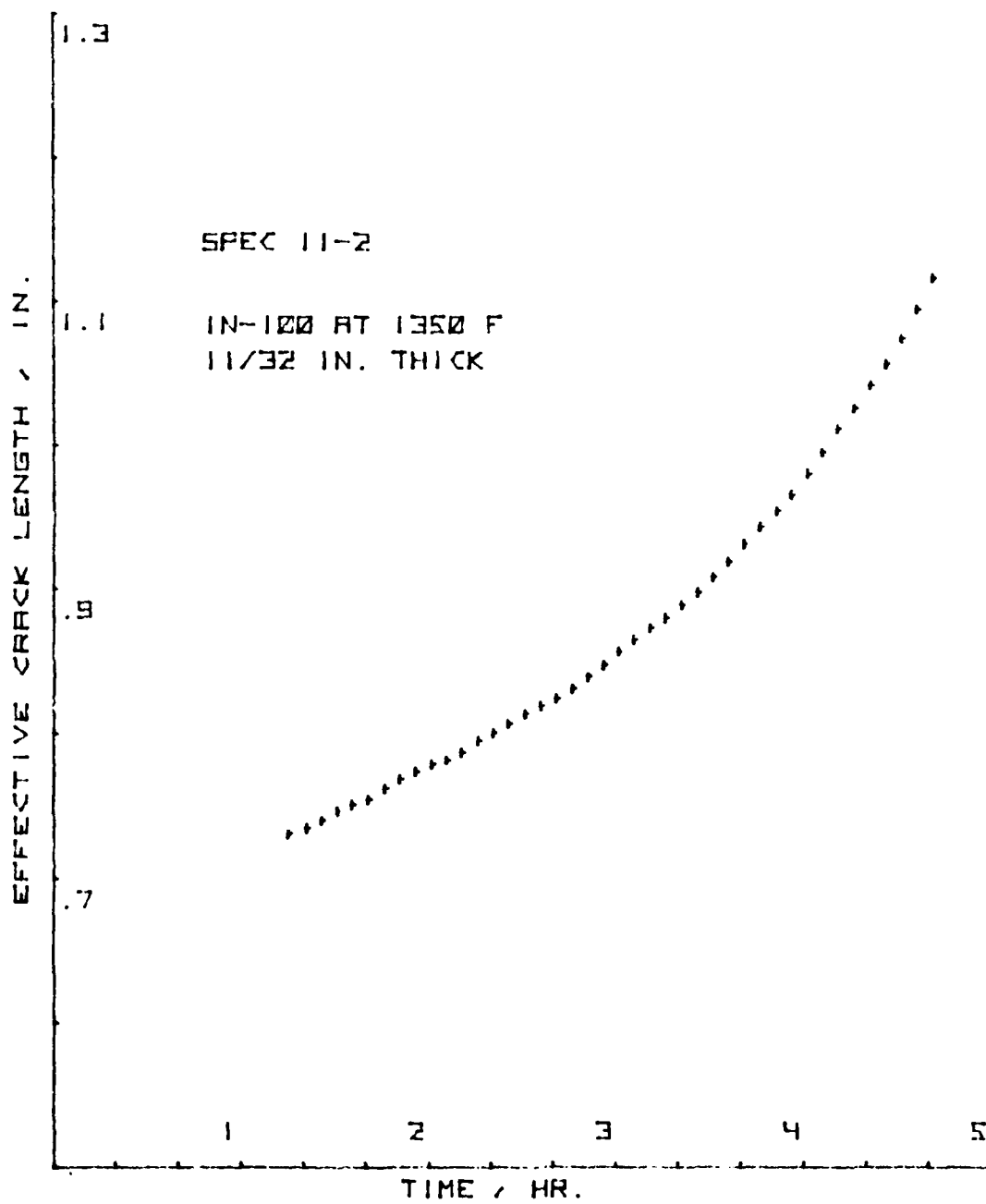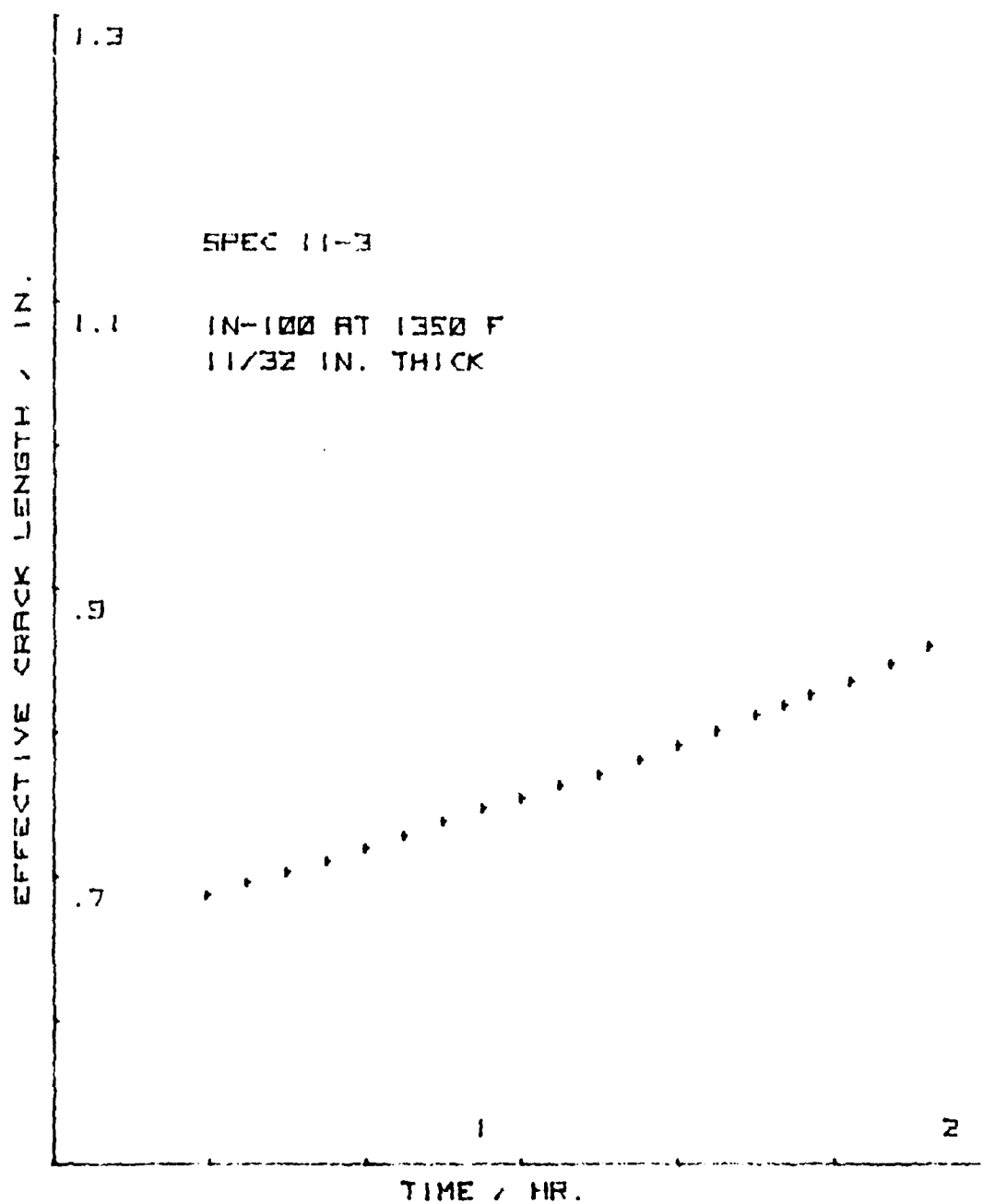
Figure 43. Effective Crack Length vs. Time Plot for CT
Specimen 11-3
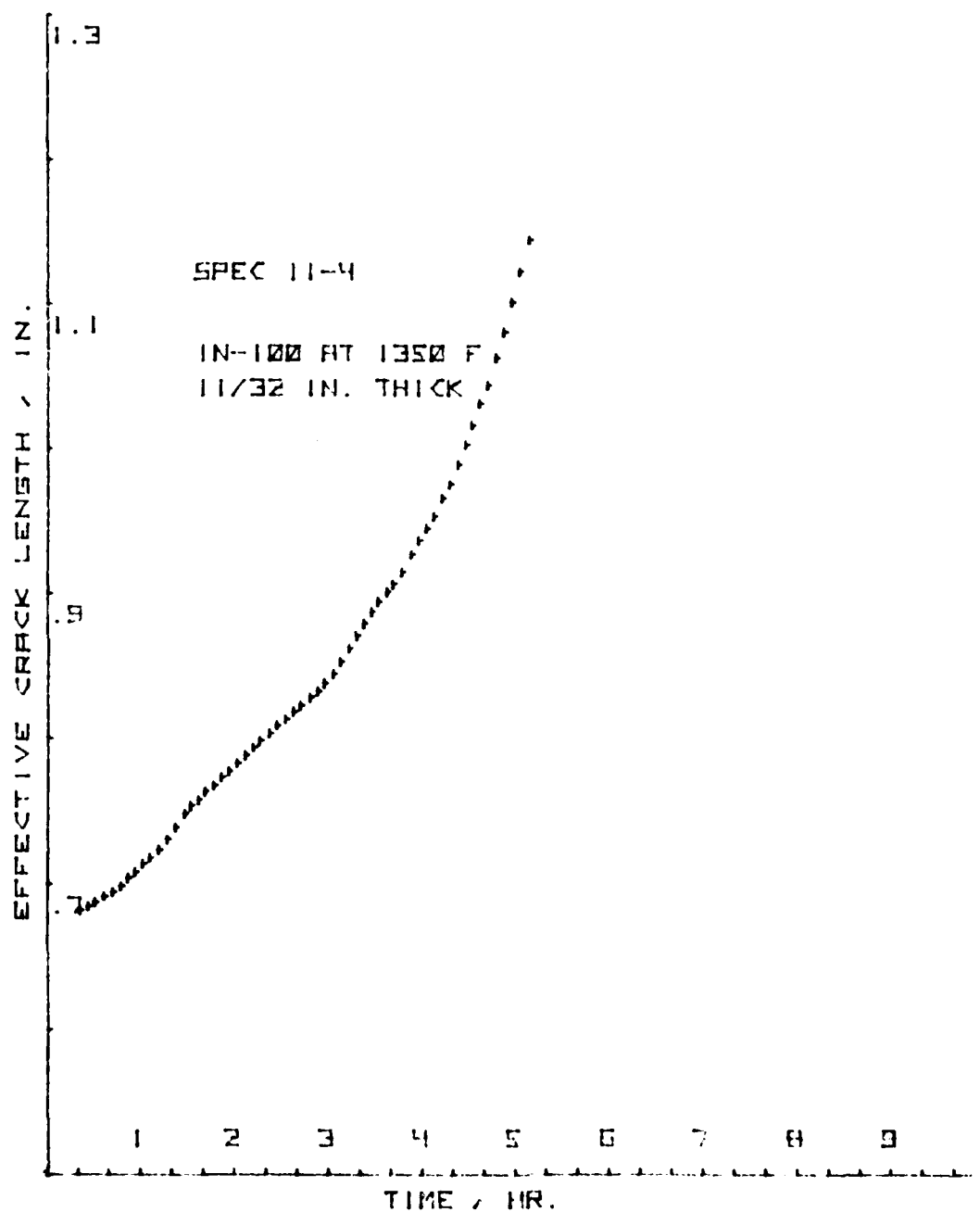
Figure 44.   Effective Crack Length vs. Time Plot for CT
Specimen 11-4

116
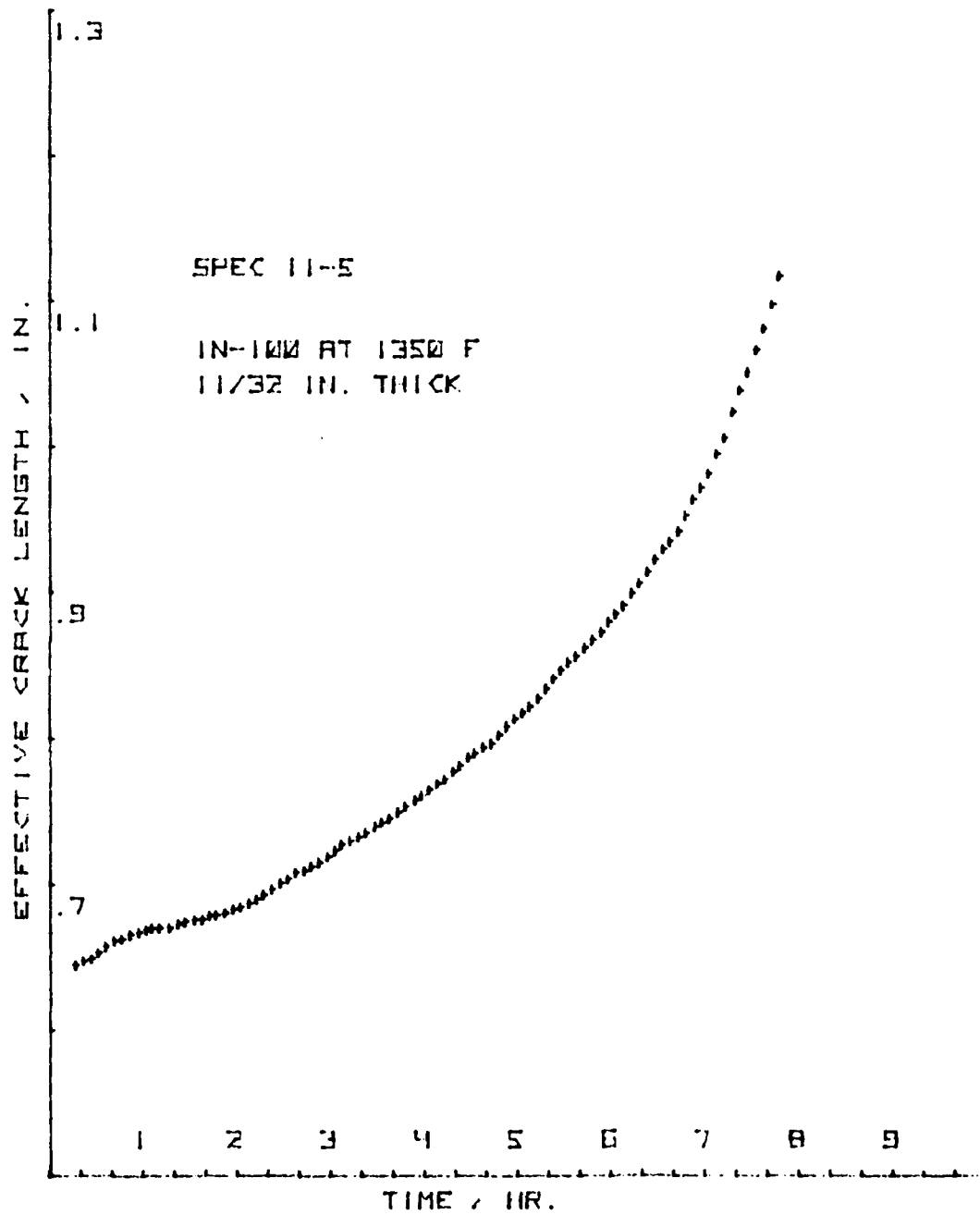
Figure 45.   Effective Crack Length vs. Time Plot for CT
Specimen 11-5
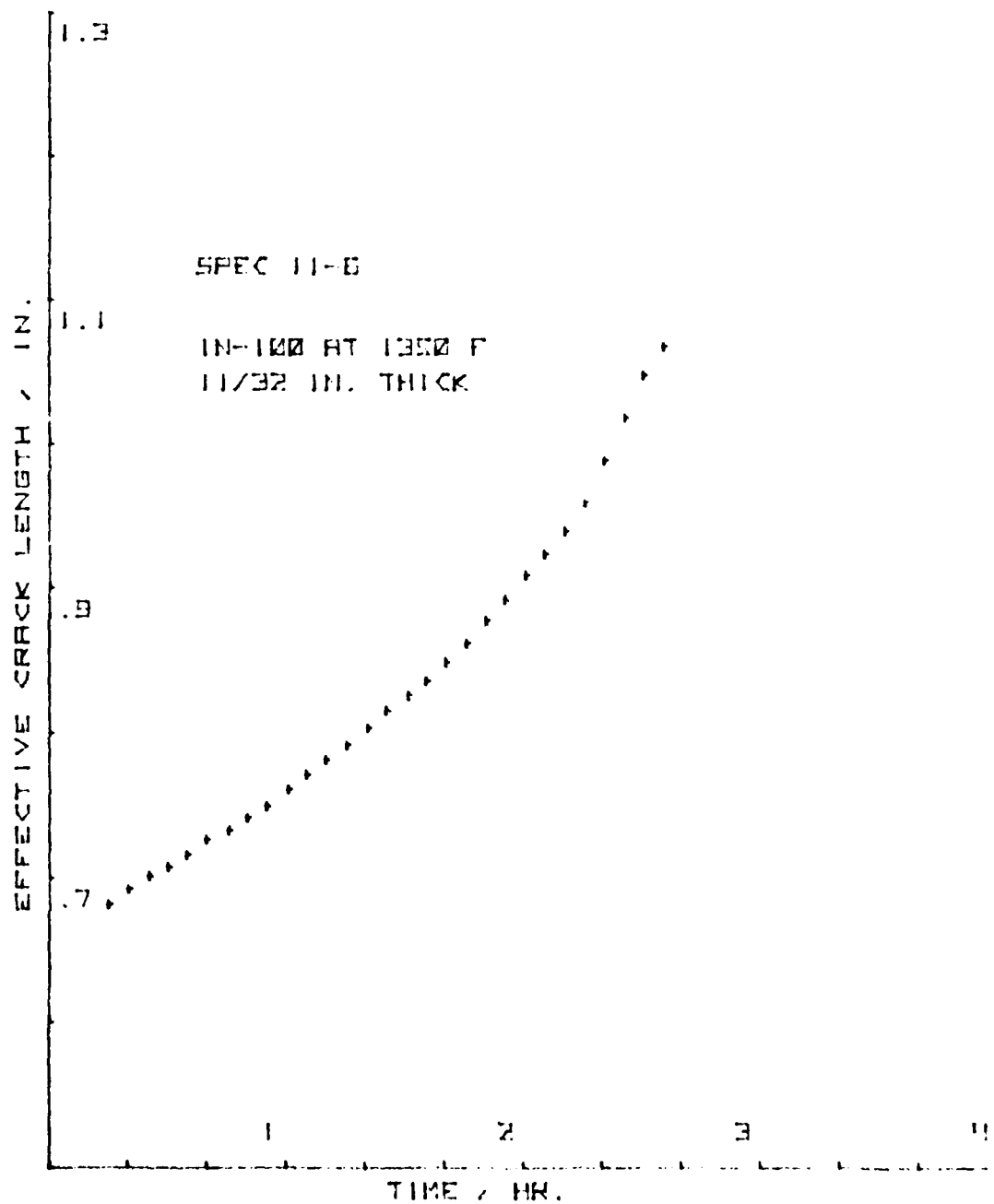
Figure 46. Effective Crack Length vs. Time Plot for CT
Specimen 11-6
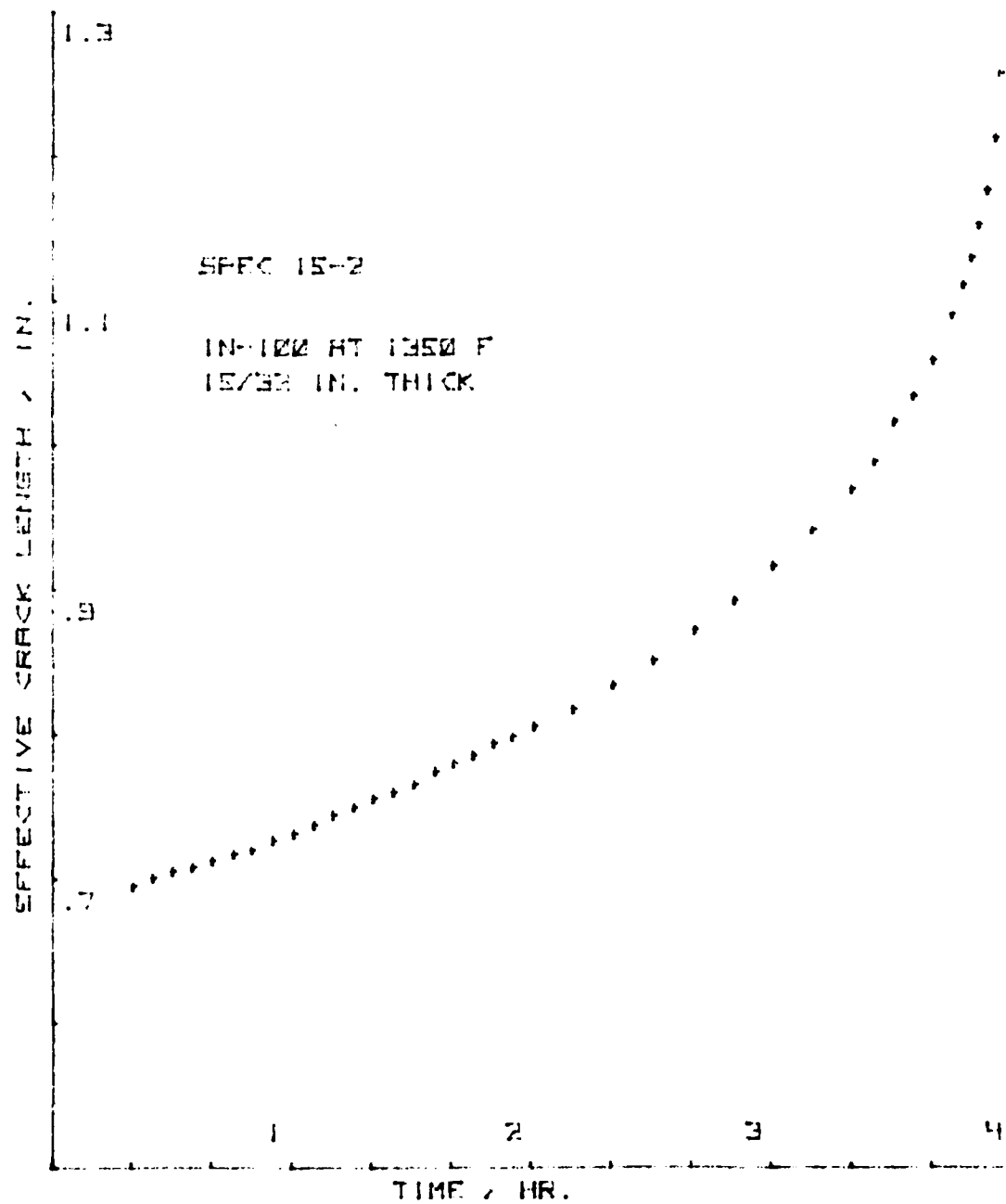
Figure 47. Effective Crack Length vs. Time Plot for CT
Specimen 15-2
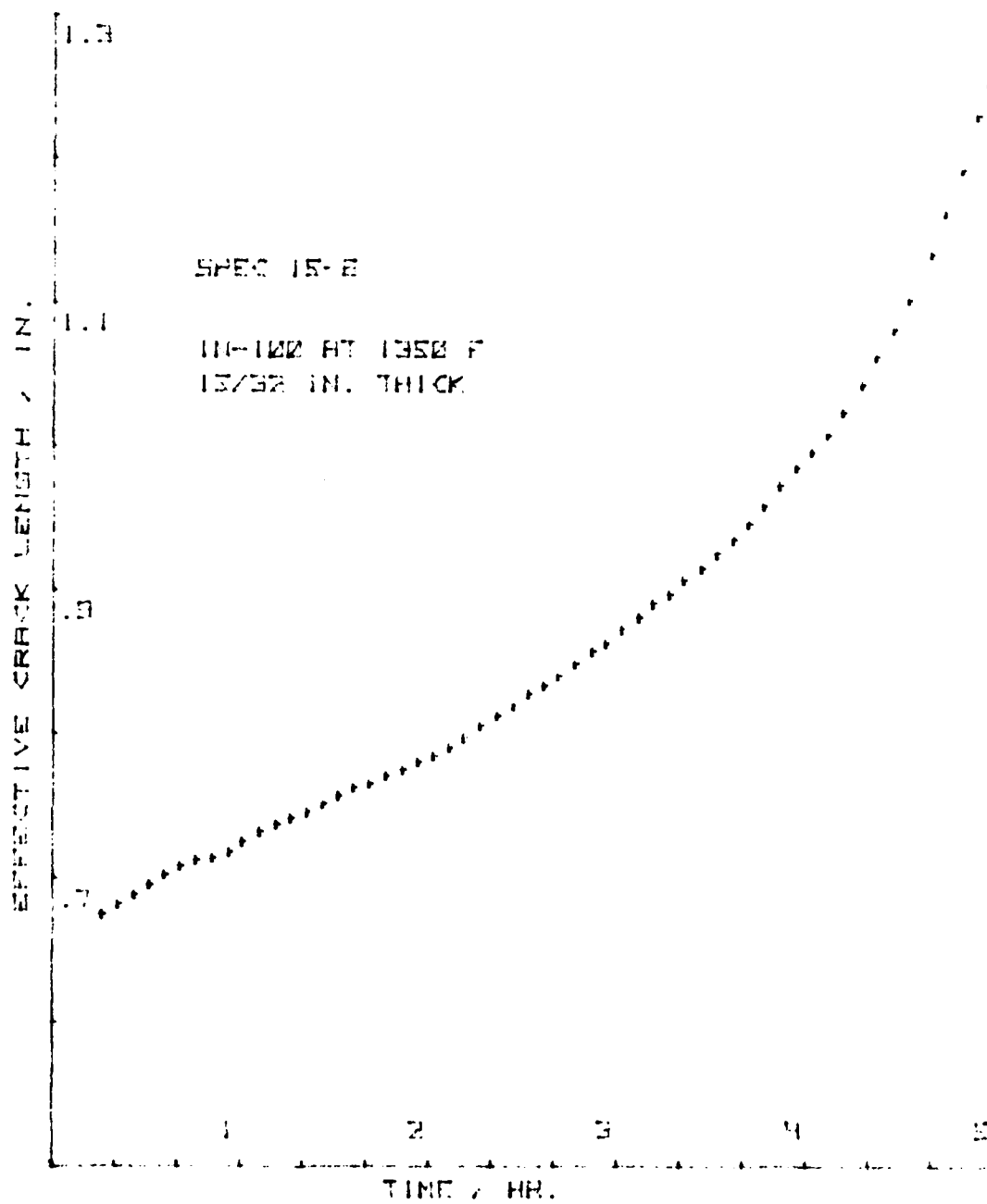
Figure 48. Effective Crack Length vs. Time Plot for CT
Specimen 15-6
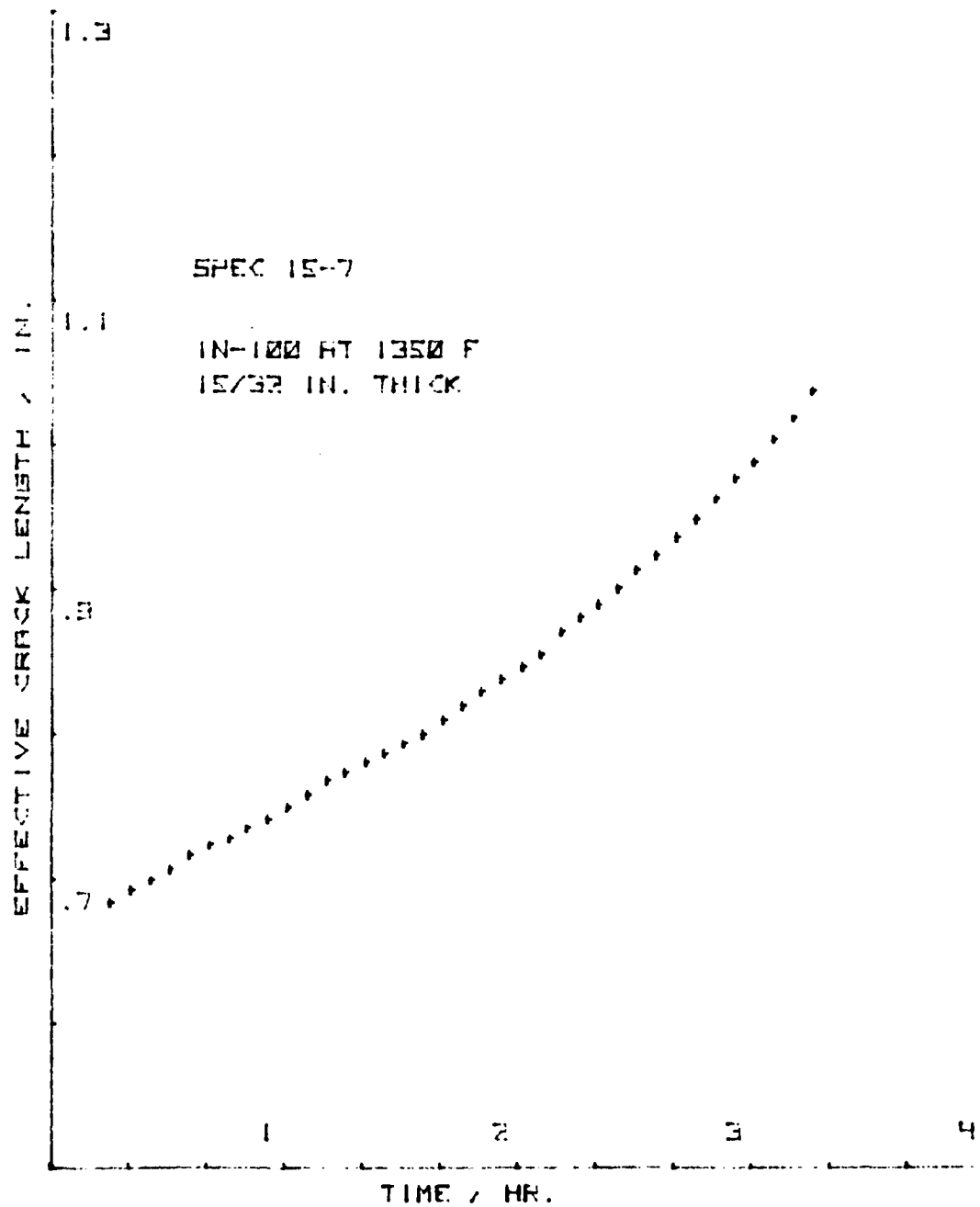
Figure 49. Effective Crack Length vs. Time Plot for CT
Specimen 15-7
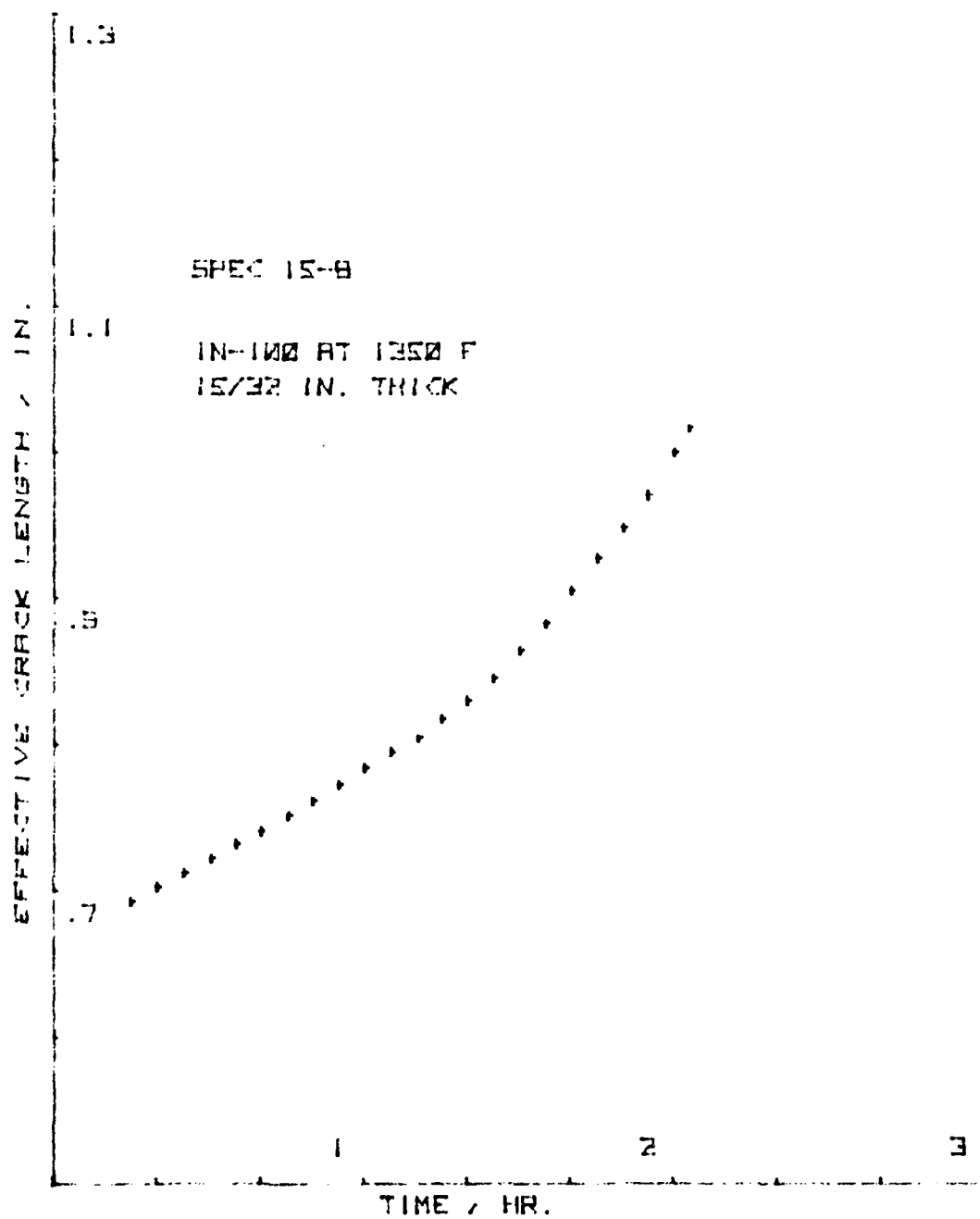
Figure 50.   Effective Crack Length vs. Time Plot for CT
Specimen 15-8
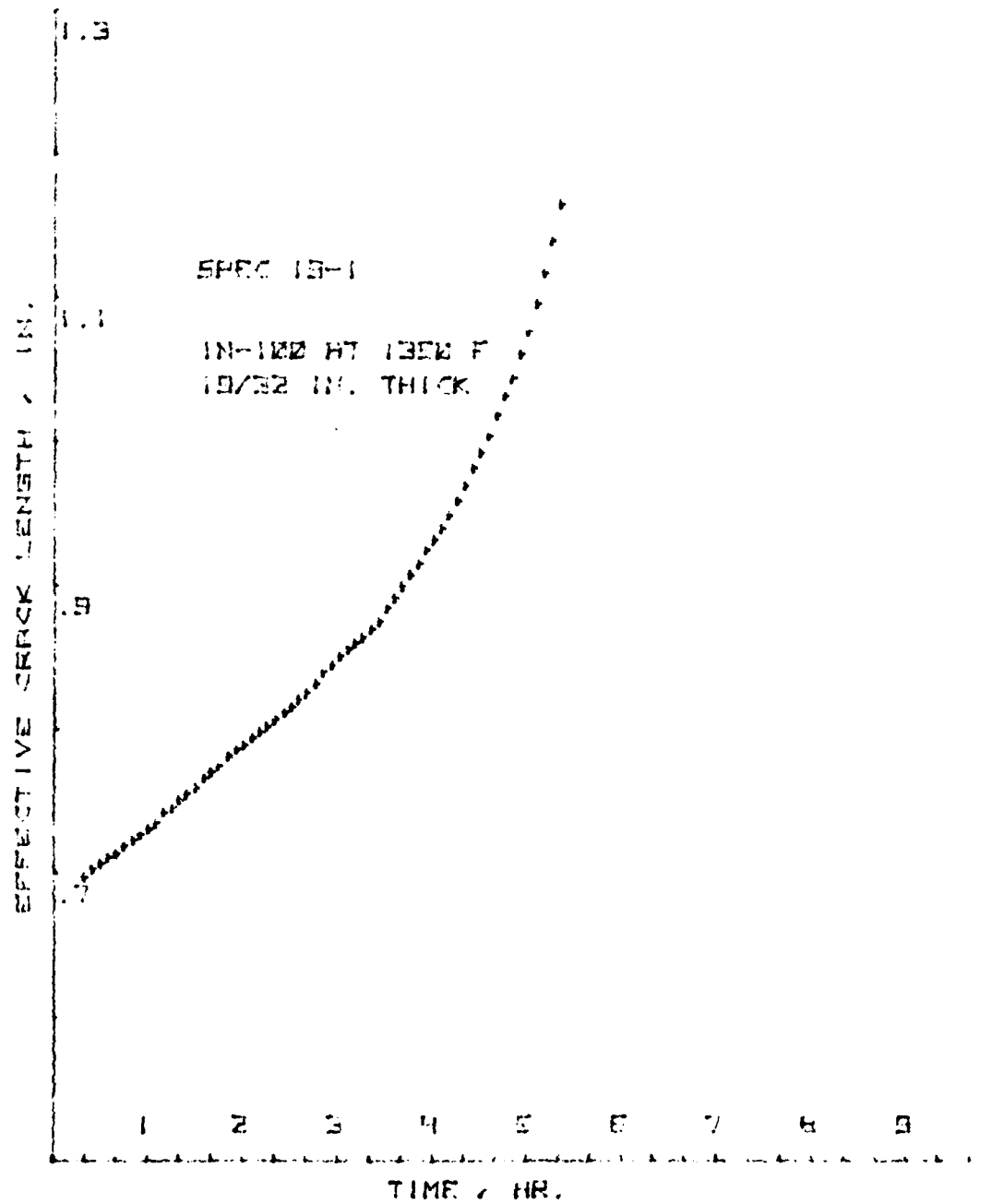
Figure 51. Effective Crack Length vs. Time Plot for CT
Specimen 19-1
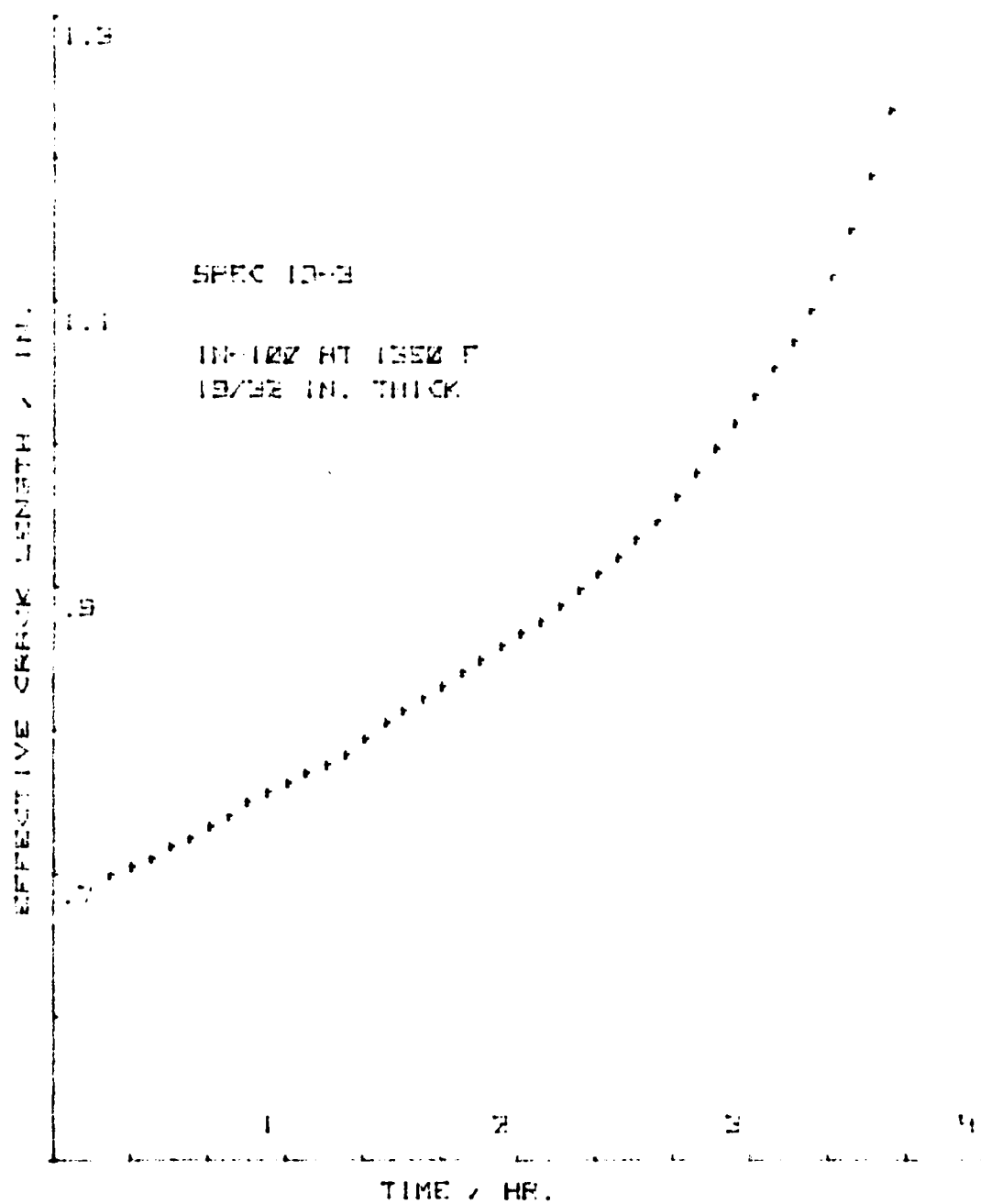
Figure 52. Effective Crack Length vs. Time Plot for CT
Specimen 19-3
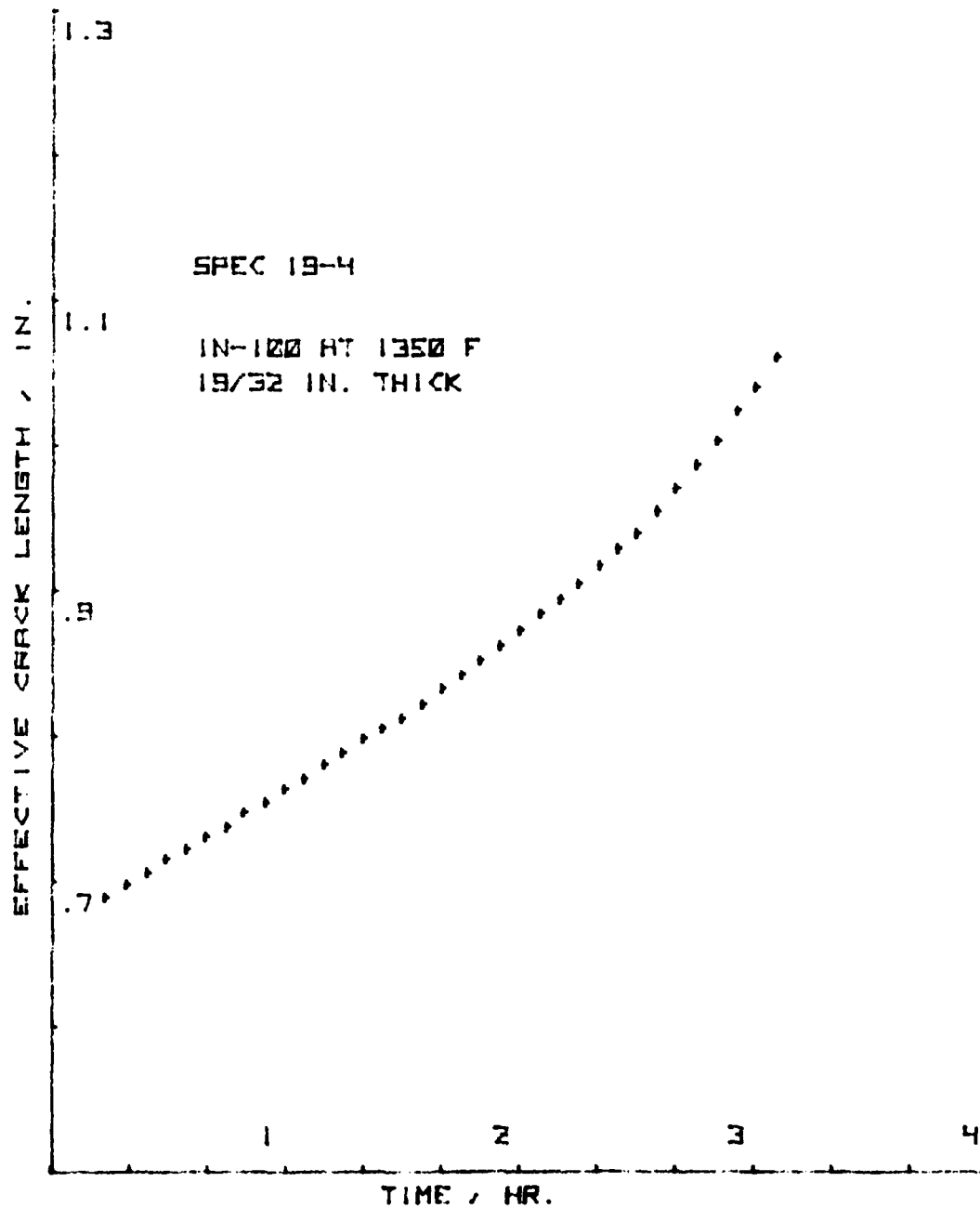
Figure 53. Effective Crack Length vs. Time Plot for CT
Specimen 19-4
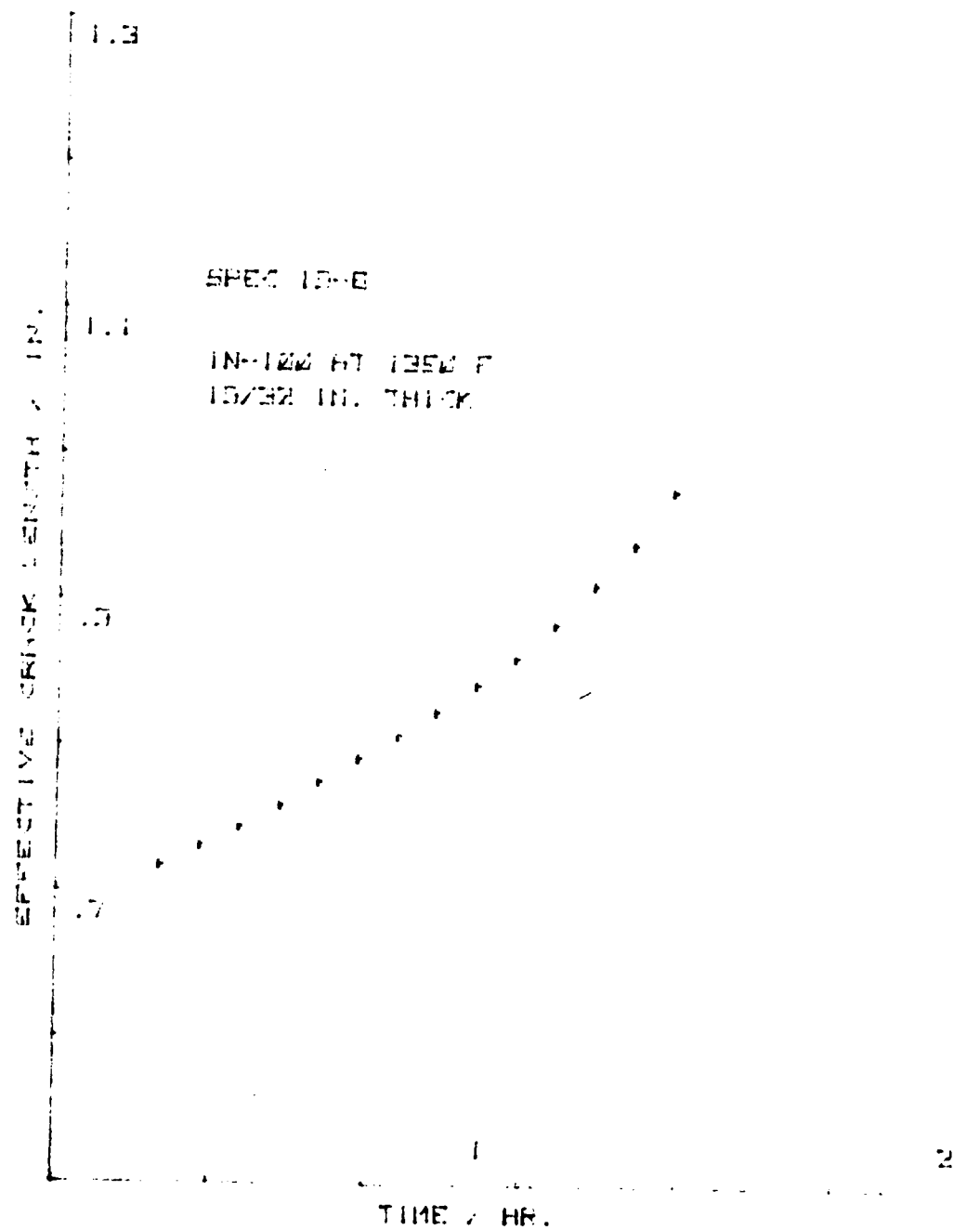
Figure 54. Effective Crack Length vs. Time Plot for CT
Specimen 19-6
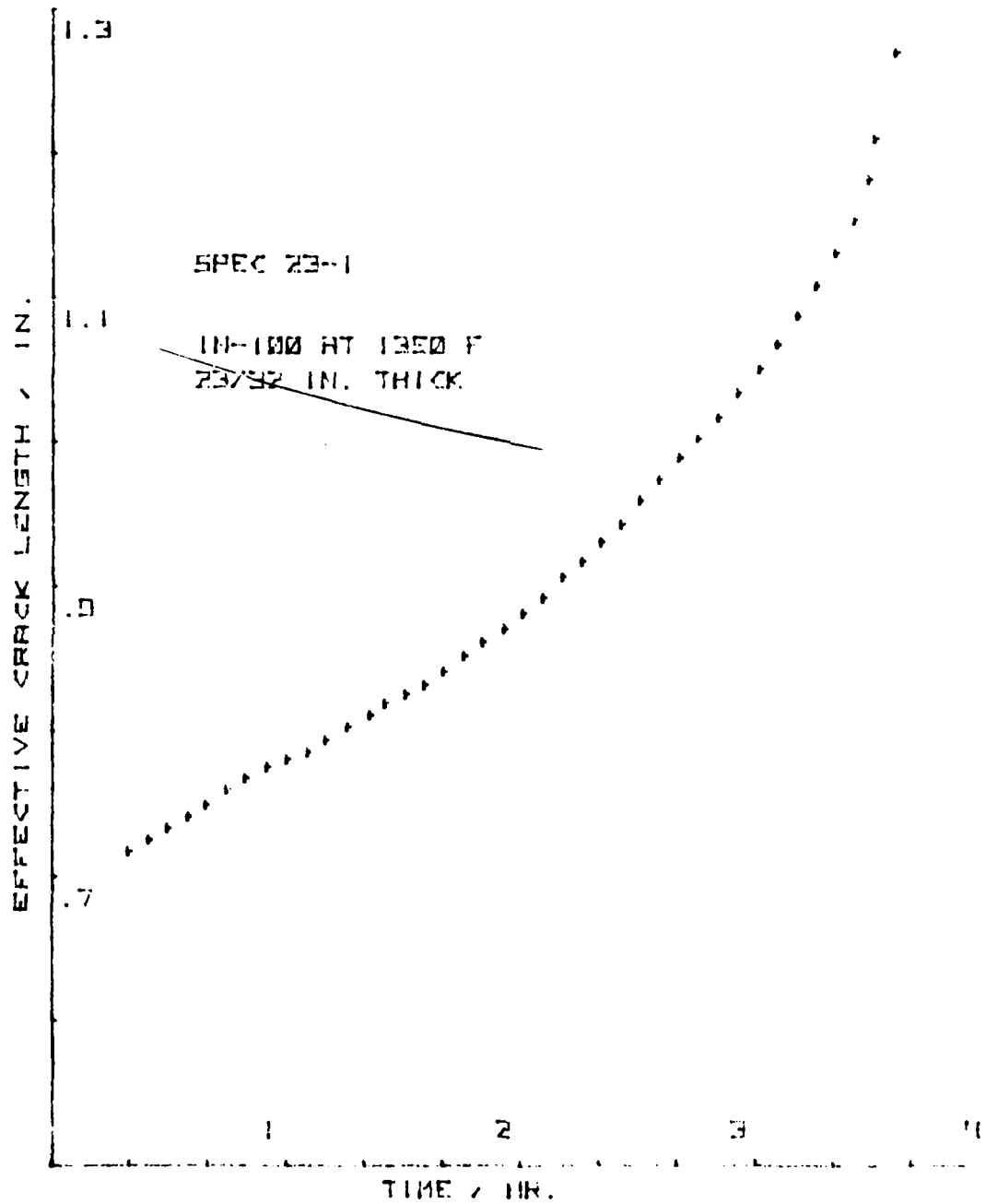
Figure 55. Effective Crack Length vs. Time Plot for CT
Specimen 23-1
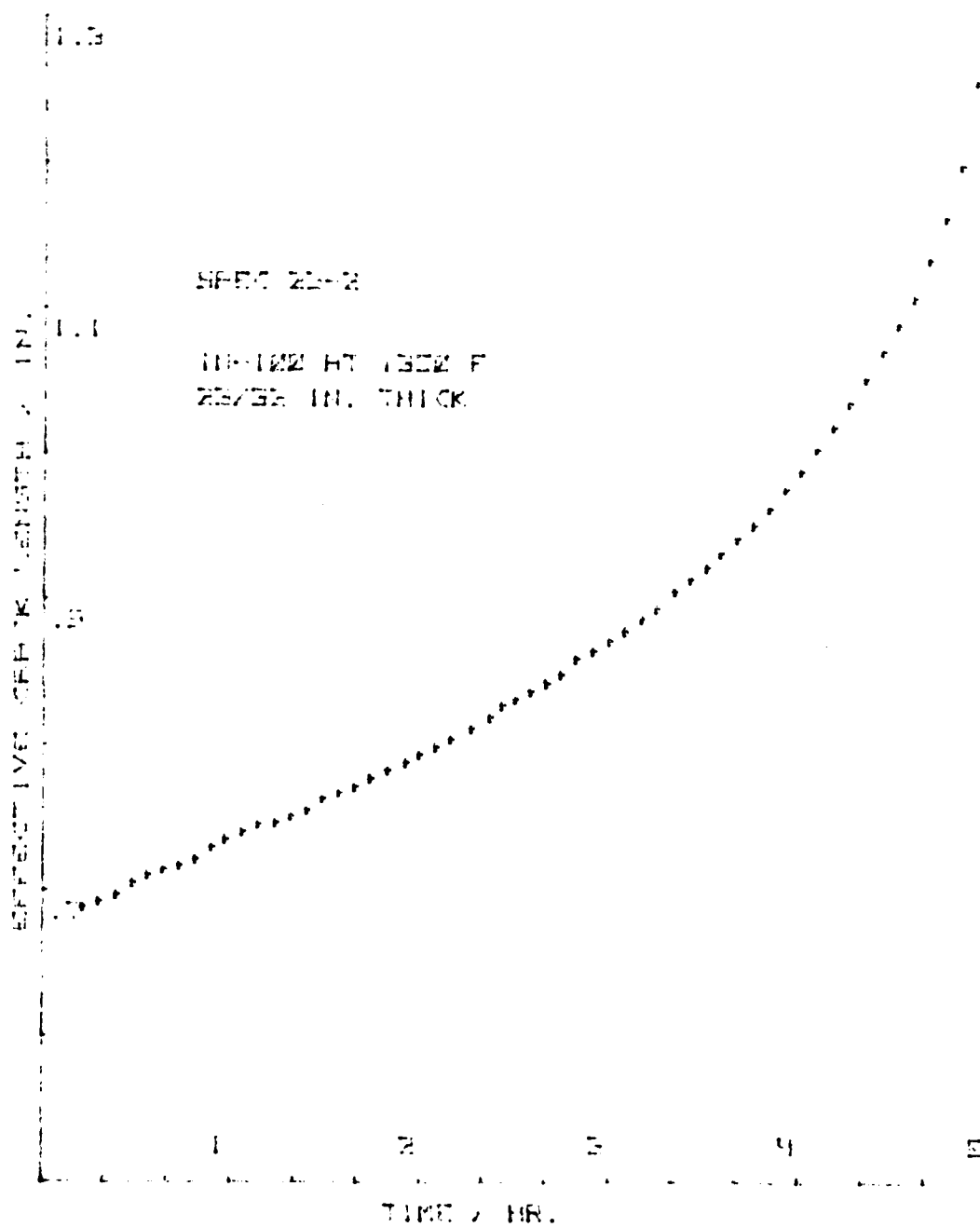
Figure 56. Effective Crack Length vs. Time Plot for CT
Specimen 23-2
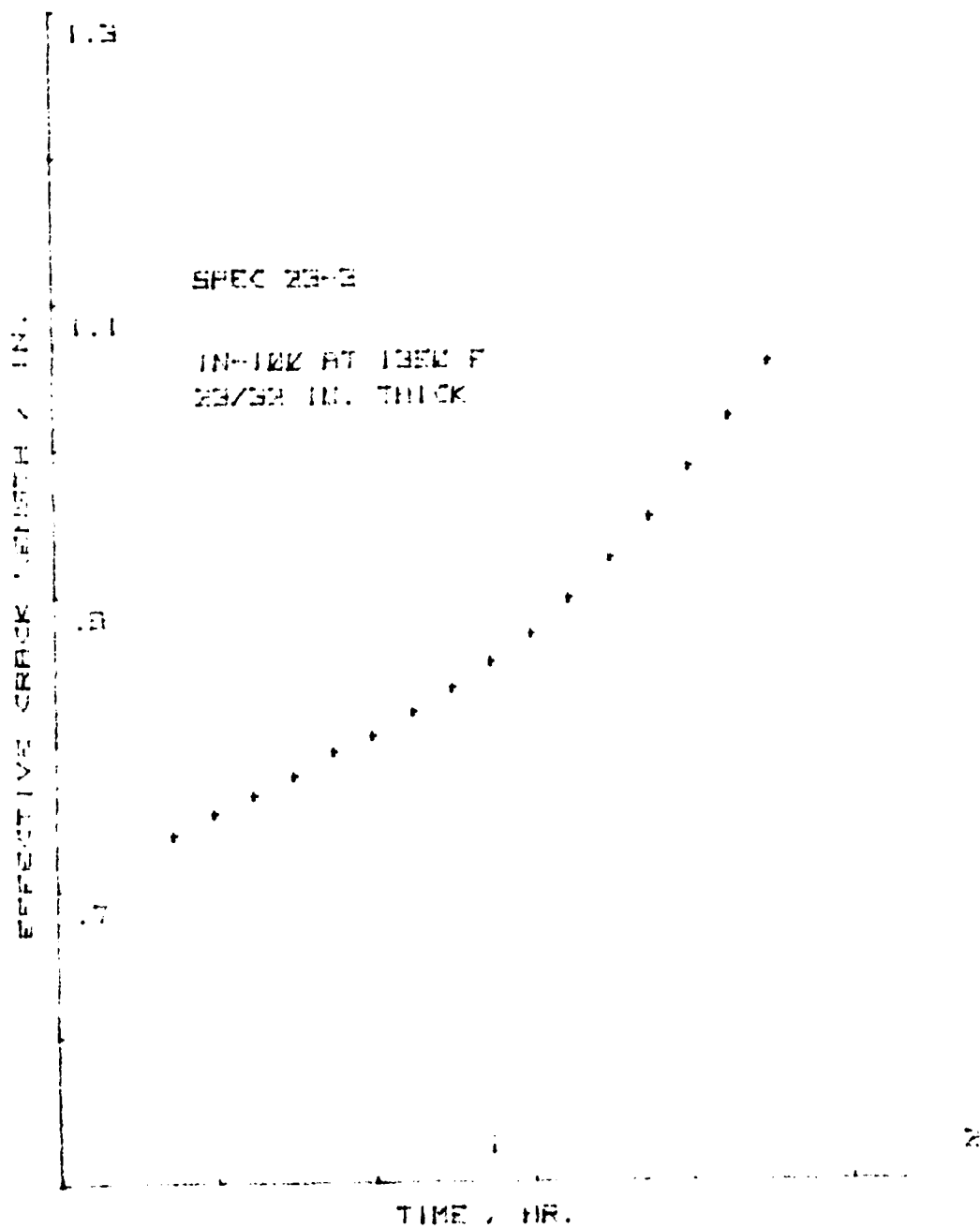
Figure 57. Effective Crack Length vs. Time Plot for CT
Specimen 23-3
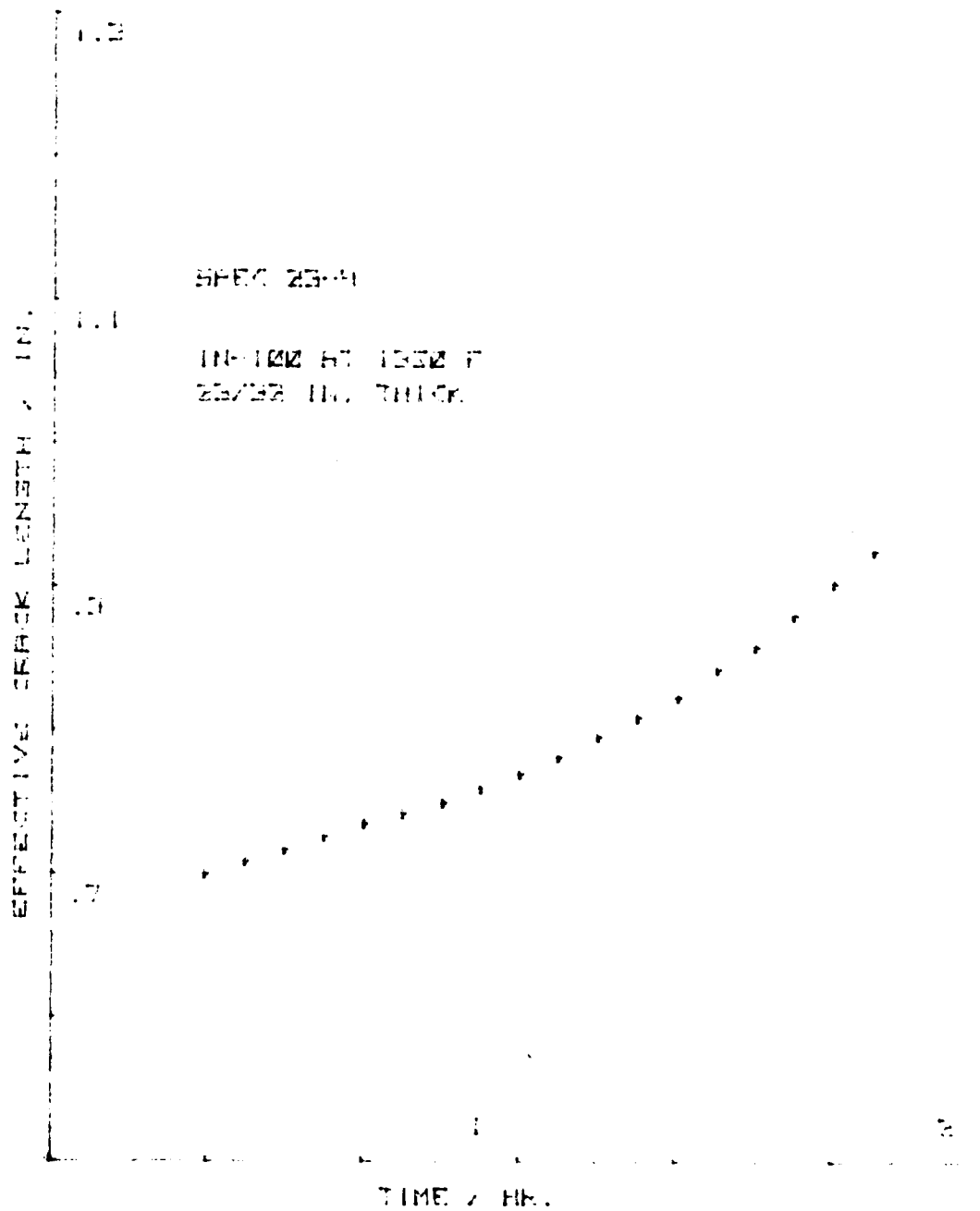
Figure 58. Effective Crack Length vs. Time Plot for CT
Specimen 23-4
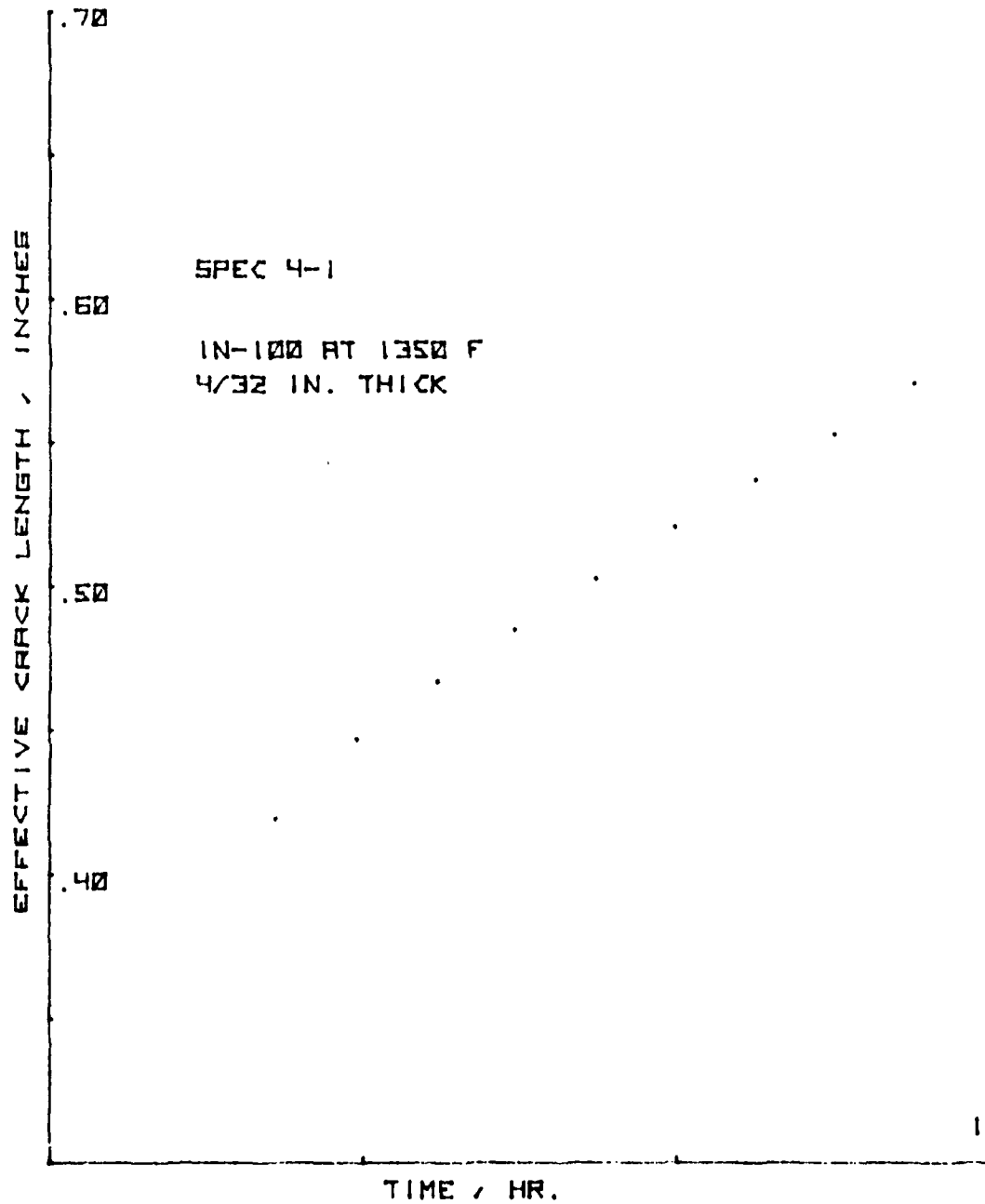
Figure 59. Effective Crack Length vs. Time Plot for Ring
Specimen 4-1

131
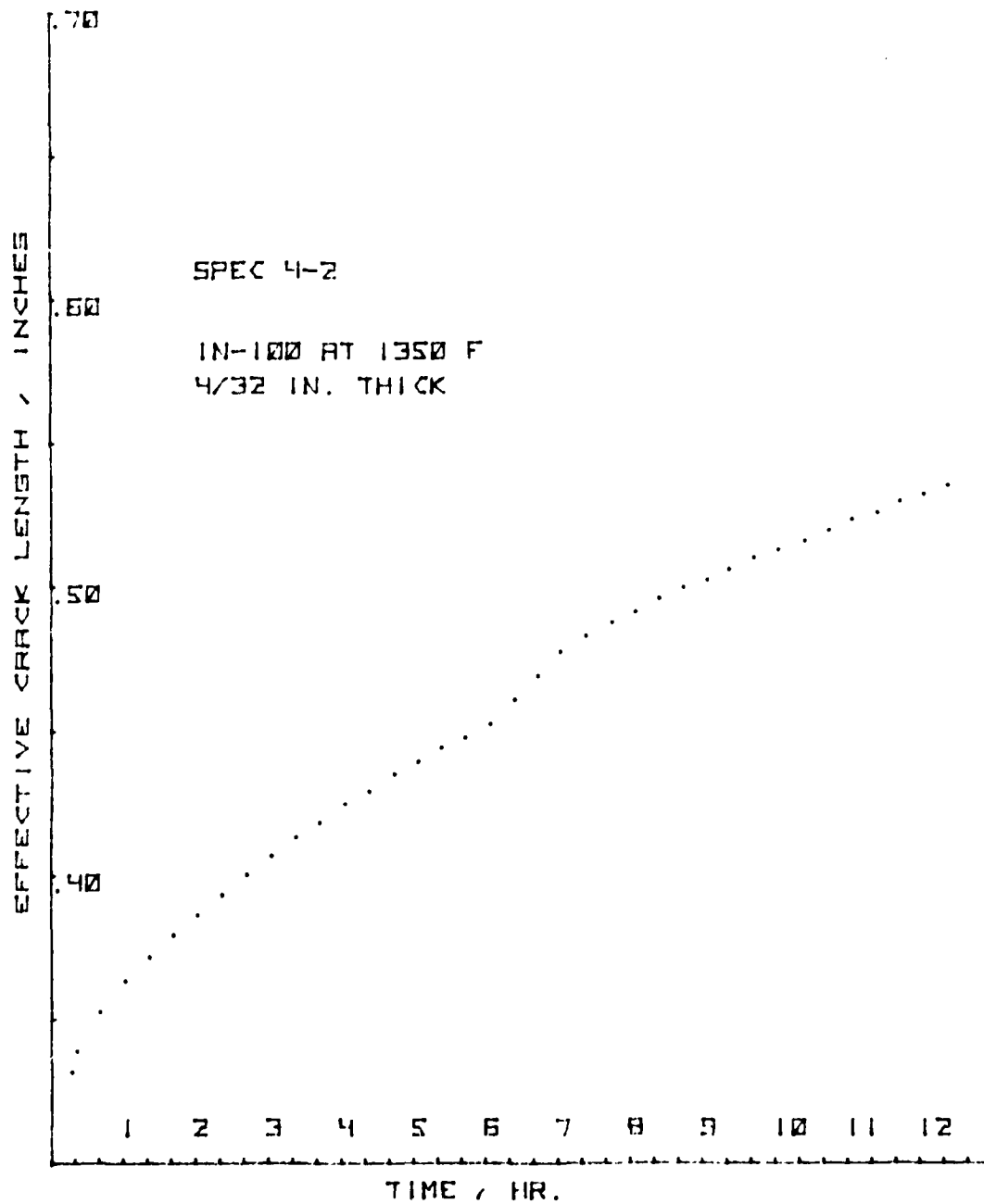
Figure 60. Effective Crack Length vs. Time Plot for Ring
Specimen 4-2

132
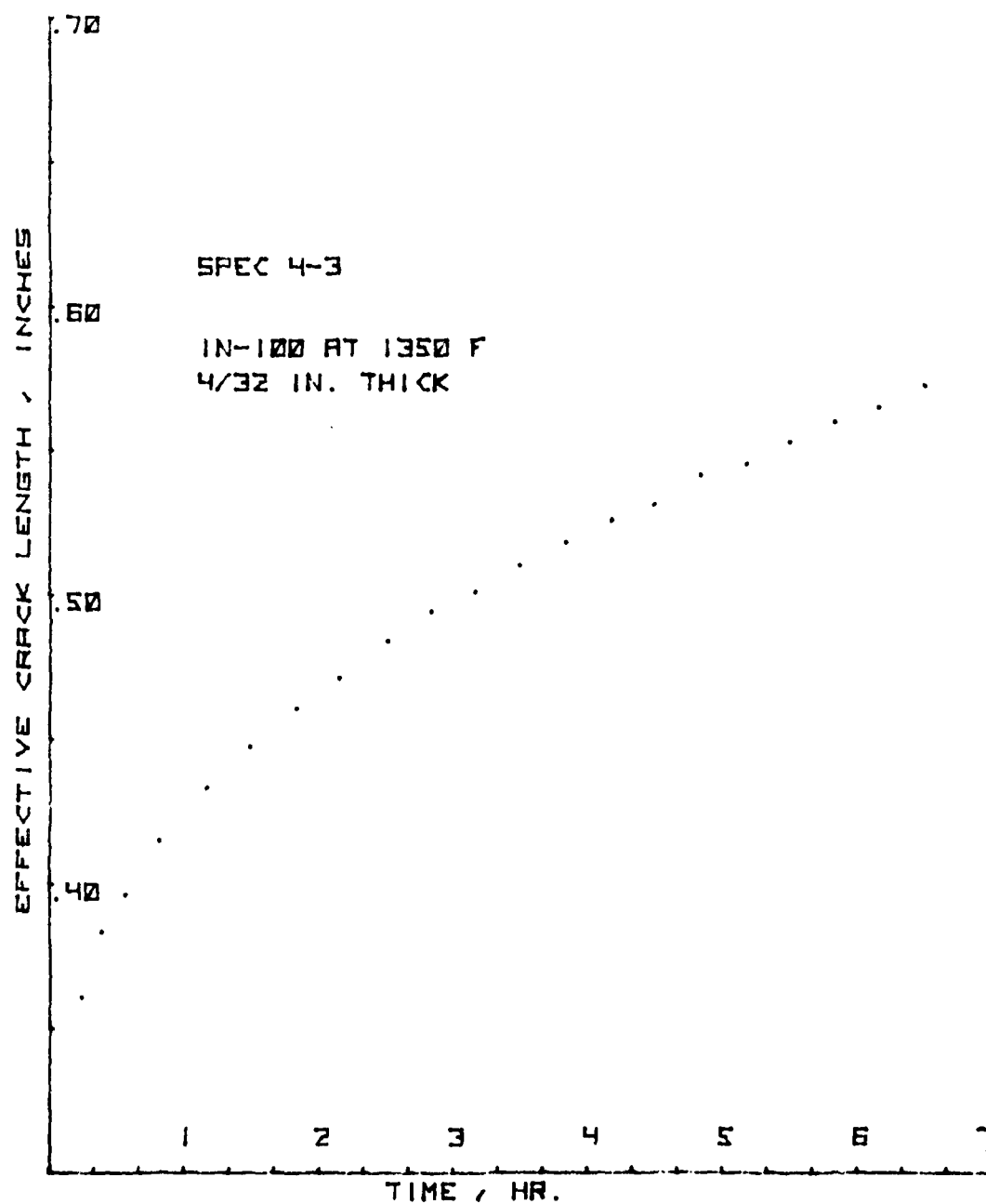
Figure 61. Effective Crack Length vs. Time Plot for Ring
Specimen 4-3
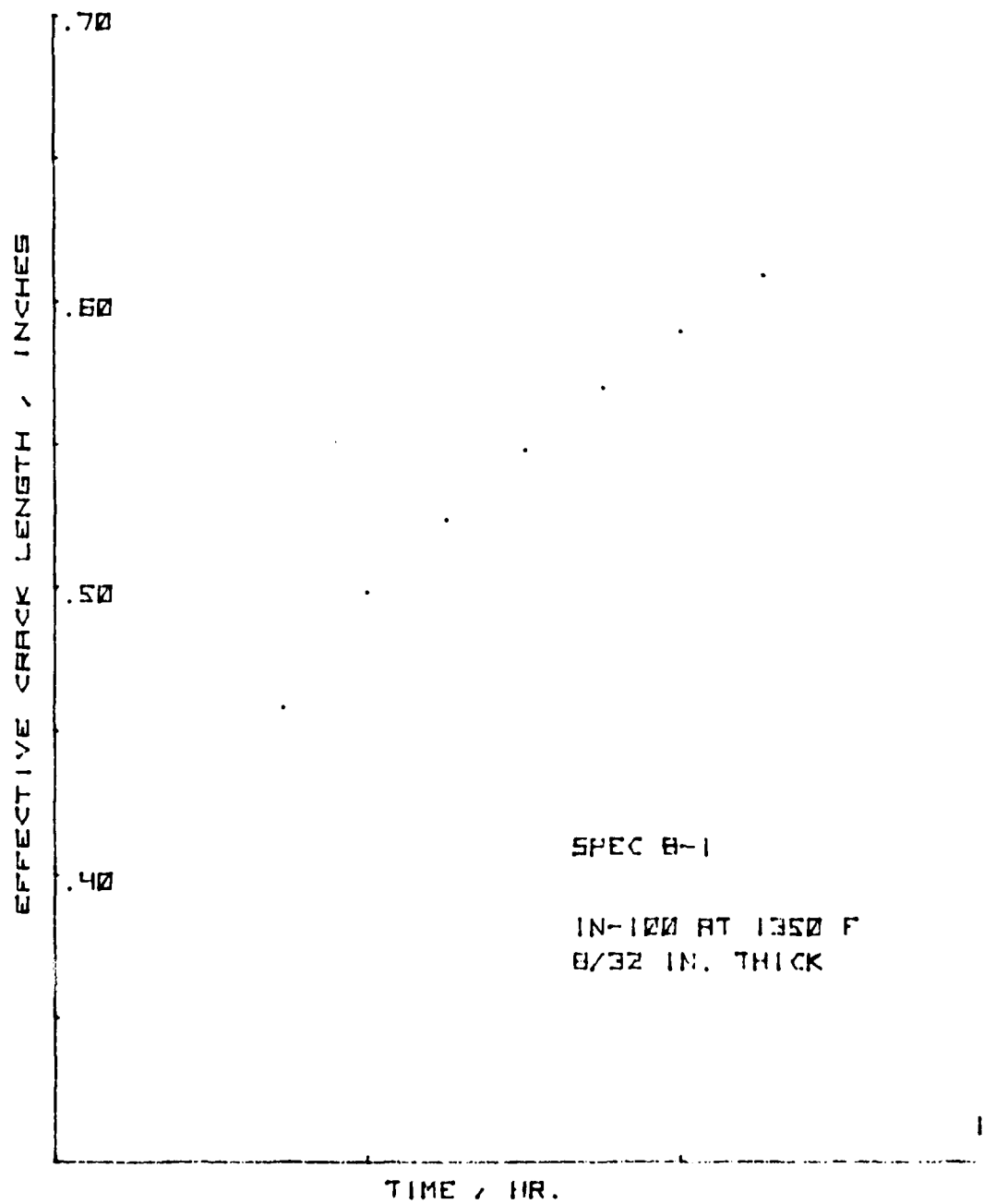
Figure 62.   Effective Crack Length vs. Time Plot for Ring
             Specimen 8-1
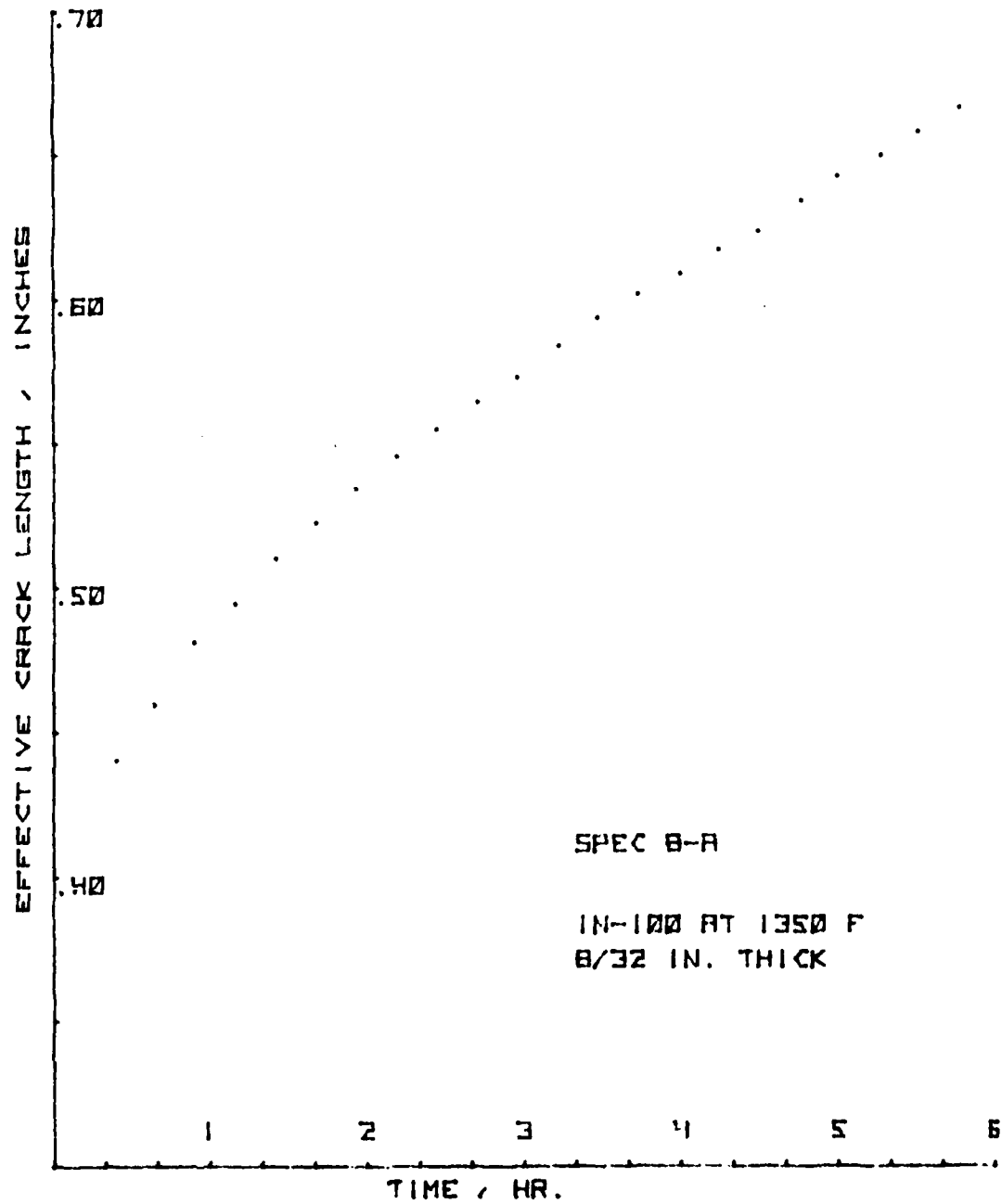
Figure 63.   Effective Crack Length vs. Time Plot for Ring
Specimen 8-A
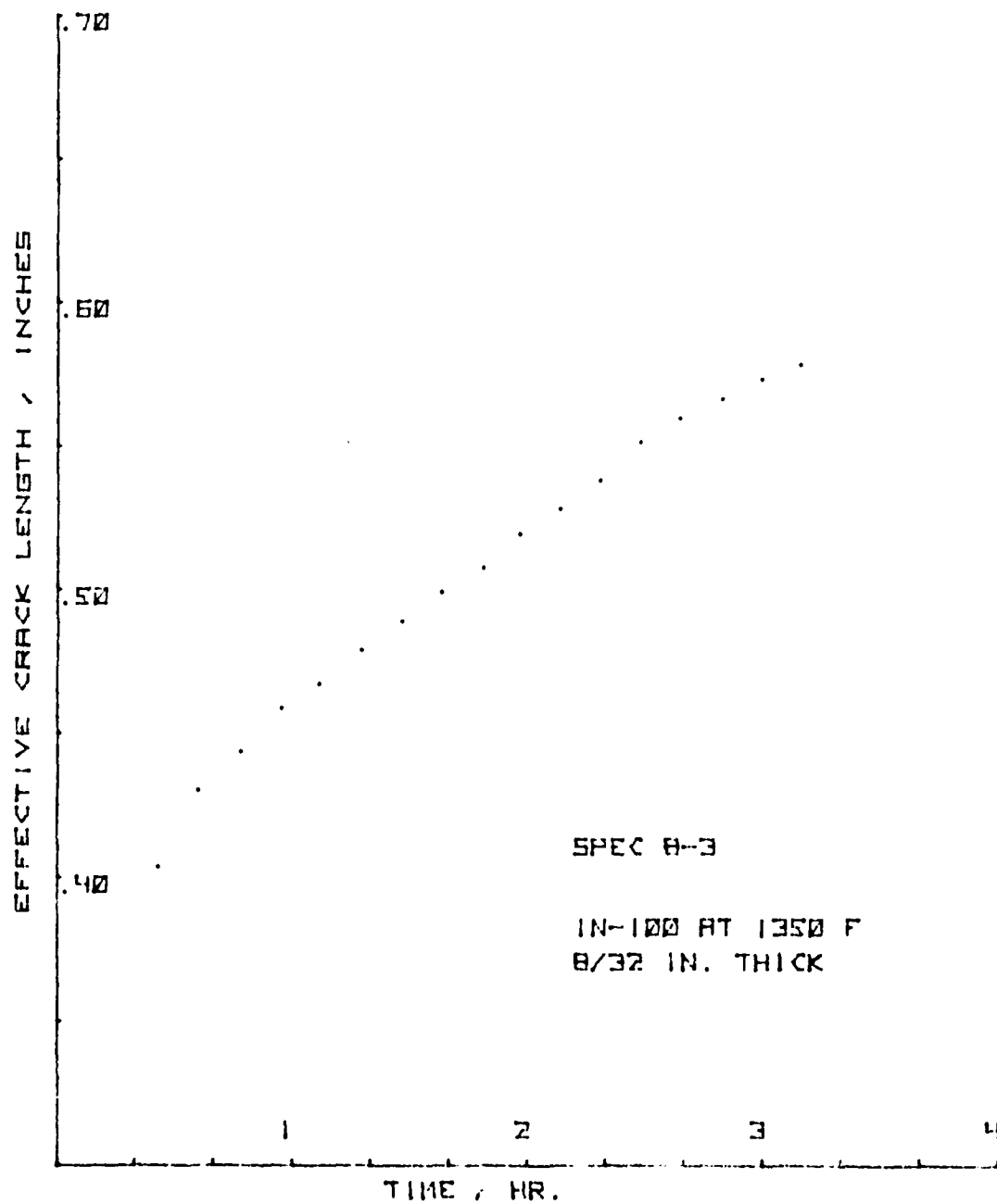
Figure 64.   Effective Crack Length vs. Time Plot for Ring
              Specimen 8-3
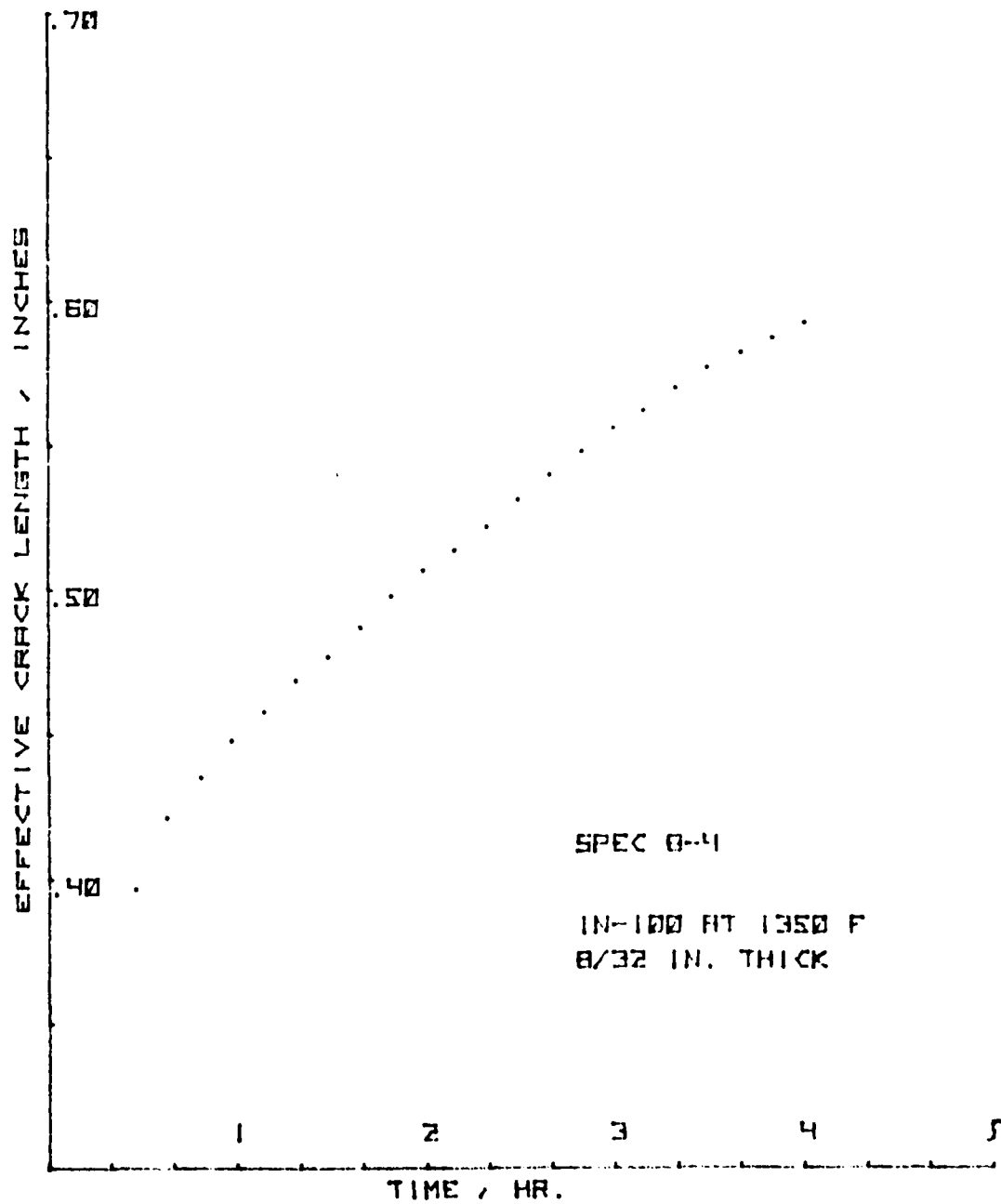
Figure 65. Effective Crack Length vs. Time Plot for Ring
            Specimen 8-4
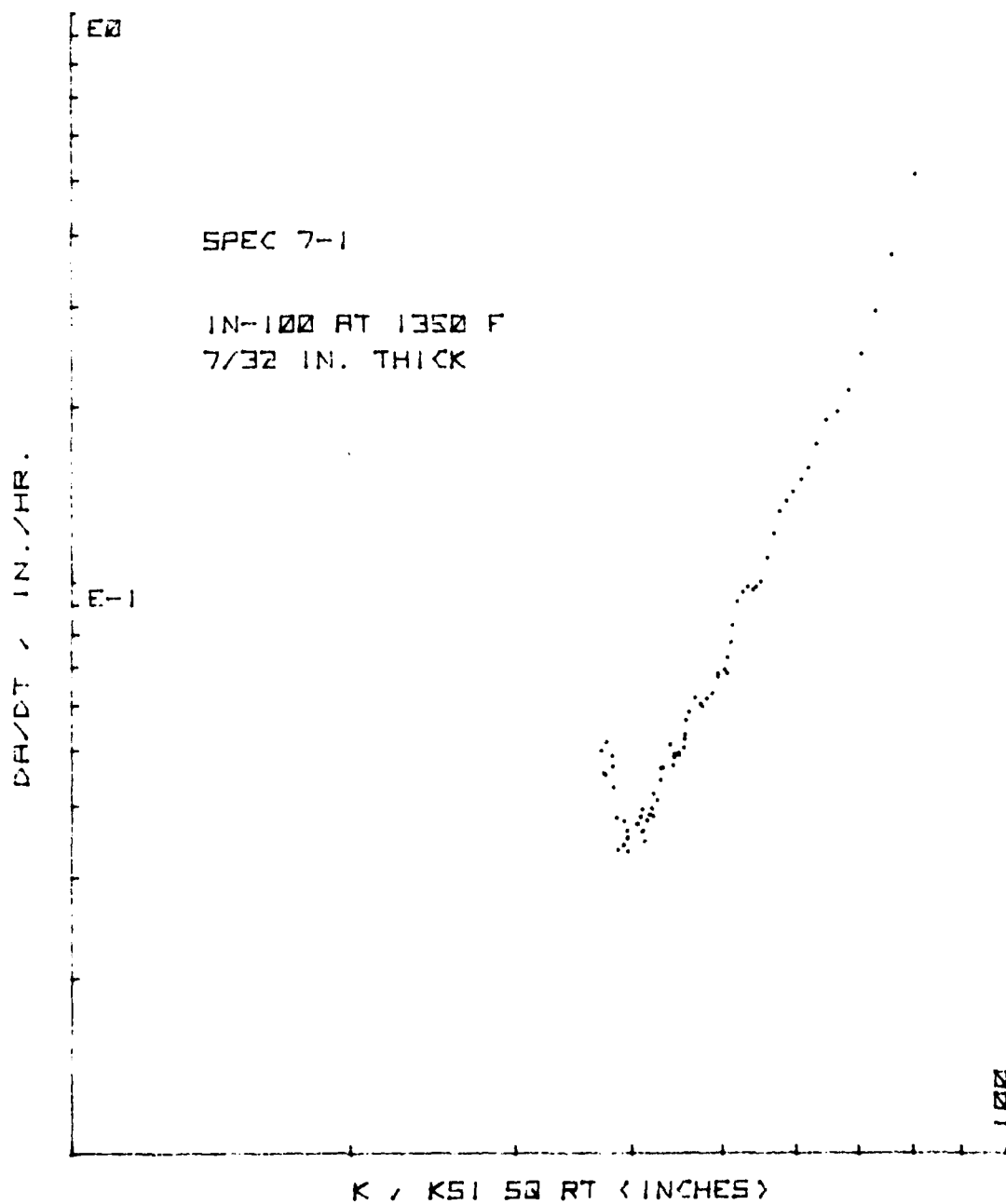
Figure 66.   Creep Crack Growth Rate vs. K for CT Specimen 7-1
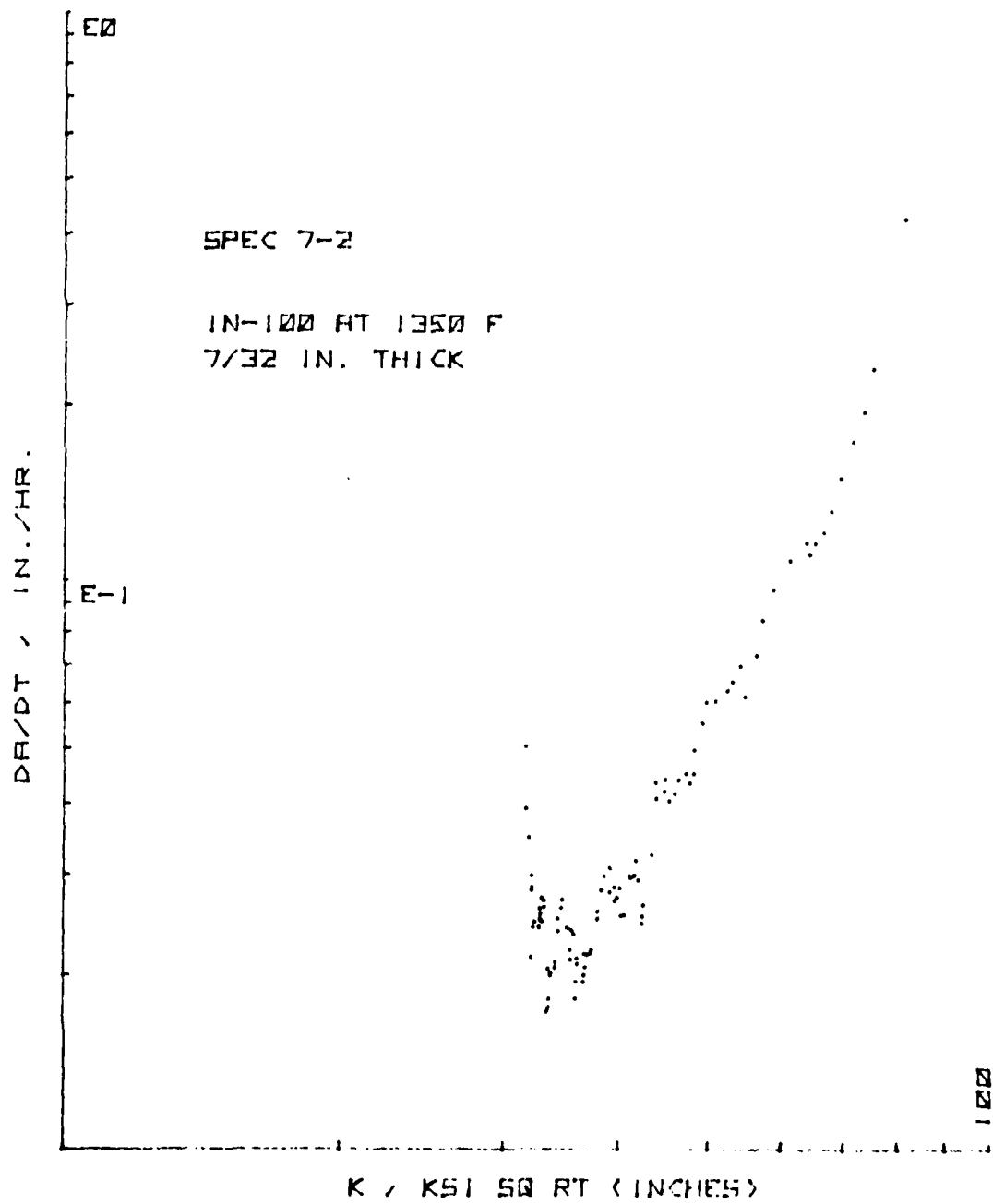
Figure 67.   Creep Crack Growth Rate vs. K for CT Specimen 7-2
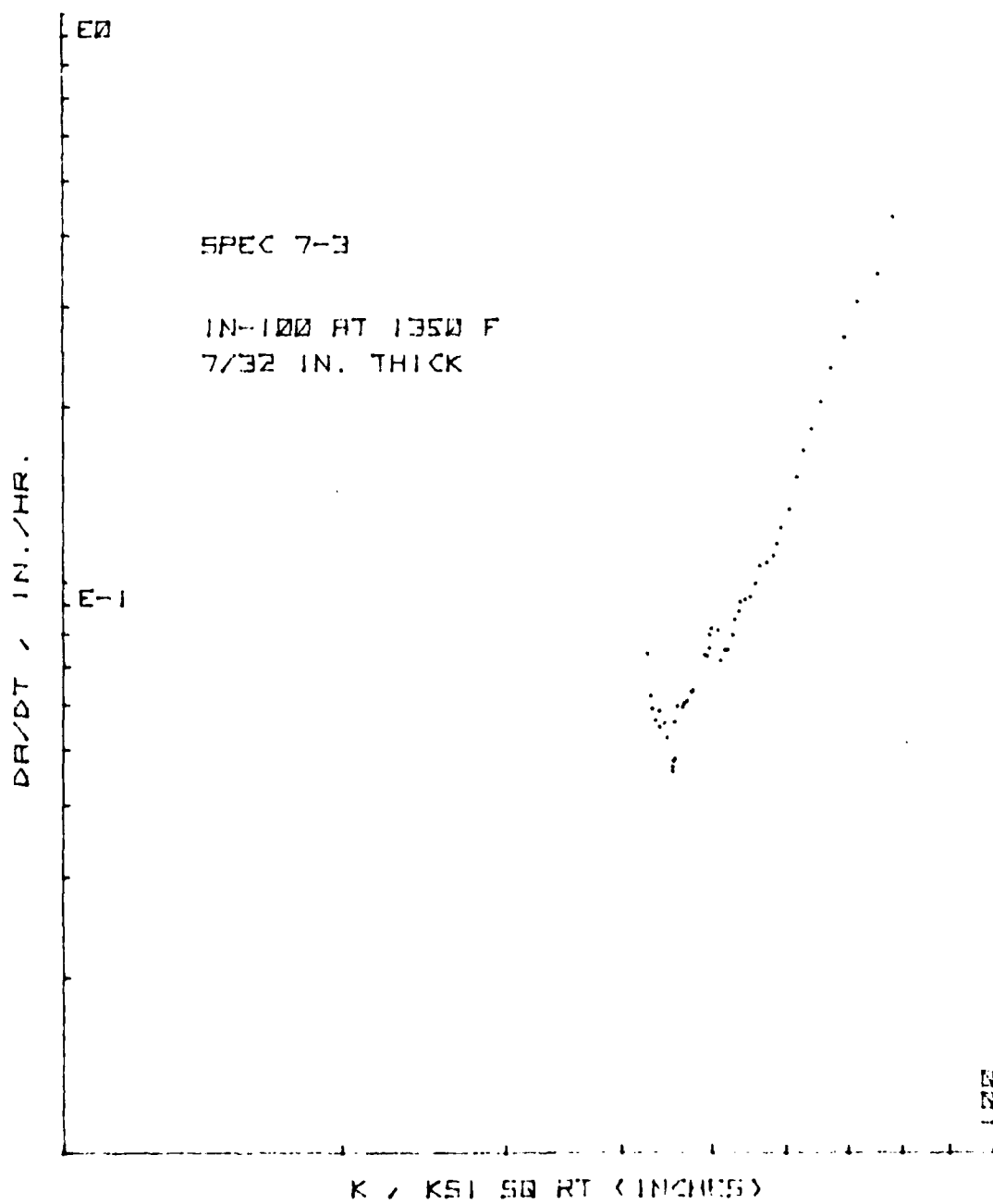
Figure 68.   Creep Crack Growth Rate vs. K for CT Specimen 7-3

Figure 69. Creep Crack Growth Rate vs. K for CT Specimen 7-4
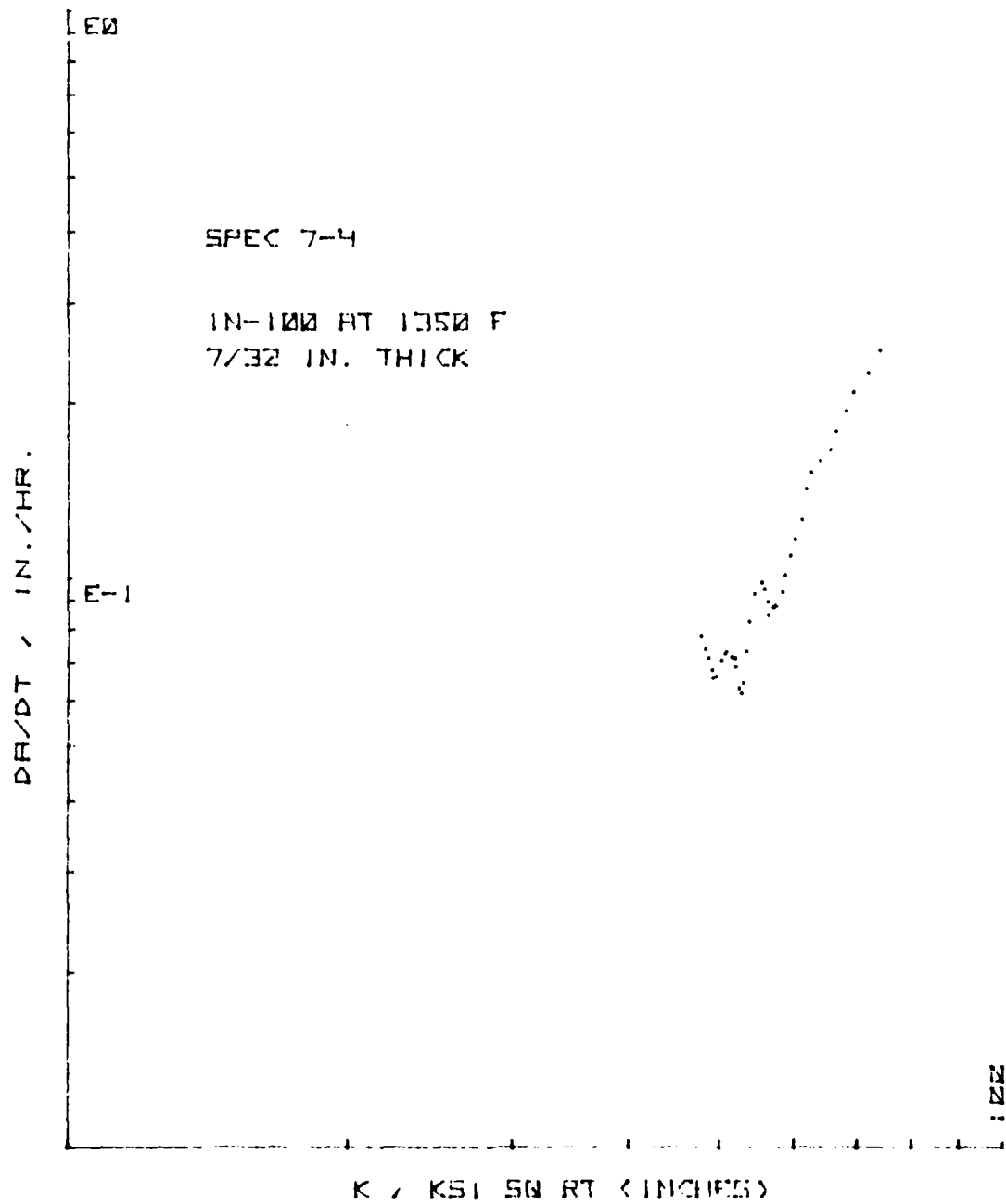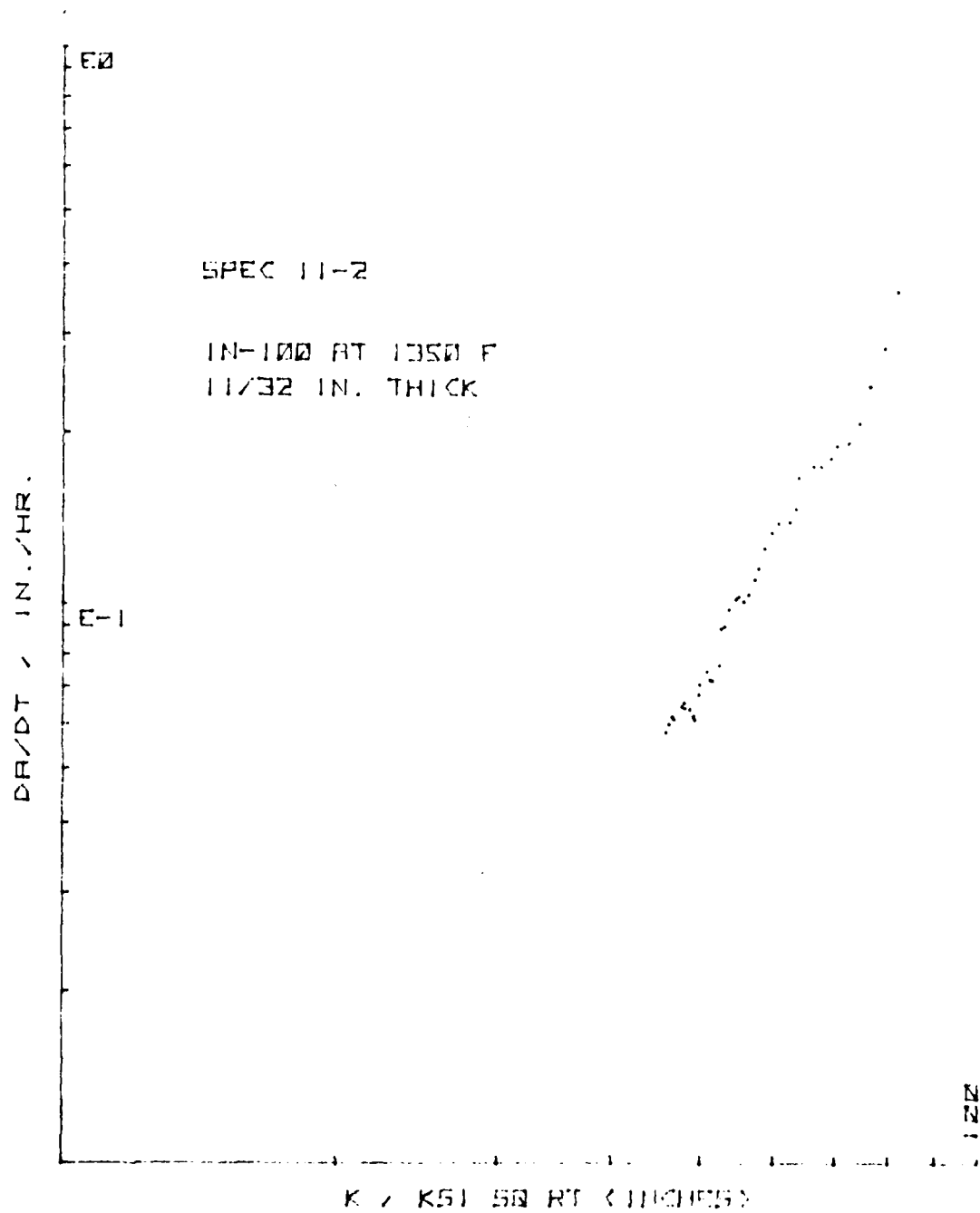
Figure 70.   Creep Crack Growth Rate vs. K for CT Specimen 11-2
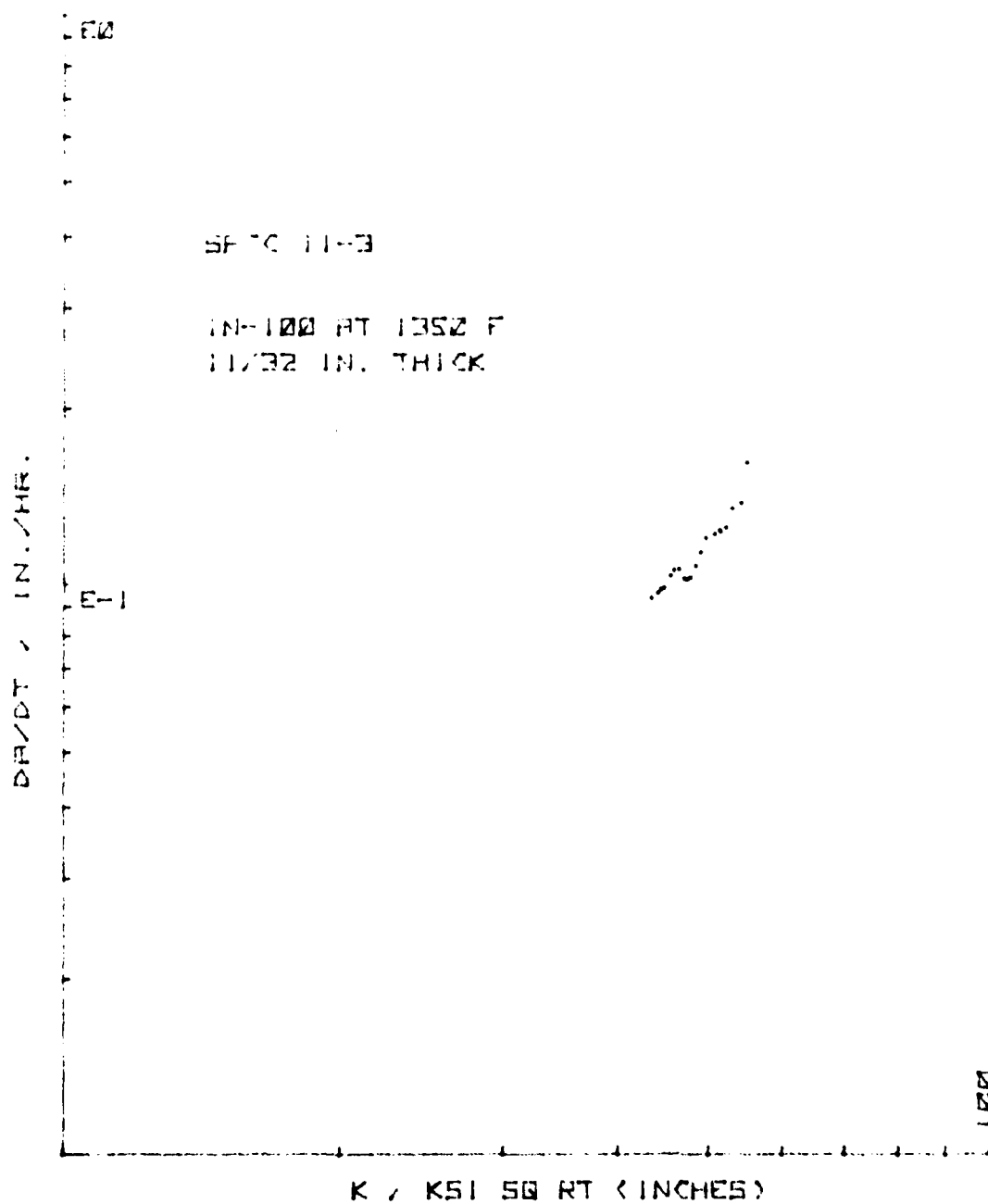
Figure 71. Creep Crack Growth Rate vs. K for CT Specimen 11-3
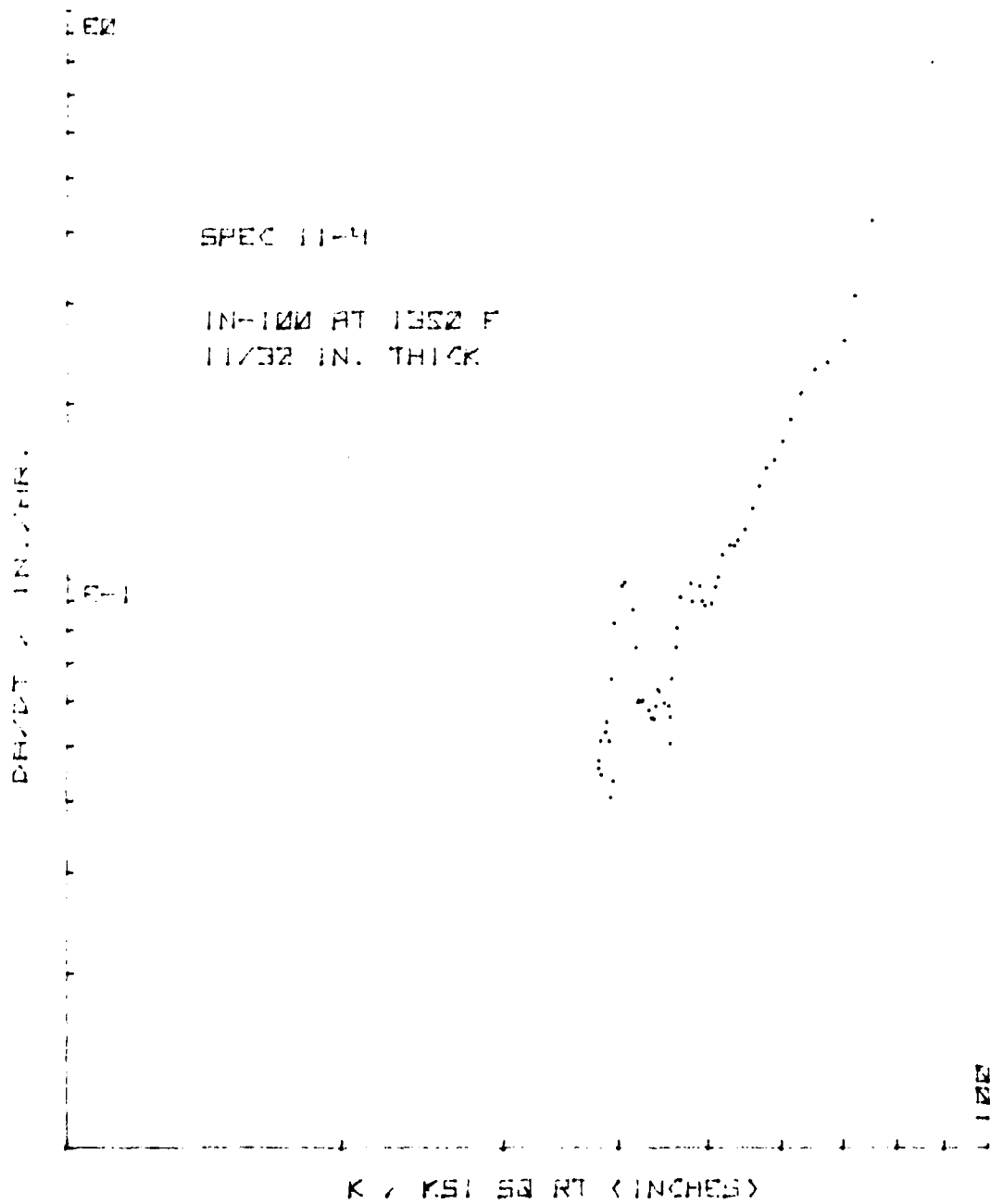
Figure 72.   Creep Crack Growth Rate vs. K for CT Specimen 11-4
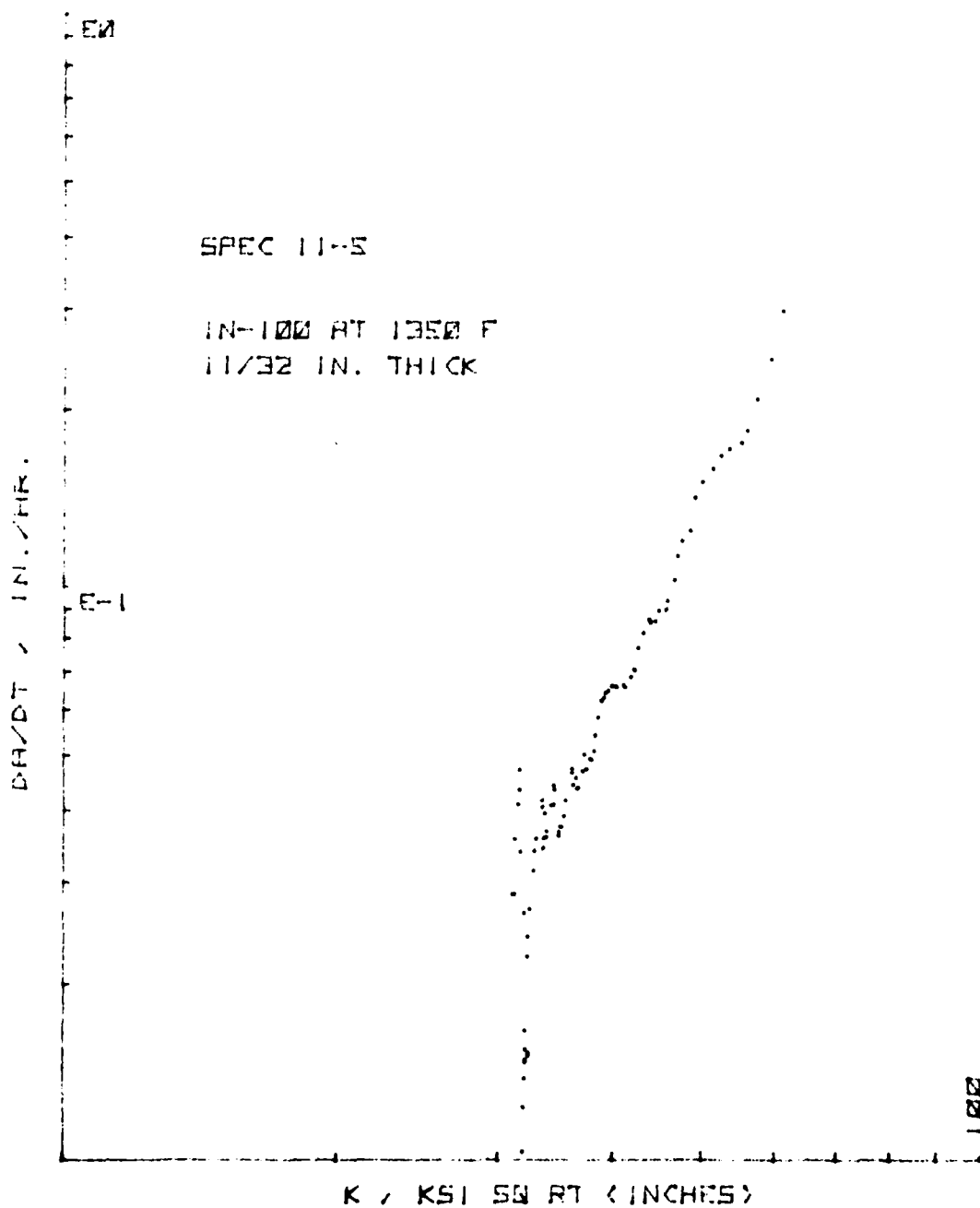
Figure 73. Creep Crack Growth Rate vs. K for CT Specimen 11-5
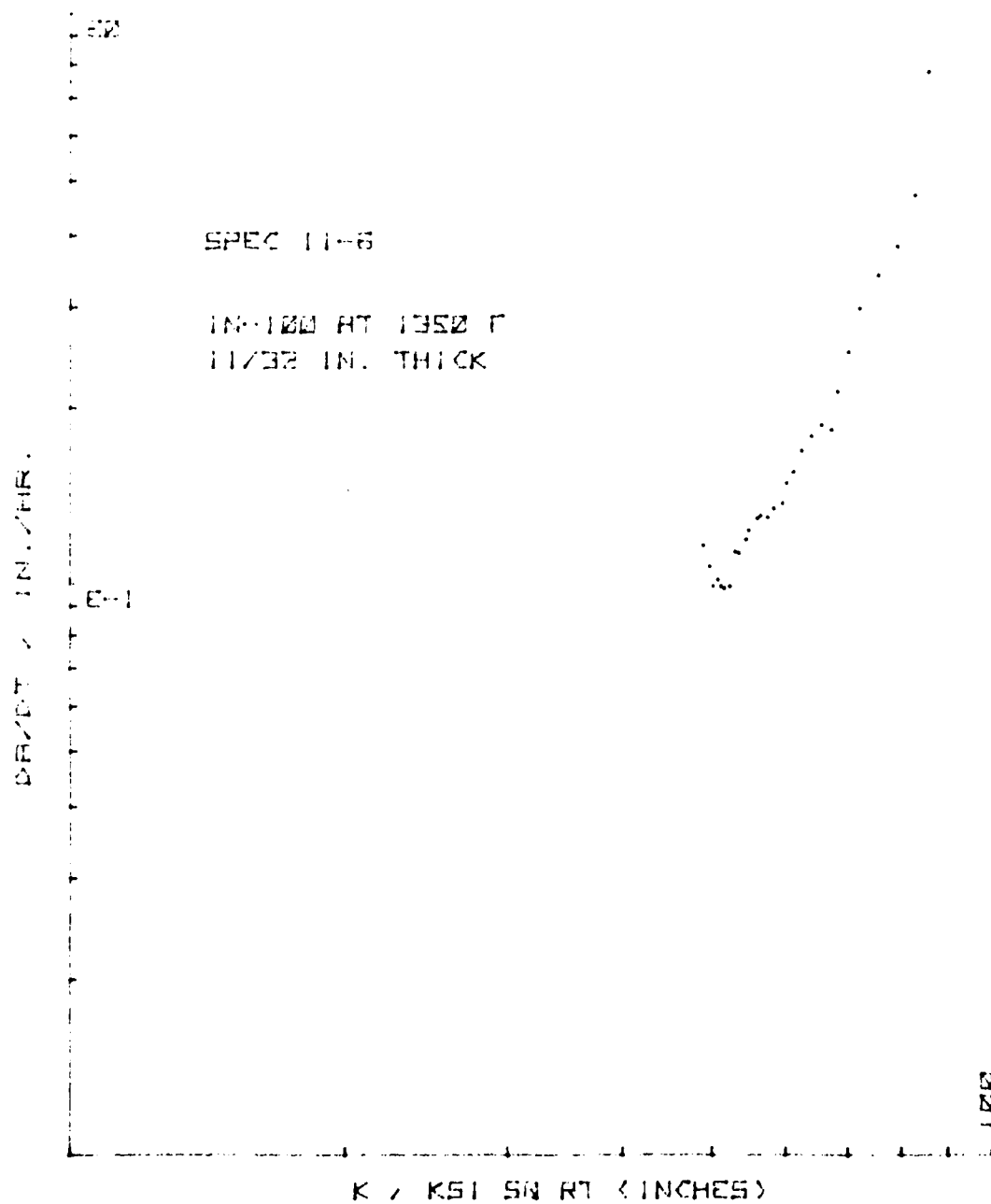
Figure 74. Creep Crack Growth Rate vs. K for CT Specimen 11-6
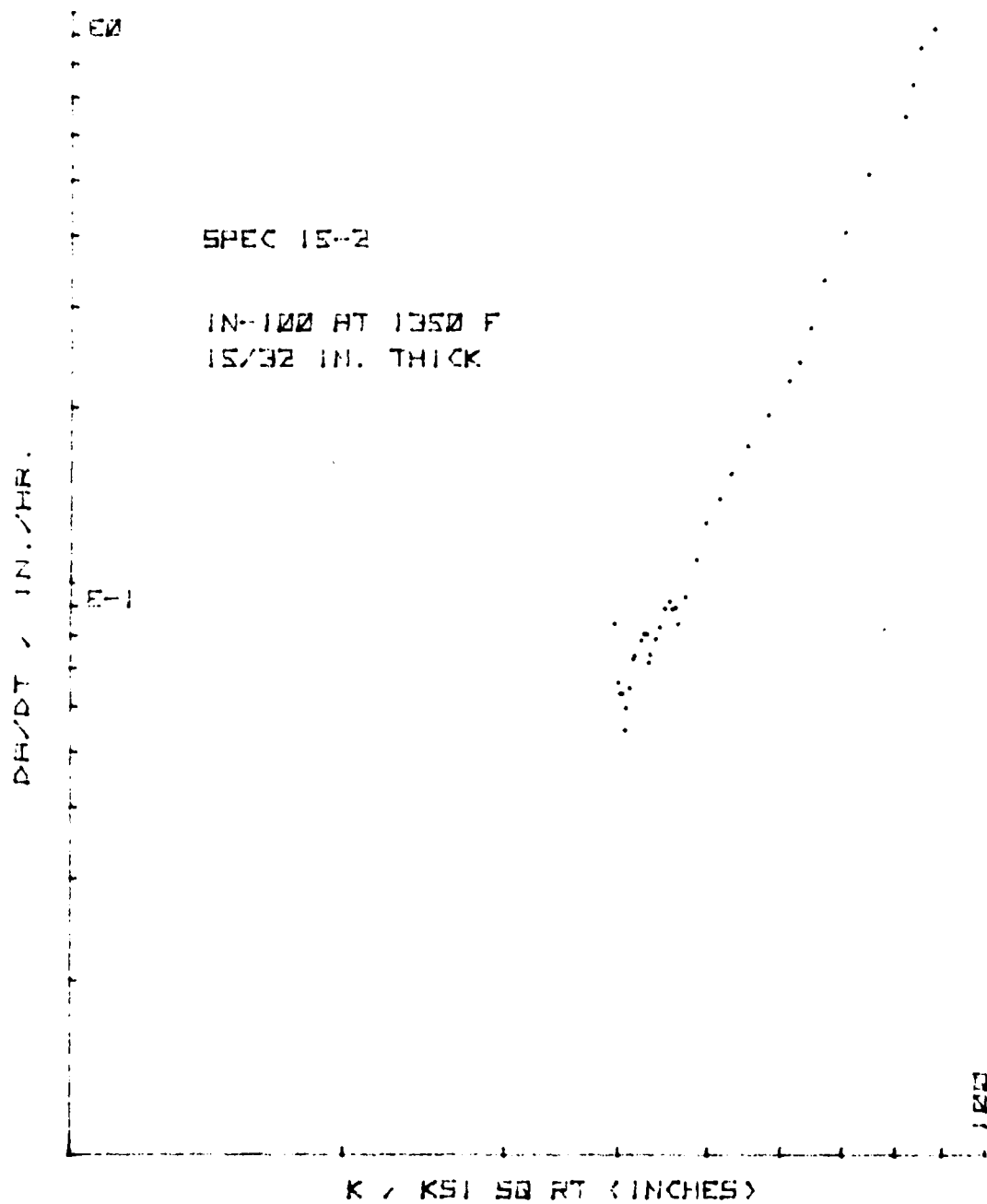
Figure 75. Creep Crack Growth Rate vs. K for CT Specimen 15-2
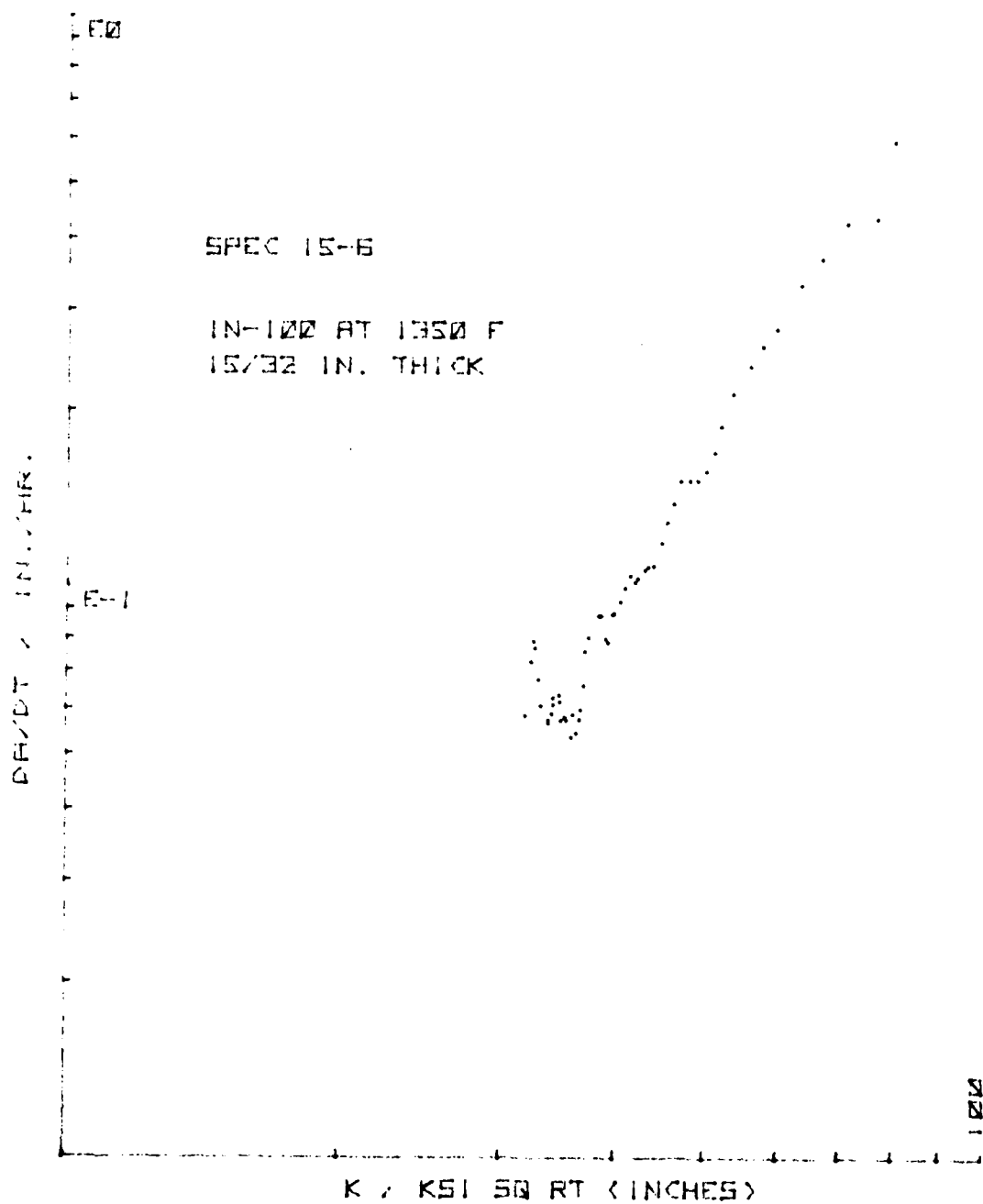
Figure 76. Creep Crack Growth Rate vs. K for CT Specimen 15-6
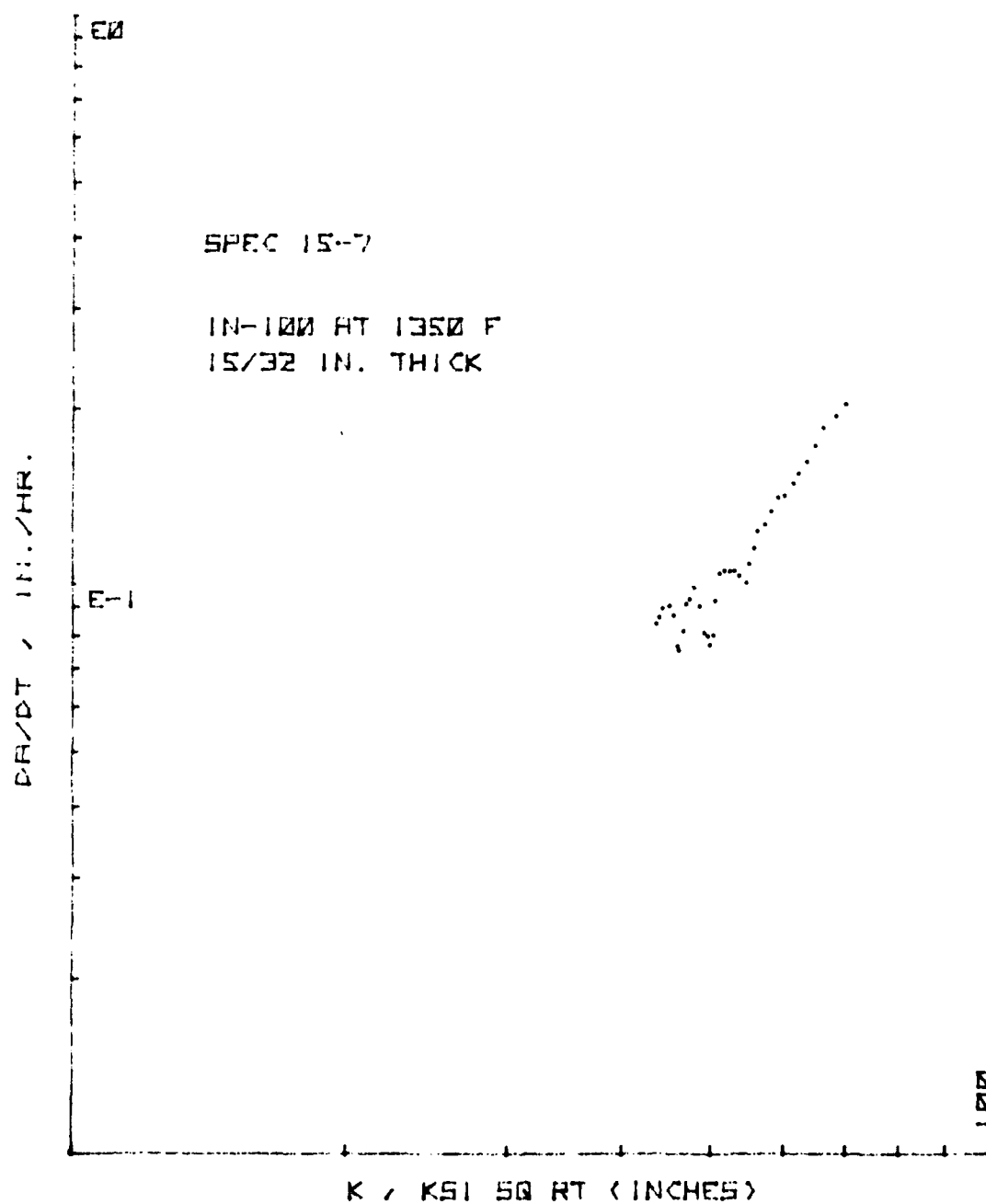
Figure 77. Creep Crack Growth Rate vs. K for CT Specimen 15-7
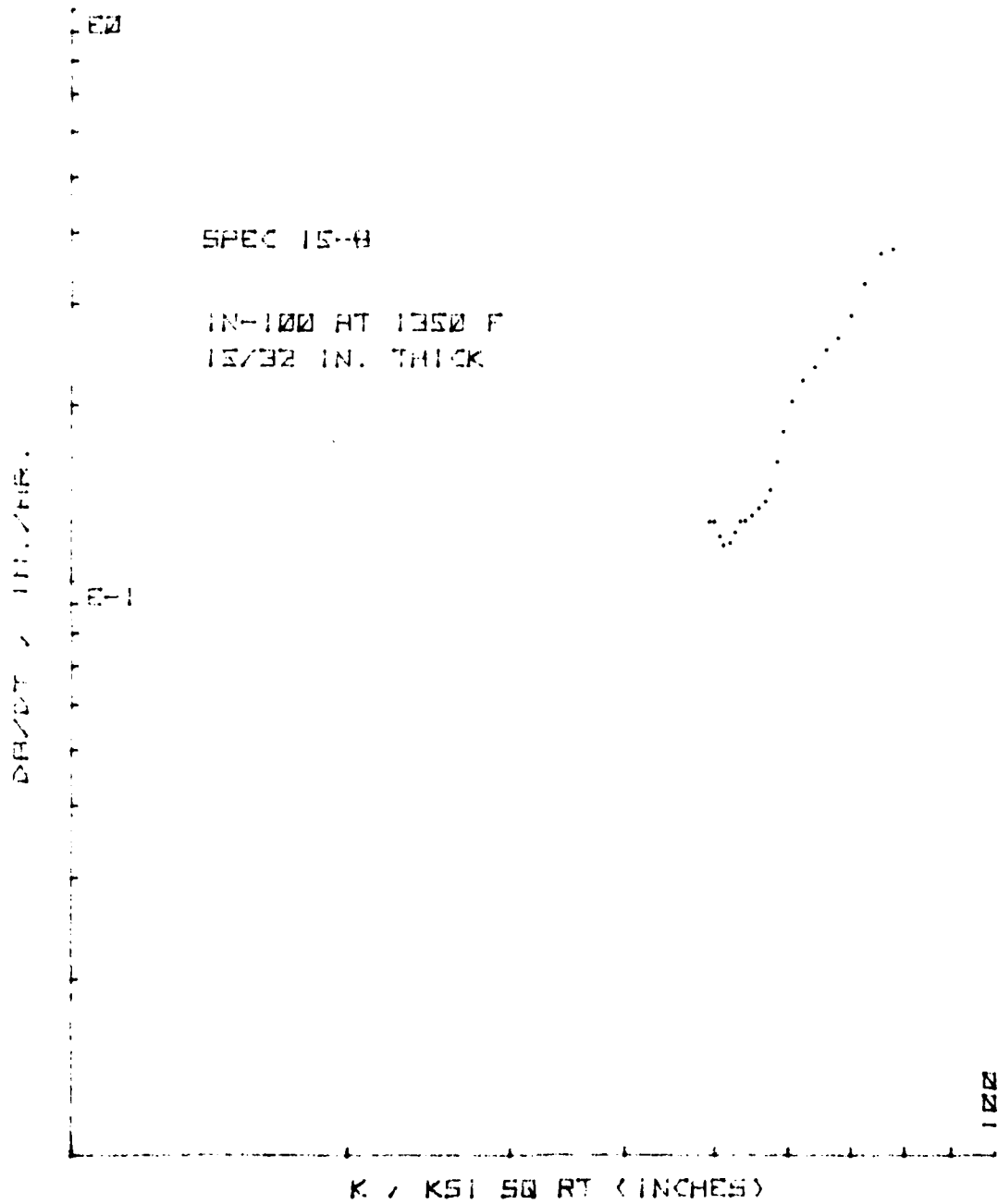
Figure 78. Creep Crack Growth Rate vs. K for CT Specimen 15-8
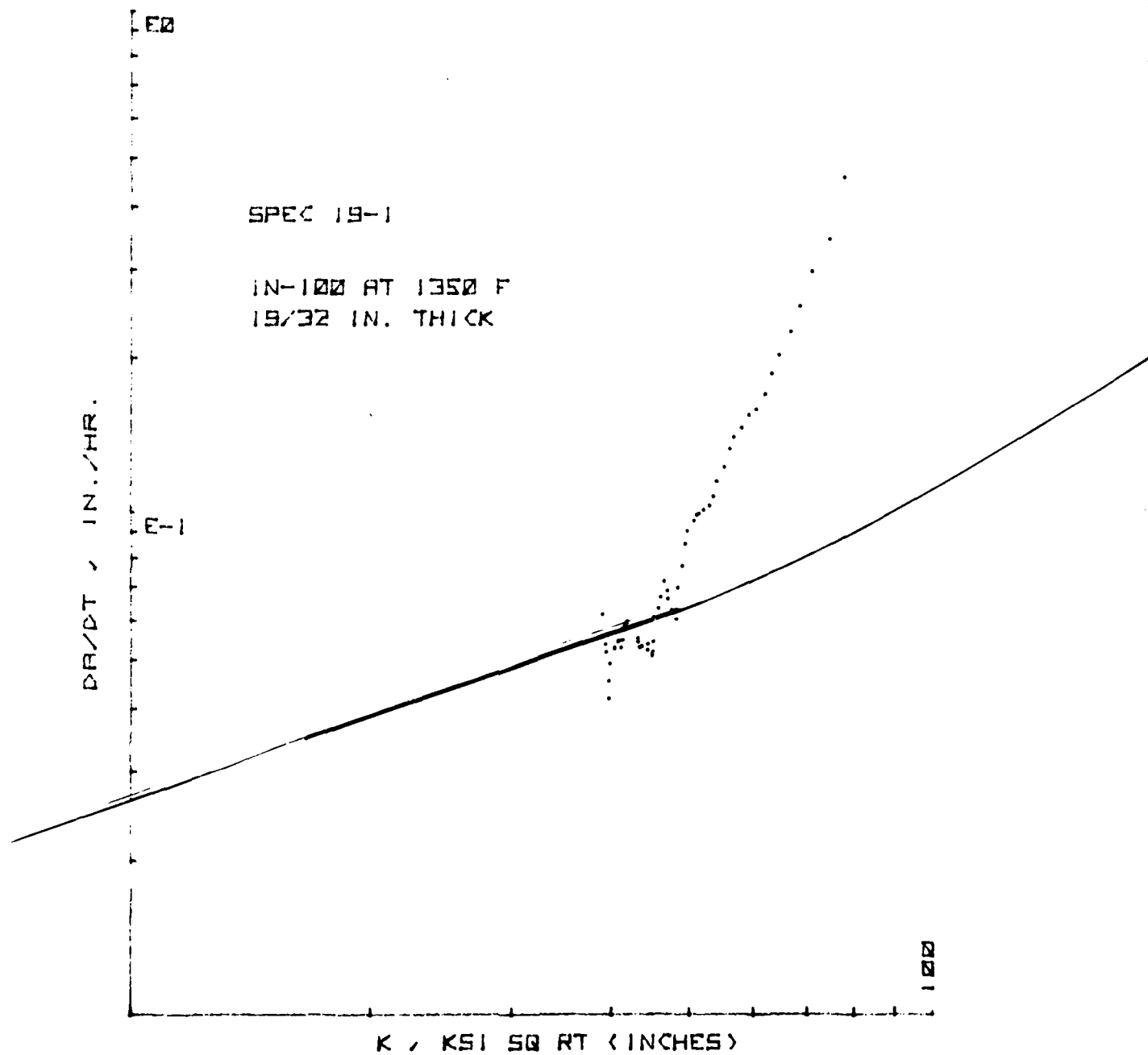
Figure 79. Creep Crack Growth Rate vs. K for CT Specimen 19-1
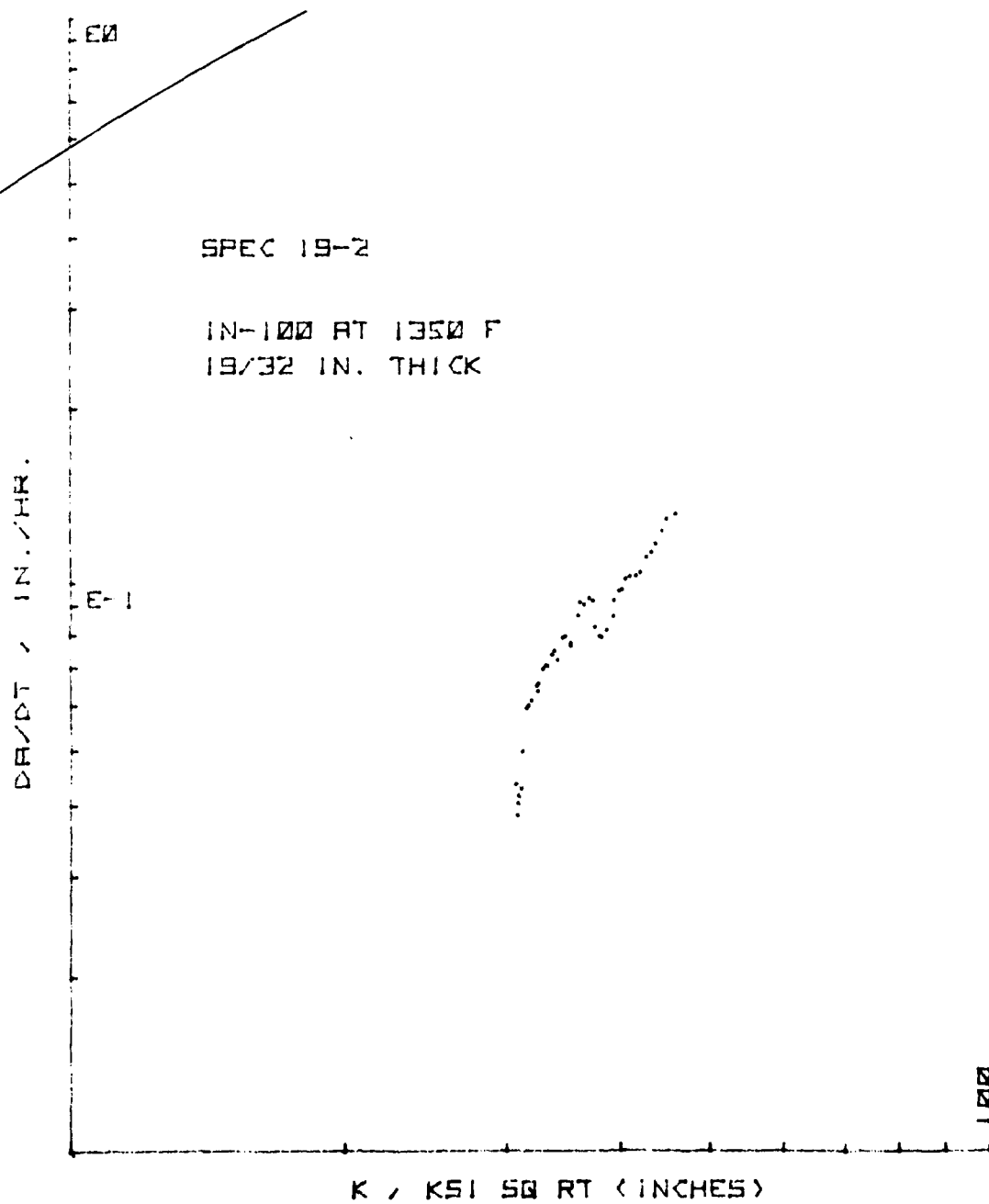
Figure 80. Creep Crack Growth Rate vs. K for CT Specimen 19-2
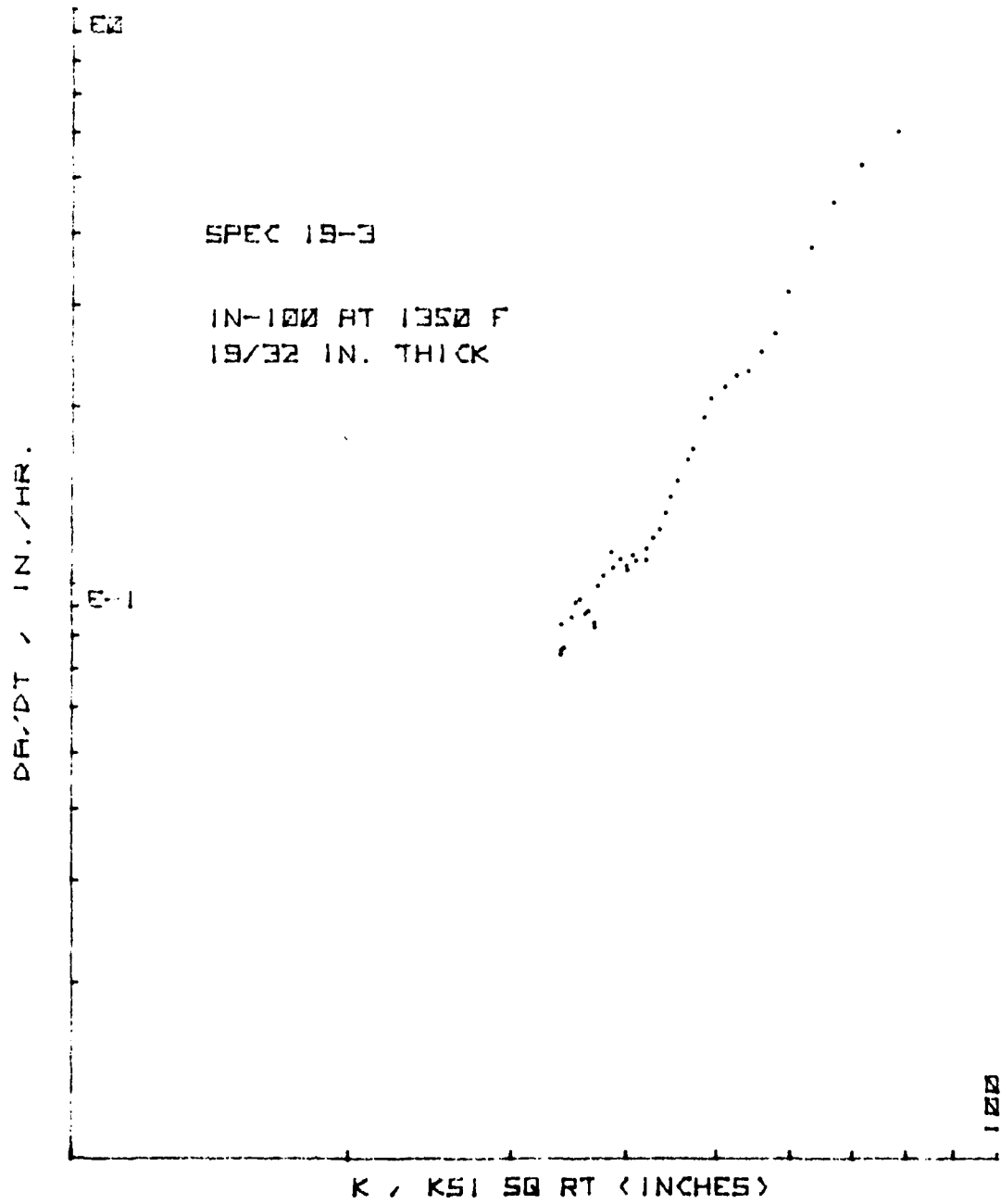
Figure 81. Creep Crack Growth Rate vs. K for CT Specimen 19-3
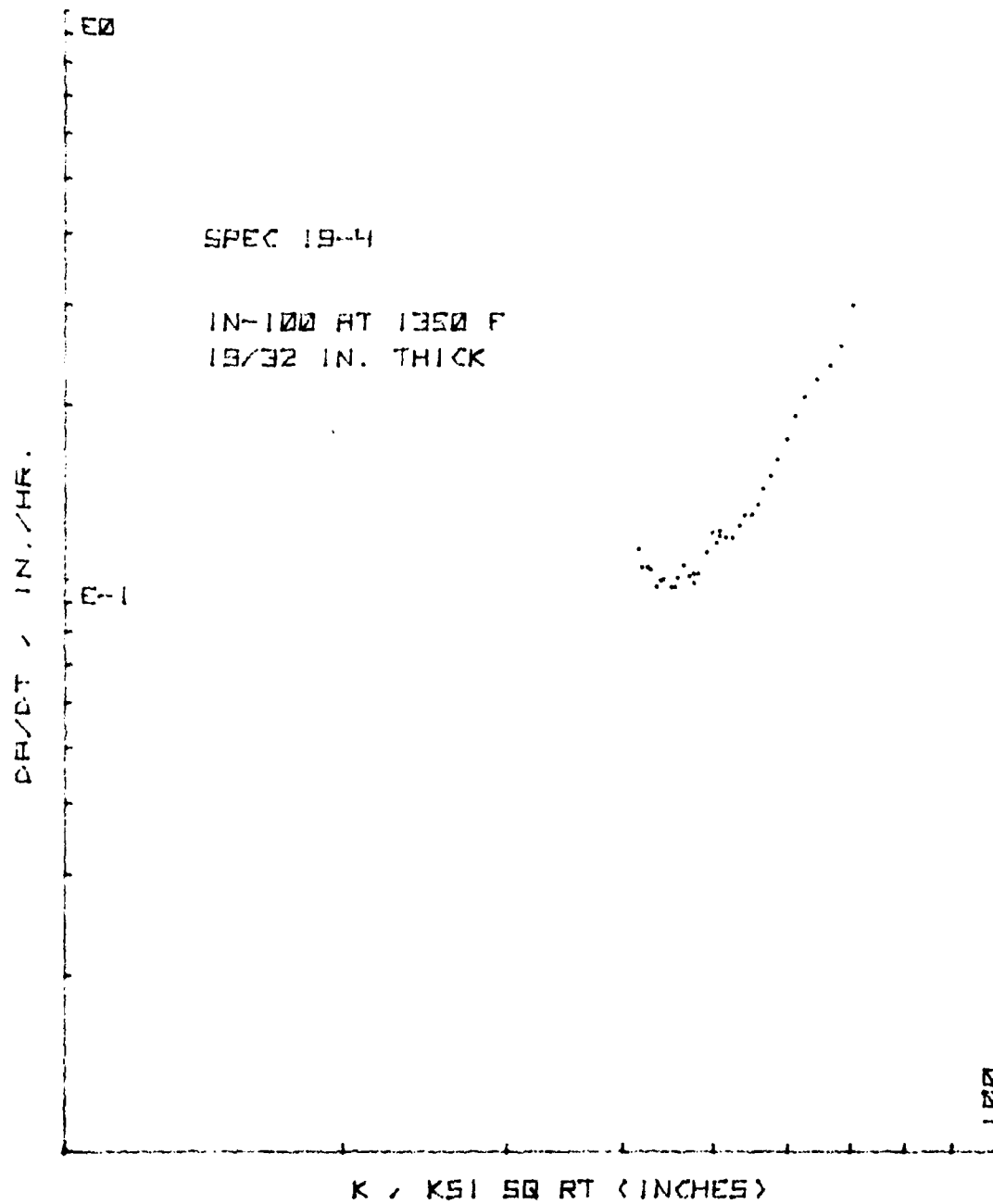
Figure 82.   Creep Crack Growth Rate vs. K for CT Specimen 19-4
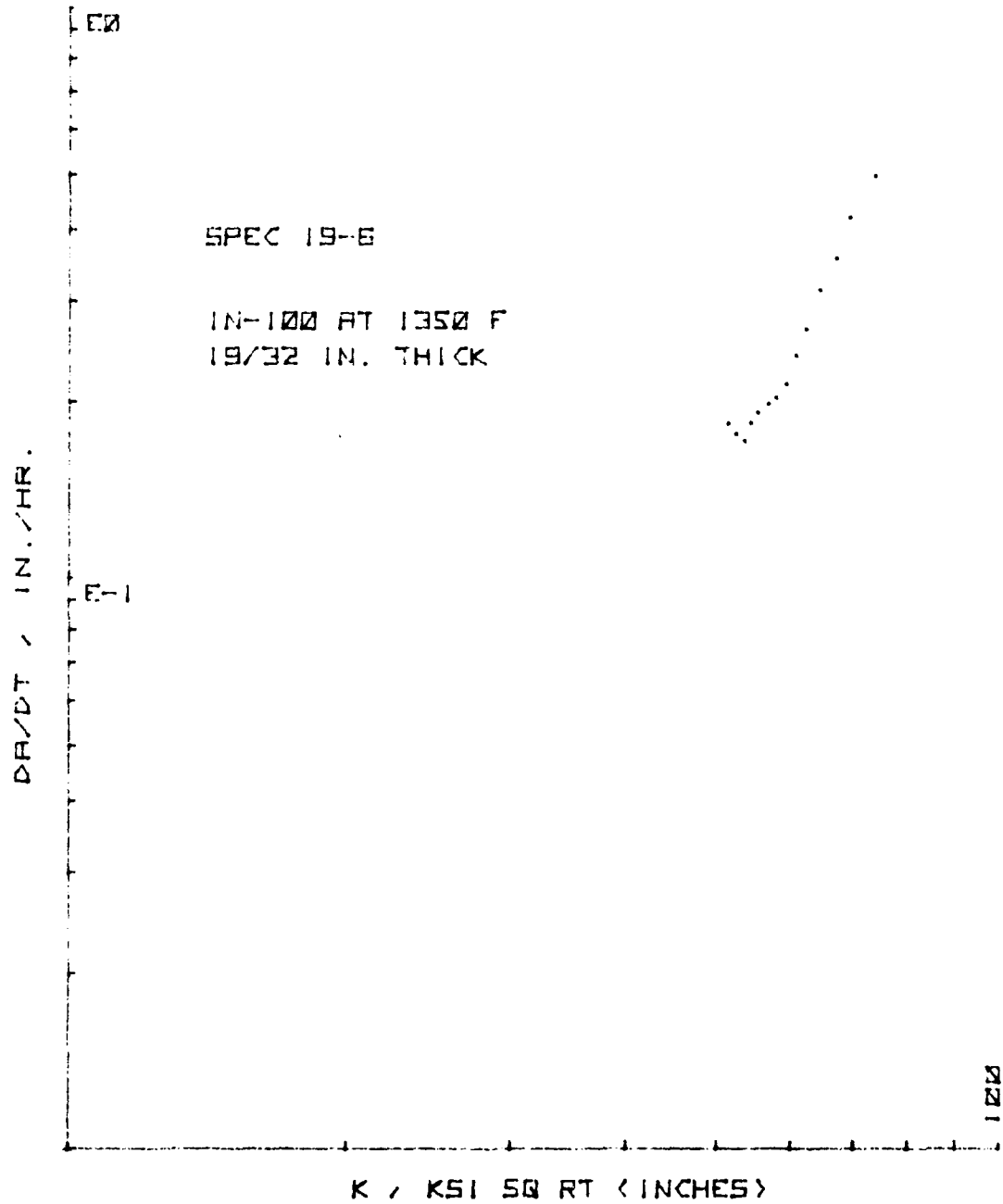
Figure 83. Creep Crack Growth Rate vs. K for CT Specimen 19-6
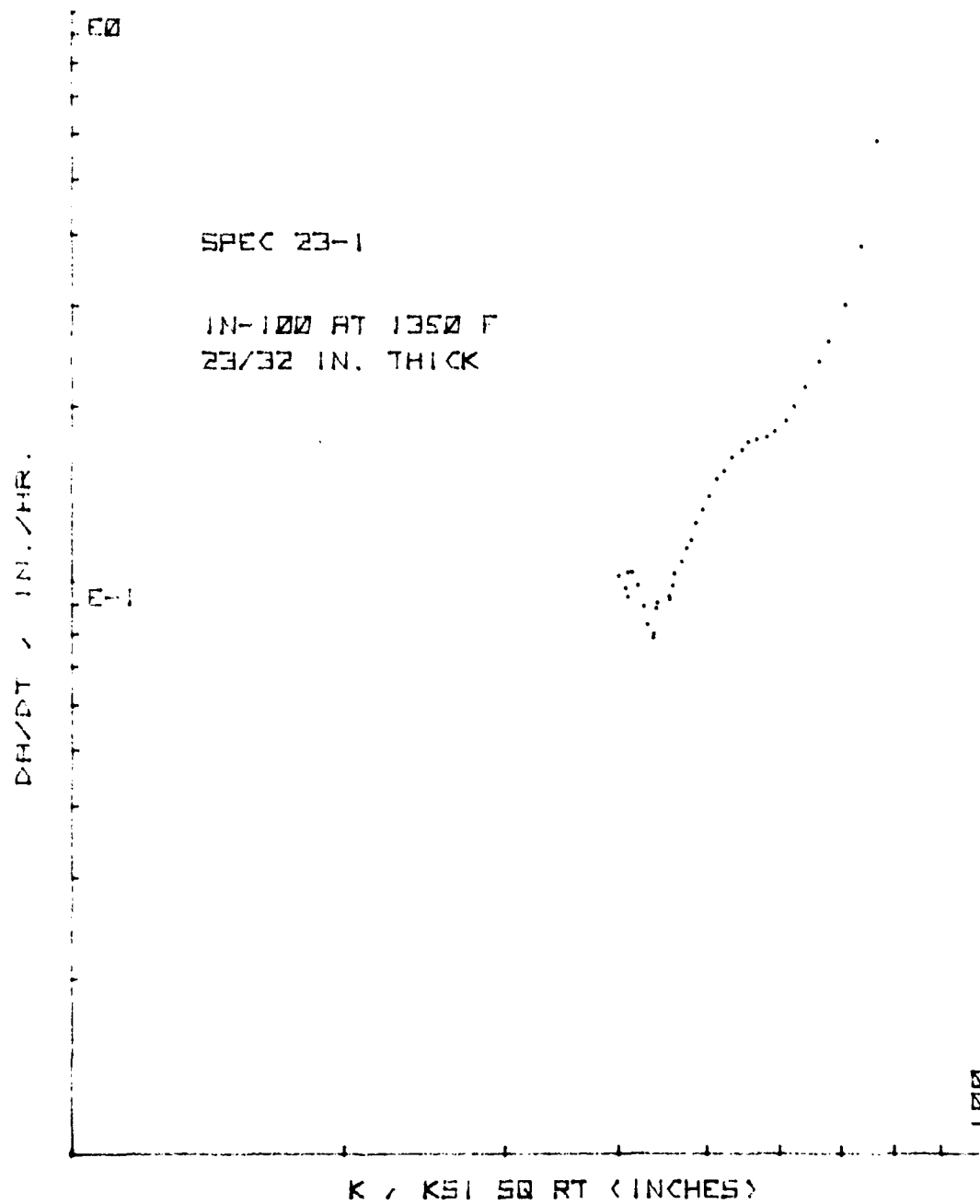
Figure 84.   Creep Crack Growth Rate vs. K for CT Specimen 23-1
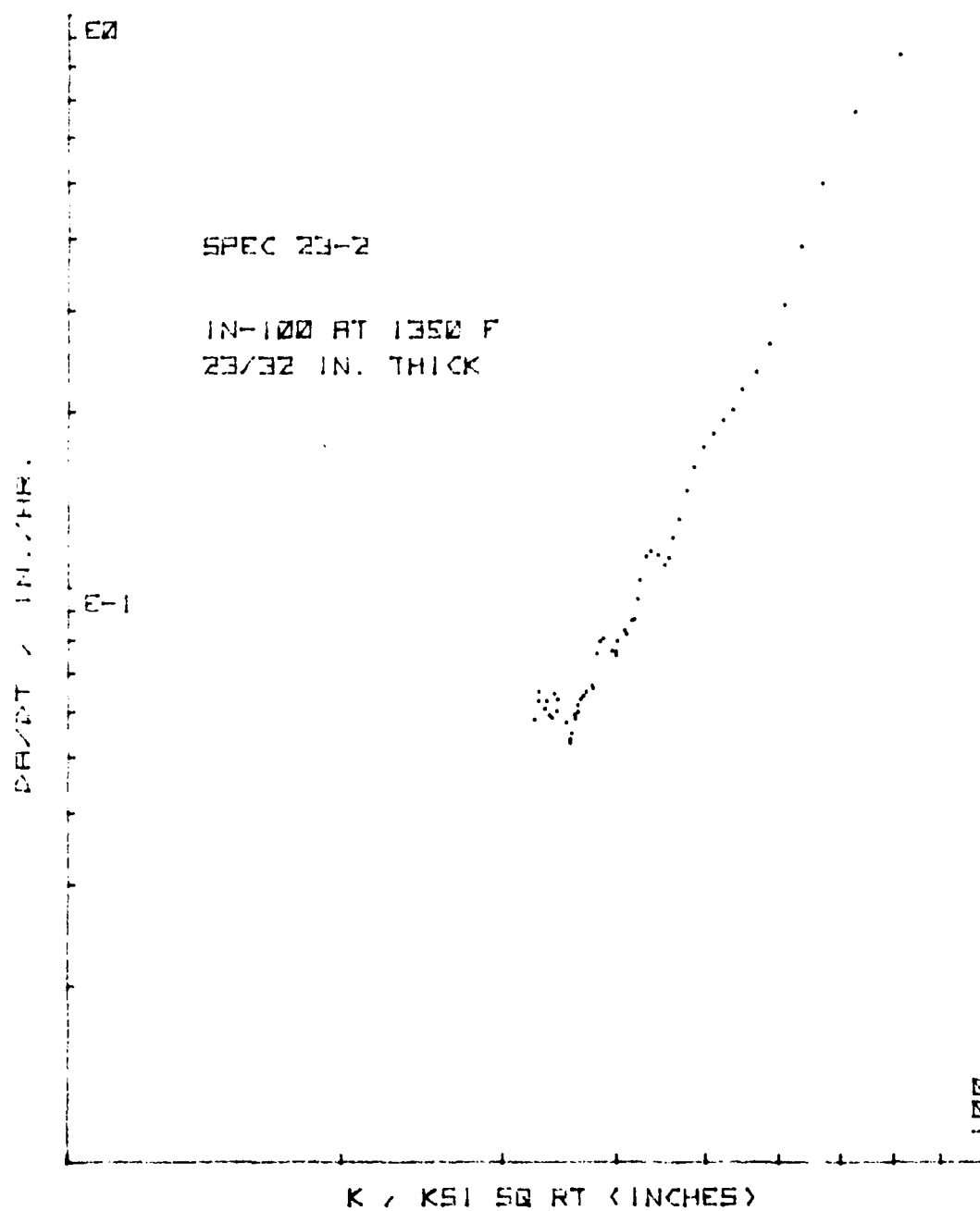
Figure 85. Creep Crack Growth Rate vs. K for CT Specimen 23-2

Figure 86.   Creep Crack Growth Rate vs. K for CT Specimen 23-3
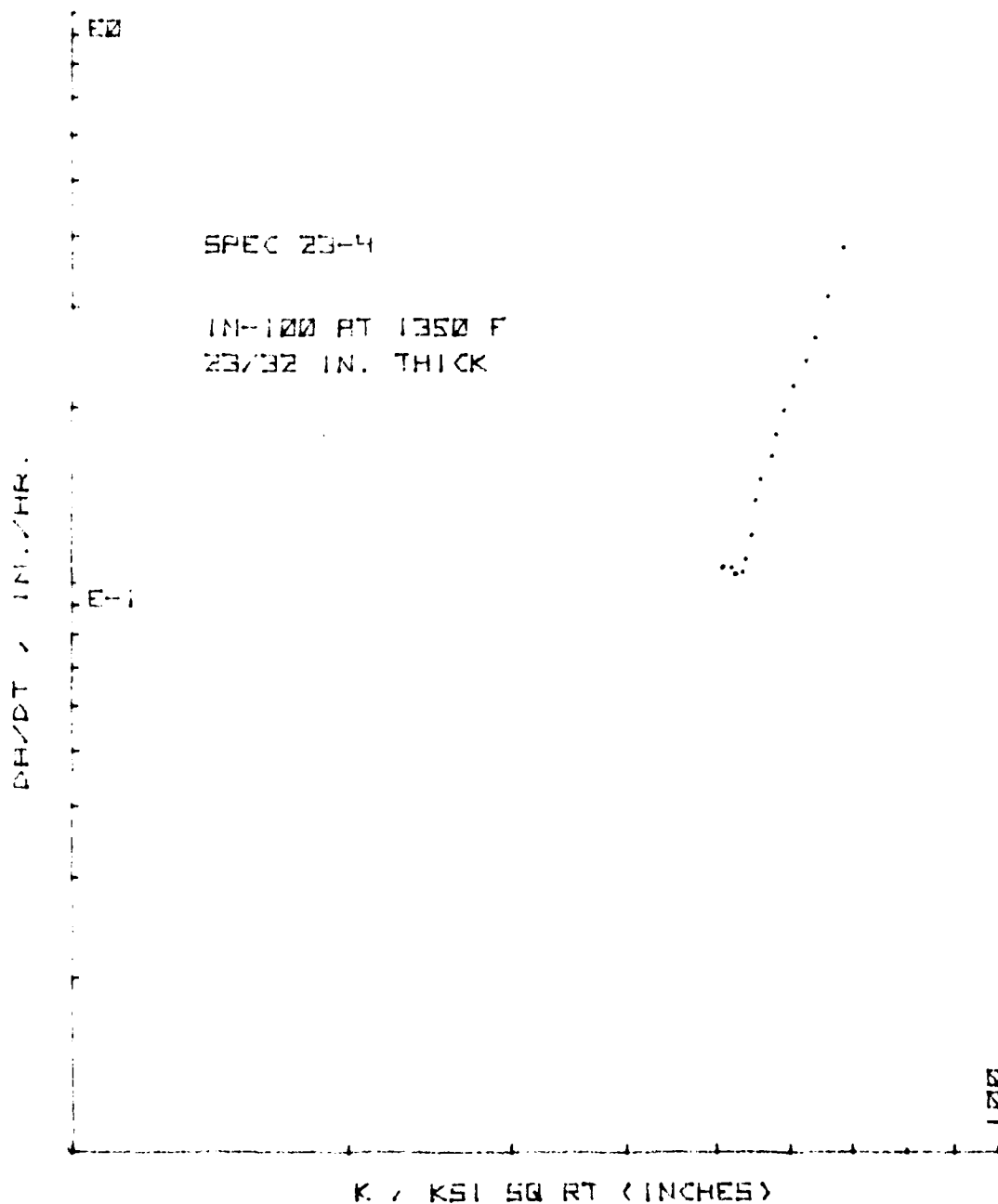
Figure 87. Creep Crack Growth Rate vs. K for CT Specimen 23-4
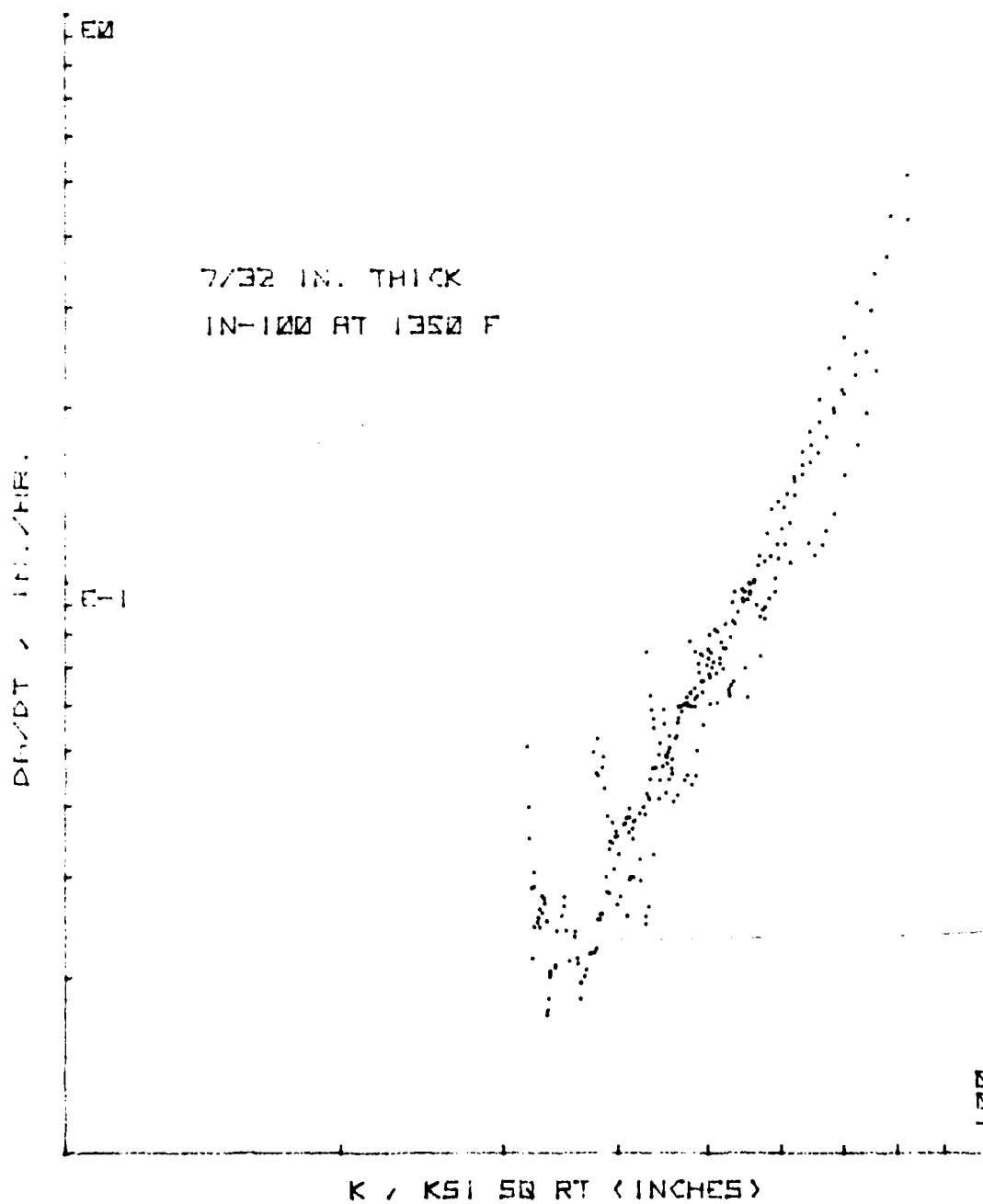
Figure 88.   da/dt vs. K - 7/32" (6 mm) Thick CT Specimen Group
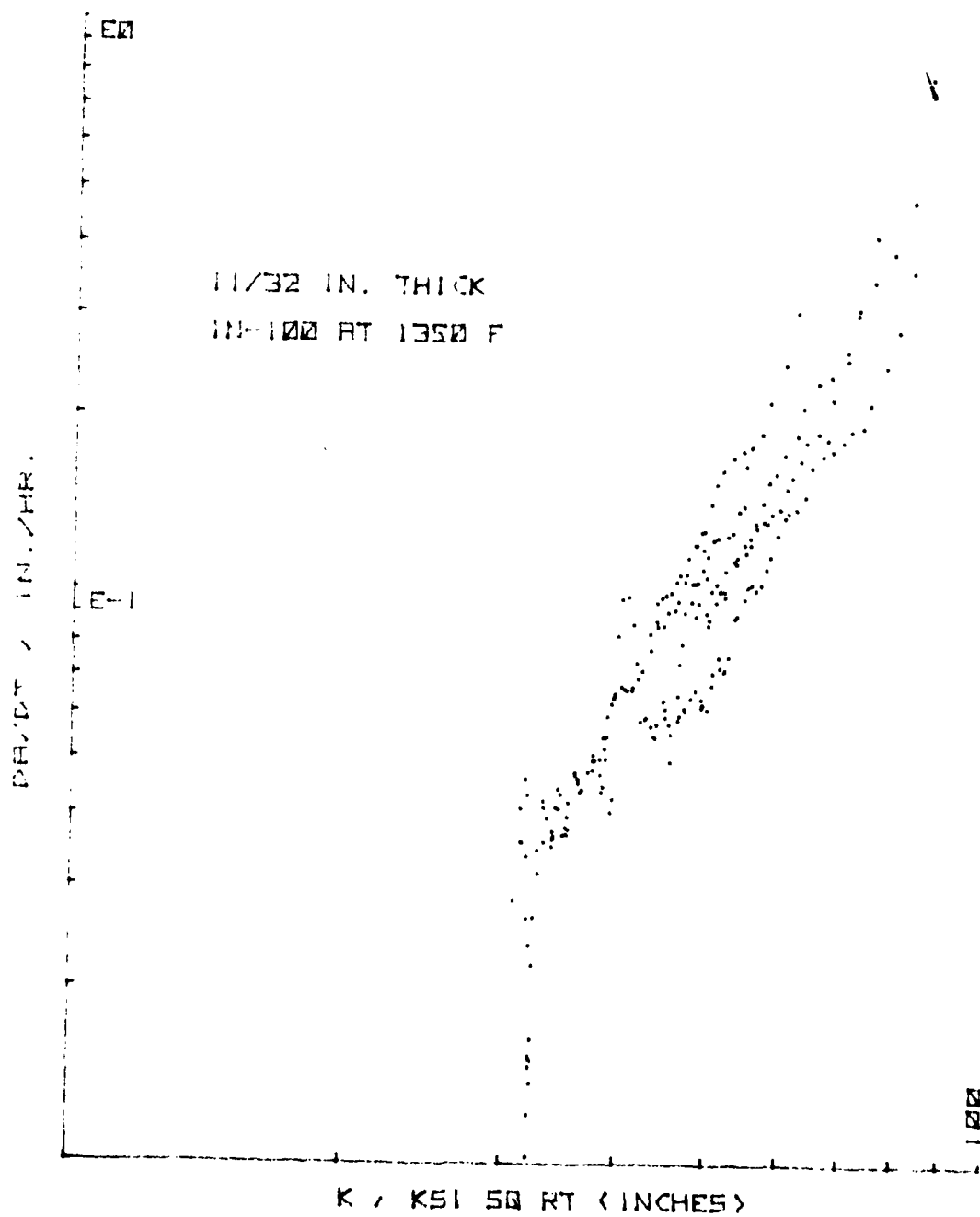
Figure 89.   da/dt vs. K - 11/32" (9 mm) Thick CT Specimen Group
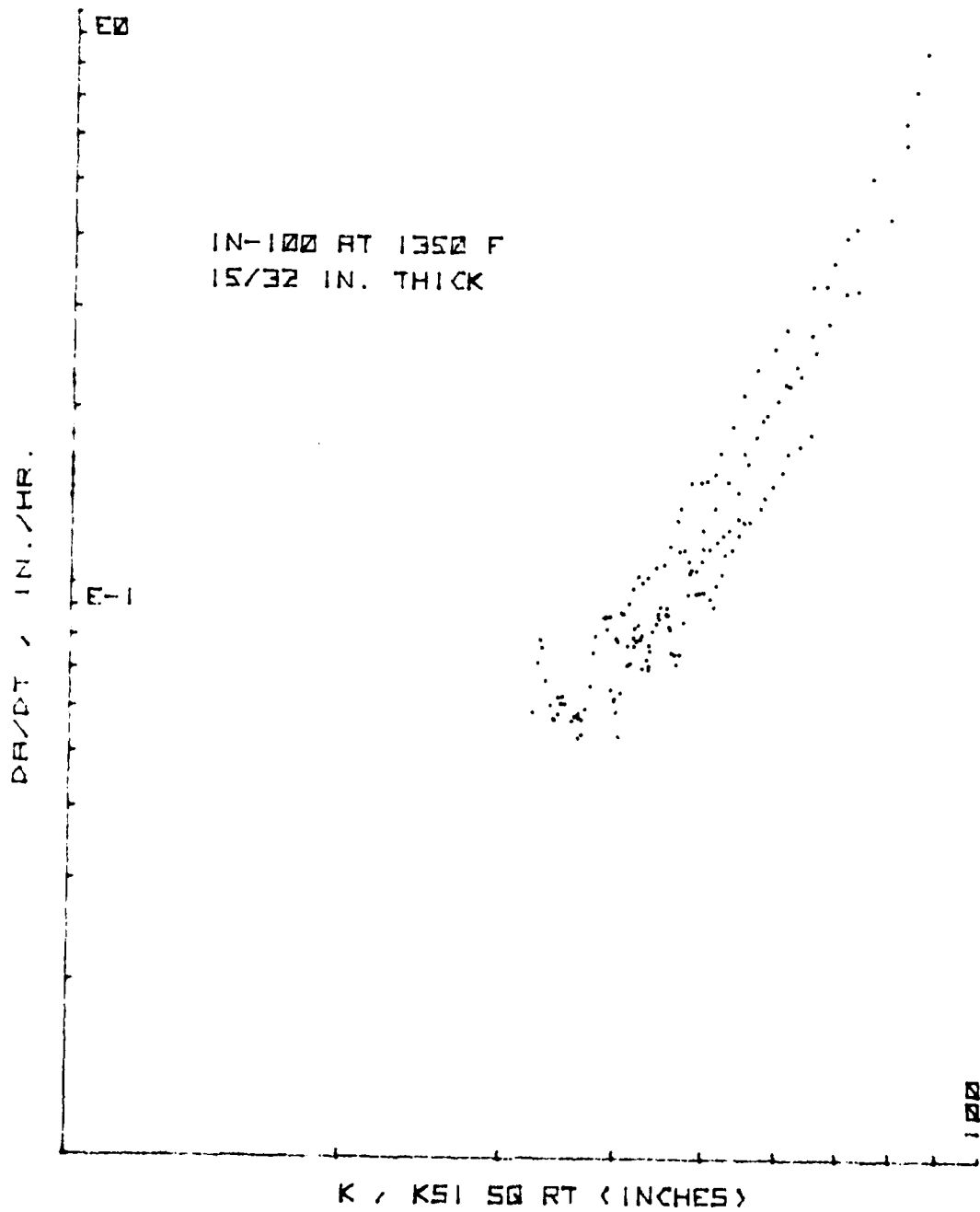
Figure 90. da/dt vs. K - 15/32" (12 mm) Thick CT Specimen Group
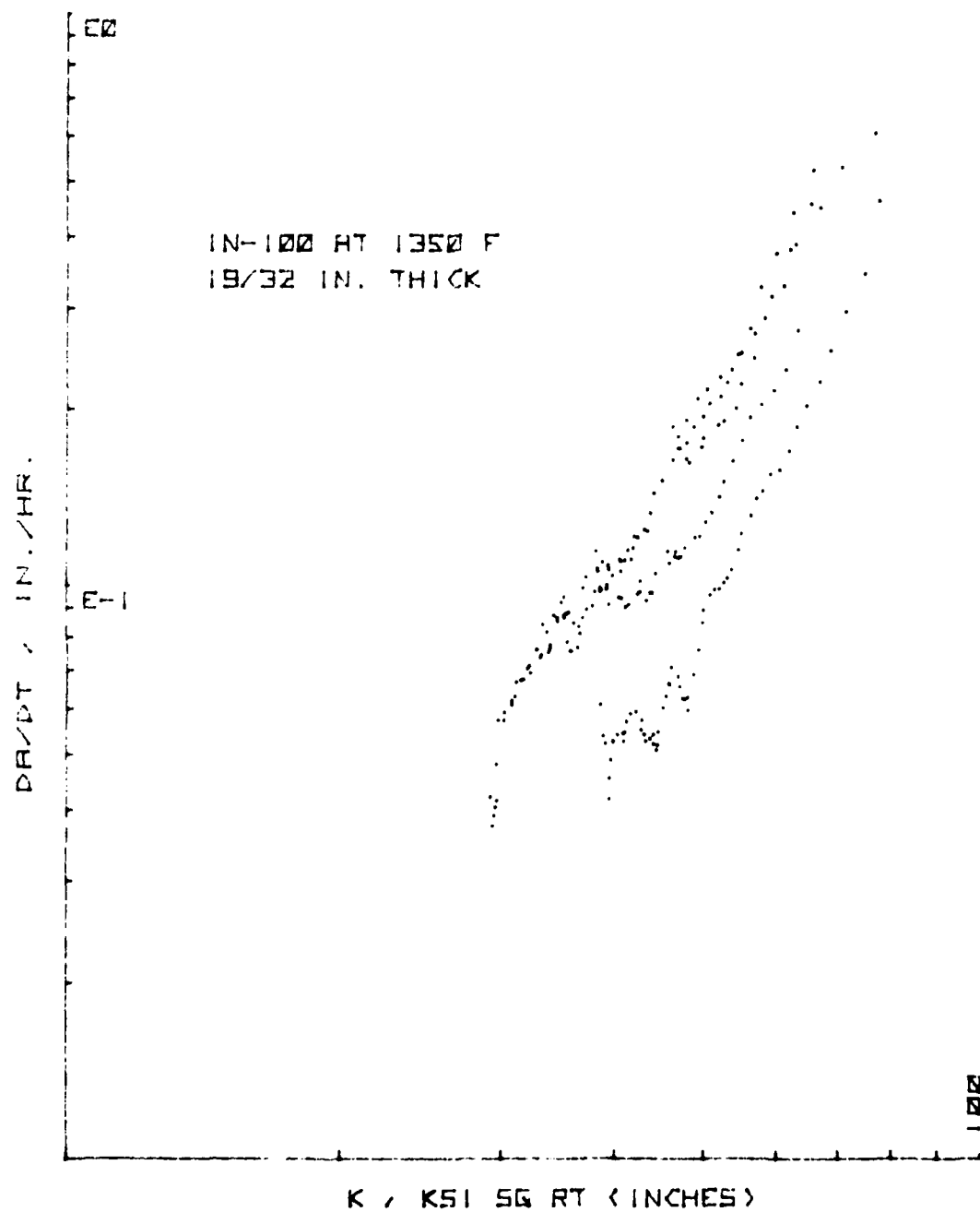
Figure 91. da/dt vs. K - 19/32" (15 mm) Thick CT Specimen Group
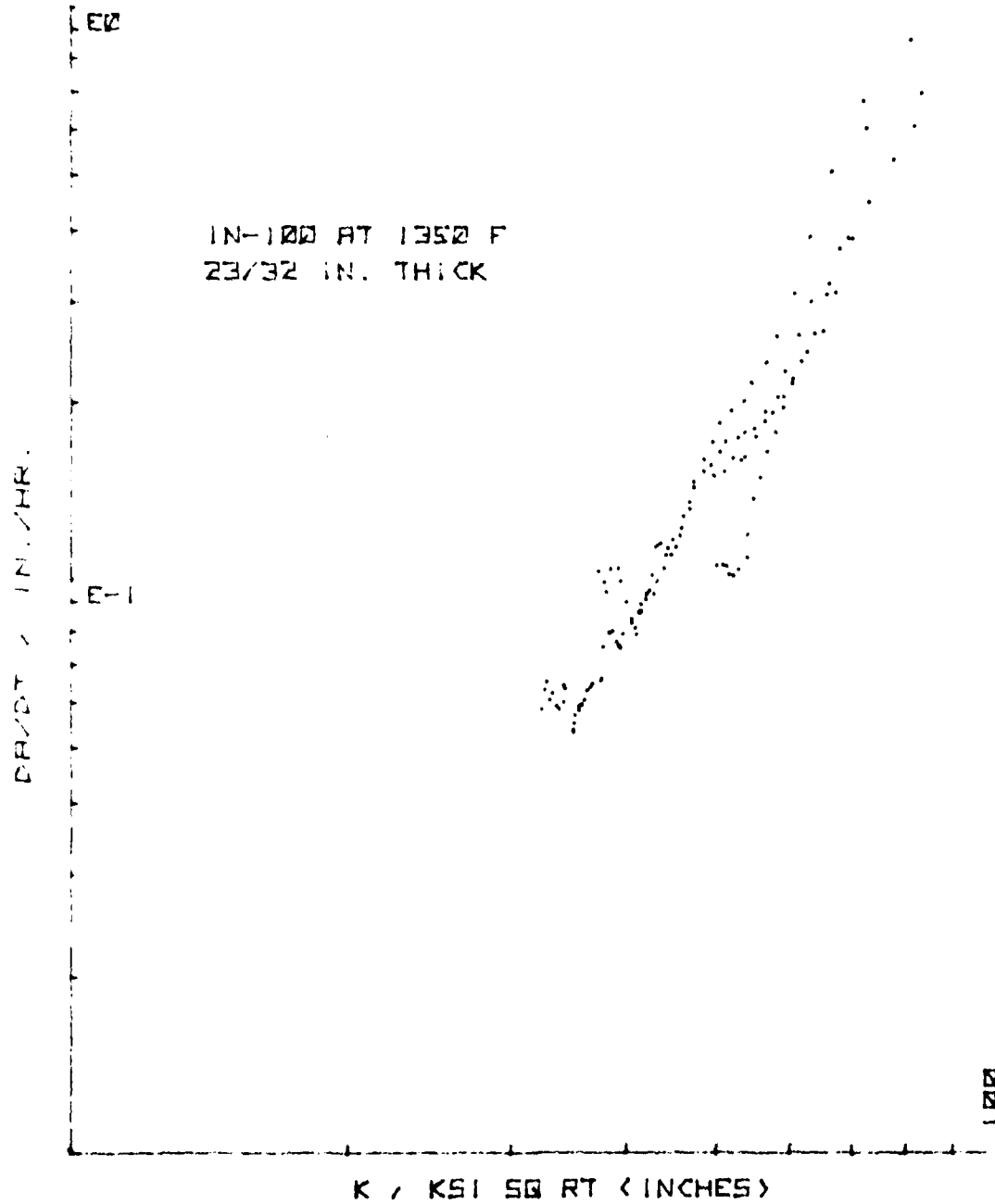
Figure 92. da/dt vs. K - 23/32" (18 mm) Thick CT Specimen Group
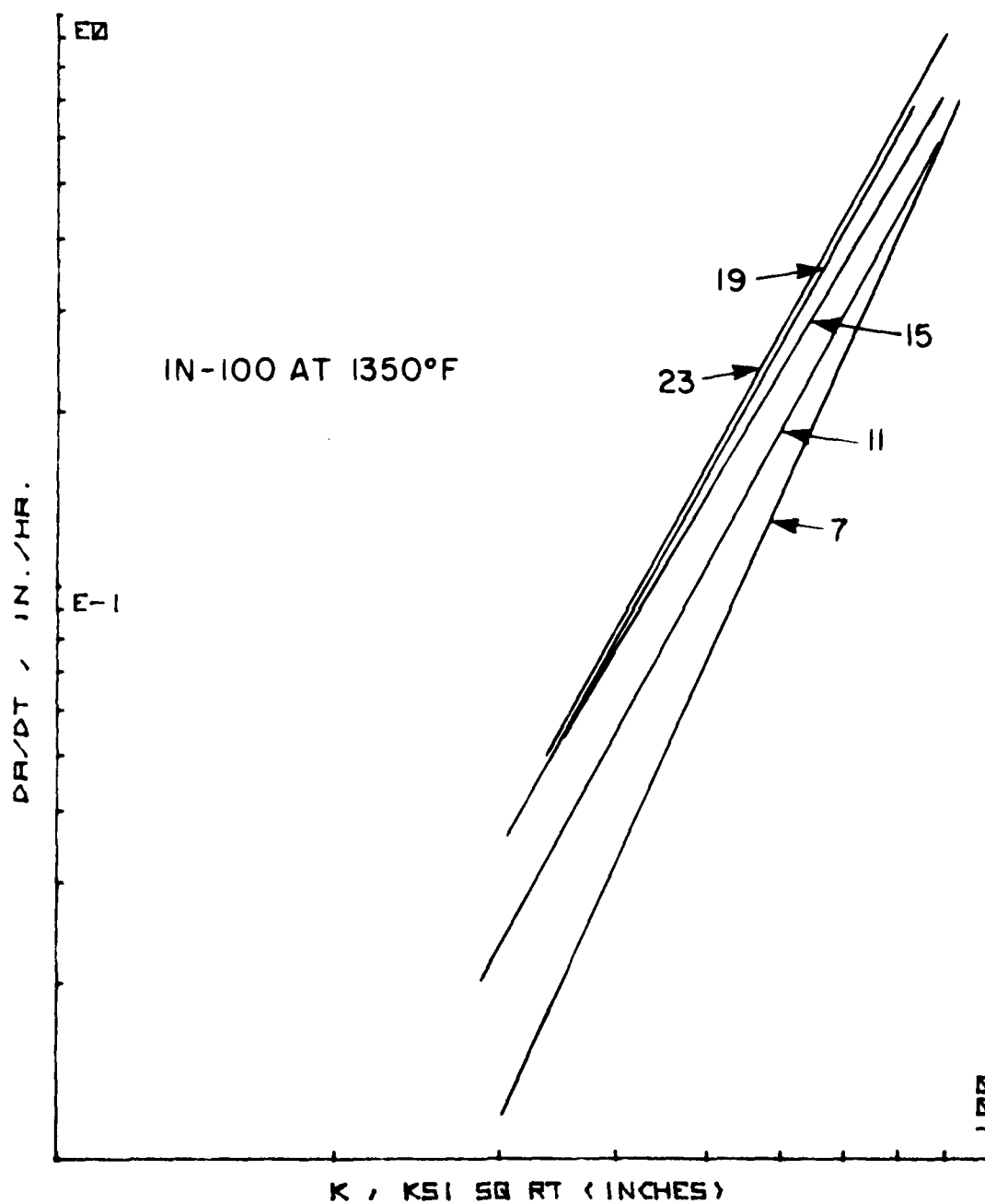
Figure 93.   da/dt - K Composite Plot for 5 Thicknesses - CT
Specimens

165
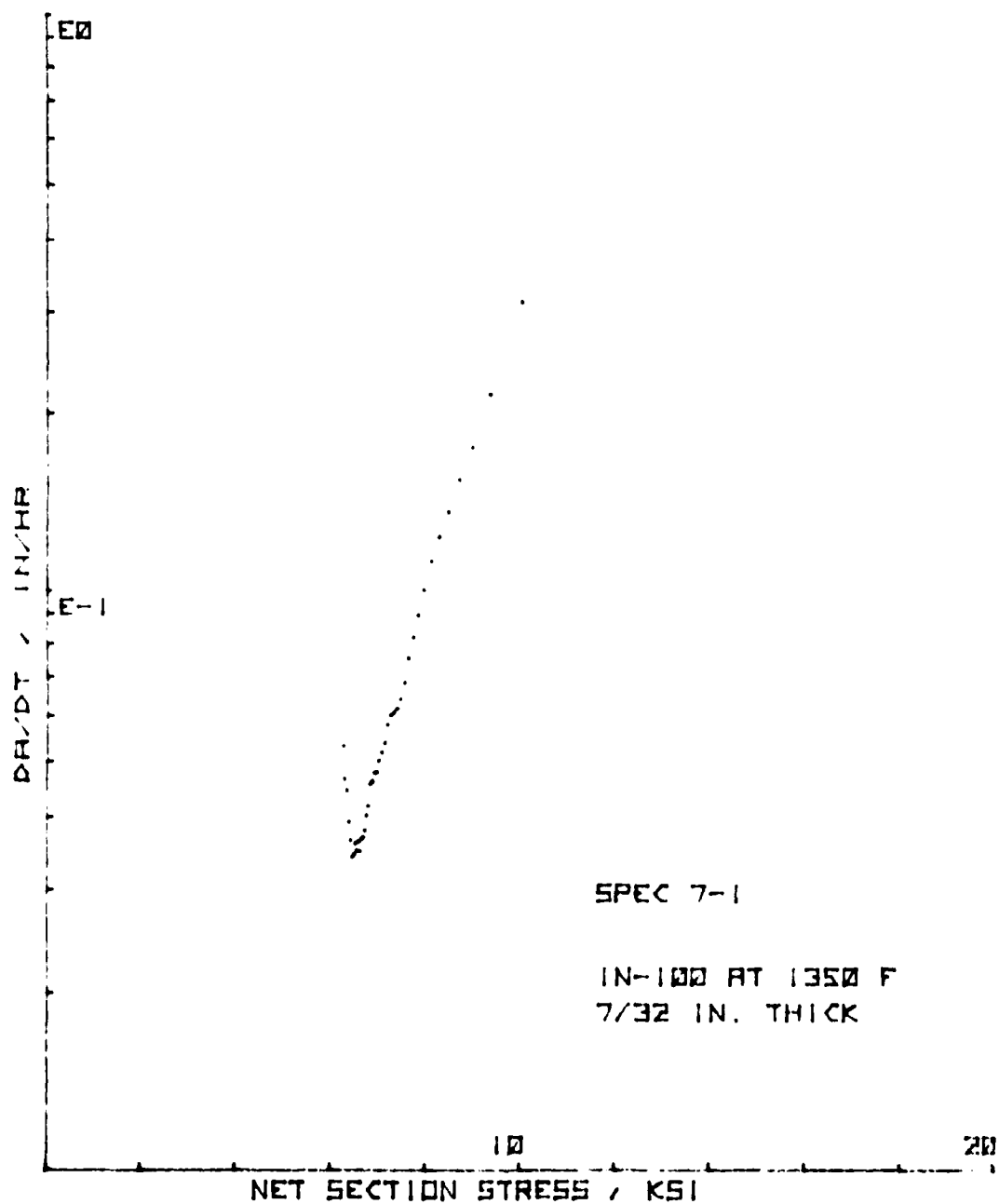
Figure 94.   da/dt vs. Net Section Stress for CT Specimen 7-1
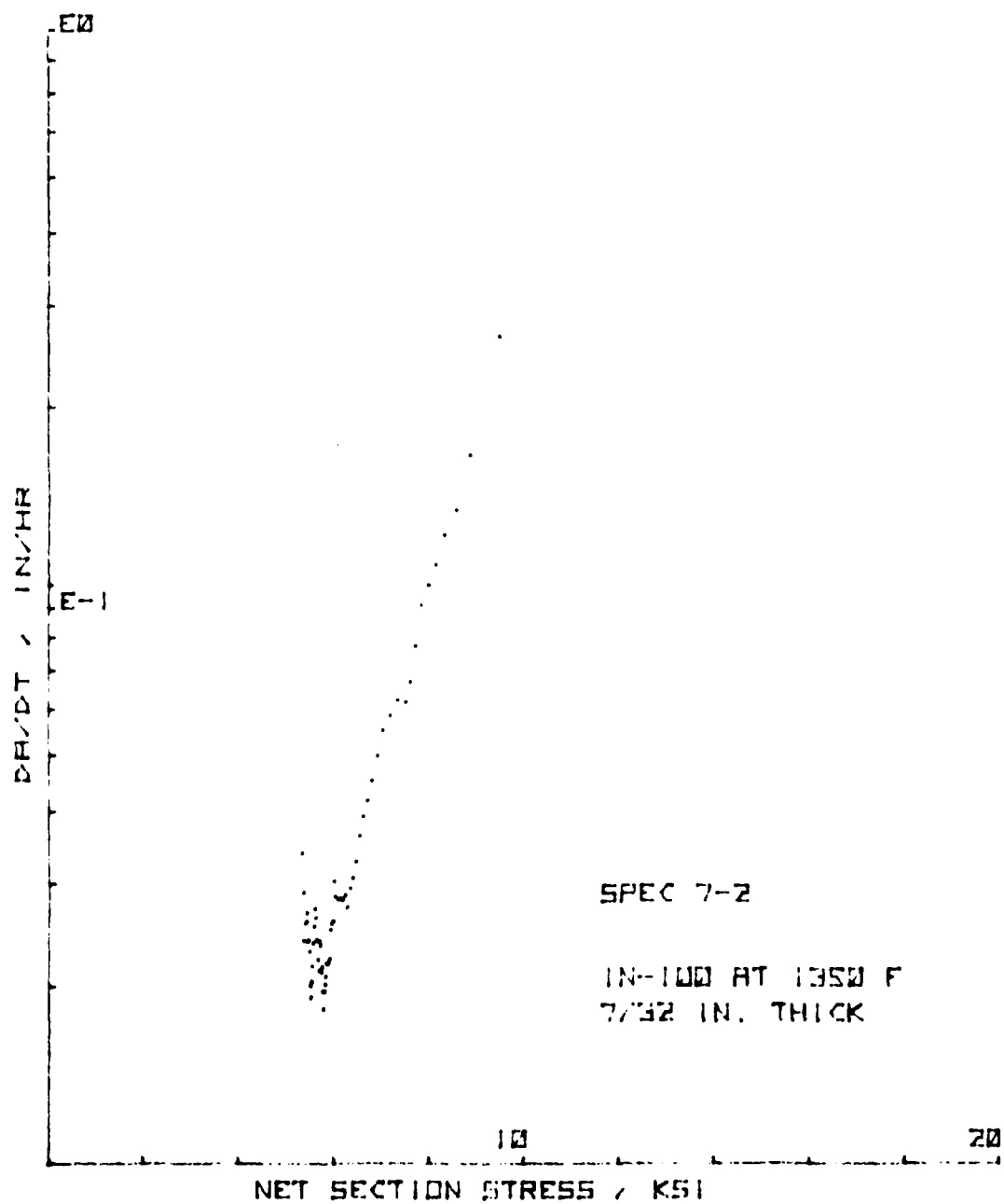
Figure 95. da/dt vs. Net Section Stress for CT Specimen 7-2
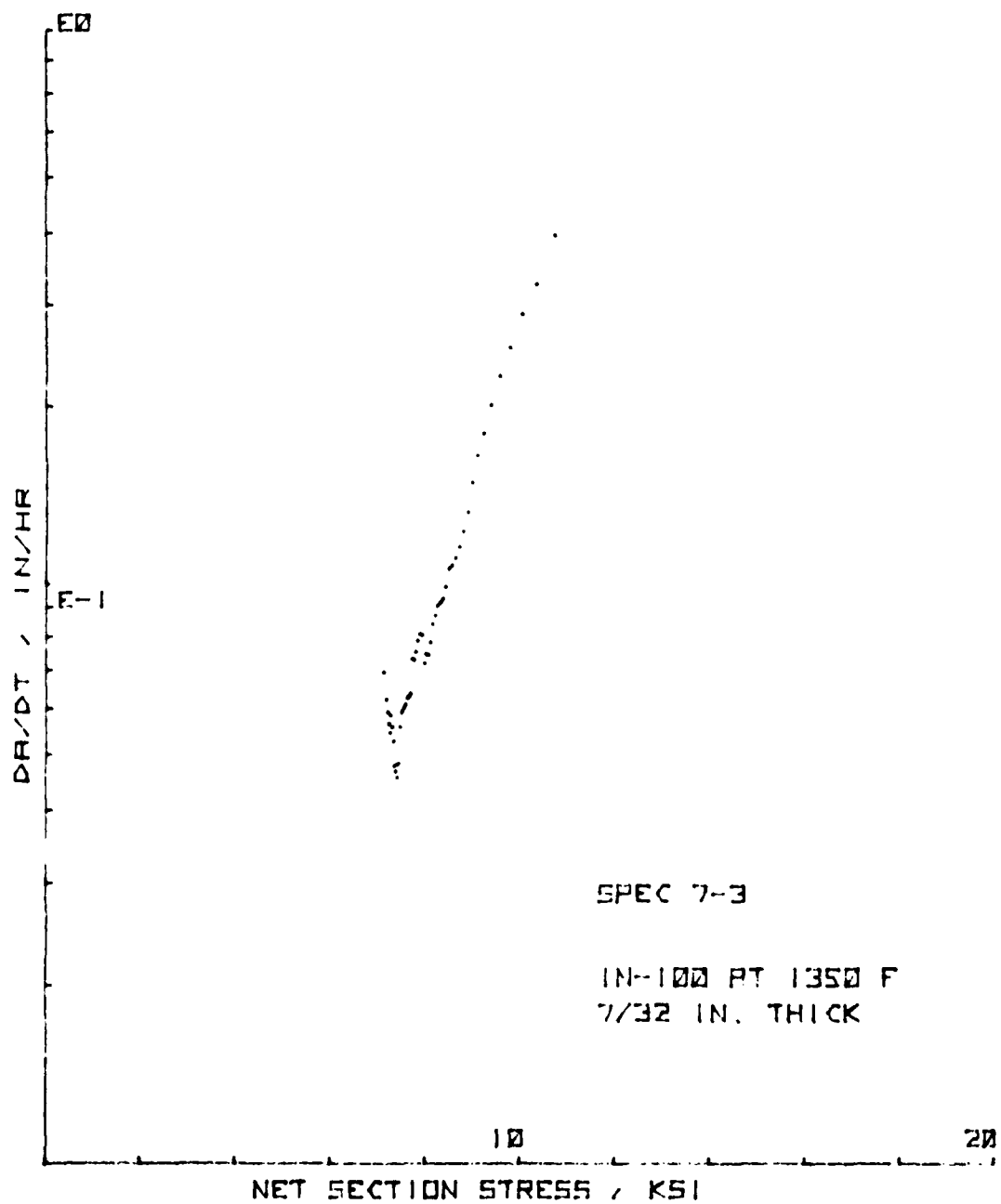
Figure 96. da/dt vs. Net Section Stress for CT Specimen 7-3
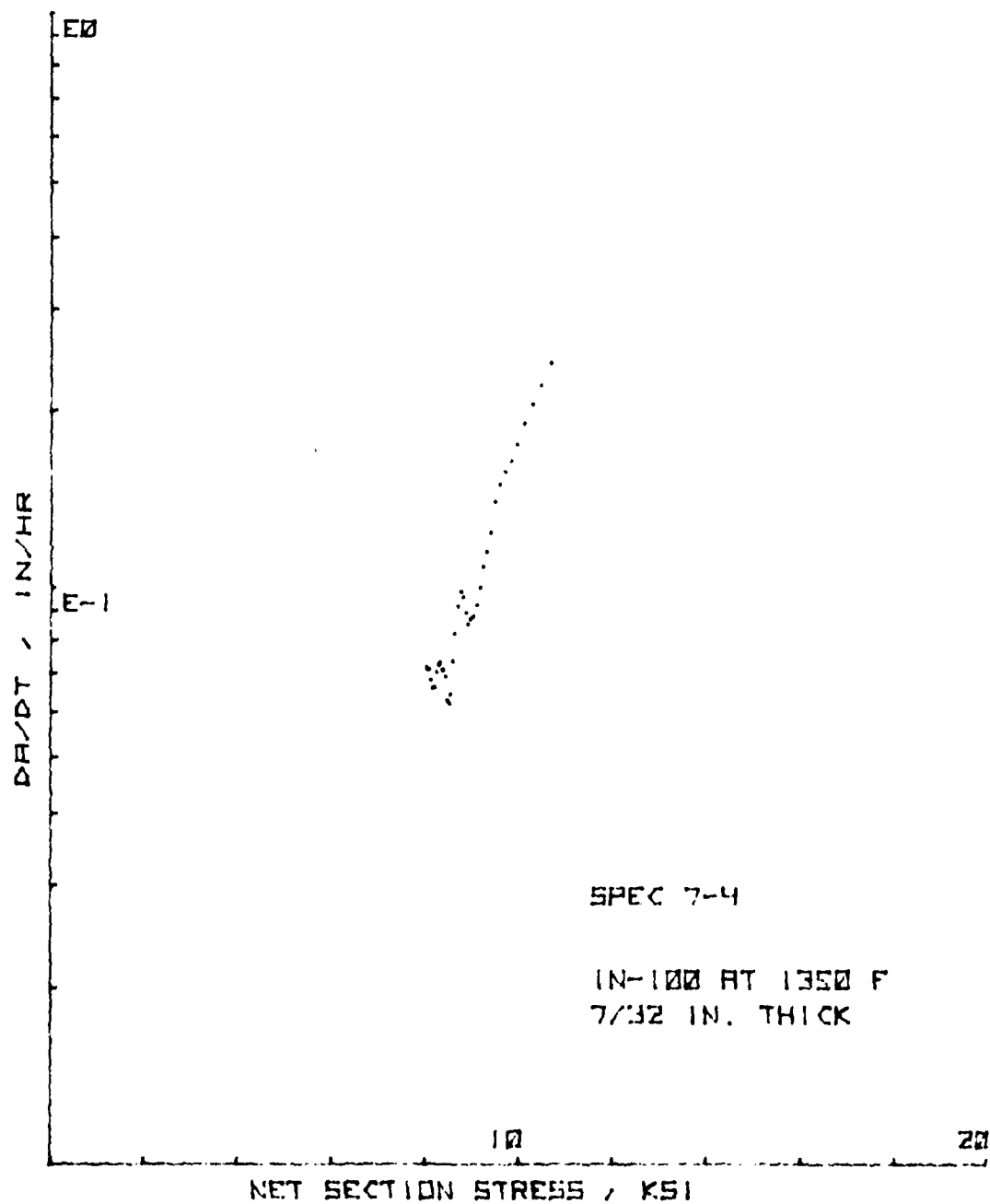
Figure 97.   da/dt vs. Net Section Stress for CT Specimen 7-4
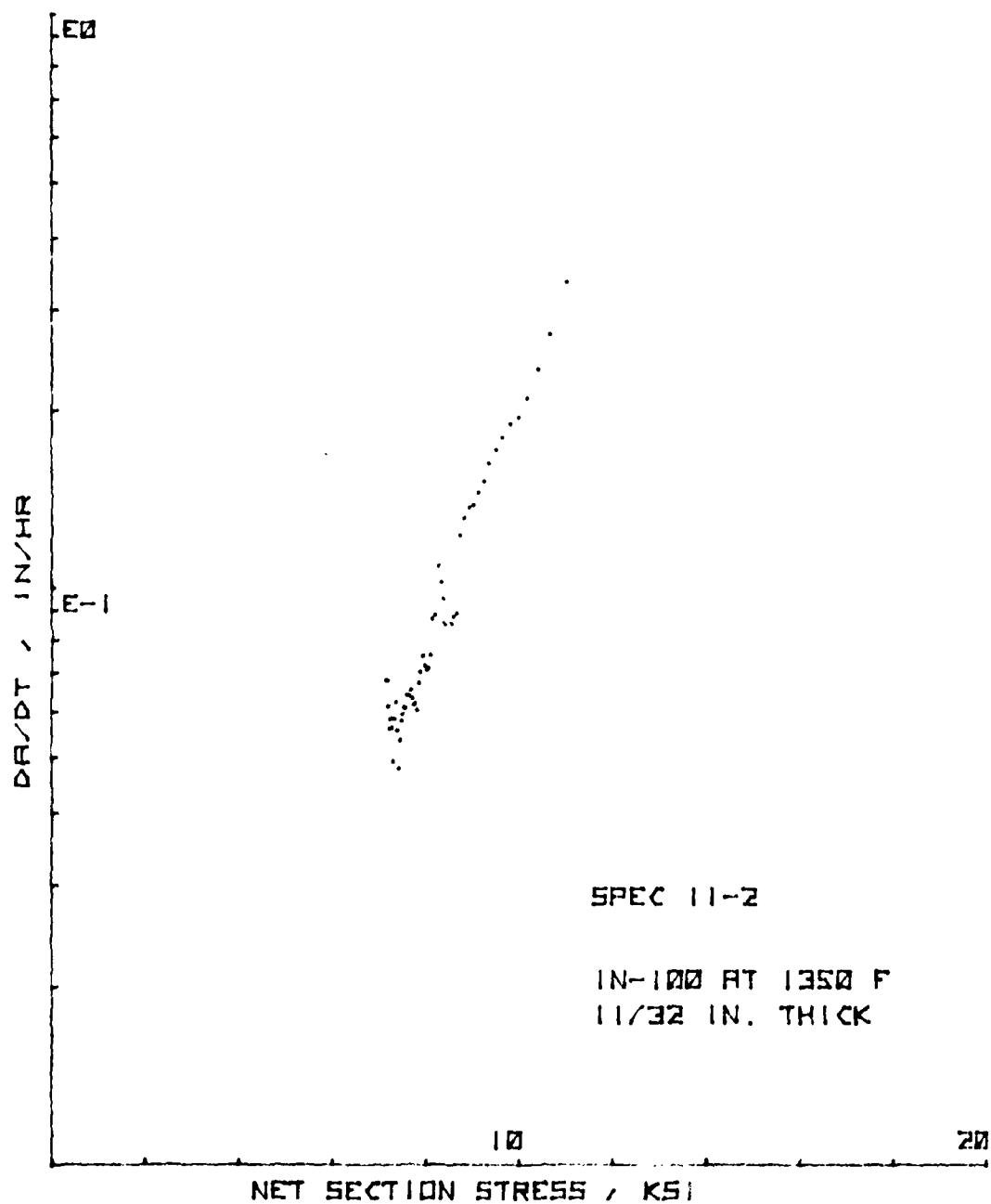
Figure 98. da/dt vs. Net Section Stress for CT Specimen 11-2
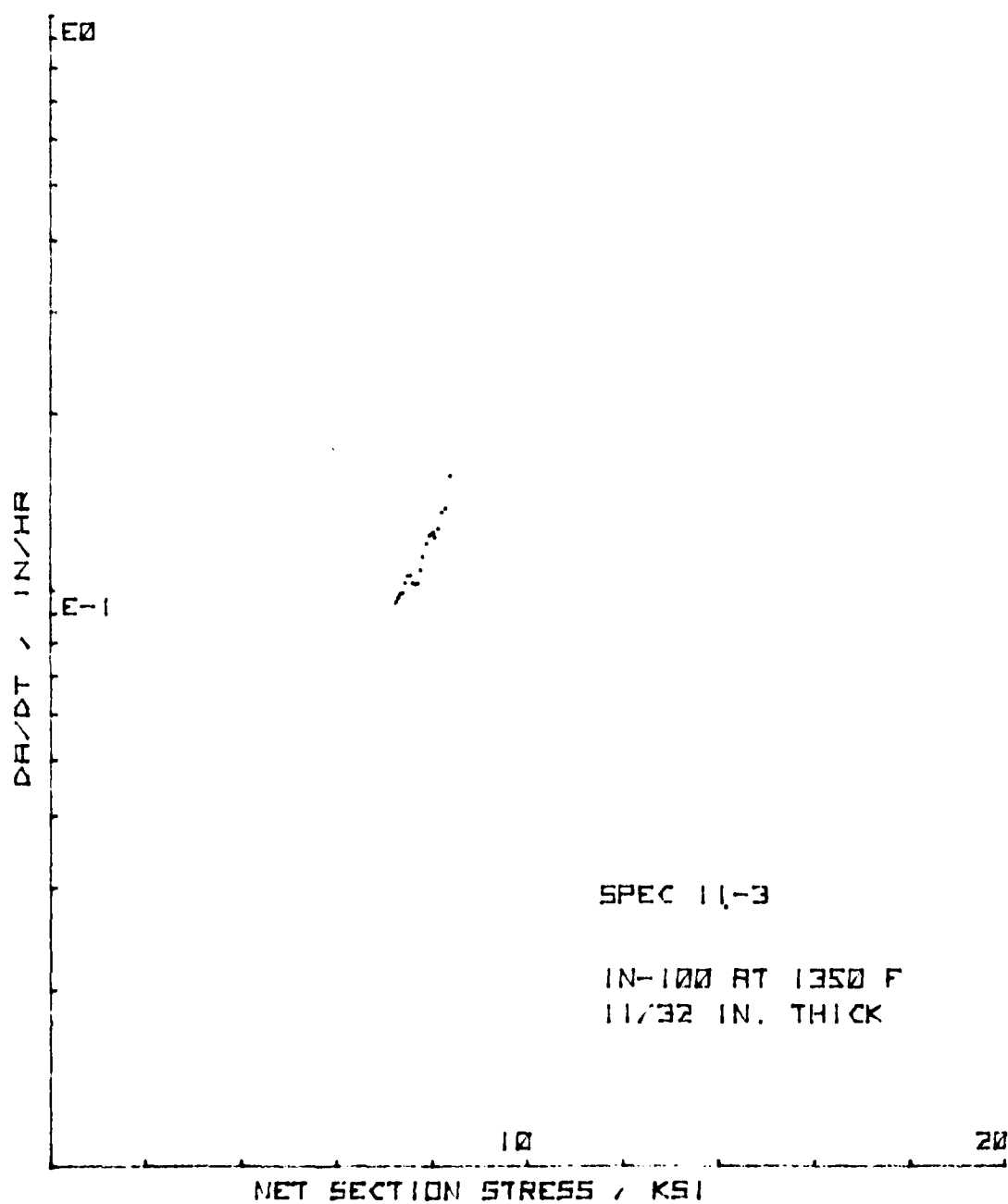
Figure 99. da/dt vs. Net Section Stress for CT Specimen 11-3

171
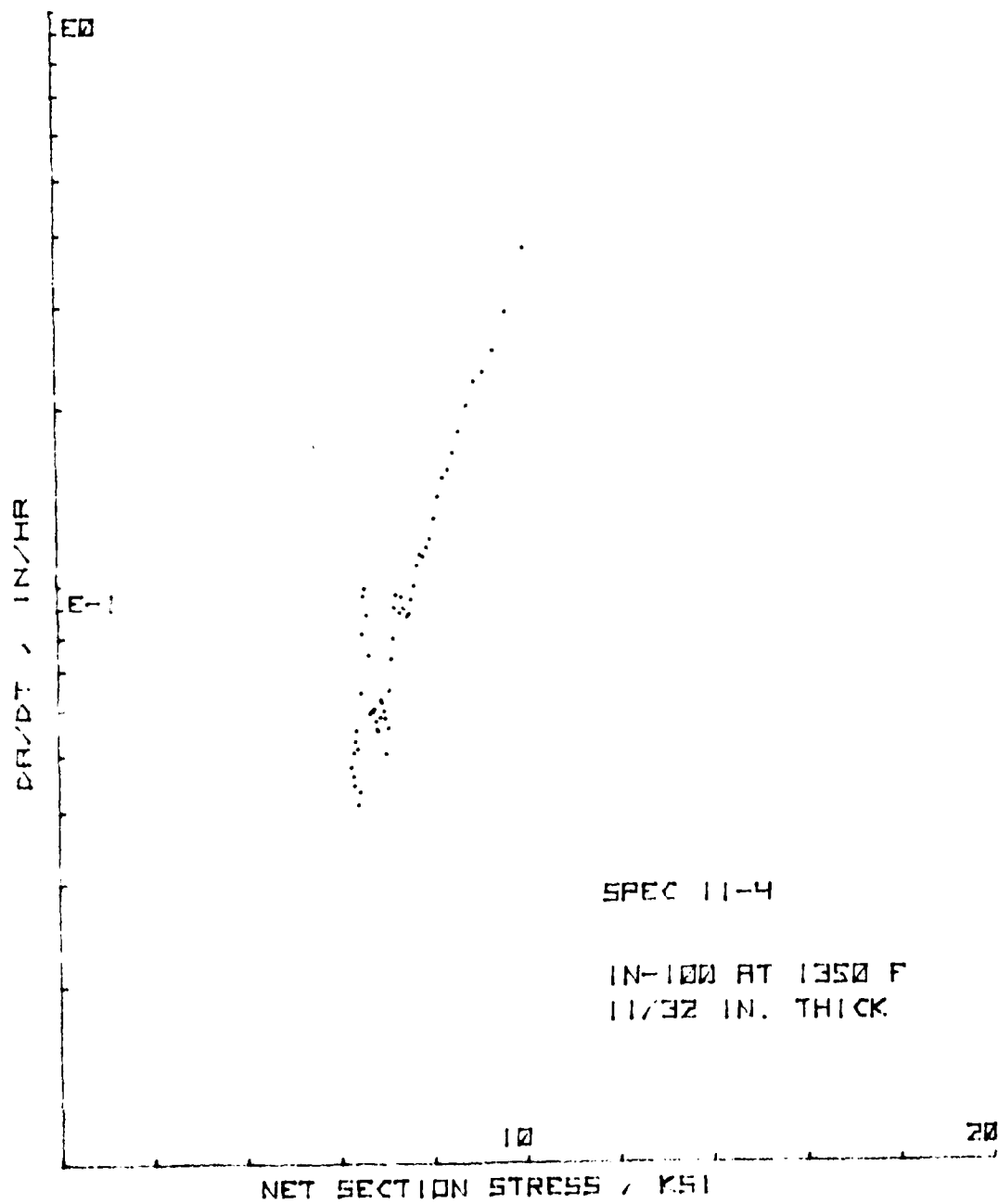
Figure 100. da/dt vs. Net Section Stress for CT Specimen 11-4
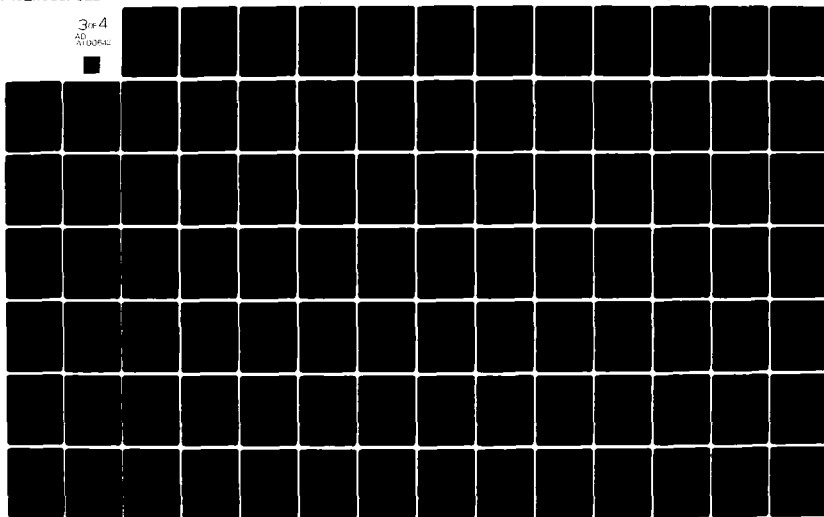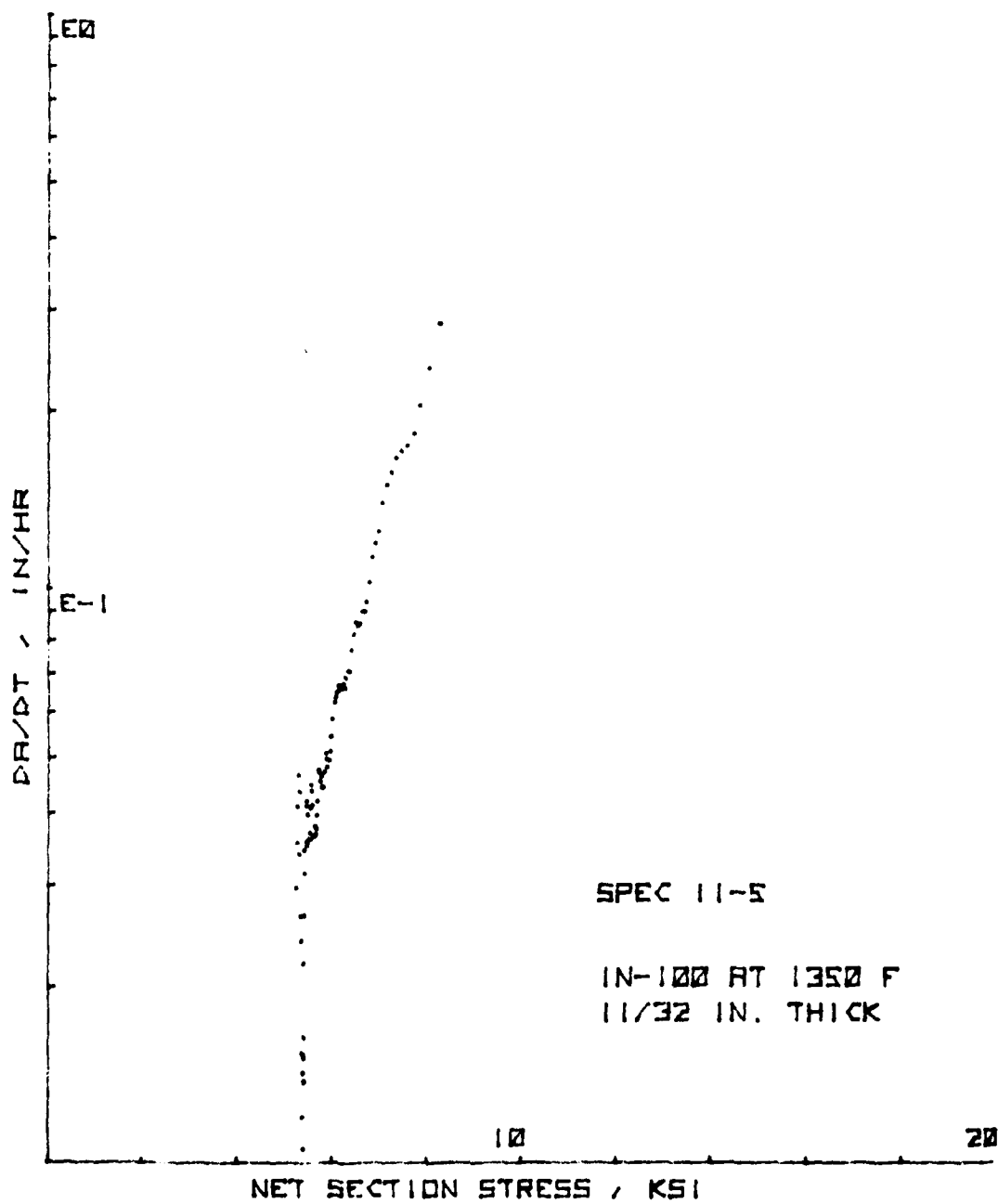
Figure 101.   da/dt vs. Net Section Stress for CT Specimen 11-5
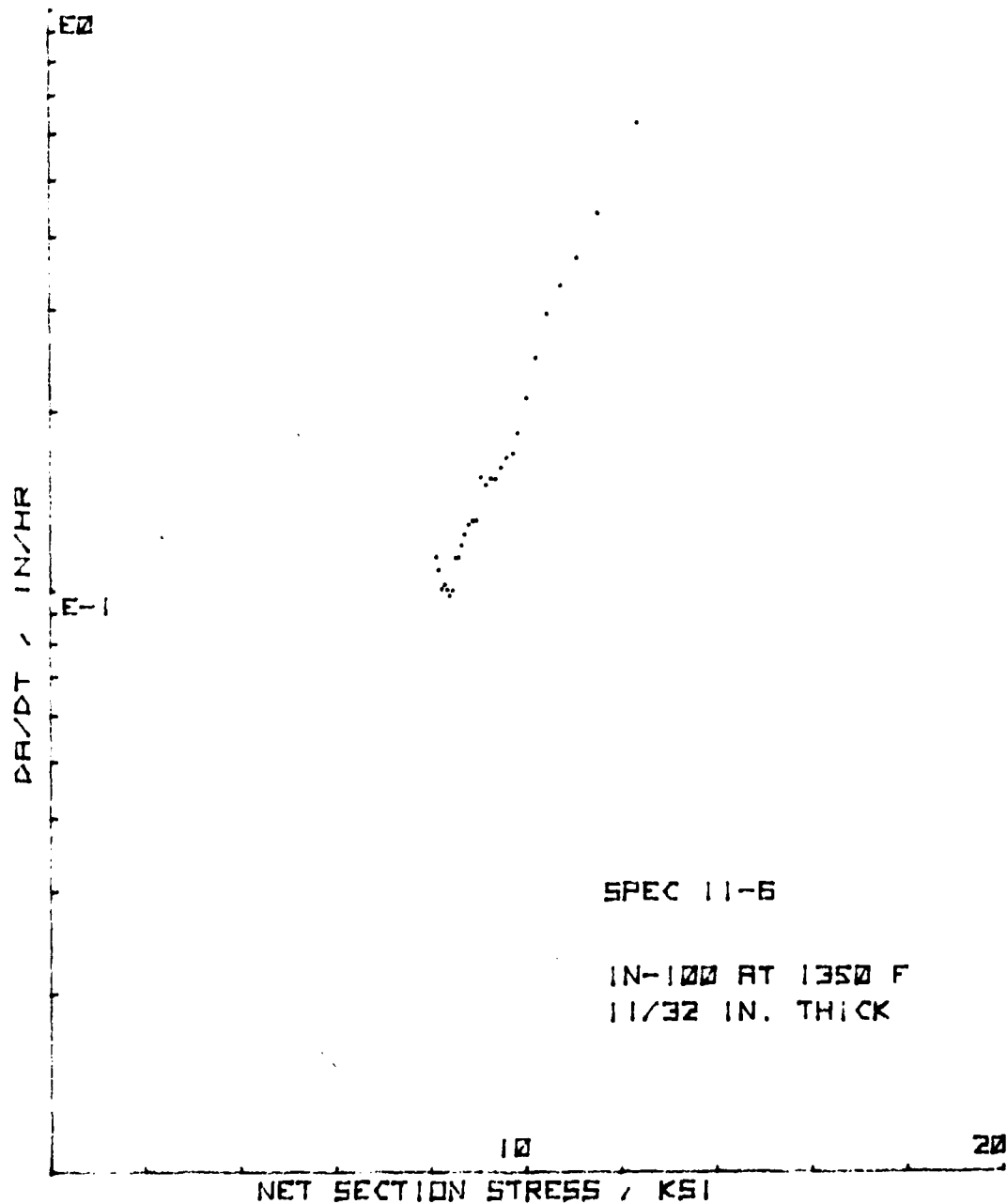
Figure 102.   da/dt vs. Net Section Stress for CT Specimen 11-6
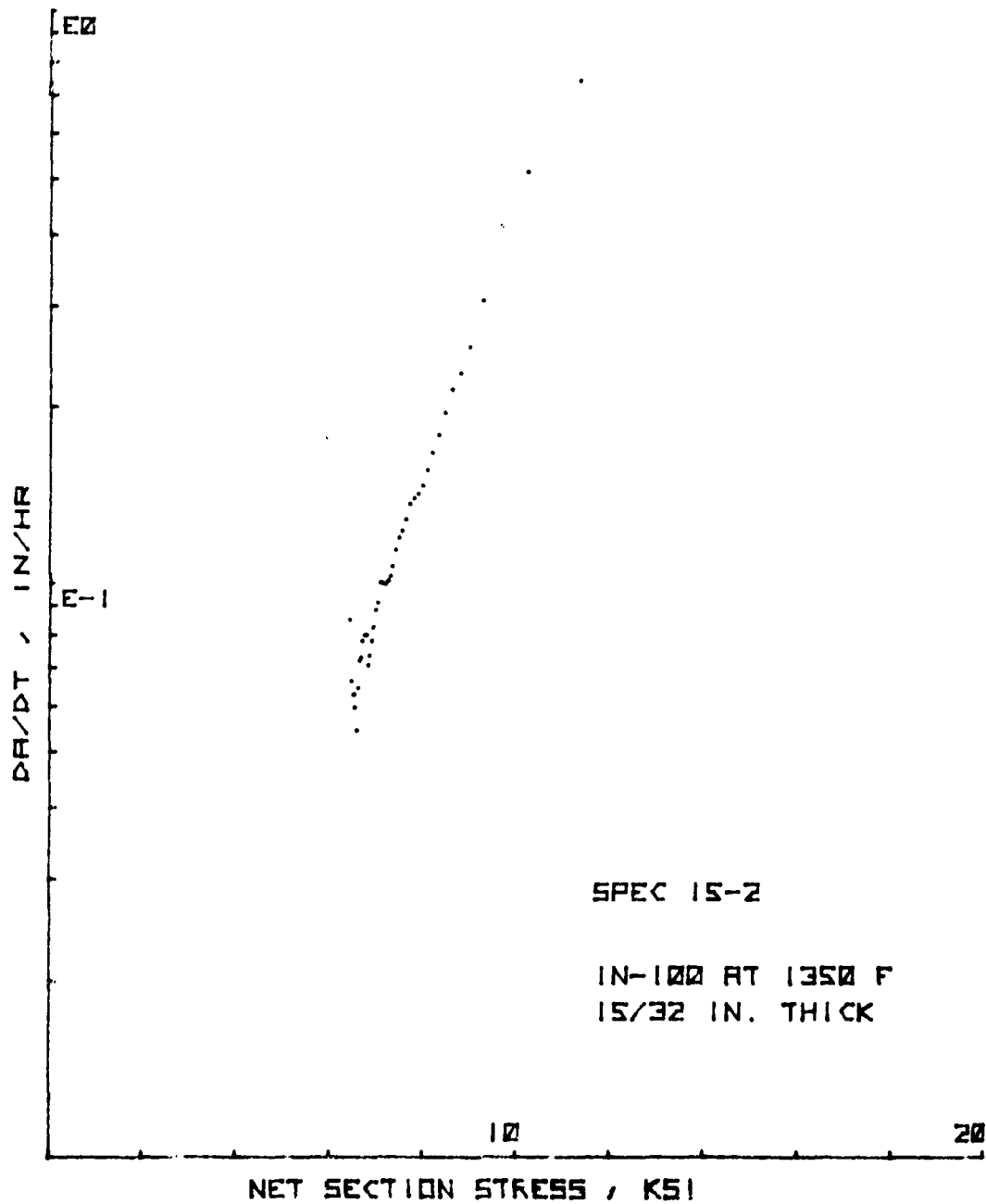
Figure 103. da/dt vs. Net Section Stress for CT Specimen 15-2
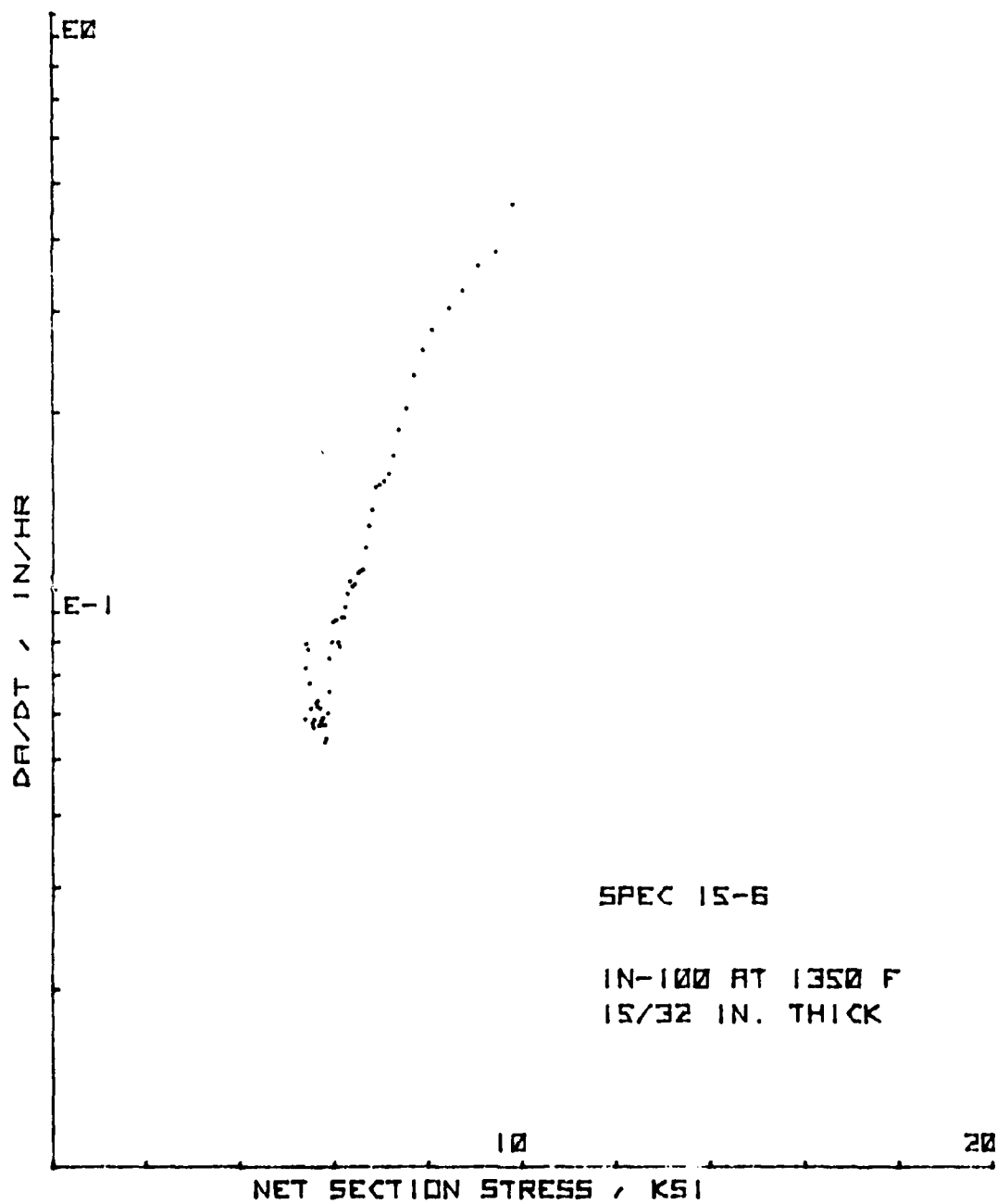
Figure 104. da/dt vs. Net Section Stress for CT Specimen 15-6
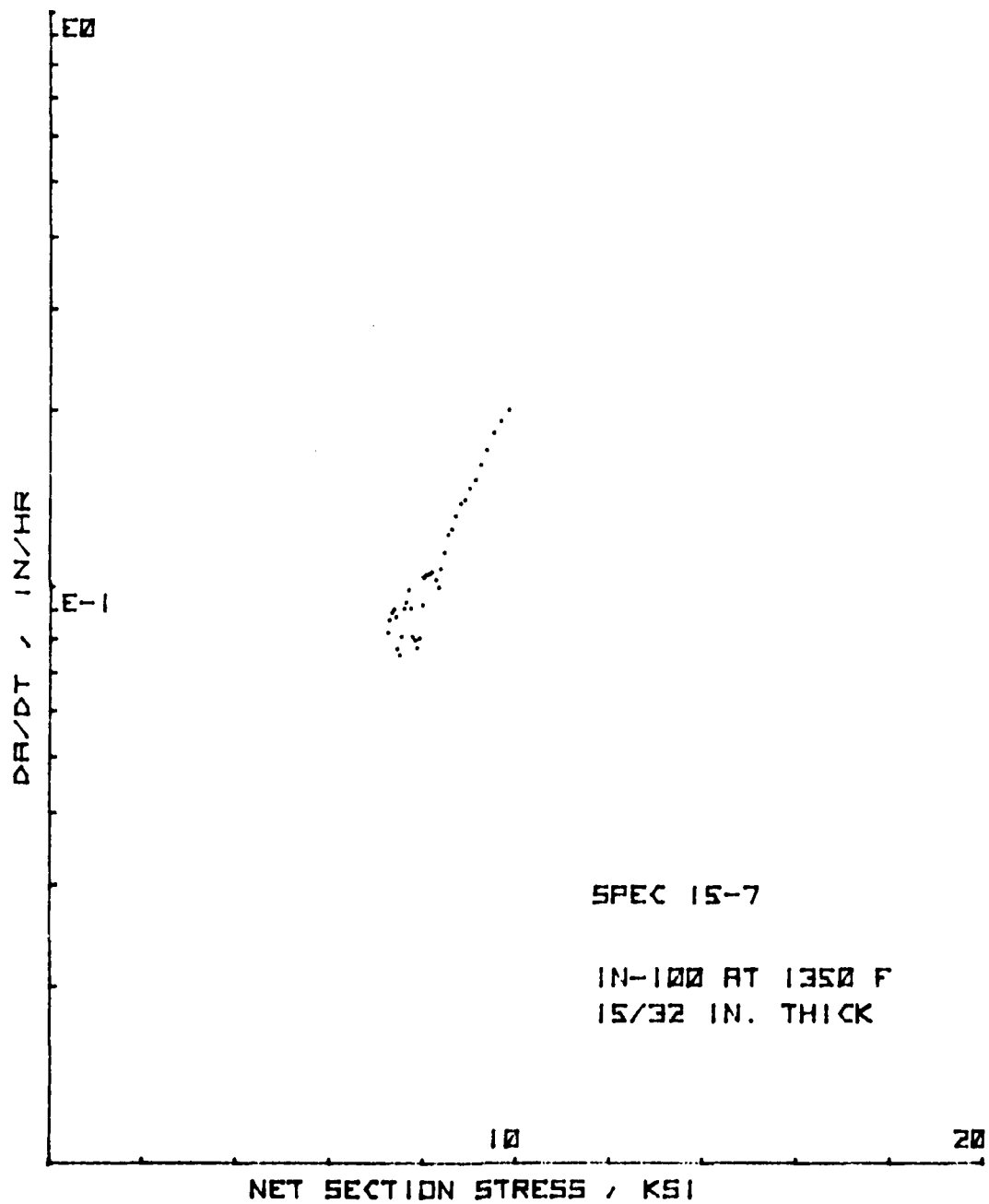
Figure 105. da/dt vs. Net Section Stress for CT Specimen 15-7
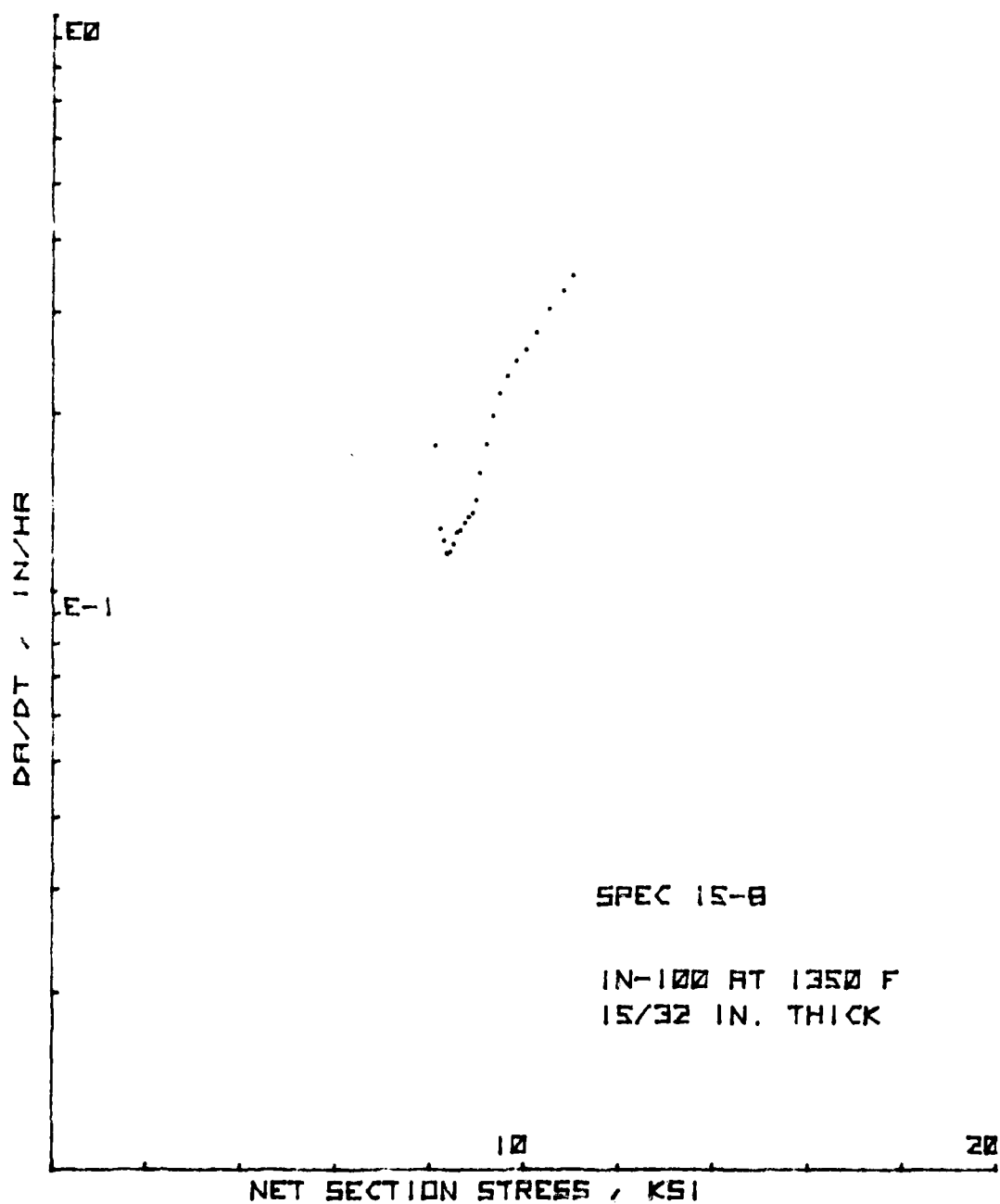
Figure 106. da/dt vs. Net Section Stress for CT Specimen 15-8
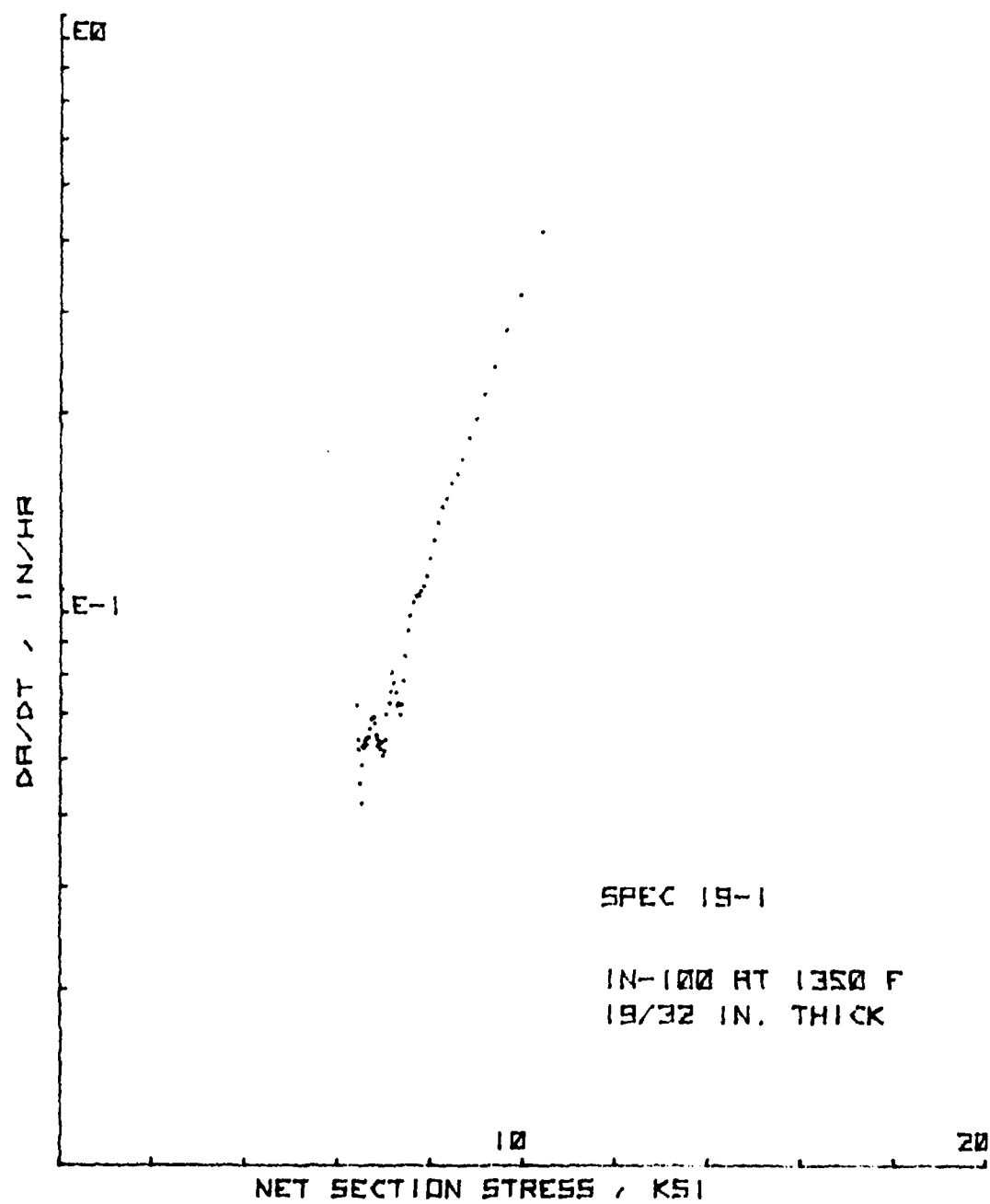
Figure 107. da/dt vs. Net Section Stress for CT Specimen 19-1
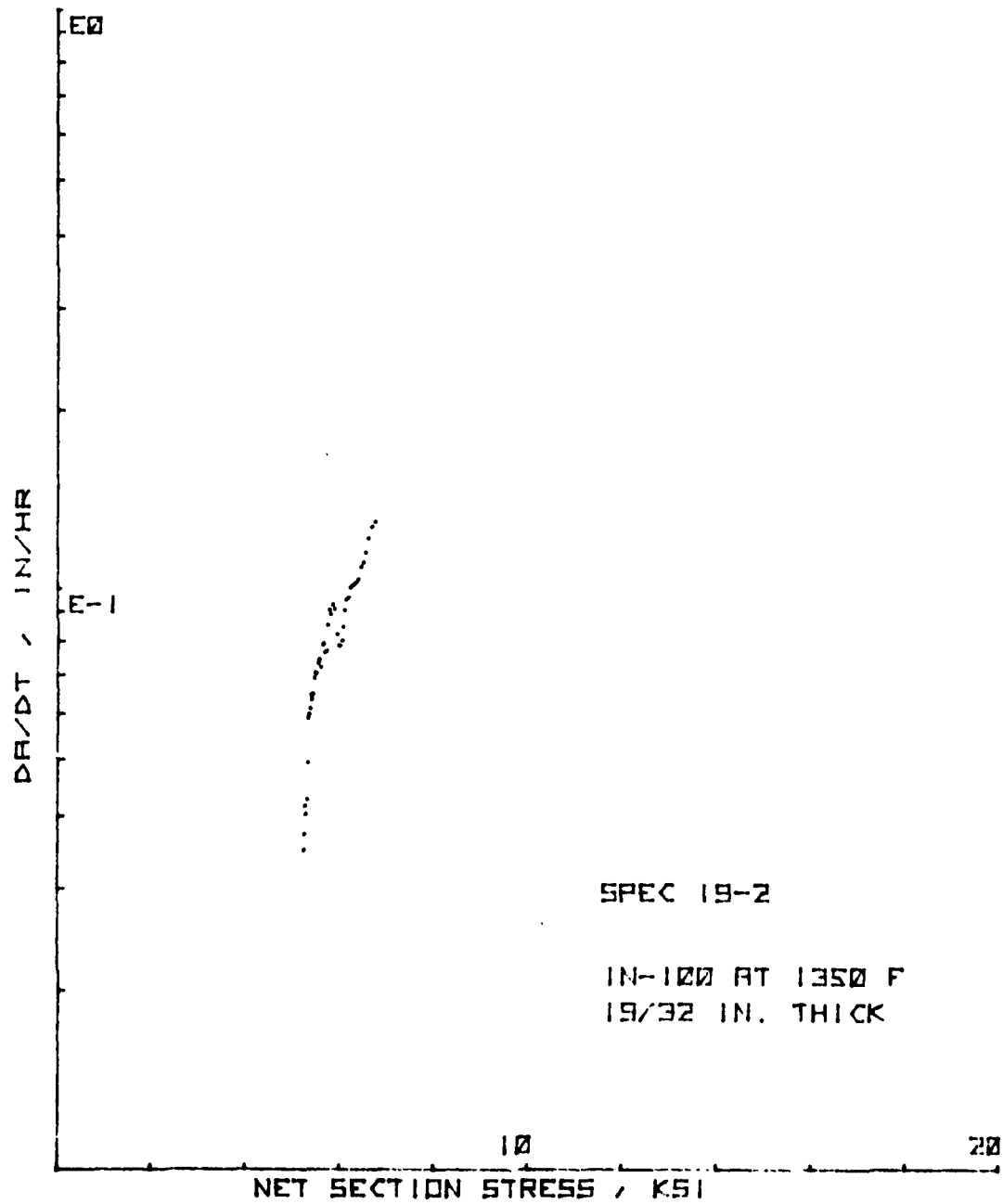
Figure 108. da/dt vs. Net Section Stress for CT Specimen 19-2
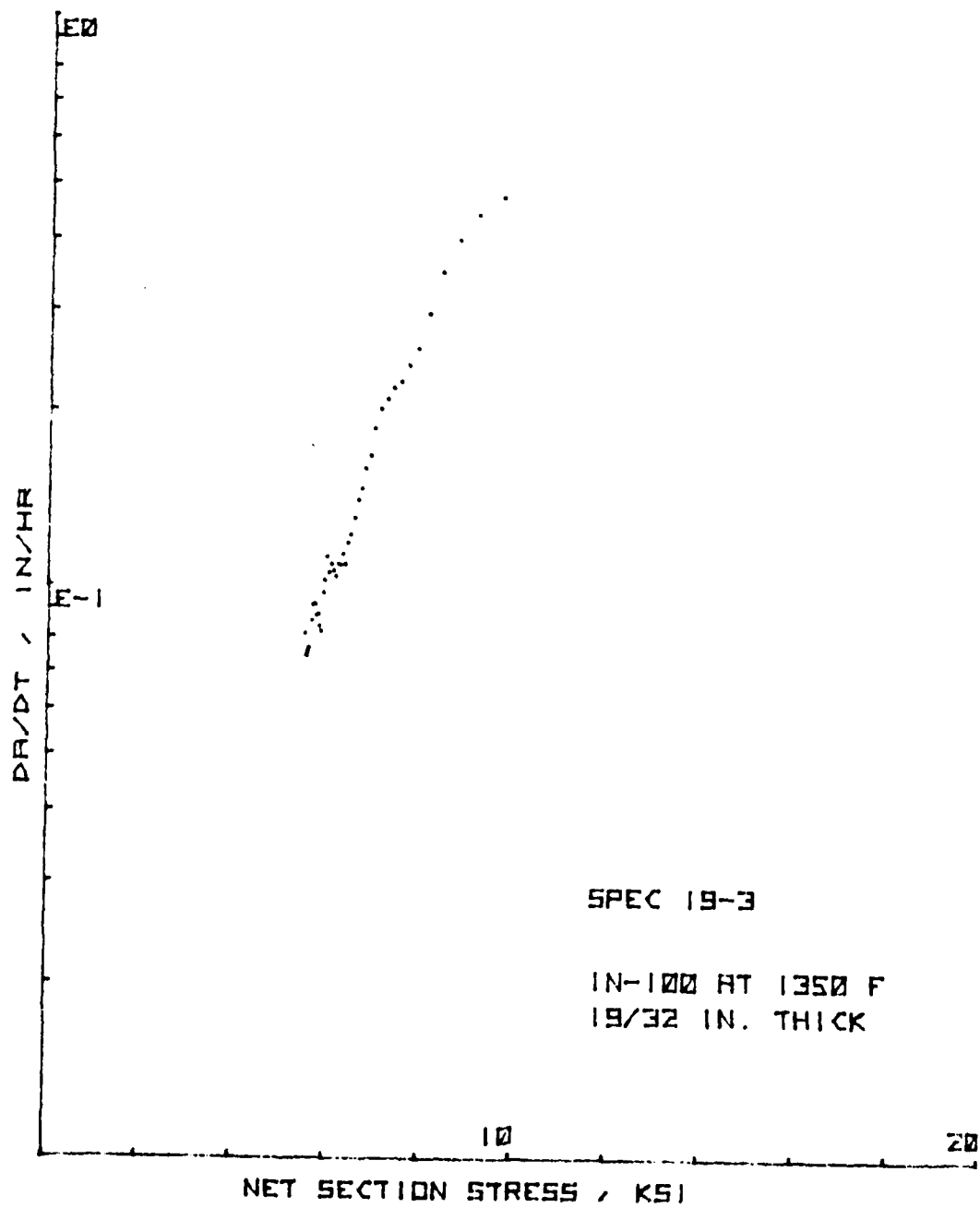
Figure 109. da/dt vs. Net Section Stress for CT Specimen 19-3
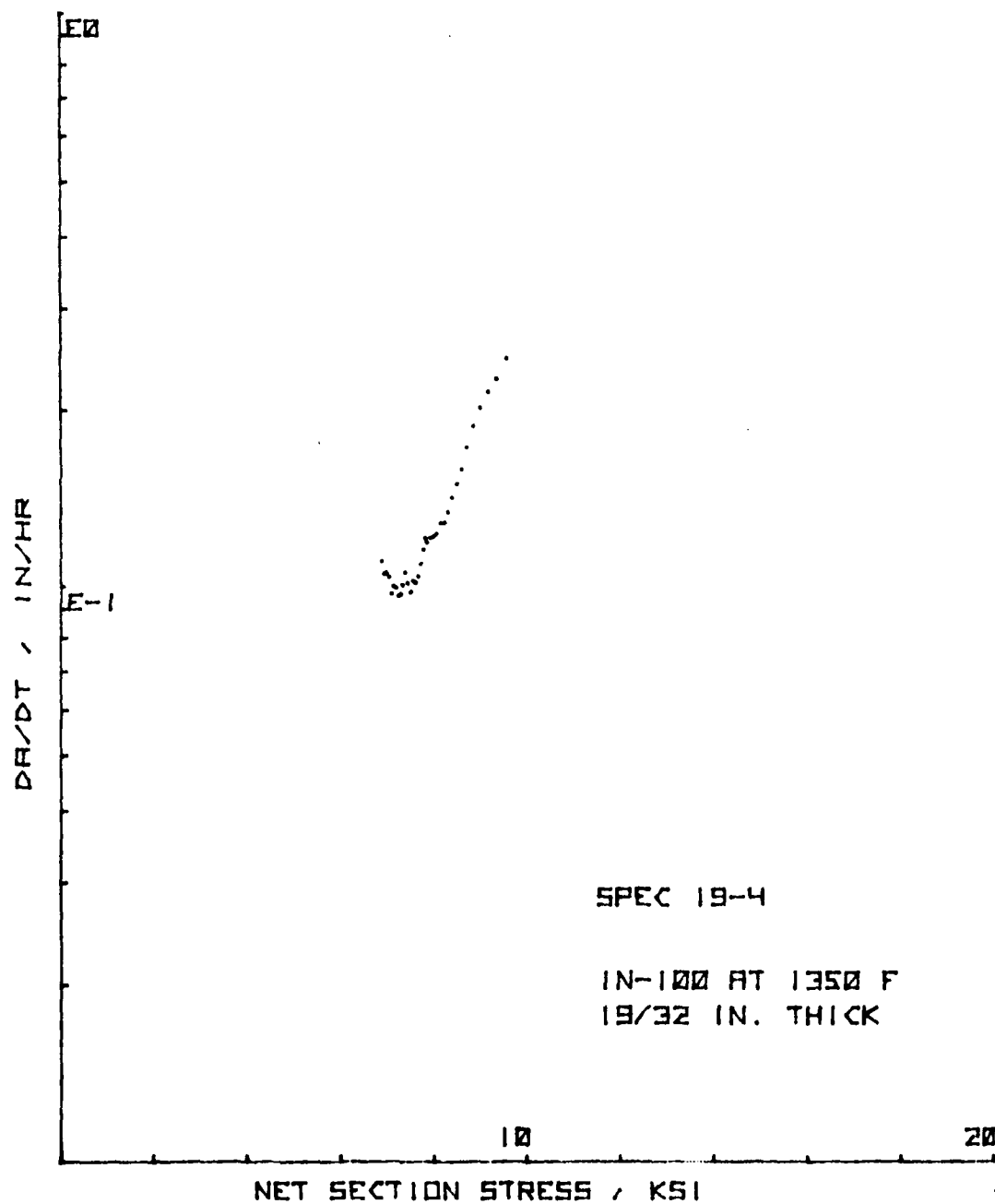
Figure 110. da/dt vs. Net Section Stress for CT Specimen 19-4
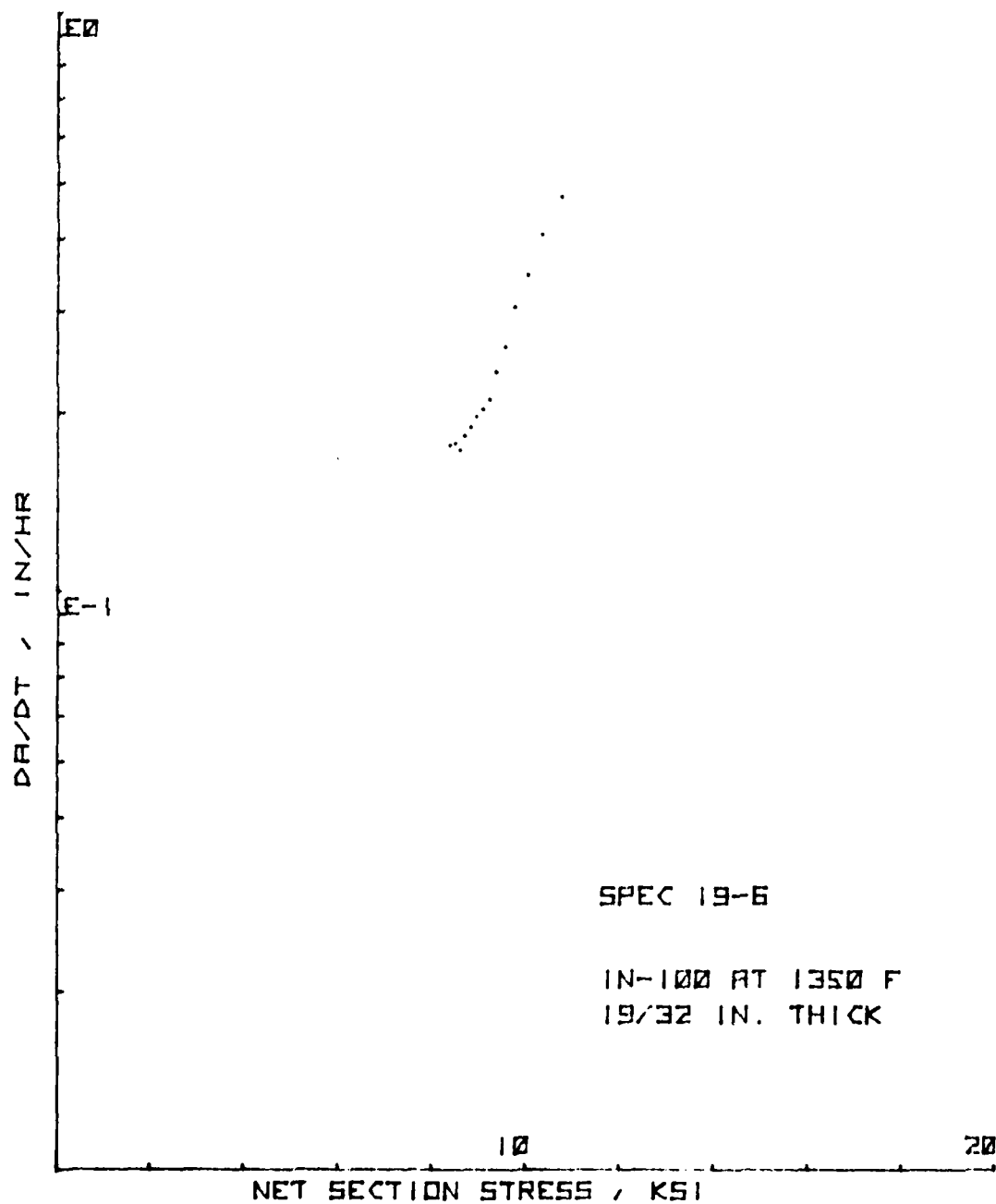
Figure 111. da/dt vs. Net Section Stress for CT Specimen 19-6
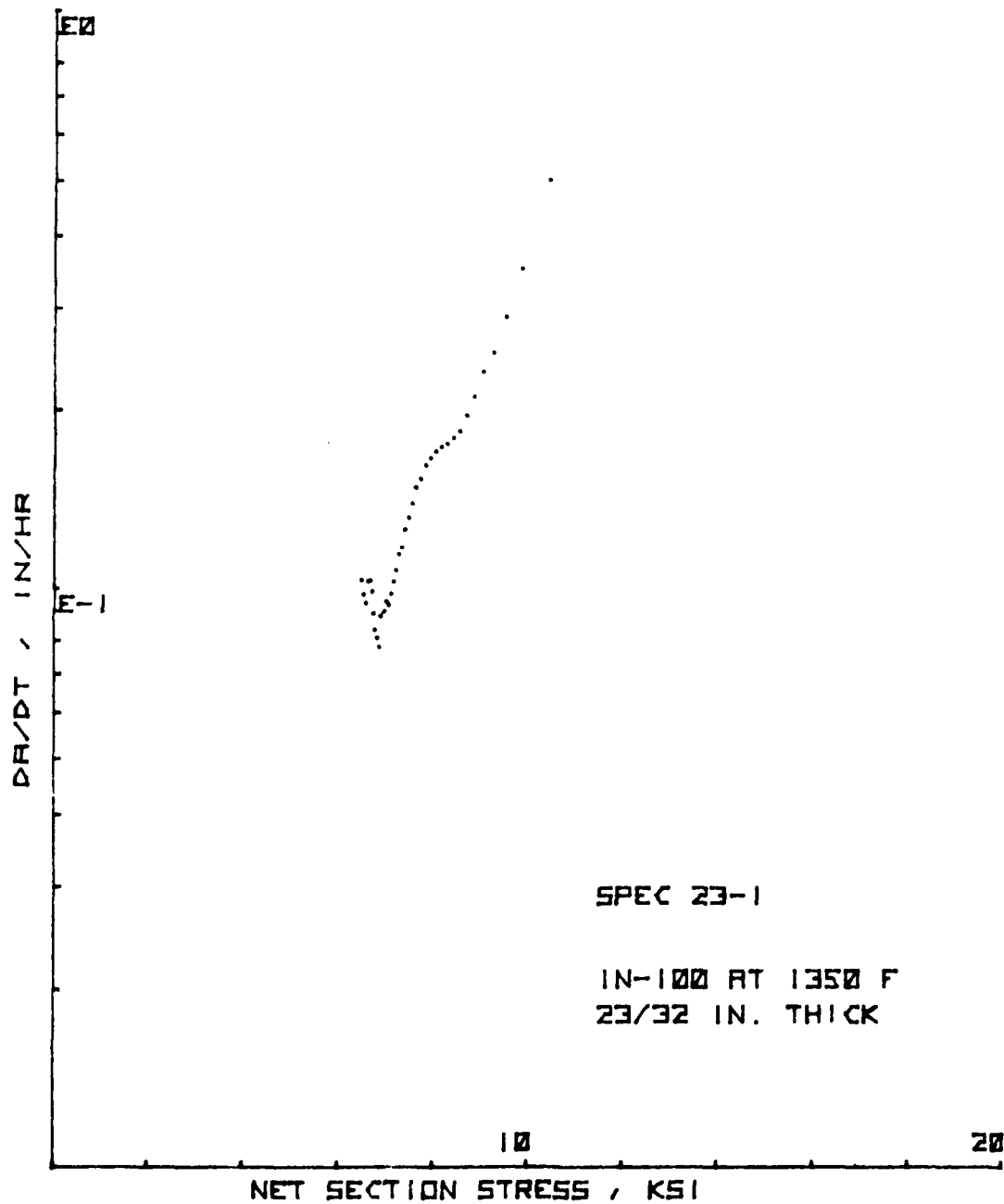
Figure 112. da/dt vs. Net Section Stress for CT Specimen 23-1
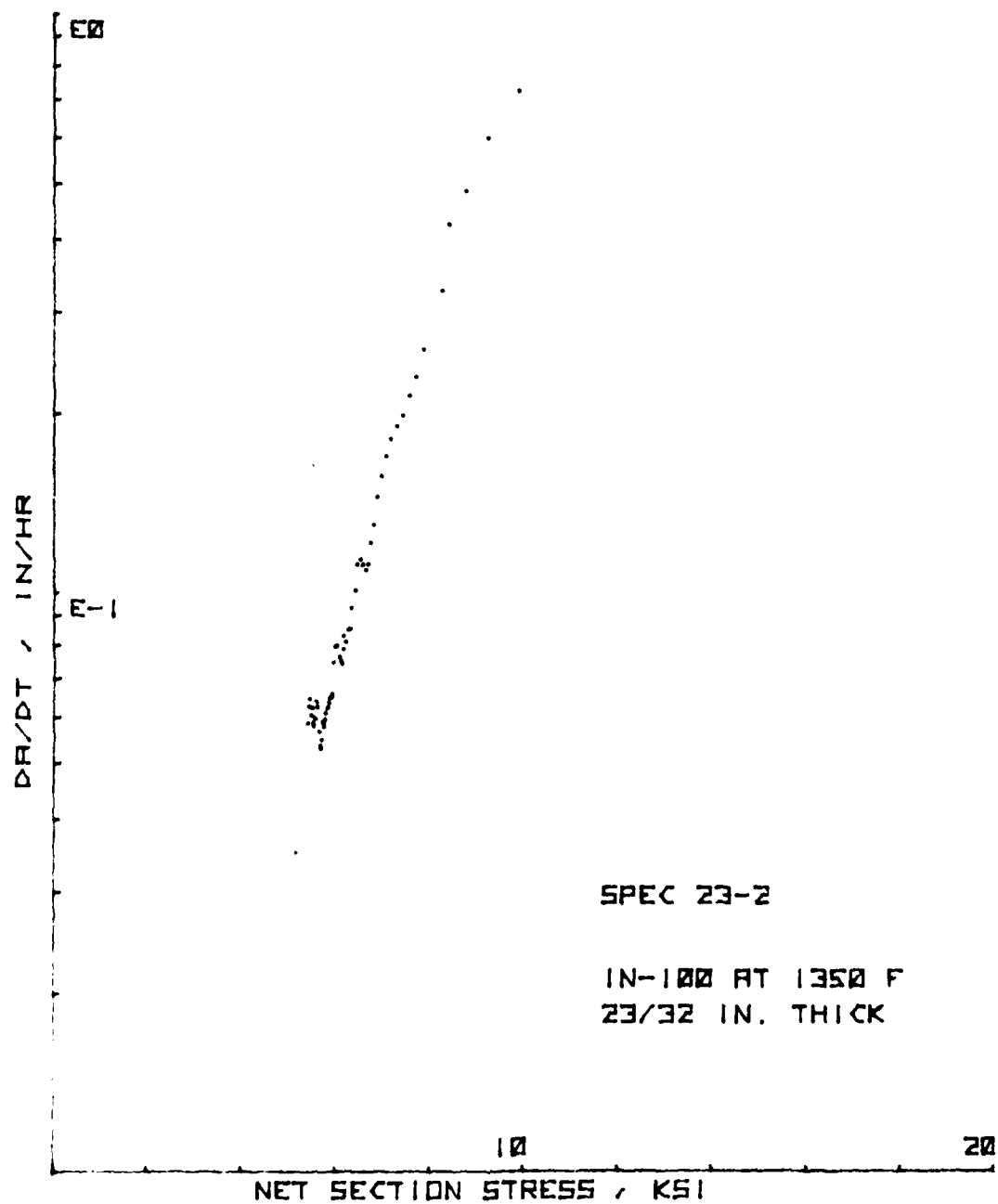
Figure 113. da/dt vs. Net Section Stress for CT Specimen 23-2
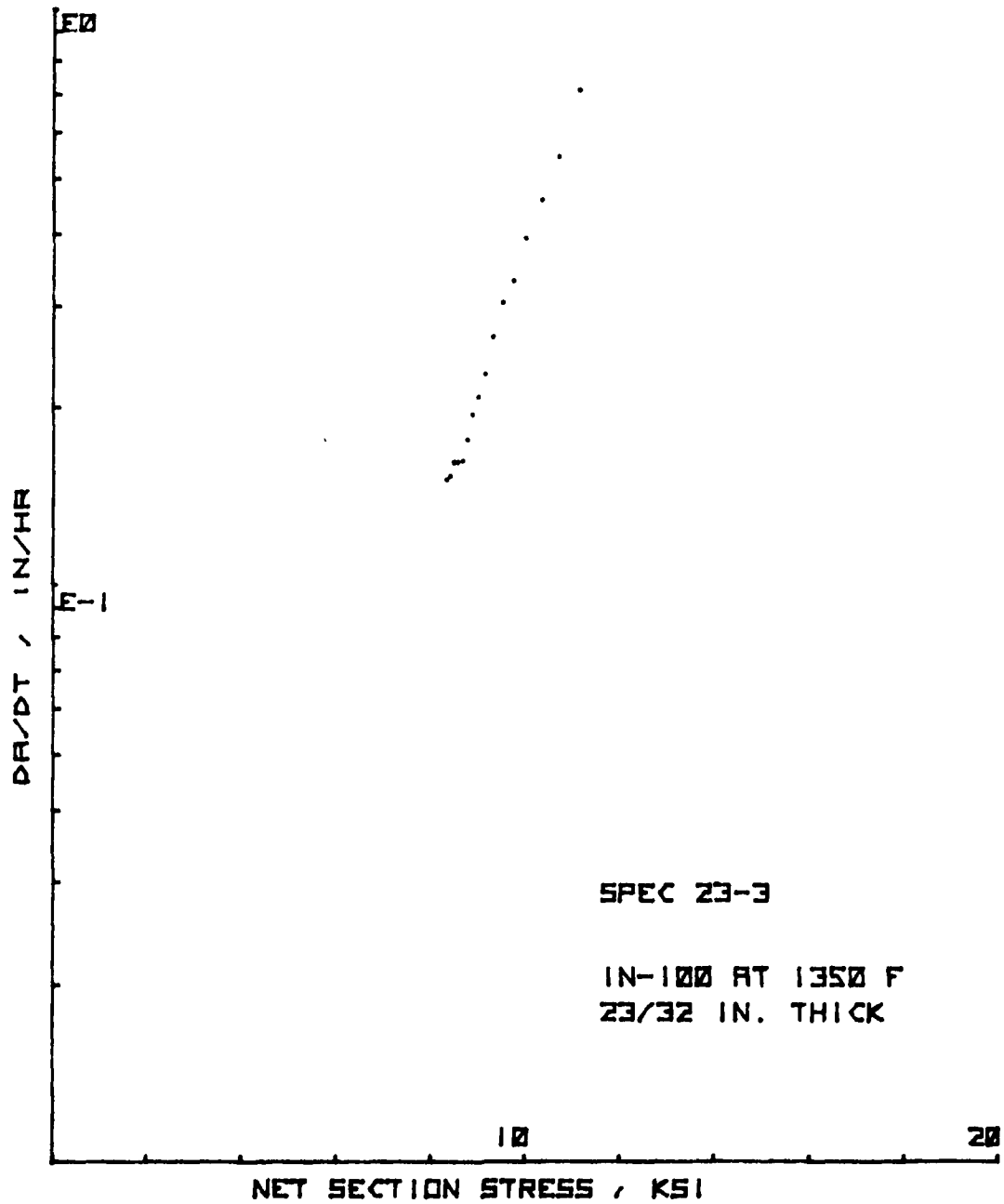
Figure 114. da/dt vs. Net Section Stress for CT Specimen 23-3
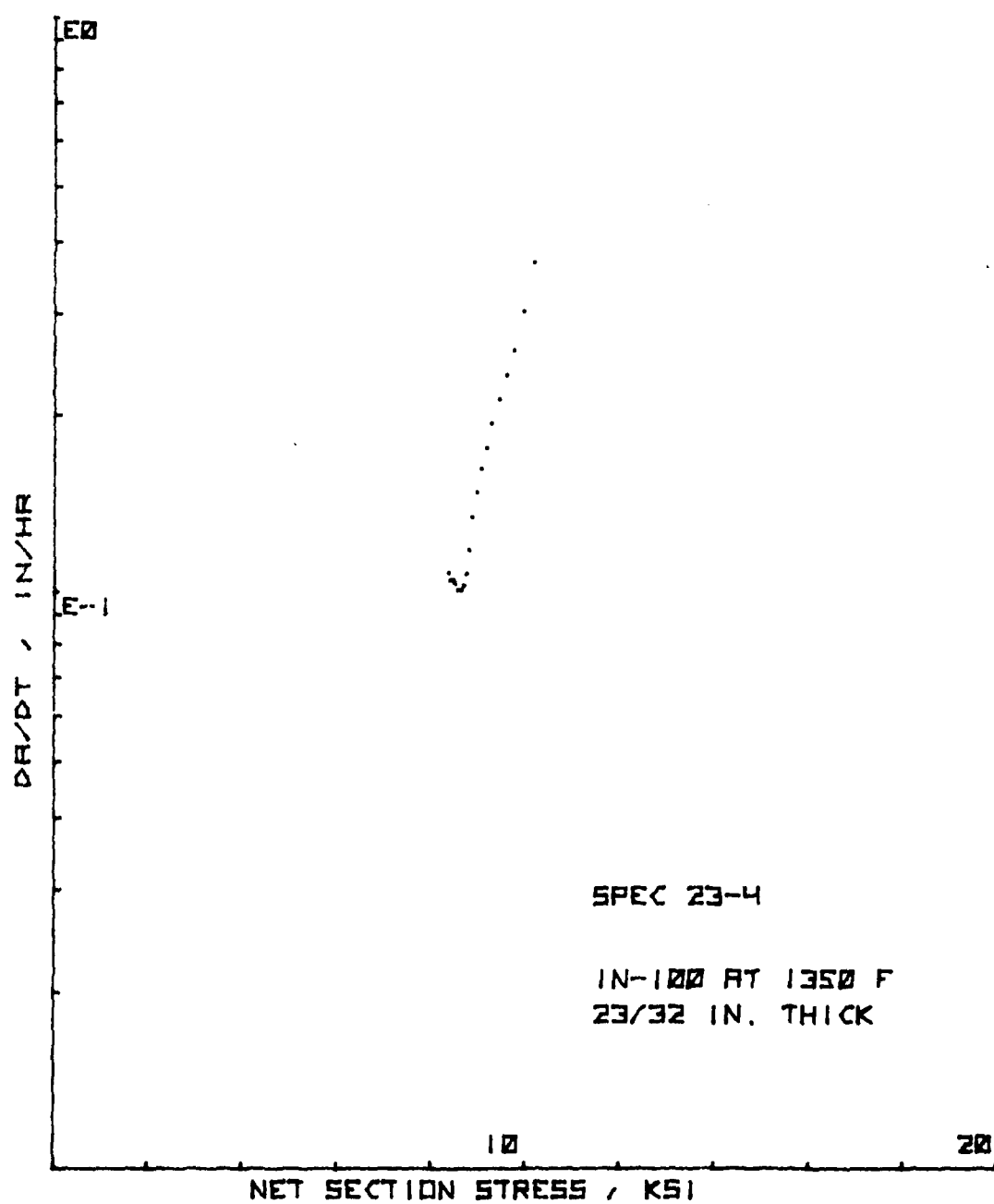
Figure 115. da/dt vs. Net Section Stress for CT Specimen 23-4
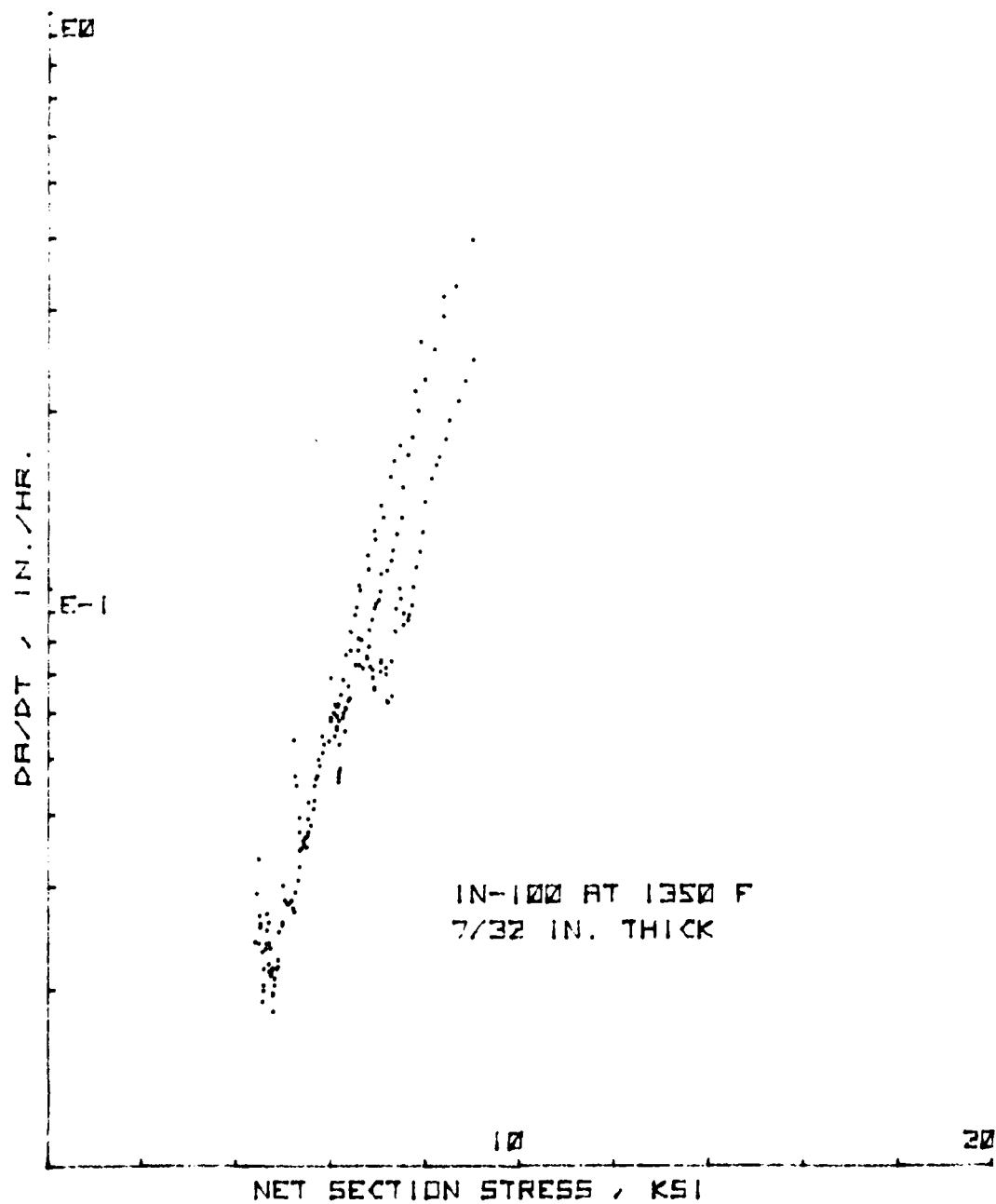
Figure 116. da/dt vs. Net Section Stress - 7/32" (6 mm) Thick
CT Specimen Group
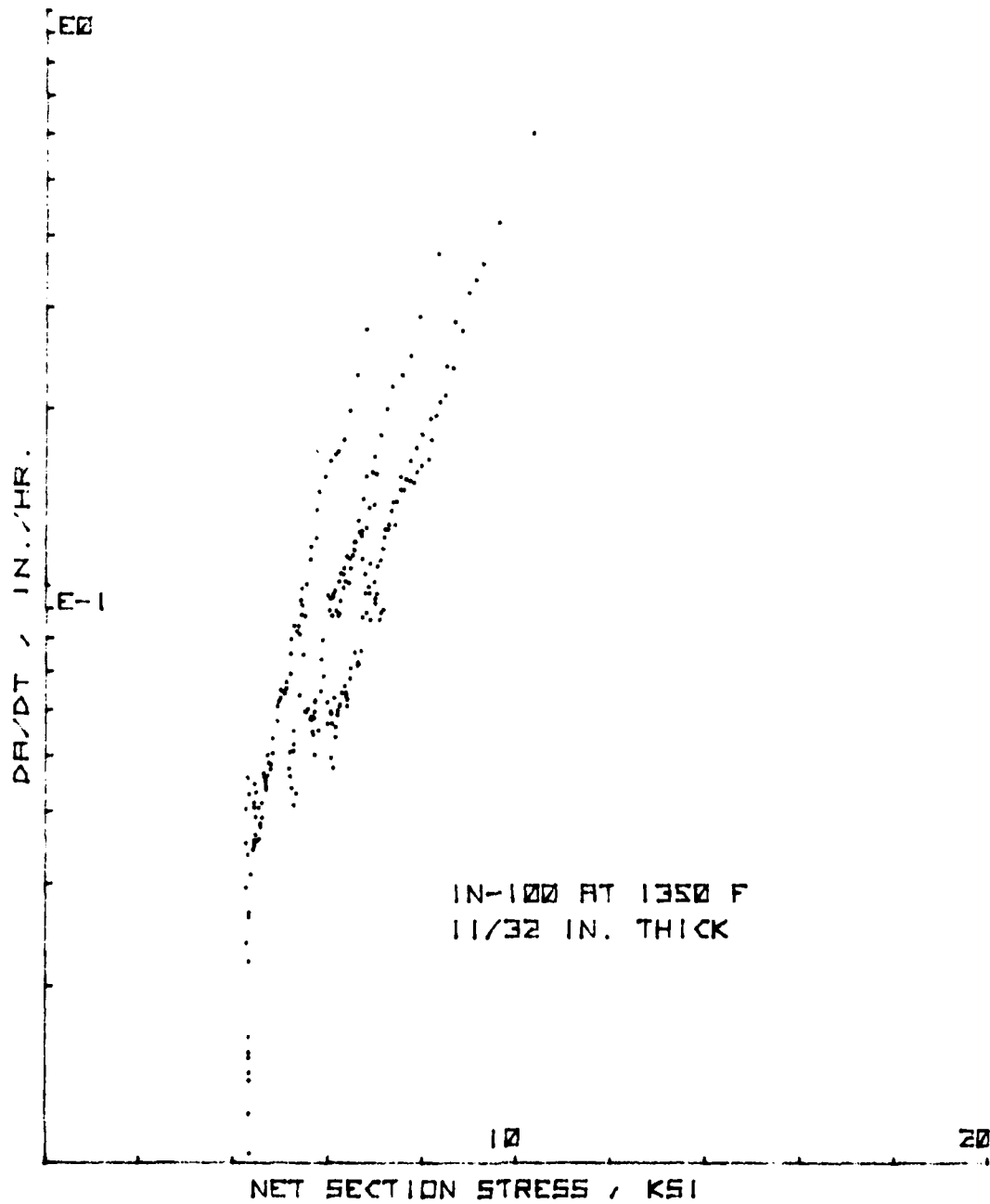
Figure 117.   da/dt vs. Net Section Stress - 11/32" (9 mm) Thick
CT Specimen Group
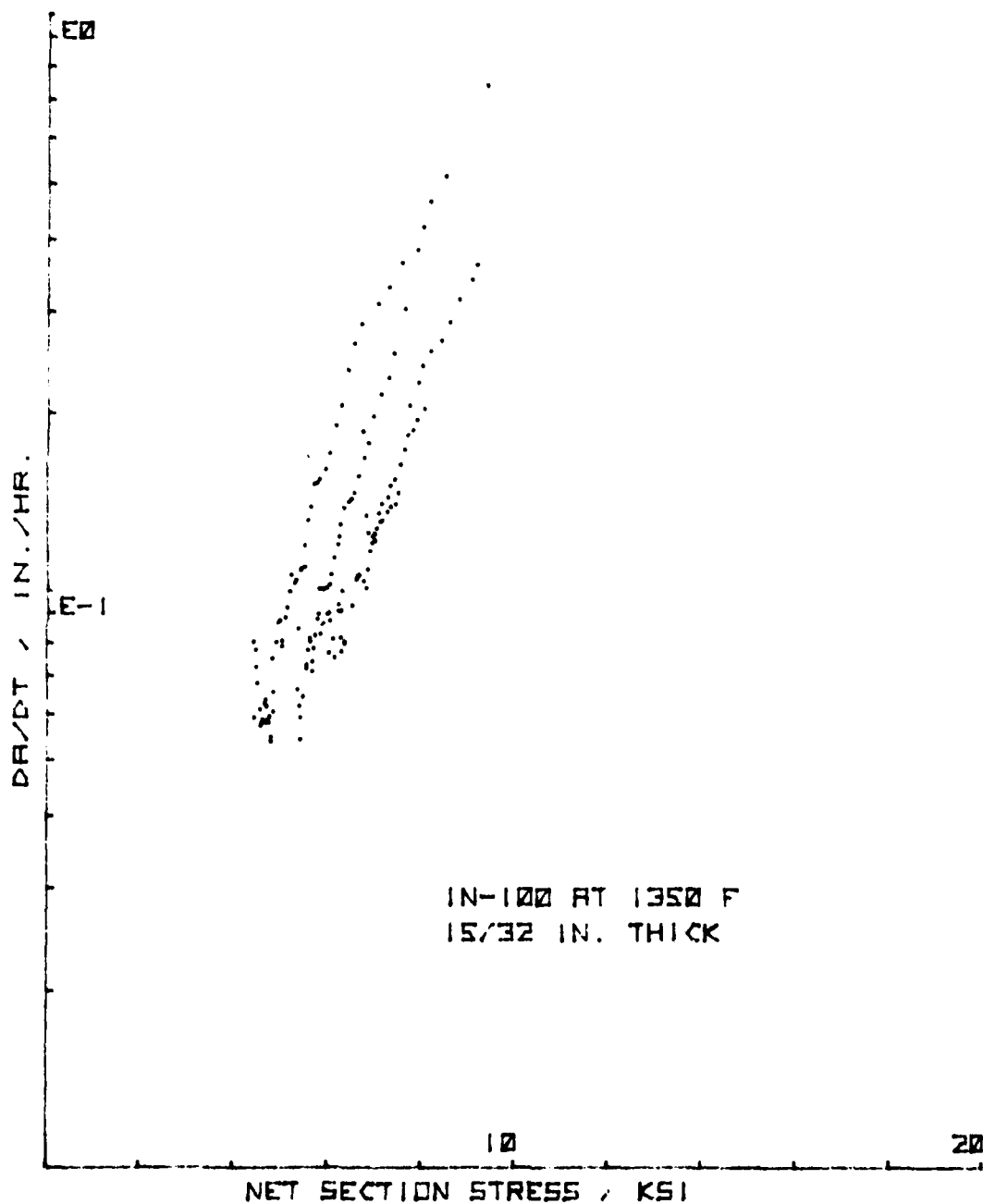
Figure 118. da/dt vs. Net Section Stress - 15/32" (12 mm) Thick
CT Specimen Group
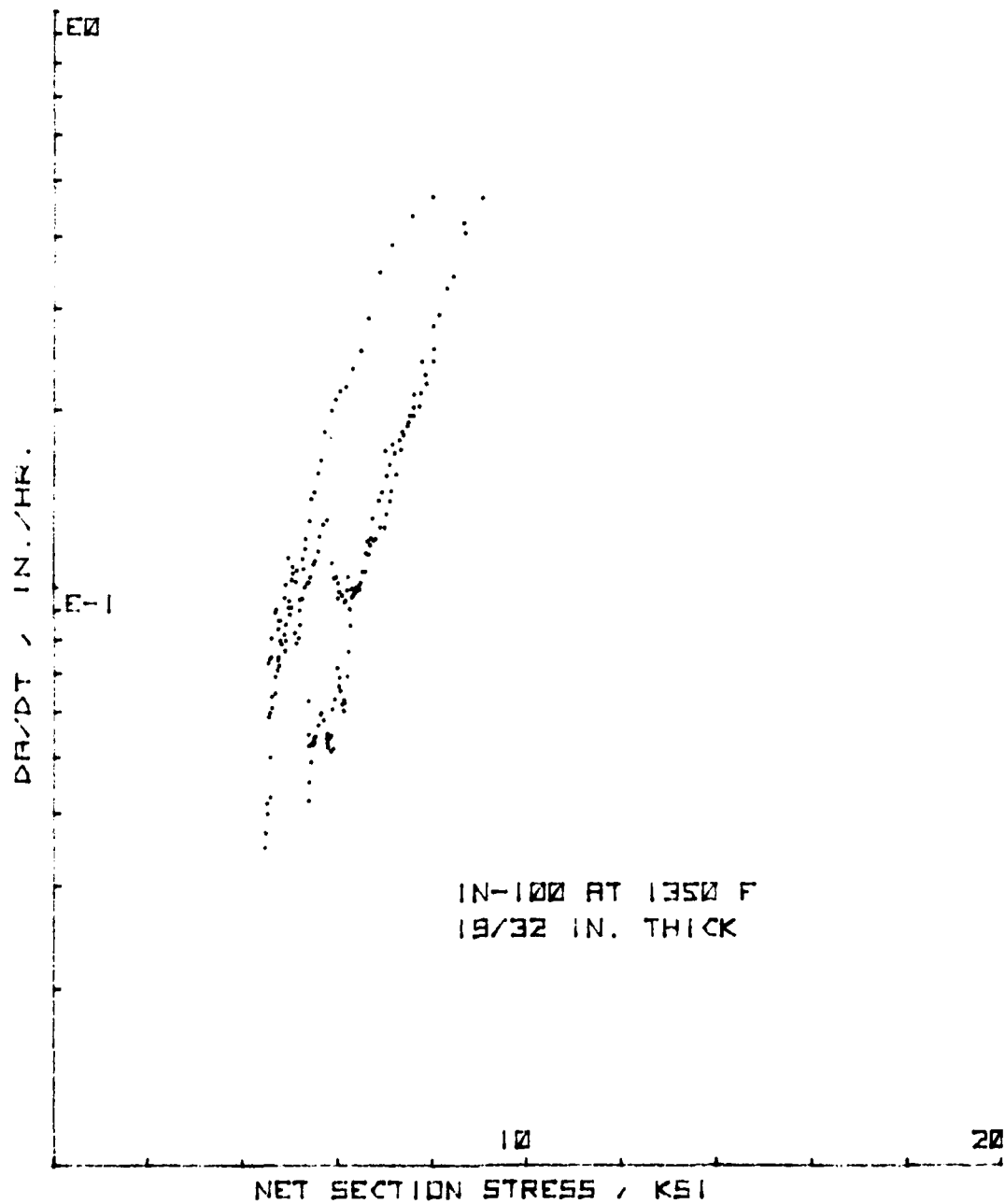
Figure 119.   da/dt vs. Net Section Stress - 19/32" (15 mm) Thick
CT Specimen Group
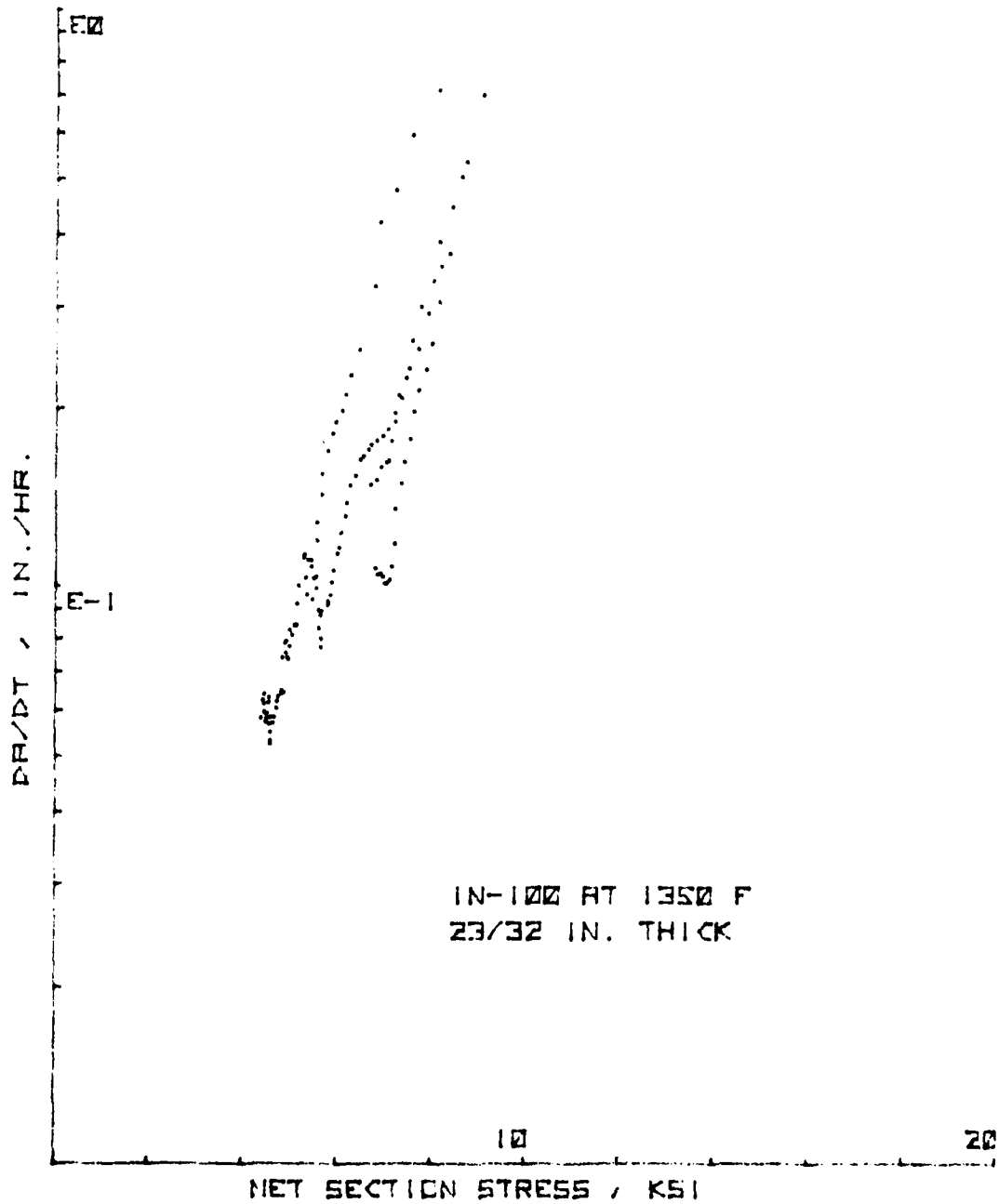
Figure 120.   da/dt vs. Net Section Stress - 23/32" (18 mm) Thick
CT Specimen Group
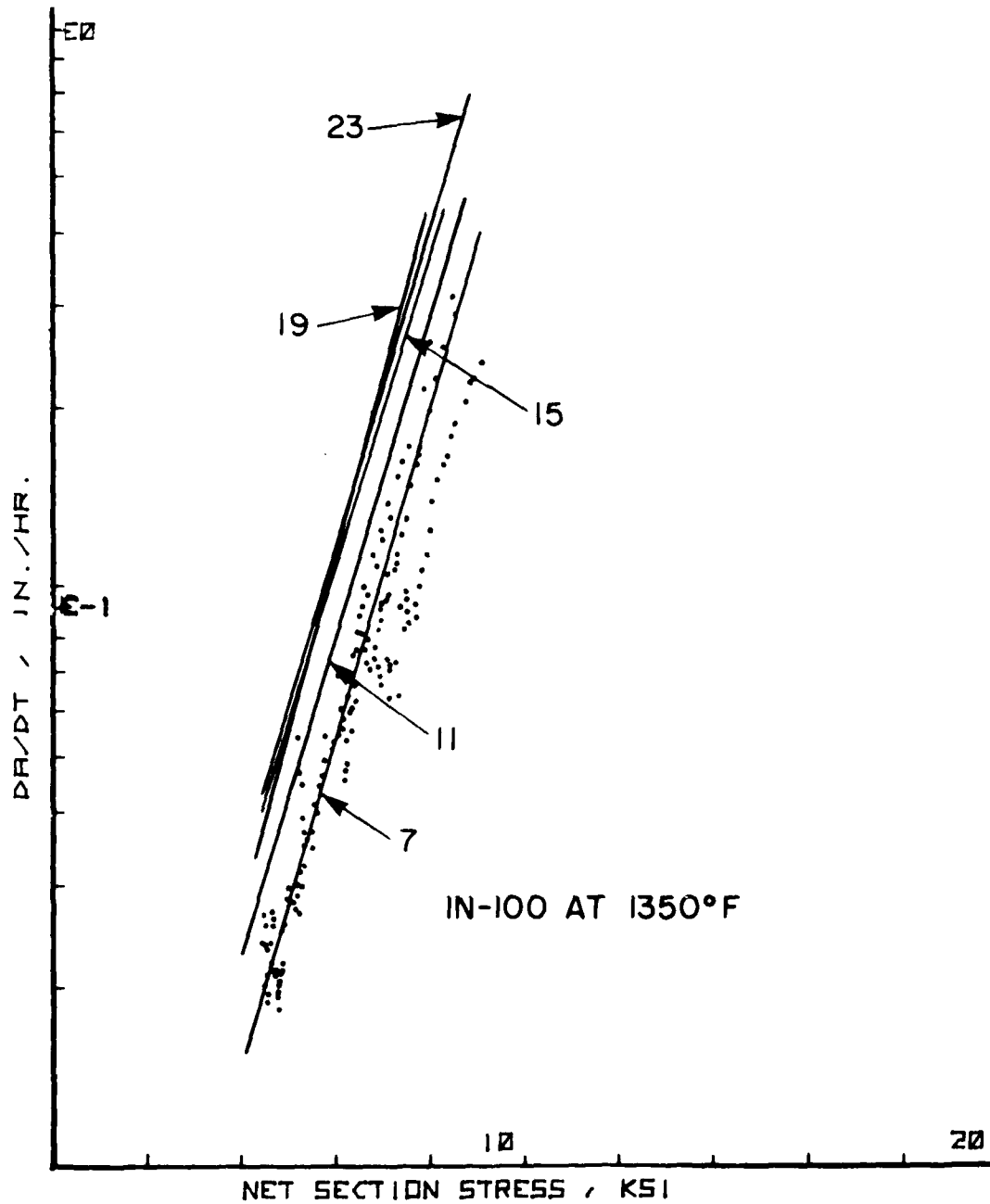
Figure 121. da/dt vs. σ_{net} Composite Plot for Five Thicknesses - CT Specimens Showing 7/32" (6 mm) Data Points
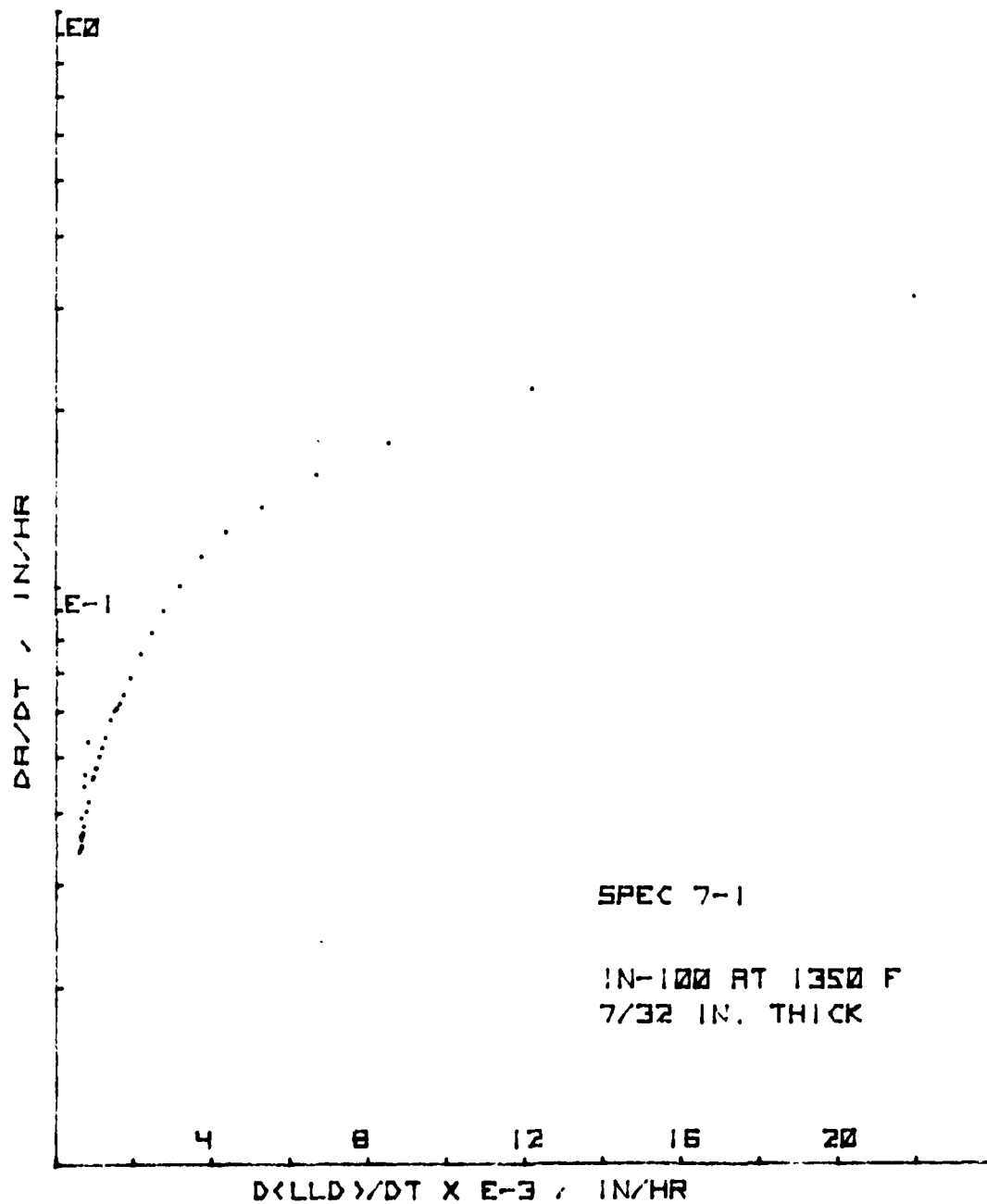
Figure 122.   da/dt vs. LLD rate for CT Specimen 7-1

194
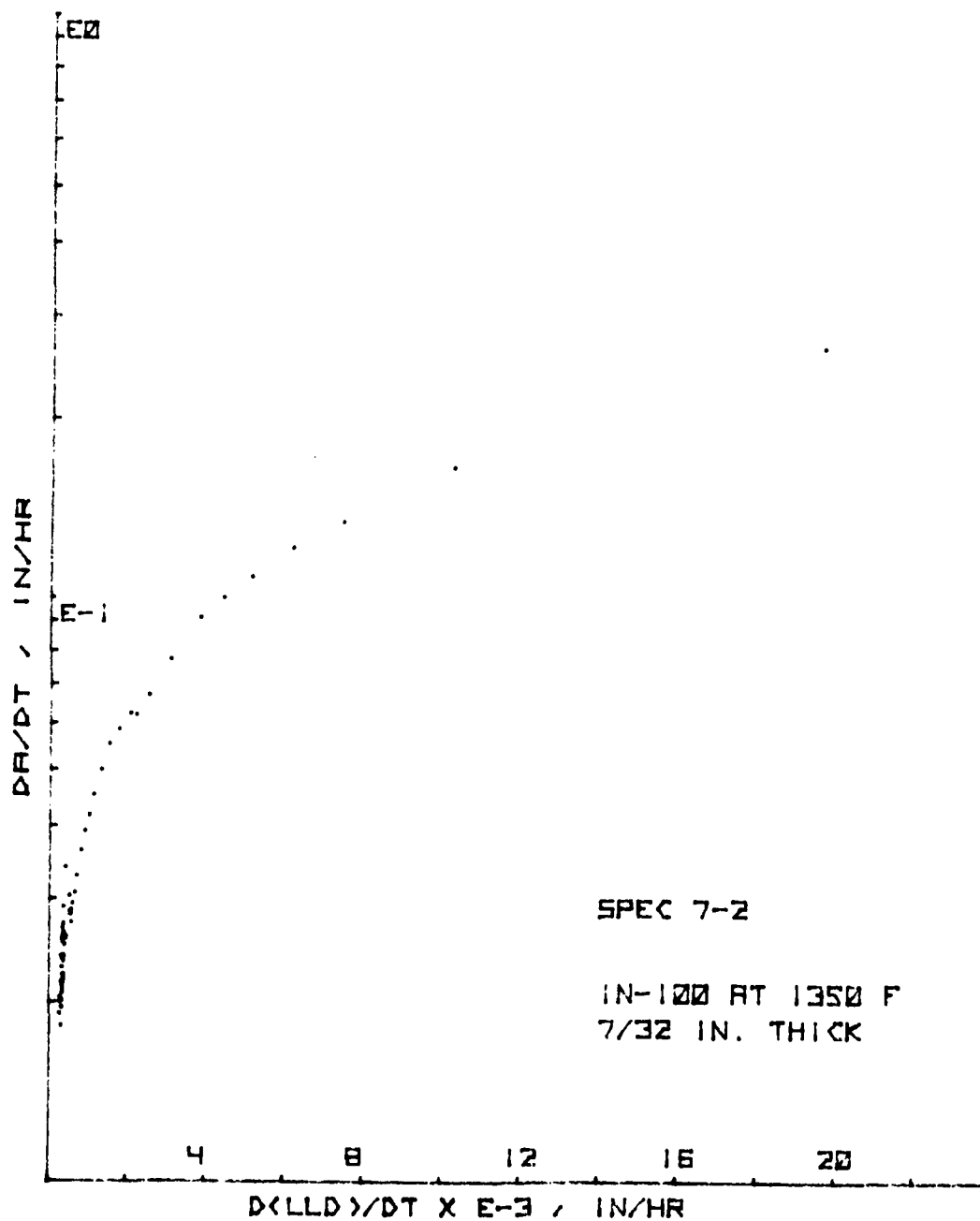
Figure 123.   da/dt vs. LLD Rate for CT Specimen 7-2
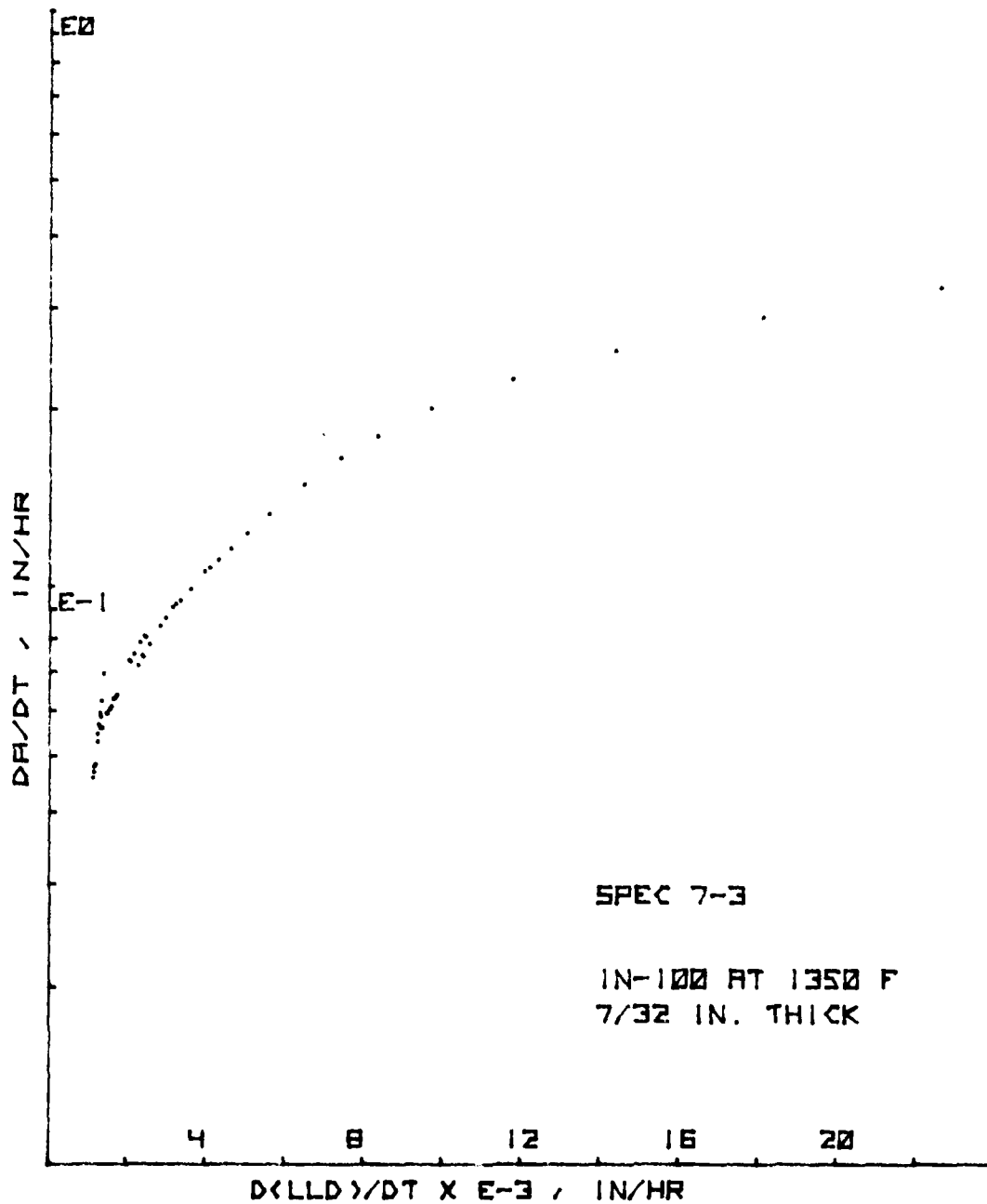
Figure 124. da/dt vs. LLD Rate for CT Specimen 7-3
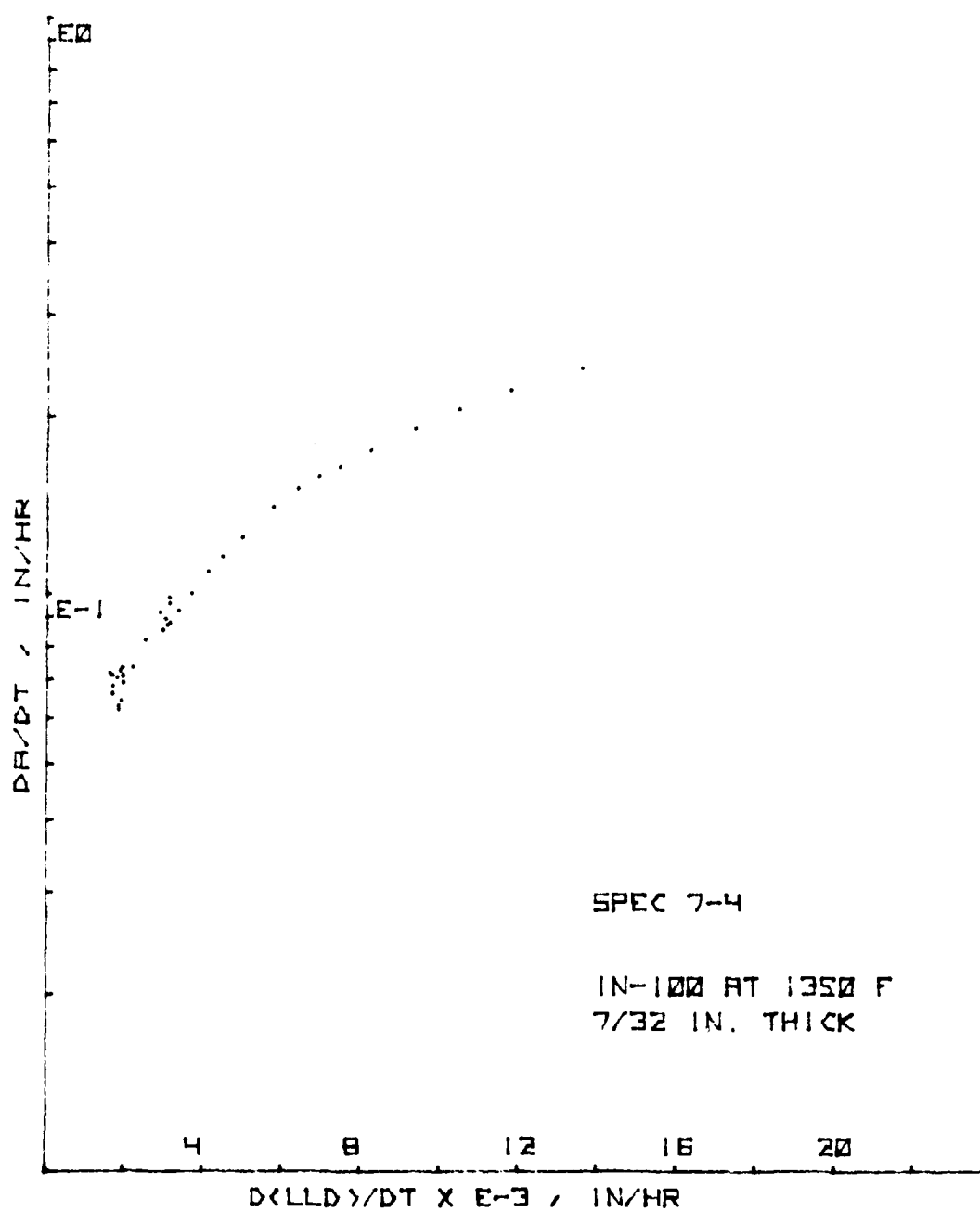
Figure 125. da/dt vs. LLD Rate for CT Specimen 7-4
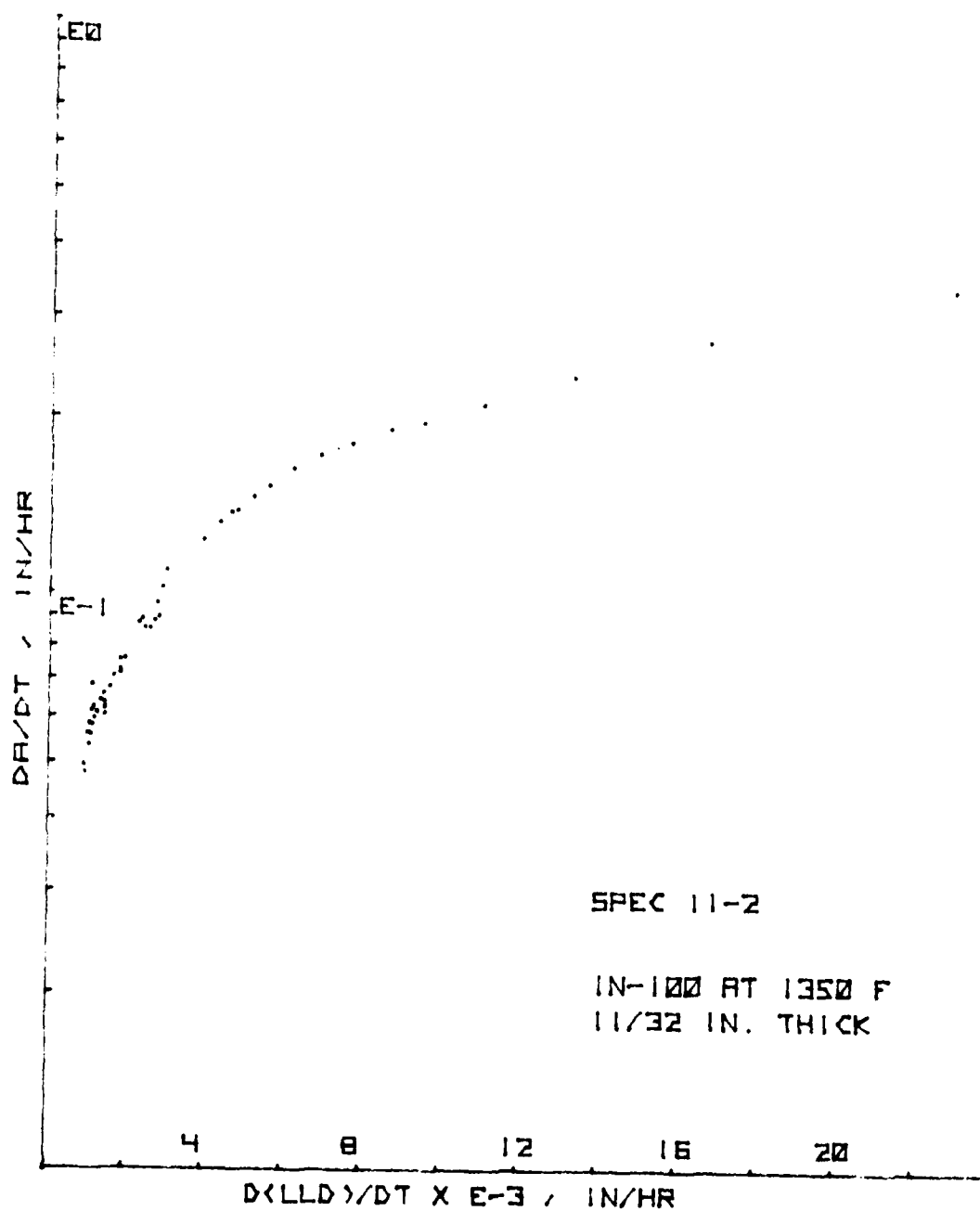
Figure 126. da/dt vs. LLD Rate for CT Specimen 11-2
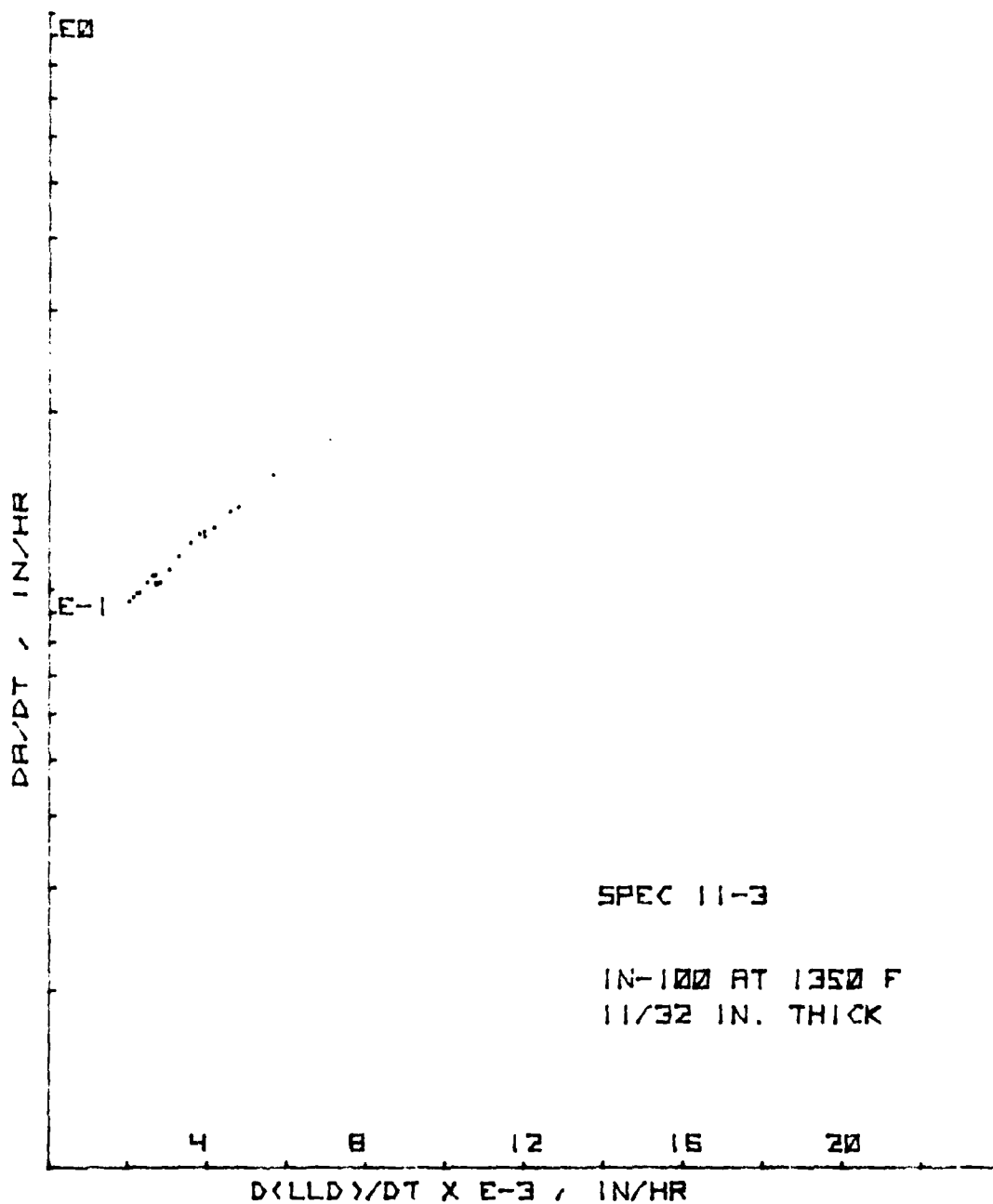
Figure 127. da/dt vs. LLD Rate for CT Specimen 11-3
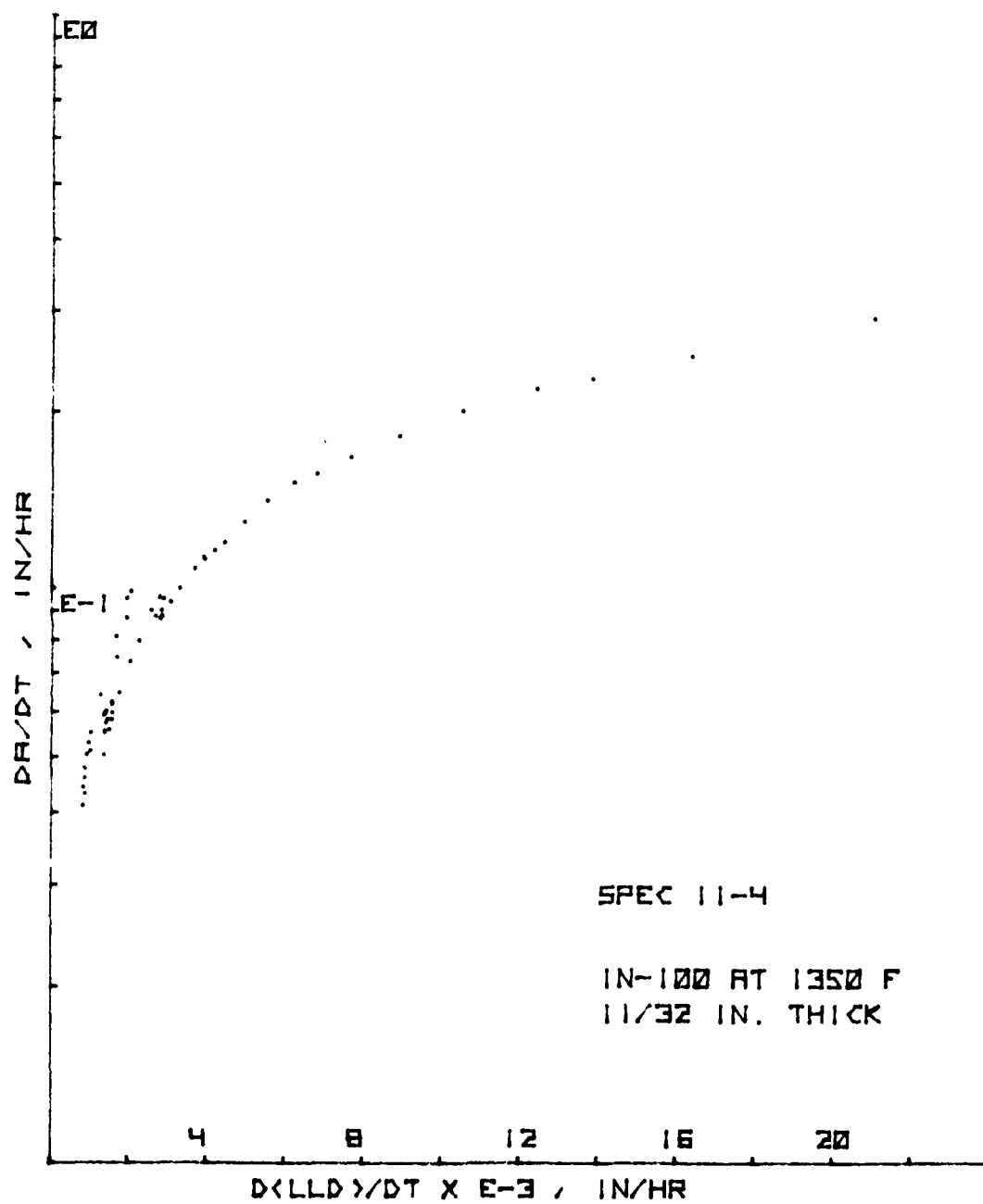
Figure 128.   da/dt vs. LLD Rate for CT Specimen 11-4
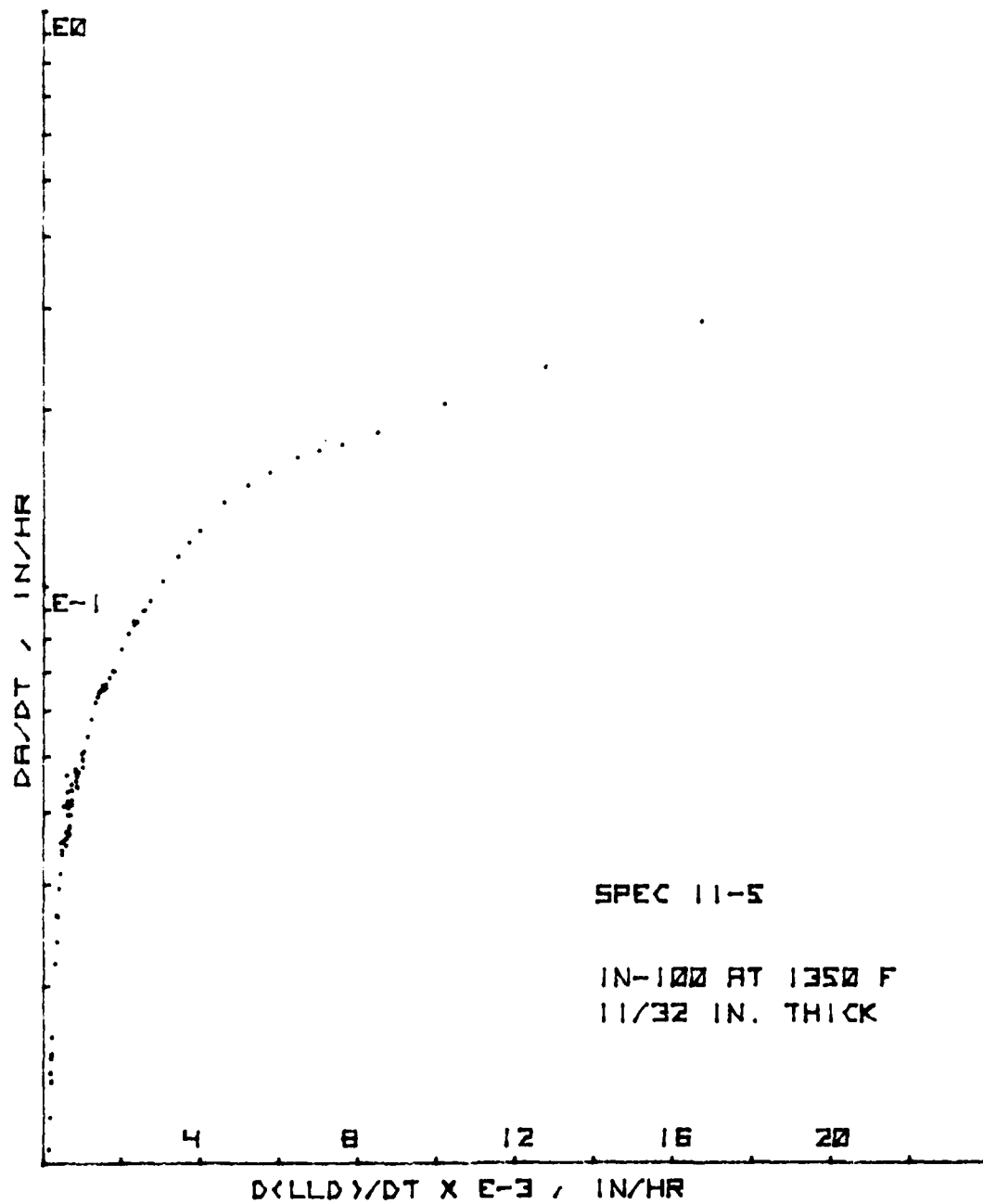
Figure 129. da/dt vs. LLD Rate for CT Specimen 11-5
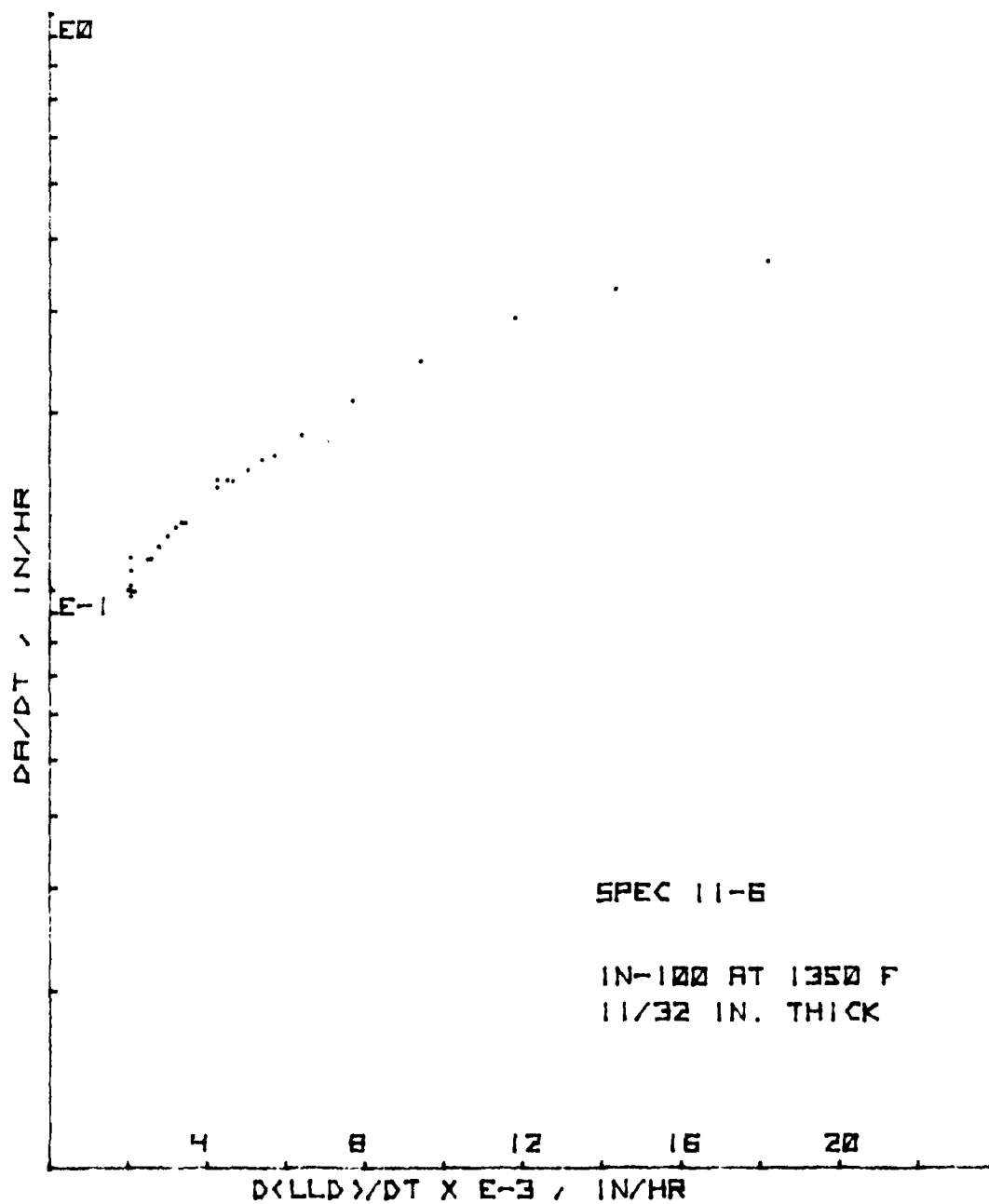
Figure 130.   da/dt vs. LLD Rate for CT Specimen 11-6
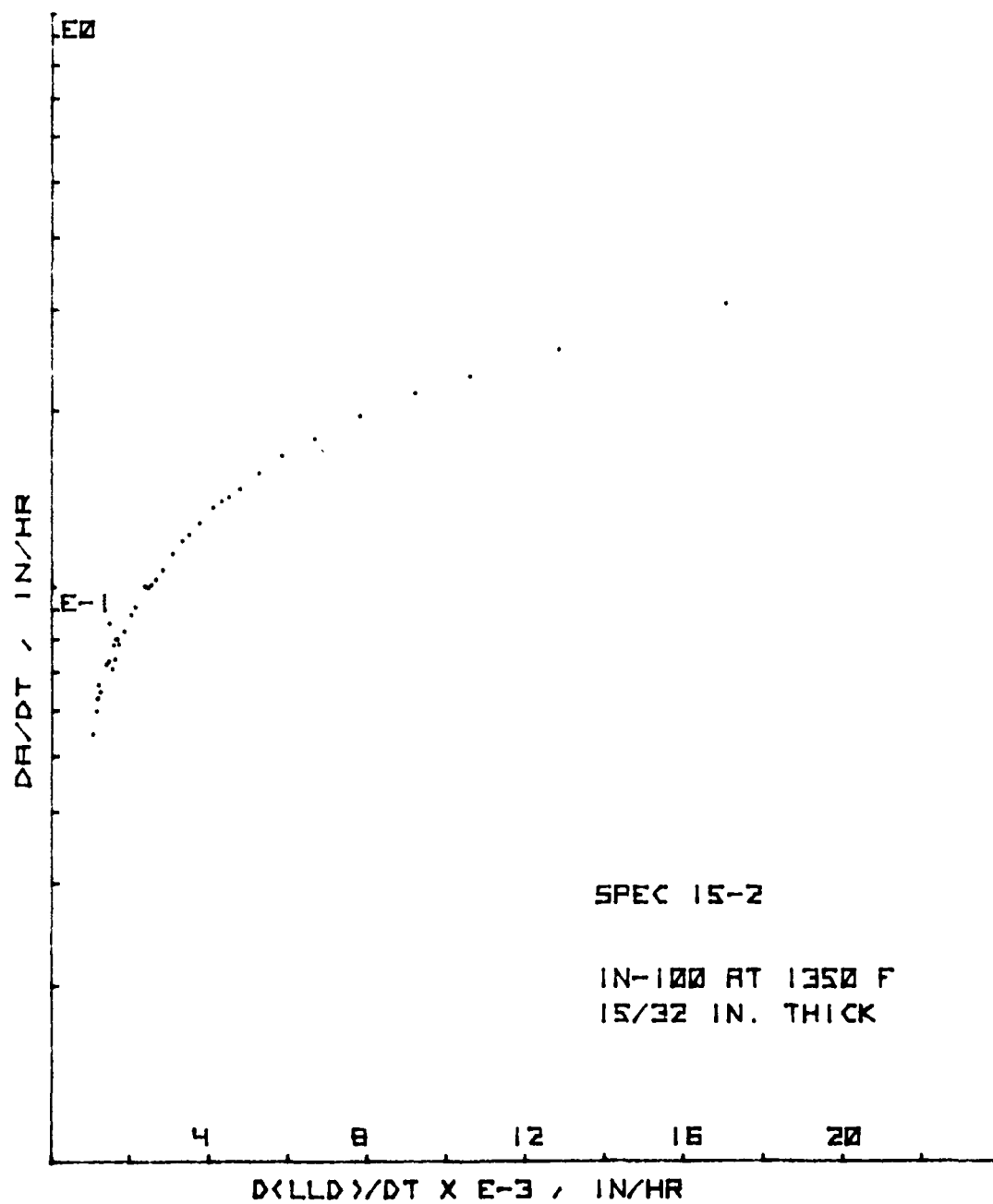
Figure 131. da/dt vs. LLD Rate for CT Specimen 15-2
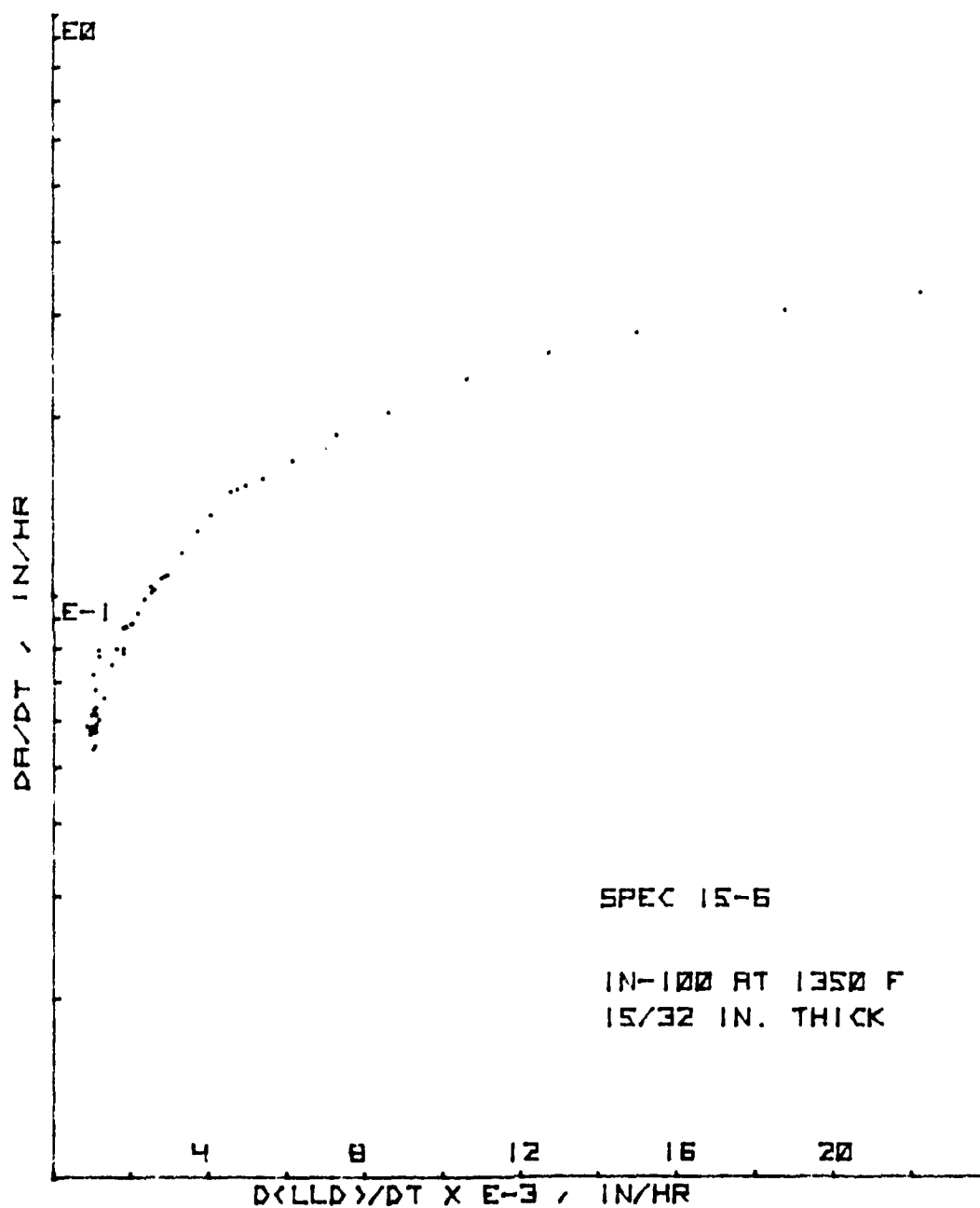
Figure 132. da/dt vs. LLD Rate for CT Specimen 15-6
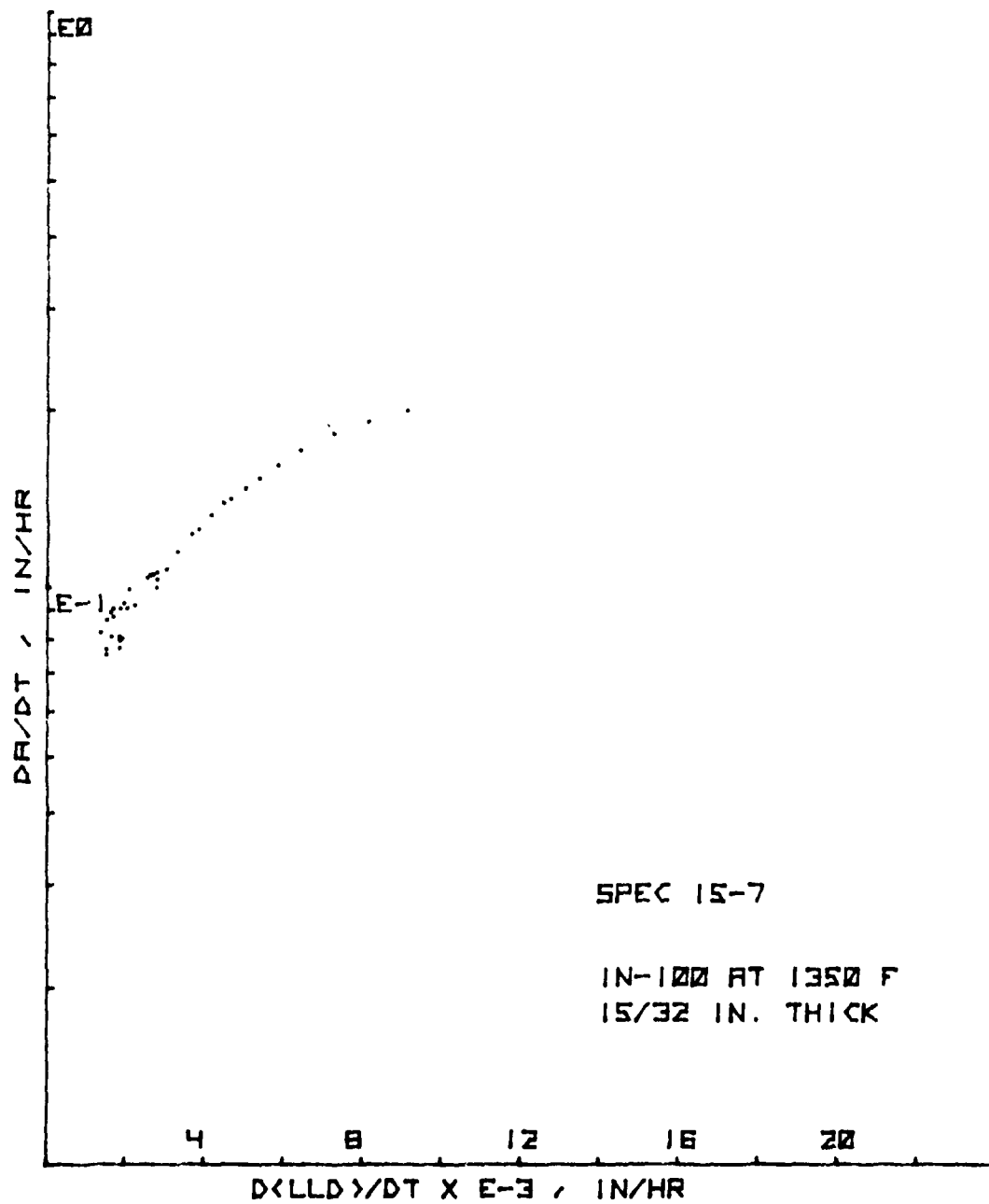
Figure 133. da/dt vs. LLD Rate for CT Specimen 15-7
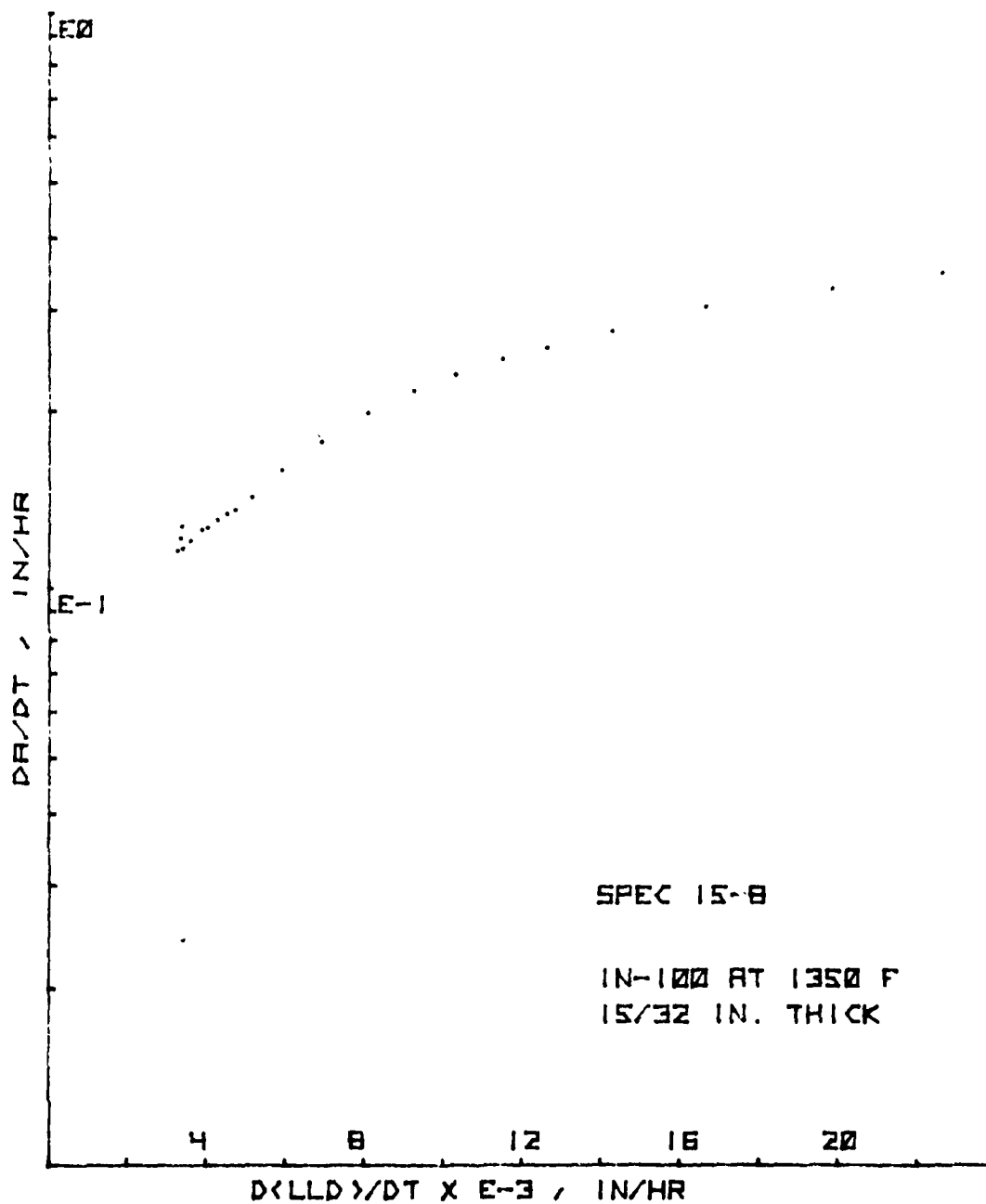
Figure 134. da/dt vs. LLD Rate for CT Specimen 15-8
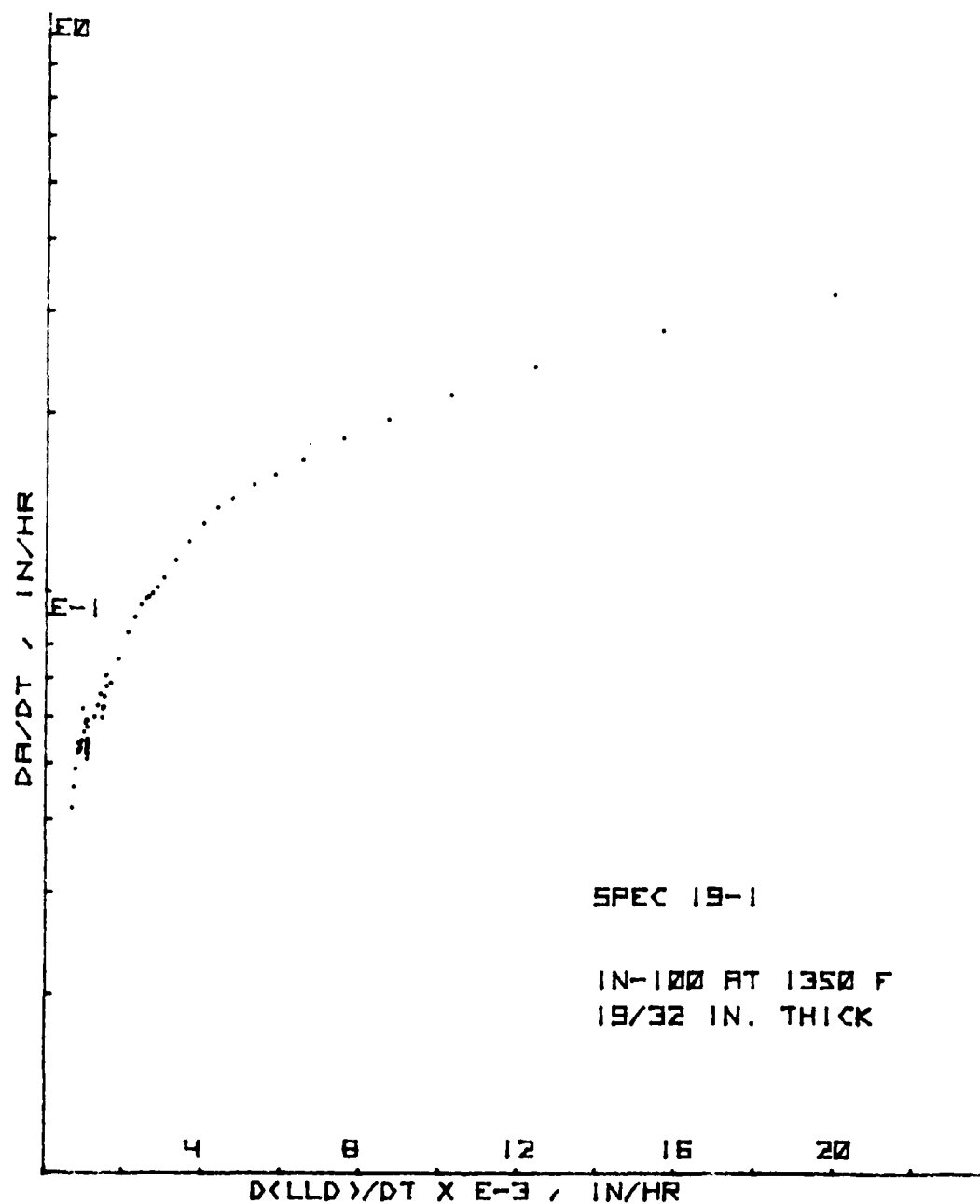
Figure 135. da/dt vs. LLD Rate for CT Specimen 19-1

E0

DA/DT , IN/HR

E-4

SPEC 19-2

IN-100 AT 1350 F
19/32 IN. THICK

4   8   12   16   20

D(LLD)/DT X E-3 , IN/HR
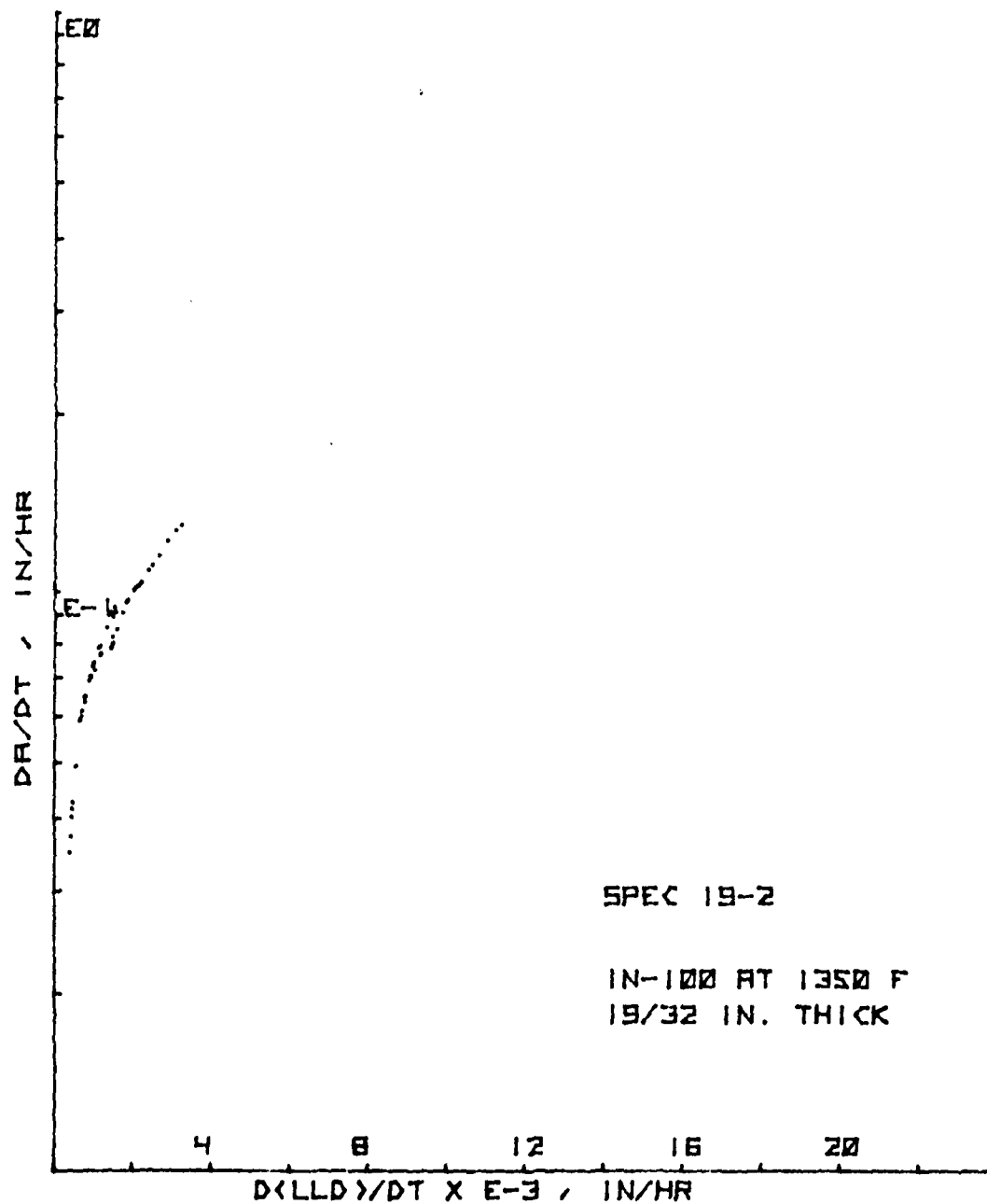
Figure 136. da/dt vs. LLD Rate for CT Specimen 19-2
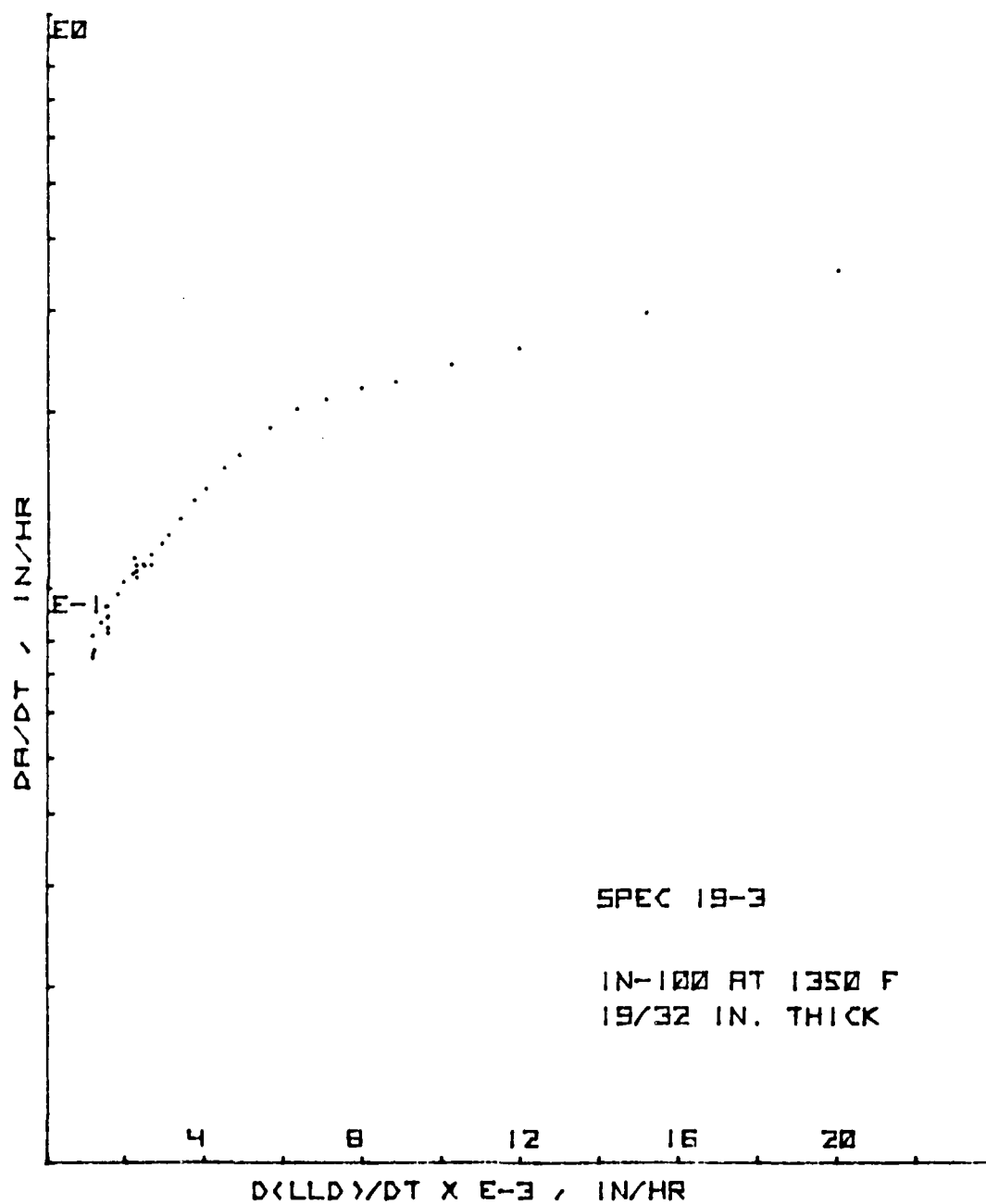
Figure 137. da/dt vs. LLD Rate for CT Specimen 19-3
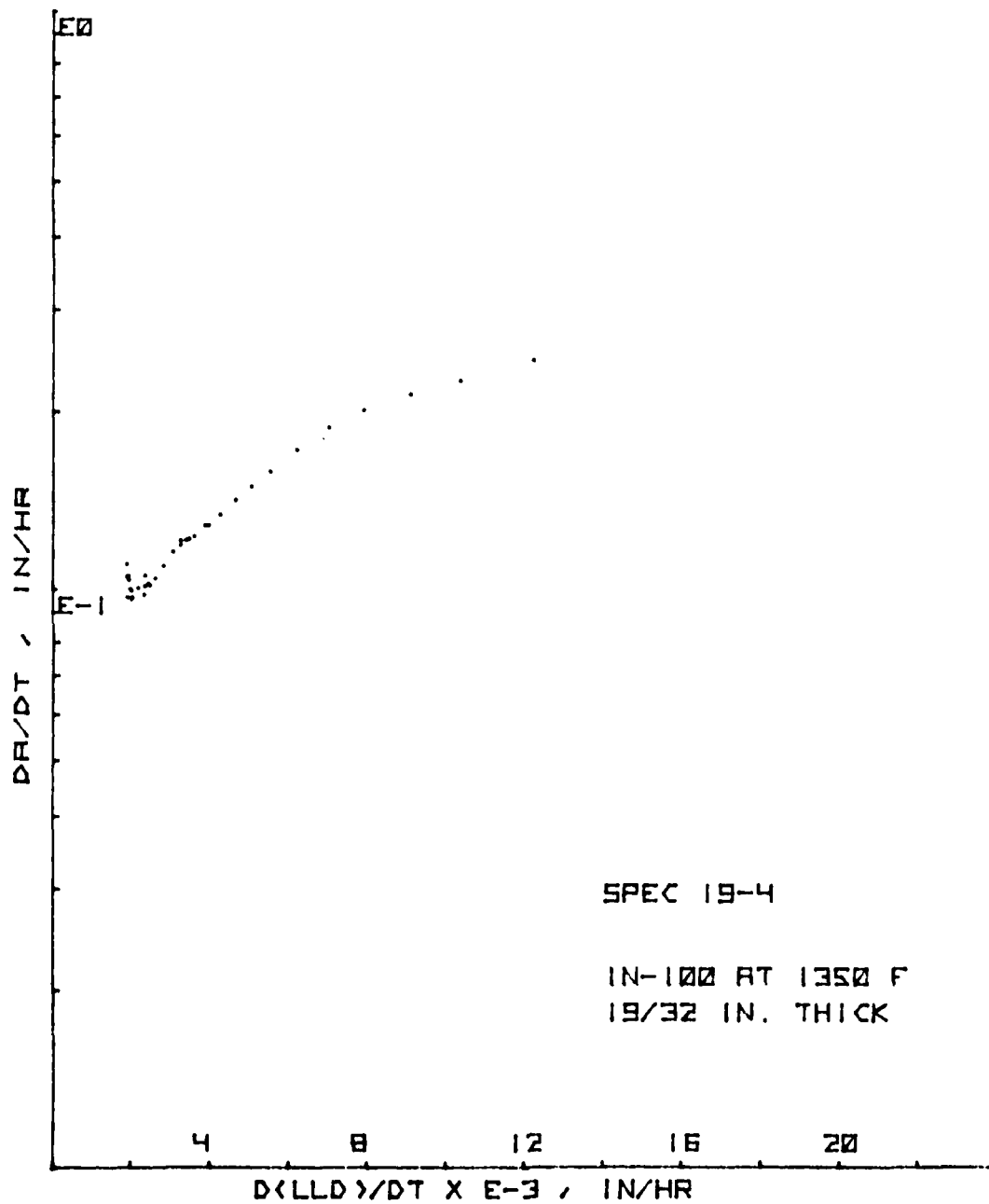
Figure 138. da/dt vs. LLD Rate for CT Specimen 19-4
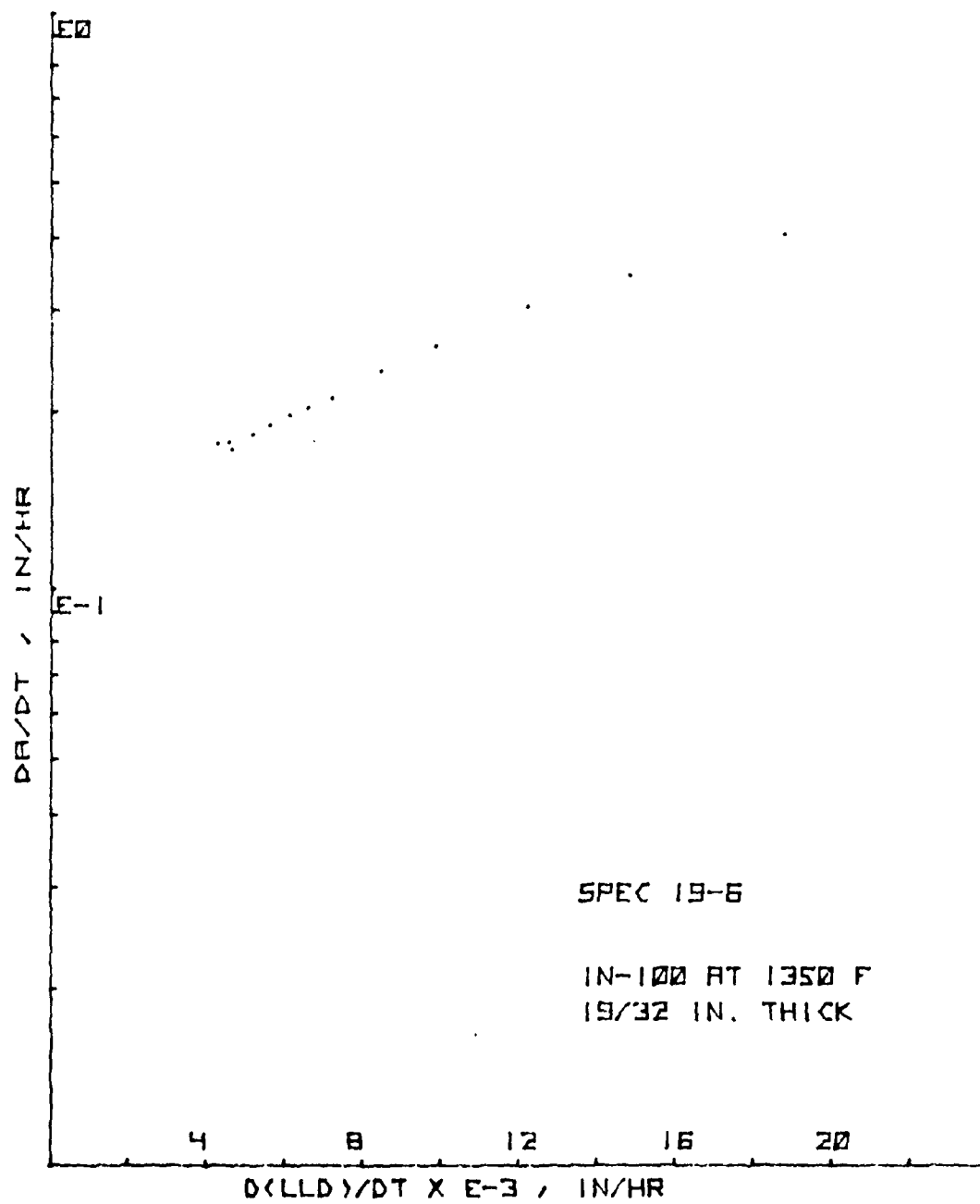
Figure 139. da/dt vs. LLD Rate for CT Specimen 19-6
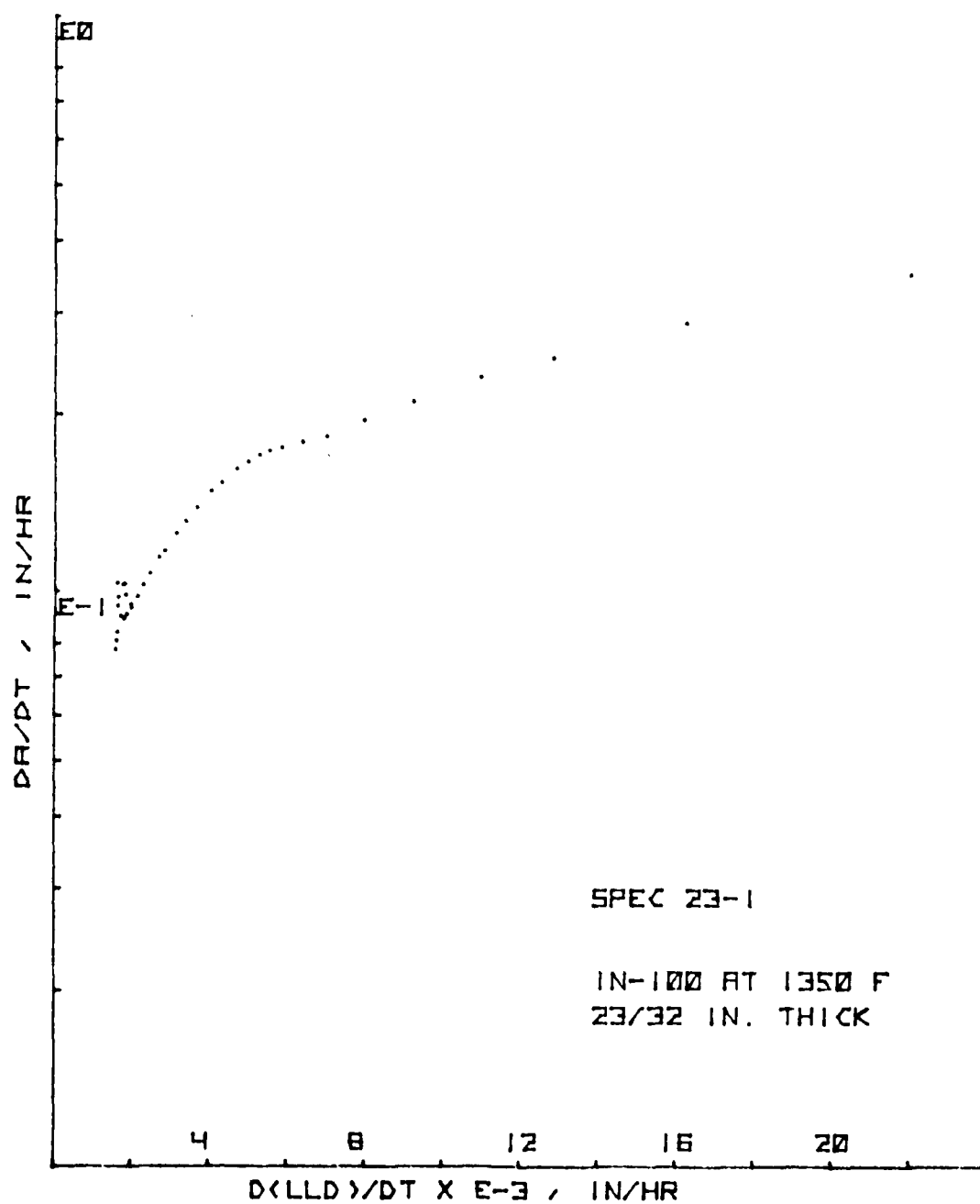
Figure 140. da/dt vs. LLD Rate for CT Specimen 23-1
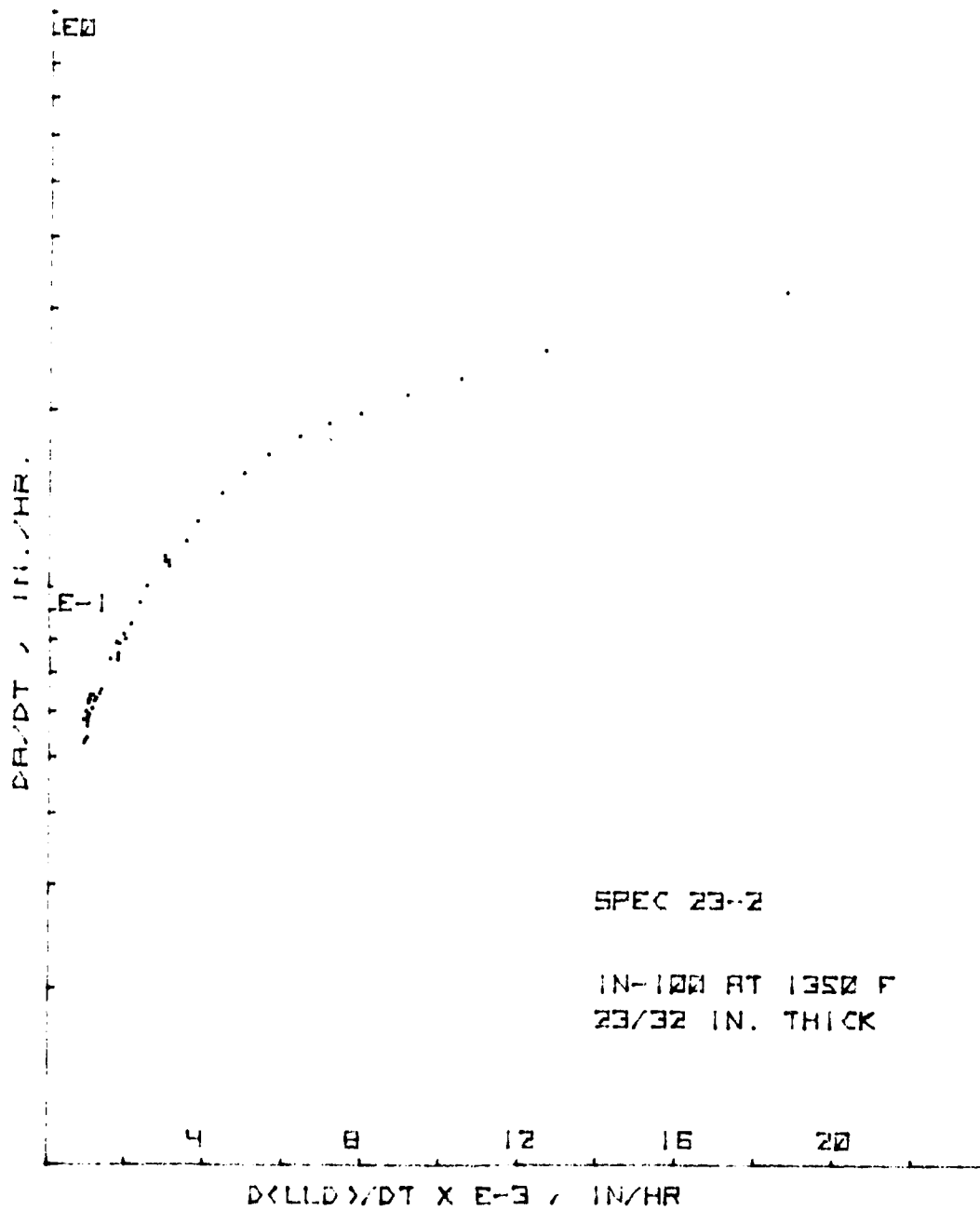
Figure 141. da/dt vs. LLD Rate for CT Specimen 23-2
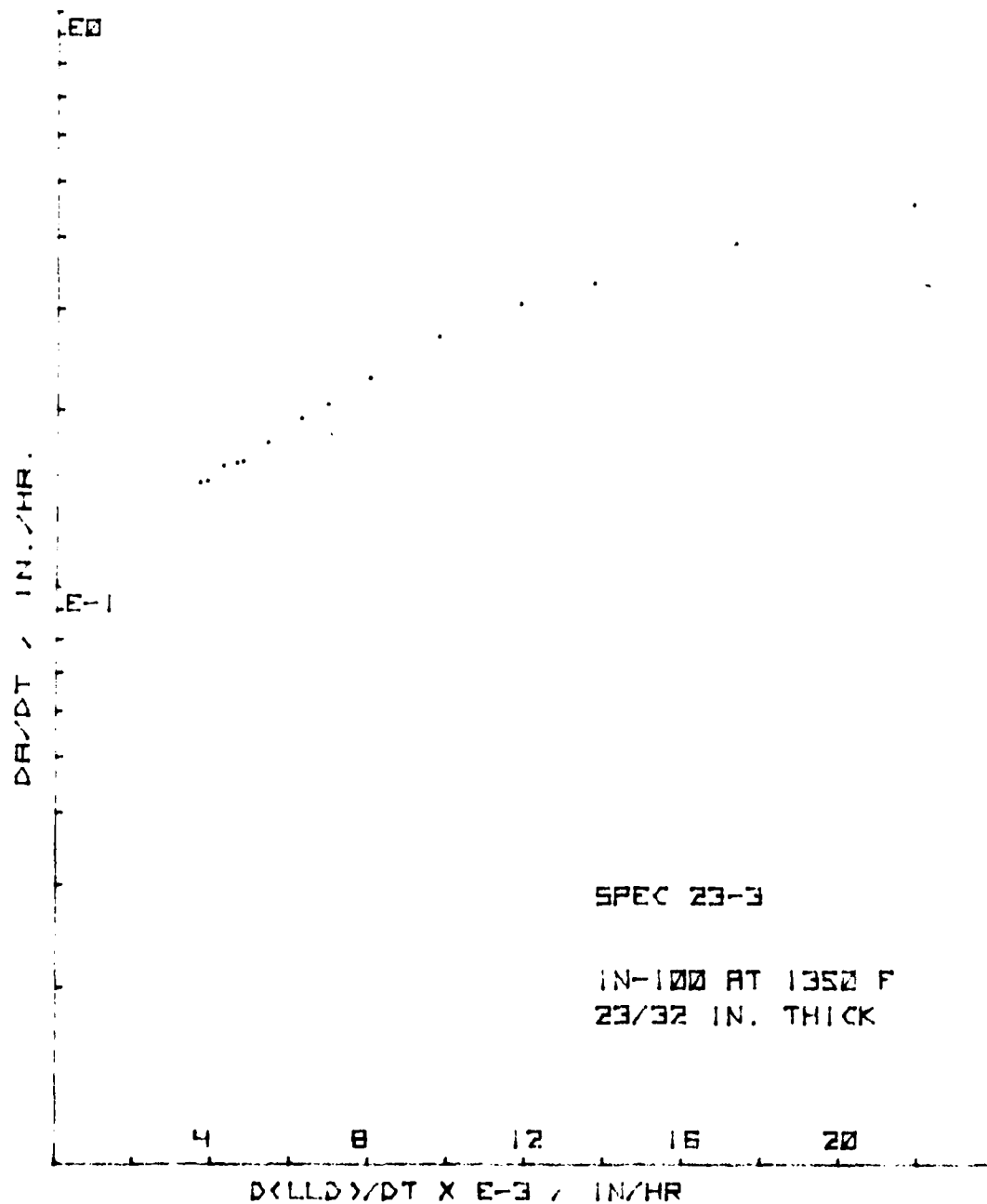
Figure 142. da/dt vs. LLD Rate for CT Specimen 23-3
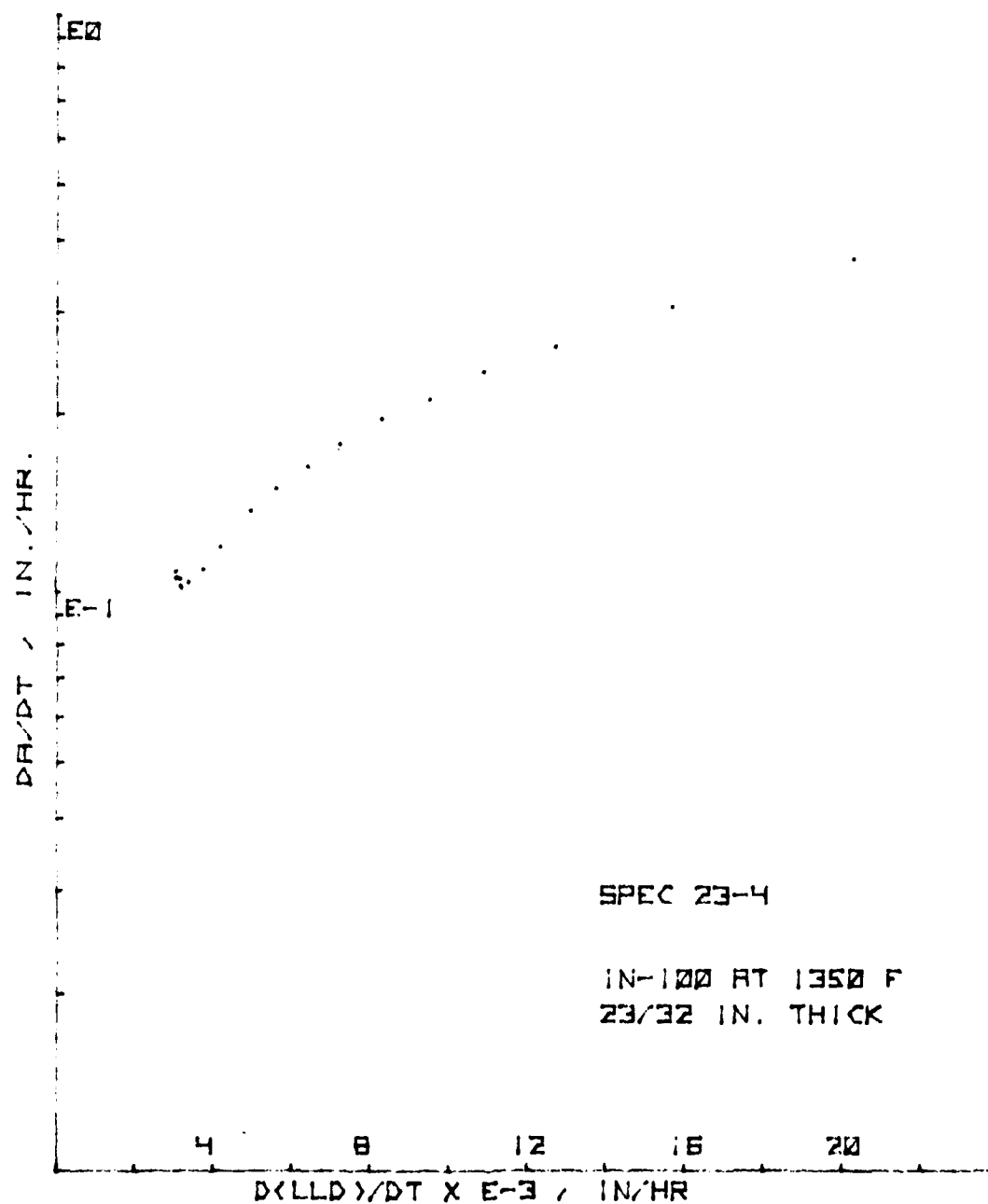
Figure 143. da/dt vs. LLD Rate for CT Specimen 23-4
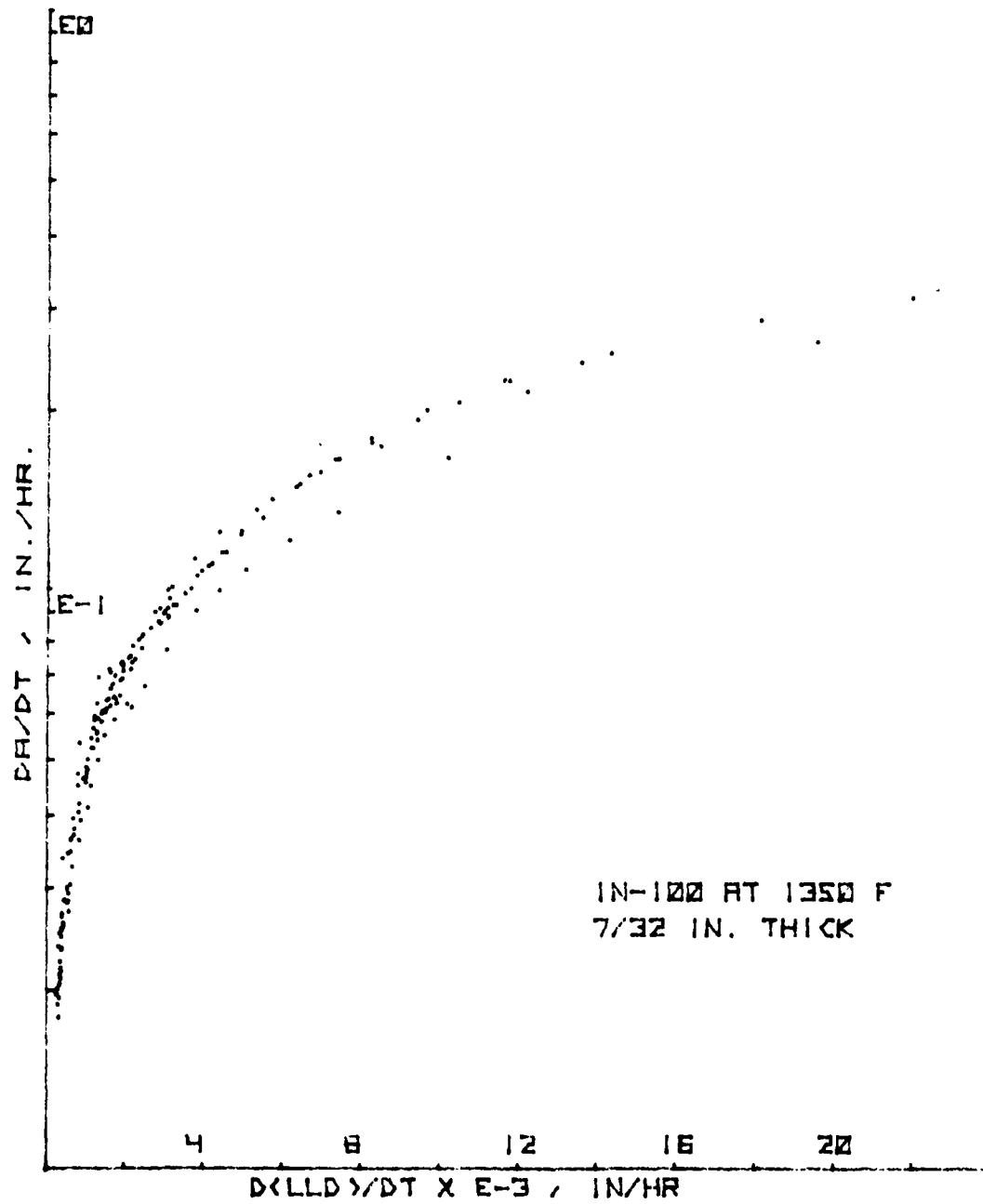
Figure 144. da/dt vs. LLD Rate - 7/32" (6 mm) Thick CT Specimen
Group

216
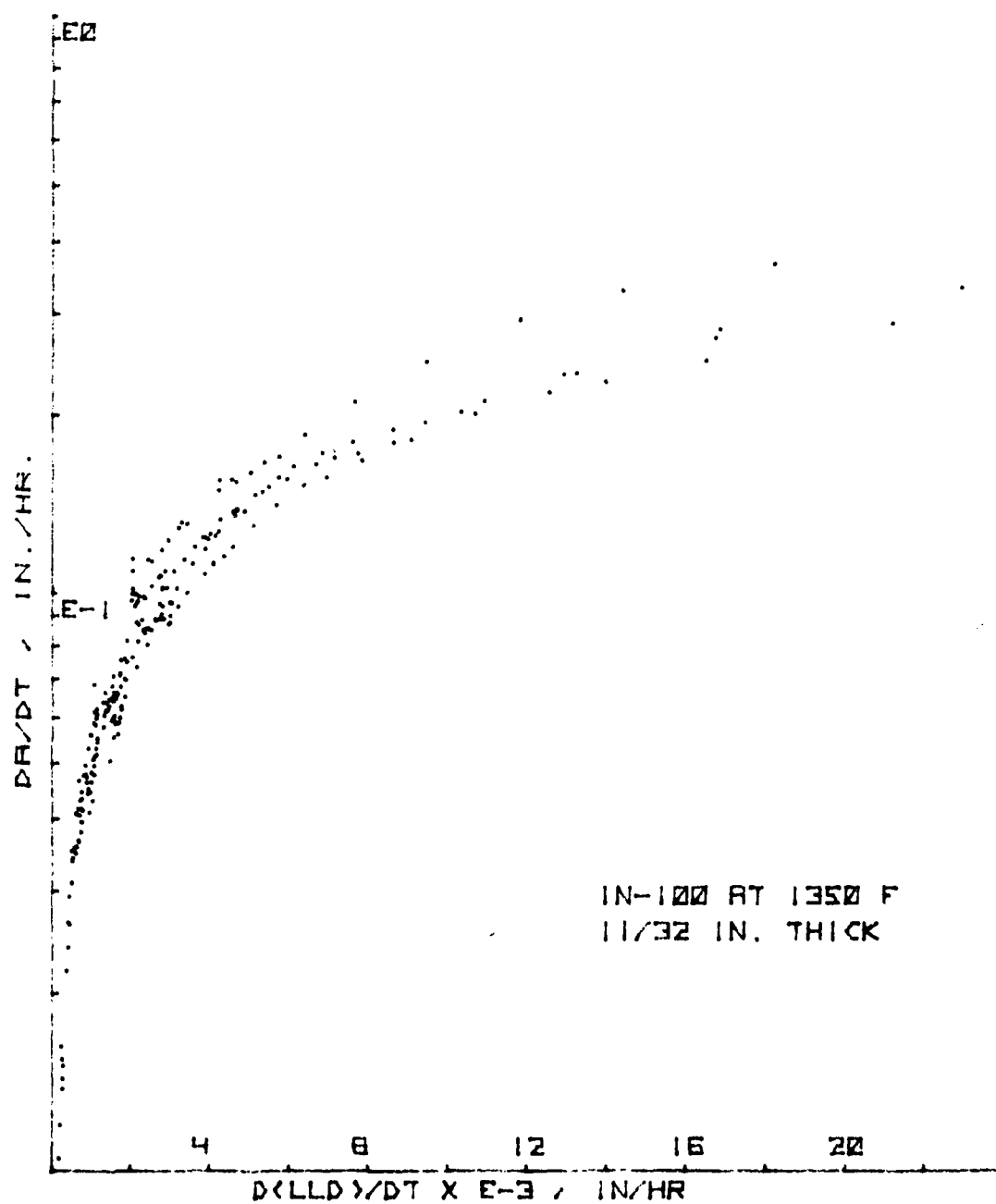
Figure 145. da/dt vs. LLD Rate - 11/32" (9 mm) Thick CT
Specimen Group
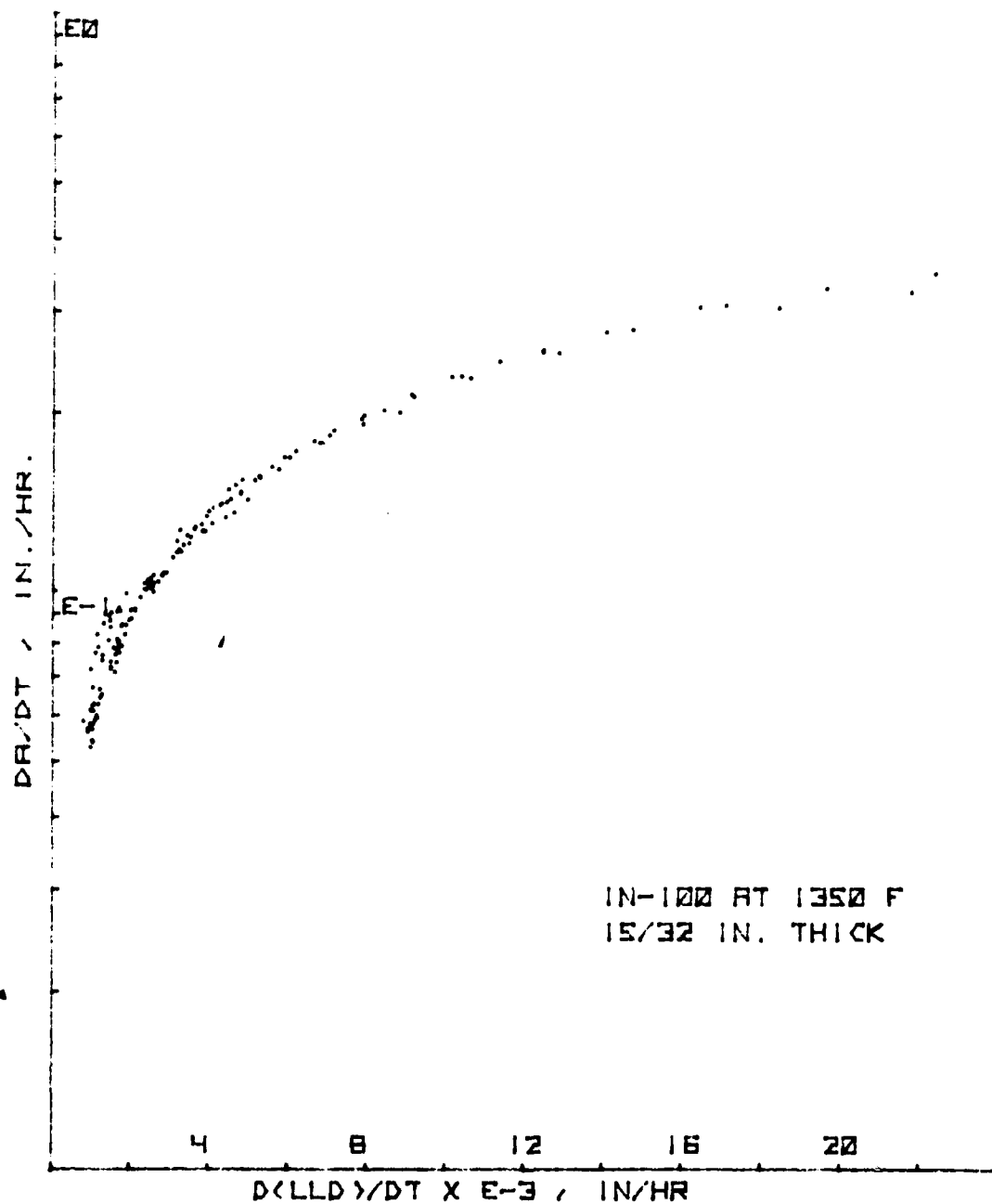
Figure 146. da/dt vs. LLD Rate - 15/32" (12 mm) Thick CT
Specimen Group
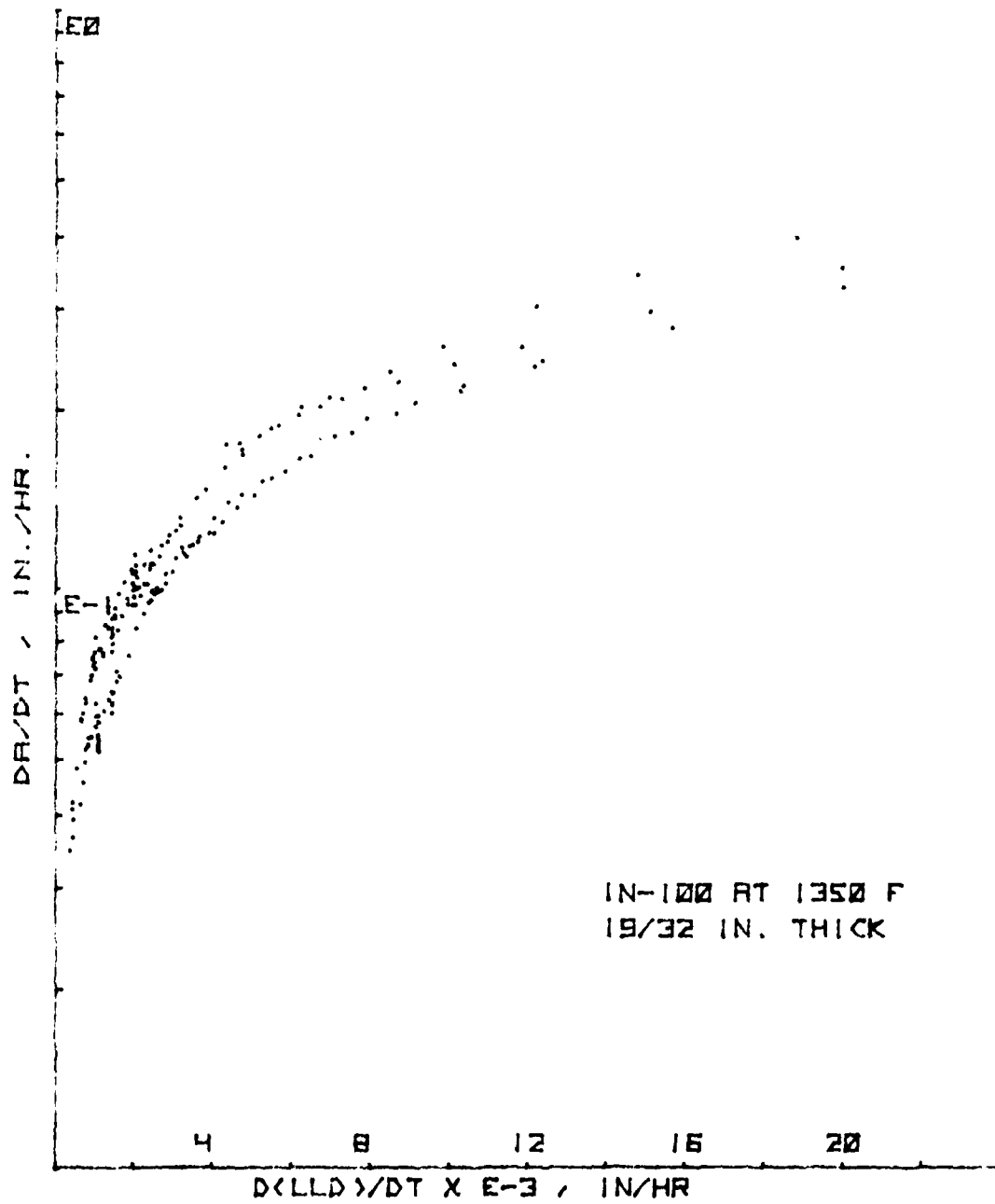
Figure 147. da/dt vs. LLD Rate - 19/32" (15 mm) Thick CT
Specimen Group
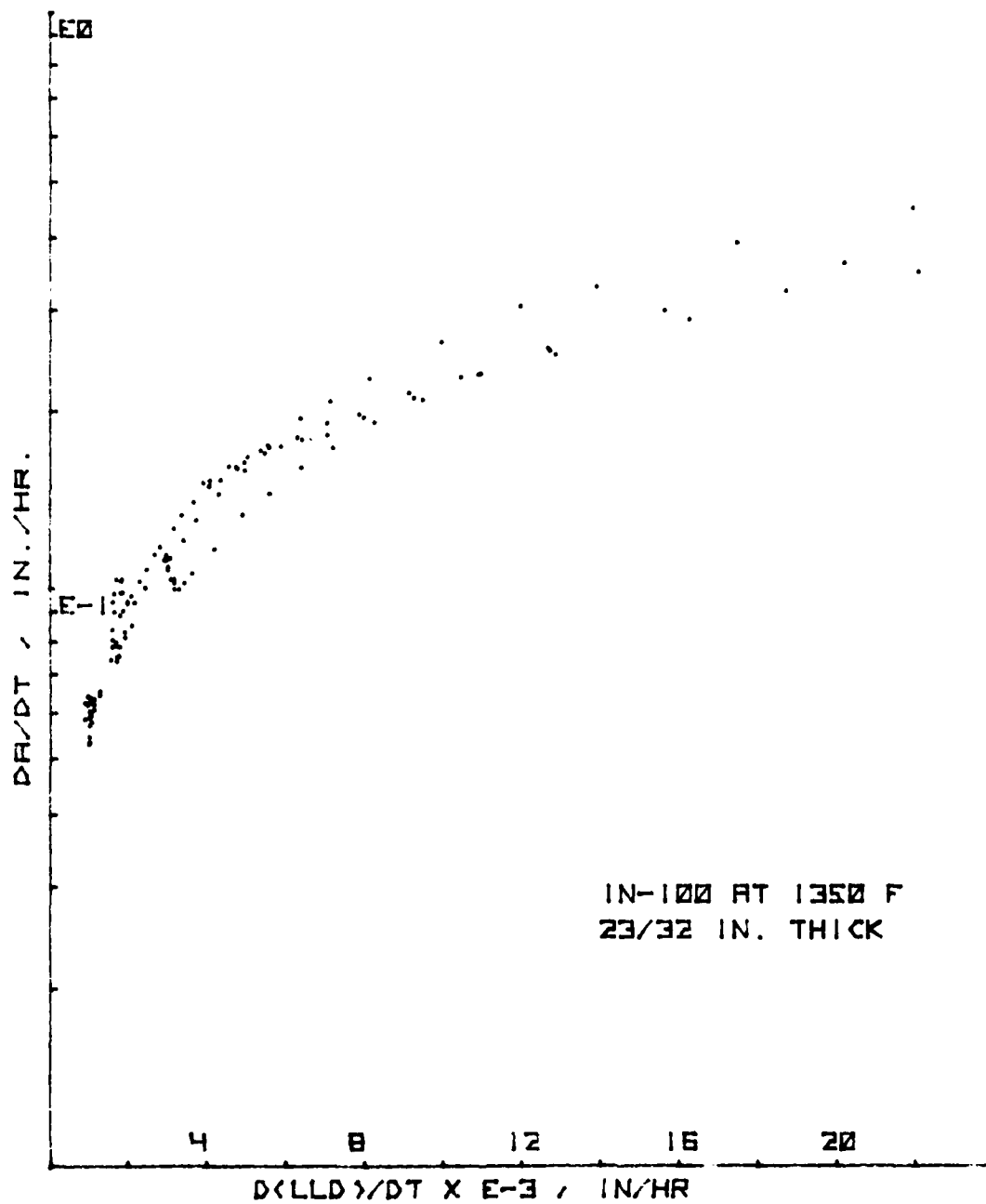
Figure 148. da/dt vs. LLD Rate - 23/32" (18 mm) Thick CT
Specimen Group
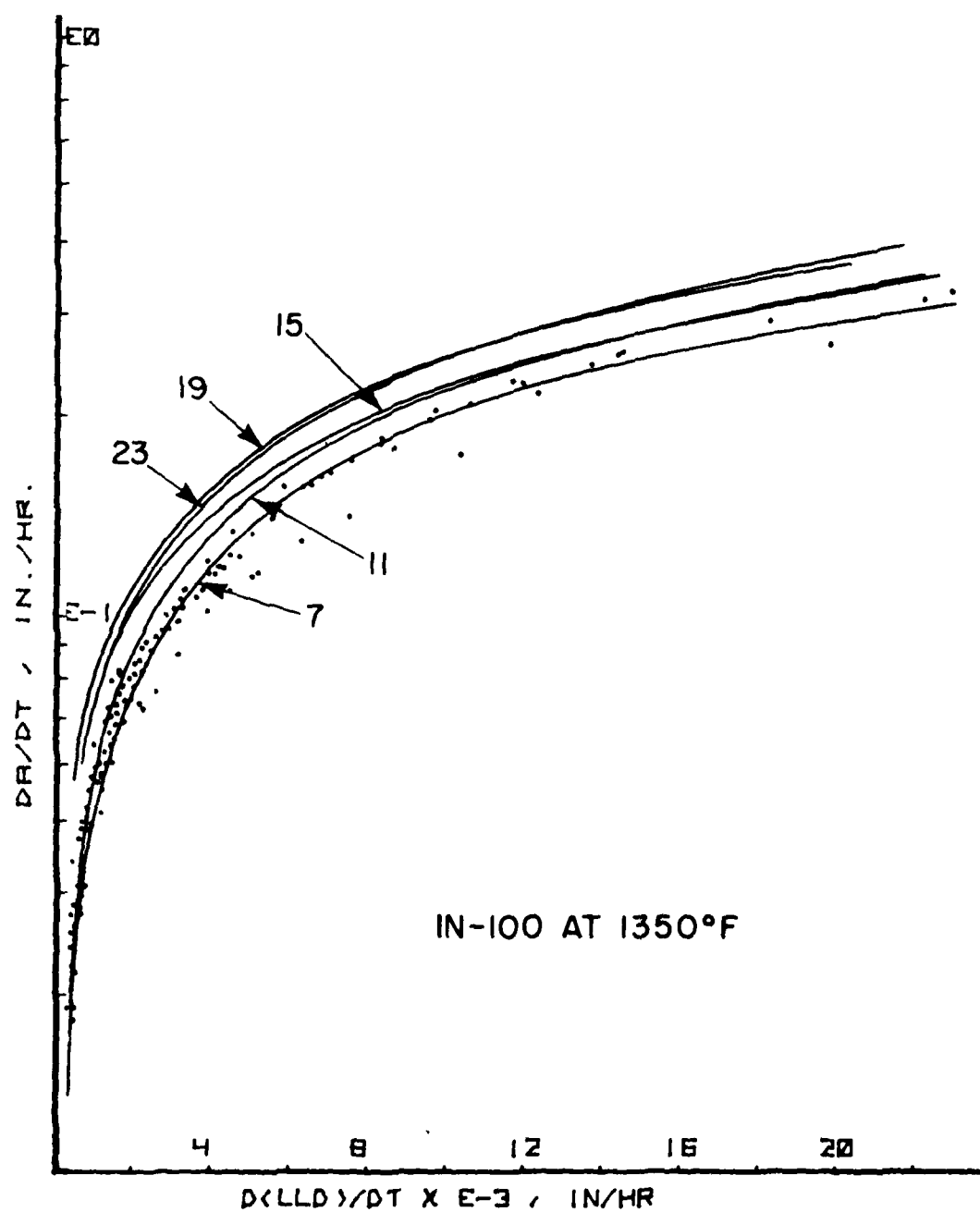
Figure 149. da/dt vs. LLD Rate Composite Plot for Five
Thicknesses - CT Specimens
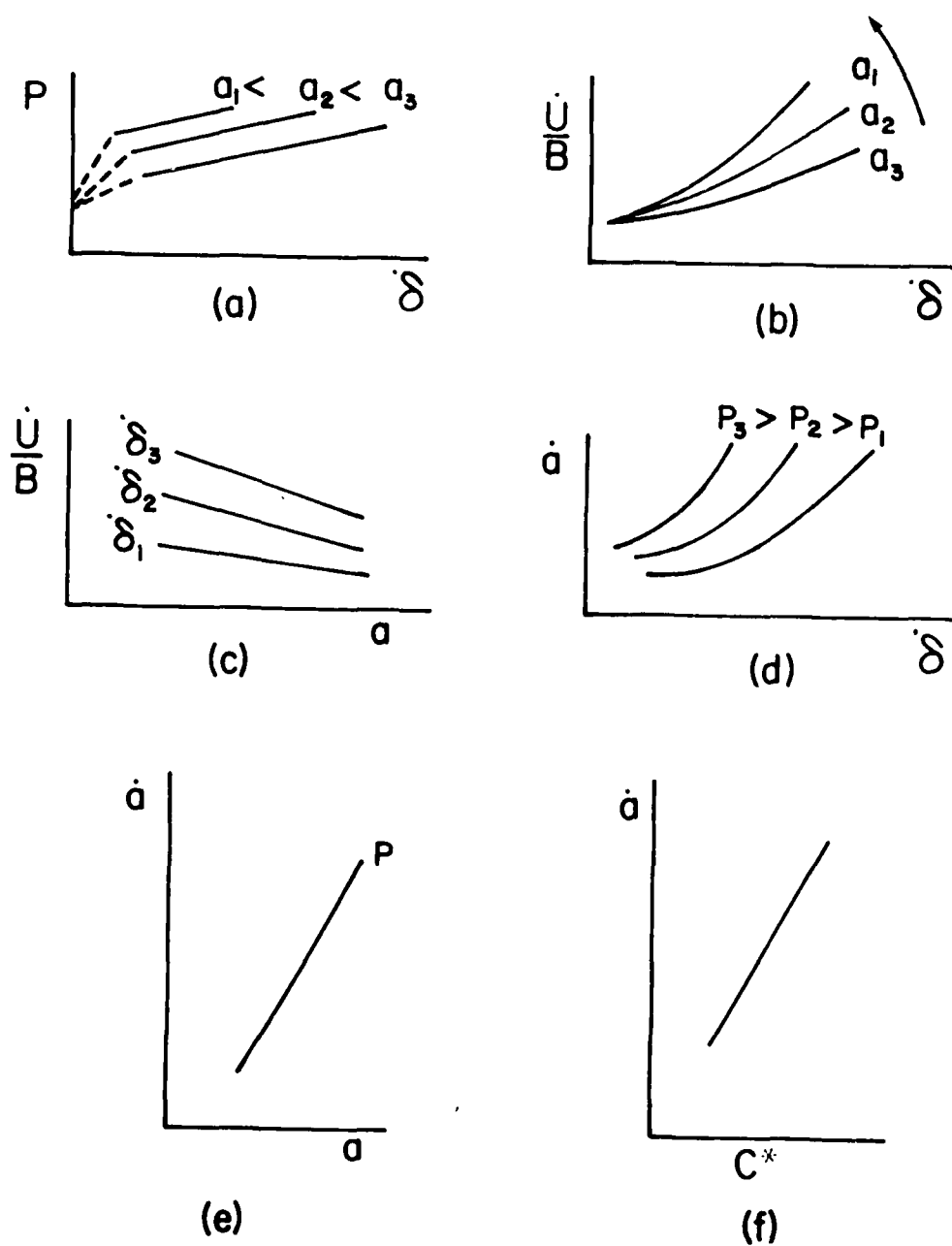
Figure 150.   A Data Reduction Scheme for C*
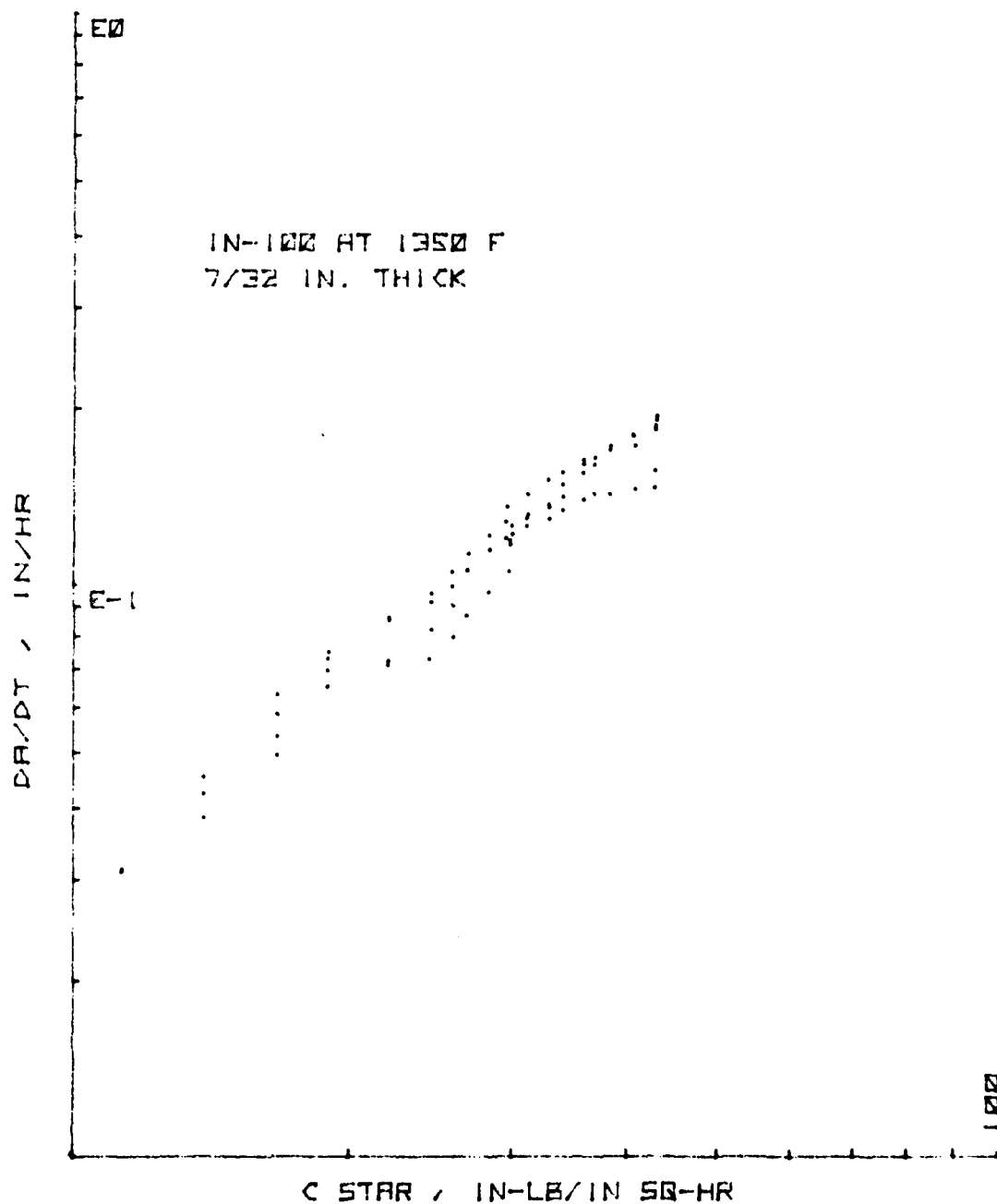
Figure 151. da/dt vs. C* Plot of the 7/32" (6 mm) Thick CT
Reduced Data
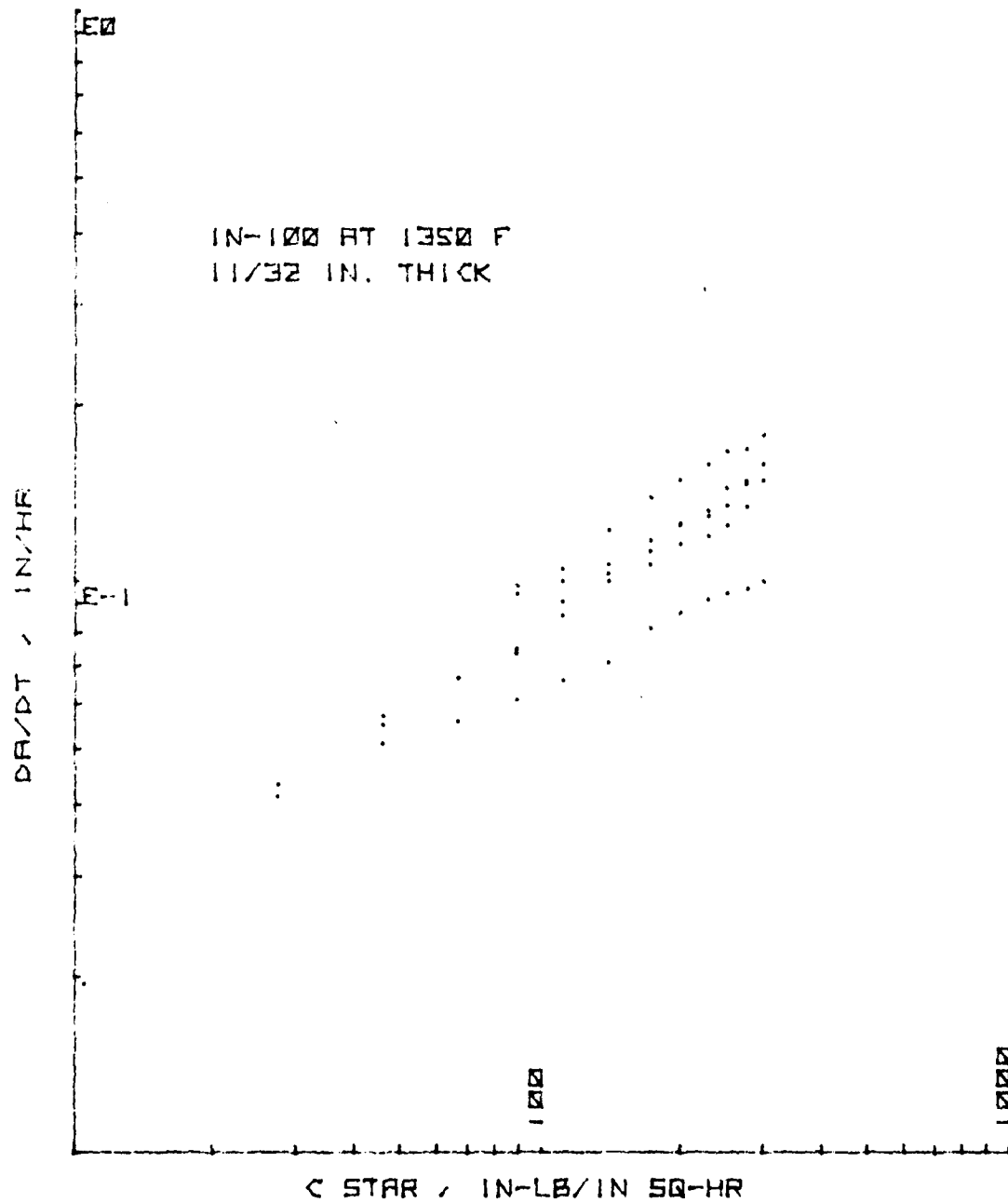
Figure 152. da/dt vs. C* Plot of the 11/32" (9 mm) Thick CT
Reduced Data
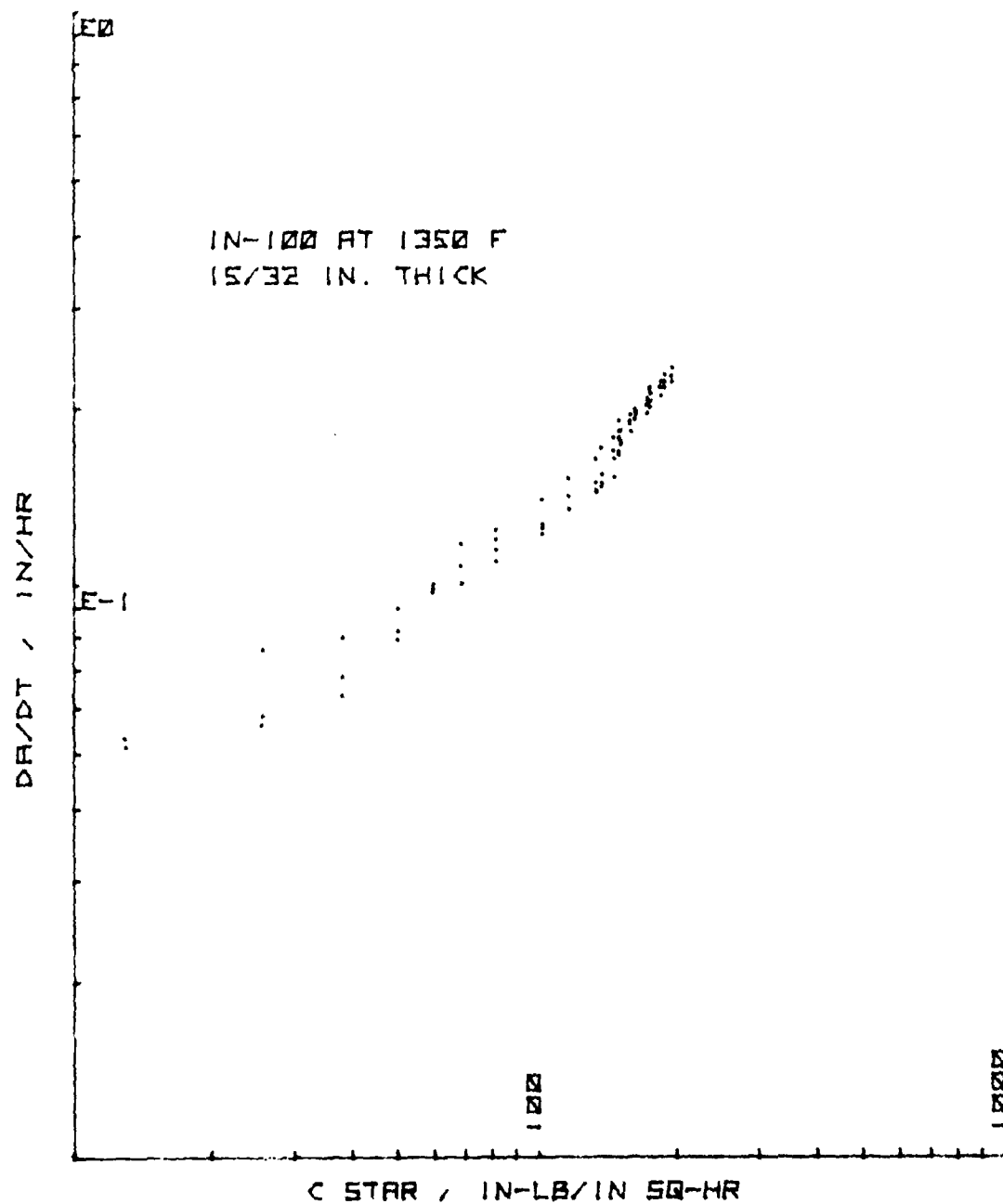
Figure 153.   da/dt vs. C* Plot of the 15/32" (12 mm) Thick CT
Reduced Data
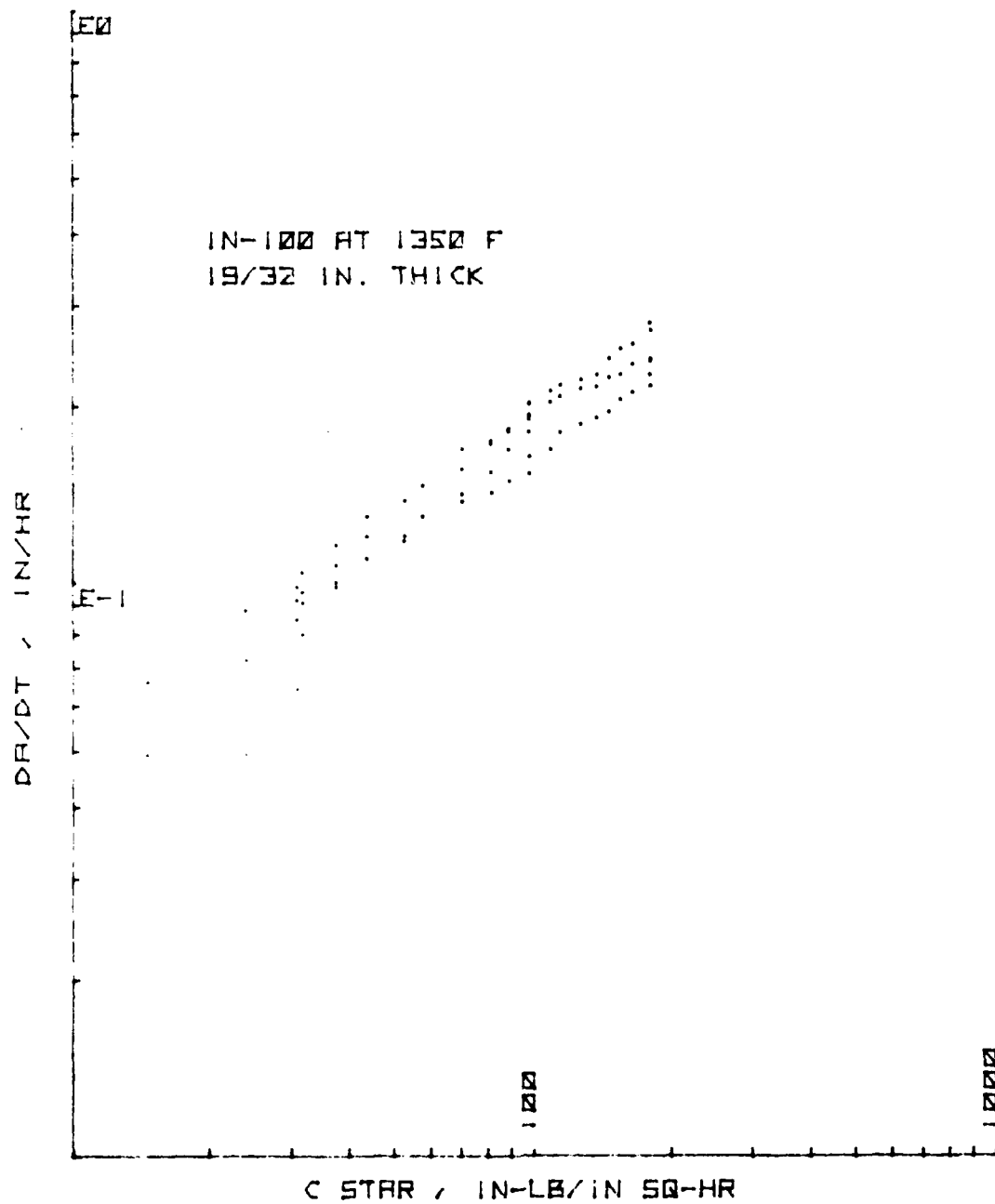
Figure 154. da/dt vs. C* Plot of the 19/32" (15 mm) Thick CT
Reduced Data
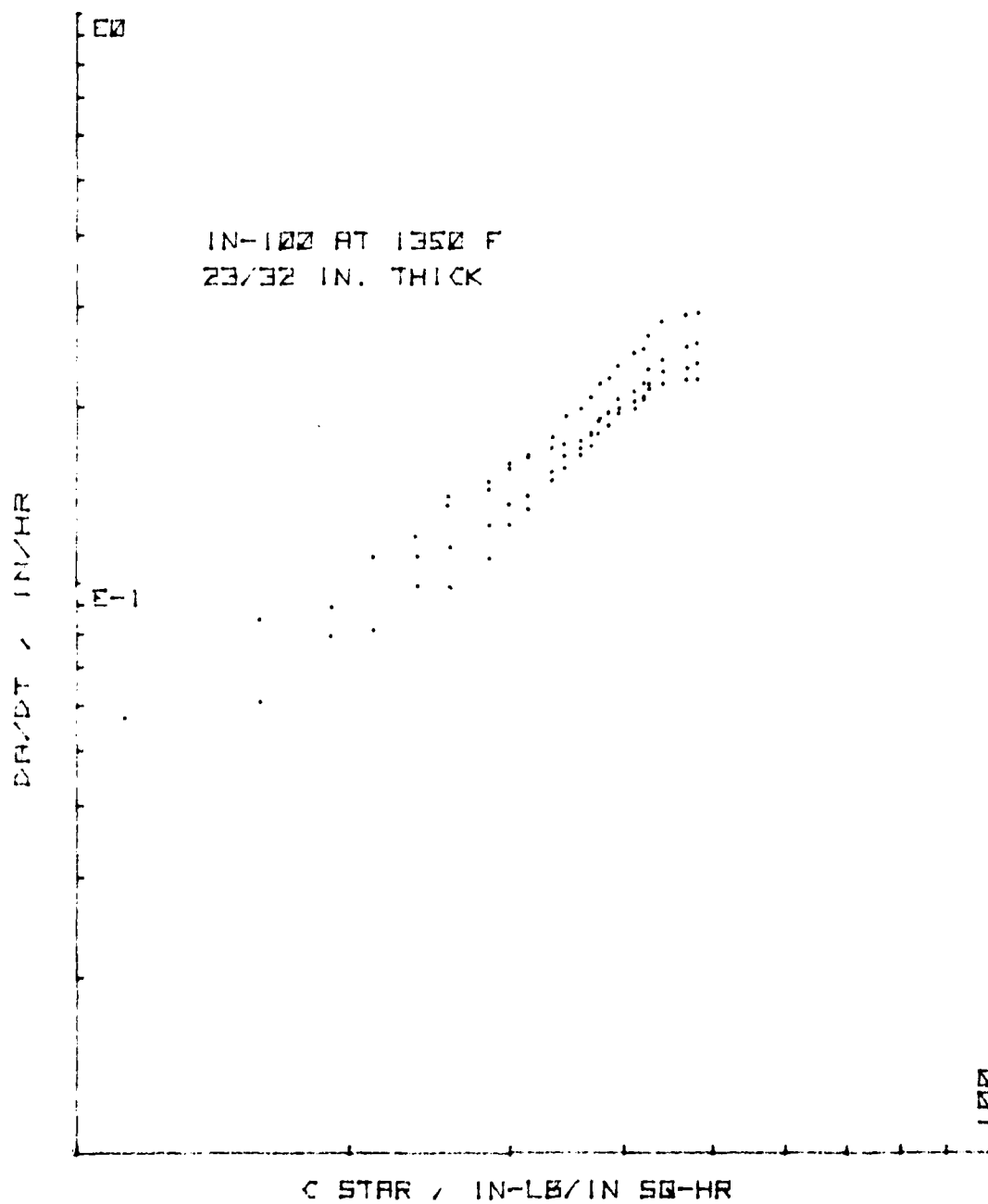
Figure 155. da/dt vs. C* Plot of the 23/32" (18 mm) Thick CT
Reduced Data
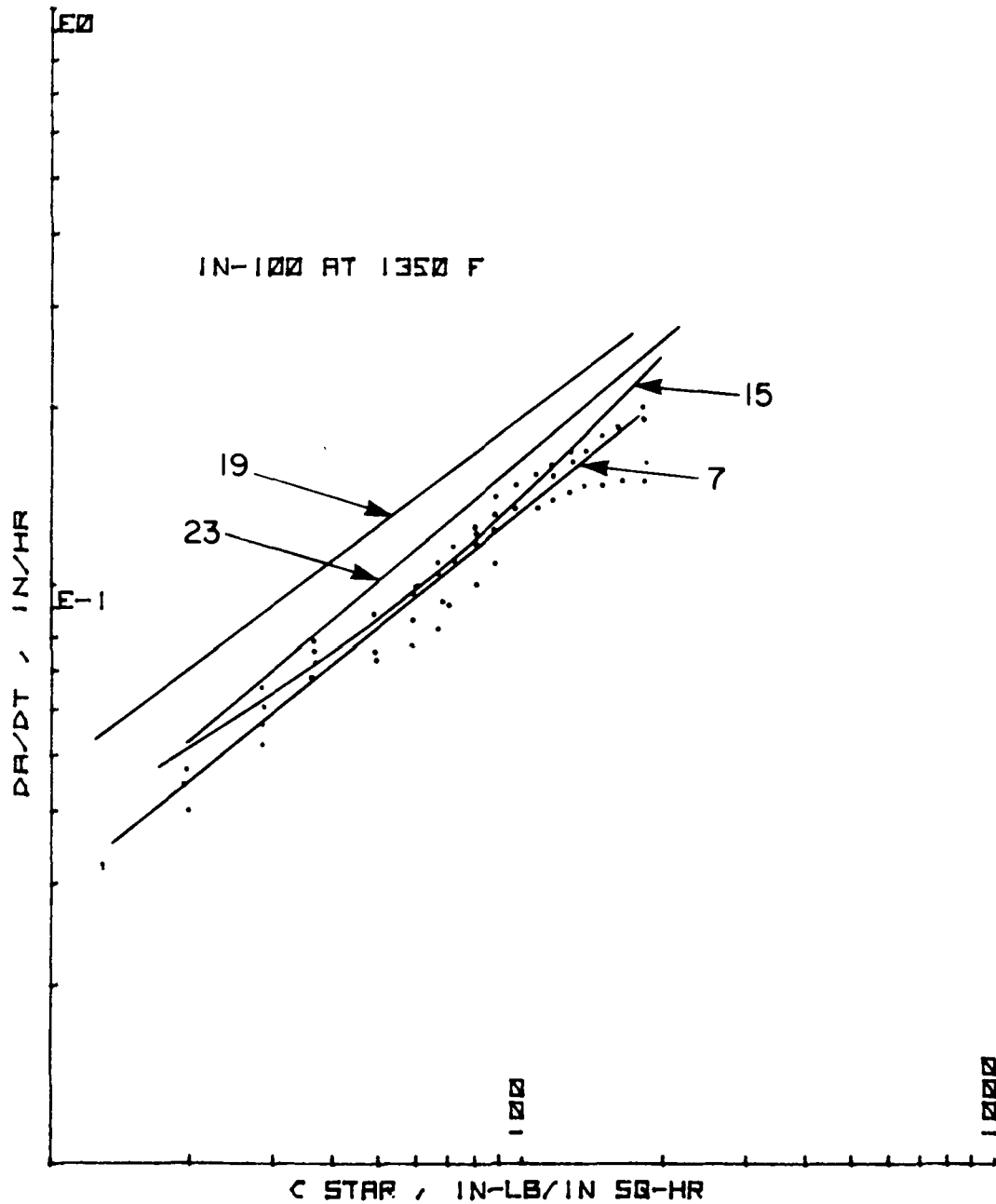
Figure 156. da/dt vs. C* Composite Plot for Five Thicknesses of CT Specimens Showing the 7/32" (6 mm) Thick Data Points
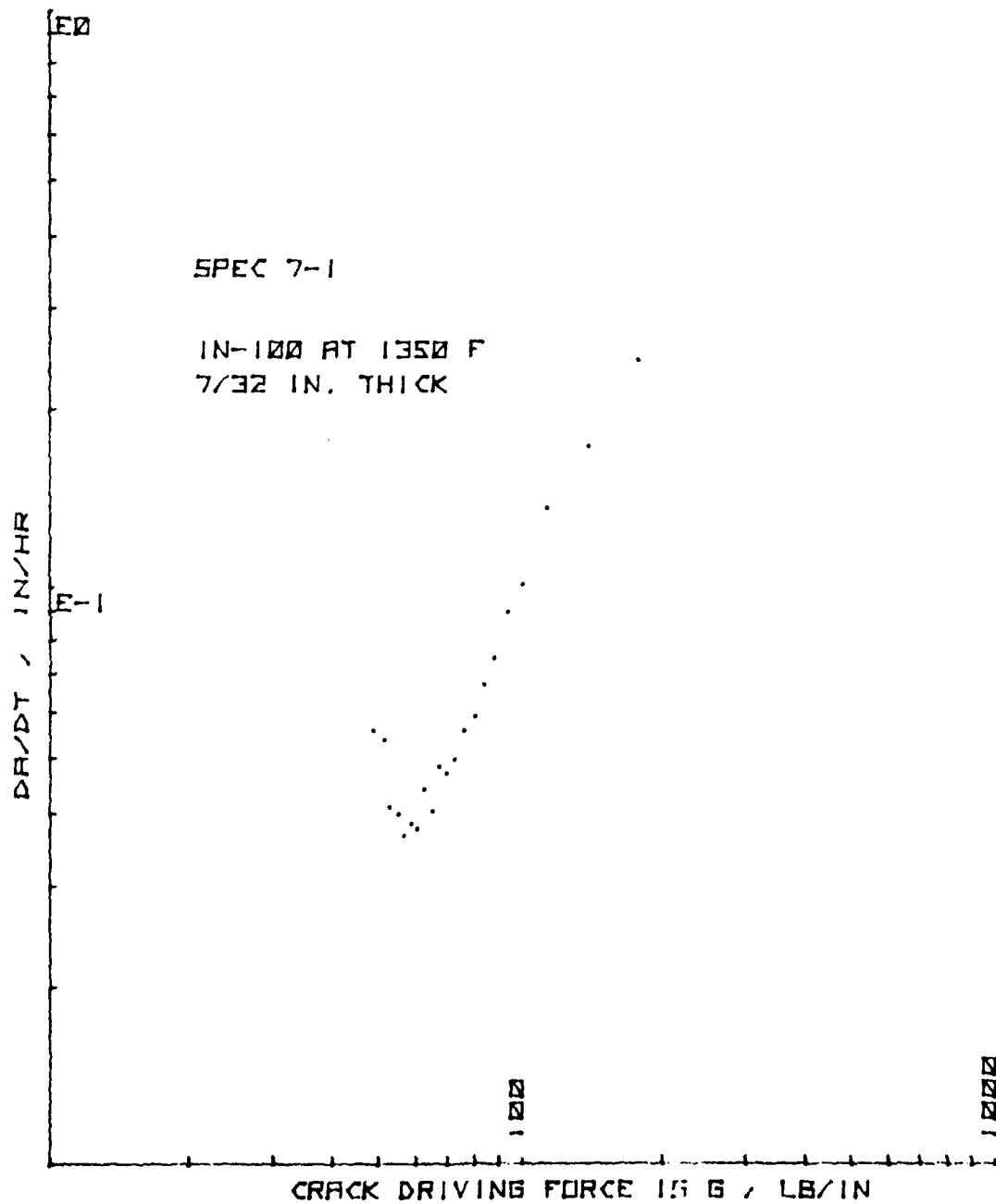
Figure 157. da/dt vs. G for CT Specimen 7-1
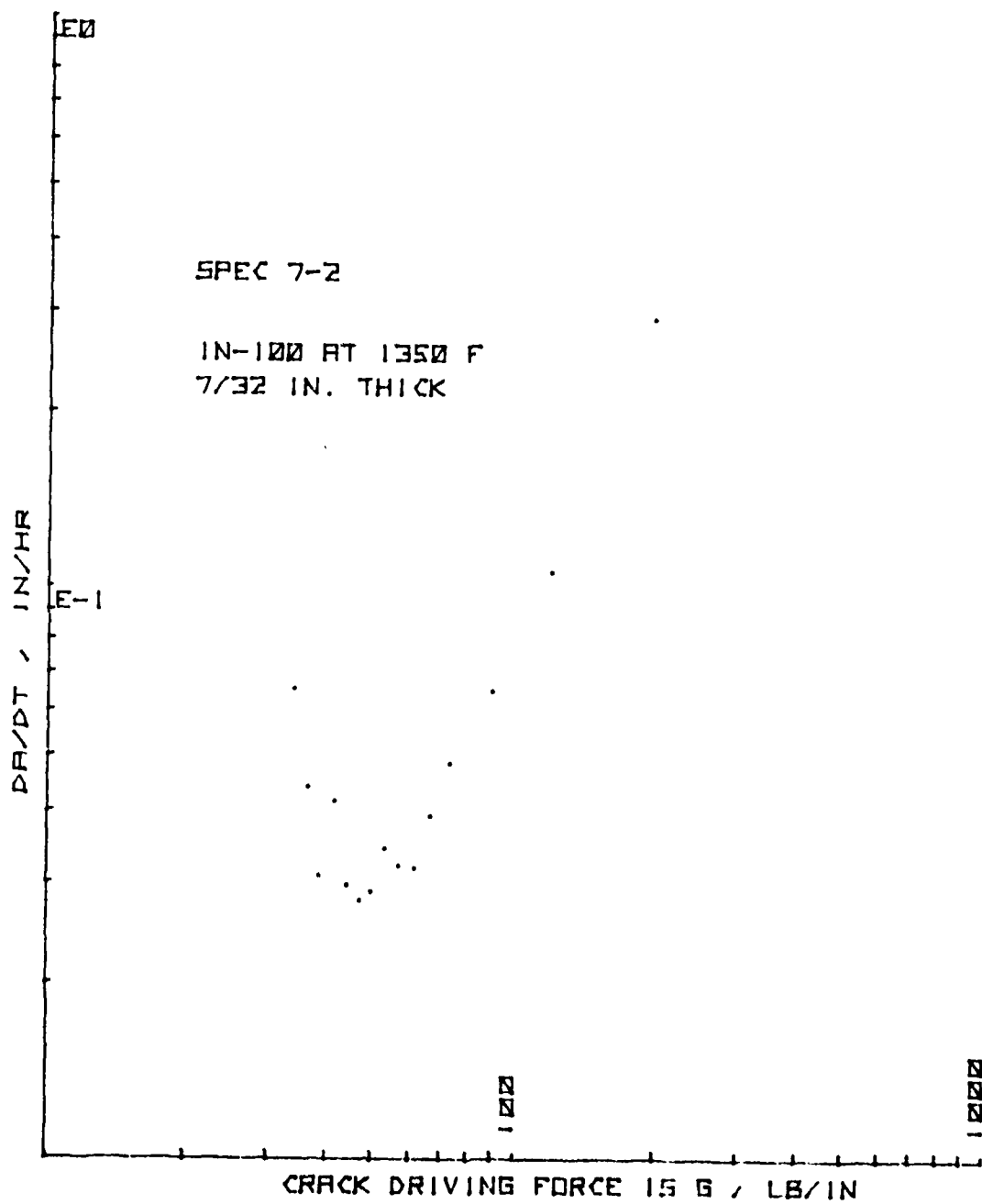
Figure 158. da/dt vs. G for CT Specimen 7-2
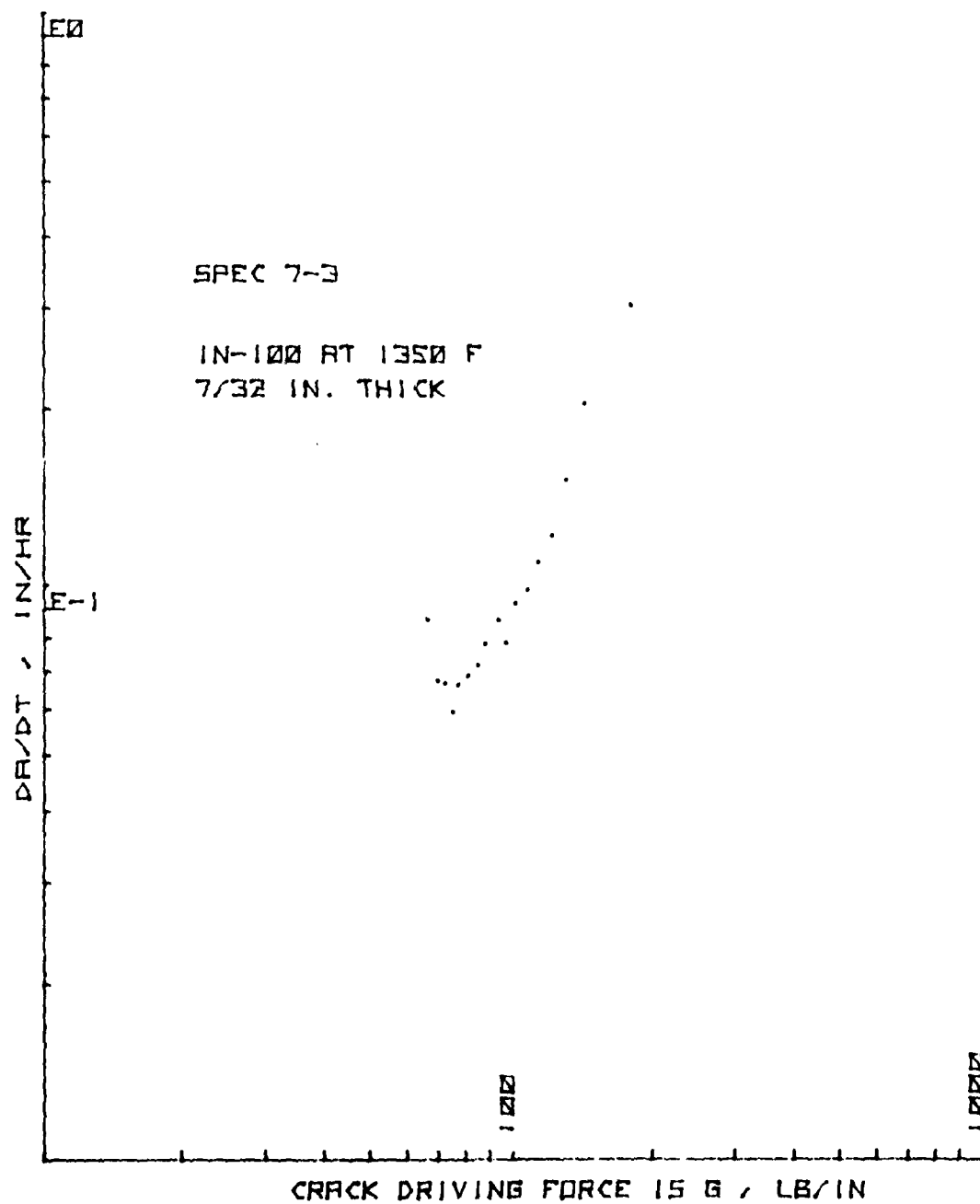
Figure 159. da/dt vs. G for CT Specimen 7-3
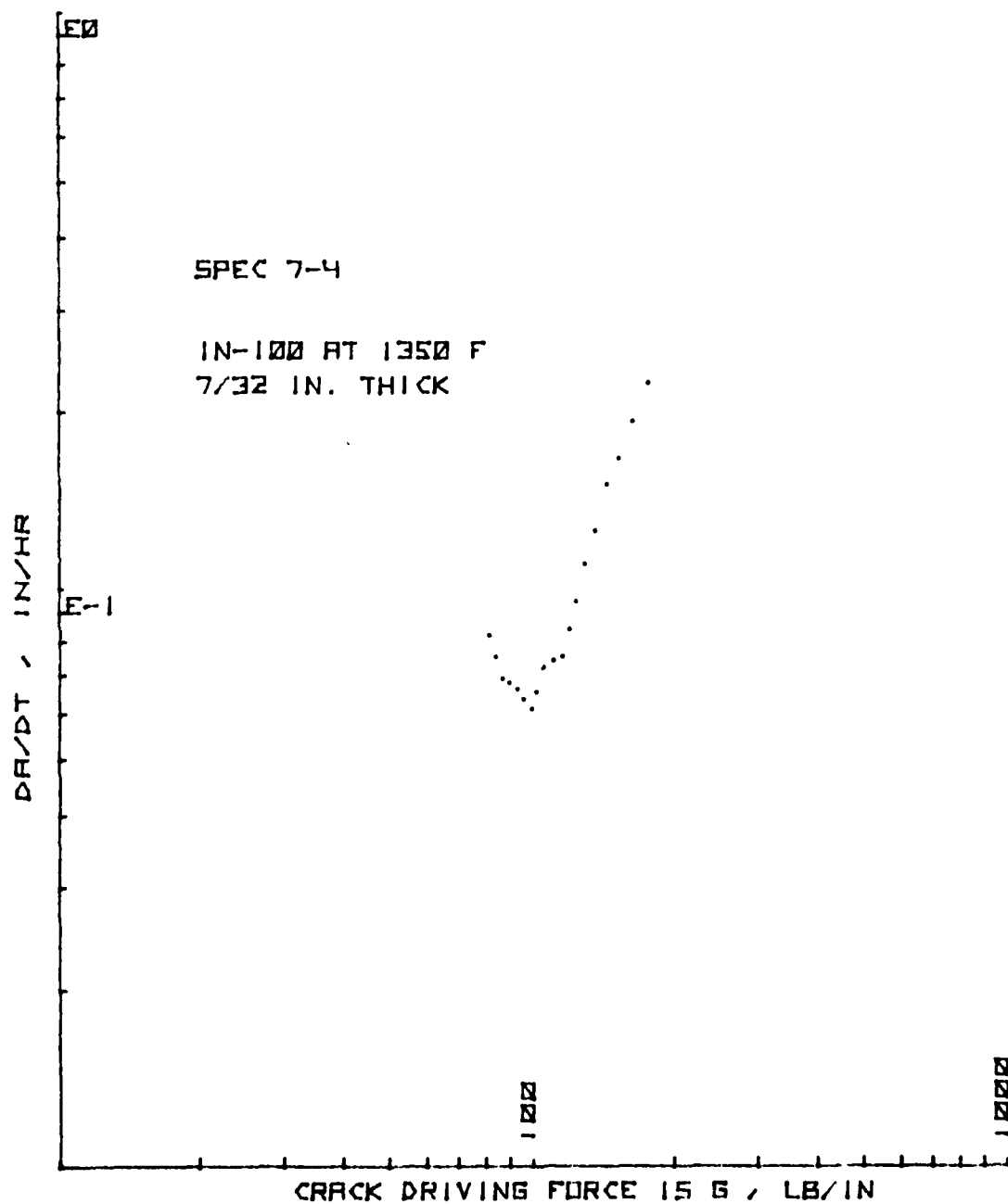
Figure 160. da/dt vs. G for CT Specimen 7-4
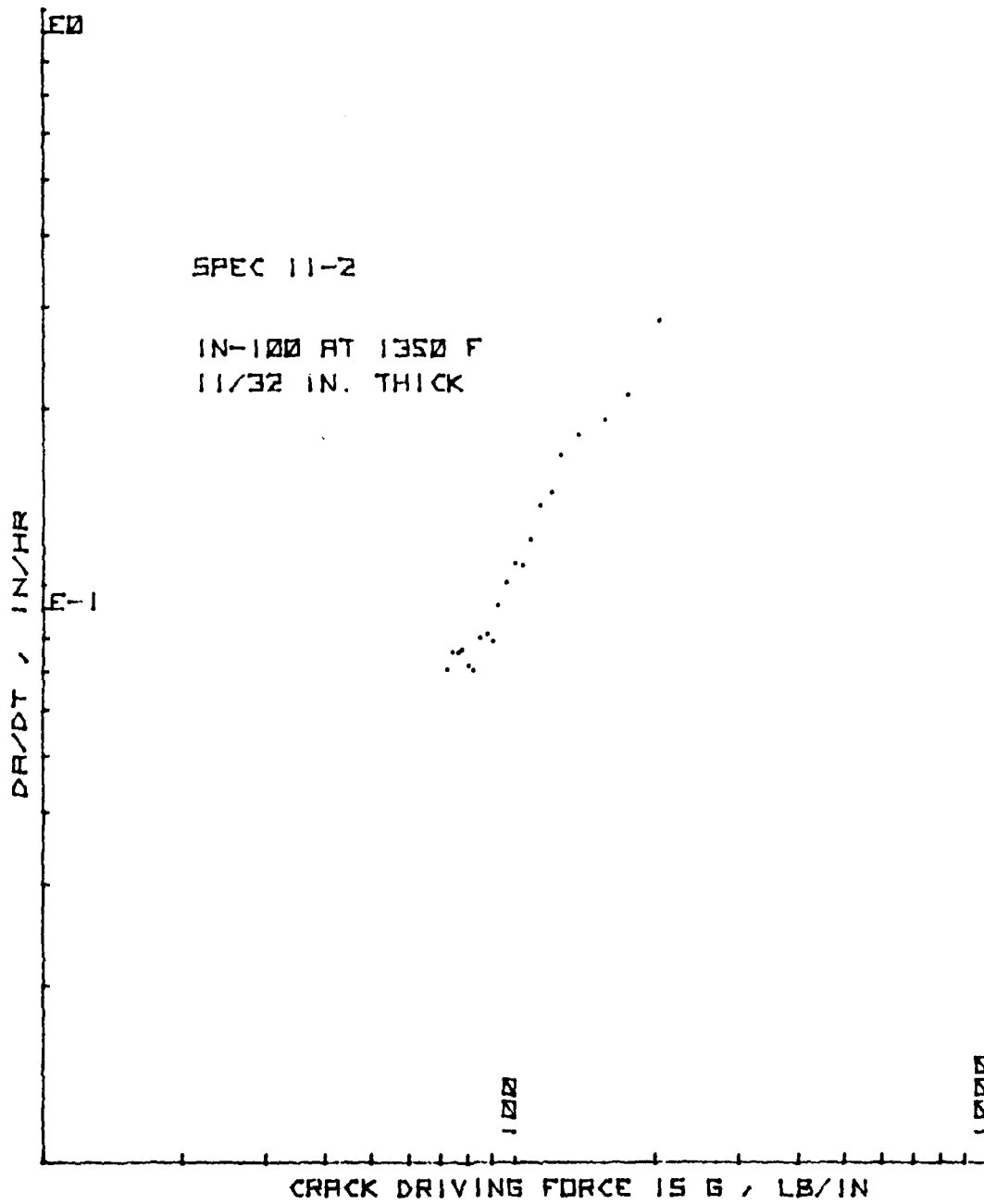
Figure 161. da/dt vs. G for CT Specimen 11-2
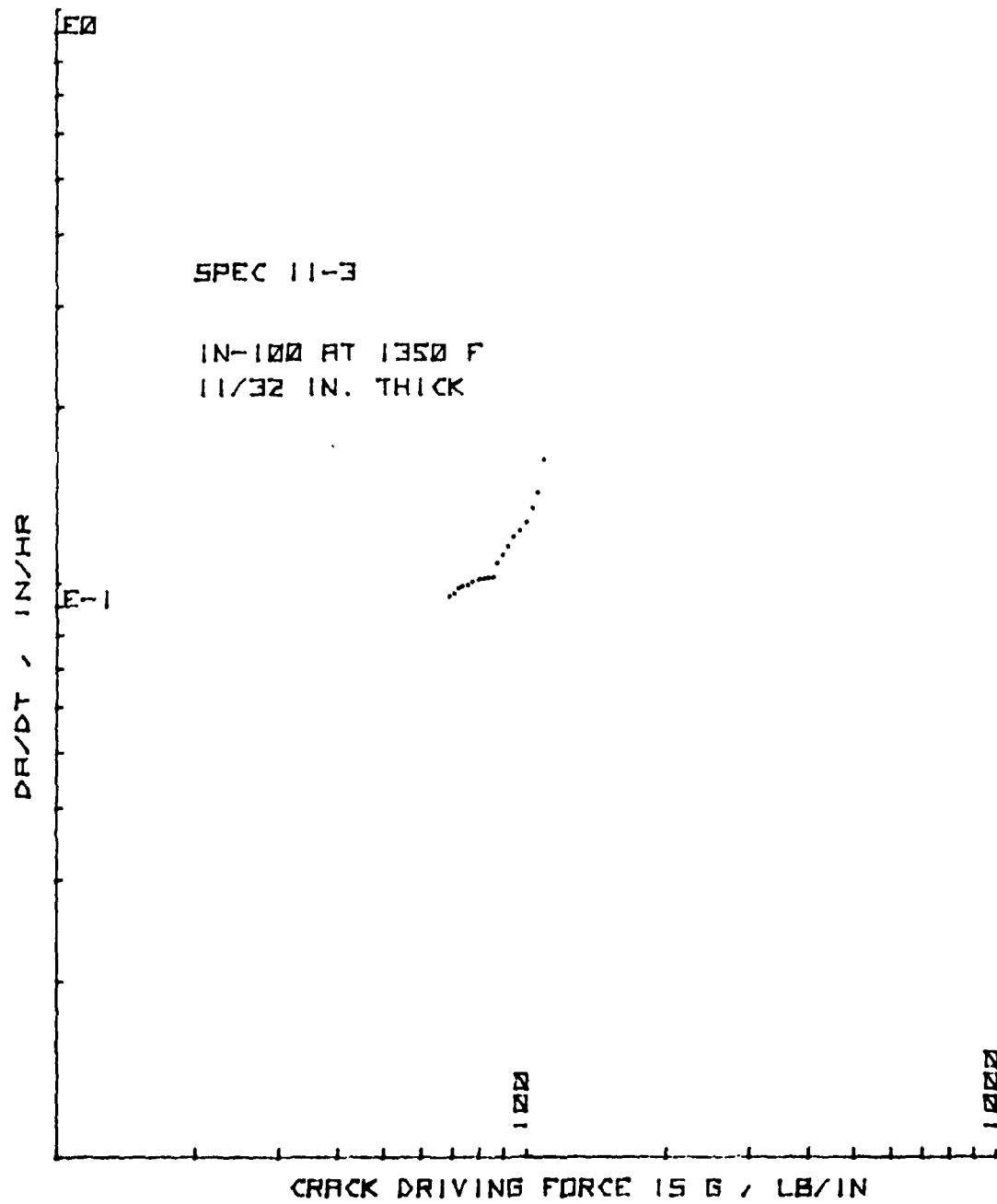
Figure 162. da/dt vs. G for CT Specimen 11-3
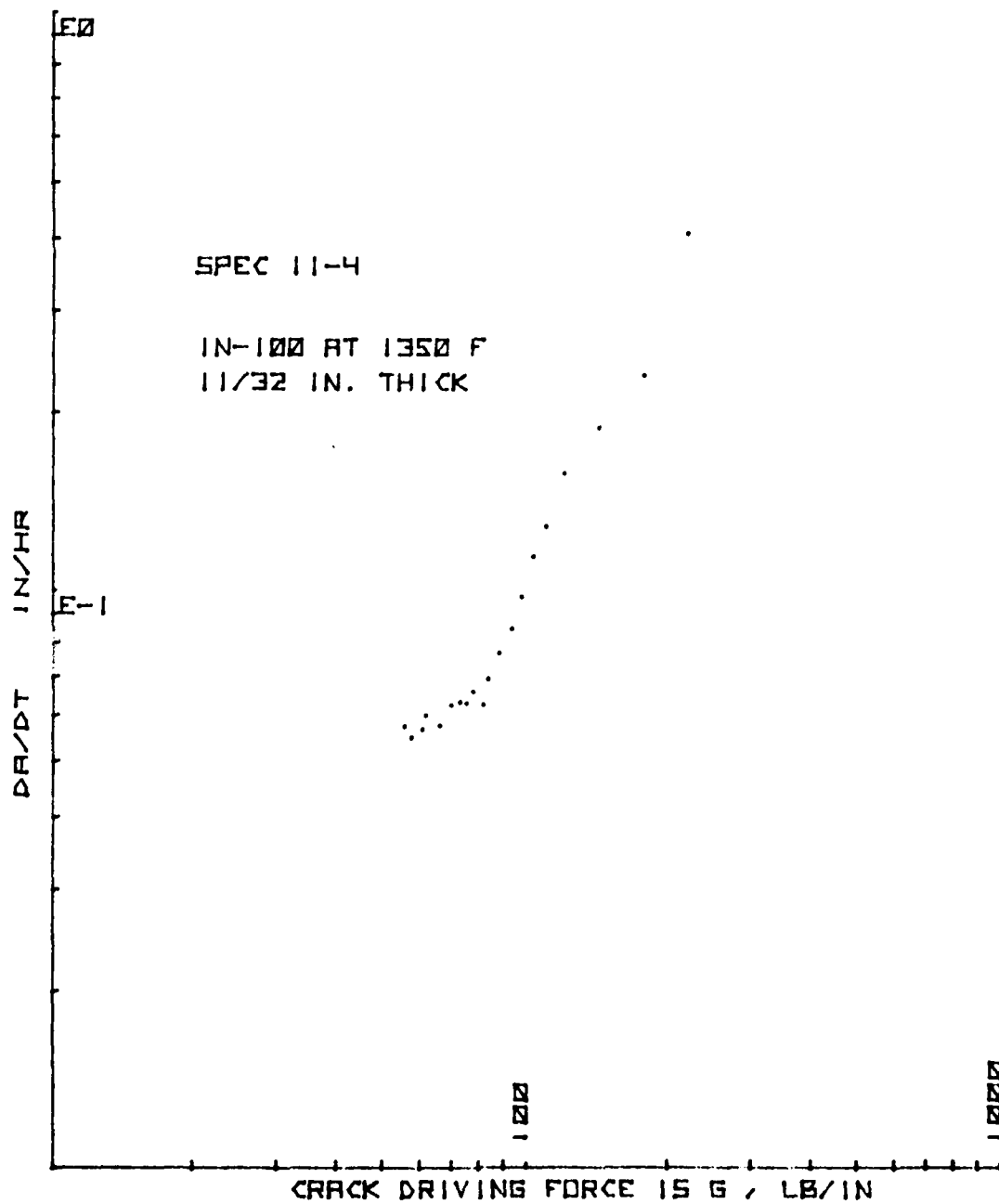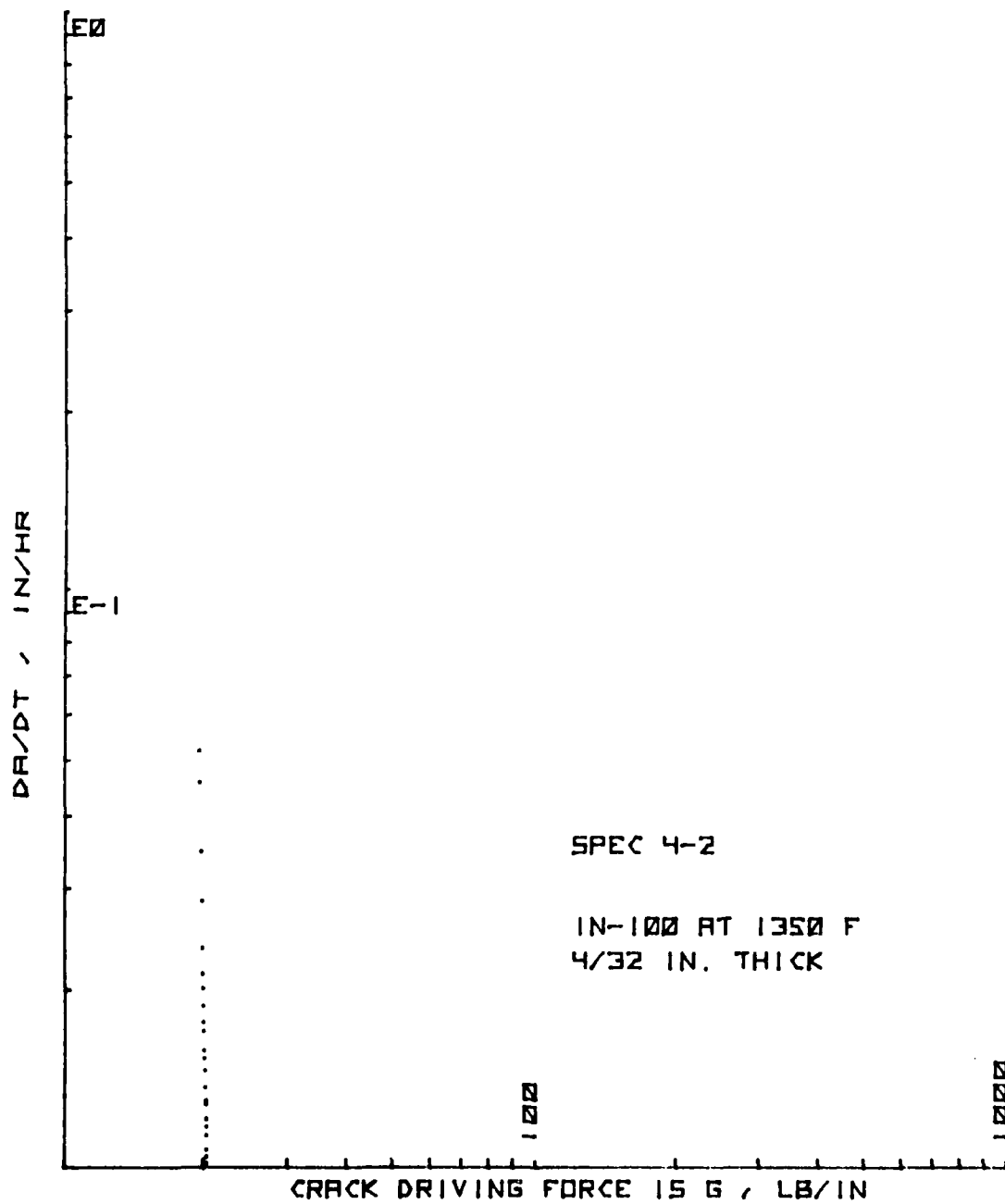
Figure 163.   da/dt vs. G for CT Specimen 11-4

235
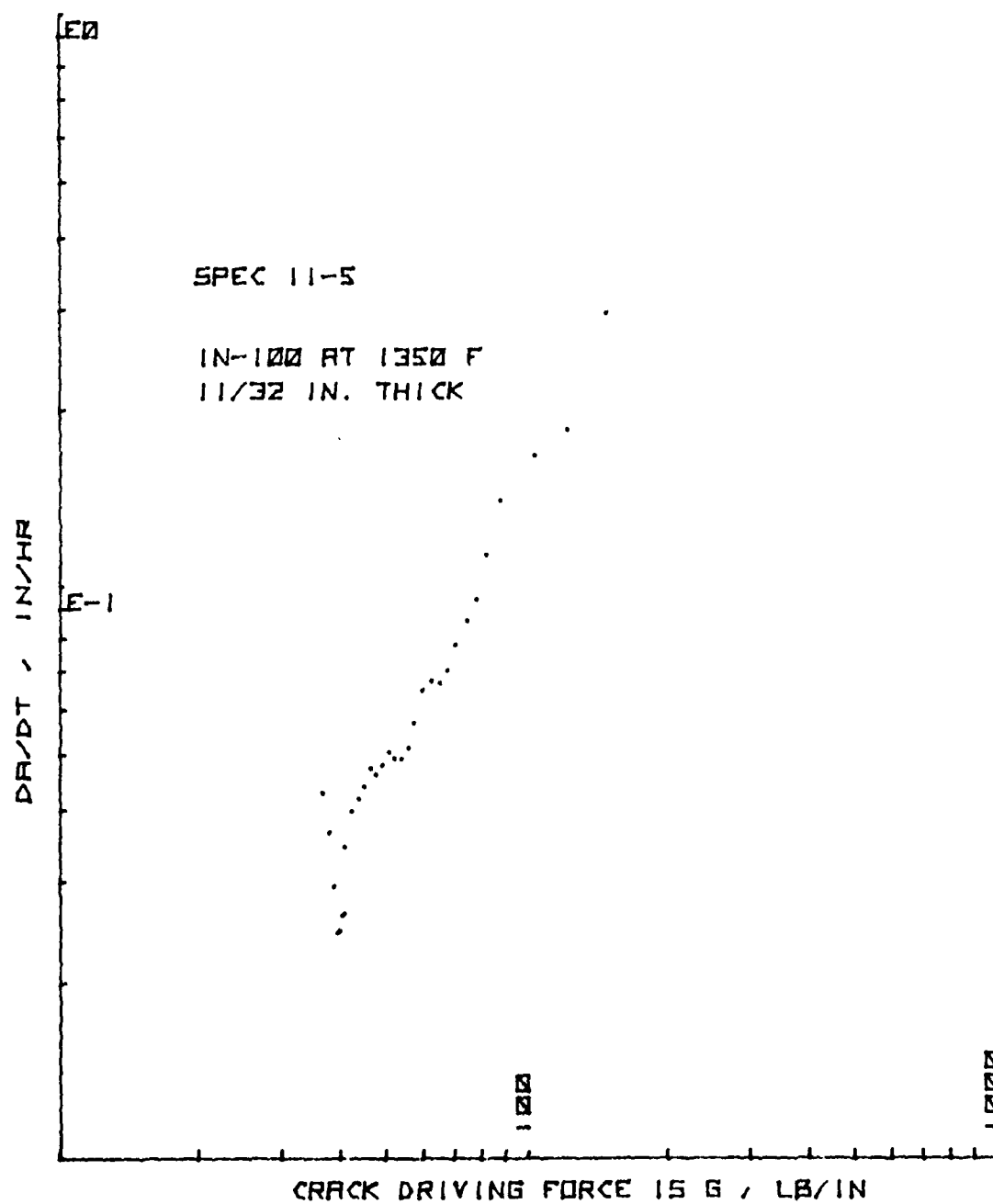
Figure 164. da/dt vs. G for CT Specimen 11-5
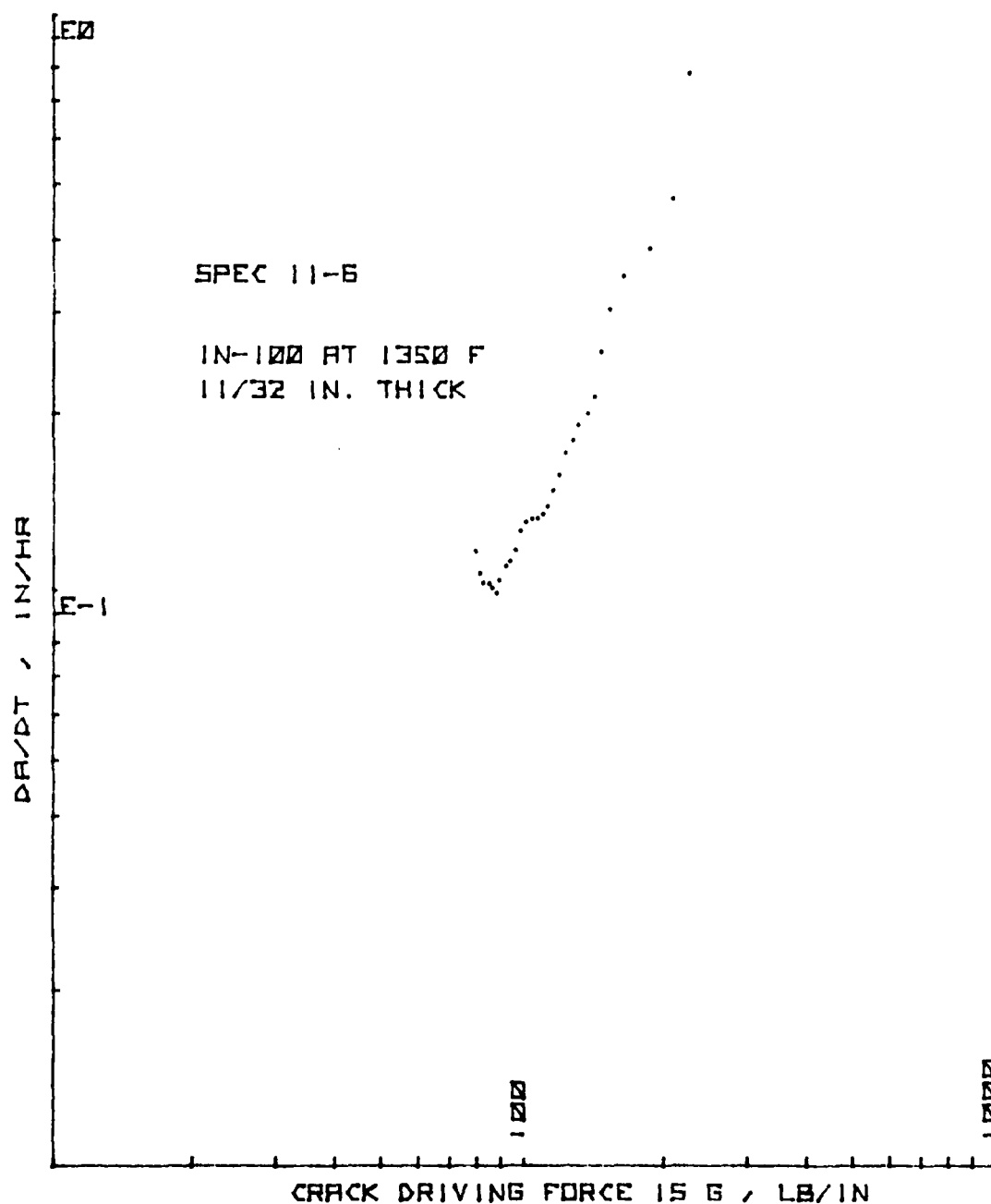
Figure 165. da/dt vs. G for CT Specimen 11-6
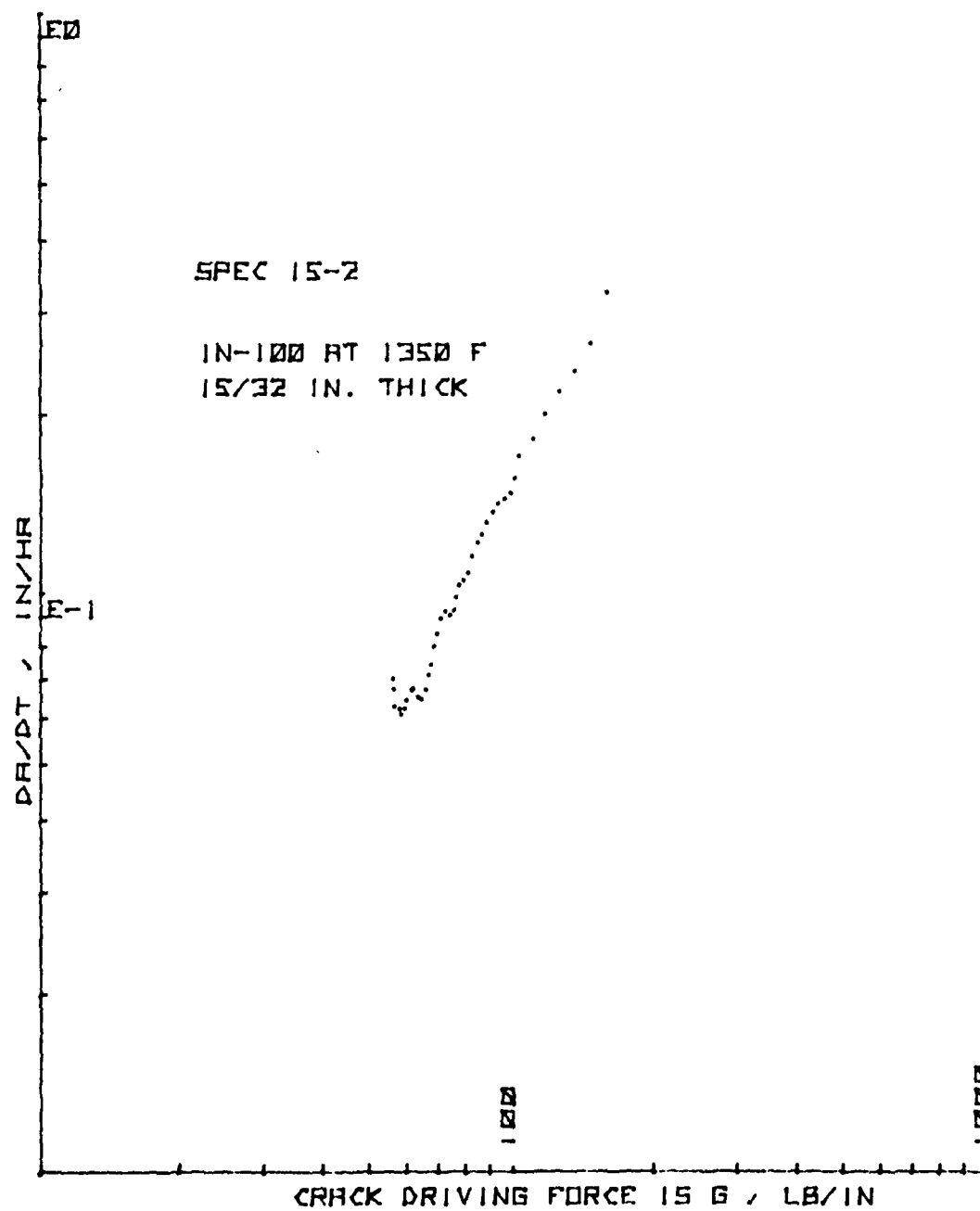
Figure 166. da/dt vs. G for CT Specimen 15-2
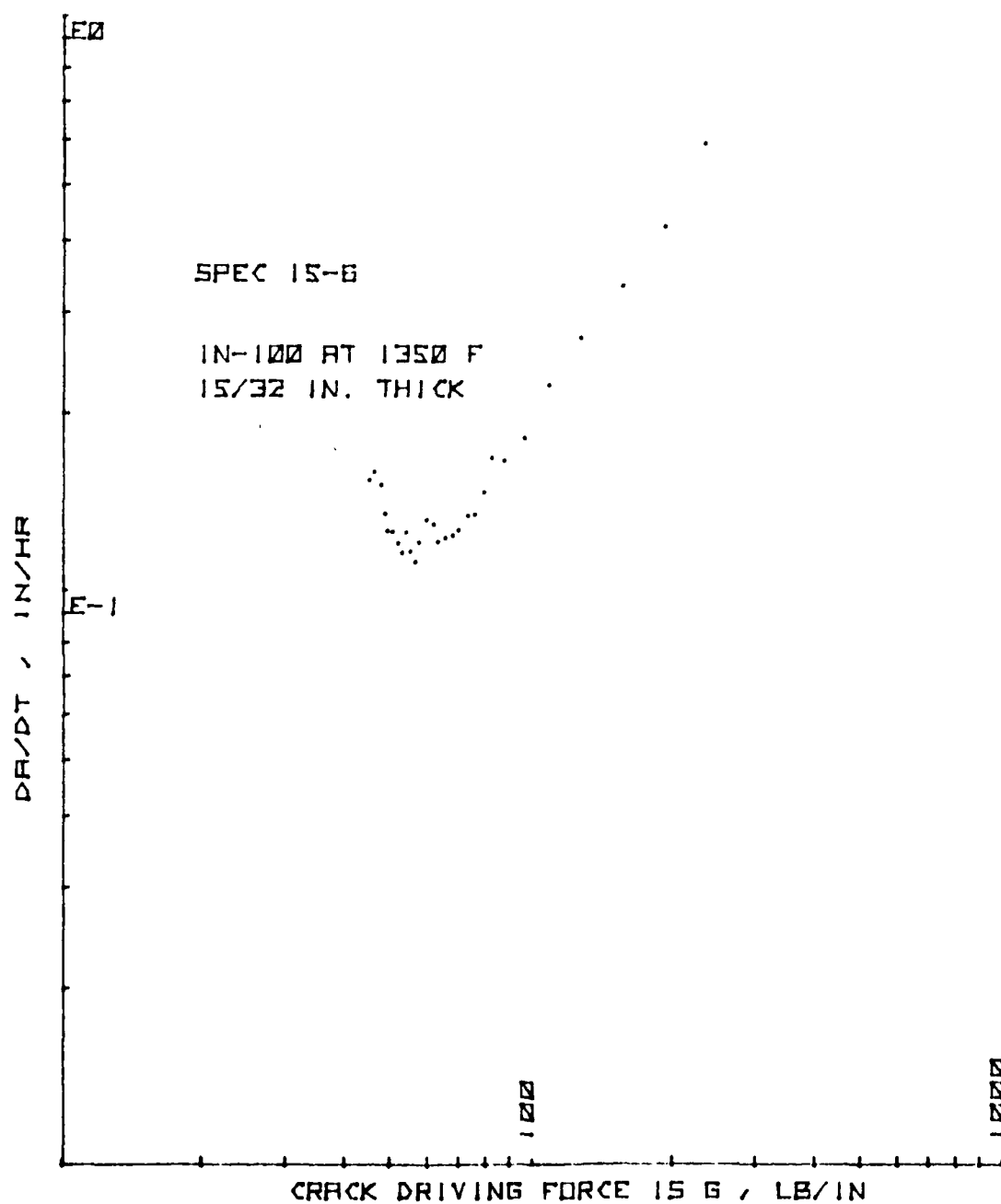
Figure 167. da/dt vs. G for CT Specimen 15-6
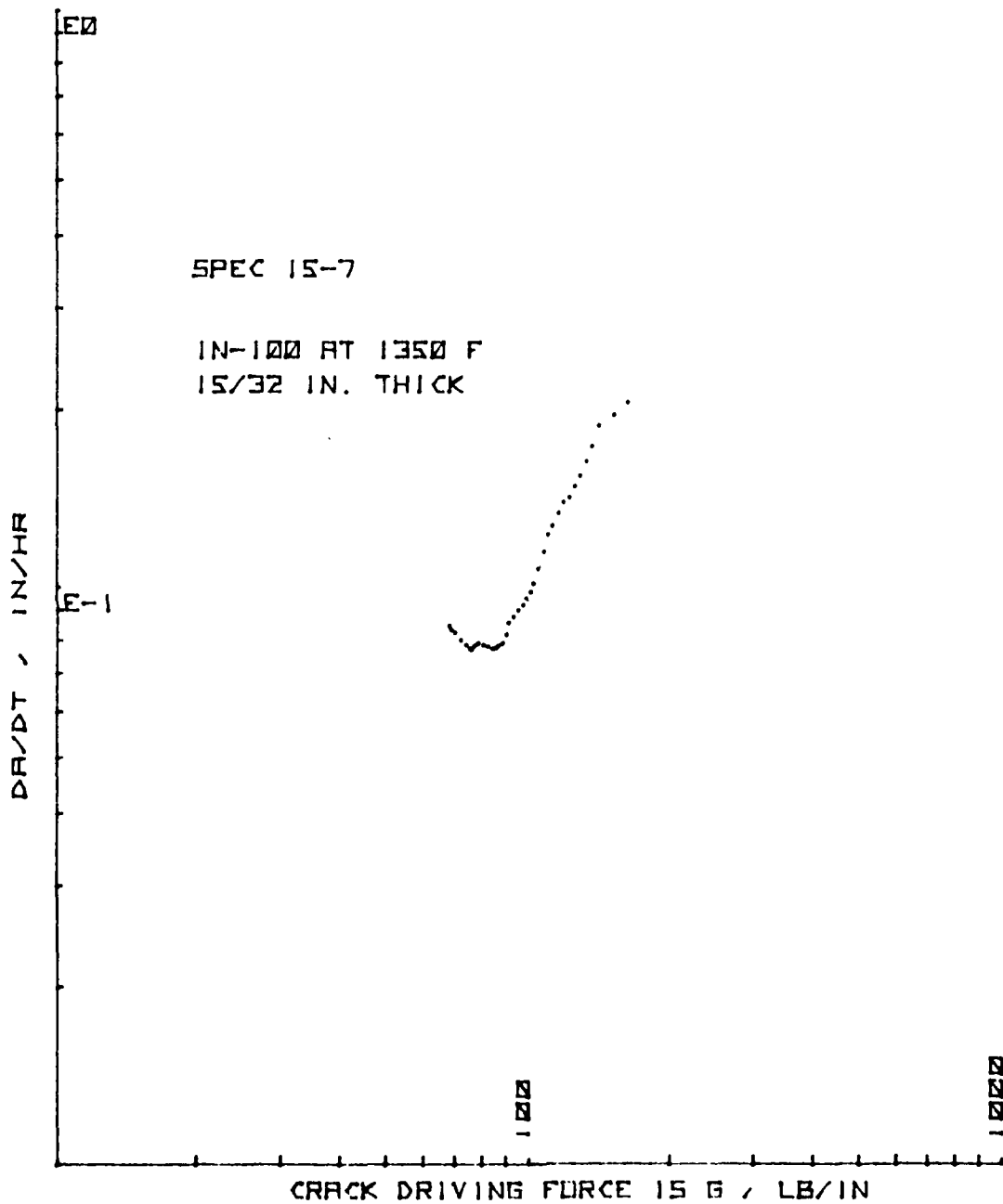
Figure 168.   da/dt vs. G for CT Specimen 15-7
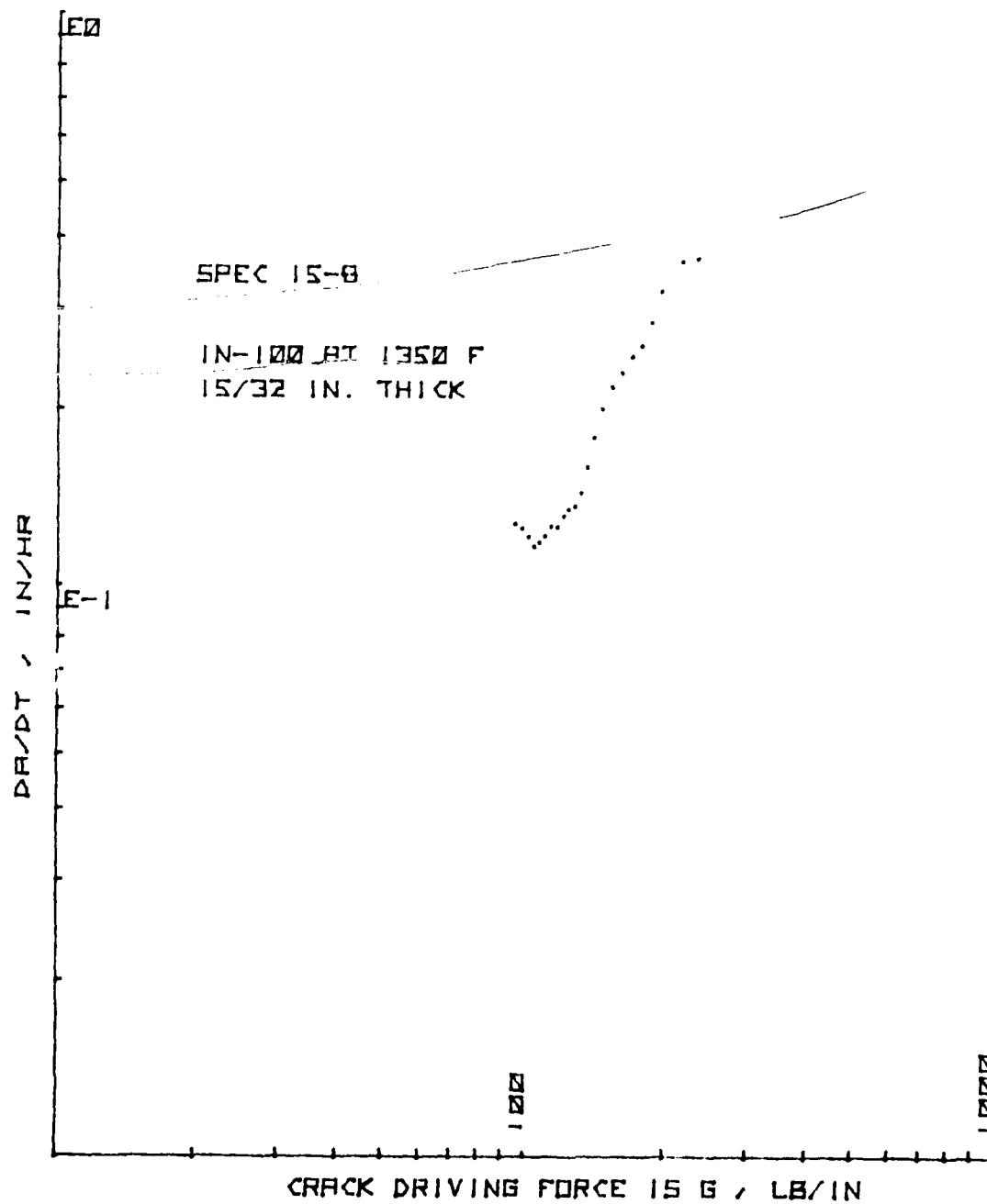
Figure 169. da/dt vs. G for CT Specimen 15-8
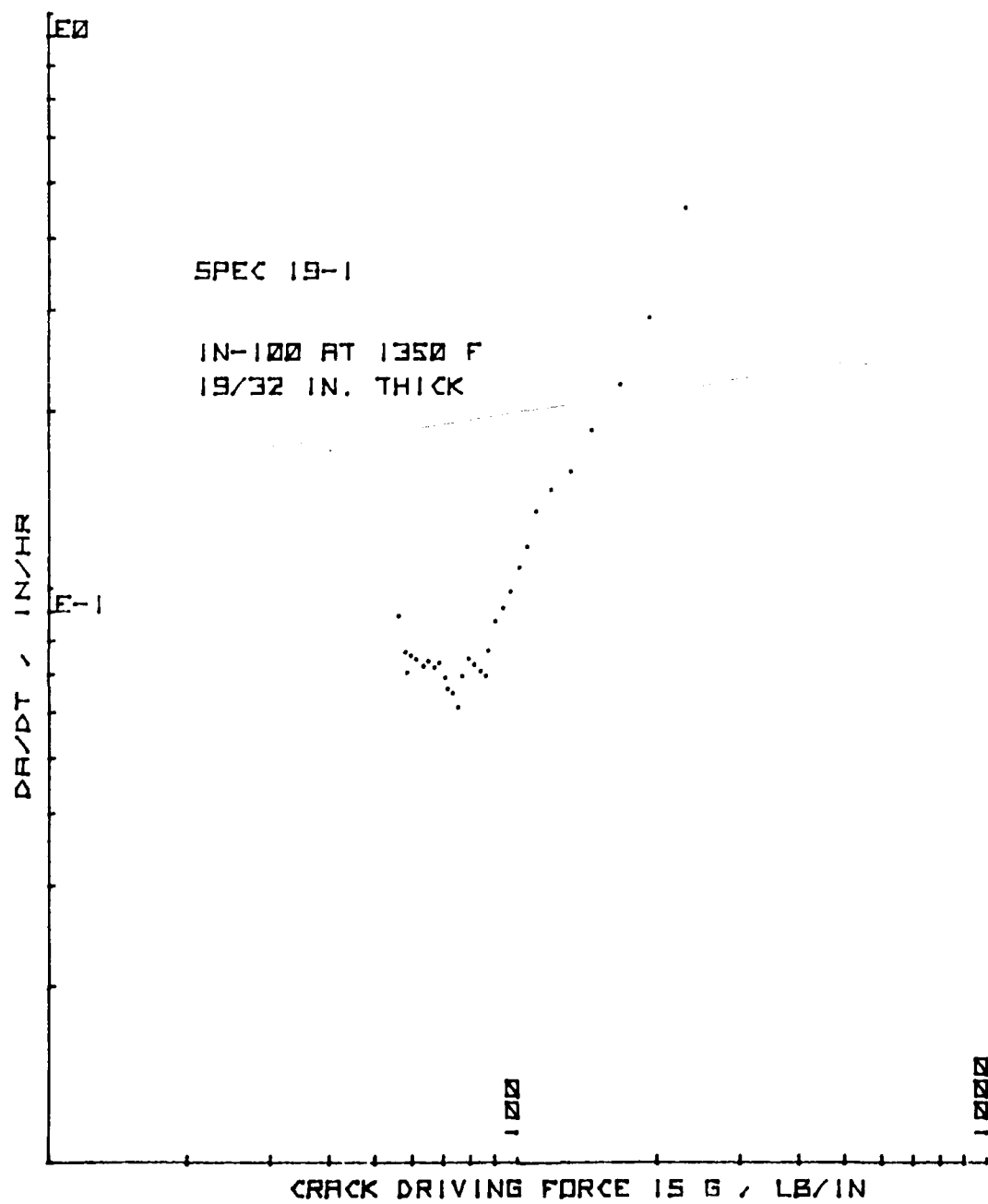
Figure 170. da/dt vs. G for CT Specimen 19-1
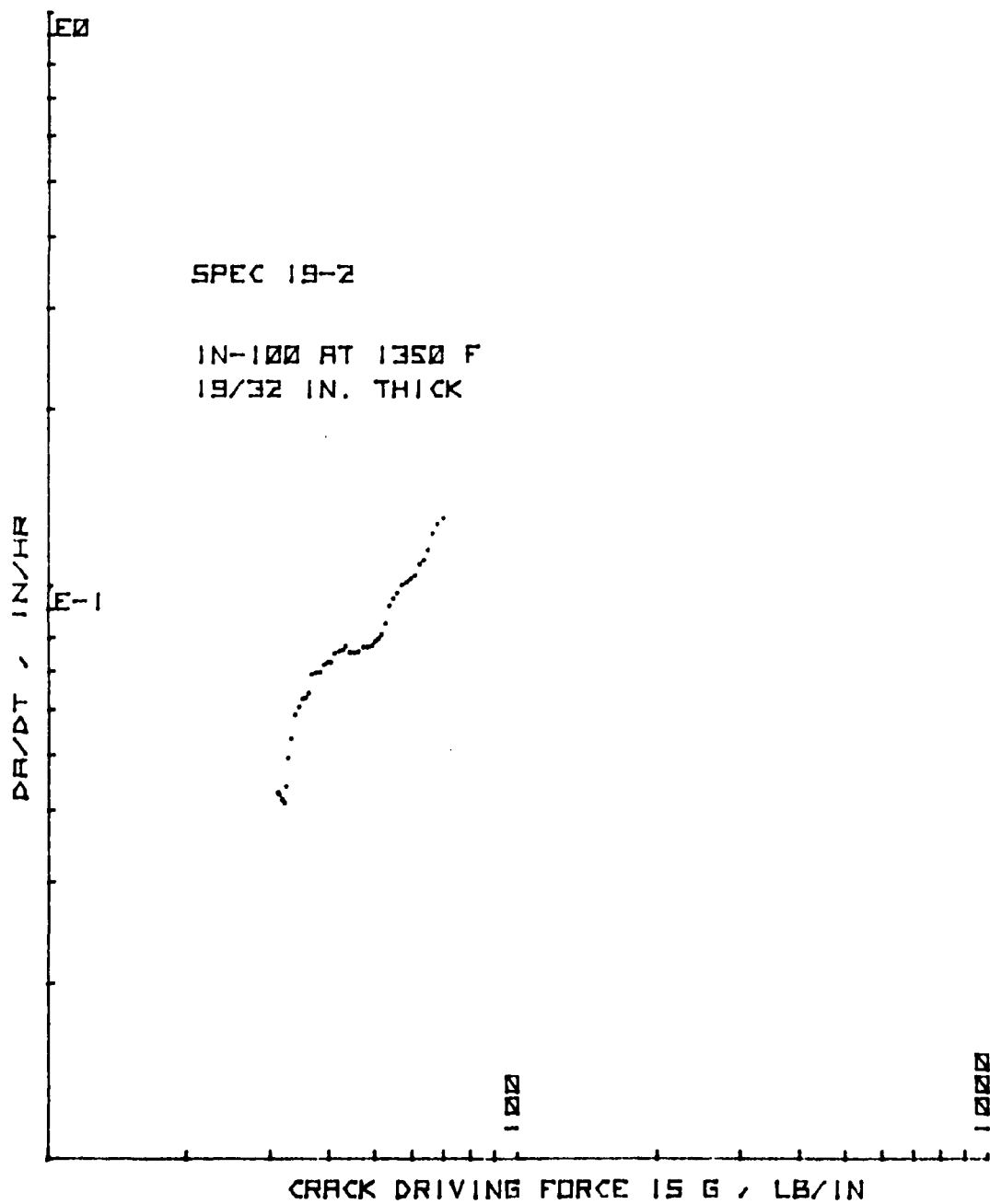
Figure 171. da/dt vs. G for CT Specimen 19-2
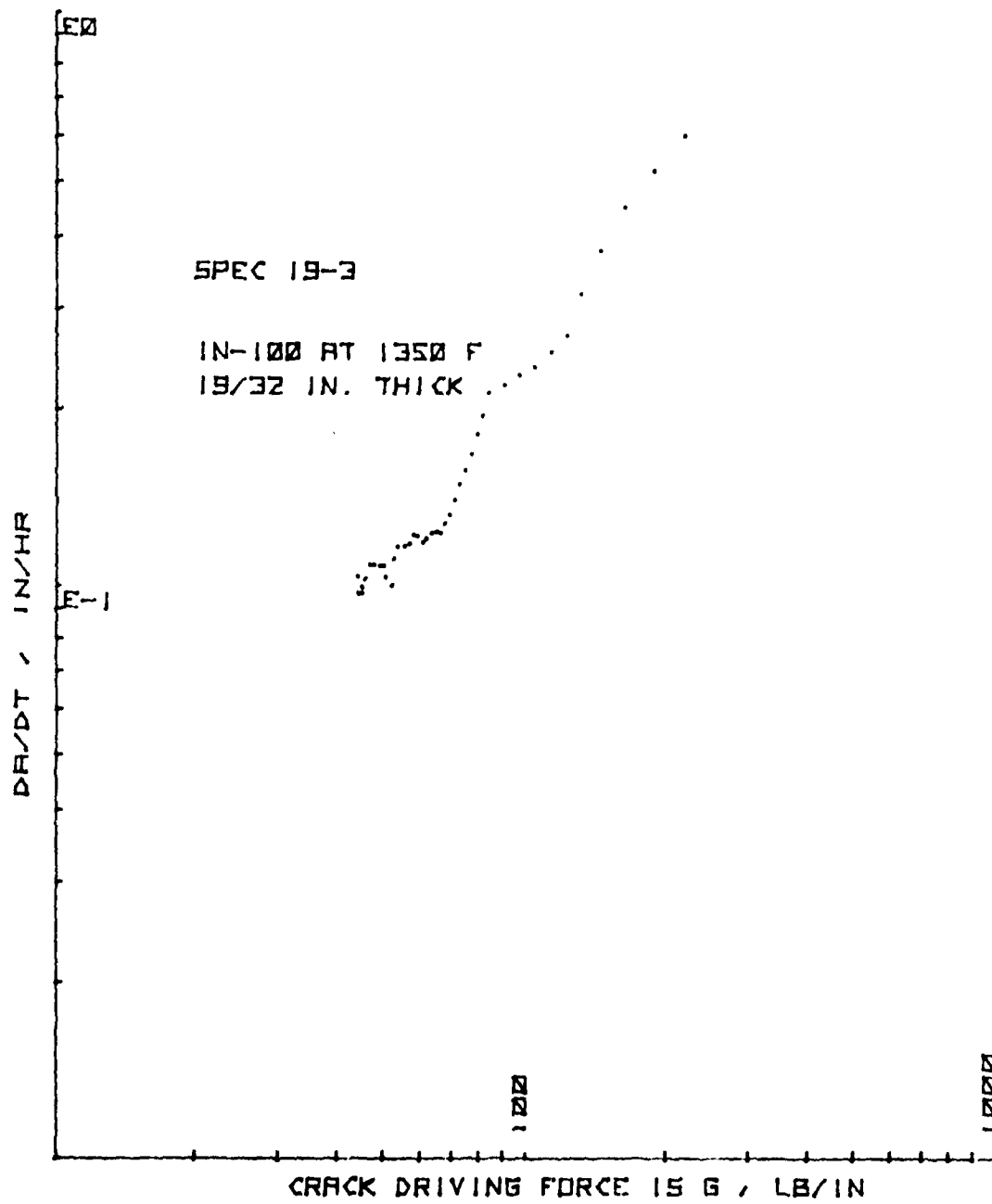
Figure 172.   da/dt vs. G for CT Specimen 19-3
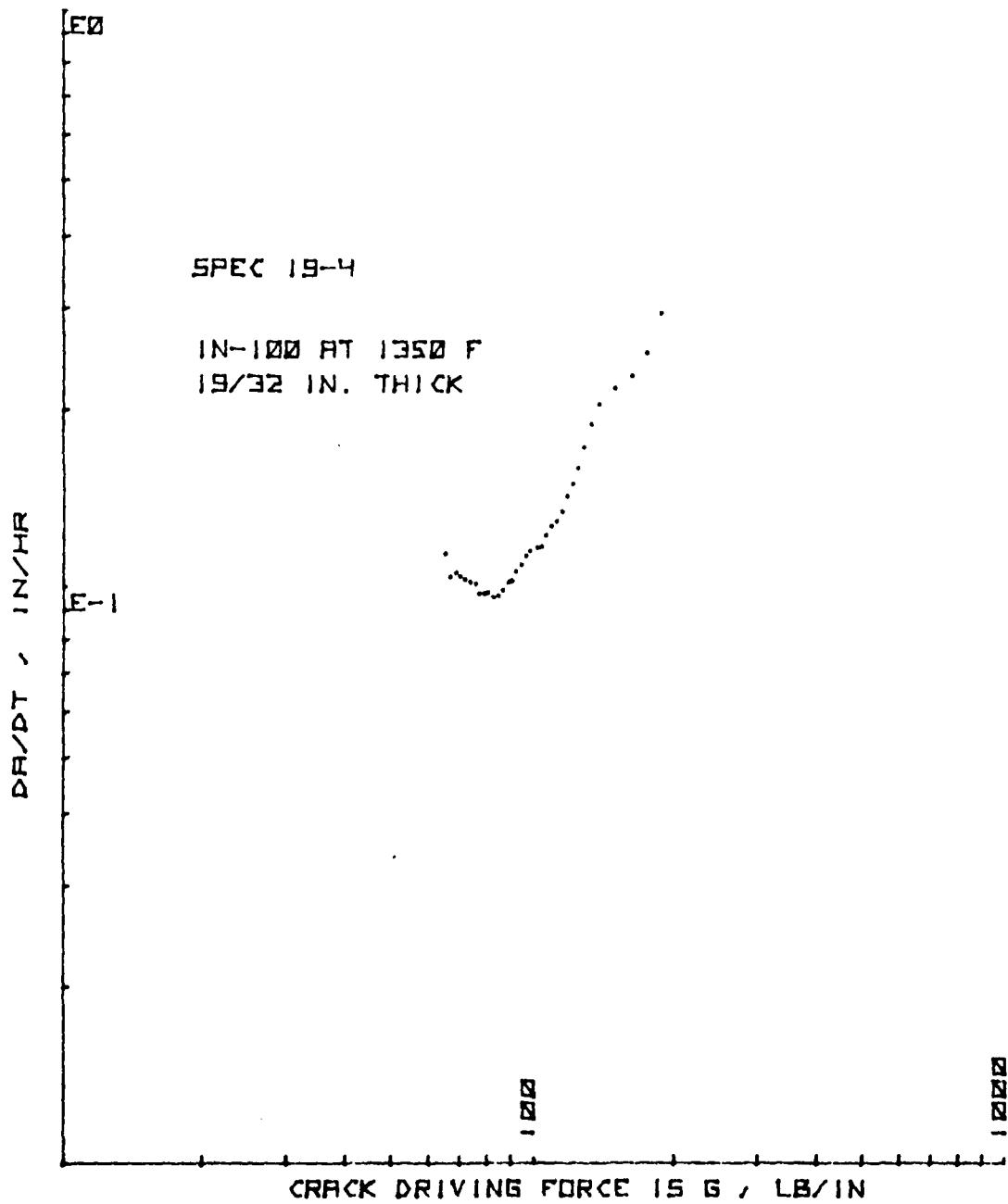
Figure 173. da/dt vs. G for CT Specimen 19-4

245
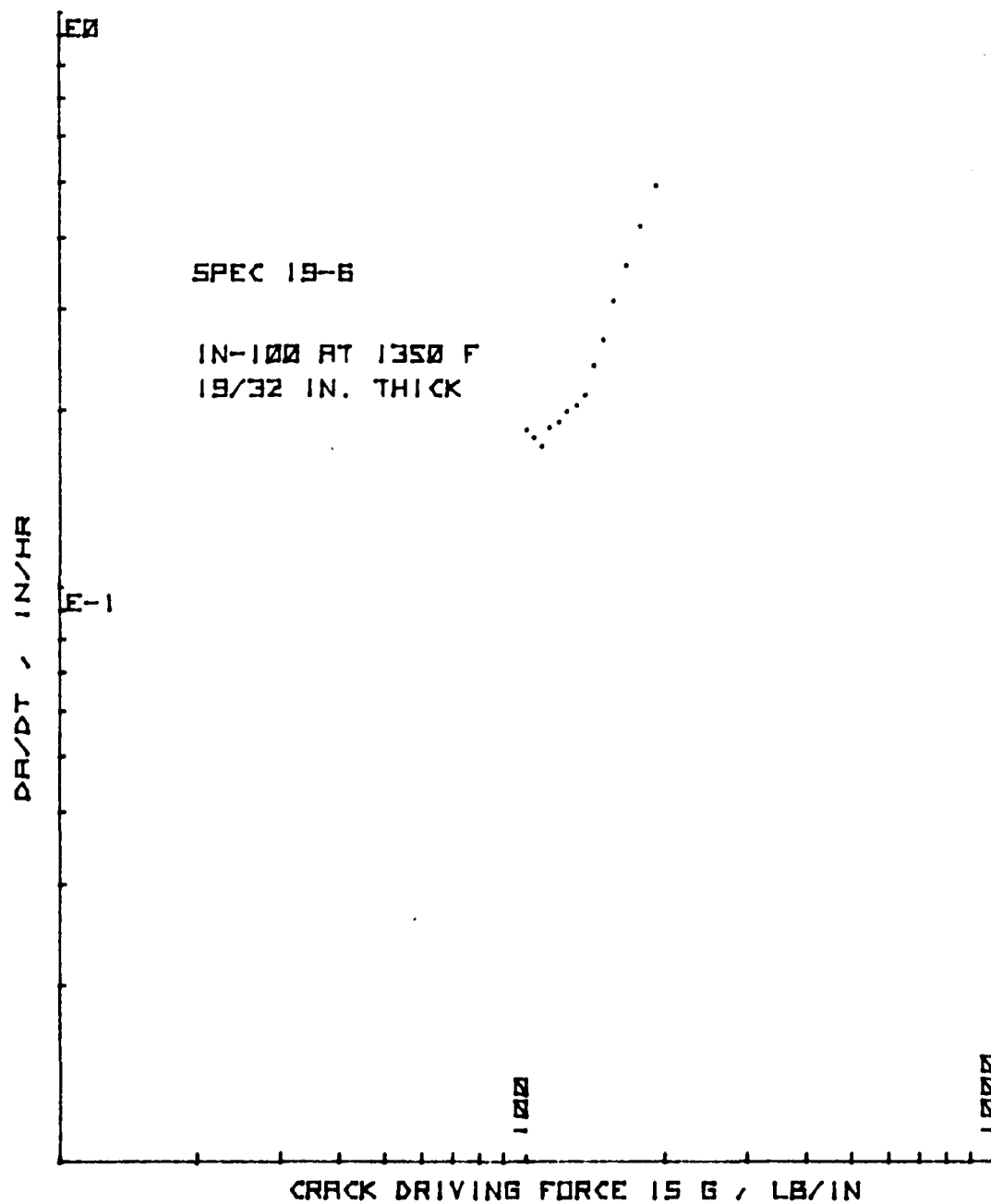
Figure 174. da/dt vs. G for CT Specimen 19-6

SPEC 23-1

IN-100 AT 1350 F
23/32 IN. THICK
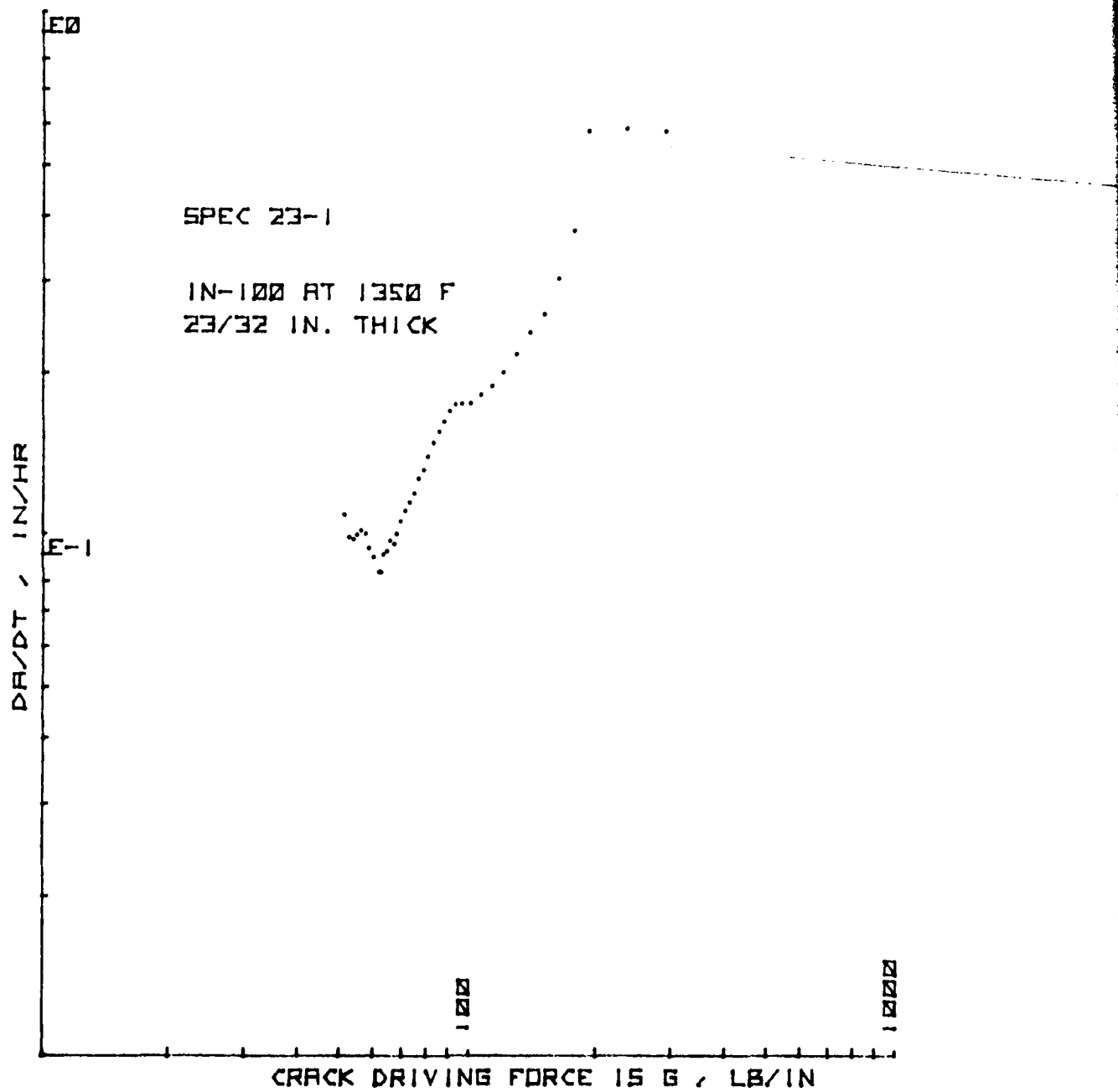
Figure 175.   da/dt vs. G for CT Specimen 23-1
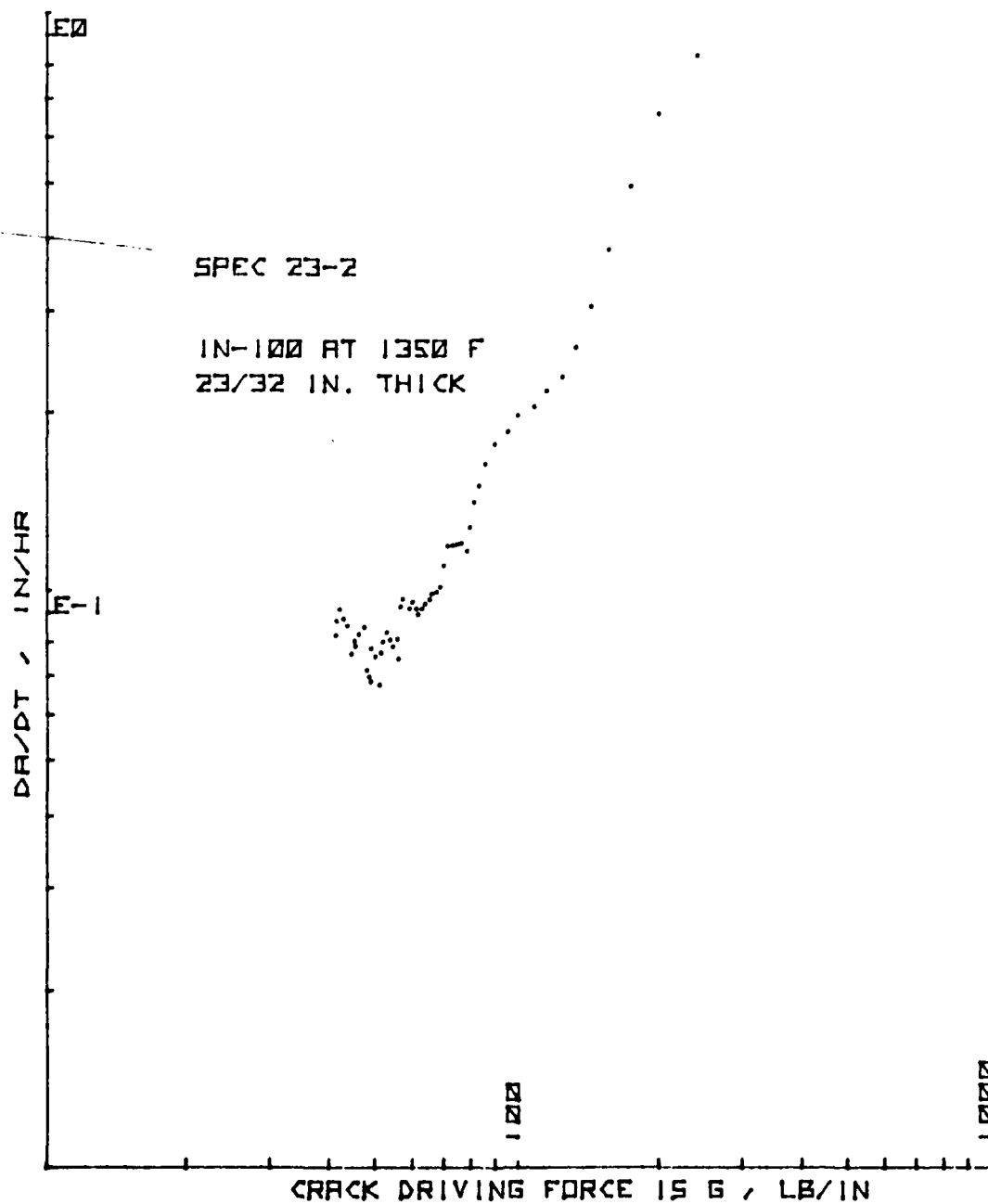
Figure 176. da/dt vs. G for CT Specimen 23-2
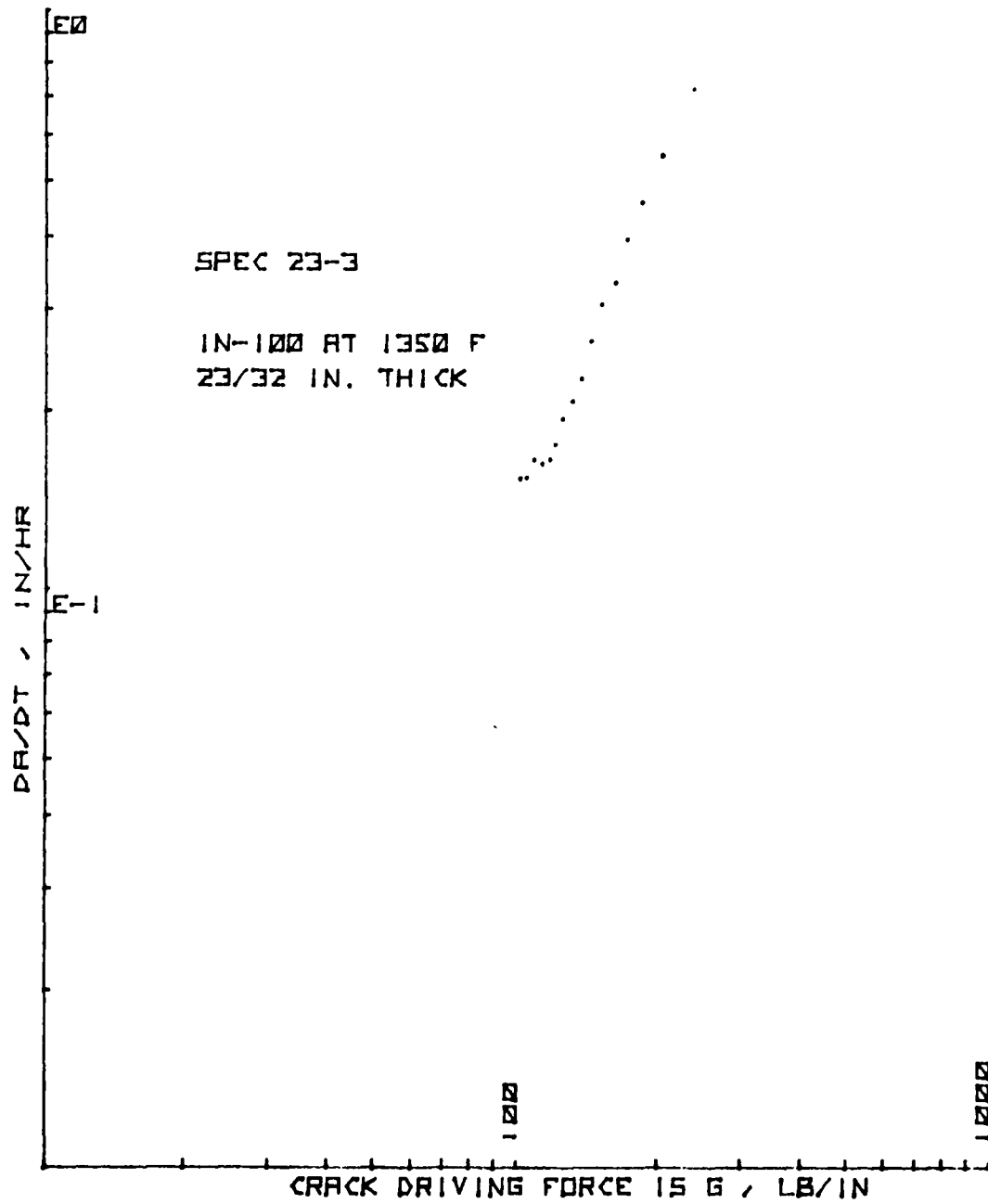
Figure 177. da/dt vs. G for CT Specimen 23-3
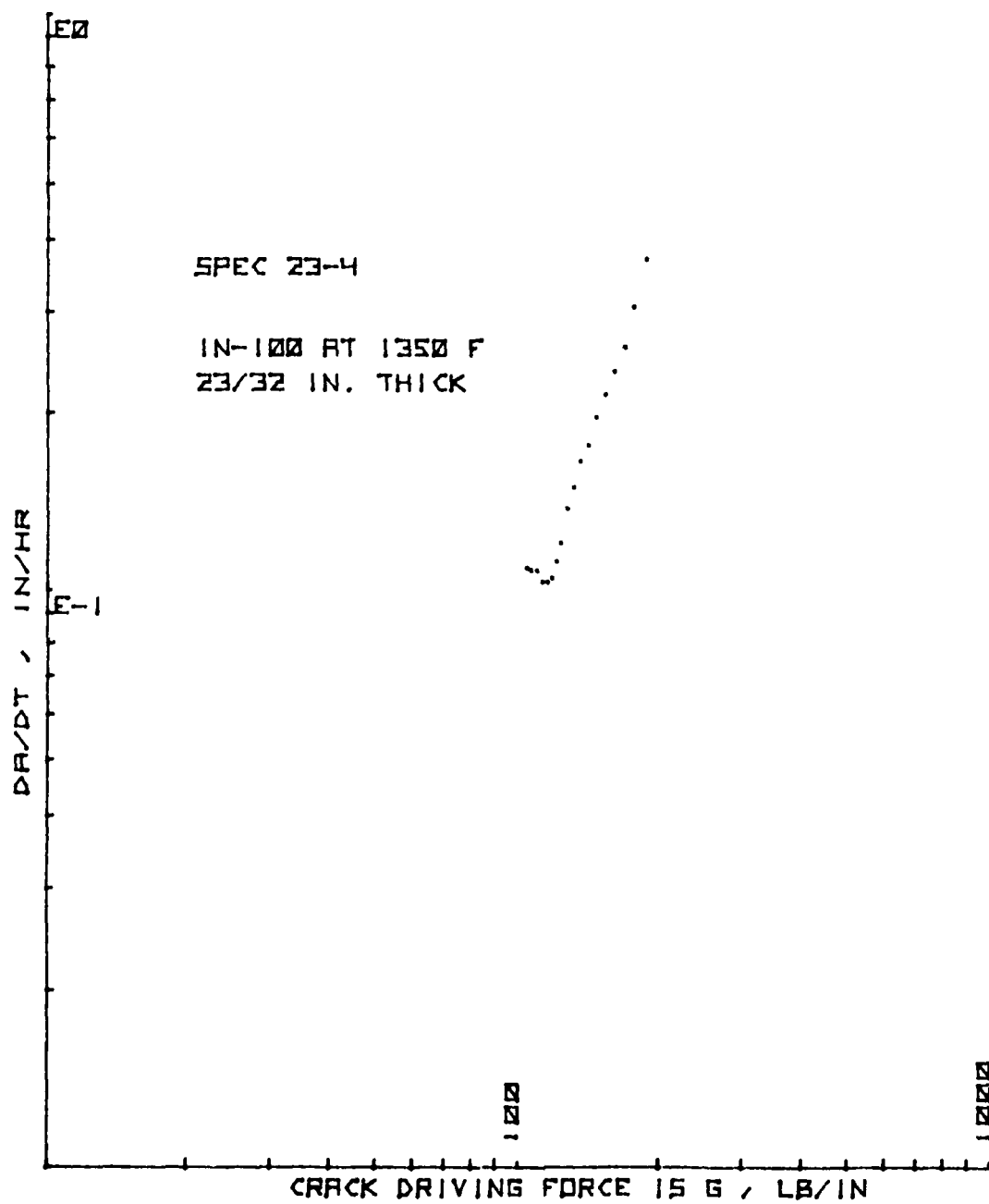
Figure 178. da/dt vs. G for CT Specimen 23-4
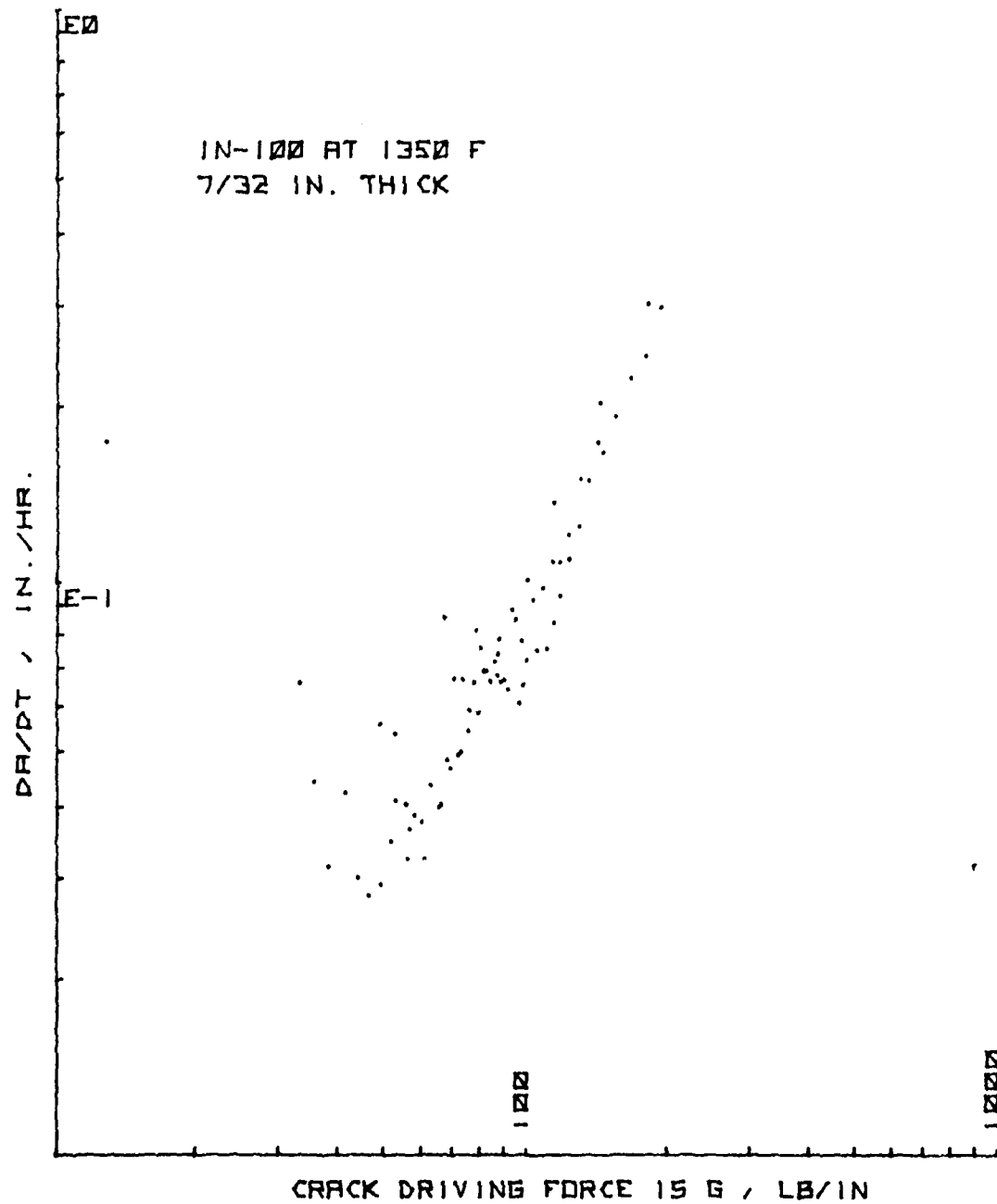
Figure 179. da/dt vs. G for the 7/32" (6 mm) Thick CT
Specimen Group
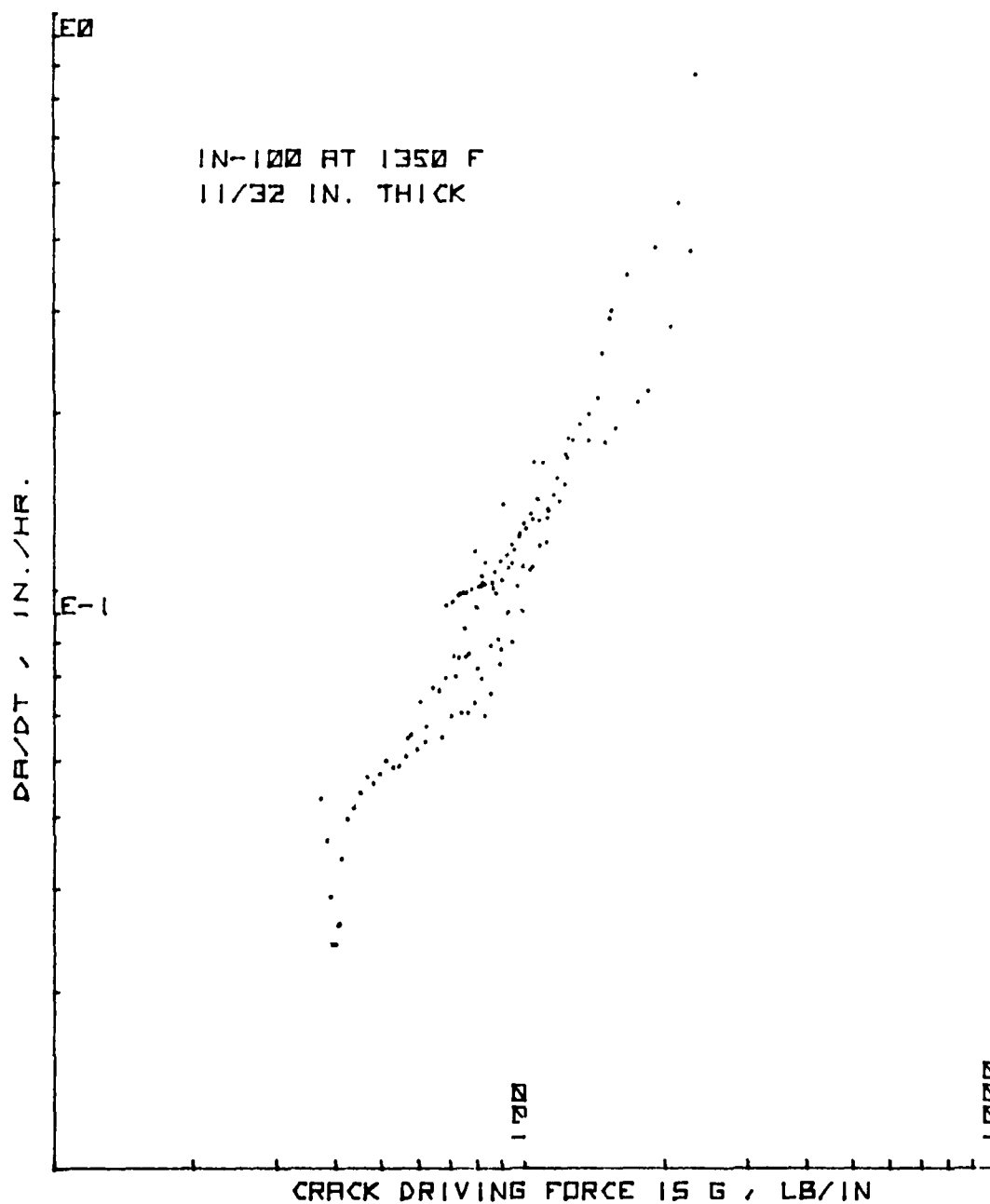
Figure 180. da/dt vs. G for the 11/32" (9 mm) Thick CT
Specimen Group

IN-100 AT 1350 F
15/32 IN. THICK
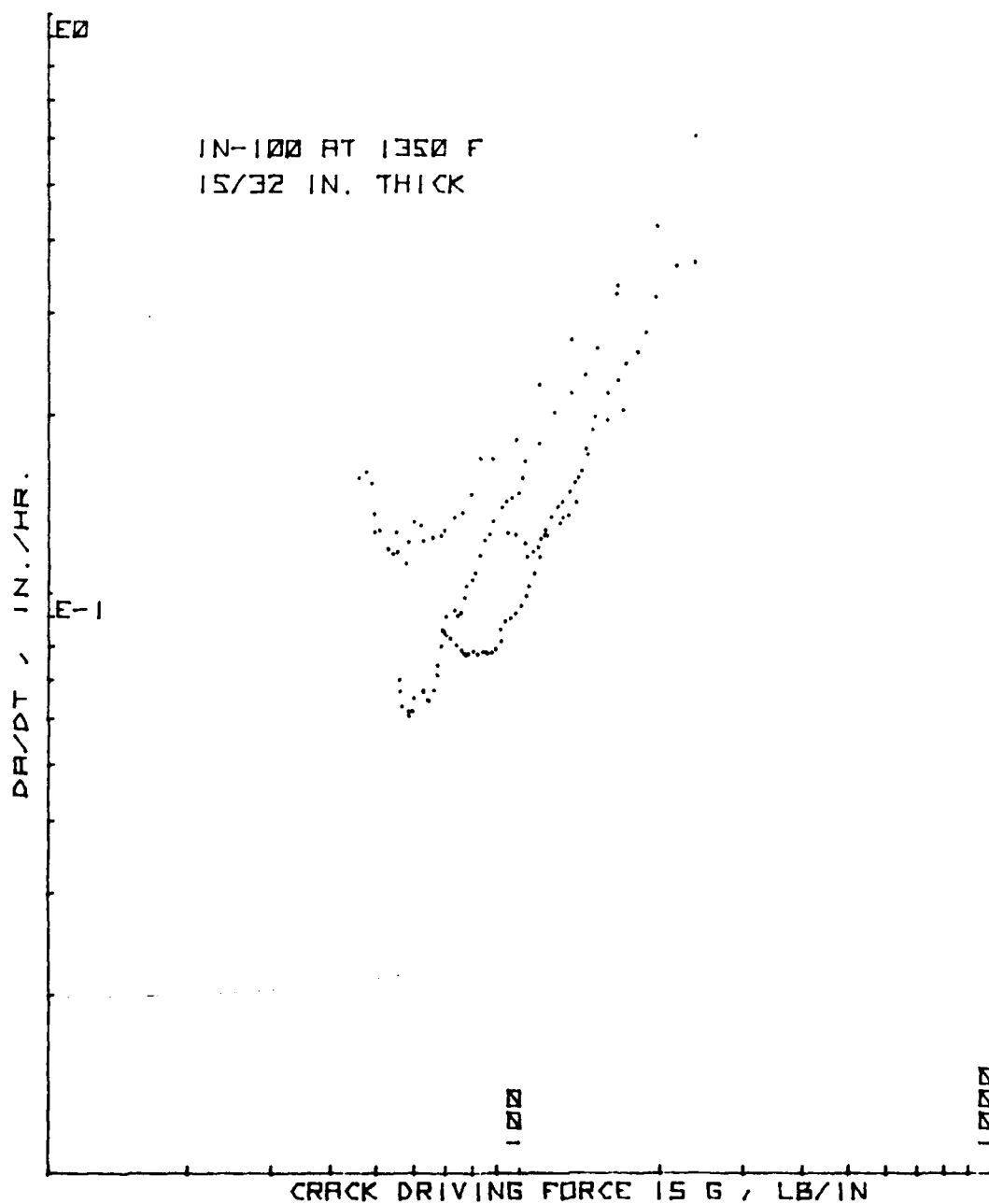
Figure 181.   da/dt vs. G for the 15/32" (12 mm) Thick CT
Specimen Group
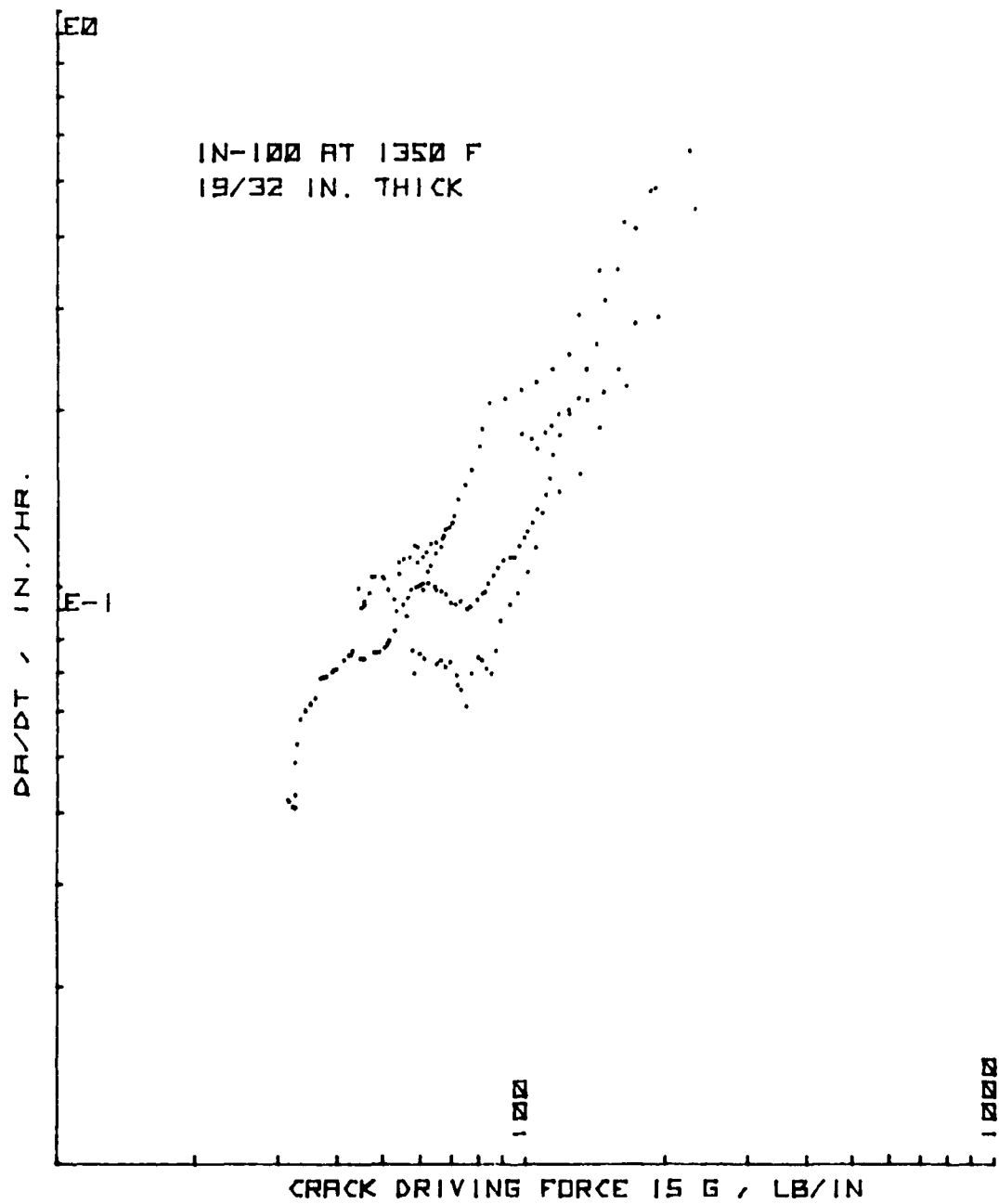
Figure 182. da/dt vs. G for the 19/32" (15 mm) Thick CT
Specimen Group
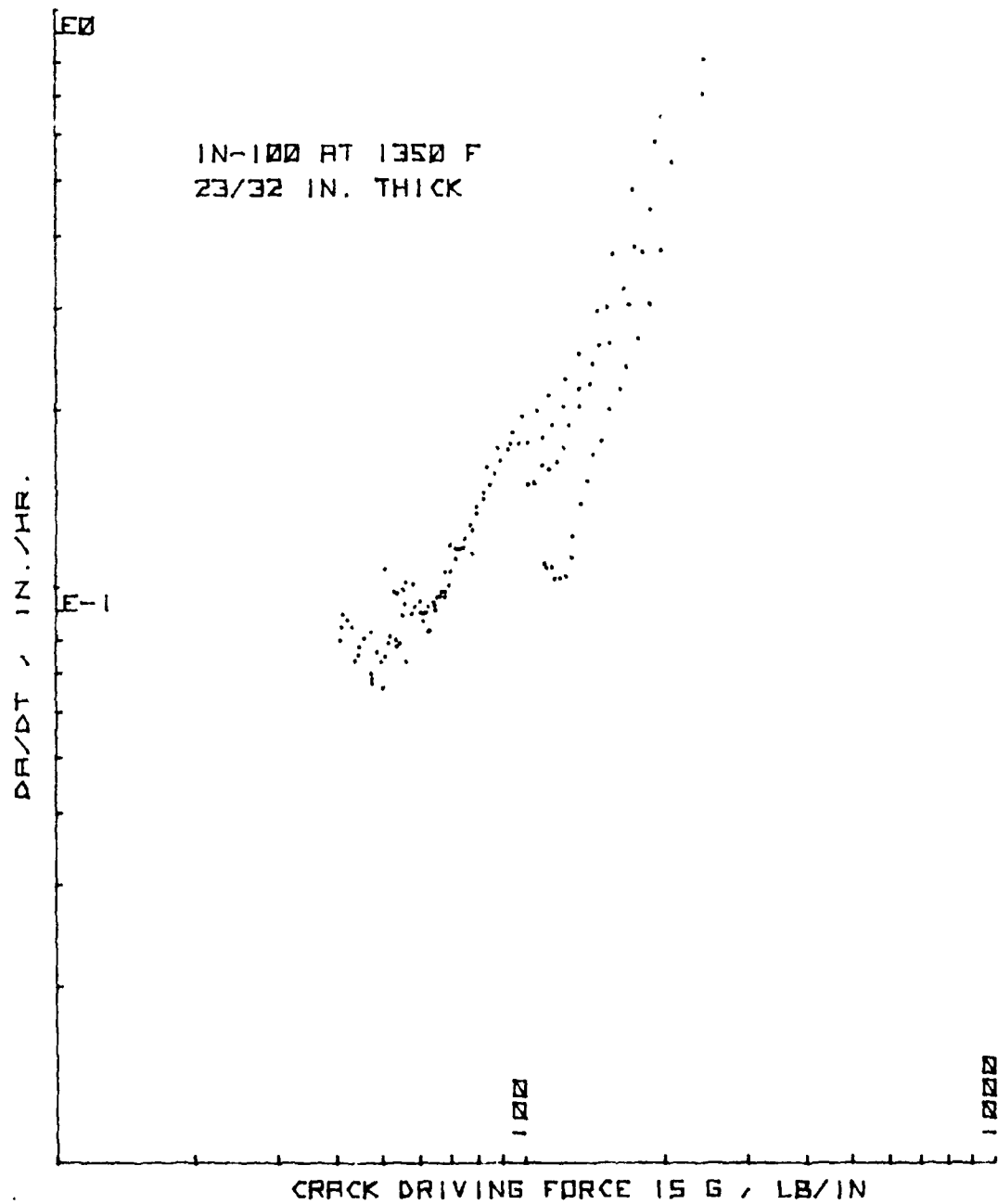
Figure 183.   da/dt vs. G for the 23/32" (18 mm) Thick CT
Specimen Group
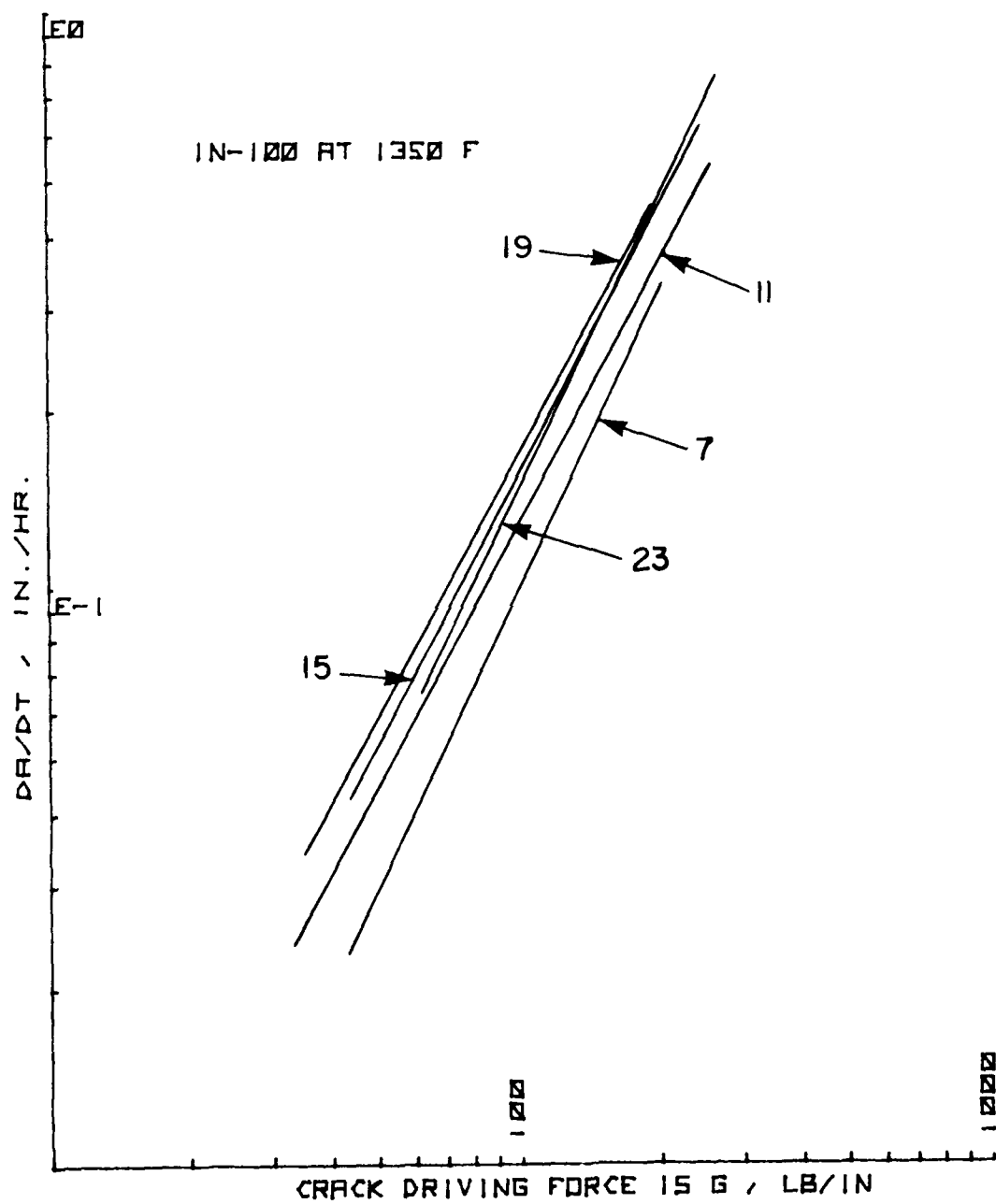
Figure 184. Crack Growth Rate Composite Plot for Crack Driving
Force, G, for Five Thicknesses of CT Specimens
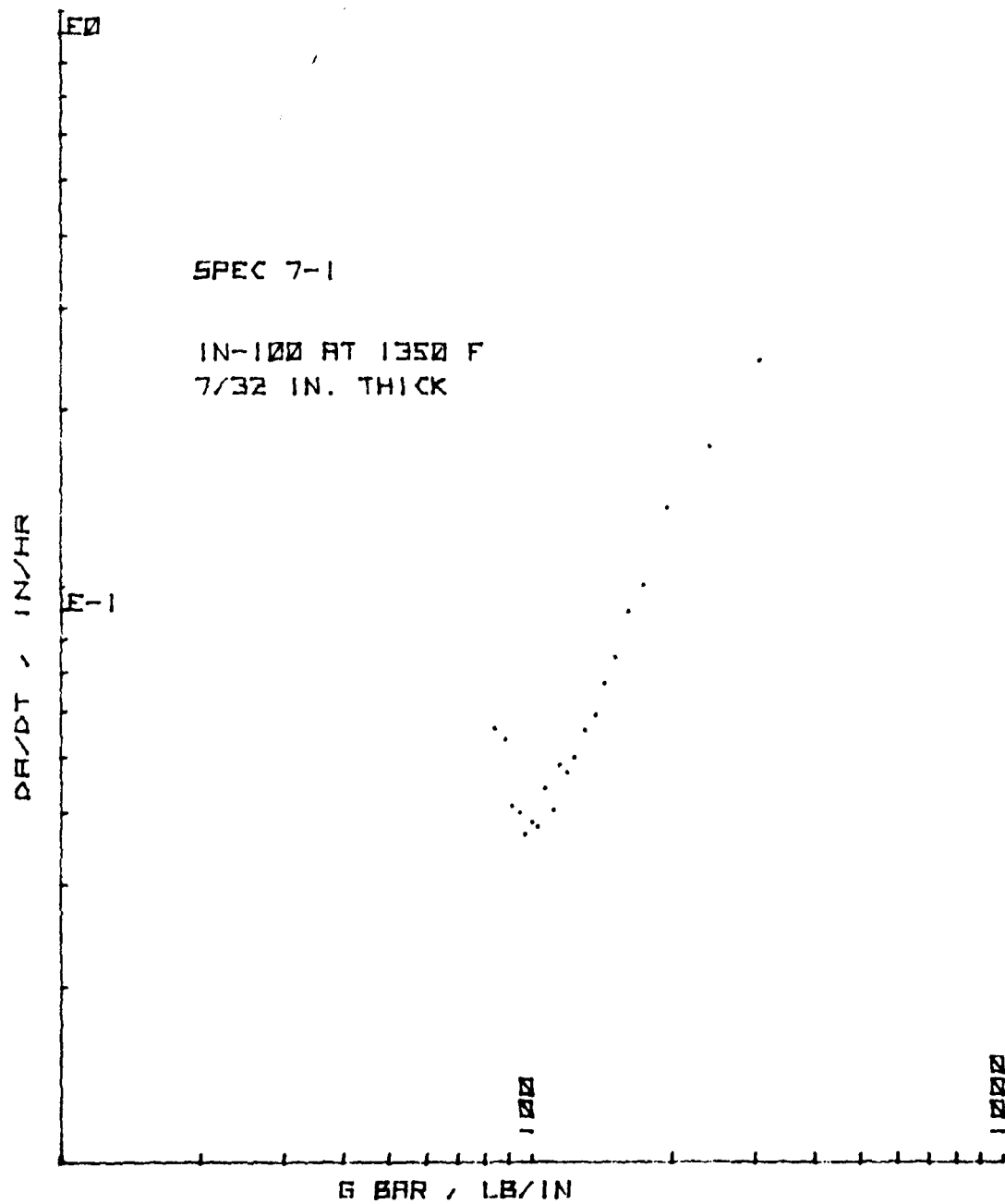
Figure 185. da/dt vs. $\bar{G}$ for CT Specimen 7-1
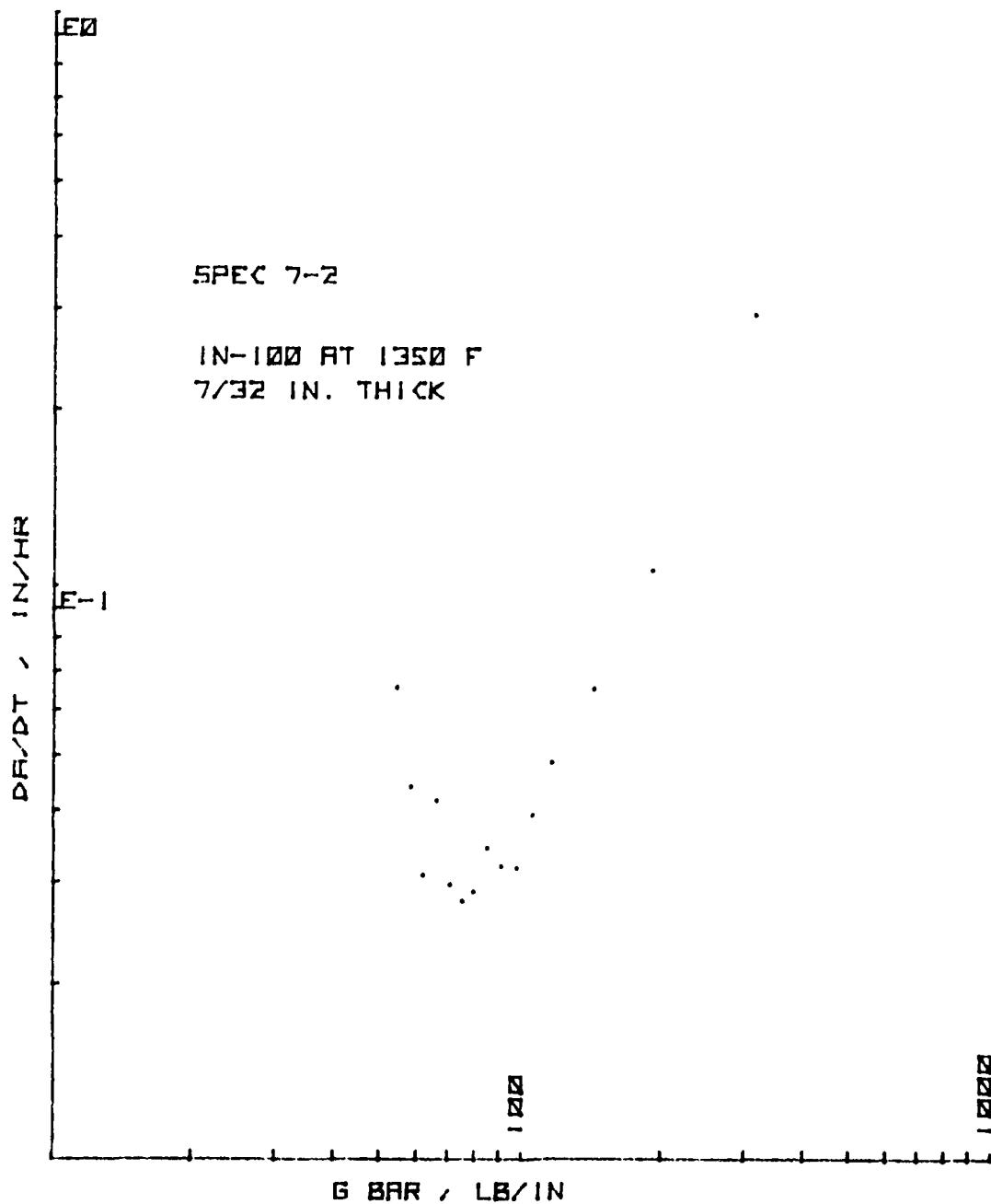
Figure 186. da/dt vs. $\overline{G}$ for CT Specimen 7-2

AFWAL-TR-80-4131
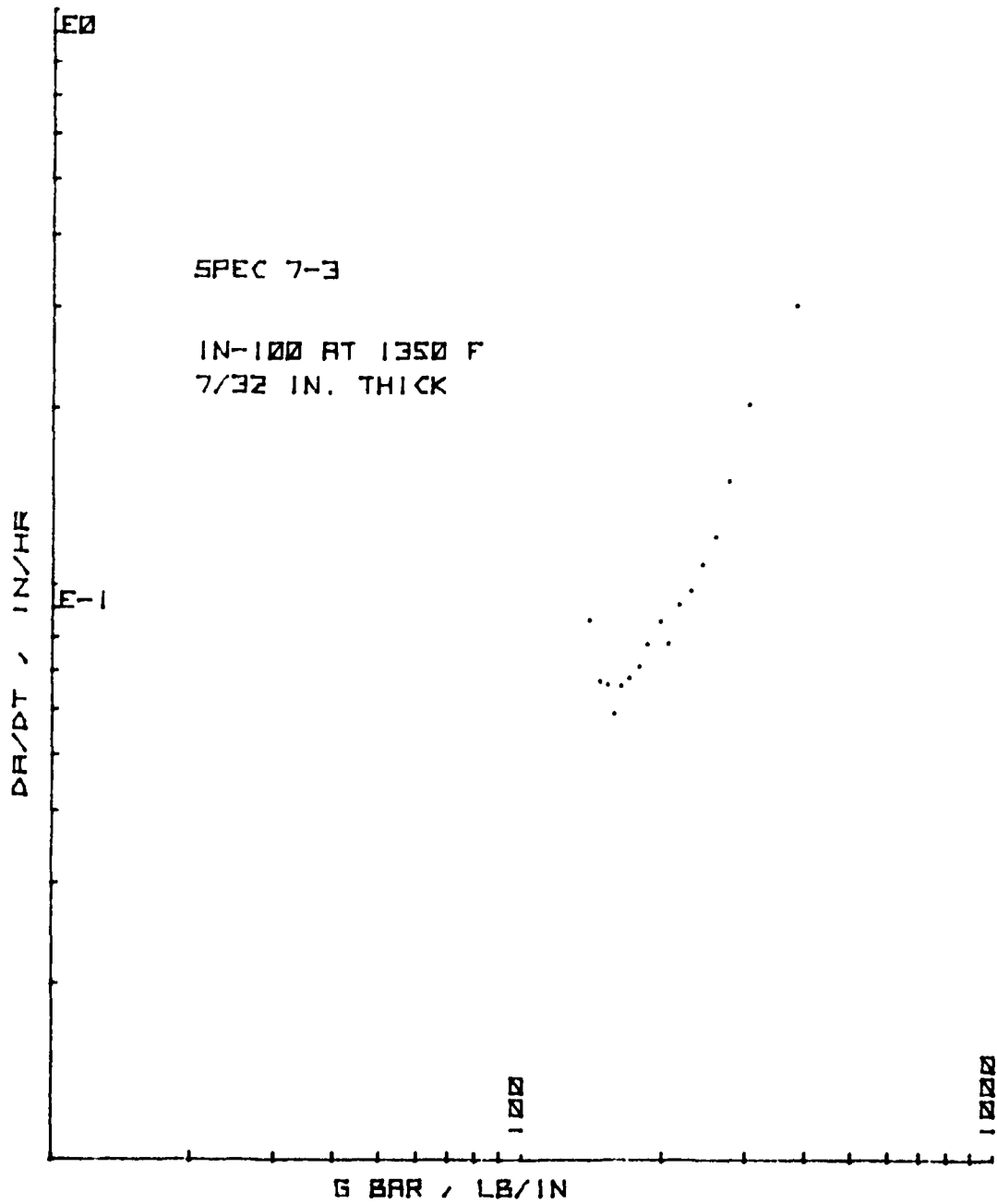
Figure 187. da/dt vs. $\overline{G}$ for CT Specimen 7-3

259
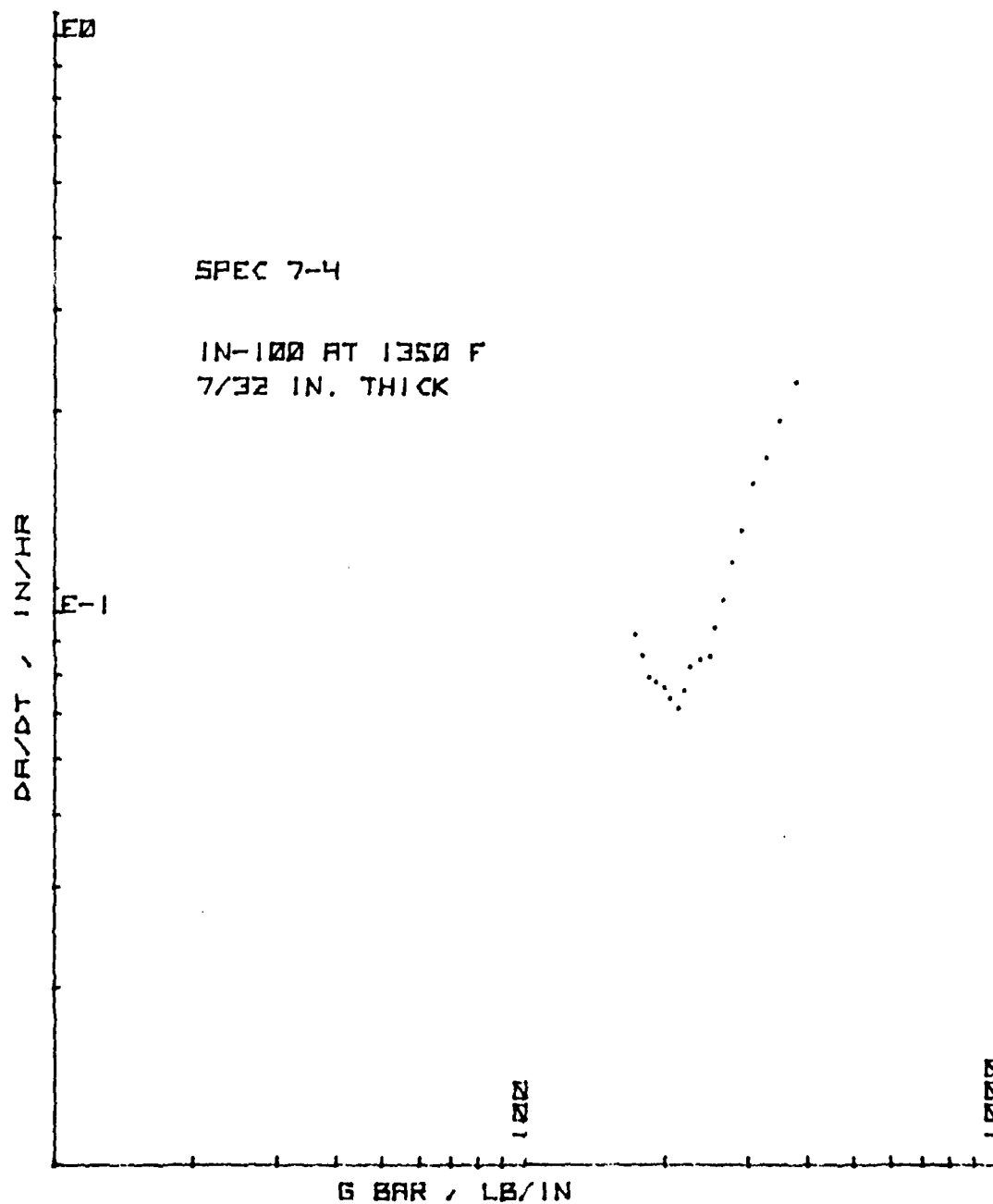
Figure 188. da/dt vs. $\bar{G}$ for CT Specimen 7-4
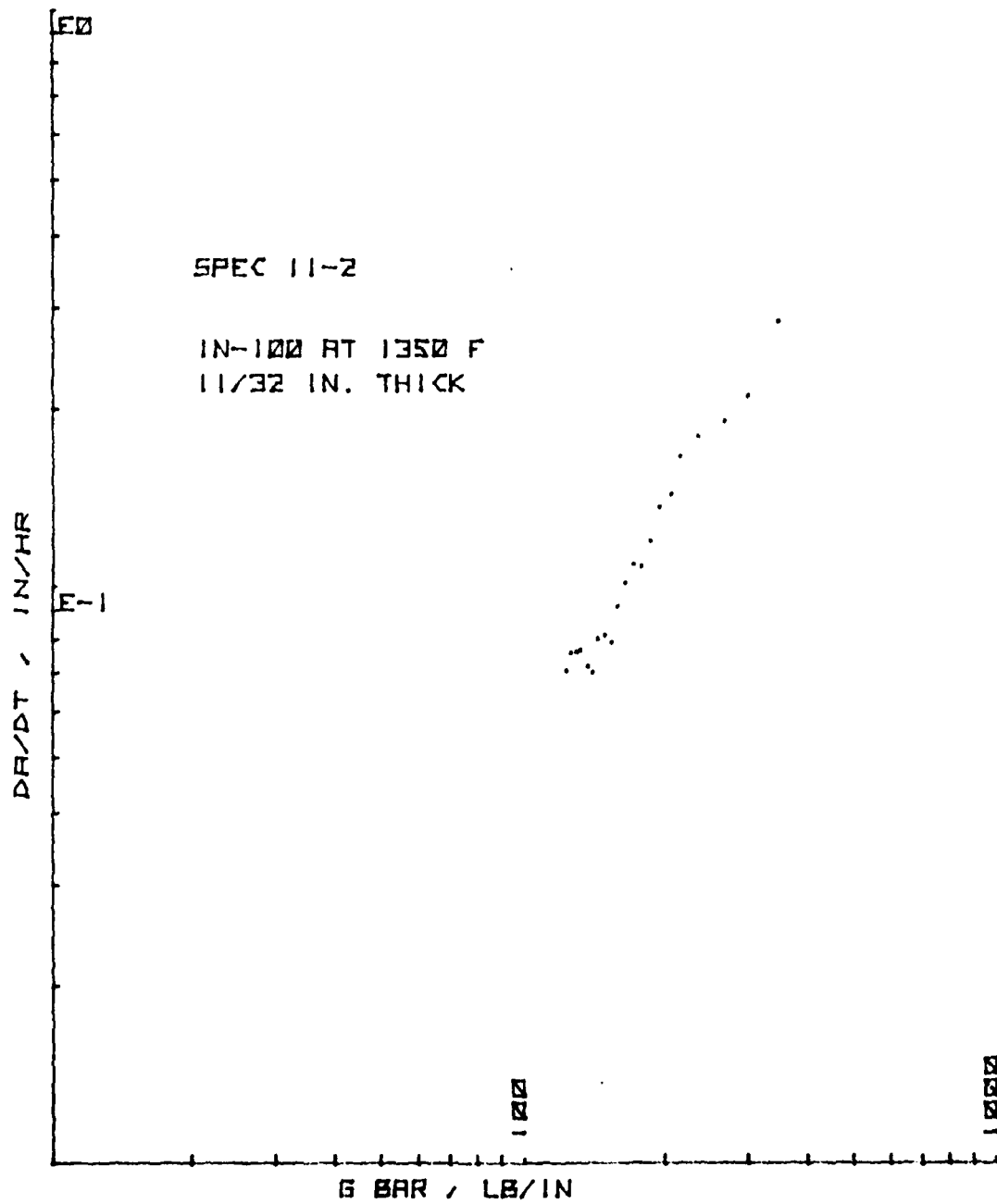
Figure 189. da/dt vs. $\overline{G}$ for CT Specimen 11-2
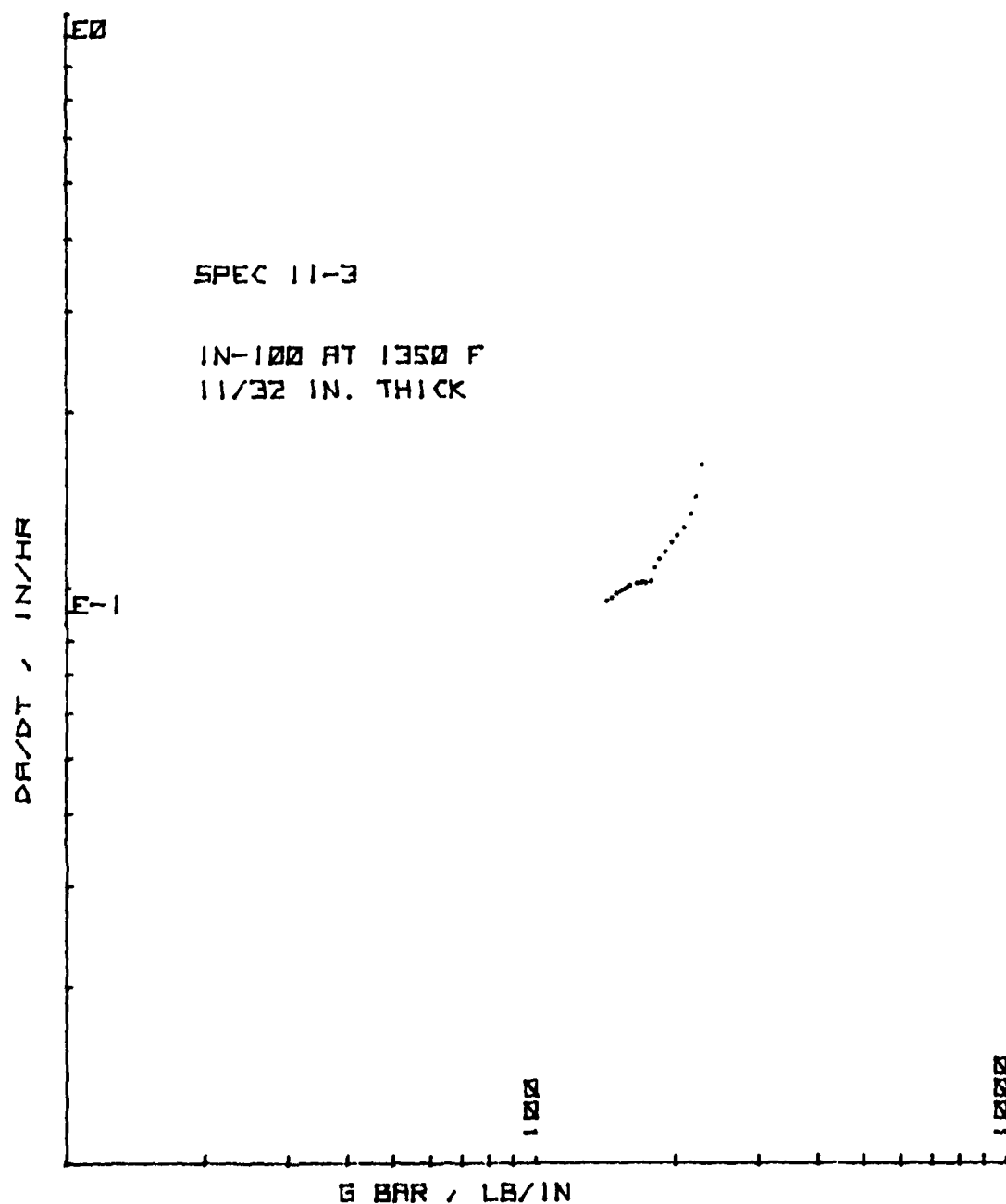
Figure 190. da/dt vs. $\overline{G}$ for CT Specimen 11-3
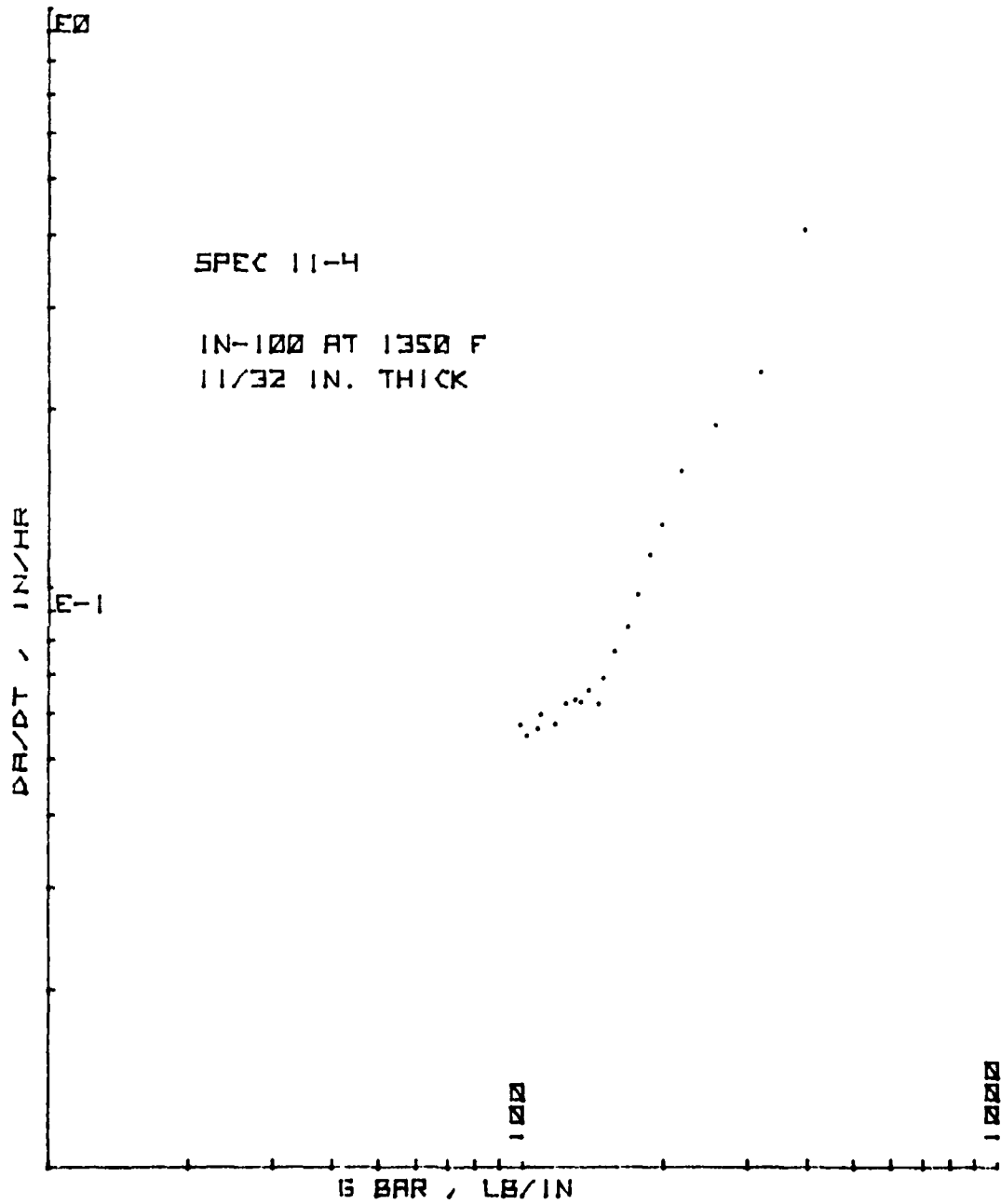
Figure 191. da/dt vs. $\bar{G}$ for CT Specimen 11-4
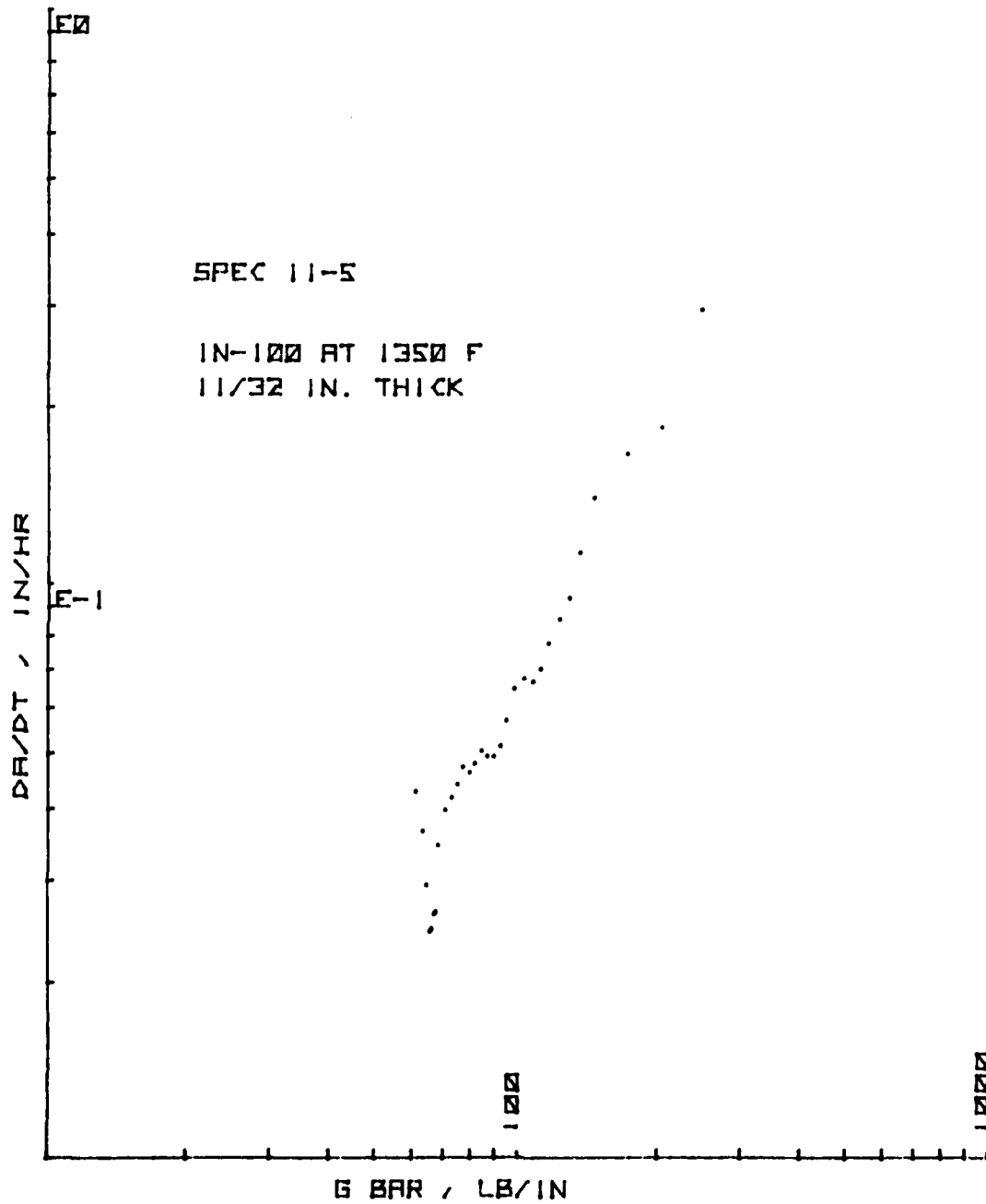
Figure 192. da/dt vs. $\overline{G}$ for CT Specimen 11-5
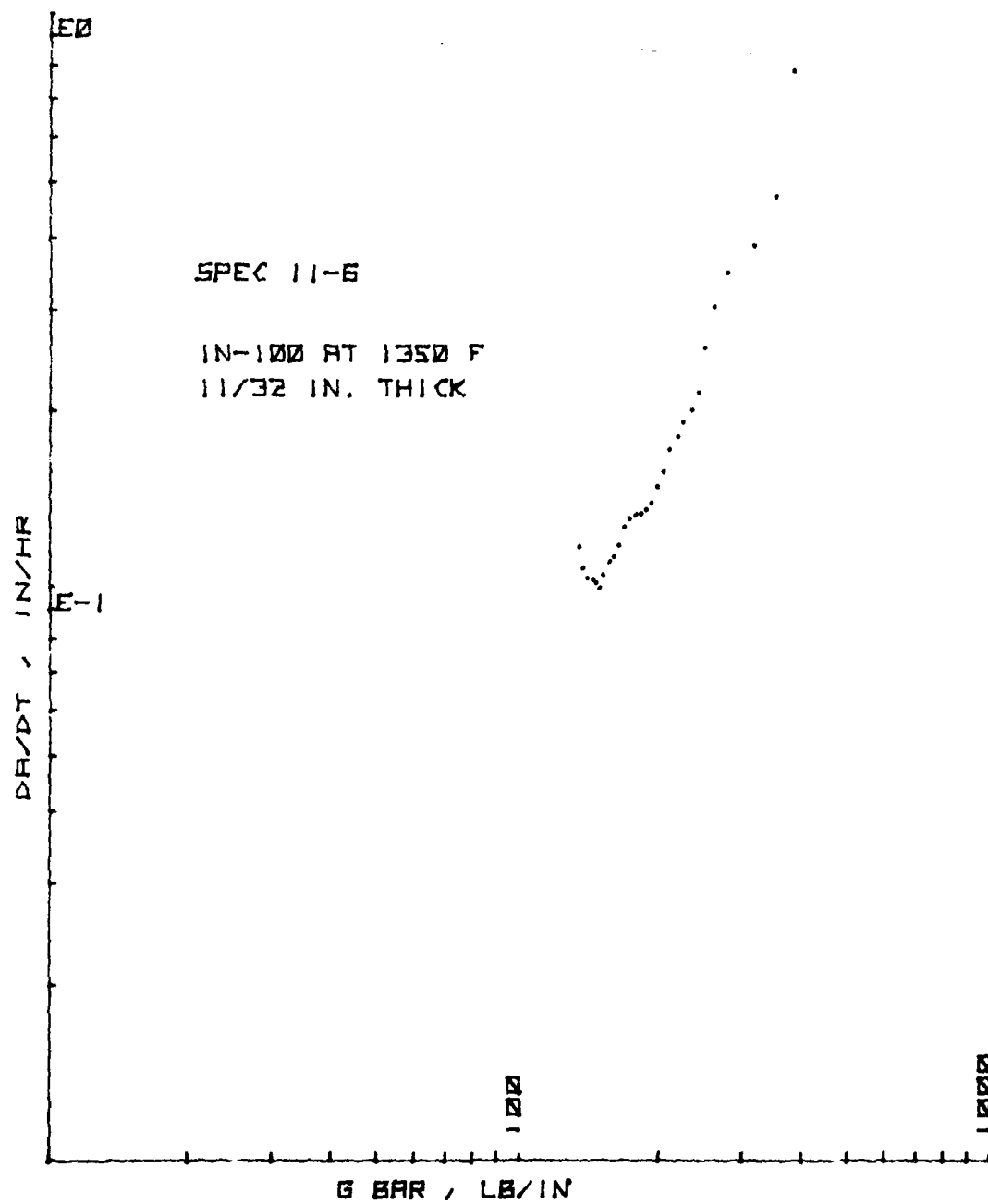
Figure 193. da/dt vs. $\overline{G}$ for CT Specimen 11-6
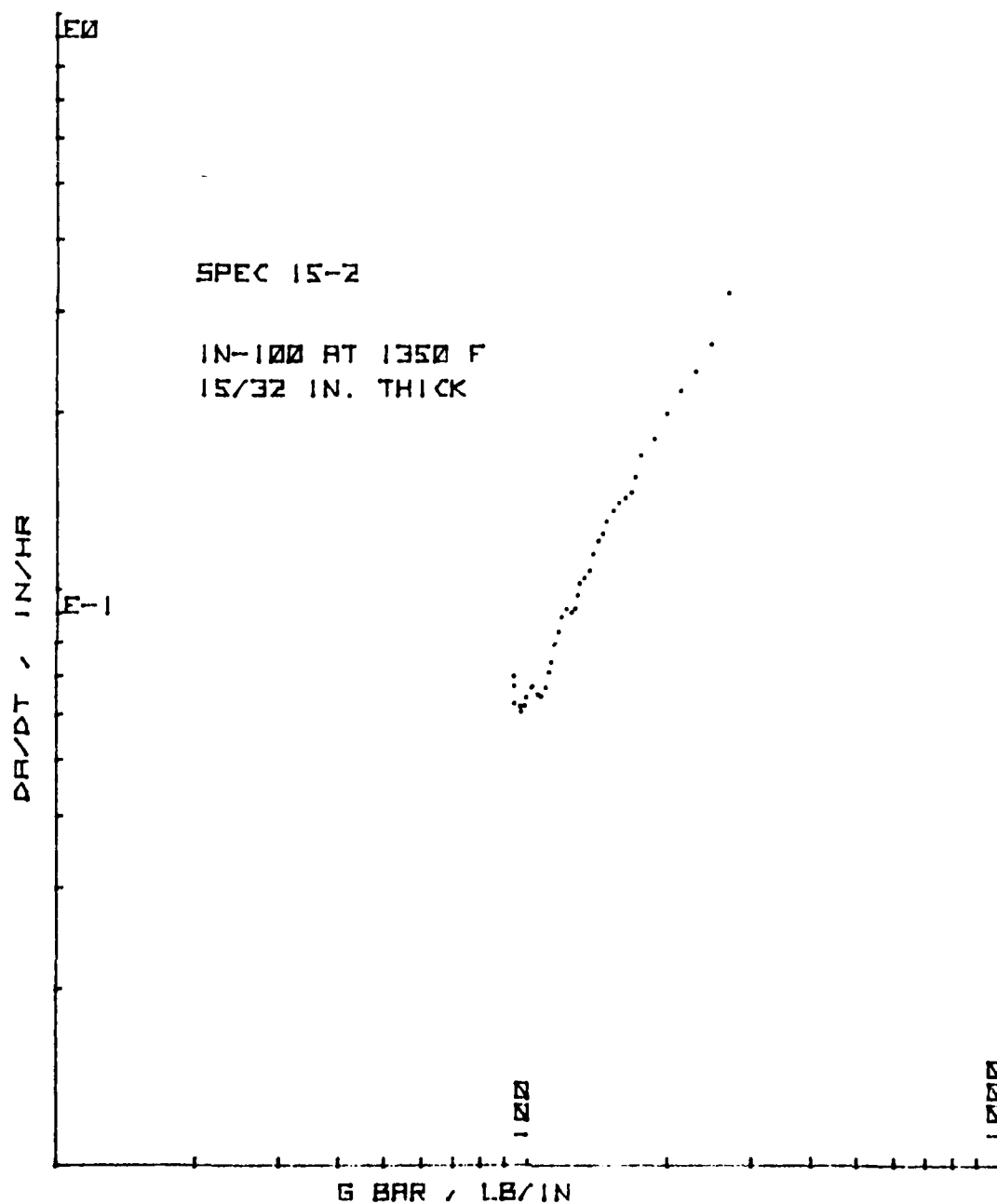
Figure 194. da/dt vs. $\bar{G}$ for CT Specimen 15-2

266
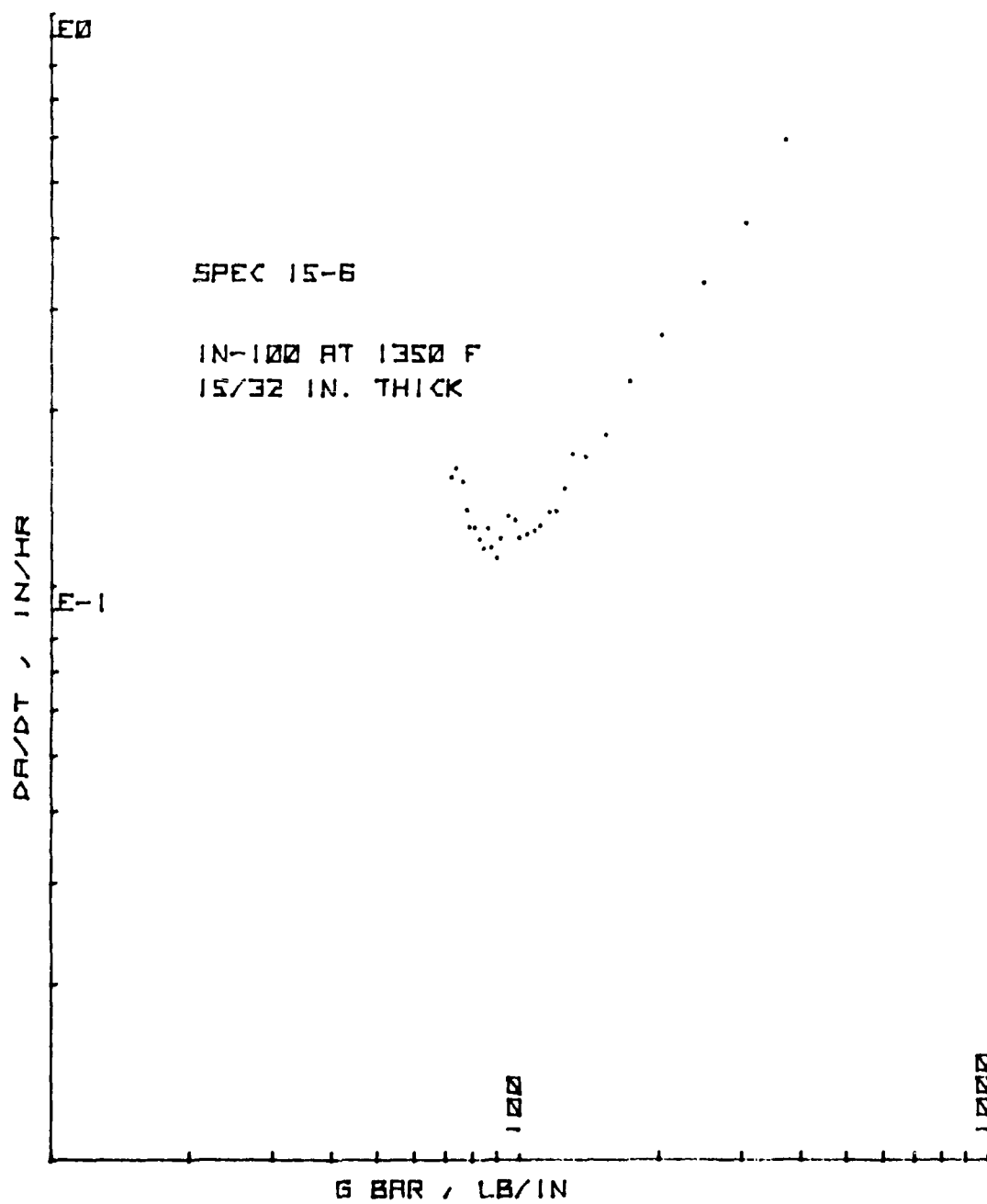
Figure 195. da/dt vs. $\bar{G}$ for CT Specimen 15-6
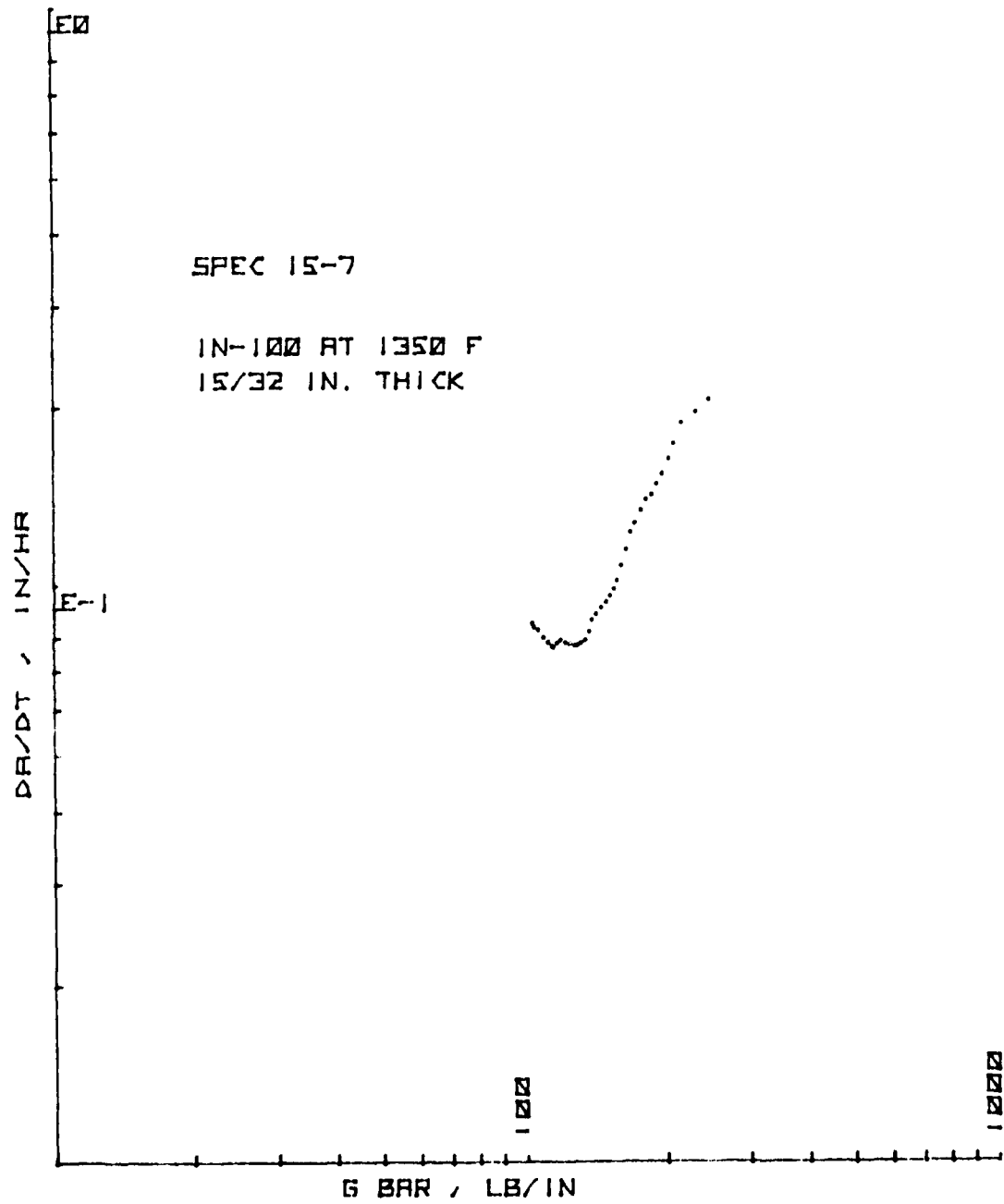
Figure 196.   da/dt vs. $\overline{G}$ for CT Specimen 15-7
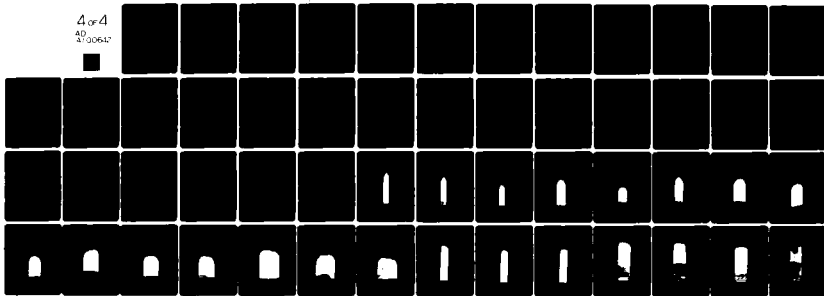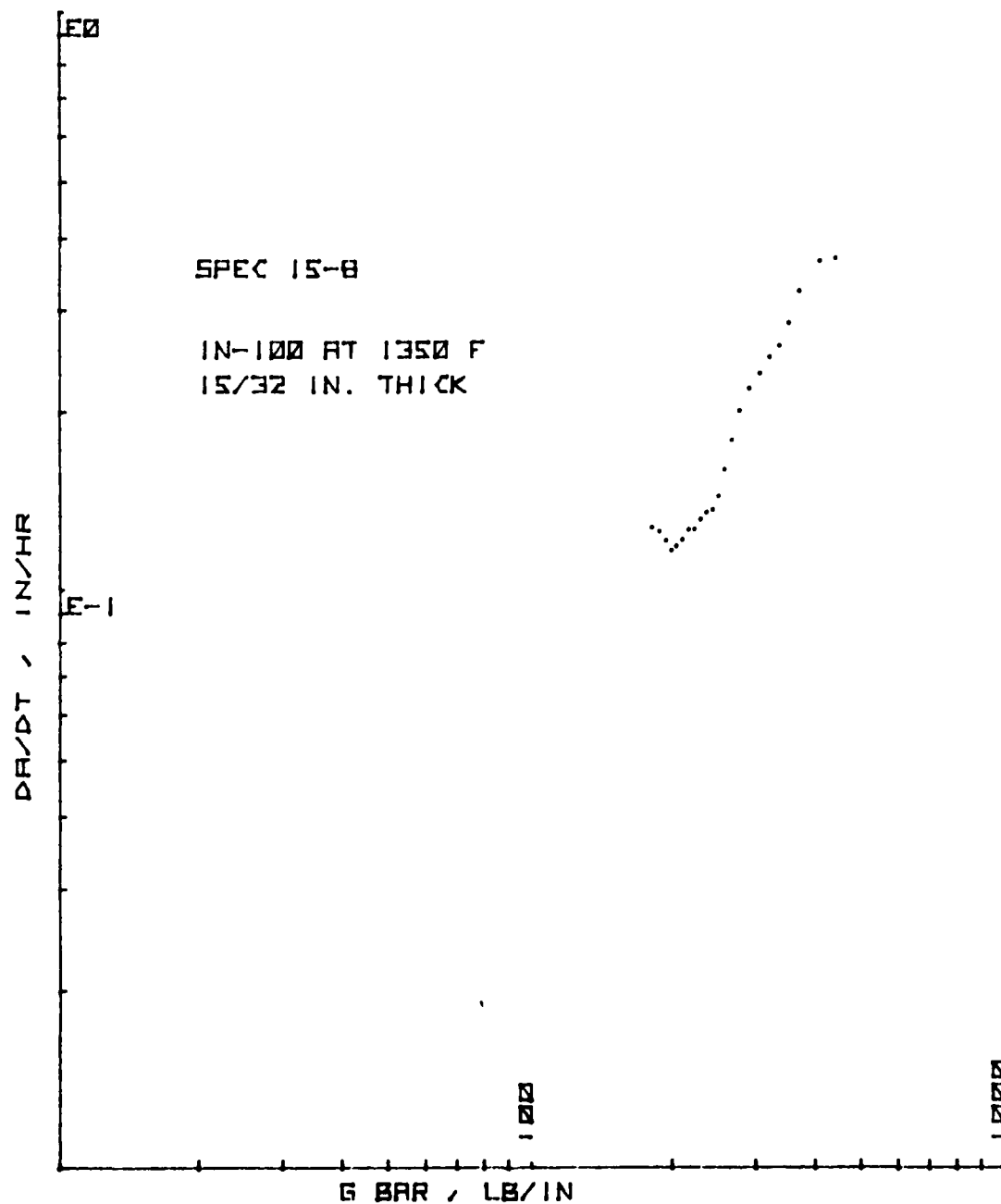
Figure 197.   da/dt vs. $\overline{G}$ for CT Specimen 15-8
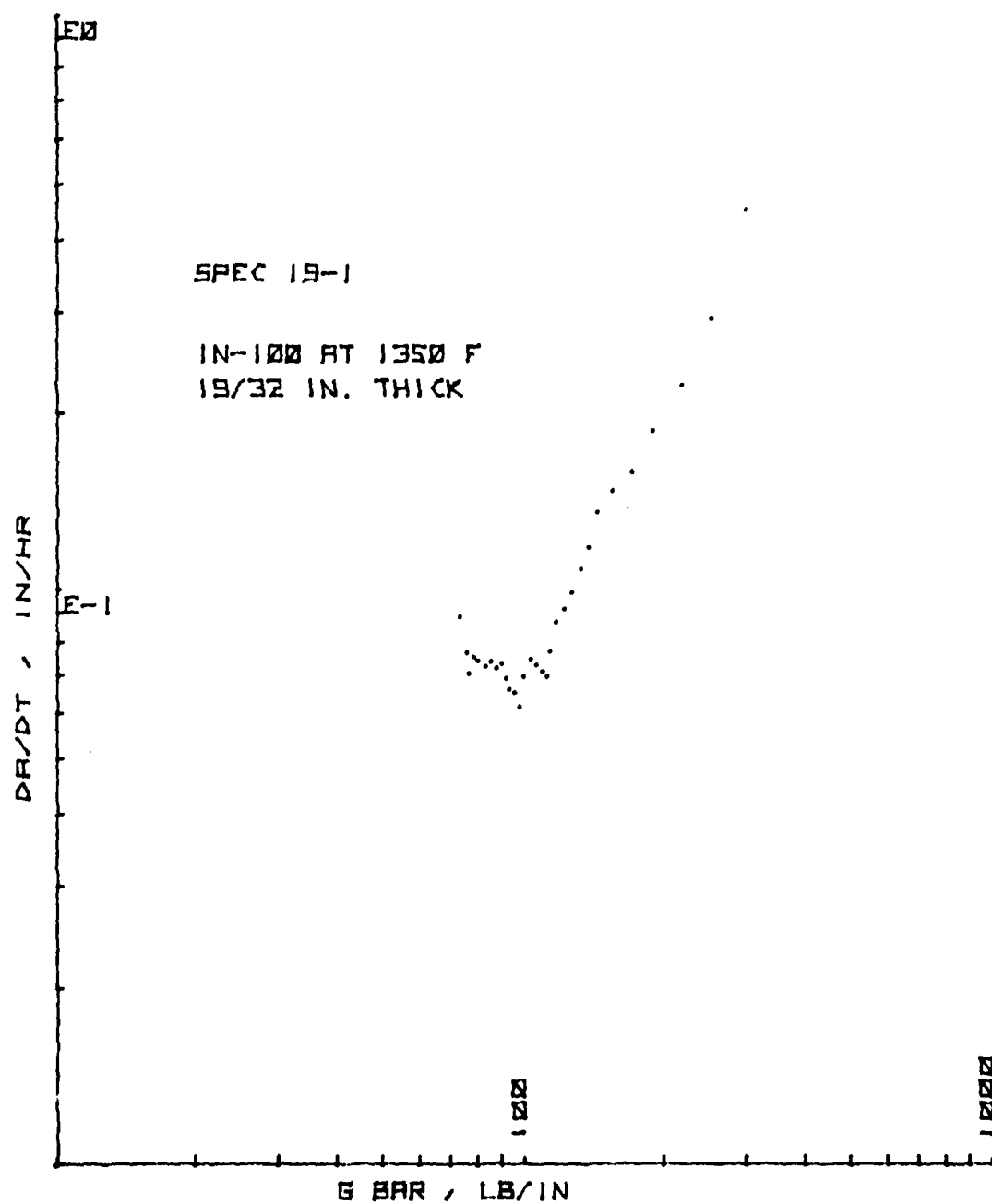
Figure 198. da/dt vs. $\overline{G}$ for CT Specimen 19-1
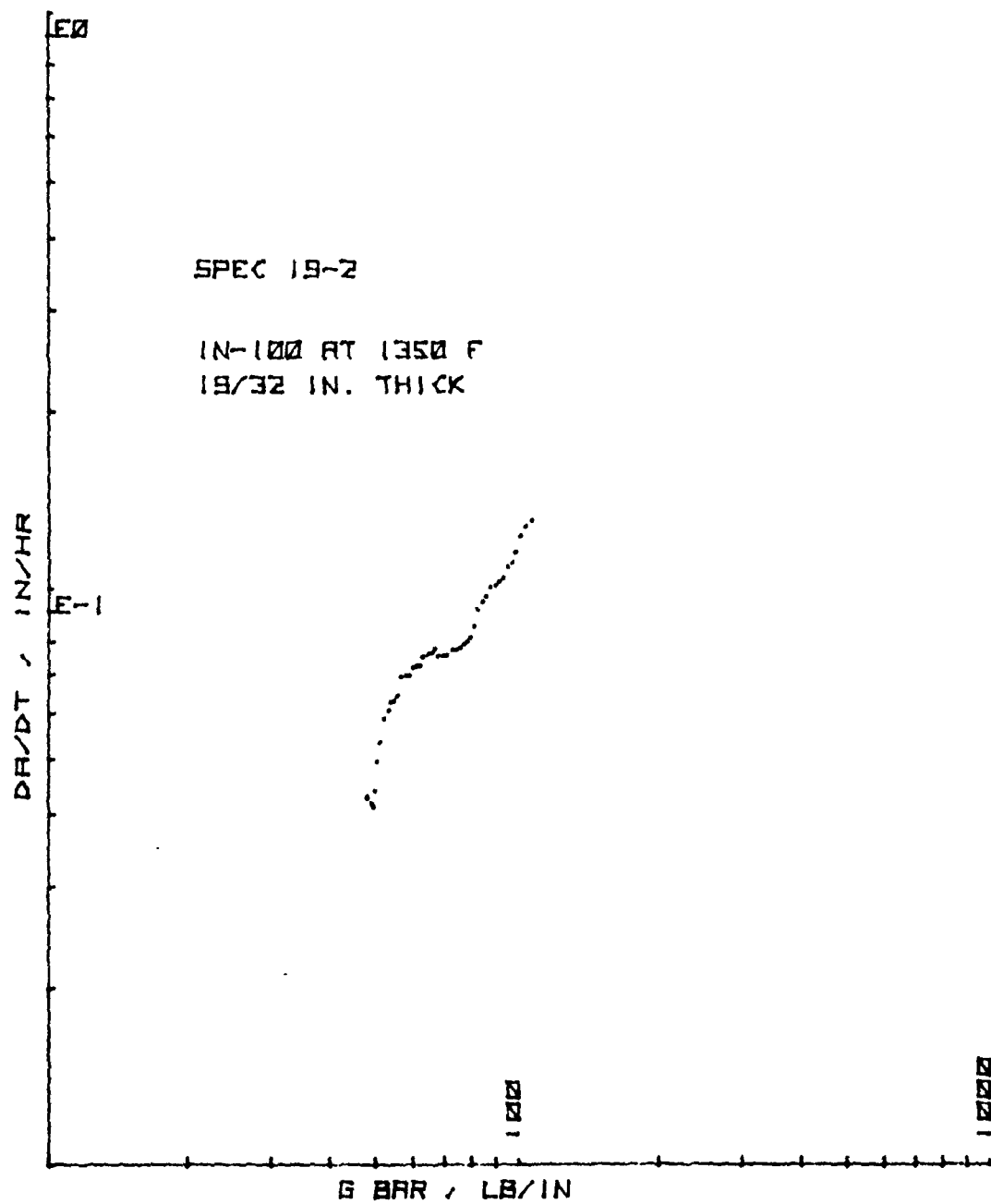
Figure 199. da/dt vs. Ḡ for CT Specimen 19-2
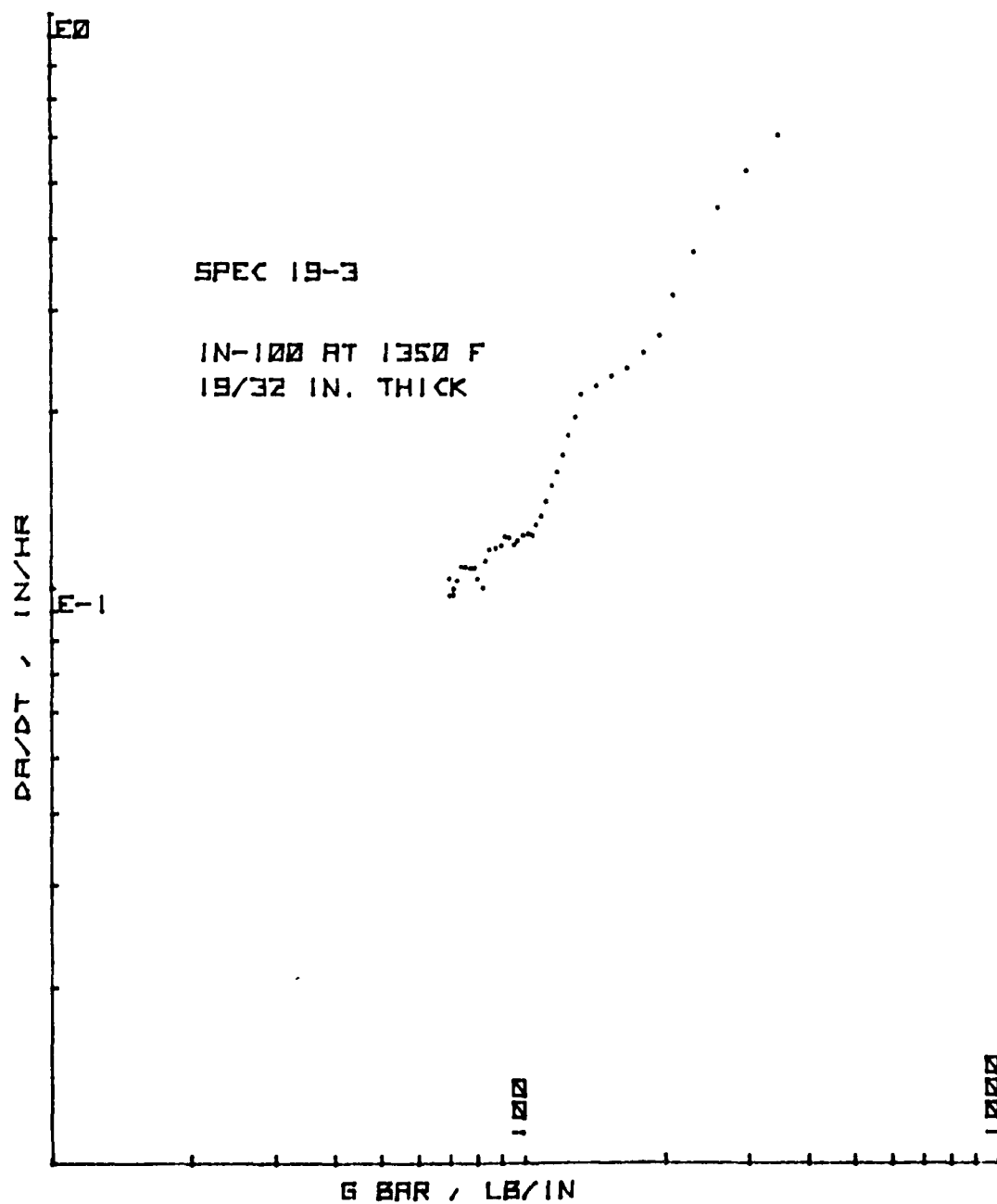
Figure 200.   da/dt vs. $\overline{G}$ for CT Specimen 19-3
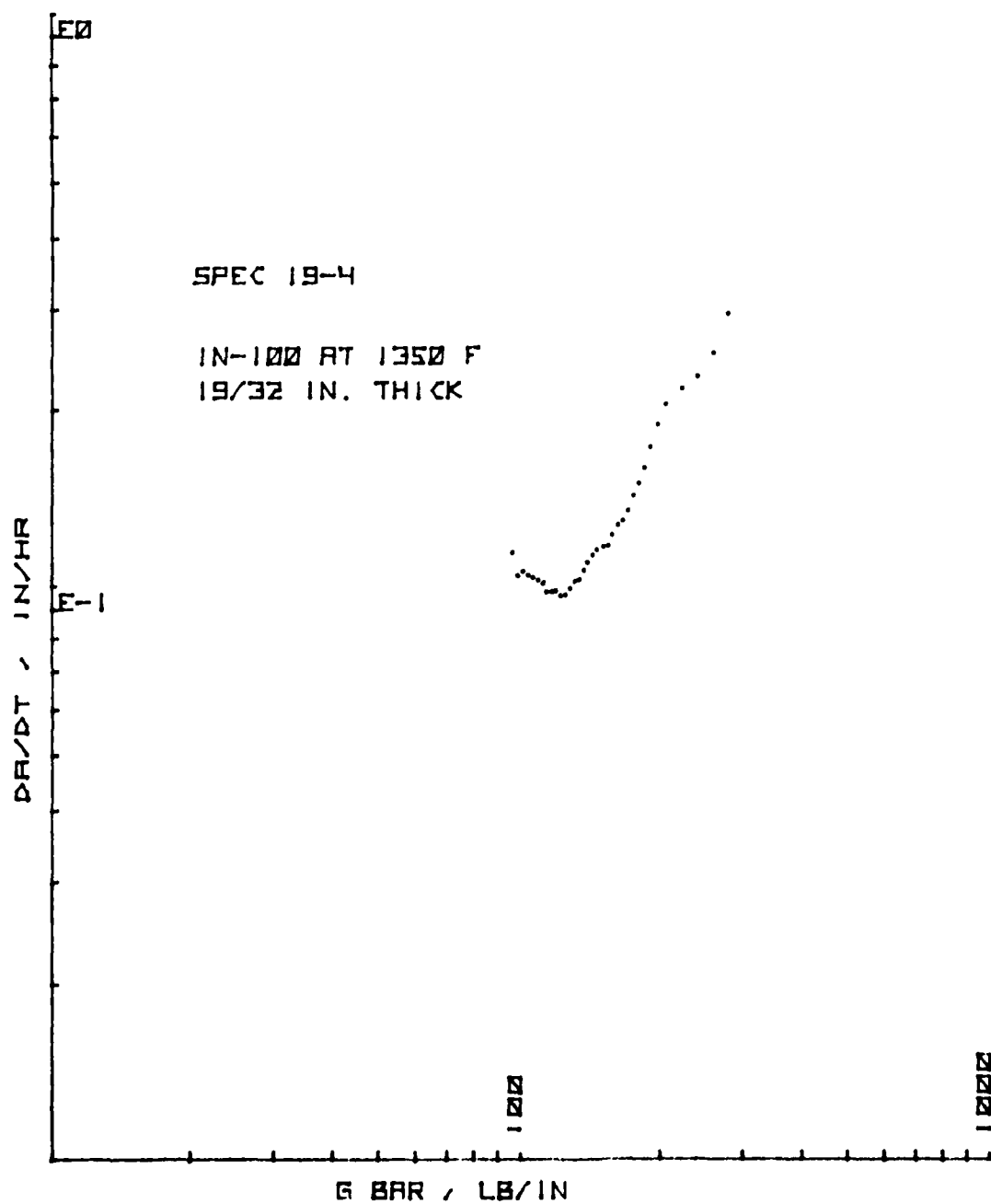
Figure 201. da/dt vs. $\overline{G}$ for CT Specimen 19-4
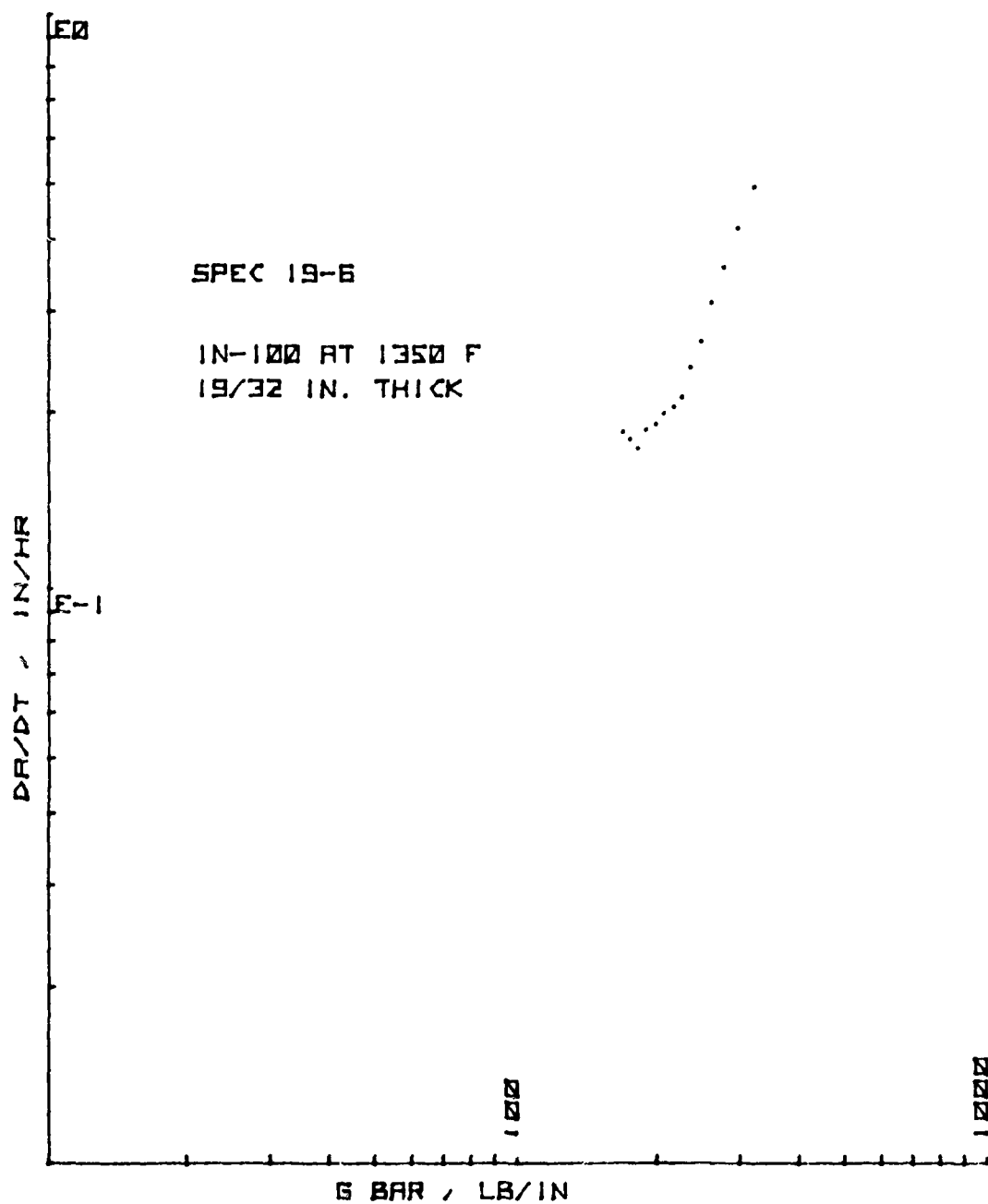
Figure 202. da/dt vs. $\overline{G}$ for CT Specimen 19-6
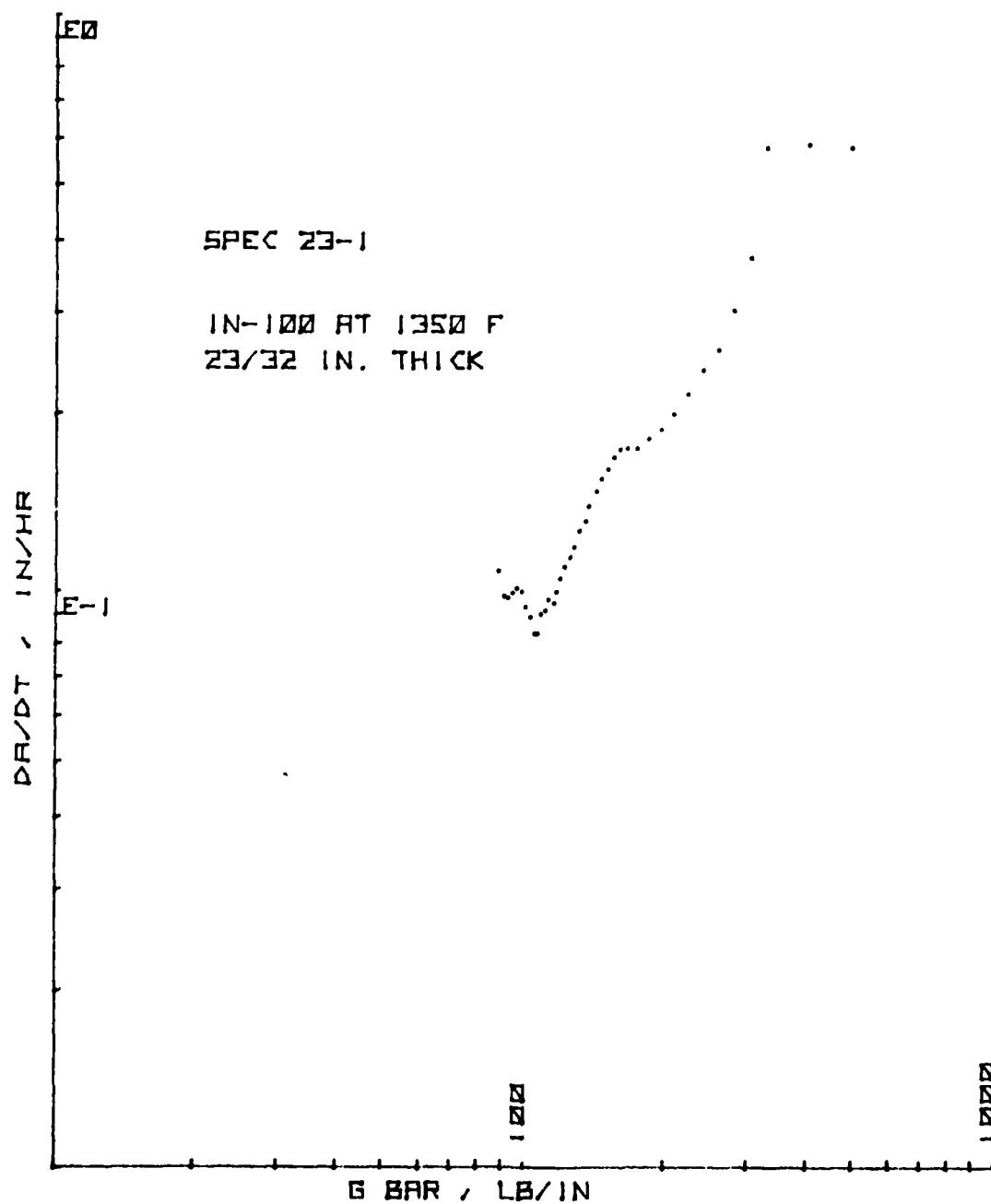
Figure 203.   da/dt vs. $\overline{G}$ for CT Specimen 23-1
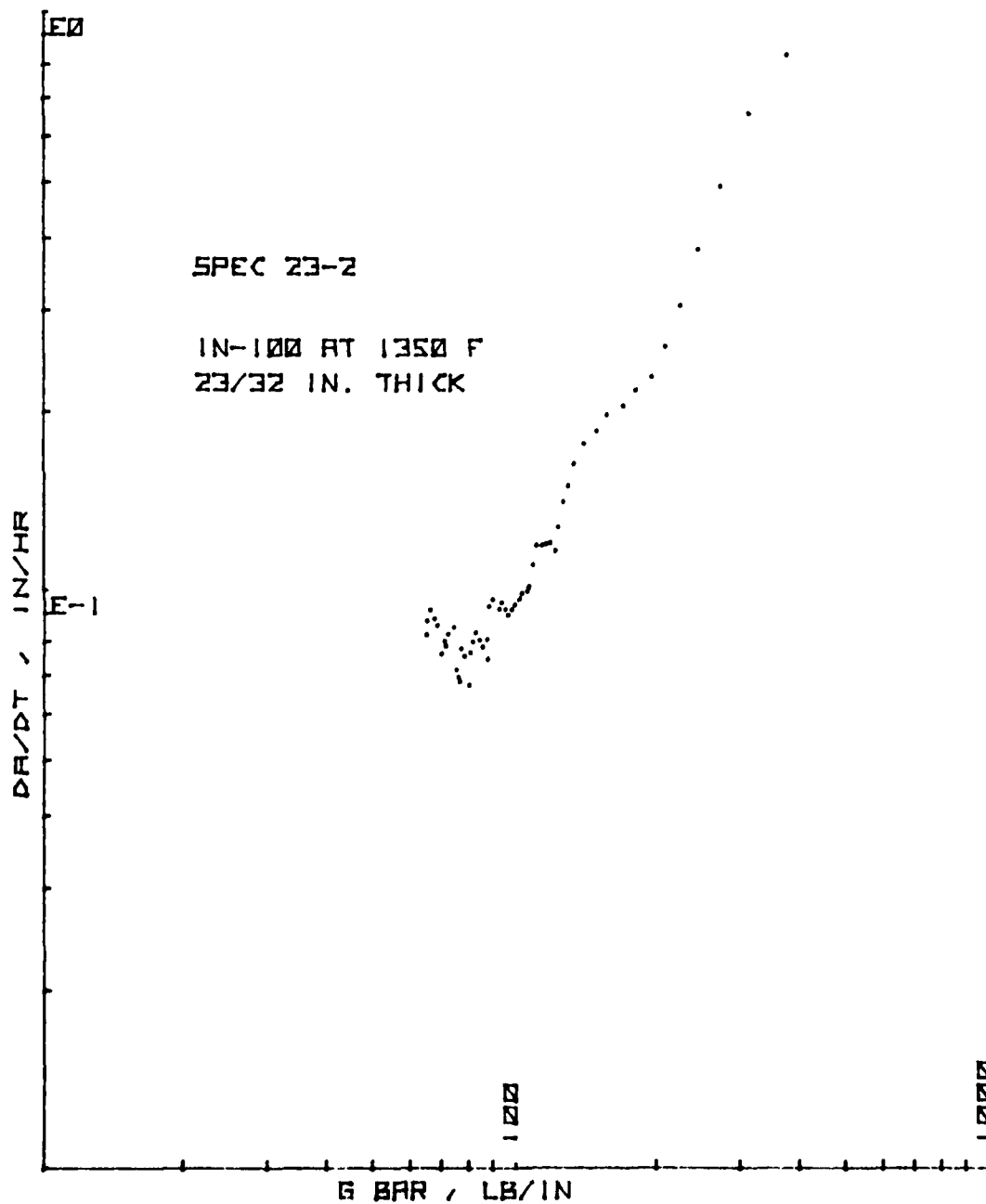
Figure 204.   da/dt vs. $\bar{G}$ for CT Specimen 23-2
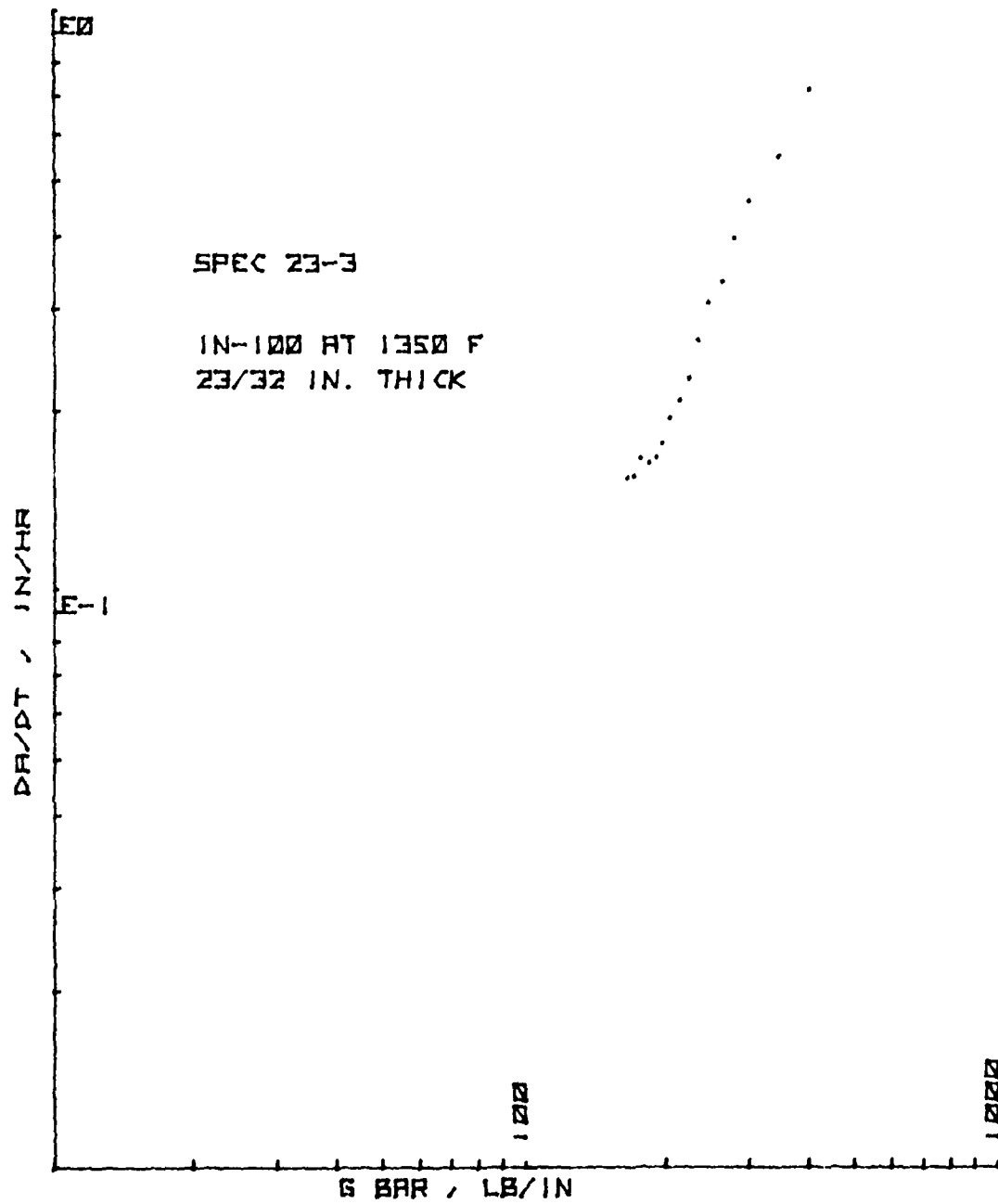
Figure 205. da/dt vs. $\overline{G}$ for CT Specimen 23-3
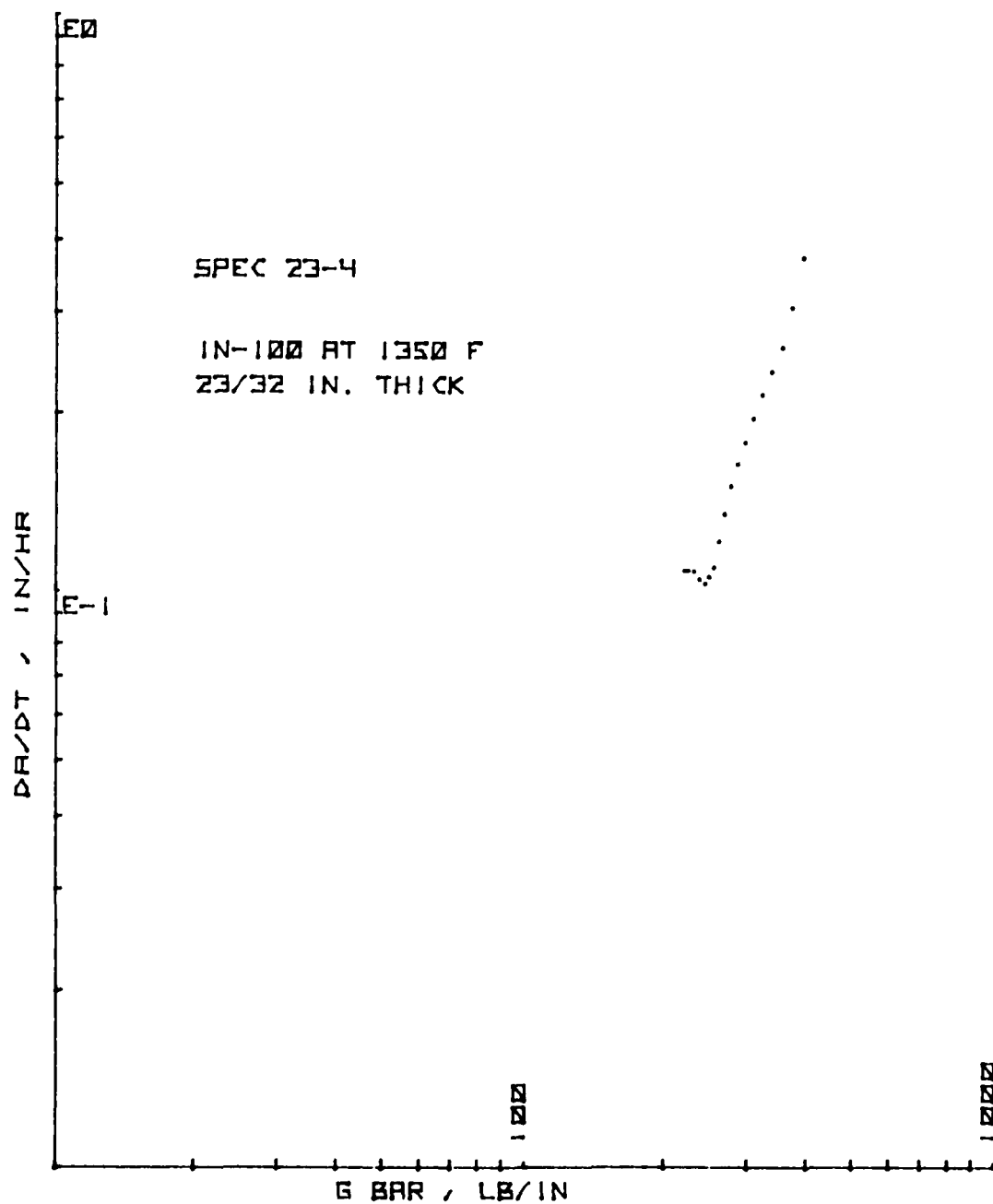
Figure 206. da/dt vs. $\bar{G}$ for CT Specimen 23-4
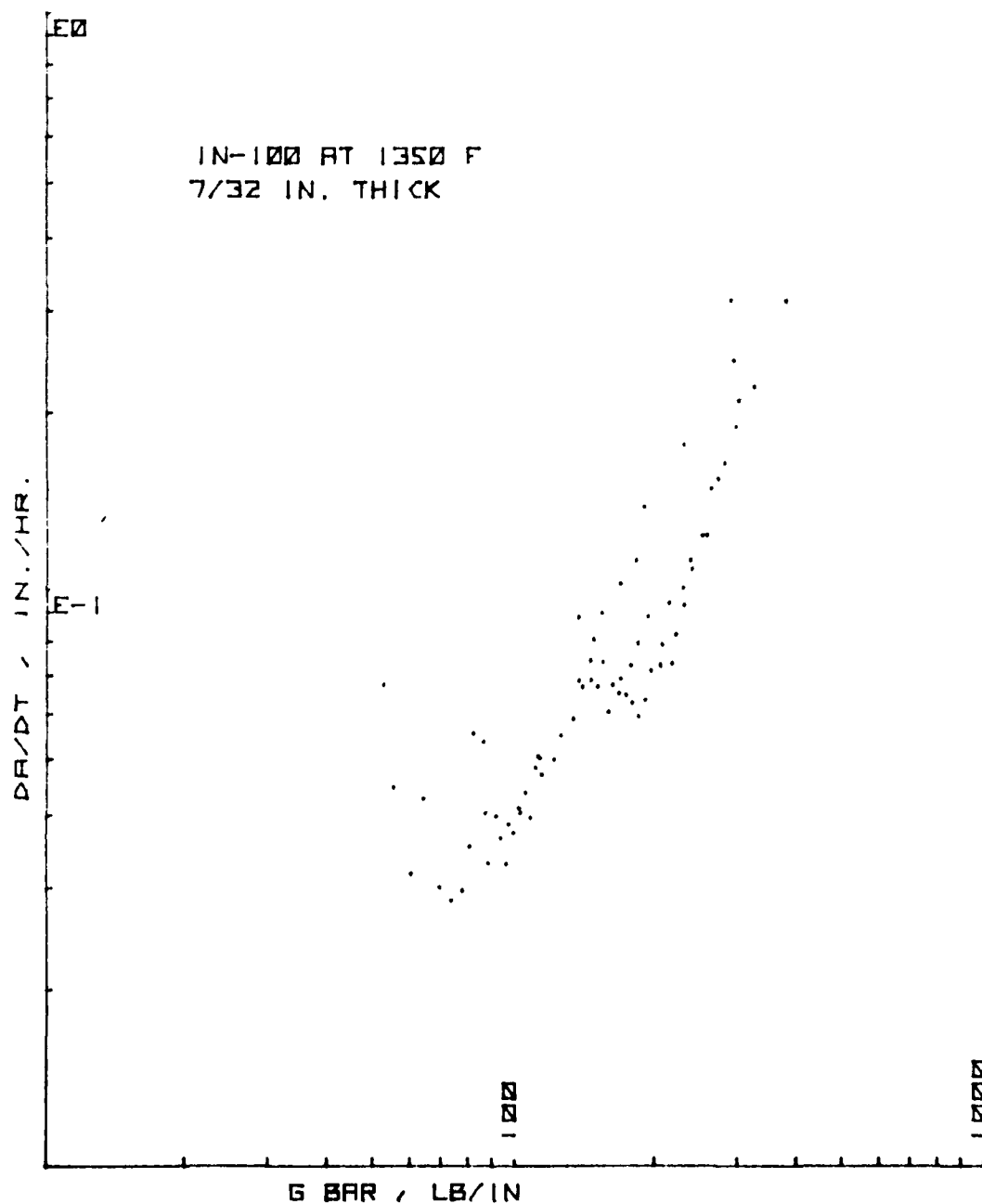
Figure 207.   da/dt vs. $\overline{G}$ for the 7/32" (6 mm) Thick CT
Specimen Group
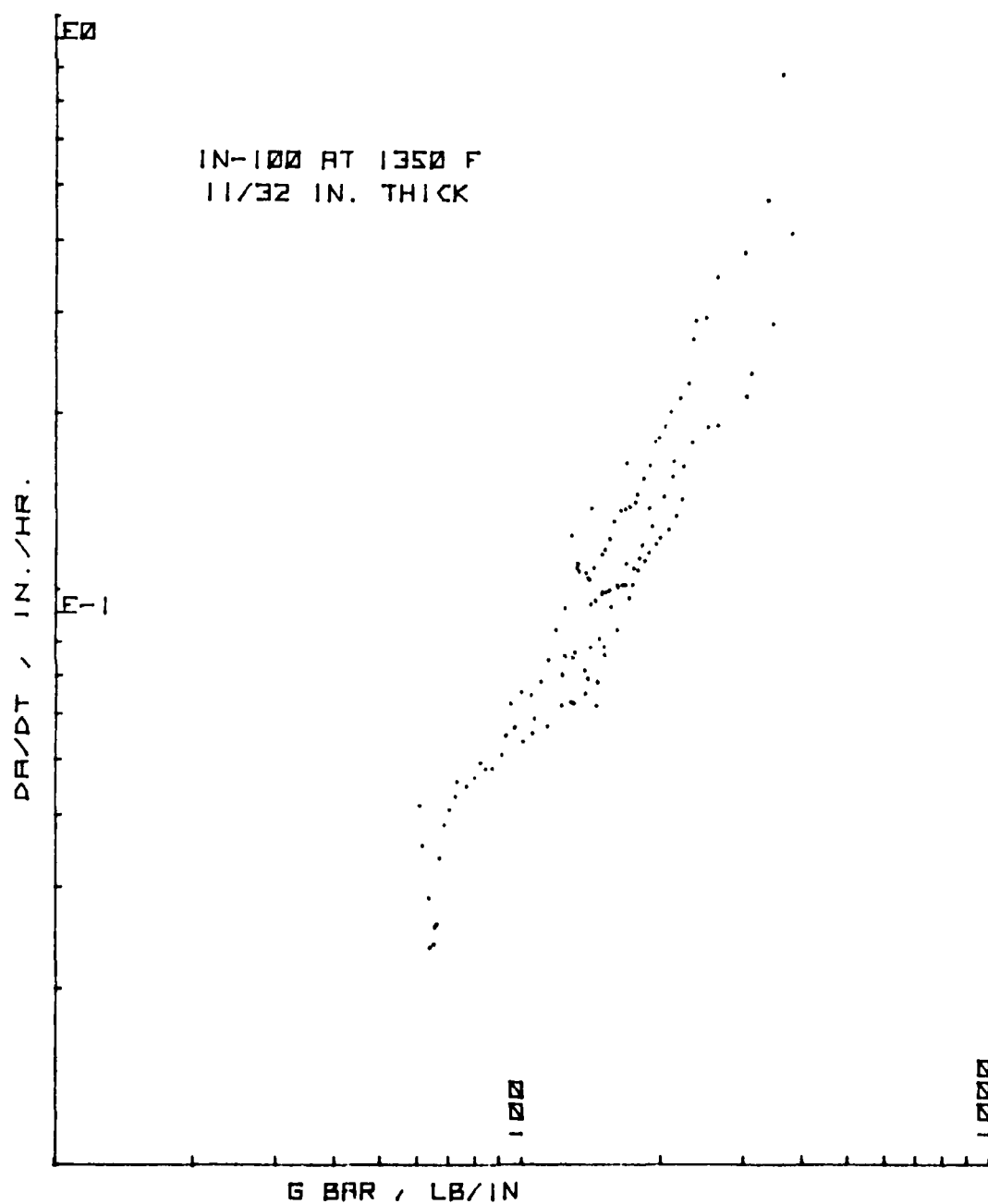
Figure 208.   da/dt vs. $\overline{G}$ for the 11/32" (9 mm) Thick CT
Specimen Group

280
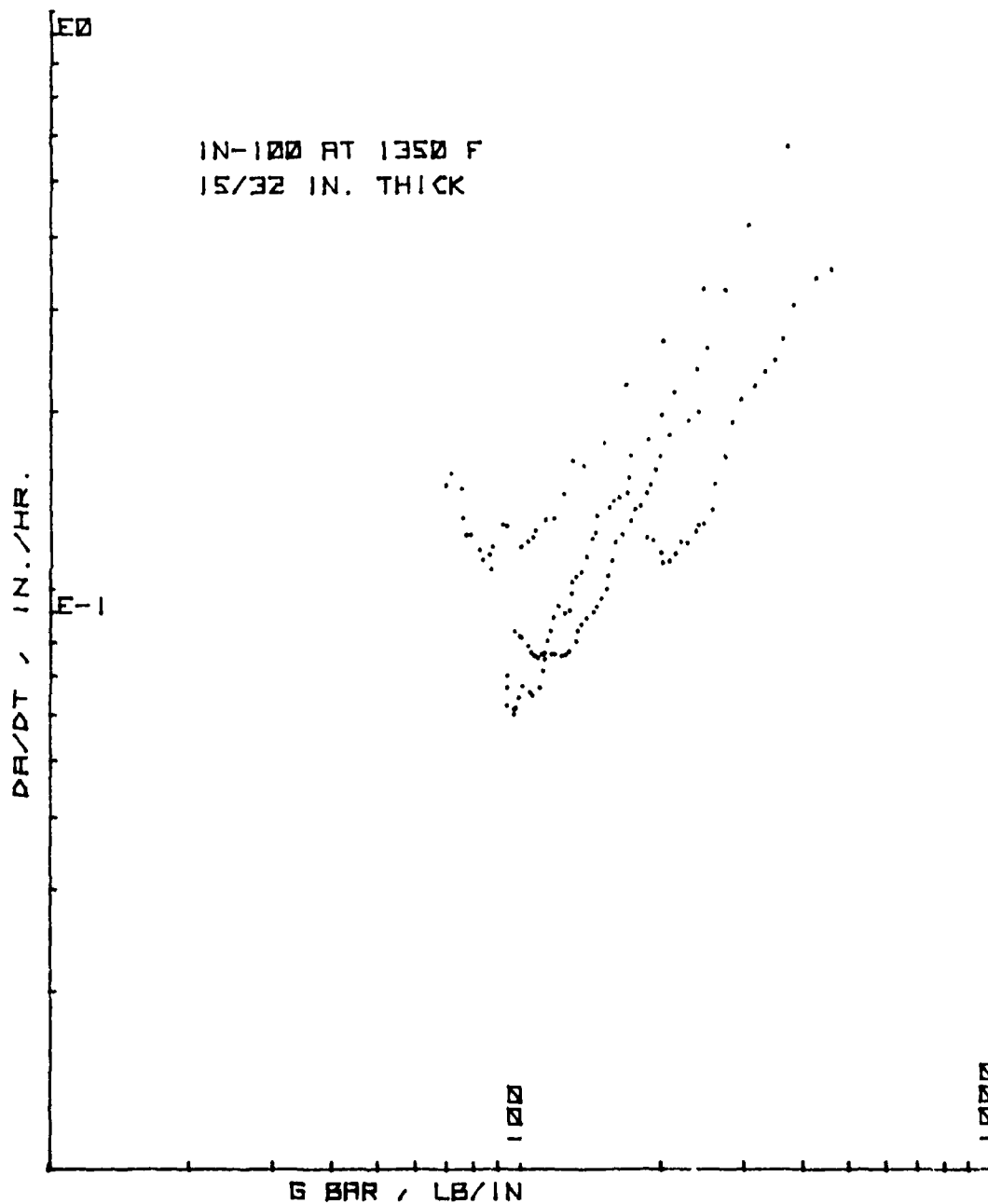
Figure 209. da/dt vs. G̅ for the 15/32" (12 mm) Thick CT Specimen Group
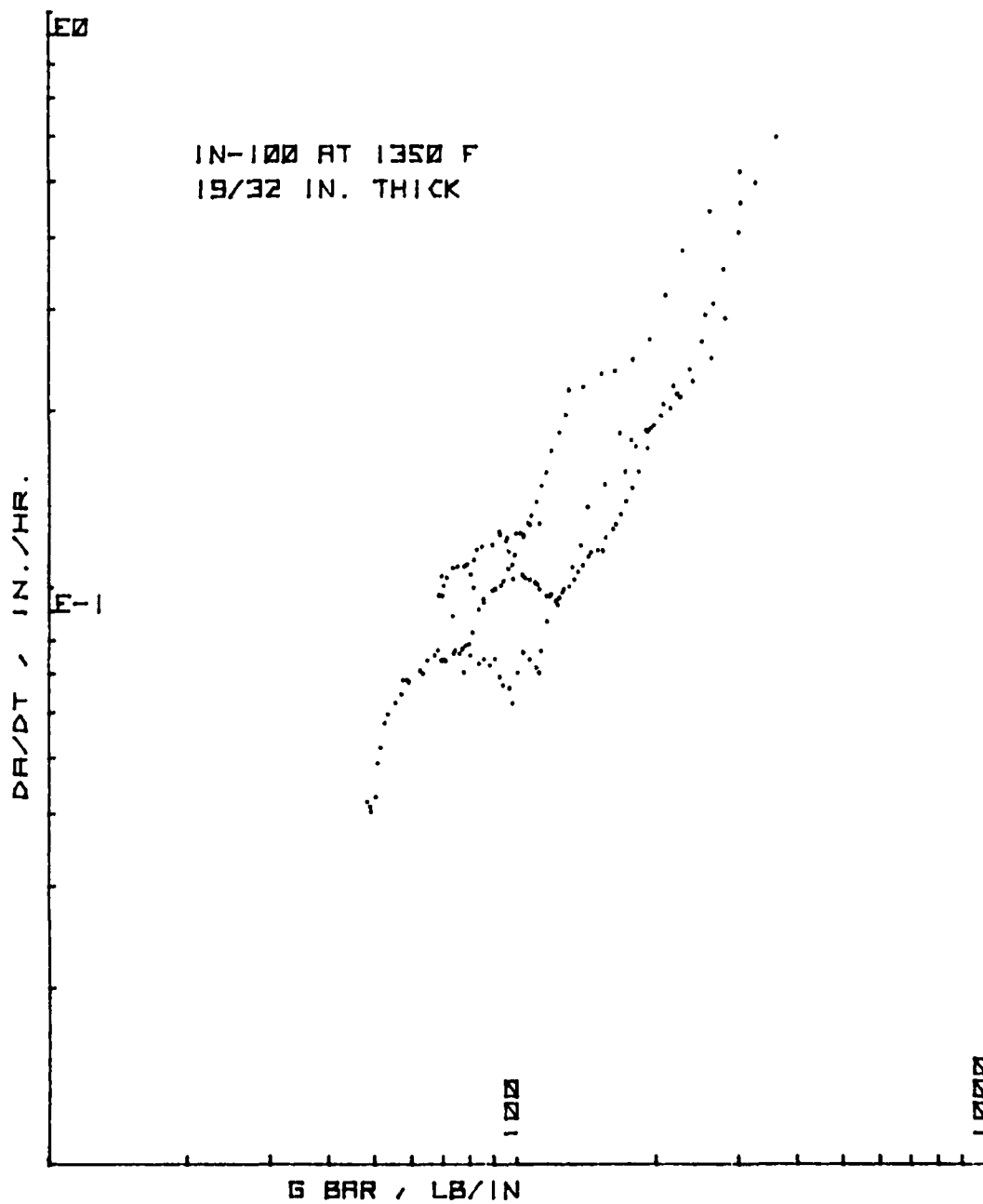
Figure 210. da/dt vs. $\overline{G}$ for the 19/32" (15 mm) Thick CT
Specimen Group
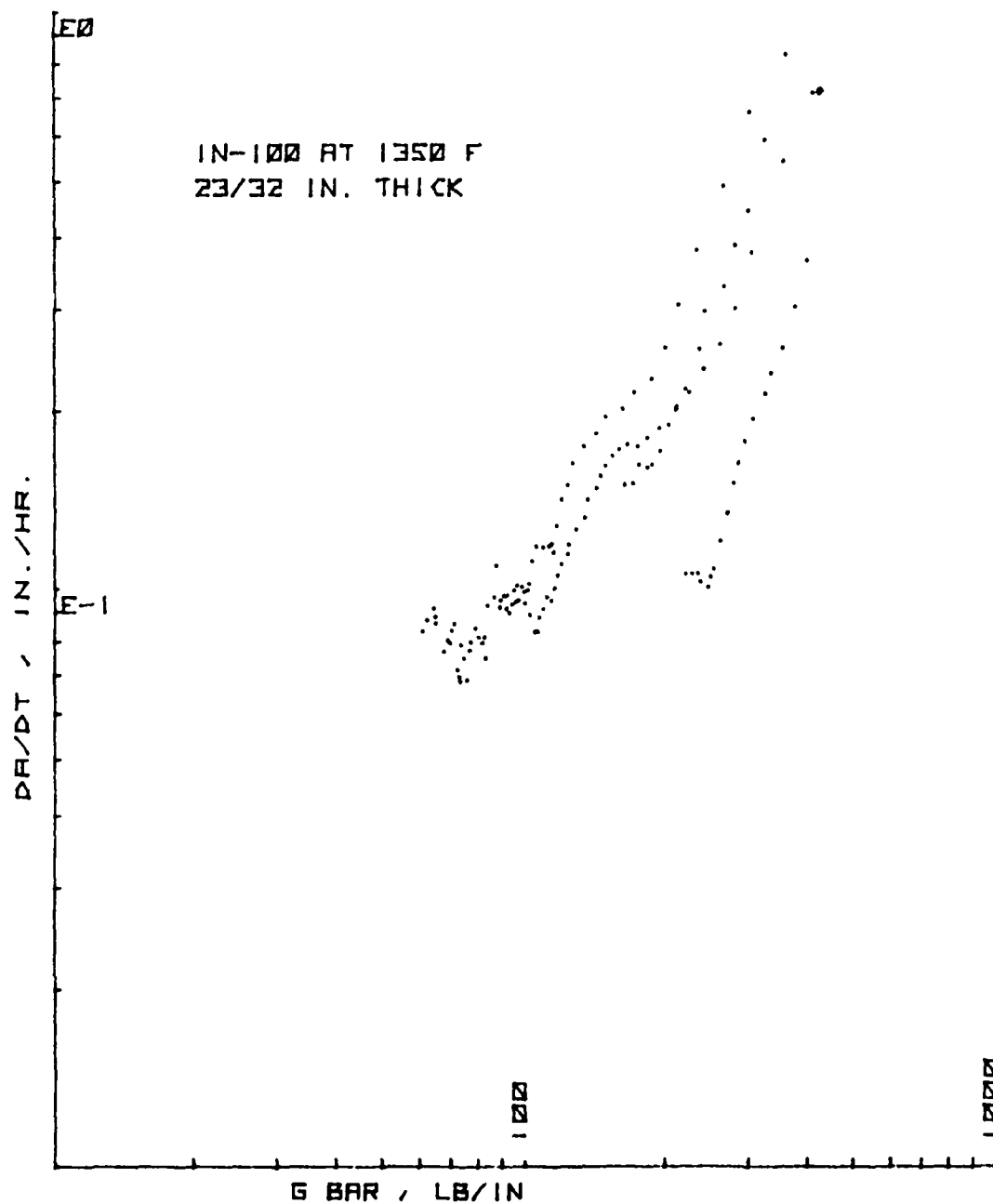
Figure 211. da/dt vs. $\overline{G}$ for the 23/32" (18 mm) Thick CT
Specimen Group
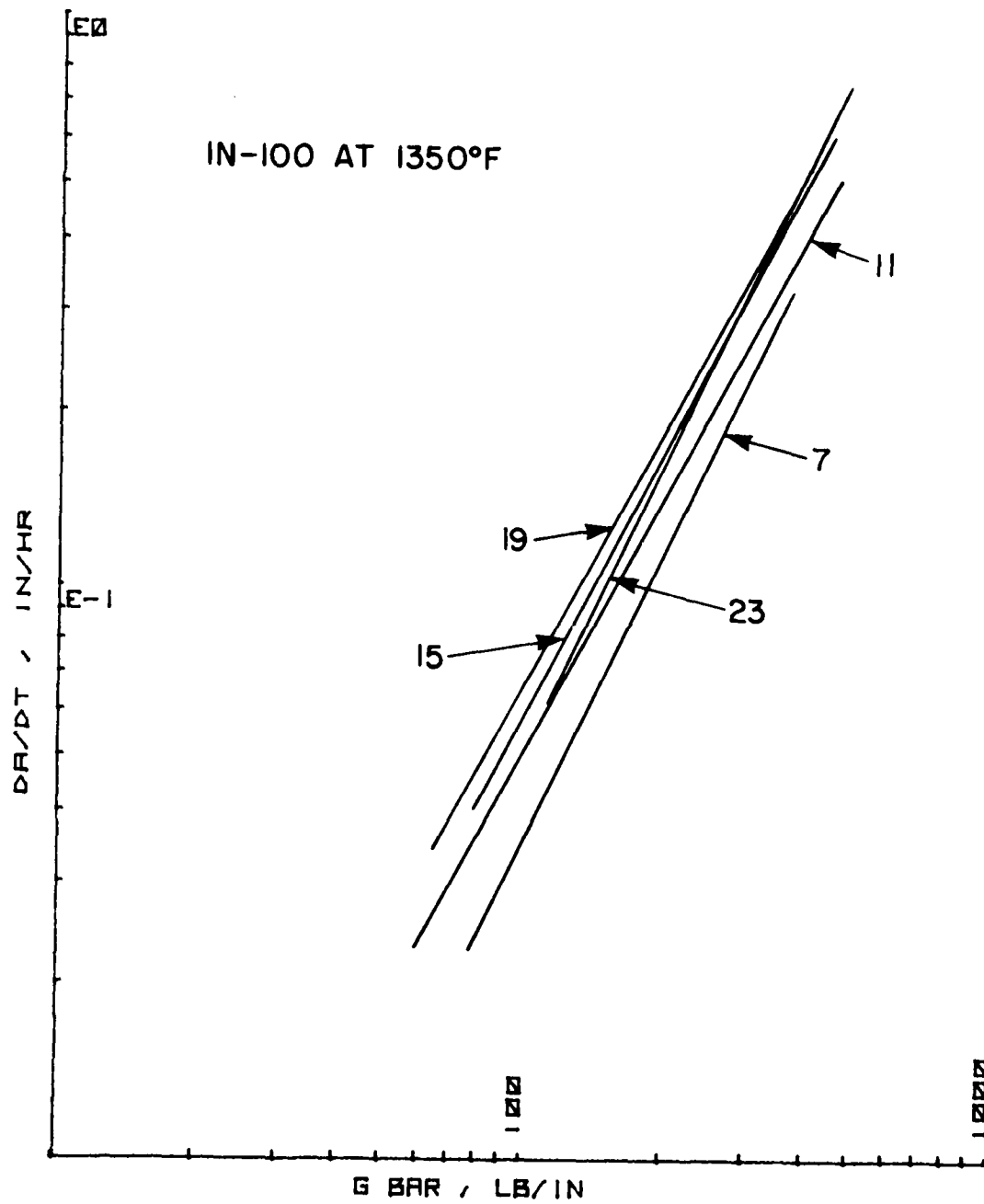
Figure 212. da/dt vs. $\bar{G}$, Composite Plot for Five Thicknesses of CT Specimens
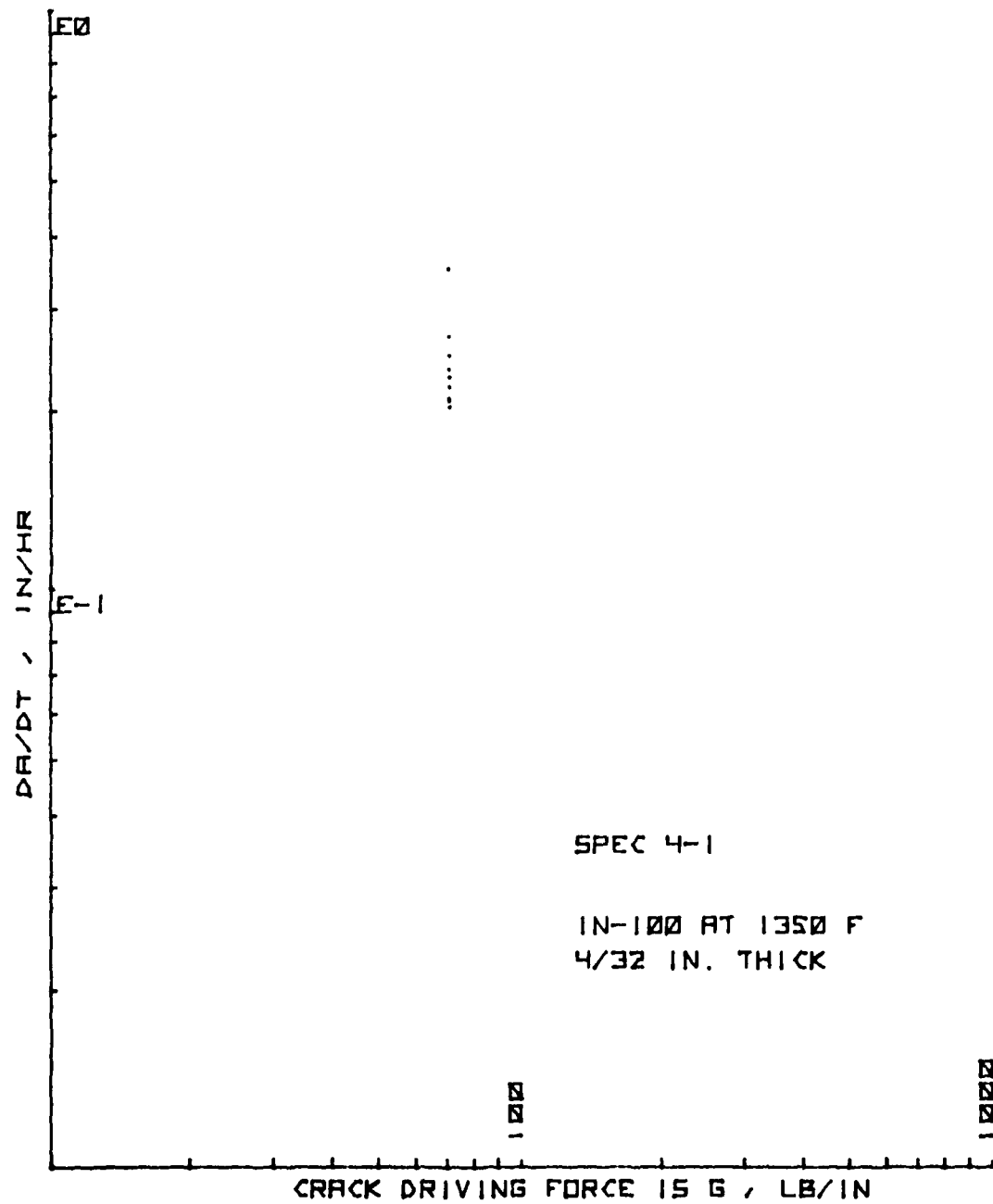
Figure 213. da/dt vs. G for Ring Specimen 4-1

Figure 214. da/dt vs. G for Ring Specimen 4-2
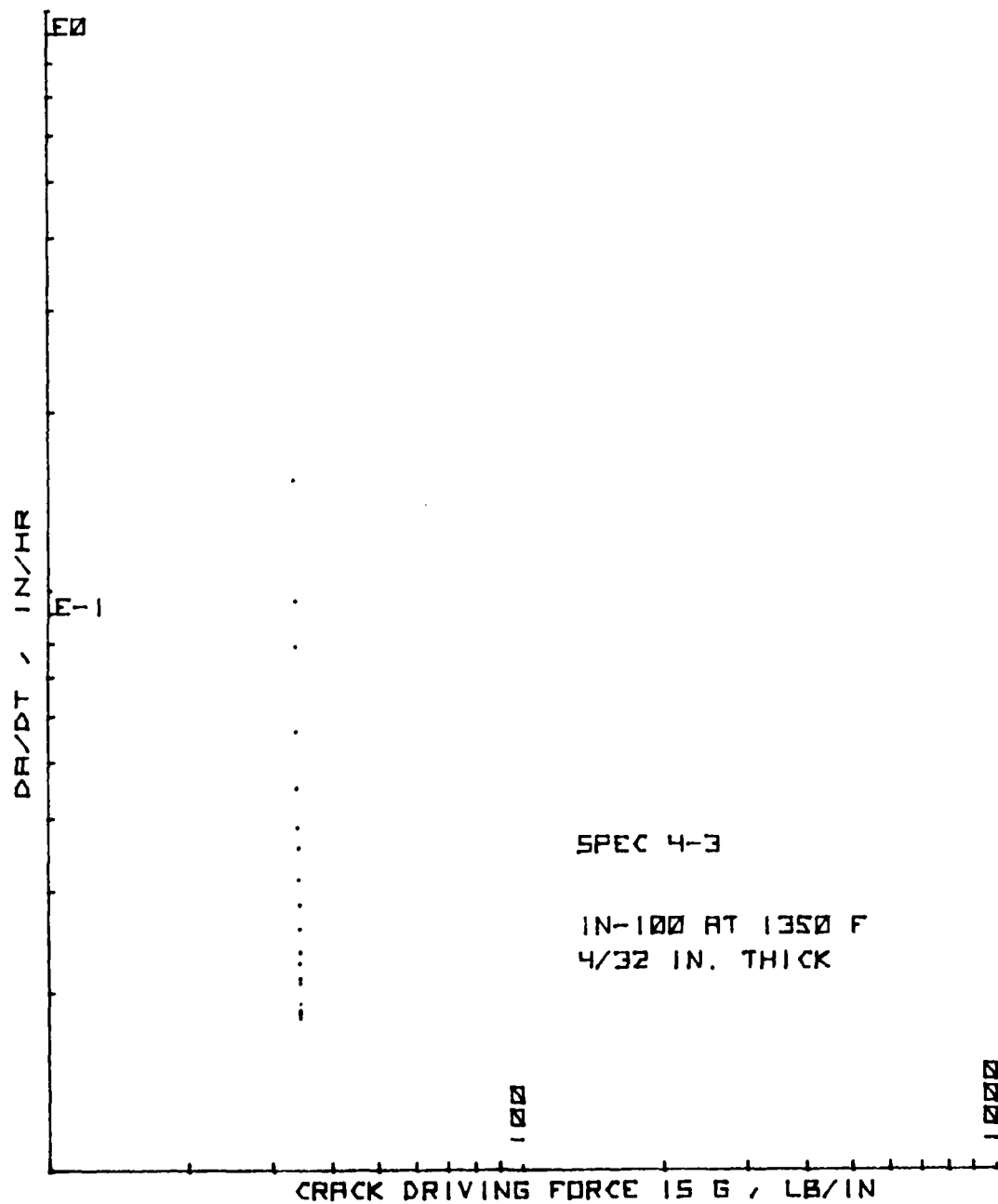
Figure 215. da/dt vs. G for Ring Specimen 4-3

EØ

DA/DT , IN/HR

E-1

SPEC 8-1

IN-1ØØ AT 135Ø F
8/32 IN. THICK

100

1000

CRACK DRIVING FORCE IS G , LB/IN
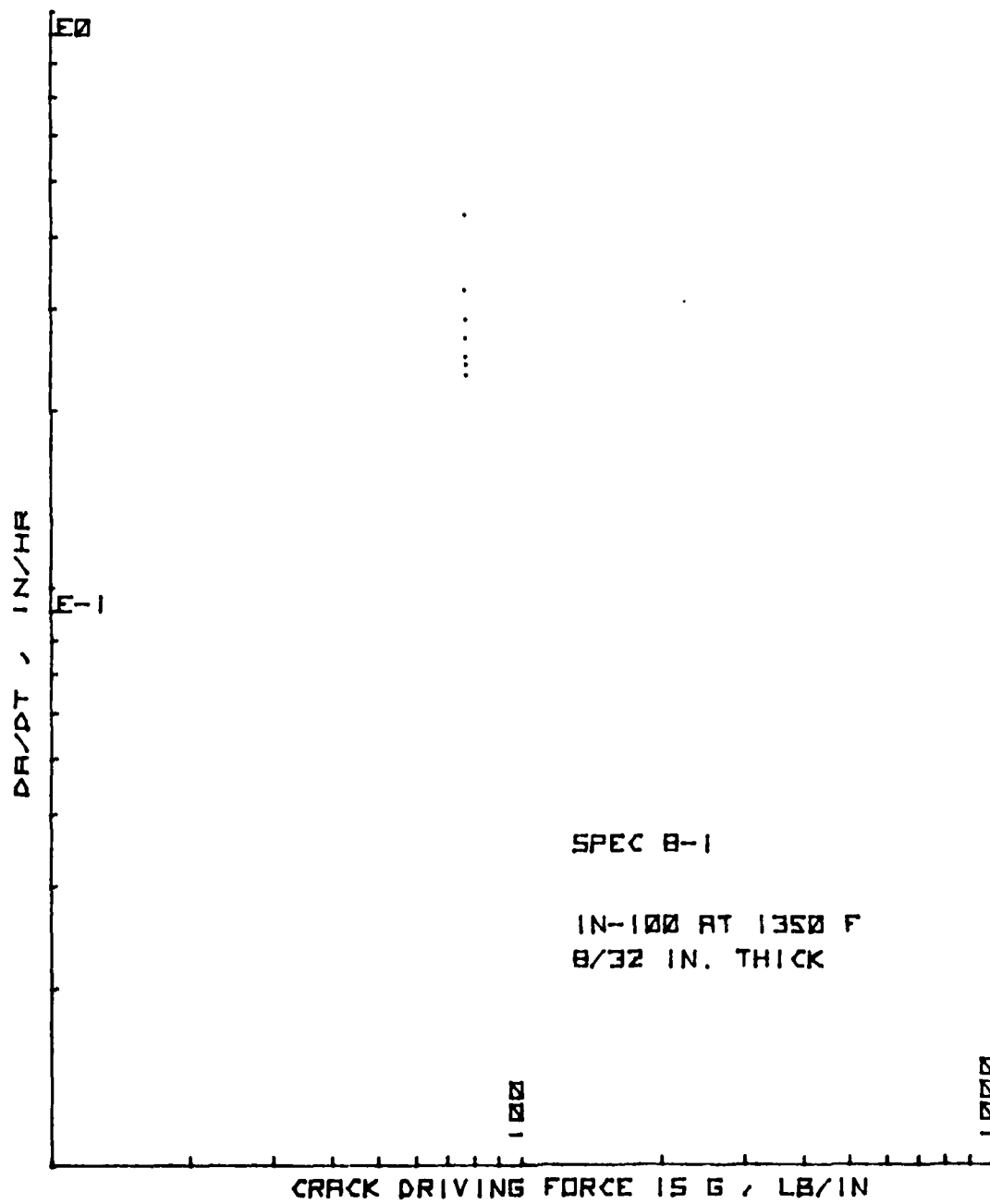
Figure 216. da/dt vs. G for Ring Specimen 8-1
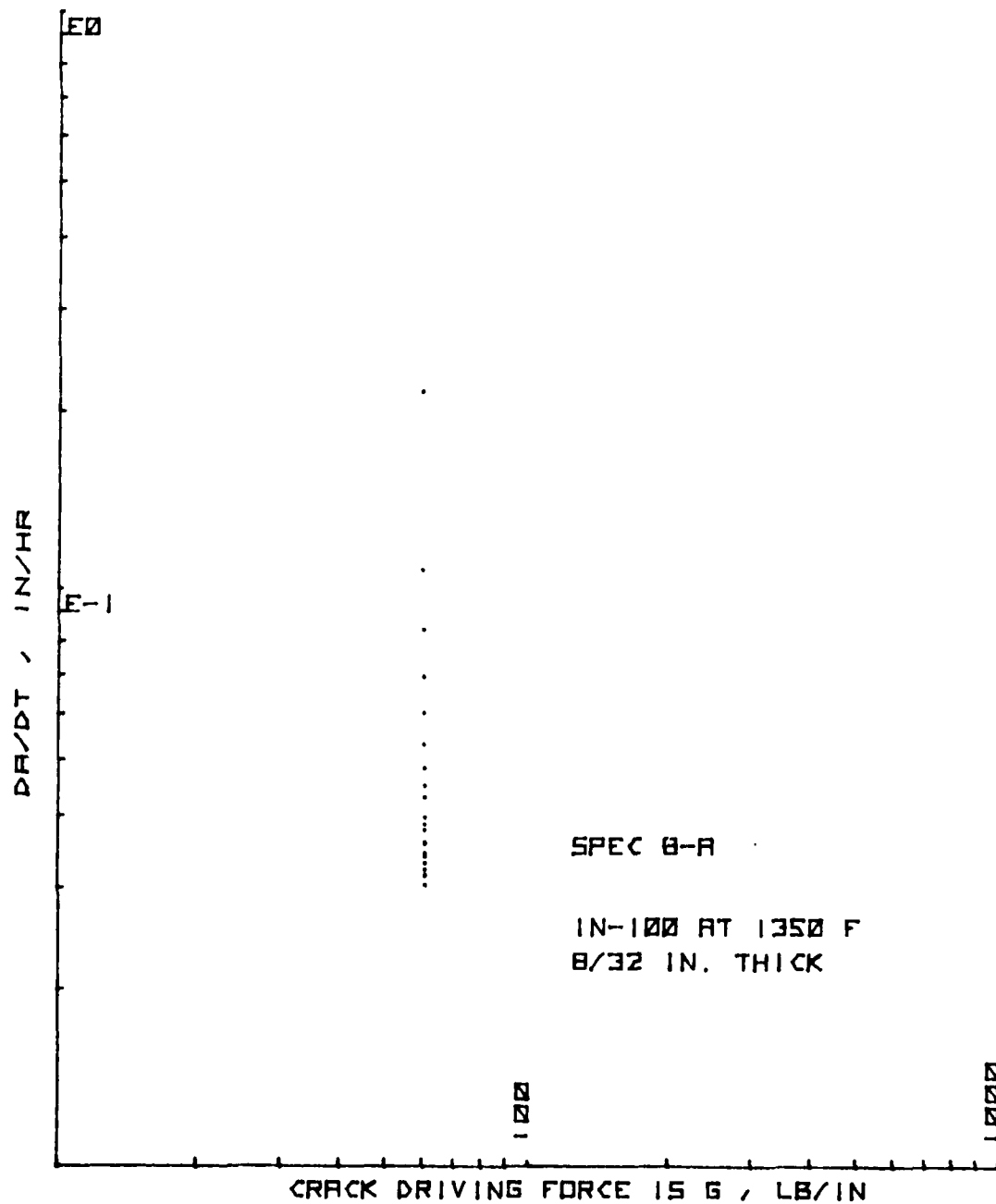
Figure 217. da/dt vs. G for Ring Specimen 8-A

Figure 218. da/dt vs. G for Ring Specimen 8-3
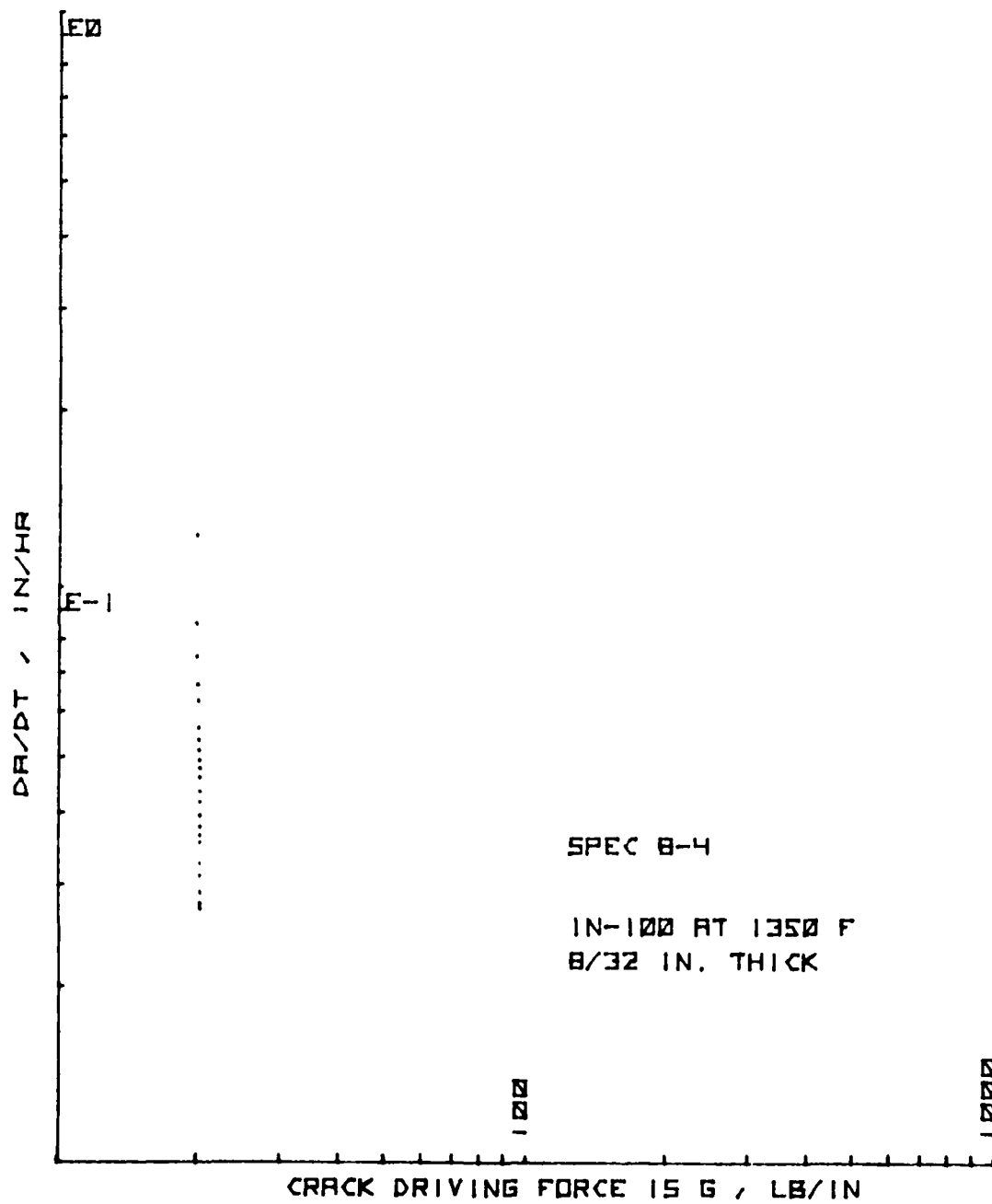
Figure 219. da/dt vs. G for Ring Specimen 8-4
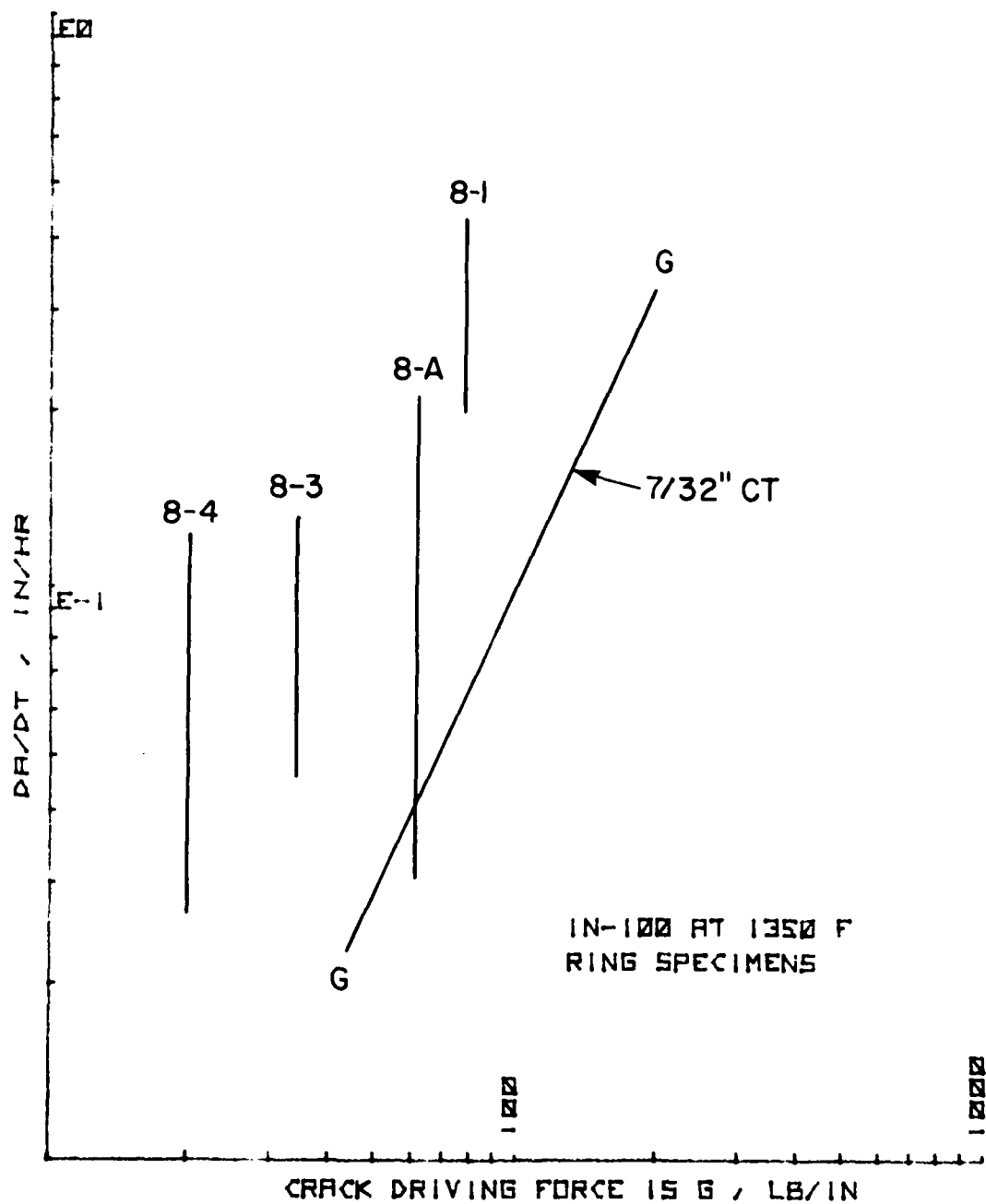
Figure 220. da/dt vs. G Plot for All the Ring Tests
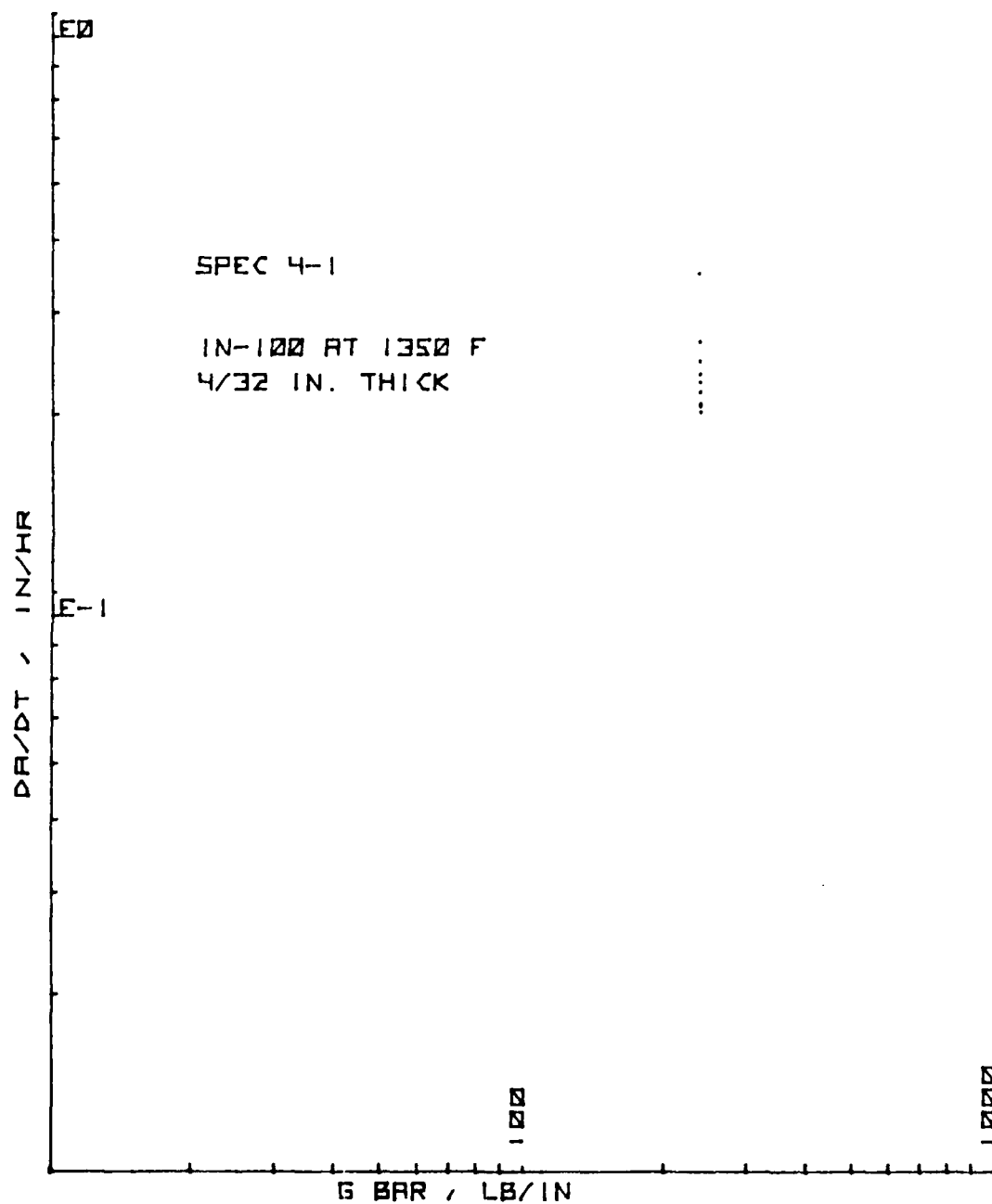
Figure 221. da/dt vs. $\bar{G}$ for Ring Specimen 4-1

293

SPEC 4-2

IN-100 AT 1350 F
4/32 IN. THICK

DA/DT , IN/HR

E0

E-1

G BAR , LB/IN

Figure 222. da/dt vs. $\overline{G}$ for Ring Specimen 4-2
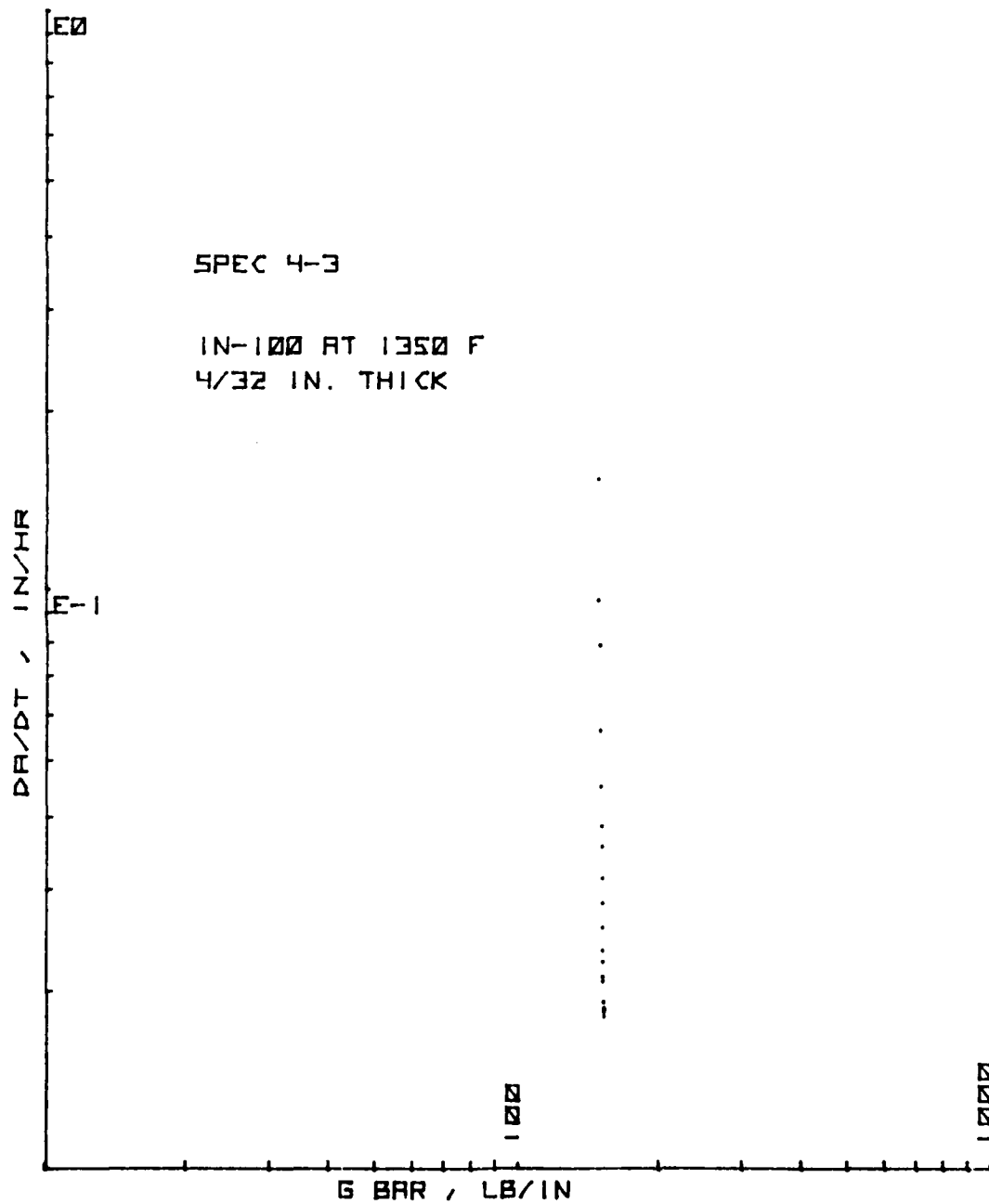
Figure 223.   da/dt vs. $\overline{G}$ for Ring Specimen 4-3
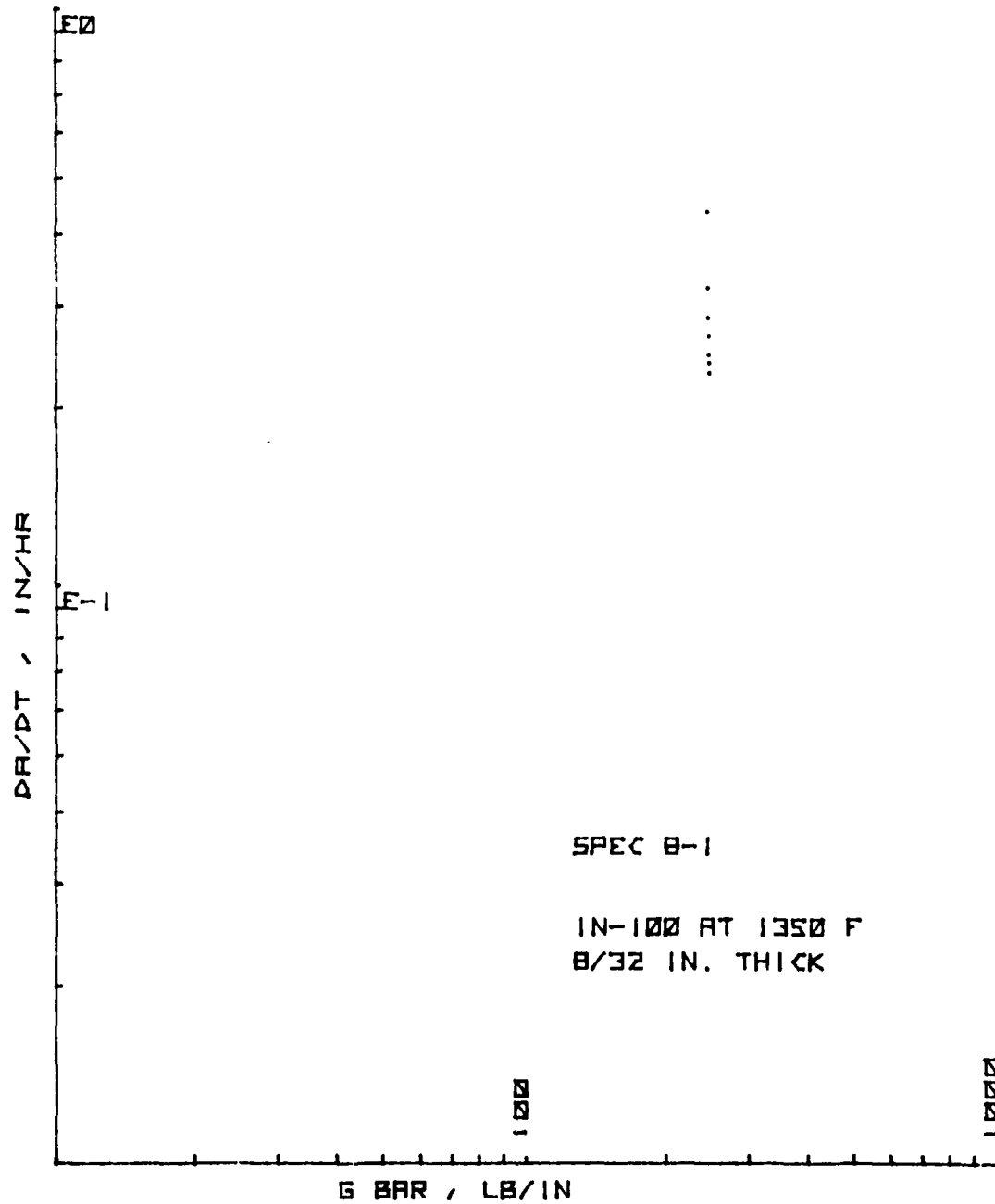
Figure 224. da/dt vs. $\overline{G}$ for Ring Specimen 8-1
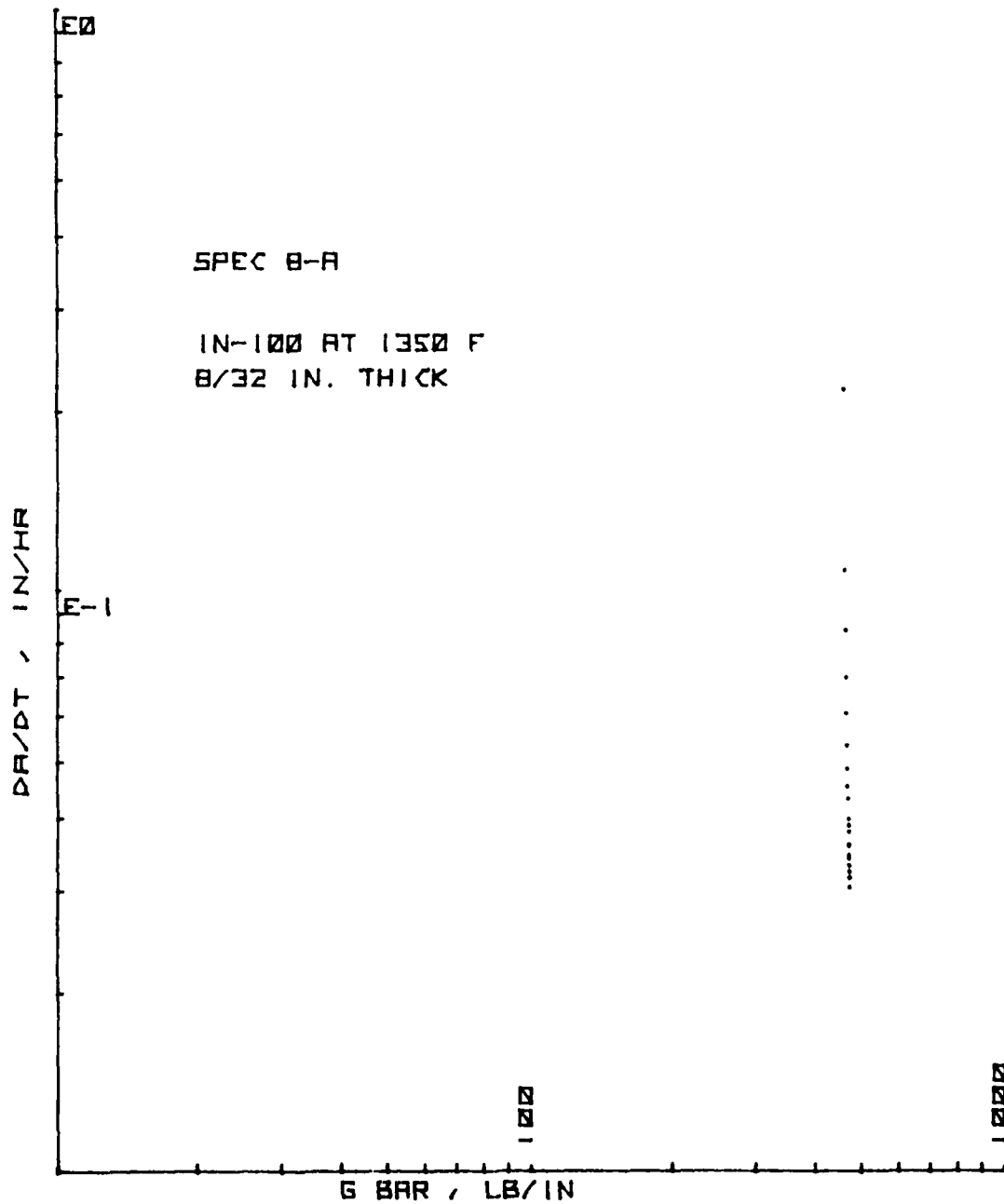
Figure 225. da/dt vs. $\overline{G}$ for Ring Specimen 8-A

SPEC 8-3

IN-100 AT 1350 F
8/32 IN. THICK

DA/DT , IN/HR

E0

E-1

G BAR , LB/IN

100

1000
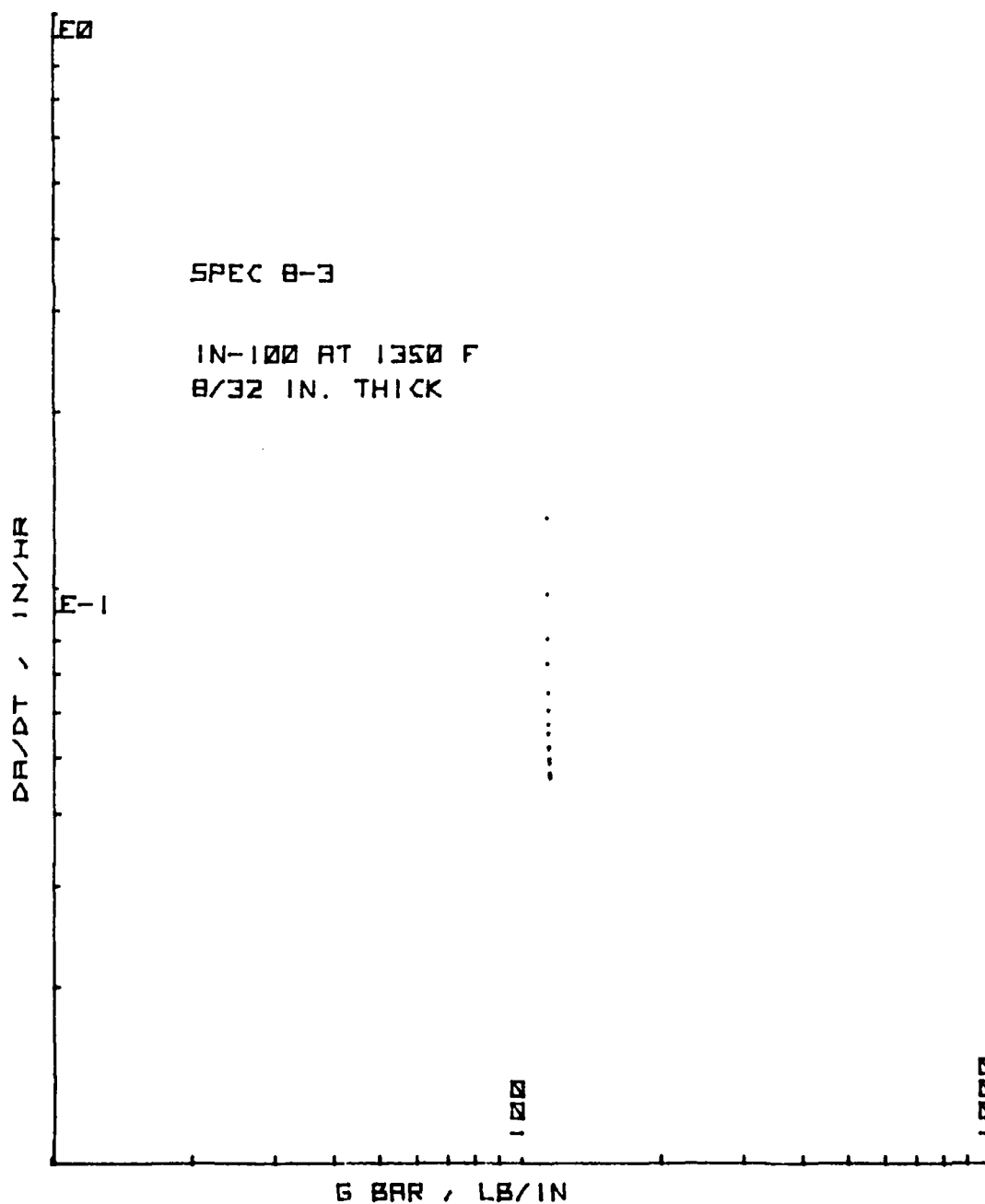
Figure 226.   da/dt vs. $\overline{G}$ for Ring Specimen 8-3
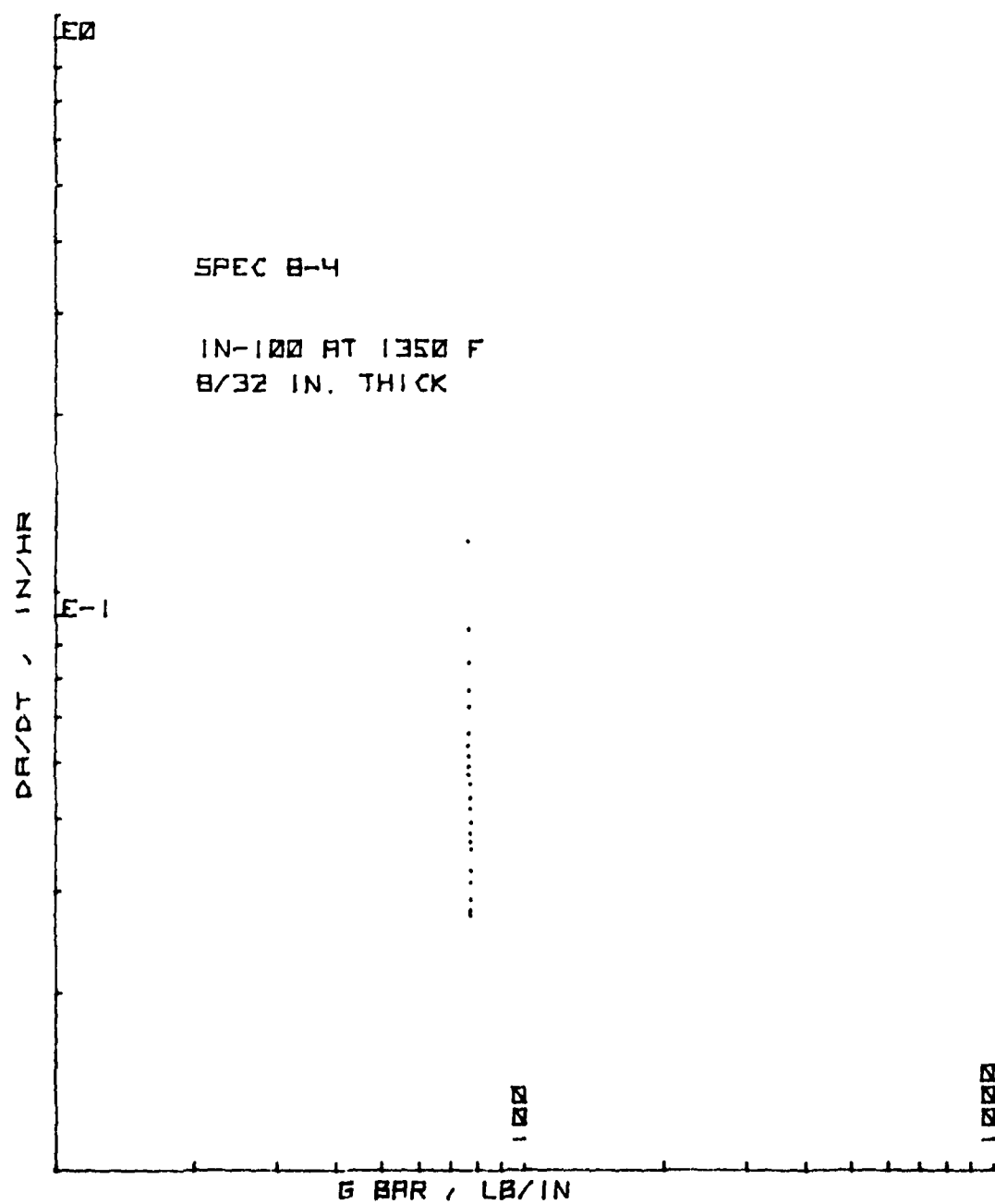
Figure 227. da/dt vs. $\overline{G}$ for Ring Specimen 8-4
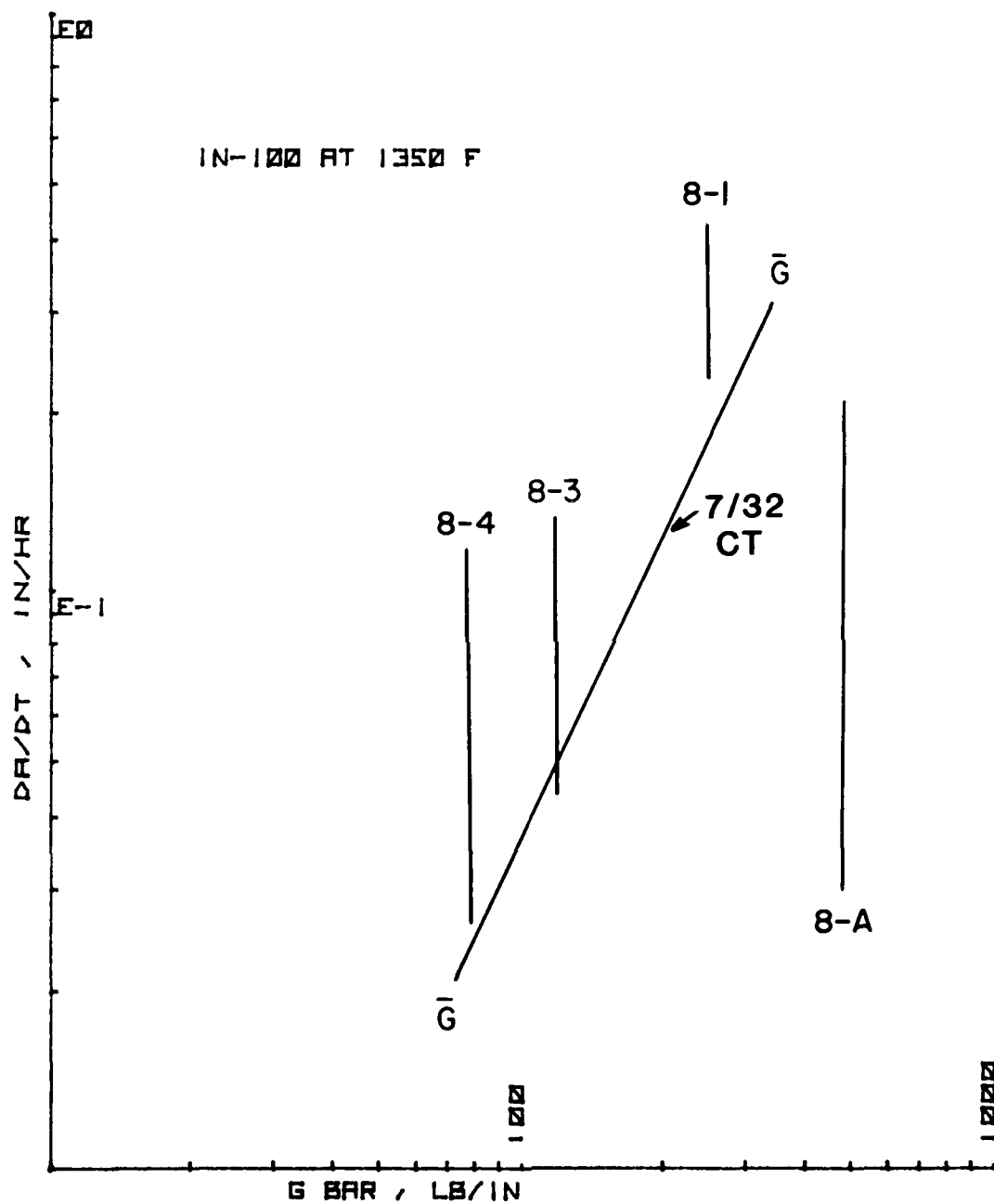
Figure 228.   da/dt vs. $\bar{G}$ Plot for All the Ring Tests
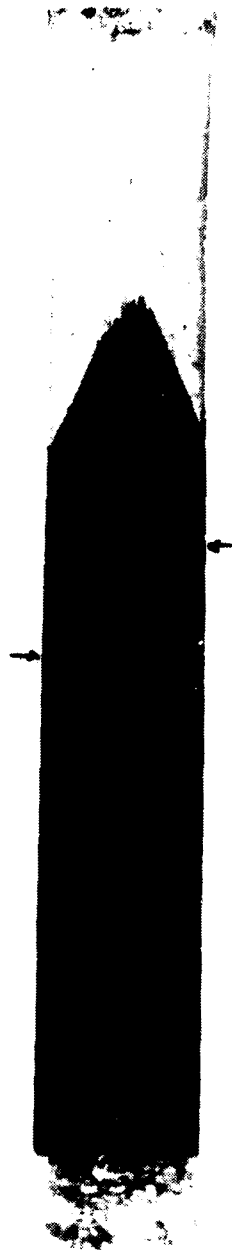
Figure 229. Fracture Surface - CT Specimen 7-2
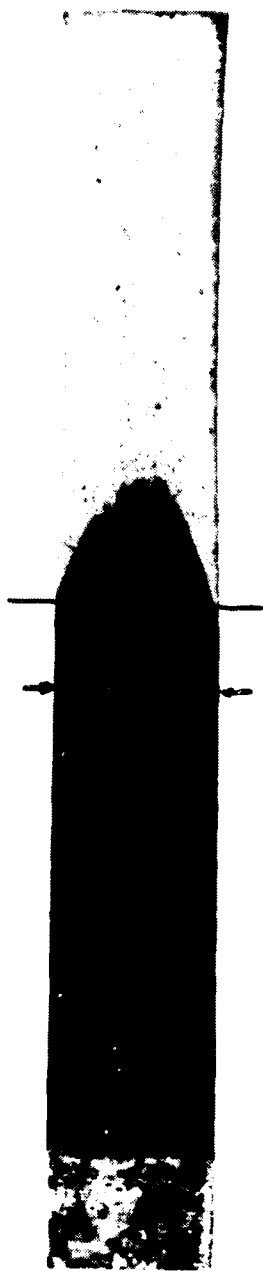
Figure 230.   Fracture Surface - CT Specimen 7-3

Figure 231.   Fracture Surface - CT Specimen 7-4
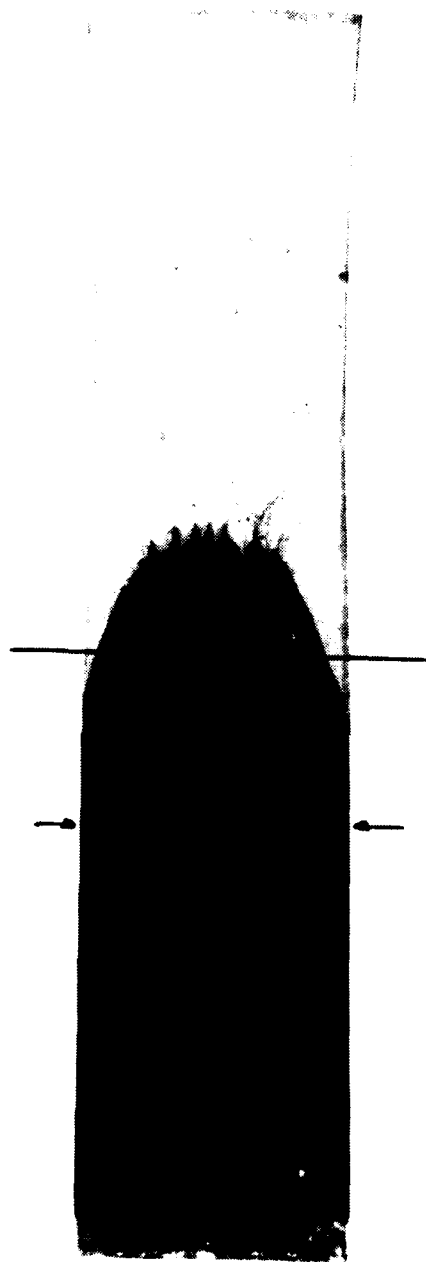
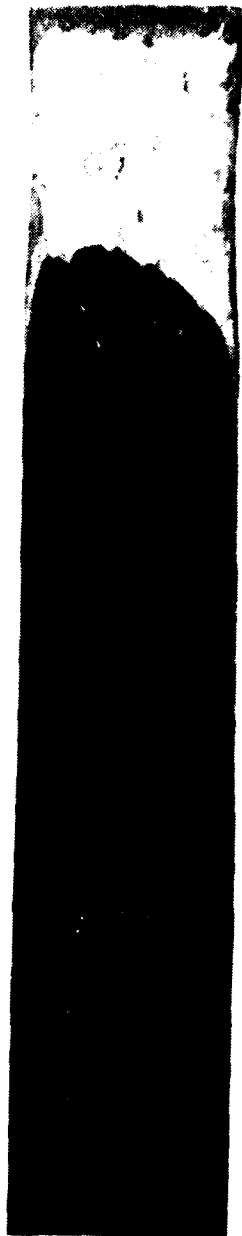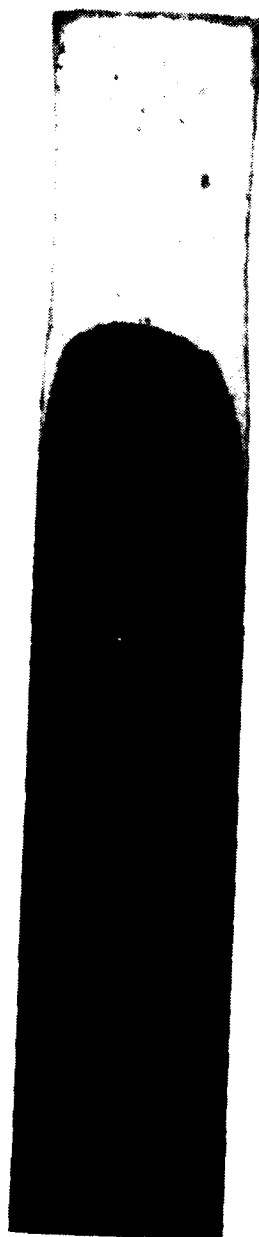Figure 232. Fracture Surface - CT Specimen 11-2
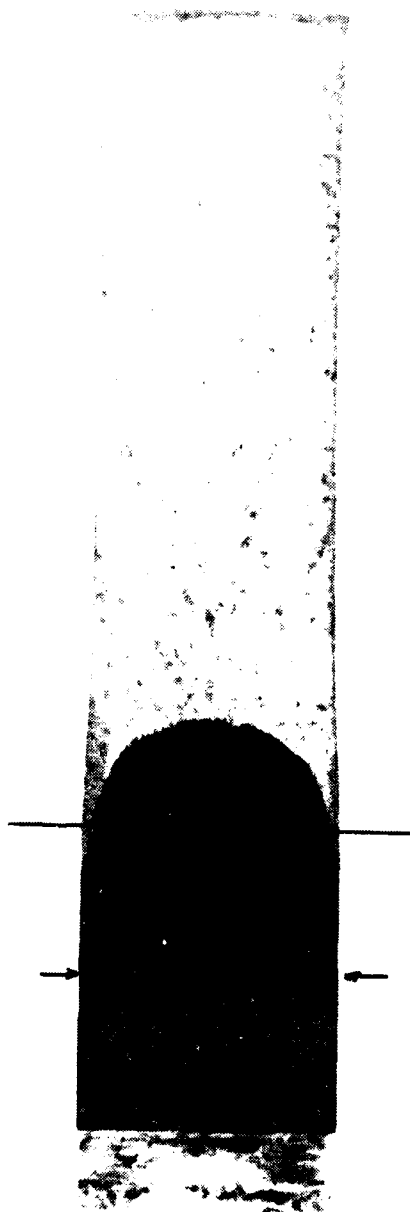
Figure 233. Fracture Surface - CT Specimen 11-3

Figure 234. Fracture Surface - CT Specimen 11-6
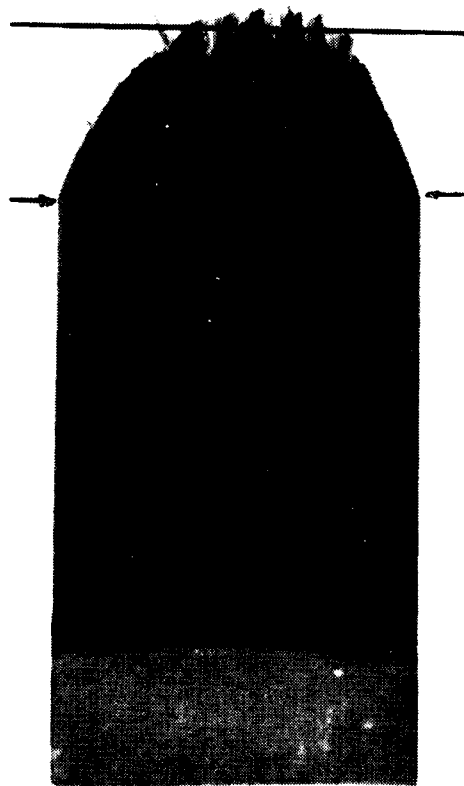
Figure 235.   Fracture Surface - CT Specimen 15-6

Figure 246. ... Specimen 15-7
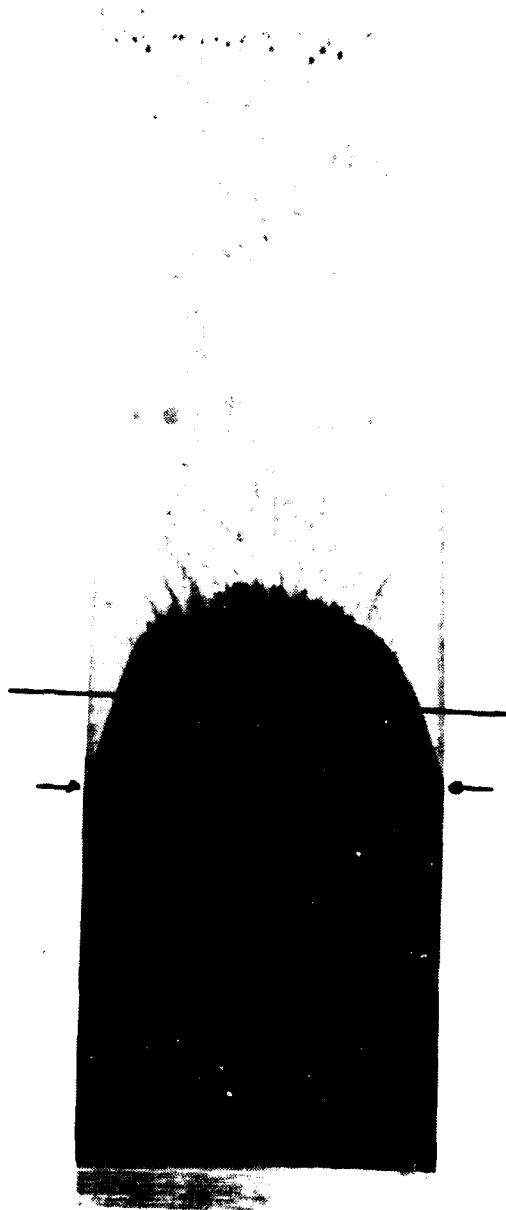
Figure 237. Fracture Surface - CT Specimen 15-8
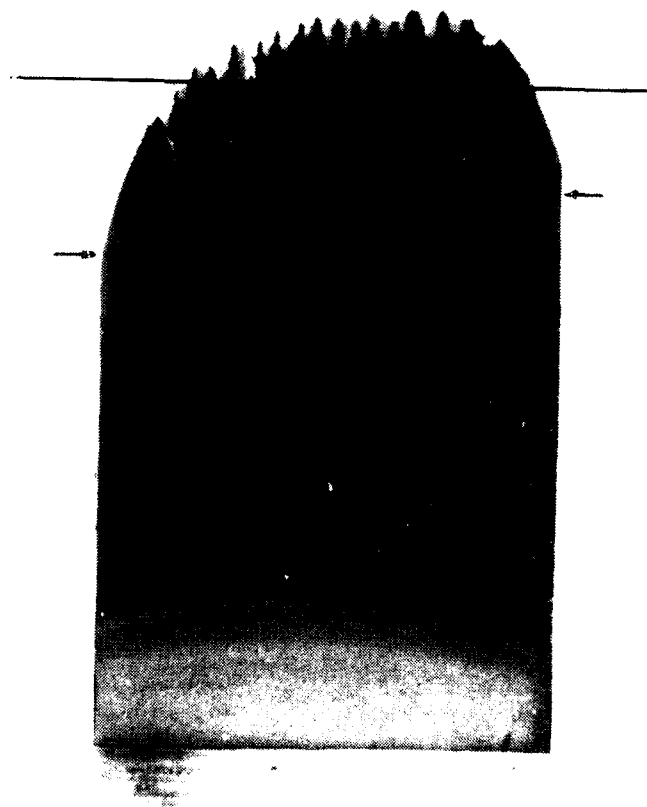
Figure 238. Fracture Surface - CT Specimen 19-3
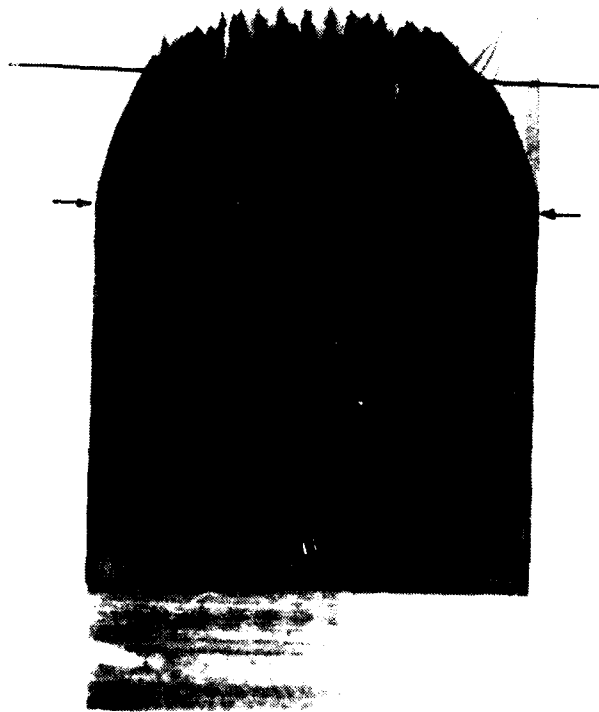
Figure 239.   Fracture Surface - CT Specimen 19-4
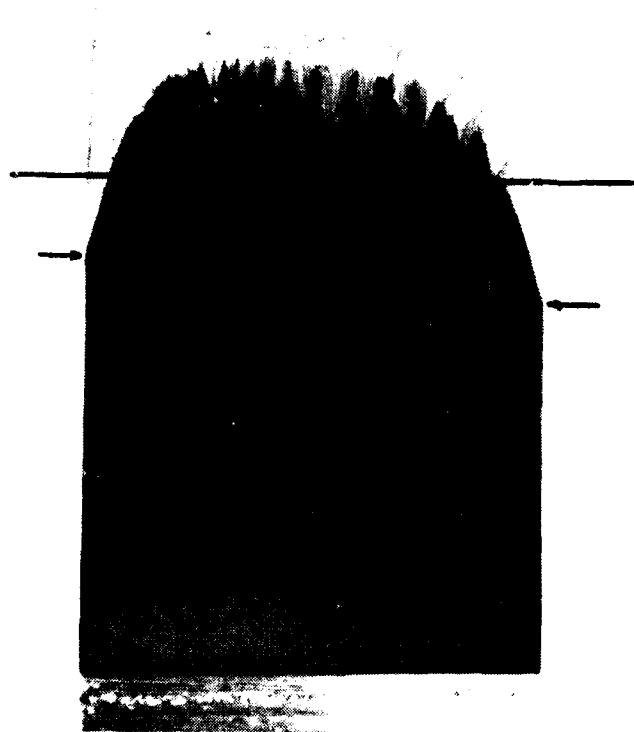
Figure 240. Fracture Surface - C1 Specimen 19-6
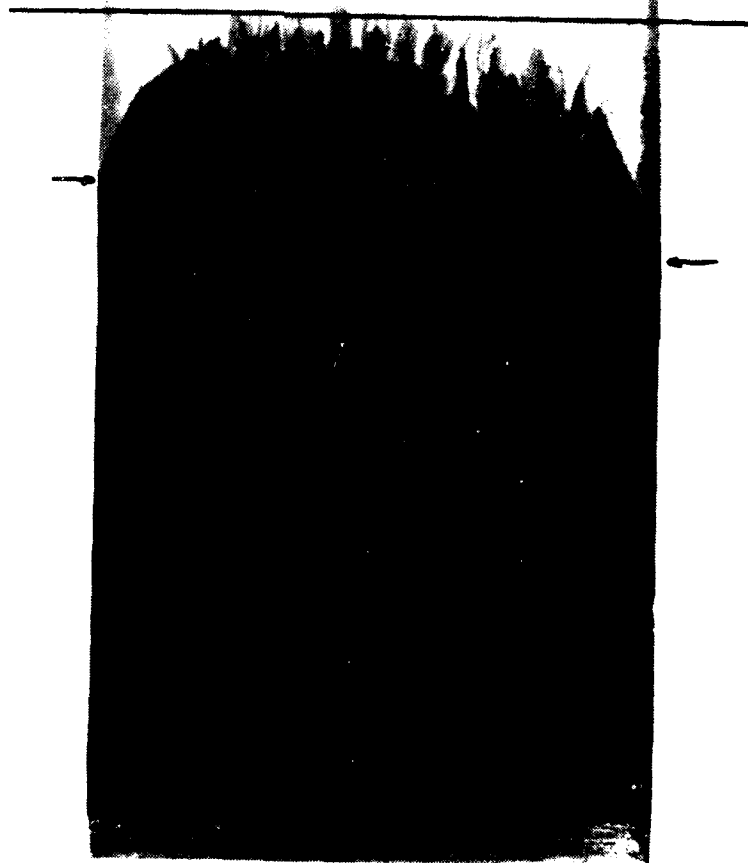
Figure 241.   Fracture Surface - CT Specimen 23-2
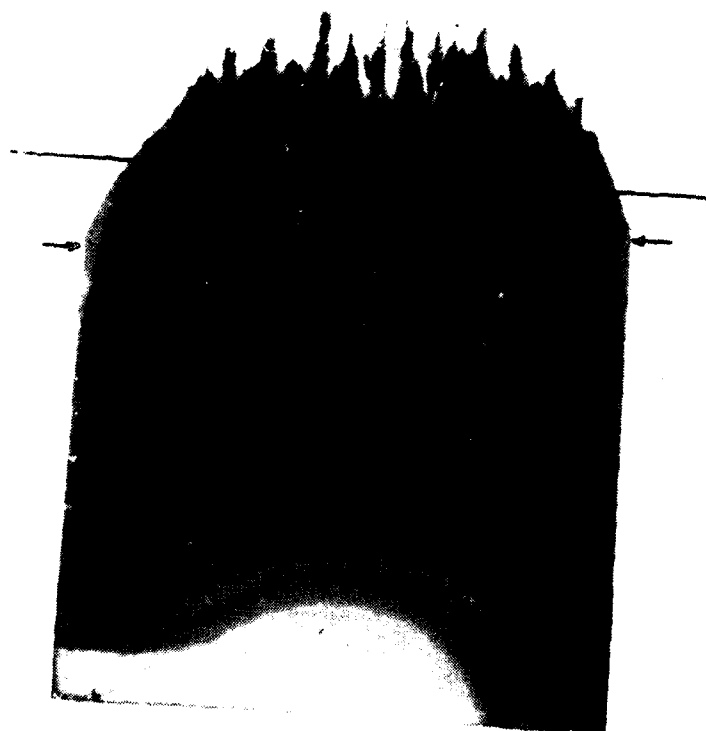
Figure 212. Fracture Surface - CT Specimen 23-3
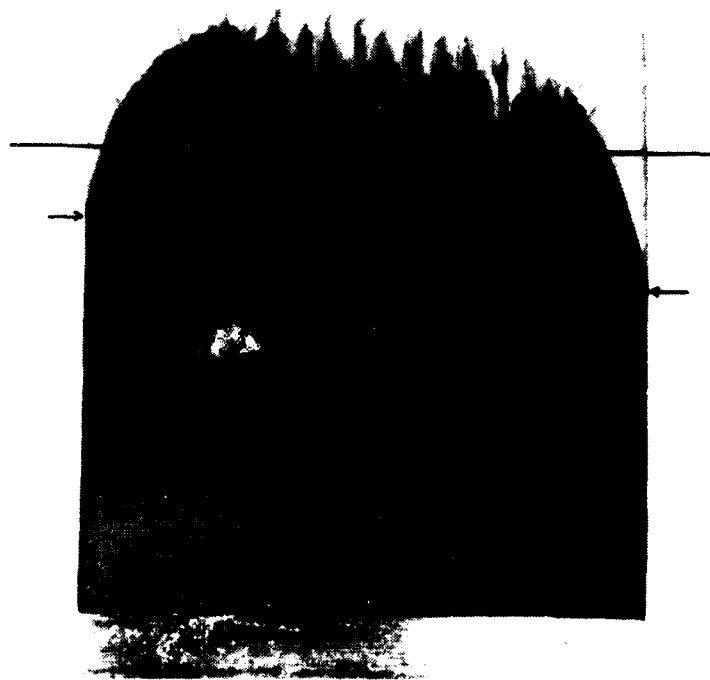
Figure 243. Fracture Surface - CT Specimen 23-4

Figure 244.   Fracture Surface - Ring Specimen 4-1

Figure 245.   Fracture Surface - Ring Specimen 4-2
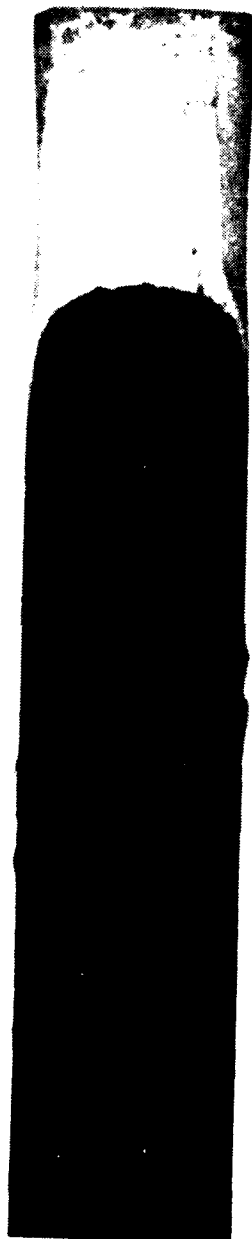
Figure 246. Fracture Surface - Ring Specimen 4-3
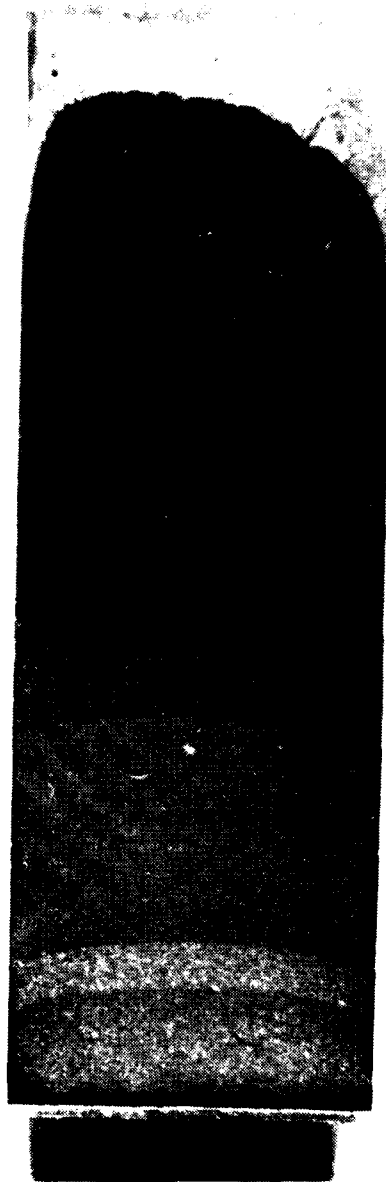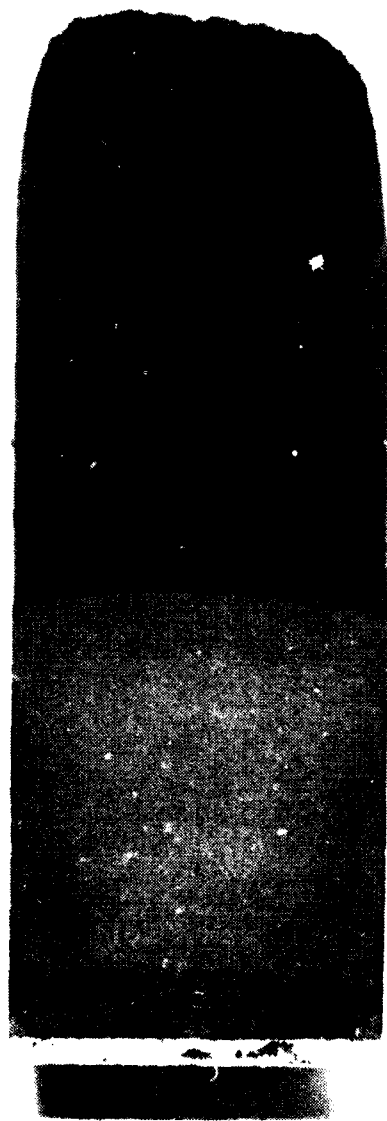
Figure 247. Fracture Surface - Ring Specimen 8-1
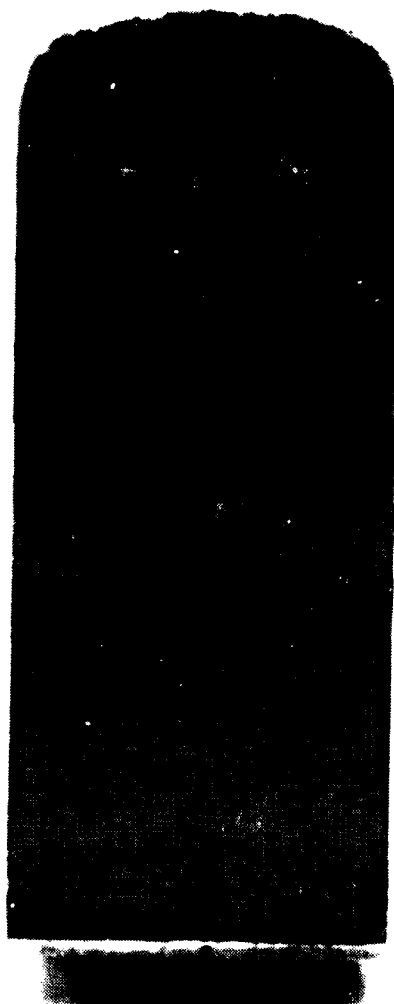
Figure 24 . . . - Ring Specimen 8-A

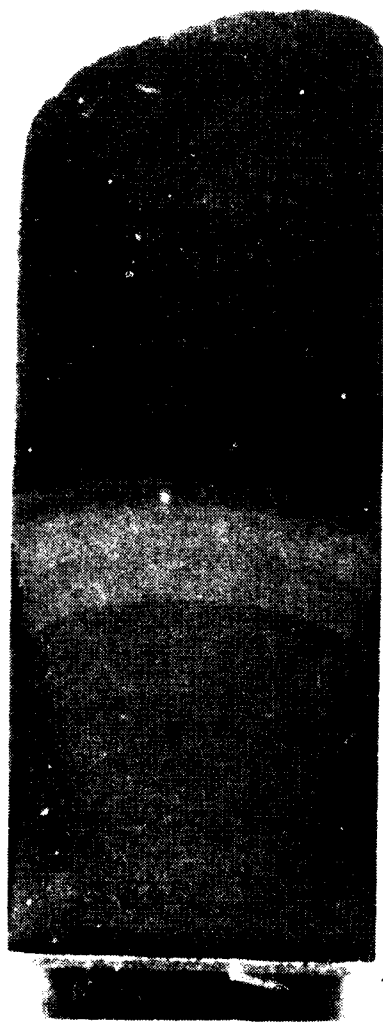Figure 249. Fracture Surface - Ring Specimen 8-3
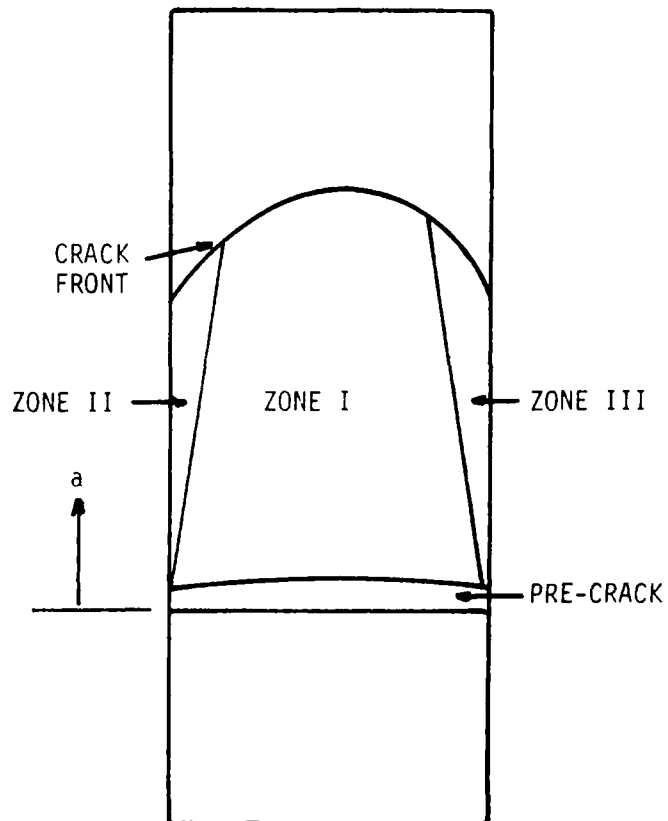
Figure 5.   Ring Specimen 8-4

Figure 251. Compact Tension Fracture Surface Schematic for
Creep Crack Growth in IN-100 at 1350°F (732°C)